


Spring 1-1-2018

Space-Time Extended Finite Element Method with Applications to Fluid-Structure Interaction Problems

Toshiki Nagai

University of Colorado at Boulder, tnagai.phys.keio@gmail.com

Follow this and additional works at: https://scholar.colorado.edu/asen_gradetds

 Part of the [Aerodynamics and Fluid Mechanics Commons](#), [Computational Engineering Commons](#), and the [Physics Commons](#)

Recommended Citation

Nagai, Toshiki, "Space-Time Extended Finite Element Method with Applications to Fluid-Structure Interaction Problems" (2018). *Aerospace Engineering Sciences Graduate Theses & Dissertations*. 198.
https://scholar.colorado.edu/asen_gradetds/198

This Dissertation is brought to you for free and open access by Aerospace Engineering Sciences at CU Scholar. It has been accepted for inclusion in Aerospace Engineering Sciences Graduate Theses & Dissertations by an authorized administrator of CU Scholar. For more information, please contact cuscholaradmin@colorado.edu.

**Space-Time Extended Finite Element Method
with Applications to Fluid-Structure Interaction Problems**

by

Toshiki Nagai

B.S., Keio University, 2008

M.S., Keio University, 2010

A thesis submitted to the
Faculty of the Graduate School of the
University of Colorado in partial fulfillment
of the requirements for the degree of
Doctor of Philosophy
Department of Aerospace Engineering Sciences
2018

This thesis entitled:
Space-Time Extended Finite Element Method
with Applications to Fluid-Structure Interaction Problems
written by T. Nagai
has been approved for the Department of Aerospace Engineering Sciences

Prof. Kurt Maute

Prof. John Evans

Date _____

The final copy of this thesis has been examined by the signatories, and we find that both the content and the form meet acceptable presentation standards of scholarly work in the above mentioned discipline.

Nagai, Toshiki (Ph.D., Aerospace Engineering Sciences)

Space-Time Extended Finite Element Method

with Applications to Fluid-Structure Interaction Problems

Thesis directed by Prof. Kurt Maute

This thesis presents a space-time extended finite element method (space-time XFEM) based on the Heaviside enrichment for transient problems with moving interfaces, and its applications to the fluid-structure interaction (FSI) analysis. The Heaviside-enriched XFEM is a promising method to discretize partial differential equations with discontinuities in space. However, significant approximation errors are introduced by time stepping schemes when the interface geometry changes in time. The proposed space-time XFEM applies the finite element discretization and the Heaviside enrichment in both space and time with elements forming a space-time slab. A simple space-time scheme is introduced to integrate the weak form of the governing equations. This scheme considers spatial intersection configuration at multiple temporal integration points. Standard spatial integration techniques can be applied for each spatial configuration. Nitsche's method and the face-oriented ghost-penalty method are extended to the proposed space-time XFEM formulation. The stability, accuracy and flexibility of the space-time XFEM for various interface conditions including moving interfaces are demonstrated with structural and fluid problems. Moreover, the space-time XFEM enables analyzing complex FSI problems using moving interfaces, such as FSI with contact. Two FSI methods using moving interfaces (full-Eulerian FSI and Lagrangian-immersed FSI) are studied. The Lagrangian-immersed FSI method is a mixed formulation of Lagrangian and Eulerian descriptions. As solid and fluid meshes are independently defined, the FSI is computed between non-matching interfaces based on Nitsche's method and projection techniques adopted from computational contact mechanics. The stabilized Lagrange multiplier method is used for contact. Numerical examples of FSI and FSI-contact problems provide insight into the characteristics of the combination of the space-time XFEM and

the Lagrangian-immersed FSI method. The proposed combination is a promising method which has the versatility for various multi-physics simulations and the applicability such as optimization.

Acknowledgements

First, I would like to thank my adviser, Prof. Maute, for his warm and patient guidance and constructive discussion in terms of my doctoral research and other technical topics. Many thanks to my defense committee members, Prof. Evans, Prof. Doostan, Prof. Felippa, and Prof. Rentschler, for their help and cooperation for my comprehensive exam, defense, lectures and technical discussions. I gratefully appreciate that Bridgestone Corporation in Japan gave me this splendid opportunity to study in the USA and the abundant financial support. I would like to acknowledge Nicholas Jenkins and Matthew Lawry for their useful research results related to my research topics, and Alvaro Mozo Gutierrez for the deep discussion about the fluid-structure interaction. I would also like to thank my lab colleagues for helpful technical discussion and advice about my research and course works. Finally, I would like to express my gratitude to my family, friends in Japan and USA, colleagues at Bridgestone Corporation, and the beautiful nature of Colorado for keeping my inner peace.

Contents

| | | |
|----------|---|-----------|
| 1 | Introduction | 1 |
| 1.1 | Motivation and Research Overview | 1 |
| 1.2 | Original Works | 7 |
| 1.3 | Thesis Outline | 11 |
| 2 | Extended Finite Element Method | 12 |
| 2.1 | Outline | 12 |
| 2.2 | Spatial Discretization based on FEM | 12 |
| 2.3 | Spatial Discretization based on XFEM (Belytschko's Method) | 13 |
| 2.4 | Spatial Discretization based on XFEM (Hansbo's Method) | 14 |
| 3 | Space-Time Extended Finite Element Method | 16 |
| 3.1 | Outline | 16 |
| 3.2 | Extended Finite Element Method (XFEM) | 17 |
| 3.3 | Space-Time Extended Finite Element Method (Space-time XFEM) | 18 |
| 3.4 | Numerical Implementation | 22 |
| 3.4.1 | Elementwise Temporal Layer Approach | 23 |
| 3.4.2 | Integration Points for Space-Time Volume | 26 |
| 3.4.3 | Integration Points for Space-Time Interface | 27 |
| 3.4.4 | Face-Oriented Ghost-Penalty Stabilization | 28 |
| 3.5 | Structural Analysis using Space-Time XFEM | 30 |
| 3.5.1 | Governing Equations and Finite Element Discretization | 31 |
| 3.5.2 | Numerical Example 1: Beam Bending due to Body Force | 34 |
| 3.6 | Fluid Analysis using Space-Time XFEM | 40 |
| 3.6.1 | Governing Equations and Finite Element Discretization | 40 |

| | | |
|----------|---|-----------|
| 3.6.2 | Numerical Example 2: Unsteady Flow around Fixed Cylinder (DFG 2D-3 Benchmark Problem) | 44 |
| 3.6.3 | Numerical Example 3: Flow around an In-line Oscillating Cylinder | 51 |
| 3.7 | Discussion | 62 |
| 4 | Fluid-Structure Interaction | 65 |
| 4.1 | Outline | 65 |
| 4.2 | Classification of Numerical Methods for FSI | 65 |
| 4.3 | Solution Method and Coupling | 66 |
| 4.4 | Physical Description and Treatment of Interface | 66 |
| 5 | Full-Eulerian FSI Method using XFEM | 72 |
| 5.1 | Outline | 72 |
| 5.2 | Mechanical Theory of Solids based on Eulerian Description | 73 |
| 5.3 | Conservative Level Set Function (CLSF) | 76 |
| 5.4 | Preliminary Study for Eulerian Solid Analysis | 77 |
| 5.4.1 | 2-Node Beam Element (BEAM2) | 77 |
| 5.4.2 | Static Beam Analysis based on Lagrangian Description | 79 |
| 5.4.3 | Dynamic Beam Analysis based on Lagrangian description | 80 |
| 5.4.4 | Dynamic Beam Analysis based on Eulerian Description | 82 |
| 5.4.5 | Numerical Example of 2D Beam Analysis | 83 |
| 5.5 | Numerical Implementation of Eulerian Solid Analysis using XFEM | 85 |
| 5.5.1 | Helmholtz smoothing Method | 85 |
| 5.5.2 | Nitsche's Method | 86 |
| 5.5.3 | Face-Oriented Ghost-Penalty Method | 89 |
| 5.6 | Eulerian Solid Analysis using XFEM | 90 |
| 5.6.1 | Strong Form of Eulerian Solid Analysis | 90 |

| | | |
|----------|--|------------|
| 5.6.2 | Weak Form of Eulerian Solid Analysis | 91 |
| 5.7 | Numerical Examples of Eulerian Solid Analysis using XFEM | 93 |
| 5.7.1 | Free Falling of Cylinder due to Body Force | 93 |
| 5.7.2 | Beam Bending due to Body Force (2D Analysis with BCs) | 95 |
| 5.8 | Theory of Full-Eulerian FSI Method | 100 |
| 5.8.1 | Artificial Advective Velocity for Level Set Function | 101 |
| 5.8.2 | Strong Form of Full-Eulerian FSI | 102 |
| 5.8.3 | Weak Form of Full-Eulerian FSI | 104 |
| 5.9 | Numerical Example of Full-Eulerian FSI using XFEM | 107 |
| 5.10 | Discussion | 115 |
| 6 | Lagrangian-Immersed FSI Method using XFEM | 117 |
| 6.1 | Outline | 117 |
| 6.2 | Physics Model | 119 |
| 6.2.1 | Eulerian System | 120 |
| 6.2.2 | Lagrangian System | 120 |
| 6.2.3 | Fluid-Structure Interaction (FSI) | 123 |
| 6.2.4 | Contact Model | 126 |
| 6.3 | Level Set Projection for Fluid-Structure Interaction | 129 |
| 6.4 | Finite Element Discretization of Lagrangian-Immersed FSI Method using XFEM | 132 |
| 6.5 | Numerical Implementation | 137 |
| 6.5.1 | Correction of Level Set Projection | 138 |
| 6.5.2 | Structure of Jacobian | 139 |
| 6.5.3 | Face-Oriented Ghost-Penalty Method | 140 |
| 6.6 | Numerical Examples | 143 |
| 6.6.1 | Stationary Beam in a Fluid Channel (COMSOL Benchmark Problem) | 143 |
| 6.6.2 | Stationary Beam in a Fluid Channel with Body Force | 150 |

| | | |
|----------|---|------------|
| 6.6.3 | Transient Structural Problem with Multibody Contact | 158 |
| 6.6.4 | Multibody FSI-Contact Problem using XFEM | 163 |
| 6.7 | Discussion | 183 |
| 7 | Lagrangian-Immersed FSI Method using Space-Time XFEM | 185 |
| 7.1 | Outline | 185 |
| 7.2 | Finite Element Discretization of Lagrangian-Immersed FSI Method using Space-Time XFEM | 187 |
| 7.3 | Numerical Implementation | 194 |
| 7.3.1 | Space-Time Slab for Lagrangian-Immersed FSI Method | 194 |
| 7.3.2 | Integration Schemes for Volume and Standard Interface | 194 |
| 7.3.3 | Integration Schemes for Face-Oriented Ghost-Penalty Method | 195 |
| 7.3.4 | Pairing of Integration Points on Non-Matching Space-Time Interfaces for FSI | 195 |
| 7.3.5 | Contact Formulation for Space-Time XFEM | 198 |
| 7.3.6 | Level Set Projection for Space-Time XFEM | 202 |
| 7.3.7 | Structure of Dynamic Jacobian | 206 |
| 7.4 | Numerical Examples | 208 |
| 7.4.1 | Falling Circular Cylinder due to Body Force | 209 |
| 7.4.2 | Turek-Hron FSI3 Benchmark Problem | 221 |
| 7.4.3 | Multibody FSI-contact problem using space-time XFEM | 241 |
| 7.5 | Discussion | 258 |
| 8 | Conclusions | 260 |
| 8.1 | Summary | 260 |
| 8.2 | Future Works | 264 |
| | Bibliography | 266 |

| | | |
|-------------------|--|------------|
| Appendix A | Material Constitutive Laws | 276 |
| A.1 | Isotropic Linear Elastic Material Constitutive Law | 276 |
| A.2 | Hyperelastic Material Constitutive Law | 277 |
| A.2.1 | Objectivity of Hyperelastic Material Constitutive Law | 278 |
| A.2.2 | Tangential Operator of Stress Tensor | 280 |
| A.2.3 | Hyperelastic Constitutive Law based on F , C and E | 280 |
| A.2.4 | Hyperelastic Constitutive Law based on Reduced Invariants of C | 281 |
| A.3 | Derivative of Determinant | 287 |
| Appendix B | Nitsche's Method for Cauchy Momentum Equation | 289 |
| B.1 | Cauchy Momentum Equation | 289 |
| B.2 | Constitutive Tensor | 290 |
| B.3 | Weak Form of Cauchy Momentum Equation | 291 |
| B.4 | Weak Form for Nitsche's Method | 292 |
| B.5 | Symmetric Nitsche Formulation | 293 |
| B.5.1 | Symmetric Nitsche Method for Pure Structural or Pure Fluid Analysis | 295 |
| B.5.2 | Symmetric Nitsche Method for FSI Analysis | 295 |
| Appendix C | Nitsche's Method for Non-Matching Interfaces | 298 |
| Appendix D | Contact Formulation based on Lagrangian Description | 303 |
| D.1 | Outline | 303 |
| D.2 | Numerical Implementation of Frictionless Contact Model (FCM) | 306 |
| D.2.1 | Gap Equation | 306 |
| D.2.2 | Residuals of Contact Formulation | 307 |
| D.2.3 | Computation of Lagrange Multiplier | 308 |
| D.2.4 | Jacobian of Contact Formulation | 309 |
| D.2.5 | Derivatives related to Residual and Jacobian | 310 |

| | |
|---|-----|
| D.3 Jacobian of Surface Area (Nanson's Formula) | 316 |
| Appendix E Correction Term due to Discontinuous Galerkin Method in Time | 317 |
| Appendix F Comparison between Simplex Triangulation Approach and Ele- mentwise Temporal Layer Approach | 319 |

List of Tables

| | | |
|------|---|-----|
| 3.1 | Notation of volume and boundary | 19 |
| 3.2 | Computational methods for structural problem | 35 |
| 3.3 | Parameters for geometry and material (structural problem) | 35 |
| 3.4 | Geometrical and material parameters (DFG 2D-3 problem) | 45 |
| 3.5 | Reference of DFG 2D-3 benchmark problem | 46 |
| 3.6 | Spatial size dependency of C_D^{\max} , C_L^{\max} and Δp^{fin} (XFEM) | 48 |
| 3.7 | Spatial size dependency of C_D^{\max} , C_L^{\max} and Δp^{fin} (space-time XFEM) | 48 |
| 3.8 | Temporal size dependency of C_D^{\max} , C_L^{\max} and Δp^{fin} (XFEM) | 49 |
| 3.9 | Temporal size dependency of C_D^{\max} , C_L^{\max} and Δp^{fin} (space-time XFEM) | 49 |
| 3.10 | Comparison between different approaches for space-time integration | 50 |
| 3.11 | Parameters for geometry and material (in-line oscillation of cylinder) | 56 |
| 3.12 | Computational results and references of C_D and C_M ($\text{Re} = 100$ and $\text{Kc} = 5$) | 59 |
| 4.1 | Computational methods for FSI | 71 |
| 5.1 | Setting of cantilever beam | 84 |
| 5.2 | Settings of free falling circular solid | 93 |
| 5.3 | Parameters of bending beam | 96 |
| 5.4 | Parameters about level set function ϕ | 97 |
| 5.5 | Parameters about boundary integrals | 97 |
| 5.6 | Models for convergence check (Eulerian solid analysis) | 98 |
| 5.7 | Parameters of full-Eulerian FSI analysis (infinitesimal strain case) | 109 |
| 5.8 | Models for convergence check | 111 |
| 5.9 | Difference between current computation and reference work | 113 |

| | | |
|------|--|-----|
| 6.1 | Parameters of COMSOL benchmark problem | 144 |
| 6.2 | Computational results of COMSOL stationary benchmark problem | 146 |
| 6.3 | Parameters of stationary beam with body force | 151 |
| 6.4 | Models of numerical example 2 of Lagrangian-immersed FSI using XFEM | 152 |
| 6.5 | parameters of multibody contact problem | 159 |
| 6.6 | Geometry parameters | 166 |
| 6.7 | Physical parameters of solid and fluid | 167 |
| 6.8 | Summary of spatial discretization (multibody FSI-contact problem) | 167 |
| 6.9 | Penalty coefficients for multibody FSI-contact problem | 168 |
| 7.1 | Notation of volume and boundary | 187 |
| 7.2 | Geometrical and material parameters for falling cylinder | 210 |
| 7.3 | Penalty coefficients for falling cylinder using space-time XFEM | 211 |
| 7.4 | Geometry of Turek-Hron FSI3 | 223 |
| 7.5 | Physical parameters of Turek-Hron CSM1 | 224 |
| 7.6 | Numerical results of Turek-Hron CSM1 | 225 |
| 7.7 | Physical parameters of Turek-Hron FSI3 | 226 |
| 7.8 | Penalty coefficients for Turek-Hron FSI3 | 227 |
| 7.9 | Numerical results of Turek-Hron FSI3 | 240 |
| 7.10 | Penalty coefficients for FSI-contact problem using space-time XFEM | 242 |
| A.1 | Notation for material constitutive law | 278 |
| D.1 | Notation for frictionless contact mechanics | 305 |
| F.1 | Number of integration points in each figure | 322 |
| F.2 | Comparison of C_D^{\max} , C_L^{\max} and Δp^{fn} | 323 |
| F.3 | Comparison using Turek-Hron FSI3 | 325 |

List of Figures

| | |
|--|----|
| 1.1 Problem of Heaviside-enriched XFEM using time stepping scheme | 3 |
| 1.2 Contact on wet surface | 5 |
| 1.3 In-vivo micro device | 6 |
| 3.1 Space-time slab | 19 |
| 3.2 Volume and boundaries in a space-time slab Q^n | 19 |
| 3.3 Temporal layers and temporal integration points (2 layers case) | 25 |
| 3.4 Temporal layers and temporal integration points (3 layers case) | 25 |
| 3.5 integration points for space-time volume | 26 |
| 3.6 integration points for space-time interface | 28 |
| 3.7 Space-time integration points for face-oriented ghost-penalty stabilization . . | 30 |
| 3.8 Model for FEM and ST-FEM | 35 |
| 3.9 Model for XFEM and ST-XFEM | 35 |
| 3.10 History of U_y^{tip} and snapshot of deformation | 37 |
| 3.11 Spatial size dependency of L2 errors of tip displacements | 37 |
| 3.12 Spatial size dependency of L2 errors of kinetic and strain energy | 38 |
| 3.13 Temporal size dependency of L2 error of tip displacements | 39 |
| 3.14 temporal size dependency of L2 error of kinetic and strain energy | 39 |
| 3.15 Model of fluid problem with fixed interface (DFG 2D-3 problem) | 44 |
| 3.16 Spatial size dependency of C_D^{\max} , C_L^{\max} and Δp^{fin} (400 time steps, $\Delta t = 0.02\text{s}$) | 46 |
| 3.17 History of C_D , C_L , Δp and vorticity in z : ω_z^f | 48 |
| 3.18 Temporal size dependency of C_D^{\max} , C_L^{\max} and Δp^{fin} ($h/D = 0.0276$) | 50 |
| 3.19 Reference results of streamlines | 53 |
| 3.20 Reference results of velocity fields | 54 |

| | | |
|------|---|-----|
| 3.21 | Reference results of in-line force | 55 |
| 3.22 | Model of in-line oscillating cylinder (time t^n) | 56 |
| 3.23 | Comparison of dimensionless in-line force f_x | 57 |
| 3.24 | Effect of face-oriented ghost-penalty method | 58 |
| 3.25 | Distribution of v_x^f and streamlines at different phase positions | 59 |
| 3.26 | Dimensionless in-line force f_x (Model 5 in Table 3.12) | 59 |
| 3.27 | Distribution of velocities at different phase positions | 61 |
| 4.1 | Category about numerical methods for FSI | 66 |
| 4.2 | Monolithic method | 67 |
| 4.3 | Image of mesh for FSI | 69 |
| 4.4 | Drawback of ALE-FSI 1 | 69 |
| 4.5 | Drawback of ALE-FSI 2 | 69 |
| 5.1 | Image of 1D advection of reference map X_x using stabilization method | 75 |
| 5.2 | Initial configuration of beam | 84 |
| 5.3 | Result of Lagrangian FEM | 85 |
| 5.4 | Result of Eulerian FEM | 85 |
| 5.5 | Intersected element | 87 |
| 5.6 | Boundaries for face-oriented ghost-penalty method | 89 |
| 5.7 | Free falling circular structure due to body force | 94 |
| 5.8 | History of velocity v_y in time | 95 |
| 5.9 | History of displacement u_y in time | 95 |
| 5.10 | System of bending beam | 96 |
| 5.11 | History of bending beam (phase, v_y and σ_{VM}) | 99 |
| 5.12 | Convergence of Eulerian solid analysis (Step 9, $t = 0.675s$) | 100 |
| 5.13 | Simple system for discussion of FSI theory | 100 |
| 5.14 | Leakage of level set function due to fluid velocity | 102 |

| | | |
|------|---|-----|
| 5.15 | System for numerical example of full-Eulerian FSI | 108 |
| 5.16 | History of solid properties | 110 |
| 5.17 | History of fluid properties | 110 |
| 5.18 | Convergence of Eulerian FSI (final time step, $t = 0.5s$) | 112 |
| 5.19 | Reference work (deformation of hyperelastic body in INS fluid) | 114 |
| 5.20 | Reference Work (L2 error corresponding to Figure 5.19) | 114 |
| 6.1 | Lagrangian and Eulerian interface | 118 |
| 6.2 | Projection of values from master interface Γ_E to slave interface Γ_L | 124 |
| 6.3 | Projection from master integration points to slave integration points | 125 |
| 6.4 | Contact interface Γ_{c0} and normal gap g_n (A : master, B : slave) | 126 |
| 6.5 | Level set projection | 131 |
| 6.6 | Correction of level set projection (early stage of Newton iteration) | 138 |
| 6.7 | Broad structure of Jacobian (Lagrangian-immersed FSI using XFEM) | 139 |
| 6.8 | Faces for face-oriented ghost-penalty method: Γ_{Lgp0} and Γ_{Egp} | 142 |
| 6.9 | System of COMSOL benchmark problem | 144 |
| 6.10 | Steady-state result of COMSOL benchmark problem | 146 |
| 6.11 | Non-matching interfaces | 147 |
| 6.12 | Deformation of fluid domain at reference work | 147 |
| 6.13 | Distribution of fluid pressure around a tip | 148 |
| 6.14 | Deformation of a Lagrangian mesh | 149 |
| 6.15 | System of stationary beam with body force | 150 |
| 6.16 | Mesh of stationary beam with body force | 152 |
| 6.17 | Steady-state velocity distribution (Model 3 of Table 6.4) | 153 |
| 6.18 | Fluid pressure and vorticity (Model 3 of Table 6.4) | 153 |
| 6.19 | Solid displacement and von Mises stress (Model 3 of Table 6.4) | 154 |
| 6.20 | L2 error of velocity and stress | 156 |

| | | |
|------|---|-----|
| 6.21 | L2 error of solid displacement and fluid pressure | 156 |
| 6.22 | L2 error of level set function | 157 |
| 6.23 | Model of transient contact problem | 158 |
| 6.24 | Results of transient contact problem | 161 |
| 6.25 | History of momentum in x | 162 |
| 6.26 | History of momentum in y | 162 |
| 6.27 | Lagrangian system 1: Ω_{L0}^1 | 163 |
| 6.28 | Lagrangian system 2: Ω_{L0}^2 | 163 |
| 6.29 | Lagrangian system 3: Ω_{L0}^3 | 163 |
| 6.30 | Lagrangian system 4: Ω_{L0}^4 | 163 |
| 6.31 | Lagrangian system 5: Ω_{L0}^5 | 164 |
| 6.32 | Eulerian system: Ω_E | 165 |
| 6.33 | FSI-contact problem using XFEM ($t = 0s$, step0) | 168 |
| 6.34 | FSI-contact problem using XFEM ($t = 1.1s$, step10) | 169 |
| 6.35 | FSI-contact problem using XFEM ($t = 2.05s$, step20) | 169 |
| 6.36 | FSI-contact problem using XFEM ($t = 3.05s$, step30) | 170 |
| 6.37 | FSI-contact problem using XFEM ($t = 4.05s$, step40) | 170 |
| 6.38 | FSI-contact problem using XFEM ($t = 4.75s$, step50) | 171 |
| 6.39 | FSI-contact problem using XFEM ($t = 5.575s$, step60) | 172 |
| 6.40 | FSI-contact problem using XFEM ($t = 6.425s$, step70) | 172 |
| 6.41 | FSI-contact problem using XFEM ($t = 7.375s$, step80) | 173 |
| 6.42 | FSI-contact problem using XFEM ($t = 8.25s$, step90) | 173 |
| 6.43 | FSI-contact problem using XFEM ($t = 9s$, step100) | 174 |
| 6.44 | FSI-contact problem using XFEM ($t = 10s$, step110) | 174 |
| 6.45 | FSI-contact problem using XFEM ($t = 11s$, step120) | 175 |
| 6.46 | FSI-contact problem using XFEM ($t = 11.9s$, step130) | 175 |

| | |
|--|-----|
| 6.47 FSI-contact problem using XFEM ($t = 12.9\text{s}$, step140) | 176 |
| 6.48 FSI-contact problem using XFEM ($t = 13.85\text{s}$, step150) | 176 |
| 6.49 FSI-contact problem using XFEM ($t = 14.75\text{s}$, step160) | 177 |
| 6.50 FSI-contact problem using XFEM ($t = 16.275\text{s}$, step180) | 177 |
| 6.51 FSI-contact problem using XFEM ($t = 17.2\text{s}$, step200) | 178 |
| 6.52 FSI-contact problem using XFEM ($t = 30.98125\text{s}$, step347) | 178 |
| 6.53 Oscillation of fluid velocity and stress ($t = 4.05\text{s}$, step40) | 179 |
| 6.54 Interpolation error due to XFEM (velocity in x) | 180 |
| 6.55 Interpolation error due to XFEM (velocity in y) | 180 |
| 6.56 Interpolation error due to XFEM (fluid pressure) | 181 |
| 6.57 Ghost fluid method | 182 |
| | |
| 7.1 Definition of volume and interfaces in a space-time slab (phase A and B) . . | 186 |
| 7.2 Lagrangian and Eulerian space-time slabs | 195 |
| 7.3 Space-time integration points for face-oriented ghost-penalty stabilization . . | 196 |
| 7.4 Node-to-surface (NTS) pairing between non-matching space-time interfaces . | 197 |
| 7.5 Space-time contact interfaces (undeformed configuration) | 198 |
| 7.6 Space-time contact interfaces (deformed configuration) | 199 |
| 7.7 Setting of integration points for space-time contact (master interface $P_{\text{co-m}}^n$) . | 200 |
| 7.8 Space-time contact interfaces and integration points (undeformed configuration) | 202 |
| 7.9 Level set projection for space-time XFEM | 203 |
| 7.10 Level set projection performed at t_-^{n+1} | 204 |
| 7.11 Procedure of level set projection for space-time XFEM | 205 |
| 7.12 Broad structure of diagonal block Jacobian ($J_n^n: t_+^n \otimes t_+^n$) | 206 |
| 7.13 Broad structure of diagonal block Jacobian ($J_{n+1}^{n+1}: t_+^{n+1} \otimes t_+^{n+1}$) | 207 |
| 7.14 Broad structure of off-diagonal block Jacobian ($J_n^{n+1}: t_+^n \otimes t_-^{n+1}$) | 207 |
| 7.15 Lagrangian system: Ω_{L0} | 209 |

| | |
|---|-----|
| 7.16 Eulerian system: Ω_E | 209 |
| 7.17 History of v_x (Lagrangian-immersed FSI using space-time XFEM) | 212 |
| 7.18 History of v_y (Lagrangian-immersed FSI using space-time XFEM) | 212 |
| 7.19 History of p^f (Lagrangian-immersed FSI using space-time XFEM) | 213 |
| 7.20 History of q^f (Lagrangian-immersed FSI using space-time XFEM) | 213 |
| 7.21 History of U_x^s (Lagrangian-immersed FSI using space-time XFEM) | 214 |
| 7.22 Comparison of F_x (XFEM and space-time XFEM) | 215 |
| 7.23 Comparison of F_y (XFEM and space-time XFEM) | 215 |
| 7.24 Comparison of P_x (XFEM and space-time XFEM) | 218 |
| 7.25 Comparison of P_y (XFEM and space-time XFEM) | 218 |
| 7.26 L2 error of force in x : F_x^{tot} | 220 |
| 7.27 L2 error of force in y : F_y^{tot} | 220 |
| 7.28 Error of momentum in x : P_x^{tot} | 220 |
| 7.29 Error of momentum in y : P_y^{tot} | 220 |
| 7.30 Model of Eulerian system Ω_E (Turek-Hron FSI3) | 222 |
| 7.31 Model of undeformed Lagrangian system Ω_{L0} (Turek-Hron FSI3) | 222 |
| 7.32 Mesh of Eulerian system (Turek-Hron FSI3) | 223 |
| 7.33 Mesh of Lagrangian system (Turek-Hron FSI3) | 223 |
| 7.34 Deformation of Turek-Hron CSM1 | 225 |
| 7.35 Convergence of tip displacements (Turek-Hron CSM1) | 225 |
| 7.36 History of velocity in x (Turek-Hron FSI3, $\Delta t = 0.005\text{s}$) | 229 |
| 7.37 History of velocity in y (Turek-Hron FSI3, $\Delta t = 0.005\text{s}$) | 230 |
| 7.38 History of fluid vorticity ω_z^f (Turek-Hron FSI3, $\Delta t = 0.005\text{s}$) | 231 |
| 7.39 Structural deformations (Turek-Hron FSI3, 7.09s-7.18s, $\Delta t = 0.005\text{s}$) | 232 |
| 7.40 Structural deformations (Turek-Hron FSI3, 7.18s-7.27s, $\Delta t = 0.005\text{s}$) | 233 |
| 7.41 Reference results of Turek-Hron FSI3 | 234 |

| | | |
|------|---|-----|
| 7.42 | Tip displacements of Turek-Hron FSI3 using $\Delta t = 0.005s$ | 235 |
| 7.43 | Drag and lift forces of Turek-Hron FSI3 using $\Delta t = 0.005s$ | 235 |
| 7.44 | Tip displacement of Turek-Hron FSI3 using $\Delta t = 0.0025s$ | 237 |
| 7.45 | Drag and lift forces of Turek-Hron FSI3 using $\Delta t = 0.0025s$ | 237 |
| 7.46 | Difference of drag force from reference (Turek-Hron FSI3, $\Delta t = 0.0025s$) | 238 |
| 7.47 | FSI-contact problem using space-time XFEM ($t = 0s$, step0) | 242 |
| 7.48 | FSI-contact problem using space-time XFEM ($t = 1s$, step10) | 243 |
| 7.49 | FSI-contact problem using space-time XFEM ($t = 2.01875s$, step23) | 243 |
| 7.50 | FSI-contact problem using space-time XFEM ($t = 3.01875s$, step33) | 244 |
| 7.51 | FSI-contact problem using space-time XFEM ($t = 4.025s$, step44) | 244 |
| 7.52 | FSI-contact problem using space-time XFEM ($t = 4.975s$, step54) | 245 |
| 7.53 | FSI-contact problem using space-time XFEM ($t = 5.9875s$, step66) | 245 |
| 7.54 | FSI-contact problem using space-time XFEM ($t = 7.0625s$, step81) | 246 |
| 7.55 | FSI-contact problem using space-time XFEM ($t = 8.06875s$, step92) | 246 |
| 7.56 | FSI-contact problem using space-time XFEM ($t = 11.0625s$, step129) | 247 |
| 7.57 | FSI-contact problem using space-time XFEM ($t = 13.16785s$, step150) | 247 |
| 7.58 | FSI-contact problem using space-time XFEM ($t = 15.5125s$, step180) | 248 |
| 7.59 | FSI-contact problem using space-time XFEM ($t = 18.33125s$, step220) | 248 |
| 7.60 | FSI-contact problem using space-time XFEM ($t = 25s$, step297) | 249 |
| 7.61 | FSI-contact problem using space-time XFEM ($t = 30.39375s$, step385) | 249 |
| 7.62 | Multibody contact in FSI-contact problem using space-time XFEM | 250 |
| 7.63 | Comparison of F_x (FSI-contact with XFEM and space-time XFEM) | 251 |
| 7.64 | Comparison of F_y (FSI-contact with XFEM and space-time XFEM) | 251 |
| 7.65 | Comparison of P_x (FSI-contact with XFEM and space-time XFEM) | 252 |
| 7.66 | Comparison of P_y (FSI-contact with XFEM and space-time XFEM) | 252 |
| 7.67 | Trajectory of centroids of solid structures (space-time XFEM, $\Delta t = 0.1s$) | 254 |

| | | |
|------|---|-----|
| 7.68 | Spatial size dependency of force (space-time XFEM, $\Delta t = 0.1s$) | 254 |
| 7.69 | Spatial size dependency of momentum (space-time XFEM, $\Delta t = 0.1s$) | 254 |
| 7.70 | L2 error of quantities at centroids (space-time XFEM, $\Delta t = 0.1s$) | 256 |
| 7.71 | L2 error of force (space-time XFEM, $\Delta t = 0.1s$) | 256 |
| 7.72 | Error of momentum (space-time XFEM, $\Delta t = 0.1s$) | 257 |
| D.1 | Contact mechanics for Lagrangian XFEM | 305 |
| F.1 | Comparison of settings of space-time volume integration points (1) | 319 |
| F.2 | Comparison of settings of space-time volume integration points (2) | 320 |
| F.3 | Comparison of settings of space-time volume integration points (3) | 321 |
| F.4 | Comparison of DFG 2D-3 benchmark problem using space-time XFEM | 323 |
| F.5 | Comparison of a falling elastic cylinder in INS fluid | 324 |
| F.6 | Comparison of tip displacements (Turek-Hron FSI3 Problem) | 326 |
| F.7 | Comparison of drag and lift forces (Turek-Hron FSI3 Problem) | 326 |

Chapter 1

Introduction

1.1 Motivation and Research Overview

Partial differential equations (PDEs) are fundamentals of continuous physical phenomenon and important mathematical background for engineering. Focusing on numerical simulation methods of a partial differential equation, finite difference method (FDM) [1, 2, 3, 4, 5, 6], finite element method (FEM) [7, 8, 9, 10, 11, 12, 13, 14, 15], finite volume method (FVM) [16, 17, 18, 19, 20, 21] and isogeometric analysis (IGA) [22, 23, 24, 25, 26] are representative methods. While there are hundreds of numerical simulation methods for a partial differential equation, the FEM is a widely used method in both academia and industry because of its mathematical background such as functional analysis, well-developed numerical techniques and its versatility for various types of application.

The FEM is based on the weak form of the PDE and discretizes an integration domain into finite-size small domains called as finite elements. The state variables are approximated by shape functions of the FEM. Interfaces in an integration domain are explicitly represented by edges of finite elements. As the quality of meshing affects results of numerical integration, various meshing techniques have been developed and the meshing part is one of the computationally most demanding parts in the finite element analysis. In particular, the FEM with moving interfaces requires continuously updating the interface and thus, remeshing is essential to track the motion of moving interfaces.

To overcome the high computational cost of meshing, immersed boundary analysis methods are alternative approaches for modeling geometry. Explicit representation of an interface such as edges of finite elements is not needed and interfaces are immersed within a compu-

tational domain implicitly. A combination of the finite element method and an immersed boundary modeling approach is the eXtended Finite Element Method (XFEM). The XFEM is an immersed boundary method that can handle discontinuity of state variables within one element by introducing enrichment functions, in addition to the standard finite element shape functions. To integrate the weak form of governing equations, the XFEM decomposes finite elements based on the intersection configuration defined by the iso-contour of the level set function ϕ [27, 28]. The kink enrichment strategy is typically used for problems with weak discontinuities (C^1 discontinuities). The Heaviside enrichment strategy is proposed for problems with strong discontinuities (C^0 discontinuities) and thus, it is applicable to a broader class of problems in comparison to kink enrichments. Hansbo and Hansbo [29] proposed one attractive XFEM formulation using the Heaviside enrichment. The spatial discretization for a two-phase problem is as follows in this case:

$$\mathbf{u}(\mathbf{x}) = \sum_{m=1}^M \left(H(-\phi(\mathbf{x})) \sum_{i=1}^{N_e} N_i(\mathbf{x}) \delta_{mq}^{A,i} \mathbf{u}_i^{A,m} + H(\phi(\mathbf{x})) \sum_{i=1}^{N_e} N_i(\mathbf{x}) \delta_{mr}^{B,i} \mathbf{u}_i^{B,m} \right), \quad (1.1)$$

where M is the number of enrichment levels, N_e is the number of nodes in the element, $N_i(\mathbf{X})$ are the shape functions, $\mathbf{u}_i^{p,m}$ is a set of state variables of enrichment level m at node i interpolating in phase p . The Heaviside function turns on/off two sets of shape functions associated with two phases A and B . For each phase, multiple enrichment levels, i.e. sets of shape functions, might be necessary to interpolate each state variable. The Kronecker delta $\delta_{mq}^{p,i}$ selects the active enrichment level q for node i such that state variables at a spatial point \mathbf{x} are interpolated by only one set of state variables defined at node i , satisfying the partition of unity principle. Benefits of (1.1) are that state variables are approximated by superposing solutions at both phase computed by the finite element method (FEM) and that non-intersected elements can be computed by the standard fashion of the FEM. Therefore, (1.1) has convenient structure for the actual implementation. The reader is also referred to Fries and Belytschko [30, 31], Khoei [32], Mohammadi [33], Makhija and Maute [34], Terada

et al. [35] and Tran et al. [36] as an introduction and general outline of the XFEM.

A drawback of the Heaviside-enriched XFEM (1.1) is the complexity of accurately predicting the response of transient problems with moving interfaces. Figure 1.1 illustrates a transient two-phase problem with a moving interface, considering four elements around an interface at previous time t^{n-1} (left) and current time t^n (right). The shaded region is phase A and the non-shaded region is phase B .

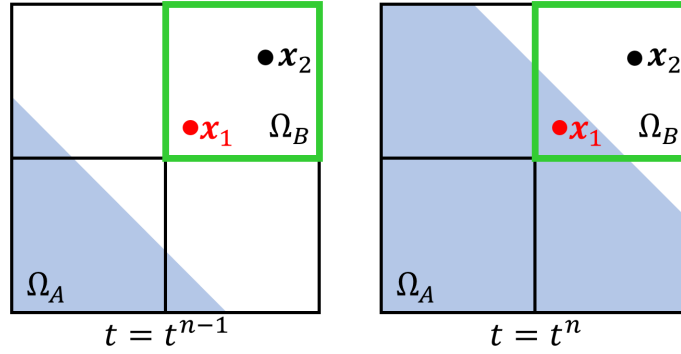


Figure 1.1: Problem of Heaviside-enriched XFEM using time stepping scheme

Focusing on the green element (top right element), this element is not intersected at $t = t^{n-1}$ and intersected at $t = t^n$ as an interface moves. The spatial point \mathbf{x}_2 belongs to phase B at both time and thus, the approximation of time derivative terms can be evaluated by time stepping schemes; e.g. $\partial \mathbf{u}^n / \partial t \sim (\mathbf{u}^n - \mathbf{u}^{n-1}) / \Delta t$. On the other hand, the phase at a spatial point \mathbf{x}_1 changes from A to B as follows:

$$\mathbf{u}^{n-1}(\mathbf{x}_1) = \sum_{i=1} N_i(\mathbf{x}_1) \mathbf{u}_i^B \quad \text{at } t^{n-1}, \quad (1.2)$$

$$\mathbf{u}^n(\mathbf{x}_1) = \sum_{i=1} N_i(\mathbf{x}_1) \mathbf{u}_i^A \quad \text{at } t^n. \quad (1.3)$$

In this case, a subtraction; $\mathbf{u}^n(\mathbf{x}_1) - \mathbf{u}^{n-1}(\mathbf{x}_1)$, is meaningless because of the phase change at t^{n-1} and t^n and thus, time stepping schemes fail to approximate time derivative terms. To mitigate this error, the ghost fluid method [37, 38, 39, 40] have been introduced.

In order to avoid time integration errors due to moving interfaces, the space-time XFEM has been proposed as a combination of the XFEM and the space-time formulation [41, 42, 43,

[44]. Chessa and Belytschko [45, 46] presented a space-time XFEM based on the Heaviside enrichment for spatially one-dimensional equations. Lehrenfeld [47] proposed a space-time XFEM approach and demonstrated its capability using a spatially three-dimensional convection diffusion equation with a moving interface. The work of [47] is restricted to linear problems because the convective velocity is analytically defined. The decomposition of a space-time domain is necessary in the space-time XFEM to generate space-time intersection configuration for numerical integration. [47] uses a four-dimensional simplex triangulation like Behr [48] and Neumüller et al. [49]. This approach is rather complex and leads to an involved implementation. Zahedi [50] also presented a space-time XFEM for spatially two-dimensional convection-diffusion equations using analytical convection velocity. [50] introduced a simple space-time integration strategy that relies on the summation of spatial integration at multiple temporal quadrature points in a space-time slab. However, this simple space-time integration leads to errors when a small intersected volume is created, because temporal quadrature points are independently defined without considering the location of space-time interfaces. This issue will be discussed in more detail later.

The XFEM suffers from ill-conditioning because of small intersected volume generated by immersed boundaries. Such configurations are frequently created by moving interfaces. The ill-conditioning causes slow convergence of linear solvers and may lead to the divergence of nonlinear solvers. To mitigate this ill-conditioning problem, several methods have been proposed such as preconditioning schemes [51, 52, 53, 54] and the face-oriented ghost-penalty method (Burman and Hansbo [55, 56]). The face-oriented ghost-penalty method penalizes the jump of numerical flux across two adjacent intersected elements and thus, controls the spatial gradients of the state variables in the vicinity of interfaces. Zahedi [50] expanded this method for the space-time XFEM and succeeded to mitigate the ill-conditioning for spatially two-dimensional convection-diffusion equations.

The realization of a stable and robust computational method for moving interfaces such

as the space-time XFEM, enhances significantly the flexibility of numerical computations for complex systems. Fluid-structure interaction (FSI) represents one class of problems which can benefit from the correct mathematical treatment of moving interfaces. FSI describes the interaction between the fluid forces that act on a structure and the change in geometry of the fluid-solid interface as a result of structural deformations. FSI is widely found in physics and various engineering applications. FSI needs to be considered in the design of industrial products such as tires, airbags, aircraft, trains, vehicles and so on. In addition, FSI plays an important role in bio-mechanics and the design of bio-mechanical devices.

A class of problems of particular interest is FSI with solid bodies undergoing mechanical contact. Tires on a wet road and inflation of an airbag are typical examples of FSI-contact problems. Similar problems are encountered in the design of bio-medical in-vivo robotic devices (Figure 1.3), which has tires made by the tread of the rubber-like material and moves on the intestinal wall with these tires to inspect the condition of organ tissues.

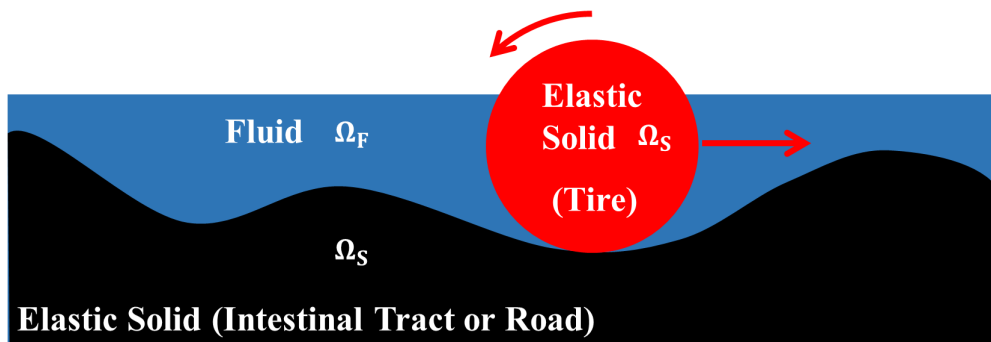


Figure 1.2: Contact on wet surface

Computational methods of the fluid-structure interaction (FSI) problems have been widely proposed. The most popular method is the Arbitrary Lagrangian and Eulerian (ALE) method (Belytschko et al. [58], Huerta et al. [59, 60], Nitikitpaiboon and Bathe [61, 62], Bathe et al. [63]). In the ALE-FSI method, the solid phase is defined by body-fitted meshes based on the Lagrangian description. The fluid phase is also represented by body-fitted meshes that deform in response to the structural deformations. The main advantage of

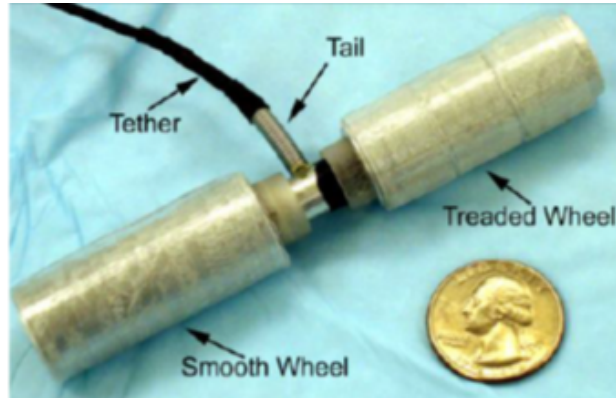


Figure 1.3: In-vivo Micro Device [57]

the ALE-FSI is that the interface between solid and fluid phase is defined explicitly because both phases are represented by the body-fitted mesh. However, the computation is not very robust, especially when body-fitted fluid mesh undergoes large deformations and fluid elements are severely distorted. Moreover, considering contact phenomena within the FSI system, the fluid phase within the contact region should be vanished. The topology of body-fitted meshes of the fluid is not preserved in this case. The flexibility of the ALE-FSI method is insufficient for problems which contains large deformation and contact like tires.

To overcome difficulties of the ALE-FSI, several non-standard FSI methods have been proposed. One of non-standard FSI methods to handle FSI-contact problems, is the full-Eulerian FSI method (Frei, Richter, et al. [64, 65], Richter [66], Kamrin et al. [67, 68]), which is based on the Eulerian description (spatial description) of both, the solid and fluid phase. As there is no body-fitted mesh, numerical instability due to the distortion of meshes does not occur. Therefore, this method is more robust than the ALE method for complex FSI problems with large deformation and contact. The main challenge of the full-Eulerian FSI method is the treatment of the solid phase using the Eulerian description. The problem of previous works of the full-Eulerian FSI method is that these works use the standard FEM or FVM and thus, very fine meshes are essential to capture reasonable interfaces. This is because an interface is represented by an immersed boundary modeling within fixed back

ground meshes, not by body-fitted meshes.

Another non-standard FSI method is the mixed Lagrangian and Eulerian formulation. Mayer, Wall, et al. [69, 70] proposed the XFEM based fixed grid approach using the ghost-fluid method to handle FSI and contact simultaneously. In the XFEM based fixed grid approach, solid and fluid phases are defined by the Lagrangian and Eulerian description respectively. The benefit of this method is that there is no limitation on the deformation of the solid because the computation of the fluid phase is always performed on a fixed background mesh. Conventional contact formulations can be directly applied. However, the ghost-fluid method is needed to treat moving interfaces in a transient problem because the XFEM based fixed grid approach uses the XFEM with the time stepping scheme. In addition, a complex technique for the update of the geometry is necessary.

1.2 Original Works

This thesis contributes to the development of the space-time XFEM and non-standard FSI method using the XFEM framework. The combination of the space-time XFEM and non-standard FSI method is a promising method for the stable and robust computation of the complex FSI system such as FSI-contact problems.

The first contribution of this thesis is a space-time XFEM based on the Heaviside enrichment for transient problems with moving interfaces. This thesis introduces a simple space-time integration based on the summation of spatial integration at multiple temporal quadrature points. Each space-time element is subdivided into multiple temporal layers along time considering its intersection configuration. Then, temporal integration points are defined in each temporal layer based on the quadrature rule and called as the temporal slices. For each temporal slice, one quadrature point is set at its central position in time. Thus, the elementwise space-time integration is performed by the summation of piece-wise constant integration in time. While the proposed integration is similar to [50], more precise

space-time integration is achieved because all small intersection configurations are taken into account for the setting of temporal quadrature points. As the proposed method only relies on the triangulation in space, the proposed space-time integration is directly applicable to spatially three-dimensional problems without simplex triangulation like [47]. This space-time integration is named as the elementwise temporal layer approach. This thesis studies spatially two-dimensional structural and fluid problems using the proposed space-time XFEM. While previous studies by [47] and [50] considered linear problems, this thesis focuses on nonlinear problems. A structural problem assumes the finite strain theory and nonlinear elastic material as a structural model. At fluid problems, this thesis uses the incompressible Navier-Stokes fluid and the variational multiscale method (Hughes et al. [71], Schott et al. [72, 73]) is applied for the stabilization of the convection and incompressibility terms. Nitsche's method of Hansbo et al. [74] is used to enforce space-time interface conditions in both structural and fluid problems. The face-oriented ghost-penalty method is applied for nonlinear elastic solid and incompressible Navier-Stokes fluid in the space-time XFEM. Numerical examples of structural and fluid problems including both fixed and moving interfaces are studied by the proposed space-time XFEM. Through these numerical examples, the proposed method, a space-time XFEM based on the elementwise temporal layer approach using the face-oriented ghost-penalty stabilization, is a stable and robust computational method for transient problems with moving interfaces.

The second contribution of this thesis is the study of non-standard FSI methods using the XFEM framework for complex FSI-contact phenomenon. The full-Eulerian FSI method using the XFEM is studied. In the full-Eulerian FSI method, the interface is driven by the propagation of the level set function. This level set function is also used for the enrichment strategy of the XFEM and thus, the XFEM has a high affinity for the full-Eulerian FSI method. The capability of the full-Eulerian FSI method using the XFEM is studied for the FSI analysis with large deformation in this thesis.

The Lagrangian-immersed FSI method using the XFEM is proposed as one of non-standard FSI methods to capture FSI-contact phenomenon. In this method, both the solid and fluid phases are defined by the Lagrangian and Eulerian description respectively. While the treatment of physical description is identical to Mayer, Wall, et al. [69, 70], there are distinct differences in terms of the update of geometry. In the proposed Lagrangian-immersed FSI method, solid and fluid are separately defined and solid structures should be immersed within the fluid mesh. To generate reasonable interfaces in the fluid phase considering the deformation of the solid phase, the level set projection method is introduced. Immersed interfaces in the fluid mesh are created by the minimization problem of level set functions between solid and fluid. The level set projection method is combined with the weak form of FSI and thus, the update of geometry is performed automatically at the solver part without any additional technique. The FSI interface integral is computed between non-matching Lagrangian and Eulerian interfaces based on Nitsche's method. The fluid-solid coupling is enforced by formulations and techniques adopted from computational contact mechanics such as a master-slave concept. Proposed Lagrangian-immersed FSI method achieved simpler implementation than [69, 70]. As the solid phase is defined by the Lagrangian description, the scheme of conventional contact formulations, e.g. the stabilized Lagrange multiplier method proposed by [75] is directly applicable. Comparing the Lagrangian-immersed FSI method to the full-Eulerian FSI method, the Lagrangian-immersed FSI method seems to be more flexible and scalable than the full-Eulerian FSI method. However, the combination of these non-standard FSI methods with the XFEM still suffers from numerical time integration errors due to moving interfaces discussed above.

The combination of the space-time XFEM and the Lagrangian-immersed FSI method is finally proposed as the third contribution of this thesis. The space-time FSI formulation and space-time contact formulation based on non-matching space-time interfaces are developed. Based on the space-time formulation, the effect of moving interfaces in the Lagrangian-

immersed FSI method is stably computed and a stable and robust FSI-contact analysis method is achieved. The proposed combination is shown to be a promising computational method for the robust and flexible FSI-contact problem and also beneficial in terms of the sensitivity analysis at the optimization scheme and gradient-based design optimization.

1.3 Thesis Outline

This thesis is organized as follows. Chapter 2 summarizes the theory of the eXtended Finite Element Method (XFEM) based on the Heaviside enrichment strategy. In Chapter 3, the space-time eXtended Finite Element Method (space-time XFEM) based on the elementwise temporal layer approach is proposed. The mathematical theory and the numerical implementation of the proposed space-time XFEM are discussed. In addition, the ease of the numerical implementation of the proposed space-time XFEM is demonstrated and applications to both structural and fluid problems including moving interfaces are presented.

The following three chapters study the fluid-structure interaction (FSI) problems using the standard XFEM and the conventional time integration scheme. Chapter 4 provides a brief summary of FSI formulations and numerical methods. Chapters 5 and 6 study non-standard computational methods for FSI problems that involve complex geometrical nonlinearity such as large deformation and contact. Chapter 5 focuses on the full-Eulerian FSI method using the XFEM and the conservative level set function (CLS F) method. In Chapter 6, the Lagrangian-immersed FSI method using the XFEM is discussed. Flexible steady-state FSI analysis methods are proposed in this chapter. Moreover, the stabilized Lagrange multiplier method for contact is described and the capability of the Lagrangian-immersed FSI method for FSI-contact problems is demonstrated. Chapter 7 summarizes the application of the proposed space-time XFEM to the Lagrangian-immersed FSI method. The theory and its numerical implementation for FSI and contact based on the space-time formulation are described. The stability and accuracy of the combination of the space-time XFEM and the Lagrangian-immersed FSI method are demonstrated using a transient FSI problem including large deformation, a well-known Turek-Hron FSI benchmark problem and a multibody FSI-contact problem. Finally, Chapter 8 summarizes the contribution of this thesis and describes the applicability of this research towards multi-physics analyses and optimization schemes.

Chapter 2

Extended Finite Element Method

2.1 Outline

The extended finite element method (XFEM) is an immersed boundary method that can handle discontinuities of state variables within one element by introducing enrichment functions in addition to finite element shape functions. The kink enrichment strategy is proposed for the weak discontinuities (C^1 discontinuities). The Heaviside enrichment strategy is proposed for problems with strong discontinuities (C^0 discontinuities) and thus, it is applicable to a broader class of problems in comparison to kink enrichments.

This chapter focuses on the Heaviside-enriched XFEM and summarizes its theory by comparing the FEM. This chapter references works of Freis [30, 76], Makhija [34], Mohammadi [33] and Song [77].

2.2 Spatial Discretization based on FEM

Consider the spatial discretization of the state variables \mathbf{u} based on the finite element method (FEM). The discretized form of the state variables is as follows:

$$\mathbf{u}(\mathbf{x}) = \sum_{i=1}^{N_e} N_i(\mathbf{x}) \mathbf{u}_i, \quad (2.1)$$

where $N_i(\mathbf{X})$ is the shape function, N_e is the number of node, and \mathbf{u}_i is a set of state variables at node i . A solution at an arbitrary point \mathbf{x} is interpolated by nodal solution vectors \mathbf{u}_i which belong to the element that contains \mathbf{x} . A set of shape functions satisfies the partition

of unity principle at any given location \mathbf{x} :

$$\sum_{i=1}^{N_e} N_i(\mathbf{x}) = 1 \quad . \quad (2.2)$$

2.3 Spatial Discretization based on XFEM (Belytschko's Method)

On the other hand, elements of the XFEM have internal interfaces. The discontinuities of state variables are captured within one finite elements along an interface. To represent internal implicit interfaces, an enrichment function is introduced. One popular form of the XFEM is Belytschko's method, which is usually applied to the crack propagation analysis. In this case, the spatial discretization based on the XFEM is denoted as follows:

$$\mathbf{u}(\mathbf{x}) = \sum_{i=1}^{N_e} N_i(\mathbf{x}) \mathbf{u}_i + \sum_{i=1}^{N_e} \hat{N}_i(\mathbf{x}) \psi(\mathbf{x}) \mathbf{a}_i \quad , \quad (2.3)$$

where $\hat{N}_i(\mathbf{x})$ is the enriched basis function, which are usually identical to the standard shape functions $N_i(\mathbf{x})$ but not necessarily identical to it. \mathbf{a}_i are an additional nodal unknown and $\psi(\mathbf{x})$ is the enrichment function. The first term of RHS is the term of the standard finite element discretization corresponding to (2.1) and the second term of RHS is the term of the local enrichment approximation. Belytschko's method represents discontinuities across the interfaces by the linear combination of regular components of the FEM and additional local components by the enrichment. But the approximation (2.3) is not correct ($\mathbf{u}(\mathbf{x}_i) \neq \mathbf{u}_i$) when the essential boundary condition is applied. To recover the Kronecker- δ property of the standard finite element approximation, (2.3) can be modified as the following shifted approximation:

$$\mathbf{u}(\mathbf{x}) = \sum_{i=1}^{N_e} N_i(\mathbf{x}) \mathbf{u}_i + \sum_{i=1}^{N_e} \hat{N}_i(\mathbf{x}) (\psi(\mathbf{x}) - \psi(\mathbf{x}_i)) \mathbf{a}_i \quad . \quad (2.4)$$

(2.4) is the shifted global enrichment of the spatial discretization based on Belytschko's method. By choosing $\hat{N}_i = N_i$ as the standard shape functions, this approximation sat-

isfies the partition of unity principle like the FEM. Extending (2.4) to the case of several enrichment levels, then:

$$\mathbf{u}(\mathbf{x}) = \sum_{i=1}^{N_e} N_i(\mathbf{x})\mathbf{u}_i + \sum_{m=1}^M \sum_{i=1}^{N_e} \hat{N}_i(\mathbf{x})(\psi^m(\mathbf{x}) - \psi^m(\mathbf{x}_i))\mathbf{a}_i^m, \quad (2.5)$$

where M is the total number of enrichment levels. There are several enrichment strategies. In this research, the Heaviside-enriched level-set based XFEM is used. The Heaviside step function H is used as the enrichment function ψ as follows:

$$\mathbf{u}(\mathbf{x}) = \sum_{i=1}^{N_e} N_i(\mathbf{x})\mathbf{u}_i + \sum_{i=1}^{N_e} \hat{N}_i(\mathbf{x})(H(\phi(\mathbf{x})) - H(\phi(\mathbf{x}_i)))\mathbf{a}_i, \quad (2.6)$$

$$H(x) = \begin{cases} 1 & (x > 0) \\ 0 & (x \leq 0) \end{cases}. \quad (2.7)$$

In (2.6), the function $\phi(\mathbf{x})$ defines the interface Γ as the iso-contour $\phi(\mathbf{x}) = 0$. This $\phi(\mathbf{x})$ is the level set function in this research.

2.4 Spatial Discretization based on XFEM (Hansbo's Method)

Hansbo and Hansbo [29] proposed an attractive XFEM formulation based on the Heaviside enrichment. This method is also based on the partition of unity and inspired by Babuska [78, 79]. Considering the spatial discretization of the state variables \mathbf{u} by the Heaviside-enriched level-set based XFEM proposed at [29], the spatial discretization is denoted as follows:

$$\mathbf{u}(\mathbf{x}) = \sum_{m=1}^M \left(H(-\phi(\mathbf{x})) \sum_{i=1}^{N_e} N_i(\mathbf{x})\delta_{mq}^{A,i} \mathbf{u}_i^{A,m} + H(\phi(\mathbf{x})) \sum_{i=1}^{N_e} N_i(\mathbf{x})\delta_{mr}^{B,i} \mathbf{u}_i^{B,m} \right). \quad (2.8)$$

The number of enrichment levels is denoted by M , N_e is the number of nodes in the element, $N_i(\mathbf{X})$ are the shape functions, $\mathbf{u}_i^{p,m}$ is a set of state variables of enrichment level m at node i interpolating in phase p . The Heaviside function turns on/off two sets of shape functions

associated with two phases A and B . For each phase, multiple enrichment levels, i.e. sets of shape functions, might be necessary to interpolate each state variable. The Kronecker delta $\delta_{mq}^{p,i}$ selects the active enrichment level q for node i such that state variables at a spatial point \mathbf{x} are interpolated by only one set of state variables defined at node i , satisfying the partition of unity principle. For further description, see Makhija and Maute [34], Terada et al. [35] and Tran et al. [36]. In non-intersected elements, the solution field is approximated by the standard finite element interpolation. The enrichment level for these elements is chosen to maintain continuous state variables across element boundaries.

Benefits of (2.8) are that state variables are approximated by superposing solutions at both phase computed by the finite element method (FEM) and that non-intersected elements can be computed by the standard fashion of the FEM. Therefore, the numerical implementation of Hansbo's method is much more convenient than Belytschko's method (2.3). The equivalence of Hansbo's method and Belytschko's method is proven by Song et al. [77]. The benefit of (2.8) is that (2.8) is only considered at the intersected elements cut by the interfaces and other non-intersected elements can be treated by the standard fashion of the FEM. This feature is very beneficial for the implementation of the XFEM and thus, this form is used in this thesis.

Chapter 3

Space-Time Extended Finite Element Method

3.1 Outline

This chapter presents a space-time XFEM based on the Heaviside enrichment for transient problems with moving interfaces, using Hansbo's method (2.8). This thesis introduces a simple space-time integration based on the summation of spatial integration at multiple temporal quadrature points. Each space-time element is subdivided into multiple temporal layers along time by considering its intersection configuration. Then, temporal integration points are defined in each temporal layer based on the quadrature rule and called as the temporal slices. While the proposed integration is similar to [50], more precise space-time integration can be achieved than [50] because all small intersection configurations are taken into account for the setting of temporal quadrature points. As this thesis only relies on the triangulation in space, the proposed space-time integration is directly applicable to spatially three-dimensional problems without the simplex triangulation like [47]. This space-time integration is named as the elementwise temporal layer approach. This thesis studies spatially two-dimensional structural and fluid problems using the proposed space-time XFEM. While the previous studies by [47] and [50] considered linear problems, this thesis focuses on nonlinear problems. The finite strain theory is assumed and a nonlinear elastic material is used as a solid model. At fluid problems, this thesis uses the incompressible Navier-Stokes fluid and the variational multiscale method [71, 72, 73] is applied for the stabilization of the convection and incompressibility terms. Nitsche's method based on Hansbo et al. [74] is used for space-time interface conditions in both structural and fluid problems. The face-oriented ghost-penalty method is also applied for nonlinear elastic solid and incompressible Navier-

Stokes fluid in the space-time XFEM. This chapter demonstrates the efficiency and stability of the proposed space-time XFEM through practical transient problems with both fixed and moving interfaces.

The remainder of this chapter is summarized as follows: Section 3.2 is a brief summary of a general weak form for the XFEM as a conventional method. Section 3.3 denotes the Heaviside-enriched space-time XFEM in comparison with Section 3.2. It should be noted that the XFEM means the Heaviside-enriched XFEM at the following discussions. In Section 3.4, characteristic numerical implementations in terms of space-time integration points and the face-oriented ghost-penalty stabilization are summarized. Section 3.5 is a numerical example of spatially two-dimensional transient structural analysis with nonlinear elastic material. Besides, two numerical examples of spatially two-dimensional transient fluid analysis using the incompressible Navier-Stokes fluid are demonstrated in Section 3.6. As a fixed interface problem, a well-known fluid benchmark problem: DFG 2D-3 problem (Schäfer and Turek [80]) is computed. As a moving interface problem, flow around an in-line oscillating cylinder is computed.

3.2 Extended Finite Element Method (XFEM)

This section is a brief summary of a general weak form for the XFEM using (2.8). The reader is referred to Chapter 3 for the outline of the XFEM. The XFEM is based on a weak form of partial differential equations, which is integrated over entire spatial domain. Assuming a transient two-phase problem, $g_i^p(\mathbf{u}^n, \dot{\mathbf{u}}^n, t^n)$ is a volume contribution of governing equations defined in the spatial volume of phase p at time t^n : $\Omega^{n,p}$, $n_i^p(\mathbf{u}^n, \dot{\mathbf{u}}^n, t^n)$ is a Neumann boundary condition of phase p at time t^n : $\Gamma_N^{n,p}$, and $h_i(\mathbf{u}^n, \dot{\mathbf{u}}^n, t^n)$ is a boundary condition including discontinuities across an interface at time t^n : Γ_{int}^n :

$$\text{Governing equations (volume):} \quad g_i^p(\mathbf{u}^n, \dot{\mathbf{u}}^n, t^n) = 0 \quad \text{in } \Omega^{n,p}, \quad (3.1)$$

$$\text{Neumann boundary conditions:} \quad n_i^p(\mathbf{u}^n, \dot{\mathbf{u}}^n, t^n) = 0 \quad \text{on } \Gamma_N^{n,p}, \quad (3.2)$$

$$\text{Interface conditions:} \quad h_i(\mathbf{u}^n, \dot{\mathbf{u}}^n, t^n) = 0 \quad \text{on } \Gamma_{\text{int}}^n . \quad (3.3)$$

A general weak form using (3.1) ~ (3.3) at time t^n can be denoted as follows:

$$\begin{aligned} & \sum_{p=A,B} \int_{\Omega^{n,p}} d\Omega w_i^p g_i^p(\mathbf{u}^n, \dot{\mathbf{u}}^n, t^n) + \sum_{p=A,B} \int_{\Gamma_N^{n,p}} d\Gamma w_i^p n_i^p(\mathbf{u}^n, \dot{\mathbf{u}}^n, t^n) \\ & + \int_{\Gamma_{\text{int}}^n} d\Gamma w_i^{\text{int}} h_i(\mathbf{u}^n, \dot{\mathbf{u}}^n, t^n) = 0 . \end{aligned} \quad (3.4)$$

Here, w_i^p is an admissible test function of phase $p = \{A, B\}$ and w_i^{int} is an admissible test function on the interface between phase A and B .

As the finite element discretization is applied only in the spatial domain, a time derivative of the state variables $\dot{\mathbf{u}}$ is approximated by the time stepping scheme. In this case, $\dot{\mathbf{u}}$ is a functional of a set of \mathbf{u} , $\dot{\mathbf{u}}$ and $\ddot{\mathbf{u}}$ up to time t^n : $\{\mathbf{u}\}^n$, $\{\dot{\mathbf{u}}\}^n$ and $\{\ddot{\mathbf{u}}\}^n$. Major approximations of $\dot{\mathbf{u}}^n$ are as follows:

$$\text{BDF1:} \quad \dot{\mathbf{u}}^n = \dot{\mathbf{u}}^n[\mathbf{u}^n, \mathbf{u}^{n-1}] = \frac{1}{\Delta t}(\mathbf{u}^n - \mathbf{u}^{n-1}) , \quad (3.5)$$

$$\text{BDF2:} \quad \dot{\mathbf{u}}^n = \dot{\mathbf{u}}^n[\mathbf{u}^n, \mathbf{u}^{n-1}, \mathbf{u}^{n-2}] = \frac{3}{2\Delta t} \left(\mathbf{u}^n - \frac{4}{3}\mathbf{u}^{n-1} + \frac{1}{3}\mathbf{u}^{n-2} \right) , \quad (3.6)$$

$$\begin{aligned} \text{Newmark:} \quad \dot{\mathbf{u}}^n &= \dot{\mathbf{u}}^n[\mathbf{u}^n, \mathbf{u}^{n-1}, \dot{\mathbf{u}}^{n-1}, \ddot{\mathbf{u}}^{n-1}] \\ &= \frac{\gamma}{\beta\Delta t}(\mathbf{u}^n - \mathbf{u}^{n-1}) + \left(1 - \frac{\gamma}{\beta}\right)\dot{\mathbf{u}}^{n-1} + \left(1 - \frac{\gamma}{2\beta}\right)\Delta t\ddot{\mathbf{u}}^{n-1} , \end{aligned} \quad (3.7)$$

where Δt is a time increment, γ and β are parameters for the Newmark method (3.7).

3.3 Space-Time Extended Finite Element Method (Space-time XFEM)

Section 3.2 shows a general weak form for the XFEM and time derivative terms are approximated by time stepping schemes. Spatial and temporal domains are distinguished as separated fields and different discretization schemes are used in both domains. However, there is no distinction between space and time as mathematical coordinate axes. Therefore, the finite element discretization also can be applied to the temporal domain.

This section summarizes the space-time extended finite element method (space-time

XFEM) as a combination of the XFEM and the space-time formulation. The space-time XFEM applies the finite element discretization in both space and time. State variables are approximated by the finite element method in a space-time domain without the need for a time stepping scheme. The weak form is integrated over an entire space-time domain. The space-time volume, which is generally denoted by Q , has one order higher dimension than the spatial volume Ω . A boundary of Q is denoted as P . Table 3.1 is the summary of the notation of volume and boundary of a space-time slab.

Table 3.1: Notation of volume and boundary

| | Spatial Domain | Space-Time Slab |
|----------|-------------------|--|
| Volume | $\Omega, d\Omega$ | $Q = \Omega \oplus T, dQ = d\Omega dt$ |
| Boundary | $\Gamma, d\Gamma$ | $P = \Gamma \oplus T, dP = d\Gamma dt$ |

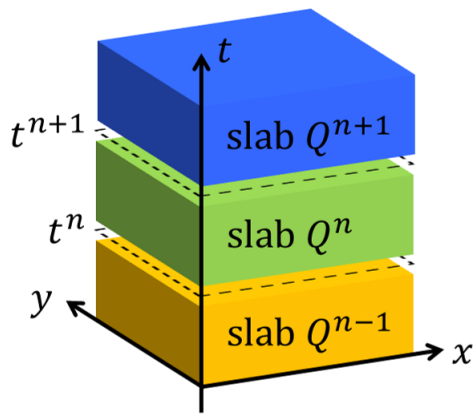


Figure 3.1: Space-time slab

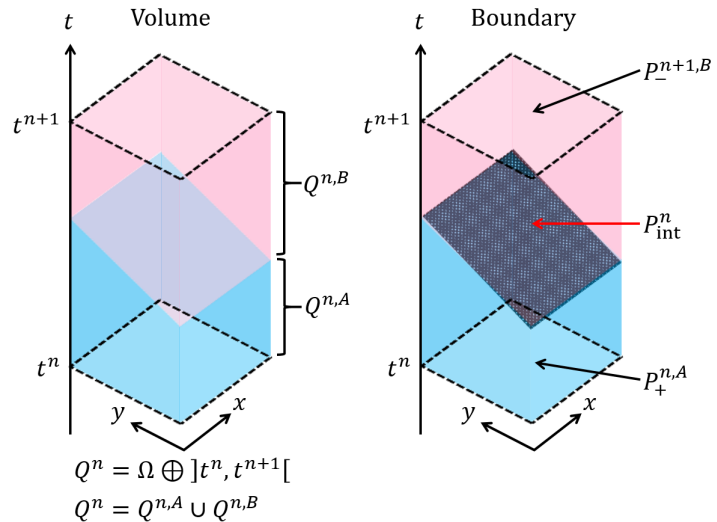


Figure 3.2: Volume and boundaries in a space-time slab Q^n

In this thesis, the space-time XFEM uses a continuous Galerkin method in space. A discontinuous Galerkin method [81, 82] is used in time to enhance the convergence by weakly averaging continuities on temporal boundaries. A key concept of the space-time XFEM is a space-time slab. A space-time slab is a subdivided portion of an entire space-time domain along time. Figure 3.1 is an image of subdivision of a space-time domain into space-time

slabs. Adjacent space-time slabs are disconnected due to a discontinuous Galerkin method to weakly enforce continuities between slabs. Figure 3.2 is an image of space-time volume and boundaries in a space-time slab Q^n (middle slab in Figure 3.1). Q^n does not contain time t^n and t^{n+1} . Its lower and upper temporal bounds are denoted as t_+^n and t_-^{n+1} , which deviate from t^n and t^{n+1} in an infinitesimal value δ like (3.8):

$$t_+^n \equiv t^n + \delta, \quad t_-^{n+1} \equiv t^{n+1} - \delta. \quad (3.8)$$

Boundary P of this slab Q^n is denoted as P^n . $P_-^{n+1,p}$ and $P_+^{n,p}$ denote boundaries on the upper temporal bound t_-^{n+1} and lower temporal bound t_+^n related to phase p . P_{int}^n denotes an interface in a space-time slab Q^n . Furthermore, a space-time slab is divided into space-time elements Q^n based on the finite element discretization. In this thesis, the number of space-time element along time axis is always one.

The space-time XFEM in this thesis applies the Heaviside-enriched XFEM (2.8) to a generalized coordinate including space and time $\mathbf{z} = (\mathbf{x}, t)$:

$$\mathbf{u}(\mathbf{z}) = \sum_{m=1}^M \left(H(-\phi(\mathbf{z})) \sum_{i=1}^{N_e^{\text{st}}} N_i(\mathbf{z}) \delta_{mq}^{A,i} \mathbf{u}_i^{A,m} + H(\phi(\mathbf{z})) \sum_{i=1}^{N_e^{\text{st}}} N_i(\mathbf{z}) \delta_{mr}^{B,i} \mathbf{u}_i^{B,m} \right), \quad (3.9)$$

where N_e^{st} is the number of nodes in a space-time element and different from N_e of a spatial element described at the previous section. A space-time element has one order higher dimension than a spatial element: if a spatial element is a 2D element (e.g. QUAD4, $N_e = 4$), a space-time element should be a 3D element (e.g. HEXA8, $N_e^{\text{st}} = 8$). This thesis focuses on spatially two-dimensional problems and thus, the space-time XFEM uses trilinear shape functions in a space-time element (spatially bilinear and temporally linear element).

To consider the weak form for the space-time XFEM, assuming $g_i^p(\mathbf{u}, \dot{\mathbf{u}}, t)$ is a volume contribution of governing equations defined in the volume of phase p in a space-time slab: $Q^{n,p}$, $n_i^p(\mathbf{u}, \dot{\mathbf{u}}, t)$ is a Neumann boundary condition of phase p of a space-time slab: $P_N^{n,p}$, and $h_i(\mathbf{u}, \dot{\mathbf{u}}, t)$ is an interface condition on P_{int}^n including discontinuities across interface

between two phases using Nitsche's method. The range of time t in this space-time slab is $t = [t_+^n, t_-^{n+1}]$:

$$\text{Governing equations (volume):} \quad g_i^p(\mathbf{u}, \dot{\mathbf{u}}, t) = \alpha_i^p \dot{u}_i^p + f_i^p(\mathbf{u}, t) = 0 \text{ in } Q^{n,p}, \quad (3.10)$$

$$\text{Neumann boundary conditions:} \quad n_i^p(\mathbf{u}, \dot{\mathbf{u}}, t) = 0 \text{ on } P_N^{n,p}, \quad (3.11)$$

$$\text{Interface conditions:} \quad h_i(\mathbf{u}, \dot{\mathbf{u}}, t) = 0 \text{ on } P_{\text{int}}^n. \quad (3.12)$$

For simplicity, this section assumes that g_i^p is separated into a term related to $\dot{\mathbf{u}}$ and the rest f_i^p which is independent of $\dot{\mathbf{u}}$ like (3.10). α_i^p is a coefficient of \dot{u}_i in this case. Using the space-time XFEM, a time derivative $\dot{\mathbf{u}}$ is constructed by the shape function in time directly because the finite element discretization is also applied in the temporal domain. Thus, additional approximation techniques for $\dot{\mathbf{u}}$ like (3.5), (3.6) and (3.7) are not necessary in this case.

As a discontinuous Galerkin method is applied along the time axis, the solution is discontinuous between space-time slabs (e.g. between Q^n and Q^{n-1}). As a correction of a discontinuous Galerkin method, the following continuity condition between is added to obtain continuous solution in time:

$$\text{Continuity between slabs:} \quad [[\alpha_i^p u_i^p]]_{\pm}^n \equiv \alpha_i^p|_+^n u_i^p|_+^n - \alpha_i^p|_-^n u_i^p|_-^n = 0 \quad \text{on } P_+^{n,p}. \quad (3.13)$$

$u_i^p|_+^n$ is a boundary value on $P_+^{n,p}$ in a current space-time slab Q^n . On the other hand, $u_i^p|_-^n$ is a boundary value on $P_-^{n,p}$ in a previous space-time slab Q^{n-1} .

Considering (3.10) - (3.13), the general weak form of governing equations in a space-time slab Q^n is written as follows:

$$\begin{aligned} & \sum_{p=A,B} \int_{Q^{n,p}} dQ w_i^p g_i^p(\mathbf{u}, \dot{\mathbf{u}}, t) + \sum_{p=A,B} \int_{P_N^{n,p}} dP w_i^p n_i^p(\mathbf{u}, \dot{\mathbf{u}}, t) \\ & + \int_{P_{\text{int}}^n} dP w_i^{\text{int}} h_i(\mathbf{u}, \dot{\mathbf{u}}, t) + \sum_{p=A,B} \int_{P_+^{n,p}} d\Omega w_i^p|_+^n [[\alpha_i^p u_i^p]]_{\pm}^n = 0. \end{aligned} \quad (3.14)$$

Here, w_i^p is an admissible test function in phase $p = \{A, B\}$, w_i^{int} is an admissible test

function on the interface of two phases A and B , and $w_i^p|_+^n$ is an admissible test function on $P_+^{n,p}$ within a current space-time slab Q^n . The forth integral of LHS of (3.14) is an additional contribution in the space-time XFEM, comparing the weak form of the XFEM (3.4). This integral is a correction term of a discontinuous Galerkin method from a continuous Galerkin method. As $P_+^{n,p}$ is purely a spatial domain, an integral over $P_+^{n,p}$ is performed only in the spatial domain $\Omega^{n,p}$. By using (3.14), a transient problem is completely discretized by the finite element discretization without time stepping schemes.

3.4 Numerical Implementation

The space-time XFEM uses the finite element discretization in space and time. Thus, integrating numerically over the space-time slab Q^n and the boundary terms in (3.14) leads to different integration points in comparison with the XFEM that uses the finite element discretization only in space. While the higher-dimensional simplex triangulation is usually used for defining integration points in a space time slab [48, 49, 47], this section proposes a simple space-time integration scheme named the elementwise temporal layer approach. First, space-time elements are subdivided into layers which correspond to different spatial intersection configurations. These layers are called as temporal layers. Then, temporal integration points are defined in each temporal layer based on the quadrature rule. Each temporal layer is cut by planes on these temporal integration points parallel to the spatial domain. The cross section created by this cut are called as the temporal slices in this thesis. Each space-time element has different number of temporal slices based on its intersection configuration. Finally, integration points for a space-time volume are distributed on each temporal slice using the same numerical integration scheme used in the standard XFEM. More precise space-time integration can be achieved than [50] by evaluating all intersection configuration including small volume created by moving interfaces.

This section summarizes the elementwise temporal layer approach and placement of in-

tegration points for space-time volume and interface in the space-time XFEM. The face-oriented ghost-penalty method is applied in the space-time XFEM like [50] to mitigate ill-conditioning problem due to small intersected space-time volume.

3.4.1 Elementwise Temporal Layer Approach

The space-time XFEM needs integration points distributed in an entire space-time slab. In general, direct decomposition methods like the simplex triangulation are used to determine the location of these integration points. Another way is the summation of spatial integration on multiple temporal integration points. Considering a fixed interface problem, the intersection configuration defined by the level set function ϕ is time-invariant. Integration points for the space-time XFEM can be defined by the duplication of integration points in the spatial domain at any time t . On the other hand, considering a moving interface problem, the location of space-time interfaces varies in time and thus, the spatial intersection configuration change in time. Therefore, an intersected space-time element has multiple types of spatial intersection configuration due to moving interfaces.

This thesis introduces an elementwise temporal layer, which is a temporal section corresponding to an individual spatial intersection configuration in an intersected space-time element. This thesis uses trilinear space-time elements (QUAD4 in space and linear in time). As the linear shape function is used along time, the level set function ϕ changes linearly in time. The detection of the change of the spatial intersection configuration is algebraically and uniquely defined by checking values of nodal level set functions. In each temporal layer, multiple temporal integration points are defined by a quadrature rule. These temporal integration points are called as temporal slices. As the linear shape function is used in time, the number of temporal slices in each temporal layer should be two or more for a full integration. The number of temporal slices changes the effective time increment. Thus, using more than two slices is beneficial from the viewpoint to use a large time increment. In this thesis, three

temporal slices are defined in each temporal layer for verifying the influence of the number of temporal slices. Finally, integration points for space-time volume are defined on each temporal slice.

3.4.1.1 One Temporal Layer Case

Just one temporal layer can be used if the intersection configuration is time-invariant. This temporal layer is identical with the entire space-time element. A standard space-time element (non-intersected element) and a space-time element cut by the time-invariant interface (fixed interface) belong to this case.

3.4.1.2 Two Temporal Layers Case

Multiple temporal layers are needed when a moving interface exists. As trilinear space-time elements (QUAD4 in space and linear in time $t = [t_+^n, t_-^{n+1}]$) are used in this thesis, temporal layers are easily detected by the change of nodal level set function values in time. The left figure of Figure 3.3 illustrates the detection of elementwise temporal layers by nodal level set function values. A nodal level set function at spatial node 3; ϕ_3 , changes from a positive to a negative value, creating two topological different intersection configurations in this space-time element. A red dashed line indicates the interface between two temporal layers. The interface is the set of all point with time t^* which is defined by ϕ_3 as follows:

$$t^* = -\frac{\phi_3(t_+^n)}{\phi_3(t_-^{n+1}) - \phi_3(t_+^n)}(t_-^{n+1} - t_+^n) + t_+^n. \quad (3.15)$$

Therefore, two layers are detected across t^* in this space-time element. Colored slices at the right figure of Figure 3.3 is called as elementwise temporal slices. These slices indicate temporal integration points. The example of Figure 3.3 has six temporal slices (three slices in each temporal layer).

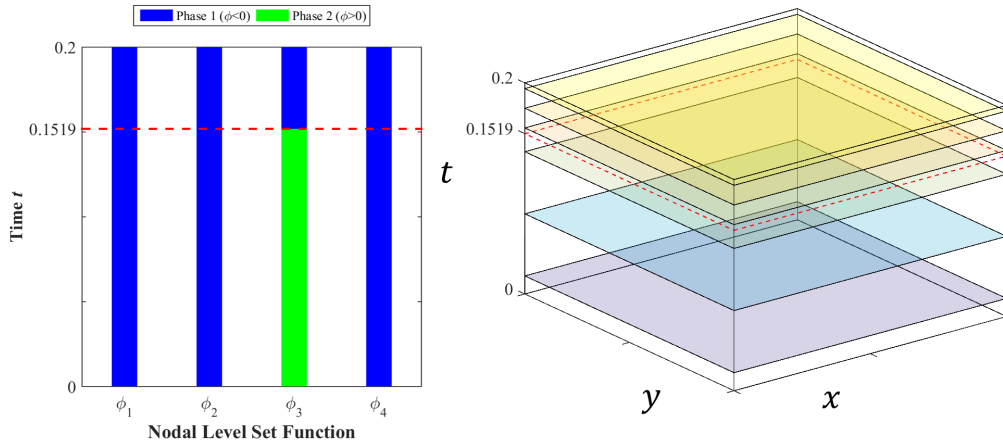


Figure 3.3: Temporal layers and temporal integration points (2 layers case)

3.4.1.3 Three Temporal Layers Case

The procedure for the three temporal layers case is identical to the case of two temporal layers. Assuming that the nodal level set functions at node 3 and 4, ϕ_3 and ϕ_4 , change from positive to negative values as shown on the left figure of Figure 3.4, the temporal layers are defined by the following two time: t^{*1} and t^{*2} ($t^{*1} < t^{*2}$), and three temporal layers are defined:

$$t^{*1} = -\frac{\phi_4(t_+^n)}{\phi_4(t_-^{n+1}) - \phi_4(t_+^n)}(t_-^{n+1} - t_+^n) + t_+^n, \quad (3.16)$$

$$t^{*2} = -\frac{\phi_3(t_+^n)}{\phi_3(t_-^{n+1}) - \phi_3(t_+^n)}(t_-^{n+1} - t_+^n) + t_+^n. \quad (3.17)$$

The right figure of Figure 3.4 shows an example of a configuration of elementwise temporal slices with nine temporal slices (three slices in each temporal layer).

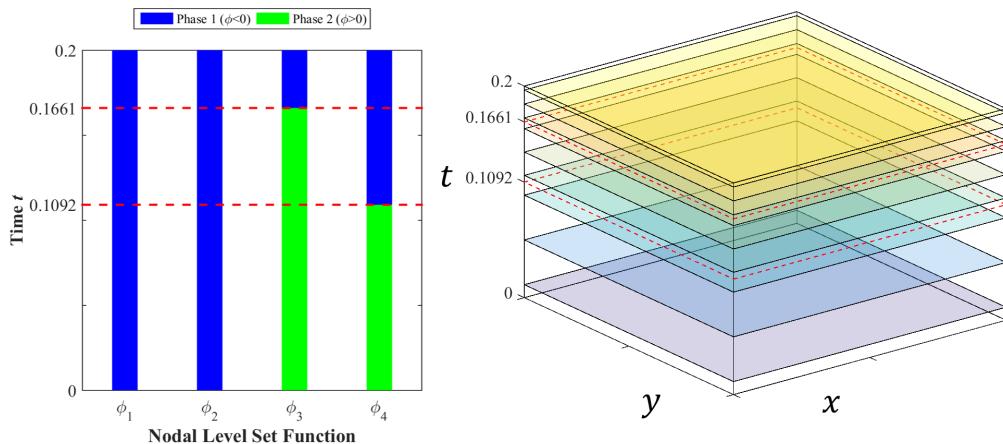


Figure 3.4: Temporal layers and temporal integration points (3 layers case)

3.4.2 Integration Points for Space-Time Volume

Integration points for the space-time volume are determined for each temporal slice based on the elementwise temporal layer approach. The method for setting volume integration points on one temporal slice is exactly identical to the standard method of the XFEM and thus, higher-dimensional simplex triangulation [48, 49, 47] is not necessary. The spatial intersection configuration is created by Delaunay triangulation on each temporal slice such that each triangle is occupied by exactly one phase and the interface is discretized by triangle edges. Integration points for space-time volume are defined on each triangle. Figure 3.5 shows two examples of the setting of integration points for space-time volume in one space-time element. The symbol $*$ marks an integration point for volume integral and red lines indicate edges of a space-time interface within the space-time element. The left and right figures of Figure 3.5 are two and three temporal layer cases corresponding to Figures 3.3 and 3.4 respectively.

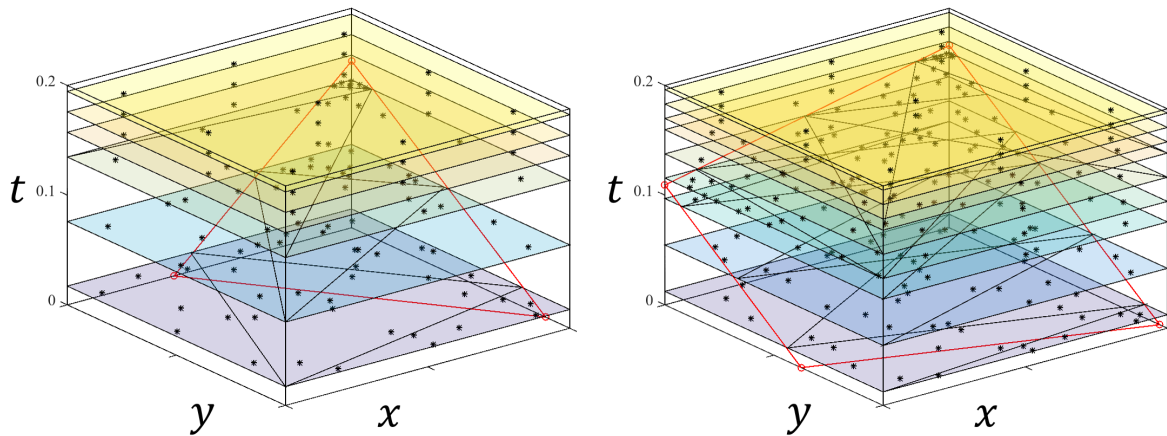


Figure 3.5: integration points for space-time volume
(left: 2 temporal layers, right: 3 temporal layers)

As Delaunay triangulation is applicable to 2D and 3D problems, the above approach is directly applicable to spatially three-dimensional problems.

Integration weights for these integration points are computed by the product of spatial

integration weights and temporal integration weights. Focusing on one temporal slice and assuming w_t as its temporal weight, integration weights of integration points for space-time volume on this temporal slice; $\tilde{\mathbf{w}}_{st}^{vol}$, are computed by w_t and spatial volume integration weights for these points; \mathbf{w}_s^{vol} :

$$\tilde{\mathbf{w}}_{st}^{vol} = w_t \mathbf{w}_s^{vol} . \quad (3.18)$$

3.4.3 Integration Points for Space-Time Interface

This section describes the approach for computing integrals over a space-time interface. In the standard XFEM for two-dimensional spatial domain, interface integration points are generated on a line corresponding to a spatial interface at some time t . On the other hand, an interface in the space-time XFEM (spatially two-dimensional case) is a three-dimensional plane (one order higher dimension space than the standard XFEM) within a space-time element. Integration points for space-time interface should be generated onto this three-dimensional plane. Therefore, these interface integration points are independent of the volume integration approach using elementwise temporal layers and temporal slices.

The shape of interfaces in a spatially two-dimensional space-time element is limited to a triangle, quadrangle, pentagon and hexagon. In this research, a space-time interface is partitioned by Delaunay triangulation and integration points for this space-time interface are defined on every triangle. Figure 3.6 shows examples of space-time interface integration points for the cases of triangle and hexagon interfaces. The case of a triangle interface (left figure) does not need Delaunay triangulation. The case of a hexagon interface (right figure) uses Delaunay triangulation to generate four triangles. The outer red line marks the configuration of a space-time interface and inner red lines indicate the edges of the triangles created by Delaunay triangulation.

Based on the proposed elementwise temporal layer approach, if the spatial dimension is d , the setting of volume integration points and interface integration points for the space-

time XFEM can be performed by the same techniques applicable to d -dimensional standard XFEM. Thus, the proposed approach does not require higher-dimensional decomposition like the simplex triangulation used by [47]. This provides a great advantage in terms of the actual implementation. Integration weights for these points are determined by the quadrature rule on each triangle defined on a space-time interface.

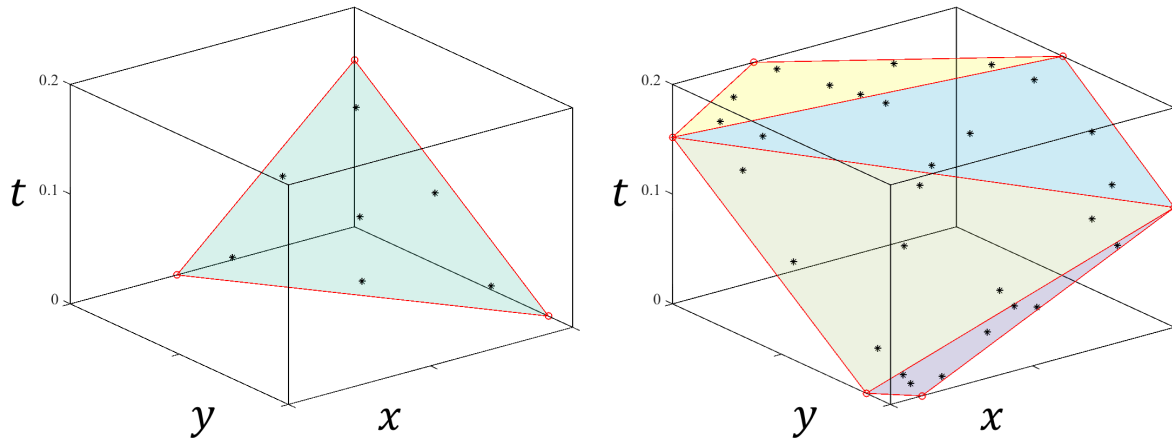


Figure 3.6: integration points for space-time interface
(left: triangle interface, right: hexagon interface)

3.4.4 Face-Oriented Ghost-Penalty Stabilization

Interfaces are immersed in the background meshes based on the iso-contour of the level set function ϕ . Intersections might produce very small space-time integration subdomains which lead an ill-conditioning problem. This ill-conditioning problem has severe impact especially for moving interface problems, because the motion of an interface usually creates tiny integration subdomains configuration when this interface moves across an elemental edge.

The main issue of this ill-conditioning is that numerical fluxes are insufficiently controlled by the weak form of the governing equations. The reader is referred to [34, 52] for the detailed discussion in terms of this ill-conditioning problem. The face-oriented ghost-penalty method [55, 56] has been proposed to mitigate this ill-conditioning problem. The main idea of the

face-oriented ghost-penalty method is to penalize a jump of numerical flux across elemental edges. A general weak form of the face-oriented ghost-penalty method as follows:

$$R_{\text{gp}} = \sum_i \sum_{m=1}^{m_i^b} \sum_{\Gamma_{\text{gp}} \in \mathcal{F}} \sum_{p=A,B} \int_{\Gamma_{\text{gp}}} d\Gamma \eta_i^{\text{gp}} \llbracket D^m w_i^p \rrbracket_{\text{gp}} \llbracket D^m u_i^p \rrbracket_{\text{gp}} , \quad (3.19)$$

where $D^m(\cdot)$ means a normal derivative of order m : $D^m(\cdot) = \frac{\partial^m(\cdot)}{\partial x_j^m} \hat{n}_j$, m_i^b is the highest order of interpolation of the i -th state variable u_i and η_i^{gp} is a penalty factor of the face-oriented ghost-penalty method related to u_i . \mathcal{F} denotes a set of elemental faces of intersected elements Γ_{gp} . $\llbracket \cdot \rrbracket_{\text{gp}}$ denotes a jump operator of a state variable across the face Γ_{gp} between two adjacent elements, element 1 Ω_e^1 and element 2 Ω_e^2 :

$$\llbracket a \rrbracket_{\text{gp}} = a|_{\Omega_e^1} - a|_{\Omega_e^2} . \quad (3.20)$$

When bilinear elements are used in space as done in this thesis, (3.19) is computed only up to the first interpolation order $m = 1$:

$$R_{\text{gp}} = \sum_i \sum_{\Gamma_{\text{gp}} \in \mathcal{F}} \sum_{p=A,B} \int_{\Gamma_{\text{gp}}} d\Gamma \eta_i^{\text{gp}} \left[\left[\frac{\partial w_i^p}{\partial x_j} \right] \right]_{\text{gp}} \hat{n}_j \left[\left[\frac{\partial u_i^p}{\partial x_k} \right] \right]_{\text{gp}} \hat{n}_k . \quad (3.21)$$

In the face-oriented ghost-penalty method, the jump terms are integrated over the entire face, individually for each phase that is considered. Thus, this method integrates twice over an intersected edge in a solid-solid problem, using different interpolation functions and state variables.

This method is also useful to mitigate an ill-conditioning problem due to small intersected space-time volume in the space-time XFEM. The extension of (3.21) for the space-time XFEM is as follows based on the same idea of [50]:

$$\tilde{R}_{\text{gp}} = \sum_i \sum_{P_{\text{gp}} \in \mathcal{G}} \sum_{p=A,B} \int_{P_{\text{gp}e}} dP \eta_i^{\text{gp}} \left[\left[\frac{\partial w_i^p}{\partial z_j} \right] \right]_{\text{gp}} \hat{N}_j \left[\left[\frac{\partial u_i^p}{\partial z_k} \right] \right]_{\text{gp}} \hat{N}_k , \quad (3.22)$$

where \mathcal{G} denotes a set of elemental faces of space-time intersected elements P_{gp} , \mathbf{z} is the generalized coordinate including space and time $\mathbf{z} = (\mathbf{x}, t)$, and \hat{N}_i denotes the space-time

normal. Integration points for (3.22) are set on faces shared by space-time element neighbors P_{gp} to stabilize the numerical flux around space-time interfaces. As a space-time slab has only one element along the time axis, P_{gp} is the $x-t$ or $y-t$ plane of an intersected space-time element. Figure 3.7 is an example of setting of these integration points between adjacent two space-time intersected elements.

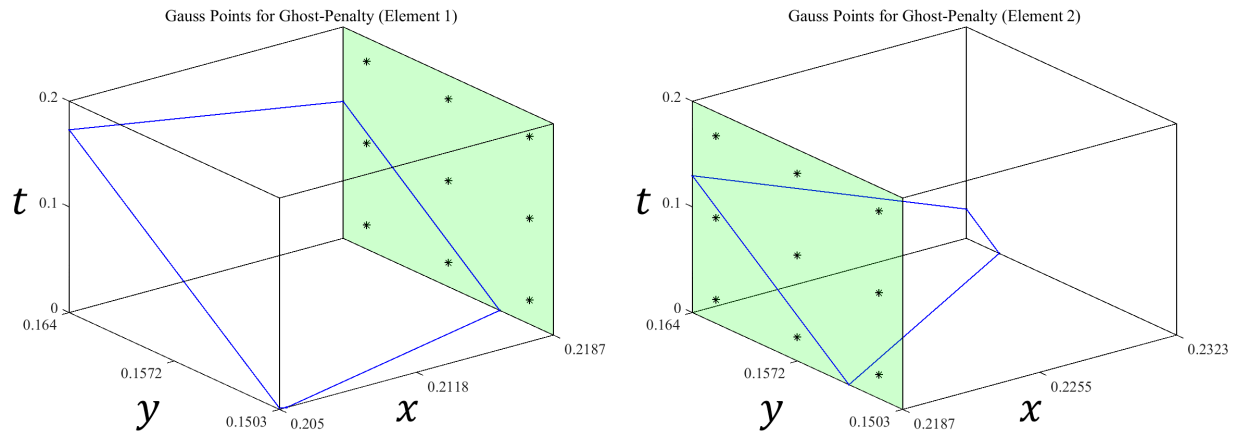


Figure 3.7: Space-time integration points for face-oriented ghost-penalty stabilization

3.5 Structural Analysis using Space-Time XFEM

This section describes a spatially two-dimensional structural problem using both the standard XFEM (XFEM that discretizes only space) and the space-time XFEM. First, the weak forms for both methods are summarized. The weak form for the space-time XFEM has an additional term due to using a discontinuous Galerkin method in time. The spatial domain is discretized by bilinear finite elements (QUAD4) in both method and the temporal domain is discretized by linear finite elements. Thus, trilinear elements are used in the space-time XFEM. This problem is a fixed interface problem and modeled by a total Lagrangian formulation of the elasto-dynamics. Therefore, the number of temporal layer is always one in the space-time XFEM. This thesis uses three temporal slices for each temporal layer in the space-time XFEM. The Newmark method (3.7: $\gamma = 0.9, \beta = 0.5$) is used to integrate

the governing equations in time when using the standard XFEM. At each time step, the nonlinear problem is solved by the Newton's method and the convergence criterion requires a drop of the norm of the residual of 10^{-6} relative to the norm of the initial residual. In each Newton step, the system of linearized equations is solved by GMRES (generalized minimal residual method) [83].

Results of both the XFEM and the space-time XFEM are compared. The proposed space-time allows for a larger time increment Δt than the standard XFEM. In addition, this example verifies the implementation of Nitsche's method for the space-time XFEM. To this end, a dummy interface is introduced, i.e. both phases represent the same material. The results of the space-time XFEM and space-time FEM without the dummy interface are compared.

3.5.1 Governing Equations and Finite Element Discretization

This section assumes the elasto-dynamics based on the finite strain theory and the hyperelastic material. The material damping is not considered in this section. Assuming a two-phase transient structural problem, the structural response is governed by the following momentum equation:

$$\rho^p \frac{\partial^2 U_i^p}{\partial t^2} = \frac{\partial \Pi_{iJ}^p}{\partial X_J} + \rho^p B_i^p \quad \text{in } \Omega_0^p . \quad (3.23)$$

Here, ρ^p is density, U_i^p is displacement, Π_{iJ}^p is the first Piola-Kirchhoff stress tensor, and B_i^p is a body force constant at phase $p = \{1, 2\}$. To use linear shape functions in time and restrict time derivative terms up to the first derivative in the space-time XFEM, (3.23) is split into two equations by introducing solid velocity V_i^p :

$$\rho^p \frac{\partial V_i^p}{\partial t} = \frac{\partial \Pi_{iJ}^p}{\partial X_J} + \rho^p B_i^p \quad \text{in } \Omega_0^p , \quad (3.24)$$

$$\frac{\partial U_i^p}{\partial t} = V_i^p \quad \text{in } \Omega_0^p . \quad (3.25)$$

A compressible neo-Hookean model (Belytschko et al. [84]) is used as a material constitutive law for the solid phase:

$$W^p = \frac{1}{2}\lambda^p (\ln(\det F^p))^2 + \frac{1}{2}\mu^p (C_{II}^p - 3 - 2 \ln(\det F^p)) , \quad (3.26)$$

$$S_{IJ}^p = 2 \frac{\partial W^p}{\partial C_{IJ}^p} = \lambda^p \ln(\det F^p) C_{IJ}^{p-1} + \mu^p (\delta_{IJ} - C_{IJ}^{p-1}) , \quad (3.27)$$

where W^p is the hyperelastic function (strain energy density function), S^p is the second Piola-Kirchhoff stress tensor, F^p is the deformation gradient tensor, C^p is the right Cauchy-Green tensor, λ^p and μ^p mean the Lamé constants at phase p . These λ^p and μ^p can be expressed in terms of Young's modulus E^p and Poisson's ratio ν^p as follows:

$$\lambda^p = \frac{\nu^p E^p}{(1 + \nu^p)(1 - 2\nu^p)} , \quad (3.28)$$

$$\mu^p = G^p = \frac{E^p}{2(1 + \nu^p)} . \quad (3.29)$$

On the outer surface, the traction free boundary condition is applied. The traction boundary condition and the continuity of displacement and velocity are applied at the interface between two phases in the initial configuration $\Gamma_{0\text{int}}$:

$$[[T_i]] = T_i^1 - T_i^2 = \Pi_{iJ}^1 \hat{n}_{0J}^1 - \Pi_{iJ}^2 \hat{n}_{0J}^2 = 0 \quad \text{on } \Gamma_{0\text{int}} , \quad (3.30)$$

$$[[U_i]] = U_i^1 - U_i^2 = 0 \quad \text{on } \Gamma_{0\text{int}} , \quad (3.31)$$

$$[[V_i]] = V_i^1 - V_i^2 = 0 \quad \text{on } \Gamma_{0\text{int}} , \quad (3.32)$$

where $\hat{\mathbf{n}}_0^p$ is an outward normal from phase p in the initial configuration.

The finite element discretization of the XFEM at time t^n is as follows based on the total Lagrangian formulation:

$$R = R_{\text{vol}} + R_{\text{int}} + R_{\text{gp}} = 0 , \quad (3.33)$$

$$R_{\text{vol}} = \sum_{p=1}^2 \left[\int_{\Omega_0^p} d\Omega \delta U_i^p \left(\rho \frac{\partial V_i^p}{\partial t} - \rho^p B_i^p \right) + \int_{\Omega_0^p} d\Omega \frac{\partial \delta U_i^p}{\partial X_J} \Pi_{iJ}^p \right]$$

$$+ \sum_{p=1}^2 \int_{\Omega_0^p} d\Omega \delta V_i^p \rho^p \left(\frac{\partial U_i^p}{\partial t} - V_i^p \right), \quad (3.34)$$

$$R_{\text{int}} = - \int_{\Gamma_{0\text{int}}} d\Gamma \llbracket \delta U_i \rrbracket \{ \Pi_{iJ} \} \hat{n}_{0J}^1 - \int_{\Gamma_{0\text{int}}} d\Gamma \{ \delta \Pi_{iJ} \} \hat{n}_{0J}^1 \llbracket U_i \rrbracket + \int_{\Gamma_{0\text{int}}} d\Gamma \llbracket \delta U_i \rrbracket \eta_u^{\text{int}} \llbracket U_i \rrbracket, \quad (3.35)$$

$$R_{\text{gp}} = \sum_{p=1}^2 \sum_{e \in \Gamma_{0\text{gp}}^p} \int_{\Gamma_{0\text{gp}e}^p} d\Gamma \eta_v^{\text{gp}} \left[\frac{\partial \delta V_i^p}{\partial X_J} \right]_{\text{gp}} \hat{n}_{0J}^p \left[\frac{\partial V_i^p}{\partial X_K} \right]_{\text{gp}} \hat{n}_{0K}^p \\ + \sum_{p=1}^2 \sum_{e \in \Gamma_{0\text{gp}}^p} \int_{\Gamma_{0\text{gp}e}^p} d\Gamma \eta_u^{\text{gp}} \left[\frac{\partial \delta U_i^p}{\partial X_J} \right]_{\text{gp}} \hat{n}_{0J}^p \llbracket \Pi_{iK}^p \rrbracket_{\text{gp}} \hat{n}_{0K}^p, \quad (3.36)$$

where δU_i^p and δV_i^p are admissible test functions for displacement U_i^p and velocity V_i^p at each phase p and Ω_0^p is a domain of phase p in the initial configuration. R_{vol} , R_{int} and R_{gp} are residuals of the volume contribution, the interface contribution and the contribution by the face-oriented ghost-penalty method, respectively. In (3.36), the first PK stress Π^p is used as numerical flux by following the work of Lawry et al. [75]. To enforce the interface conditions (3.30)-(3.36), the interface contribution (3.35) is computed by the symmetric Nitsche method. When using a time stepping scheme, time derivative terms are approximated by the Newmark method (3.7) as a standard time stepping scheme.

On the other hand, the finite element discretization is applied also to approximate the time derivative terms in the space-time XFEM. The weak form of the space-time XFEM is defined in a space-time slab Q^n as follows:

$$\tilde{R} = \tilde{R}_{\text{vol}} + \tilde{R}_{\text{int}} + \tilde{R}_{\text{disc}} + \tilde{R}_{\text{gp}} = 0, \quad (3.37)$$

$$\tilde{R}_{\text{vol}} = \sum_{p=1}^2 \left[\int_{Q_0^{n,p}} dQ \delta U_i^p \left(\rho^p \frac{\partial V_i^p}{\partial t} - \rho^p B_i^p \right) + \int_{Q_0^{n,p}} dQ \frac{\partial \delta U_i^p}{\partial X_J} \Pi_{iJ}^p \right] \\ + \sum_{p=1}^2 \int_{Q_0^{n,p}} dQ \delta V_i^p \rho^p \left(\frac{\partial U_i^p}{\partial t} - V_i^p \right), \quad (3.38)$$

$$\tilde{R}_{\text{int}} = - \int_{P_{0\text{int}}^n} dP \llbracket \delta U_i \rrbracket \{ \Pi_{iJ} \} \hat{N}_{0J}^p - \int_{P_{0\text{int}}^n} dP \{ \delta \Pi_{iJ} \} \hat{N}_{0J}^p \llbracket U_i \rrbracket \\ + \int_{P_{0\text{int}}^n} dP \llbracket \delta U_i \rrbracket \eta_u^{\text{int}} \llbracket U_i \rrbracket, \quad (3.39)$$

$$\tilde{R}_{\text{disc}} = \sum_{p=1}^2 \int_{P_{0+}^{n,p}} d\Omega \delta U_i^p|_+^n \rho^p [U_i^p]_{\pm}^n + \sum_{p=1}^2 \int_{P_{0+}^{n,p}} d\Omega \delta V_i^p|_+^n \rho^p [V_i^p]_{\pm}^n, \quad (3.40)$$

$$\begin{aligned} \tilde{R}_{\text{gp}} = & \sum_{p=1}^2 \sum_{e \in P_{0\text{gp}}^{n,p}} \int_{P_{0\text{gp}}^{n,p}} dP \eta_v^{\text{gp}} \left[\left[\frac{\partial \delta V_i^p}{\partial Z_J} \right]_{\text{gp}} \hat{N}_{0J}^p \left[\left[\frac{\partial V_i^p}{\partial Z_K} \right]_{\text{gp}} \hat{N}_{0K}^p \right. \\ & \left. + \sum_{p=1}^2 \sum_{e \in P_{0\text{gp}}^{n,p}} \int_{P_{0\text{gp}}^{n,p}} dP \eta_u^{\text{gp}} \left[\left[\frac{\partial \delta U_i^p}{\partial Z_J} \right]_{\text{gp}} \hat{N}_{0J}^p [\Pi_{iK}^p]_{\text{gp}} \hat{N}_{0K}^p \right], \end{aligned} \quad (3.41)$$

where $\hat{\mathbf{N}}_0^p$ is an outward space-time normal from phase p in the initial configuration, and \mathbf{Z} is a generalized coordinate including space and time; $\mathbf{Z} = (\mathbf{X}, t)$. As fixed interfaces are always used based on the total Lagrangian formulation, a space-time normal $\hat{\mathbf{N}}_0^p$ is always parallel to a corresponding spatial normal $\hat{\mathbf{n}}_0^p$ (temporal component of $\hat{\mathbf{N}}_0^p$ is always zero). \tilde{R}_{vol} , \tilde{R}_{int} and \tilde{R}_{gp} are residuals of the volume contribution, the interface contribution and the contribution by the face-oriented ghost-penalty method, respectively. \tilde{R}_{disc} is an additional residual computed on the lower bound of a space-time slab $P_{0+}^{n,p}$ due to the discontinuous Galerkin method used in time.

3.5.2 Numerical Example 1: Beam Bending due to Body Force

The first benchmark problem of the space-time XFEM is a transient structural problem. Through this example, the efficiency of the space-time method versus the Newmark time stepping scheme is demonstrated. The implementation of Nitsche's method is verified by comparing results of the space-time XFEM and space-time FEM without interface. The computational approaches compared in this example are summarized at Table 3.2 along with the abbreviations are used in the following discussions. The rows of Table 3.2 denote spatial discretization methods and columns of Table 3.2 denote temporal discretization methods.

Figure 3.8 shows a computational domain for FEM and ST-FEM in the initial configuration. Fixed Dirichlet boundary conditions ($U_x = U_y = V_x = V_y = 0$) are applied on the left boundary Γ_{dbc} and the solid phase deforms due to the body force acting downwards in vertical direction. Figure 3.9 shows the computational domain for the XFEM and ST-XFEM. The

Table 3.2: Computational methods for structural problem

| | Standard Time Stepping (Newmark method) | Space-Time Method |
|--------------------------------|--|-------------------|
| standard Finite Element Method | FEM | ST-FEM |
| eXtended Finite Element Method | XFEM | ST-XFEM |

spatial domain consists of two phase Ω_0^1 and Ω_0^2 which are made by identical solid materials and an interface is introduced as a dummy interface to verify the implementation of Nitsche's method. The parameters for geometry and material are summarized in Table 3.3. As the interface in Figure 3.9 is just a dummy interface, different spatial discretization (FEM and XFEM) should compute exactly identical results in this problem.

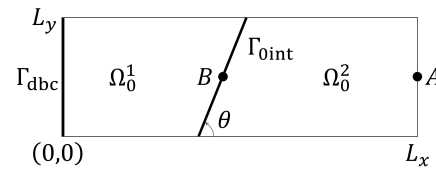
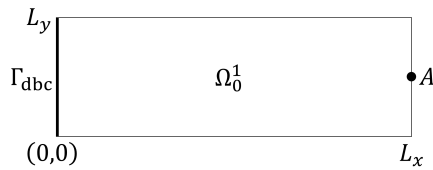


Figure 3.8: Model for FEM and ST-FEM Figure 3.9: Model for XFEM and ST-XFEM

Table 3.3: Parameters for geometry and material (structural problem)

| Group | Description | Parameter |
|----------|--------------------|--|
| Geometry | domain size | $L_x = 1.50\text{m}$ $L_y = 0.50\text{m}$ |
| | point A | $(L_x, L_y/2) = (1.50, 0.25)\text{m}$ |
| | point B | $(0.44L_x, L_y/2) = (0.66, 0.25)\text{m}$ |
| | angle of interface | $\theta = \pi/8\text{rad}$ |
| | Solid | density |
| | Young's modulus | $E^1 = E^2 = 1\text{MPa}$ |
| | Poisson's ratio | $\nu^1 = \nu^2 = 0.4$ |
| | body force | $\mathbf{b}^1 = \mathbf{b}^2 = (0, -10)\text{m/s}^2$ |

The structural response is simulated up to time $t = 1.782\text{s}$. The size of the spatial discretization h is set as $h = 0.25, 0.125, 0.0625, 0.03125, 0.02083\text{m}$ and the size of the temporal discretization Δt is set as $\Delta t = 0.162, 0.054, 0.018\text{s}$ respectively. The reference solution for the convergence study is the result of FEM (standard finite element computed by the

Newmark method) with the finest spatial and temporal discretization ($h = 0.0125\text{m}$ and $\Delta t = 0.001\text{s}$).

The structural response is monitored by the tip displacements at point A in Figures 3.8 and 3.9, U_x^{tip} and U_y^{tip} , the strain energy E_{str} and the kinetic energy E_{kin} :

$$U_x^{\text{tip}} = U_x^1|_A \quad \text{or} \quad U_x^2|_A, \quad (3.42)$$

$$U_y^{\text{tip}} = U_y^1|_A \quad \text{or} \quad U_y^2|_A, \quad (3.43)$$

$$E_{\text{str}} = \sum_{p=1}^2 \int_{\Omega_0^p} d\Omega W^p, \quad (3.44)$$

$$E_{\text{kin}} = \sum_{p=1}^2 \int_{\Omega_0^p} d\Omega \frac{1}{2} \rho^p \mathbf{V}^{p2}, \quad (3.45)$$

where W^p is the hyperelastic function of phase p defined in (3.26). In Figure 3.10, the left diagram shows the histories of U_y^{tip} using both the XFEM and the space-time XFEM with the finest model ($h = 0.02083\text{m}$). The green solid line is the history of reference solution. The other solid lines represent the histories of the space-time XFEM and dashed lines mean histories of the XFEM using three time step sizes, Δt . Results of the space-time XFEM with $\Delta t < 0.054\text{s}$ exactly overlap with the line of a reference solution. The top right figure shows the initial phases at $t = 0\text{s}$ and the bottom right figure is a snapshot at $t = 1.35\text{s}$ colored by the von Mises stress using the space-time XFEM ($h = 0.02083\text{m}$ and $\Delta t = 0.18\text{s}$). The red solid line in the left figure is the configuration that corresponds to these snapshots. As the face-oriented ghost-penalty method is applied in both the spatial XFEM and the space-time XFEM, the condition number of the Jacobian is reduced (e.g. from the order of 10^{20} to the order of 10^{12} using the space-time XFEM with $h = 0.02083\text{m}$ and $\Delta t = 0.054\text{s}$).

Figures 3.11 and 3.12 illustrate the spatial size dependency of the normalized L2 errors against the reference solution. The normalized L2 errors are defined as follows:

$$\text{Err}(a) = \sqrt{\frac{\int dt (a - a_{\text{ref}})^2}{\int dt a_{\text{ref}}^2}} \quad (a = U_x^{\text{tip}}, U_y^{\text{tip}}, E_{\text{str}} \text{ and } E_{\text{kin}}). \quad (3.46)$$

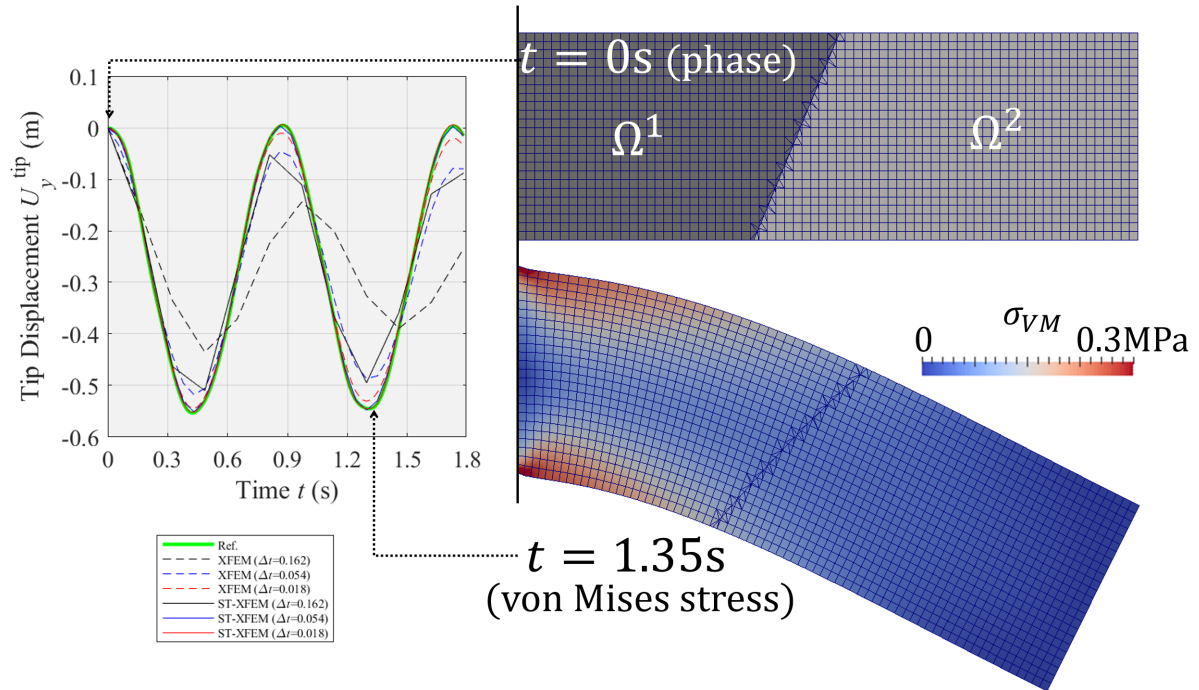


Figure 3.10: History of U_y^{tip} and snapshot of deformation (right figures: results of space-time XFEM with $h = 0.02083\text{m}$ and $\Delta t = 0.18\text{s}$)

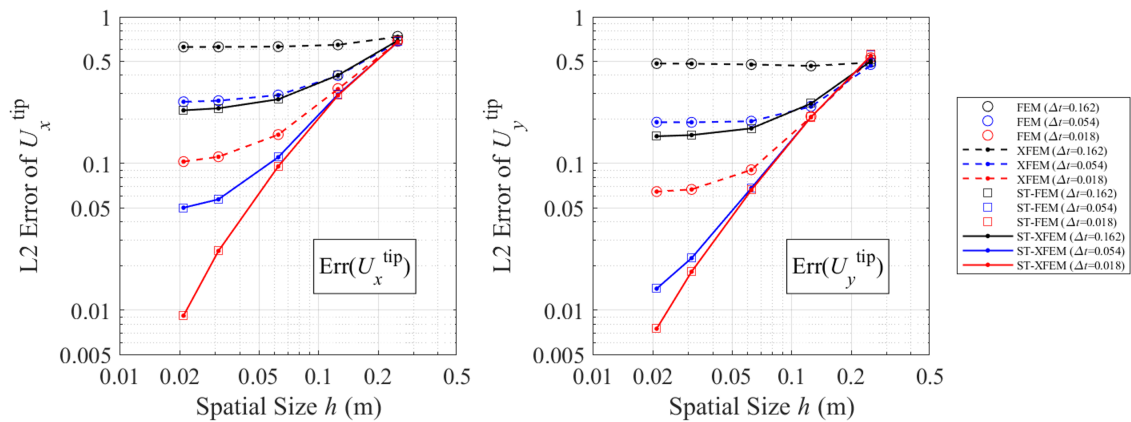


Figure 3.11: Spatial size dependency of L2 errors of tip displacements U_x^{tip} and U_y^{tip}

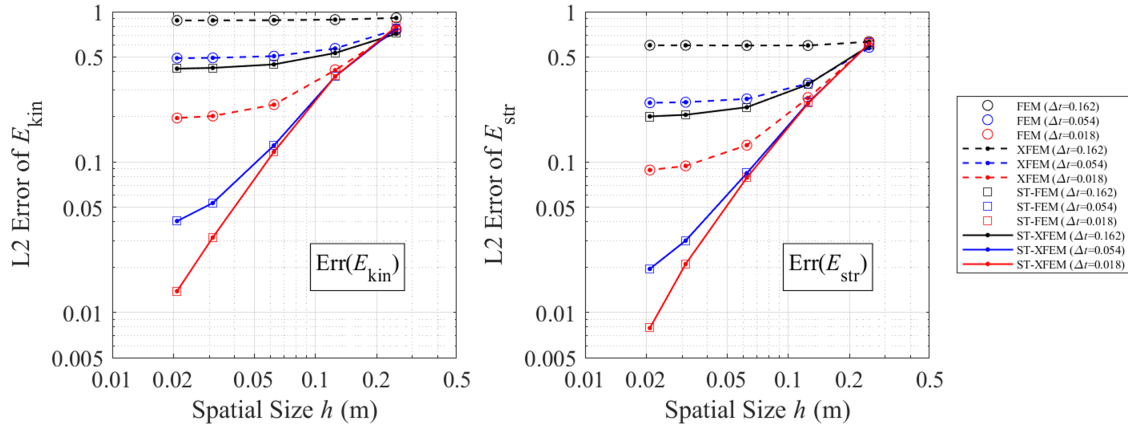


Figure 3.12: Spatial size dependency of L2 errors of kinetic energy E_{kin} and strain energy E_{str}

Circle and square markers denote the results of the spatial and space-time FEM (FEM and ST-FEM, no interface case). Dashed and solid lines represent the results of the spatial and space-time XFEM (XFEM and ST-XFEM). Each color represents a different time step size. First, it is confirmed that the L2 errors of the FEM and XFEM (ST-FEM and ST-XFEM) agree well in both spatial method and space-time method. The implementation of Nitsche's method in the space-time XFEM was verified. Second, comparing the XFEM (dashed lines) and the space-time XFEM (solid lines), the rate of convergence of the space-time XFEM is higher than the one of the XFEM. The space-time XFEM uses three temporal quadrature points in each temporal layer and $\Delta t/3$ is an approximate time increment substantially. This interpretation is confirmed by the fact that results of the XFEM with $\Delta t = 0.054\text{s}$ (blue dashed line) and results of the space-time XFEM with $\Delta t = 0.162\text{s}$ (black solid line) are almost identical. As the effective time step in the space-time XFEM is smaller than in the spatial XFEM, the space-time XFEM has a higher rate of convergence. The error also plateaus at a larger nominal time step; the error stagnates even reducing the time step size as the error is dominated by the spatial discretization error.

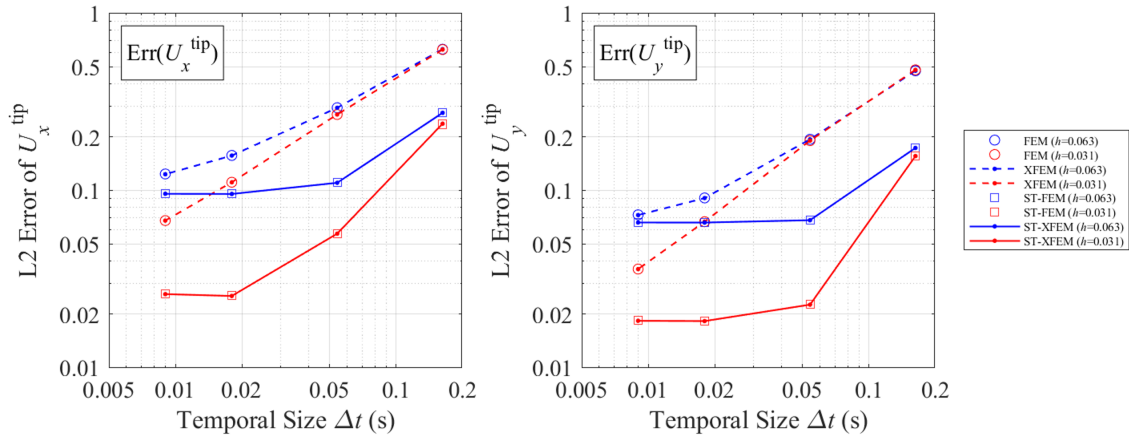


Figure 3.13: Temporal size dependency of L2 error of tip displacements U_x^{tip} and U_y^{tip}

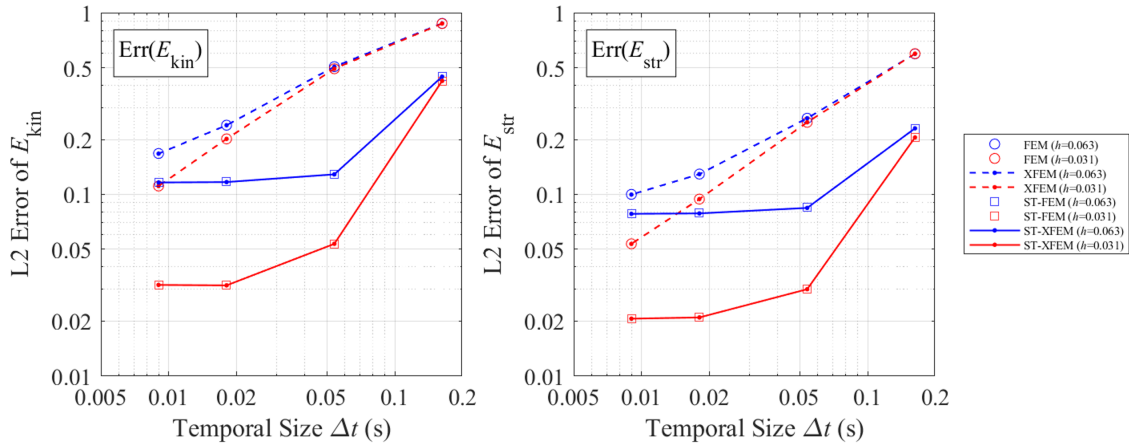


Figure 3.14: Temporal size dependency of L2 error of kinetic energy E_{kin} and strain energy E_{str}

Figures 3.13 and 3.14 show the temporal size dependency of the normalized L2 errors. Different colors represent different spatial element sizes. As the effective time increment of the space-time XFEM is about $\Delta t/3$, the convergence of the space-time XFEM is higher than the one of the spatial XFEM. The results of the spatial XFEM is nearly reproduced by the space-time XFEM with three times larger Δt , when $\Delta t > 0.05$. The space-time XFEM plateaus for large Δt when compared with the standard XFEM. The efficiency of the proposed space-time XFEM was confirmed from this structural problem.

3.6 Fluid Analysis using Space-Time XFEM

This section summarizes spatially two-dimensional fluid problems using both the XFEM (XFEM that discretizes only space) and the space-time XFEM. The flow is modeled by the incompressible Navier-Stokes fluid in this section. The spatial domain is discretized by bilinear finite elements (QUAD4) in both methods and the temporal domain is discretized by linear finite elements in the space-time XFEM. Thus, trilinear elements are used in the space-time XFEM. In the space-time XFEM, three temporal slices are defined in each temporal layer. At each time step, the nonlinear problem is solved by the Newton's method and the convergence criterion requires a drop of the norm of the residual of 10^{-6} relative to the norm of the initial residual. In each Newton step, the system of linearized equations is solved by GMRES.

There are two examples in this section. Numerical example 2 (Section 3.6.2) is a spatially two-dimensional unsteady fluid problem around a fixed cylinder, which is the well-known DFG 2D-3 benchmark problem proposed by Schäfer and Turek et al. [80]. Numerical example 3 (Section 3.6.3) is a transient fluid problem with a moving interface. This problem was studied previously by Dütsch et al. [85] and Guilmineau et al. [86].

3.6.1 Governing Equations and Finite Element Discretization

This section summarizes the weak forms of a transient fluid problem for both the XFEM and the space-time XFEM, assuming a spatially two-dimensional fluid domain around a solid structure. Governing equations are the momentum equation and the continuity equation of the incompressible Navier-Stokes fluid as follows:

$$\rho^f \frac{\partial v_i^f}{\partial t} + \rho^f v_j^f \frac{\partial v_i^f}{\partial x_j} = \frac{\partial \sigma_{ij}^f(\mathbf{v}^f, p^f)}{\partial x_j} + \rho^f b_i^f \quad \text{in } \Omega^{n,f}, \quad (3.47)$$

$$\frac{\partial v_i^f}{\partial x_i} = 0 \quad \text{in } \Omega^{n,f}, \quad (3.48)$$

where v_i^f , p^f and ρ^f are the velocity, the pressure and the density of the fluid. b_i^f is the body force and $\Omega^{n,f}$ denotes the fluid domain at time t^n , σ_{ij}^f is the Cauchy stress tensor of a Newtonian fluid:

$$\sigma_{ij}^f(\mathbf{v}^f, p^f) = -p^f \delta_{ij} + \mu^f \left(\frac{\partial v_i^f}{\partial x_j} + \frac{\partial v_j^f}{\partial x_i} \right), \quad (3.49)$$

where μ^f is the dynamic viscosity of a fluid. As an interface condition at the fluid-solid interface, the continuity of velocity is prescribed:

$$v_i^f = v_i^{\text{struct}} \quad \text{on } \Gamma_{\text{int}}^{n,f}, \quad (3.50)$$

where $\Gamma_{\text{int}}^{n,f}$ means an interface at time t^n and v_i^{struct} is the velocity of the structure, which is zero at the case of a fixed interface and non-zero at the case of a moving interface.

The finite element discretization of the standard XFEM at time t^n is defined by the following weak form defined in the current configuration.

$$R^f = R_{\text{vol}}^f + R_{\text{int}}^f + R_{\text{gp}}^f, \quad (3.51)$$

$$\begin{aligned} R_{\text{vol}}^f &= \int_{\Omega^{n,f}} d\Omega \delta v_i^f \rho^f \left(\frac{\partial v_i^f}{\partial t} + v_j^f \frac{\partial v_i^f}{\partial x_j} - b_i^f \right) + \int_{\Omega^{n,f}} d\Omega \frac{\partial \delta v_i^f}{\partial x_j} \sigma_{ij}^f(\mathbf{v}^f, p^f) \\ &\quad + \int_{\Omega^{n,f}} d\Omega \delta p^f \frac{\partial v_i^f}{\partial x_i} + \sum_{e \in \Omega^{n,f}} \int_{\Omega_e^{n,f}} d\Omega \tau_m^f \left(v_j^f \frac{\partial \delta v_i^f}{\partial x_j} + \frac{1}{\rho^f} \frac{\partial \delta p^f}{\partial x_i} \right) \bar{r}_i^f(\mathbf{v}^f, p^f) \\ &\quad + \sum_{e \in \Omega^{n,f}} \int_{\Omega_e^{n,f}} d\Omega \tau_c^f \frac{\partial \delta v_j^f}{\partial x_j} \frac{\partial v_i^f}{\partial x_i}, \end{aligned} \quad (3.52)$$

$$\begin{aligned} R_{\text{int}}^f &= - \int_{\Gamma_{\text{int}}^n} d\Gamma \delta v_i^f \sigma_{ij}^f(\mathbf{v}^f, p^f) \hat{n}_j - \int_{\Gamma_{\text{int}}^n} d\Gamma \delta p^f \hat{n}_i^f (v_i^f - v_i^{\text{struct}}) \\ &\quad - \int_{\Gamma_{\text{int}}^n} d\Gamma \tilde{\sigma}_{ij}^f(\delta \mathbf{v}^f) \hat{n}_j^f (v_i^f - v_i^{\text{struct}}) + \int_{\Gamma_{\text{int}}^n} d\Gamma \eta^{\text{int}} \delta v_i^f v_i^f, \end{aligned} \quad (3.53)$$

$$\begin{aligned} R_{\text{gp}}^f &= \sum_{e \in \Gamma_{\text{GP}}^{n,f}} \int_{\Gamma_{\text{GP}e}^{n,f}} d\Gamma \eta_v^{\text{gp}} \left[\left[\frac{\partial \delta v_i^f}{\partial x_j} \right]_{\text{gp}} \right] \hat{n}_j^f \left[\left[\frac{\partial v_i^f}{\partial x_k} \right]_{\text{gp}} \right] \hat{n}_k^f \\ &\quad + \sum_{e \in \Gamma_{\text{GP}}^{n,f}} \int_{\Gamma_{\text{GP}e}^{n,f}} d\Gamma \eta_p^{\text{gp}} \left[\left[\frac{\partial \delta p^f}{\partial x_i} \right]_{\text{gp}} \right] \hat{n}_i^f \left[\left[\frac{\partial p^f}{\partial x_j} \right]_{\text{gp}} \right] \hat{n}_j^f. \end{aligned} \quad (3.54)$$

R_{vol}^f is the volume contribution; here the residual-based variational multiscale method [71] is

applied for the convection and incompressibility stabilizations in (3.52). The WTSE option ($\partial v_i^f / \partial t$ term is excluded) is applied (Tezduyar et al. [87]). τ_m^f and τ_c^f are elementwise stabilization parameters for the advection and continuity terms:

$$\tau_m^f = \left[\left(\frac{2\rho^f}{\Delta t} \right)^2 + \rho^{f2} \mathbf{v}^{fT} G \mathbf{v}^f + \mu^{f2} \right]^{-1/2}, \quad (3.55)$$

$$\tau_c^f = \left[\tau_m^f \text{Tr}(G) \right]^{-1}, \quad (3.56)$$

where $G_{ij} = \sum_{k=1}^2 (\partial \xi_k / \partial x_i) (\partial \xi_k / \partial x_j)$ and ξ_k is the isoparametric coordinate of each element. In (3.52), $\tilde{\sigma}_{ij}^f$ is a deviatoric part of the fluid Cauchy stress, \hat{n}_i^f is an outward facing normal from the fluid phase and \bar{r}_i^f is a scalar residual of the momentum equation defined as follows:

$$\bar{r}_i^f(\mathbf{v}^f, p^f) = \rho^f \frac{\partial v_i^f}{\partial t} + \rho^f v_j^f \frac{\partial v_i^f}{\partial x_j} - \frac{\partial \sigma_{ij}^f(\mathbf{v}^f, p^f)}{\partial x_j} - \rho^f b_i^f. \quad (3.57)$$

R_{int}^f is the interface contribution based on the symmetric Nitsche method. The second term of RHS of (3.53) is the mass-preserving adjoint consistency term (negative sign is correct) based on Schott et al. [73]. While there are several versions of Nitsche's method, this thesis chooses empirically the above version of Nitsche's method because of its stability at computations in the proposed space-time XFEM. R_{gp}^f is the additional contribution by the face-oriented ghost-penalty method to stabilize numerical flux at small intersected elements. η^{int} is the penalty factor of Nitsche's method, and η_v^{gp} and η_p^{gp} are the penalty factors of the face-oriented ghost-penalty method defined as follows [72, 73]:

$$\eta^{\text{int}} = \alpha^{\text{int}} \left(\frac{\mu^f}{h} + \frac{\rho^f \|\mathbf{v}^f\|_{\infty}}{6} + \frac{\rho^f h}{12\Delta t} \right), \quad (3.58)$$

$$\eta_v^{\text{gp}} = \alpha_v^{\text{gp}} h \left(\mu^f + \frac{\rho^f h^2}{10\Delta t} \right), \quad (3.59)$$

$$\eta_p^{\text{gp}} = \alpha_p^{\text{gp}} h^2 \left(\frac{\mu^f}{h} + \frac{\rho^f \|\mathbf{v}^f\|_{\infty}}{6} + \frac{\rho^f h}{12\Delta t} \right)^{-1}, \quad (3.60)$$

where α^{int} , α_v^{gp} and α_p^{gp} are dimensionless scalar and these are set as $\alpha^{\text{int}} = 50$, $\alpha_v^{\text{gp}} = 10^{-3}$ and $\alpha_p^{\text{gp}} = 10^{-4}$ respectively. h is a representative spatial size and $\|\mathbf{v}^f\|_{\infty}$ is the infinity norm of the fluid velocity.

On the other hand, the finite element discretization for the space-time XFEM is defined as follows. The discontinuous Galerkin method is applied in time. The symmetric Nitsche method on the interface and the face-oriented ghost-penalty method are also applied:

$$\tilde{R}^f = \tilde{R}_{\text{vol}}^f + \tilde{R}_{\text{int}}^f + \tilde{R}_{\text{disc}}^f + \tilde{R}_{\text{gp}}^f, \quad (3.61)$$

$$\begin{aligned} \tilde{R}_{\text{vol}}^f &= \int_{Q^{n,f}} dQ \delta v_i^f \rho^f \left(\frac{\partial v_i^f}{\partial t} + v_j^f \frac{\partial v_i^f}{\partial x_j} - b_i^f \right) + \int_{Q^{n,f}} dQ \frac{\partial \delta v_i^f}{\partial x_j} \sigma_{ij}^f(\mathbf{v}^f, p^f) \\ &\quad + \int_{Q^{n,f}} d\Omega \delta p^f \frac{\partial v_i^f}{\partial x_i} + \sum_{e \in Q^{n,f}} \int_{Q_e^{n,f}} dQ \tau_m^f \left(v_j^f \frac{\partial \delta v_i^f}{\partial x_j} + \frac{1}{\rho^f} \frac{\partial \delta p^f}{\partial x_i} \right) \bar{r}_i^f(\mathbf{v}^f, p^f) \\ &\quad + \sum_{e \in Q^{n,f}} \int_{Q_e^{n,f}} dQ \tau_c^f \frac{\partial \delta v_j^f}{\partial x_j} \frac{\partial v_i^f}{\partial x_i}, \end{aligned} \quad (3.62)$$

$$\begin{aligned} \tilde{R}_{\text{int}}^f &= - \int_{P_{\text{int}}^n} dP \delta v_i^f \sigma_{ij}^f(\mathbf{v}^f, p^f) \hat{N}_j^f - \int_{P_{\text{int}}^n} dP \delta p^f \hat{N}_i^f (v_i^f - v_i^{\text{struct}}) \\ &\quad - \int_{P_{\text{int}}^n} dP \tilde{\sigma}_{ij}^f(\delta \mathbf{v}^f) \hat{N}_j^f (v_i^f - v_i^{\text{struct}}) + \int_{P_{\text{int}}^n} dP \eta^{\text{int}} \delta v_i^f (v_i^f - v_i^{\text{struct}}), \end{aligned} \quad (3.63)$$

$$\tilde{R}_{\text{disc}}^f = \int_{P_+^{n,f}} d\Omega \delta v_i^f |_{+}^n \rho^f [v_i^f]_{\pm}^n, \quad (3.64)$$

$$\begin{aligned} \tilde{R}_{\text{gp}}^f &= \sum_{e \in P_{\text{gp}}^{n,f}} \int_{P_{\text{gp}^e}^{n,f}} dP \eta_v^{\text{gp}} \left[\frac{\partial \delta v_i^f}{\partial z_j} \right]_{\text{gp}} \hat{N}_j^f \left[\frac{\partial v_i^f}{\partial z_k} \right]_{\text{gp}} \hat{N}_k^f \\ &\quad + \sum_{e \in P_{\text{gp}}^{n,f}} \int_{P_{\text{gp}^e}^{n,f}} dP \eta_p^{\text{gp}} \left[\frac{\partial \delta p^f}{\partial z_i} \right]_{\text{gp}} \hat{N}_i^f \left[\frac{\partial p^f}{\partial z_j} \right]_{\text{gp}} \hat{N}_j^f, \end{aligned} \quad (3.65)$$

where \hat{N}^f is an outward space-time normal from the fluid phase. \tilde{R}_{vol}^f and \tilde{R}_{int}^f are the volume and interface contributions of the weak form of the space-time XFEM. $\tilde{R}_{\text{disc}}^f$ is the additional residual comparing with the XFEM (3.51), which is defined on the boundary between the current and the past space-time slabs and originated from applying the discontinuous Galerkin method in time. \tilde{R}_{vol}^f is the contribution of the face-oriented ghost-penalty method in the space-time XFEM. z_i is the generalized coordinate including space and time. Penalty coefficients for Nitsche's method and the face-oriented ghost-penalty method are the same as those of the XFEM (3.58) - (3.60).

3.6.2 Numerical Example 2: Unsteady Flow around Fixed Cylinder (DFG 2D-3 Benchmark Problem)

To demonstrate the efficiency of the space-time XFEM, a transient fluid problem with a fixed interface is studied. This second benchmark problem is a spatially two-dimensional fluid problem for the unsteady flow around a fixed cylinder, which is well-known as DFG 2D-3 benchmark problem proposed by Schäfer, Turek, et al. [80]. A fixed cylinder located at $(x^{\text{cyl}}, y^{\text{cyl}}) = (0.2, 0.2)\text{m}$ is embedded in an Eulerian fluid domain which is modeled by the incompressible Navier-Stokes equations (3.49). Figure 3.15 shows the geometry of this problem. The geometric parameters and the material parameters are summarized in Table 3.4. These parameters are identical to settings of [80]. As the cylinder is fixed, the spatial domain $\Omega^{n,f}$, the spatial interface $\Gamma_{\text{int}}^{n,f}$, the space-time volume $Q^{n,f}$ and the space-time interface $P_{\text{int}}^{n,f}$ of fluid are time-invariant and thus, upper subscripts n for the volume and boundary terms are omitted in this numerical example like $\Omega^{n,f} \rightarrow \Omega^f$. Inlet velocities are prescribed on the left edge Γ_{inlet} and defined by the time-dependent functions:

$$v_x^{\text{inlet}}(0, y, t) = 4\bar{U} \frac{y(L_y - y)}{L_y^2} \sin\left(\frac{\pi t}{8}\right), \quad v_y^{\text{inlet}}(0, y, t) = 0\text{m/s} \quad \text{on } \Gamma_{\text{inlet}}, \quad (3.66)$$

$$v_x^{\text{int}} = v_y^{\text{int}} = 0\text{m/s} \quad \text{on } \Gamma_{\text{int}}. \quad (3.67)$$

No-slip boundary condition is applied on the upper and lower edges, Γ_{noslip} , and on the interface around a fixed cylinder, Γ_{int} . The right edge of this domain is a traction-free boundary Γ_{free} . The time interval of this simulation is $0 \leq t \leq 8\text{s}$.

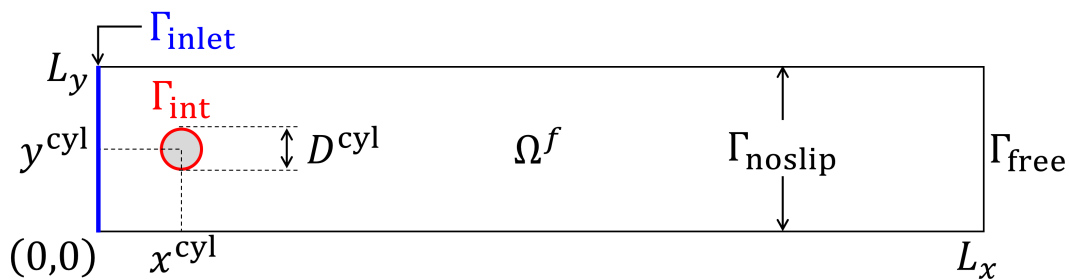


Figure 3.15: Model of fluid problem with fixed interface (DFG 2D-3 problem)

Table 3.4: Geometrical and material parameters (DFG 2D-3 problem)

| Group | Description | Parameter |
|----------|---|---|
| Whole | size | $L_x = 0.41\text{m}$ |
| Domain | | $L_y = 2.20\text{m}$ |
| Cylinder | diameter | $D = 0.1\text{m}$ |
| | center | $x^{\text{cyl}} = 0.2\text{m}$ |
| | | $y^{\text{cyl}} = 0.2\text{m}$ |
| Fluid | density | $\rho^f = 1000\text{kg/m}^3$ |
| | kinematic viscosity | $\nu^f = 10^{-3}\text{m}^2/\text{s}$ |
| | body force | $\mathbf{b}^f = (0, 0)\text{m/s}^2$ |
| | maximum inlet velocity | $\bar{U} = 1.5\text{m/s}$ |
| | inlet velocity on Γ_{inlet} | $v_x^{\text{inlet}} = 4\bar{U}L_y^{-2}(L_y - y)y \sin(\pi t/8)$ |
| | interface velocity on Γ_{int} | $v_x^{\text{cyl}} = v_y^{\text{cyl}} = 0\text{m/s}$ |

The accuracy of the flow solution is monitored by the drag coefficient; C_D , lift coefficient; C_L , and pressure difference around the cylinder; Δp , as functions of time in $0 \leq t \leq 8\text{s}$:

$$C_D(t) = \frac{F_D(t)}{1/2\rho^f\bar{U}^2D} = \frac{1}{1/2\rho^f\bar{U}^2D} \int_{\Gamma_{\text{int}}} d\Gamma \left[\mu^f \left(\frac{\partial v_x^f}{\partial y} - \frac{\partial v_y^f}{\partial x} \right) n_y^{\text{cyl}} - p^f n_x^{\text{cyl}} \right], \quad (3.68)$$

$$C_L(t) = \frac{F_L(t)}{1/2\rho^f\bar{U}^2D} = \frac{1}{1/2\rho^f\bar{U}^2D} \int_{\Gamma_{\text{int}}} d\Gamma \left[-\mu^f \left(\frac{\partial v_x^f}{\partial y} - \frac{\partial v_y^f}{\partial x} \right) n_x^{\text{cyl}} - p^f n_y^{\text{cyl}} \right], \quad (3.69)$$

$$\begin{aligned} \Delta p(t) &= p^f(x^{\text{cyl}} - D/2, y^{\text{cyl}}, t) - p^f(x^{\text{cyl}} + D/2, y^{\text{cyl}}, t) \\ &= p^f(0.15\text{m}, 0.2\text{m}, t) - p^f(0.25\text{m}, 0.2\text{m}, t), \end{aligned} \quad (3.70)$$

where $\mathbf{n}^{\text{cyl}} = (n_x^{\text{cyl}}, n_y^{\text{cyl}})$ is the outward normal of the cylinder. The computation of the drag and lift forces; F_D and F_L , are based on the method of John [88], considering the condition of the interface velocities $v_x^{\text{int}} = v_y^{\text{int}} = 0$. Δp is the difference between the left and right of the cylinder like (3.70). In particular, the maximum C_D ; C_D^{max} , the maximum C_L ; C_L^{max} and the pressure difference Δp at time $t = 8\text{s}$ (final time); Δp^{fin} are representative numerical properties of the DFG 2D-3 benchmark problem. Reference values of [80] are summarized in Table 3.5. As the face-oriented ghost-penalty method is applied in both the XFEM and the space-time XFEM, the condition number of the Jacobian is reduced (e.g. from the order of 10^{13} to the order of 10^6 using the space-time XFEM with $h/D = 0.1615$ and $\Delta t = 0.02\text{s}$).

Table 3.5: Reference of DFG 2D-3 benchmark problem [80]

| | C_D^{\max} | C_L^{\max} | Δp^{fin} |
|-------------|--------------|--------------|-------------------------|
| lower bound | 2.9300 | 0.4700 | -0.1150 |
| upper bound | 2.9700 | 0.4900 | -0.1050 |

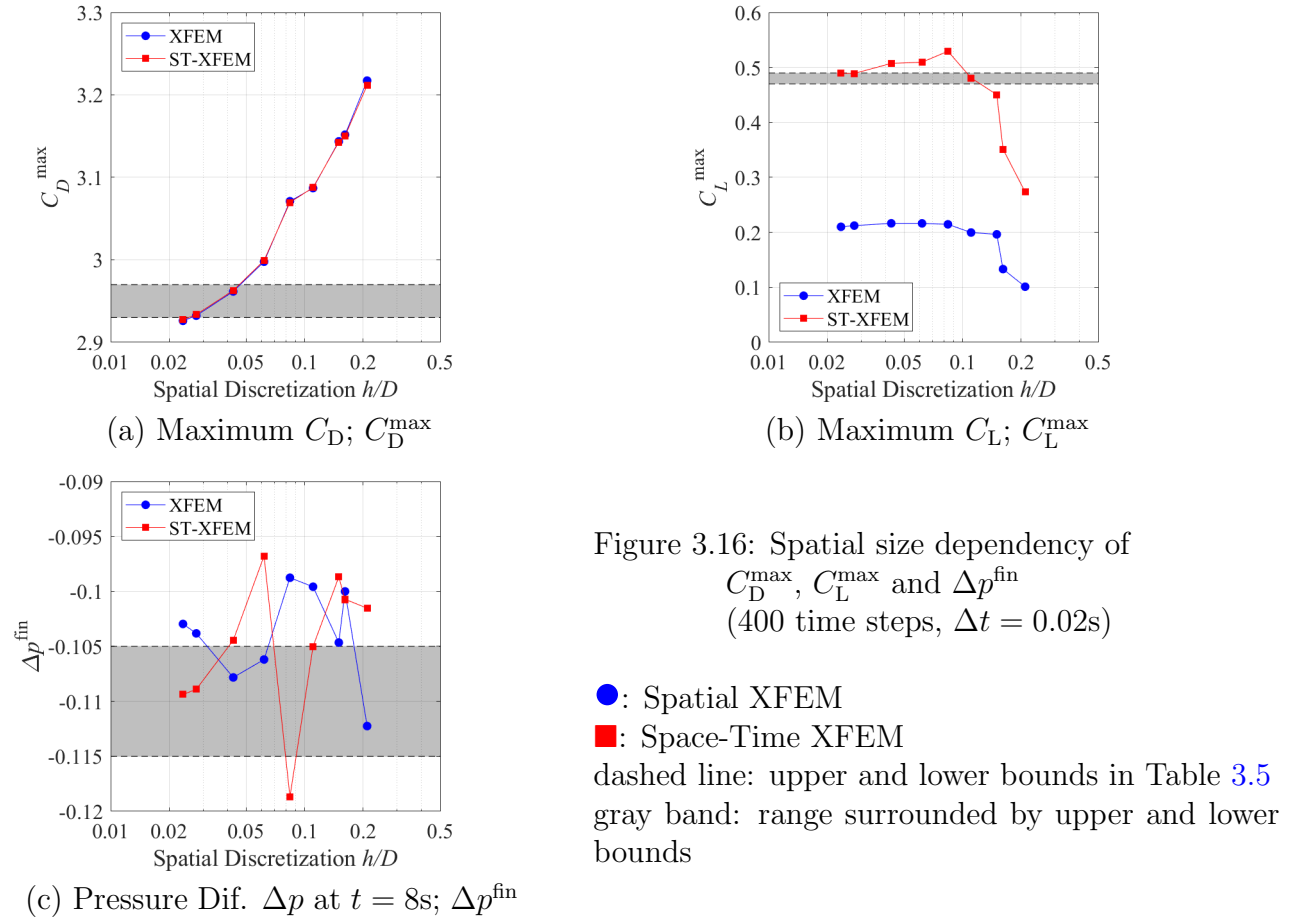


Figure 3.16 illustrates the spatial size dependency of C_D^{\max} , C_L^{\max} and Δp^{fin} using both the XFEM and the space-time XFEM with $\Delta t = 0.02s$. h/D is a normalized spatial size by the cylinder diameter D . Blue circles denote results of the XFEM and red squares denote results of the space-time XFEM. Black dashed lines show the upper and lower bounds of the reference work given in Table 3.5 and gray bands surrounded by dashed lines represent the reasonable range within its upper and lower bounds. Tables 3.6 and 3.7 summarize the data used in Figure 3.16. $t(C_D^{\max})$ and $t(C_L^{\max})$ denote the time when C_D^{\max} and C_L^{\max} occur.

In terms of C_D^{\max} (Figure 3.16(a)), the computational results of both the XFEM and the space-time XFEM overlap and C_D^{\max} of both methods converge to its lower bound of the reference with almost the same rate of convergence. On the other hand, the spatial size dependency of C_L^{\max} using both method is completely different in Figure 3.16(b). It is confirmed that the influence of the time integration scheme is significant for the evaluation of C_L^{\max} , unlike C_D^{\max} . The standard XFEM underestimates C_L^{\max} when $\Delta t = 0.2s$ and this fact indicates that the standard XFEM needs a smaller time increment. The space-time XFEM predicts larger C_L^{\max} than the XFEM and converges to the values that are within the range of the reference work. This is because the space-time XFEM uses three integration points along time axis and thus, the time increment is almost one-third of the XFEM when the same Δt is used in both method. Considering the finest model for the space-time XFEM (model at the bottom of Table 3.7), C_D^{\max} and C_L^{\max} are obtained at $t(C_D^{\max}) = 3.9400s$ and $t(C_L^{\max}) = 5.7000s$ respectively. Figure 3.17 shows the history of C_D , C_L and Δp of the corresponding model and snapshots of vorticity at time $t = 4, 5.6$ and $8s$. While the flow field around $t(C_D^{\max})$ is at steady-state (top right figure of Figure 3.17), the flow field around $t(C_L^{\max})$ (middle right figure of Figure 3.17) is obviously unsteady. As C_L^{\max} is determined at the unsteady region as a dynamical property, the influence of a time integration scheme is significant and the space-time XFEM captures dynamic properties more efficiently because the efficient time increment is smaller than the XFEM. Although Δp^{fin} does not exhibit a clear convergence with the spatial size in Figure 3.16(c), Δp^{fin} computed by the space-time XFEM converges in a gray band using finer mesh models.

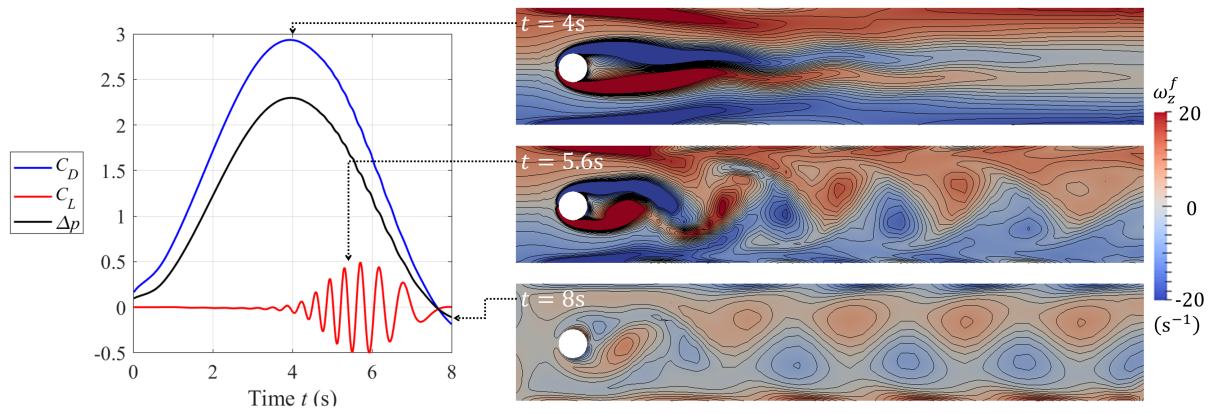


Figure 3.17: History of C_D , C_L , Δp and vorticity in z : ω_z^f
(bottom model in Table 3.9)

Table 3.6: Spatial size dependency of C_D^{\max} , C_L^{\max} and Δp^{fin} (XFEM)

| Spatial Active DOFs | Time Steps | h/D (-) | Δt (s) | C_D^{\max} (-) | C_L^{\max} (-) | Δp^{fin} (kPa) | $t(C_D^{\max})$ (s) | $t(C_L^{\max})$ (s) |
|------------------------|---------------|--------------|-------------------|---------------------|---------------------|----------------------------------|------------------------|------------------------|
| 3552 | 400 | 0.2100 | 0.0200 | 3.2173 | 0.0992 | -0.1122 | 3.9600 | 7.2000 |
| 4278 | 400 | 0.1615 | 0.0200 | 3.1518 | 0.1332 | -0.1000 | 3.9400 | 6.8600 |
| 4530 | 400 | 0.1500 | 0.0200 | 3.1437 | 0.1847 | -0.1047 | 3.9400 | 6.1400 |
| 5859 | 400 | 0.1105 | 0.0200 | 3.0870 | 0.1997 | -0.0996 | 3.9400 | 6.6200 |
| 7635 | 400 | 0.0840 | 0.0200 | 3.0711 | 0.1985 | -0.0988 | 3.9400 | 6.5200 |
| 13144 | 400 | 0.0618 | 0.0200 | 2.9977 | 0.2163 | -0.1062 | 3.9400 | 6.4600 |
| 19444 | 400 | 0.0429 | 0.0200 | 2.9616 | 0.2164 | -0.1078 | 3.9400 | 6.4000 |
| 37888 | 400 | 0.0276 | 0.0200 | 2.9323 | 0.2123 | -0.1038 | 3.9400 | 6.3400 |
| 45872 | 400 | 0.0236 | 0.0200 | 2.9260 | 0.2101 | -0.1030 | 3.9400 | 6.3400 |

Table 3.7: Spatial size dependency of C_D^{\max} , C_L^{\max} and Δp^{fin} (space-time XFEM)

| Space-Time Active DOFs | Time Steps | h/D (-) | Δt (s) | C_D^{\max} (-) | C_L^{\max} (-) | Δp^{fin} (kPa) | $t(C_D^{\max})$ (s) | $t(C_L^{\max})$ (s) |
|---------------------------|---------------|--------------|-------------------|---------------------|---------------------|----------------------------------|------------------------|------------------------|
| 7104 | 400 | 0.2100 | 0.0200 | 3.2116 | 0.2735 | -0.1015 | 3.9600 | 6.2200 |
| 8556 | 400 | 0.1615 | 0.0200 | 3.1502 | 0.3512 | -0.1007 | 3.9400 | 6.0400 |
| 9060 | 400 | 0.1500 | 0.0200 | 3.1428 | 0.4504 | -0.0987 | 3.9400 | 6.0000 |
| 11718 | 400 | 0.1105 | 0.0200 | 3.0877 | 0.4809 | -0.1050 | 3.9400 | 5.9000 |
| 15270 | 400 | 0.0840 | 0.0200 | 3.0696 | 0.5295 | -0.1187 | 3.9400 | 5.8400 |
| 26288 | 400 | 0.0618 | 0.0200 | 2.9992 | 0.5094 | -0.0968 | 3.9400 | 5.7800 |
| 38888 | 400 | 0.0429 | 0.0200 | 2.9629 | 0.5073 | -0.1044 | 3.9400 | 5.7400 |
| 74776 | 400 | 0.0276 | 0.0200 | 2.9336 | 0.4890 | -0.1098 | 3.9400 | 5.7200 |
| 91744 | 400 | 0.0236 | 0.0200 | 2.9274 | 0.4893 | -0.1094 | 3.9400 | 5.7000 |

Figure 3.18 illustrates the temporal size dependency of C_D^{\max} , C_L^{\max} and Δp^{fin} using a mesh with spatial size $h/D = 0.0276$. Tables 3.8 and 3.9 give the corresponding data of Figure 3.18. Δt means a discrete time increment in the XFEM and a length along the time axis of a space-time slab Q^n in the space-time XFEM. The temporal size dependency of C_D^{\max} of both methods is similar because the steady-state like behavior is dominant when the maximum C_D is obtained. In terms of C_L^{\max} (Figure 3.18(b)), the results of the XFEM become dramatically larger as Δt decreases, but a much smaller Δt is essential to reach the range between upper and lower bounds (gray band). On the other hand, C_L^{\max} of the space-time XFEM has a flat distribution with respect to Δt around the reference upper bound. The space-time XFEM can use larger Δt than the XFEM to obtain converged solutions. The distribution of Δp of the space-time XFEM is also flatter than the XFEM, and these values are located within the range between bounds. This temporal dependency study suggests that the space-time XFEM can compute unsteady fluid problems more efficiently than the XFEM.

Table 3.8: Temporal size dependency of C_D^{\max} , C_L^{\max} and Δp^{fin} (XFEM)

| Spatial Active DOFs | Time Steps | h/D (-) | Δt (s) | C_D^{\max} (-) | C_L^{\max} (-) | Δp^{fin} (kPa) | $t(C_D^{\max})$ (s) | $t(C_L^{\max})$ (s) |
|------------------------|---------------|--------------|-------------------|---------------------|---------------------|----------------------------------|------------------------|------------------------|
| 37888 | 250 | 0.0276 | 0.0320 | 2.9327 | 0.0862 | -0.1058 | 3.9360 | 7.4560 |
| 37888 | 400 | 0.0276 | 0.0200 | 2.9323 | 0.2123 | -0.1038 | 3.9400 | 6.3400 |
| 37888 | 800 | 0.0276 | 0.0100 | 2.9310 | 0.3327 | -0.1001 | 3.9400 | 5.7600 |
| 37888 | 1000 | 0.0276 | 0.0080 | 2.9302 | 0.3649 | -0.1023 | 3.9360 | 5.7520 |
| 37888 | 1200 | 0.0276 | 0.0067 | 2.9290 | 0.3670 | -0.1039 | 3.9400 | 6.2200 |

Table 3.9: Temporal size dependency of C_D^{\max} , C_L^{\max} and Δp^{fin} (space-time XFEM)

| Space-Time Active DOFs | Time Steps | h/D (-) | Δt (s) | C_D^{\max} (-) | C_L^{\max} (-) | Δp^{fin} (kPa) | $t(C_D^{\max})$ (s) | $t(C_L^{\max})$ (s) |
|---------------------------|---------------|--------------|-------------------|---------------------|---------------------|----------------------------------|------------------------|------------------------|
| 74776 | 250 | 0.0276 | 0.0320 | 2.9342 | 0.4620 | -0.1087 | 3.9360 | 5.7280 |
| 74776 | 400 | 0.0276 | 0.0200 | 2.9336 | 0.4890 | -0.1089 | 3.9400 | 5.7200 |
| 74776 | 800 | 0.0276 | 0.0100 | 2.9320 | 0.5032 | -0.1090 | 3.9400 | 5.7100 |
| 74776 | 1000 | 0.0276 | 0.0080 | 2.9311 | 0.5041 | -0.1090 | 3.9360 | 5.7120 |
| 74776 | 1200 | 0.0276 | 0.0067 | 2.9300 | 0.5042 | -0.1090 | 3.9333 | 5.7133 |

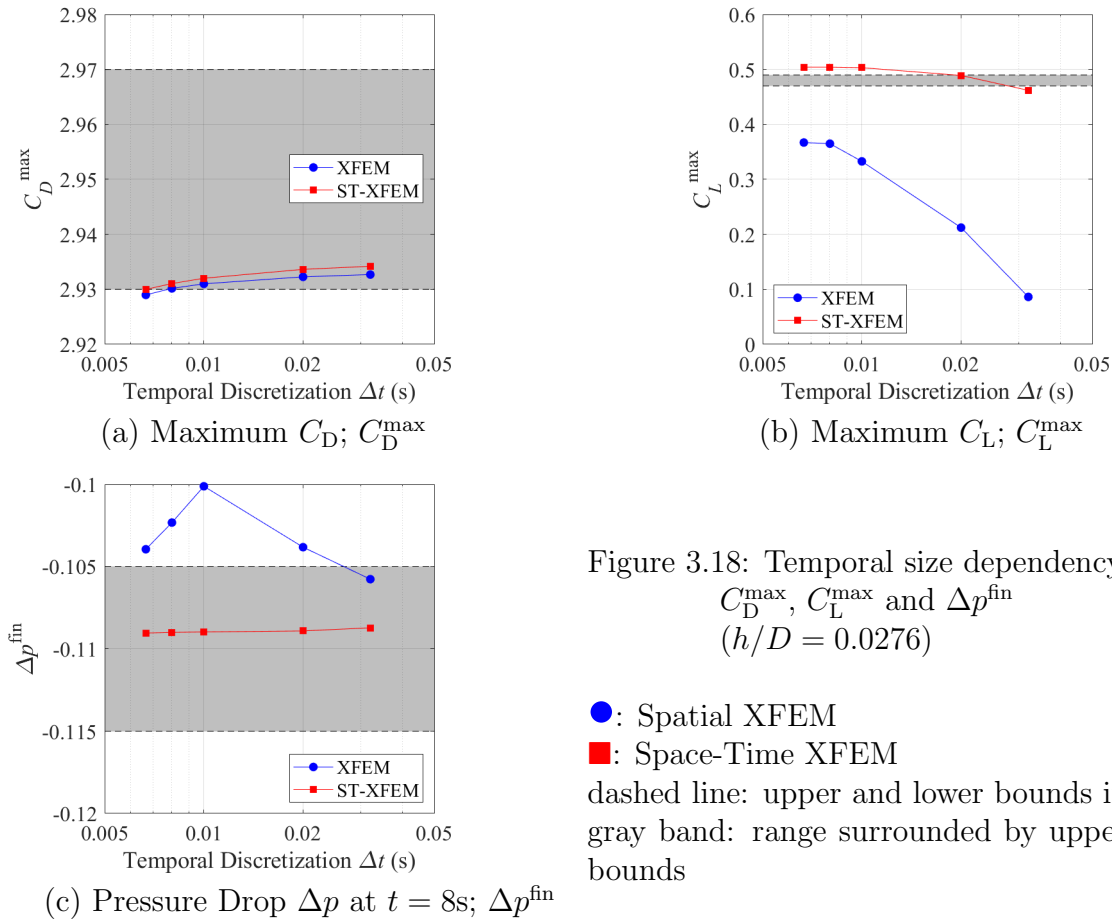


Figure 3.18: Temporal size dependency of C_D^{\max} , C_L^{\max} and Δp^{fin} ($h/D = 0.0276$)

●: Spatial XFEM

■: Space-Time XFEM

dashed line: upper and lower bounds in Table 3.5
gray band: range surrounded by upper and lower bounds

This numerical example is studied to compare the proposed space-time XFEM based on the elementwise temporal layer and the space-time XFEM based on the simplex triangulation like [47] (direct decomposition of a space-time slab). Table 3.10 summarizes the computational results using space-time XFEM based on both approaches. As can be seen, two approaches converge to the same results. At least for this example, the proposed elementwise temporal layer approach is equivalent to the simplex triangulation approach. The details of this comparison is summarized in Appendix F.

Table 3.10: Comparison between different approaches for space-time integration

| Approach | C_D^{\max} (-) | C_L^{\max} (-) | Δp^{fin} (kPa) | $t(C_D^{\max})$ (s) | $t(C_L^{\max})$ (s) |
|----------------------------|---------------------|---------------------|----------------------------------|------------------------|------------------------|
| Simplex triangulation | 3.0876 | 0.4812 | -0.1049 | 3.9600 | 5.9000 |
| Elementwise temporal layer | 3.0877 | 0.4809 | -0.1050 | 3.9400 | 5.9000 |

($\Delta t = 0.2s$, $h/D = 0.1105$, 11718 DOFs, 400 time steps)

3.6.3 Numerical Example 3: Flow around an In-line Oscillating Cylinder

The third benchmark problem for the space-time XFEM is a spatially two-dimensional transient fluid problem with a moving interface. The purpose of this numerical example is to demonstrate the stability of the space-time XFEM for moving interface problems. In this numerical example, there is an in-line oscillating circular cylinder which generates a moving interface within a fluid that is initially at rest. The Reynolds number; Re , is 100 and the Keulegan-Carpenter number; Kc (ratio of drag force and inertial force), is 5 based on the experiment of Dütsch et al. [85]. Flow induced by an in-line oscillating cylinder with $Re = 100$ and $Kc = 5$ was characterized in a region that results in the stable, symmetric and periodic vortex shedding; see Tatsuno and Bearman [89]. The characteristic numbers Re and Kc are defined as follows:

$$Re = \frac{V_x D}{\nu^f}, \quad (3.71)$$

$$Kc = \frac{V_x}{f D}, \quad (3.72)$$

where D is the diameter of the cylinder, V_x is the maximum velocity in x direction, and f is the frequency of the motion of the cylinder. The fluid kinematic viscosity ν^f is determined by $\nu^f = V_x D / Re$ based on (3.71). The motion of the center of the cylinder is described by:

$$x^{cyl}(t) = -A \sin(2\pi f t), \quad (3.73)$$

$$v_x^{cyl}(t) = -2\pi f A \cos(2\pi f t) = -V_x \cos(2\pi f t), \quad (3.74)$$

$$a_x^{cyl}(t) = 4\pi^2 f^2 A \sin(2\pi f t). \quad (3.75)$$

Parameter A is the amplitude of the cylinder motion in x direction and A is computed by $A = Kc D / 2\pi$. The in-line force acting on the cylinder at time t^n : $F_x(t^n)$ is computed by:

$$F_x(t^n) = \int_{\Gamma_{int}^n} d\Gamma \sigma_{ij}^f(\mathbf{v}^f, p^f) \hat{n}_j^{cyl} = - \int_{\Gamma_{int}^n} d\Gamma p^f \hat{n}_i^{cyl} + \int_{\Gamma_{int}^n} d\Gamma \tilde{\sigma}_{ij}^f(\mathbf{v}^f) \hat{n}_j^{cyl}, \quad (3.76)$$

where Γ_{int}^n denotes the moving interface at time t^n , $\tilde{\sigma}_{ij}^f$ is the deviatoric part of σ_{ij}^f and \hat{n}_j^{cyl} is the outward normal of the cylinder ($\hat{\mathbf{n}}^{\text{cyl}} = -\hat{\mathbf{n}}^f$).

As this numerical example is an important model for engineering structures such as offshore platforms, there is a well-known approximation of the in-line force F_x called the Morison equation. The Morison equation consists of contributions of the drag force and the inertial force as follows (Chakratarti [90]):

$$F_x(t) = C_D \frac{1}{2} \rho^f D |v_x^{\text{cyl}}(t)| v_x^{\text{cyl}}(t) + C_M \frac{1}{4} \rho^f \pi D^2 a_x^{\text{cyl}}(t) . \quad (3.77)$$

C_D and C_M are the drag and the added-mass coefficients respectively. These parameters are characteristic measures of this benchmark problem. To evaluate C_D and C_M from computational results through the Morison equation, the following dimensionless in-line force is useful instead of (3.77):

$$f_x(\tau) = \frac{F_x(t)}{1/2 \rho^f V_x^2 D} = -C_D |\cos(2\pi\tau)| \cos(2\pi\tau) + C_M \frac{\pi^2}{\text{Kc}} \sin(2\pi\tau) , \quad (3.78)$$

where τ is a cycle $\tau = t/T = ft$ of the cylinder motion. C_D and C_M can be computed by the Fourier integral of (3.78):

$$C_D = -\frac{3\pi}{4} \int_{\tau_0}^{\tau_0+1} d\tau f_x(\tau) \cos(2\pi\tau) , \quad (3.79)$$

$$C_M = \frac{2\text{Kc}}{\pi^2} \int_{\tau_0}^{\tau_0+1} d\tau f_x(\tau) \sin(2\pi\tau) , \quad (3.80)$$

(3.79) and (3.80) correspond to the integration of one period starting from an arbitrary cycle position τ_0 .

Numerical studies of this problem were reported by Dütsch et al. [85] and Guilmineau and Queutey [86]. In these works, the flow was solved on an O-type structured fixed grid using the FEM. The influence of the in-line oscillation of the cylinder is considered as a time-dependent boundary condition on the fixed interface and thus, these computations are based on the Lagrangian description because the cylinder does not move. Figures 3.19 - 3.21

are reference results provided by [86]. In these figures, the results of [85] are also included.

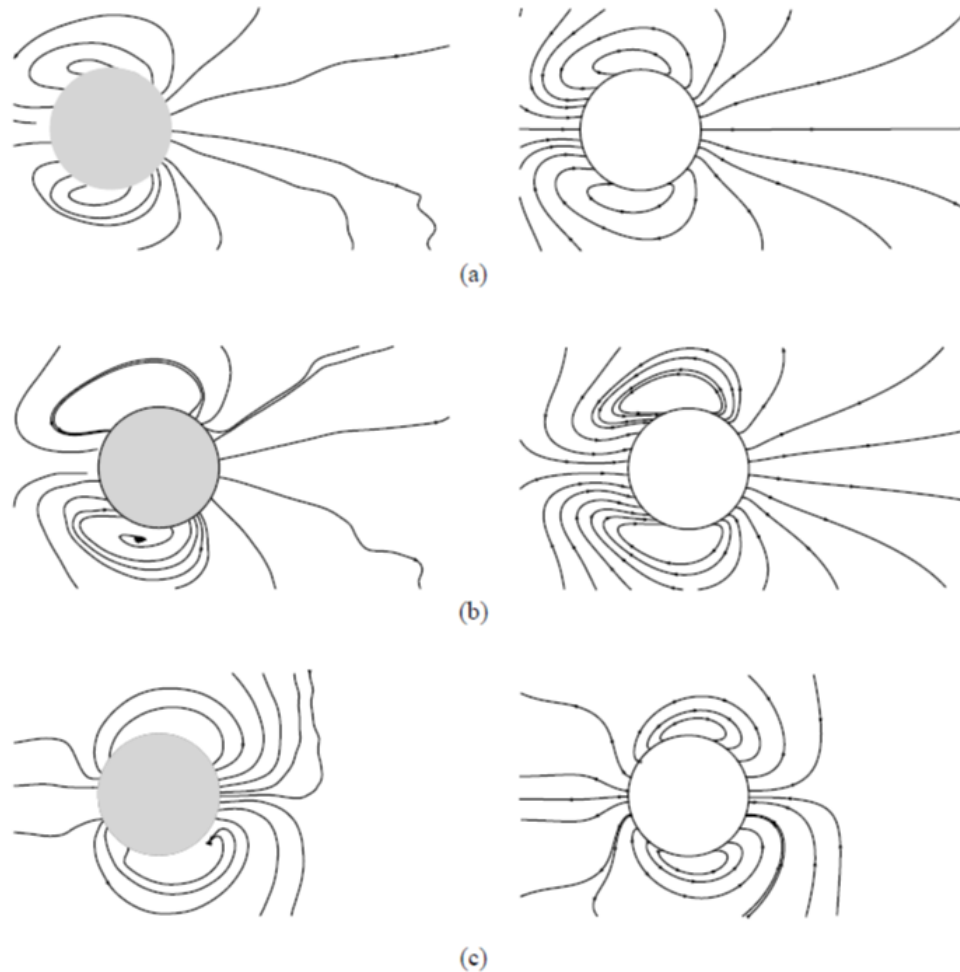


Figure 7. Measured Dutsch *et al.* (1998) (left) and computed streamlines (right) in the vicinity of the cylinder at $Re=100$ and $KC=5$ at different phase positions (phase position $= 2\pi f_c t$): (a) 180° ; (b) 210° ; (c) 330° .

Figure 3.19: Reference results of streamlines (Figure 7 of [86])

Another computational approach for this problem is an Eulerian approach, which computes the flow on a fixed background mesh. The cylinder moves within a fixed grid based on the Eulerian description. As the amplitude A of the in-line motion is not negligibly small relative to the diameter D in this problem ($A/D = Kc/2\pi \simeq 0.8$), the ALE approach is not appropriate because of the limitation of the deformation of ALE meshes. On the other hand, the XFEM with an immersed moving interface can handle this problem based on the Eulerian

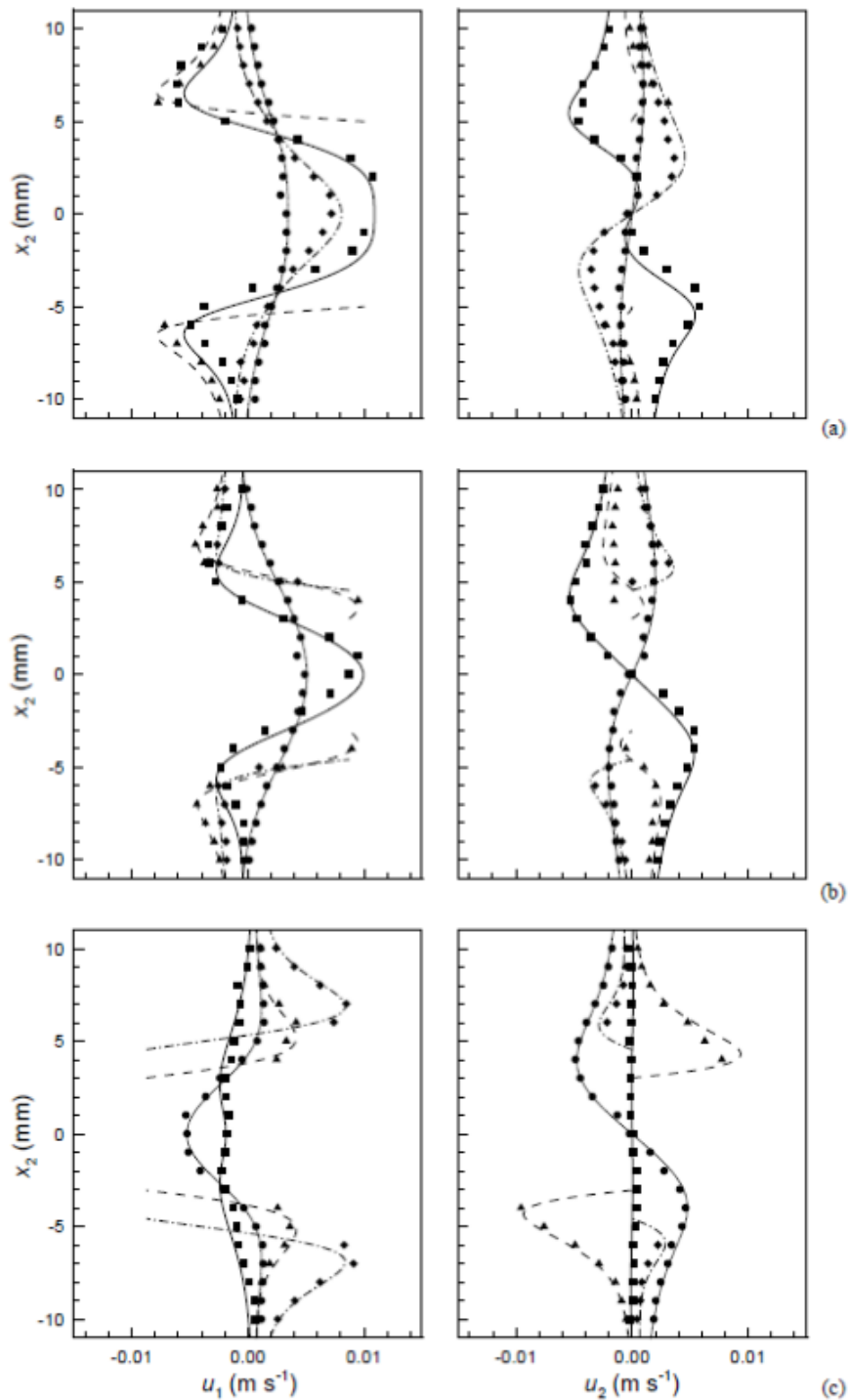


Figure 8. Comparison of the velocity components for $Re = 100$ and $KC = 5$ between present computation and experimental investigation Dütsch *et al.* (1998) at different phase positions (phase position $= 2\pi f_c t$): (a) 180° ; (b) 210° ; (c) 330° ; —, ■, computation and experiments, $x = -6$ mm; - - -, ▲, computation and experiments, $x = 0$ mm; - · - · - ·, ◆, computation and experiments, $x = 6$ mm; ·····, ●, computation and experiments, $x = 12$ mm.

Figure 3.20: Reference results of velocity fields (Figure 8 of [86])

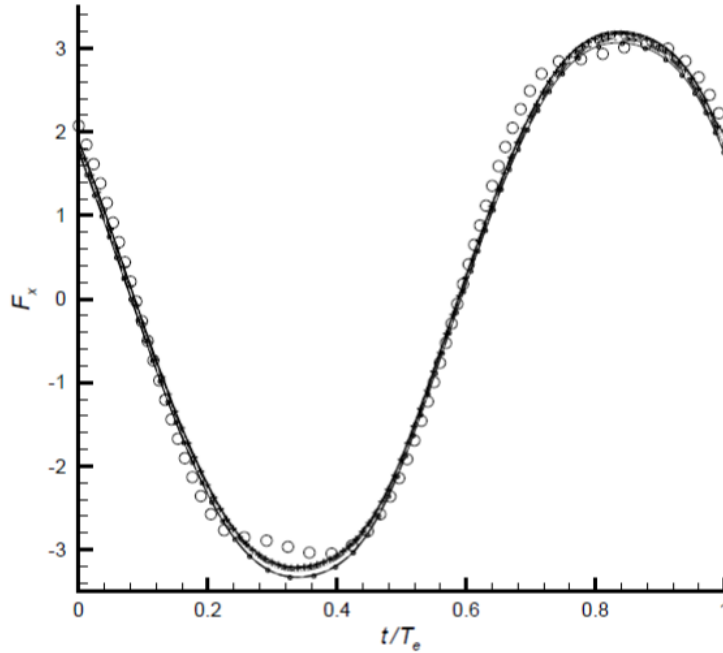


Figure 9. In-line force computed on different grid levels for $Re=100$ and $KC=5$: —○—, mesh = 120×100 ; - - - -, mesh = 120×200 ; - · - ·, mesh = 180×100 ; ·····, mesh = 180×200 ; — — — —, mesh = 240×100 ; - - - -, mesh = 240×200 ; — + —, mesh = 360×300 ; — + —, mesh = 480×400 ; ○, Morison equation.

Figure 3.21: Reference results of in-line force (Figure 9 of [86])

description. When the XFEM with time stepping schemes is used, results have an error due to a moving interface described in Section 3.1. This is because different discretization methods are applied in space and time respectively. In this case, additional treatments like the ghost-fluid method [37, 38, 39, 40] are necessary to mitigate this error. On the other hand, the proposed space-time XFEM does not suffer from this error because the finite element discretization is applied in both space and time. Hence, the space-time XFEM is suitable for this benchmark problem. The parameters for geometry and material are summarized in Figure 3.22 and Table 3.11. The center region of $|x/D| \leq 1.5$ and $|y/D| \leq 1.5$ (Region A in Tables 3.11 and 3.12) is discretized by fine square meshes ($m \times m$ meshes) and the outside of this region ($1.5 < |x/D| \leq 51.5$ or $1.5 < |y/D| \leq 51.5$) is discretized by exponentially coarsened rectangle meshes. The “do-nothing” boundary conditions (traction free boundary condition) are applied on the outer boundaries ($x = \pm L_x$ or $y = \pm L_y$).

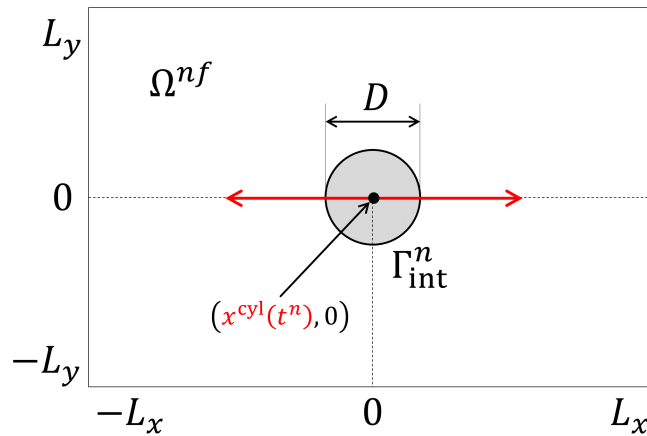
Figure 3.22: Model of in-line oscillating cylinder (time t^n)

Table 3.11: Parameters for geometry and material (in-line oscillation of cylinder)

| Group | Description | Parameter |
|----------|----------------------------------|--|
| Cylinder | diameter | $D = 0.01\text{m}$ |
| | frequency of in-line oscillation | f |
| | amplitude of x^{cyl} | $A = \text{Kc}D/2\pi$ |
| | center position | $x^{\text{cyl}}(t) = -A \sin(2\pi ft)$ $y^{\text{cyl}} = 0$ |
| | maximum velocity in x | $V_x = \max(v_x^{\text{cyl}}) = 2\pi f A$ |
| Grid | whole size | $L_x/D = L_y/D = 51.5$ |
| | fine mesh region (Region A) | $ x/D \leq 1.5, y/D \leq 1.5$ |
| Fluid | Reynolds number | $\text{Re} = 100$ |
| | Keulegan-Carpenter number | $\text{Kc} = 5$ |
| | kinematic viscosity | $\nu^f = V_x D / \text{Re}$ |
| | body force | $\mathbf{b}^f = (0, 0)\text{m/s}^2$ |

The weak form of the space-time XFEM is (3.61). In this example, the spatial coordinates x and y are non-dimensionalized by the diameter of the cylinder D . The time t is also non-dimensionalized by the period T (or frequency f) as a cycle τ . The computation is performed at $-0.75 \leq \tau \leq 5$ and a temporal size of a space-time slab $\Delta\tau = \Delta t/T = 1/480$. It should be noted that the ghost-fluid method [37, 38, 39, 40] is not used here.

The in-line force is generated by the periodic motion of the moving cylinder as a periodic sinusoidal wave. Figure 3.23 is a comparison of the dimensionless in-line force f_x computed by

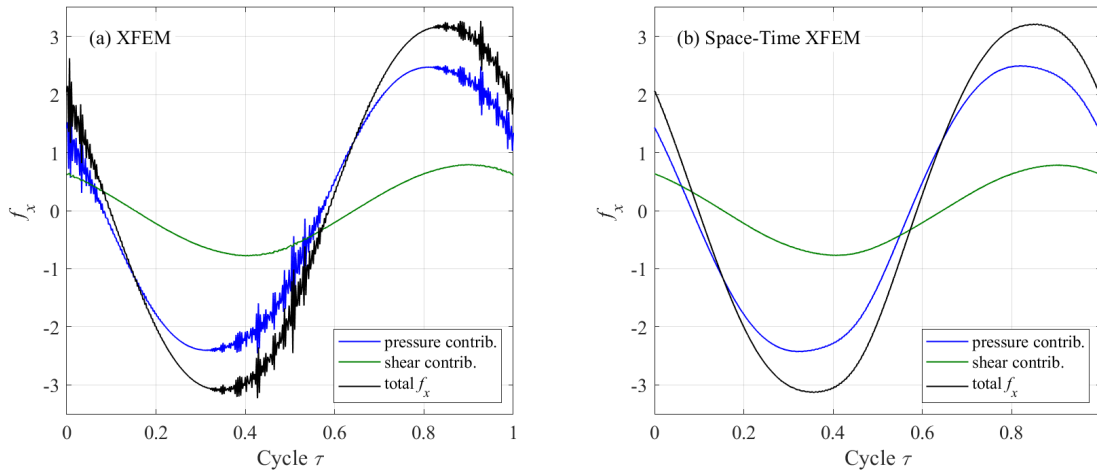


Figure 3.23: Comparison of dimensionless in-line force f_x
 (a) XFEM (b) space-time XFEM
 (Model 5 in Table 3.12, $0 \leq \tau \leq 1$)

the XFEM and the space-time XFEM. Pressure contribution of f_x computed by the XFEM (Figure 3.23(a)) highly oscillates and this oscillation is entirely due to a computational error as comparison of the numerical results against the reference experiment [85] (Figure 3.21). The XFEM with time stepping schemes cannot guarantee the continuity of state variables along time because the approximation of the time derivative terms fails due to moving interfaces; see Section 3.1. Therefore, the XFEM with time stepping schemes is not meaningful to evaluate C_D and C_M . On the other hand, f_x computed by the space-time XFEM (Figure 3.23(b)) has a smooth distribution which agrees well the experimental result (Figure 10 of [85]) and computational results using the body-fitted FEM (Figure 9 of [86]). As the finite element discretization is applied to both space and time in the space-time XFEM, the effect of a moving interface is successfully captured and the continuity of state variables along time is guaranteed.

Figure 3.24 shows the effect of the face-oriented ghost-penalty method in the space-time XFEM. The left figure is the history of the condition number of the Jacobian as an indicator of ill-conditioning. The right figure is the history of f_x . Using the space-time XFEM without

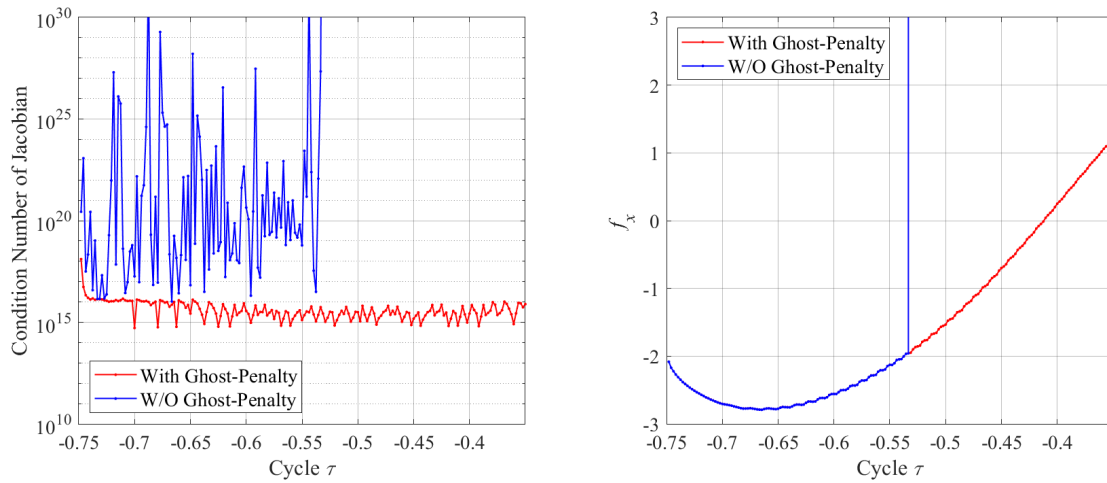


Figure 3.24: Effect of face-oriented ghost-penalty method
(Model 3 in Table 3.12)

the face-oriented ghost-penalty method (blue line in Figure 3.24), the condition number of the Jacobian is large and fluctuates largely due to the creation of small intersected volume by a moving interface. Finally, the transient analysis diverges at $\tau = -0.53125$ at an early stage due to ill-conditioning. On the other hand, the space-time XFEM with the face-oriented ghost-penalty method (red line in Figure 3.24) reduces the condition number of the Jacobian and its fluctuation. As the ill-conditioning problem is mitigated by the face-oriented stabilization, stable computation is achieved in this case. The results shown in Figures 3.23 and 3.24 suggest that the space-time XFEM with the face-oriented ghost-penalty method is a stable and efficient method for moving interface problems.

Figure 3.25 is the distribution of velocity in x : v_x^f using Model 5 in Table 3.12. There is a good agreement between Figure 3.25 and Figure 3.19 (Figure 7 of [86]). Figure 3.27 shows the distribution of normalized velocity v_x^f/V_x and v_y^f/V_x at four x locations in different phase positions corresponding to Figure 3.25. These distributions agree well with the ones in Figure 3.20 (Figure 8 of [85] and [86]). Thus, the results again suggest that the proposed method can reproduce numerical reference results using a moving interface problem.

Representative measures of this problem: drag coefficient C_D and added-mass coefficient

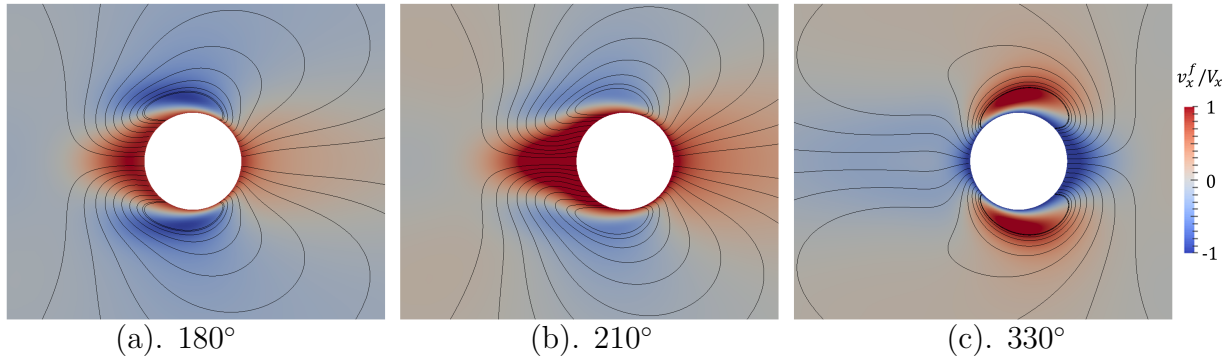


Figure 3.25: Distribution of v_x^f and streamlines at different phase positions θ
 $(\theta = 2\pi\tau = 2\pi ft)$

Table 3.12: Computational results and references of C_D and C_M ($Re = 100$ and $Kc = 5$)

| Model | Mesh (Region A) | Space-Time Active DOFs at $\tau = 5$ | h/D (Region A) | $\Delta\tau$ ($\Delta t/T$) | C_D | C_M |
|-------|--|--|---------------------|----------------------------------|--------|--------|
| 1 | 39×39 | 27816 | 1/13 | 1/480 | 2.0319 | 1.4315 |
| 2 | 59×59 | 45784 | 3/59 | 1/480 | 2.0633 | 1.4026 |
| 3 | 79×79 | 68216 | 3/79 | 1/480 | 2.0911 | 1.4117 |
| 4 | 99×99 | 94992 | 1/33 | 1/480 | 2.1142 | 1.4239 |
| 5 | 119×119 | 126112 | 3/119 | 1/480 | 2.1198 | 1.4236 |
| Ref.1 | Table 1, Set C of [85] | | | (experiment) | 2.0900 | 1.4500 |
| Ref.2 | Table 2, Mesh 480×400 of [86] | | | 1/720 | 2.0800 | 1.4340 |

(Region A: $|x/D| \leq 3$ and $|y/D| \leq 3$)

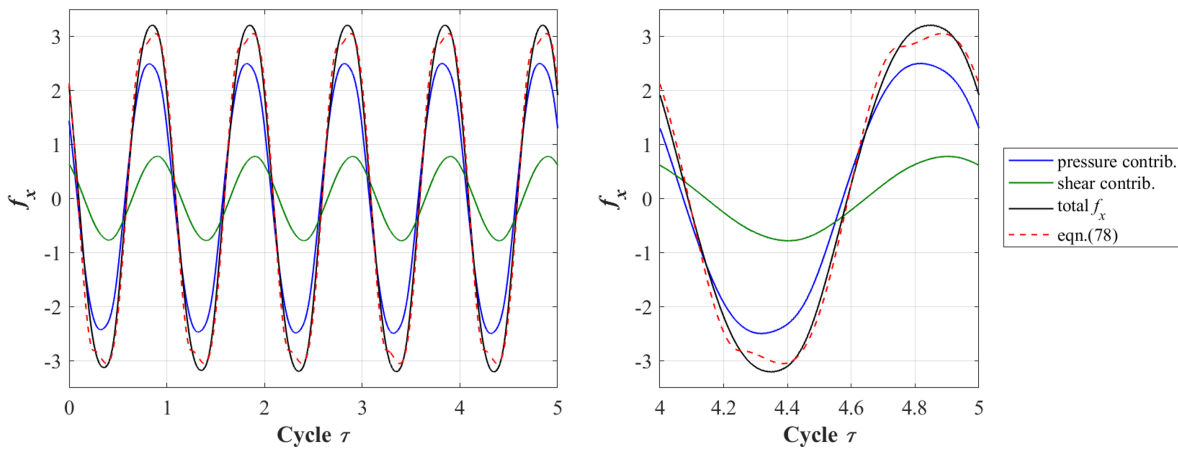


Figure 3.26: Dimensionless in-line force f_x (Model 5 in Table 3.12)

C_M are computed by the Fourier integral of the Morison equation (3.78)~(3.80). Table 3.12 shows the dependency of C_D and C_M with respect to the spatial discretization size h/D and reference solutions of [85] and [86]. C_D and C_M are evaluated at the fifth period ($4 \leq \tau \leq 5$: $\tau_0 = 4$ at (3.79) and (3.80)). The converged solution is obtained using the finest model (Model 5) of Table 3.12. Using Model 5, the values of C_D and C_M are $C_D = 2.1198$ and $C_M = 1.4236$. The difference of C_D and C_M with respect to results of Dütsch et al. [85] are 1.4% and -1.8% respectively. Figure 3.26 shows the history of dimensionless in-line force using Model 5. The total f_x (black line) is the summation of the pressure contribution (blue line) and the velocity contribution (green line) in this figure. The right figure is the history at the fifth period which is actually used for computations of C_D and C_M . The red line represents the approximation by the Morison equation (3.78). As [85] and [86] reported, an approximation of f_x by the Morison equation always has discrepancy around peaks of f_x like Figure 3.26 and this discrepancy reveals a limitation of the Morison equation. Guilmineau et al. [86] also referenced Dütsch et al. [85] and the difference of C_D and C_M were -0.5% and -1.1% respectively using an O-type structured fixed grid and a fixed interface assuming time-dependent interface condition. Although the difference of C_D and C_M of the proposed space-time XFEM is larger than [86], the difference of the proposed method from the reference is less than 2% and thus, this computational result is still acceptable. In addition, the proposed method handles a moving interface directly and thus, the space-time XFEM with the face-oriented ghost-penalty method is an attractive method which has the applicability for various moving interface problems.

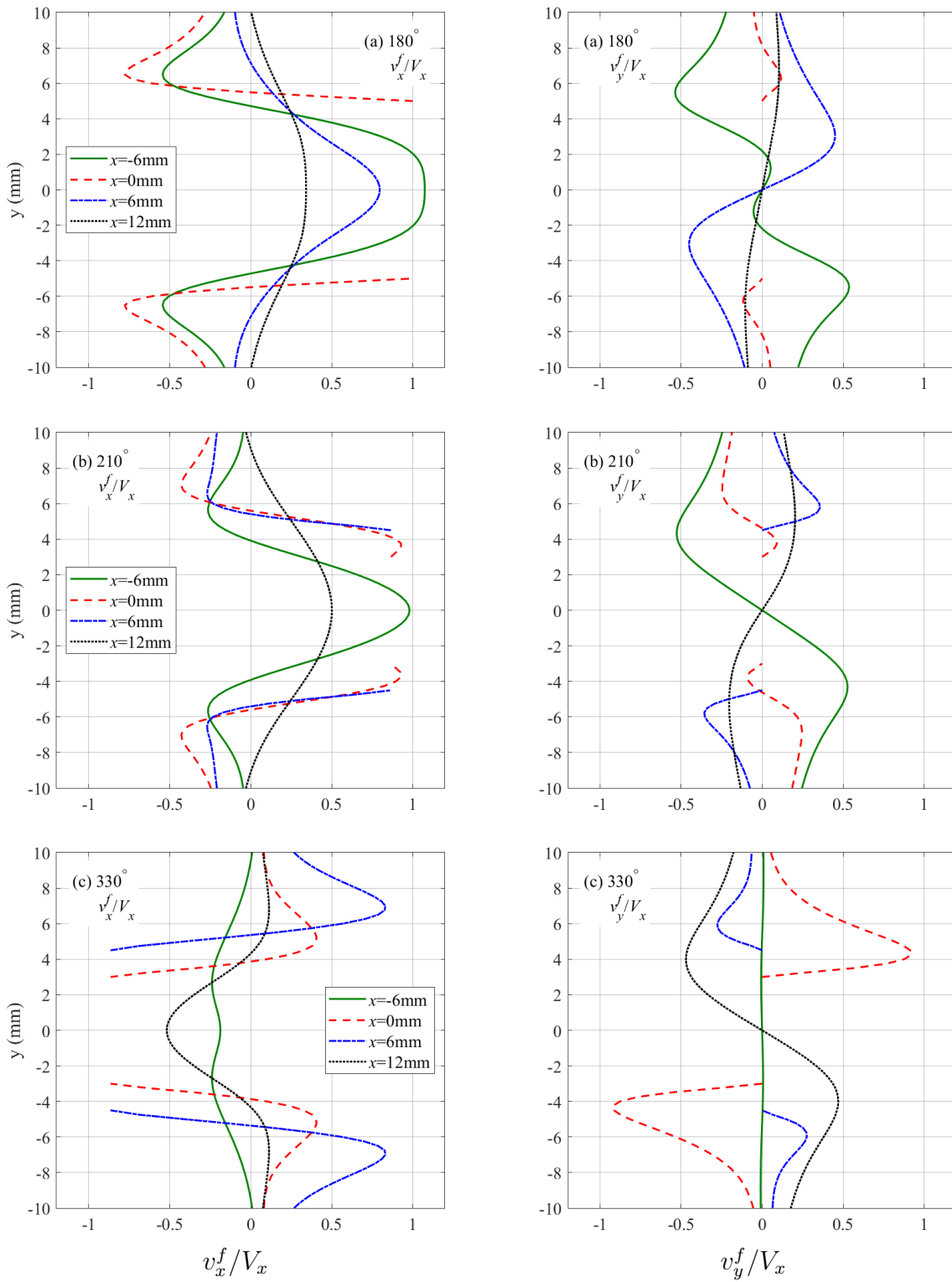


Figure 3.27: Distribution of velocities at different phase positions: (a)180°, (b)210°, (c)330° (Model 5 in Table 3.12, corresponding to Figure 8 of Guilmineau et al. [86])

3.7 Discussion

This chapter presents a space-time extended finite element method (space-time XFEM) based on the elementwise temporal layer approach using the Heaviside enrichment and the face-oriented ghost-penalty stabilization. for moving interface problems. A simple space-time integration based on the summation of spatial integration at multiple temporal quadrature points was introduced as the elementwise temporal layer approach. Each space-time element is subdivided into multiple temporal layers along time by considering its intersection configuration. Furthermore, temporal integration points are defined in each temporal layer and each temporal layer is cut by planes on these points parallel to the spatial domain. The cross sections created by this cut are called as the temporal slices in this thesis. As the number of temporal slices in each temporal layer affects the effective time increment, a larger number of slices is beneficial from the viewpoint to get a faster convergence in terms of the time evolution. In this thesis, three temporal integration points are defined in each temporal slice. Integration points for a space-time volume are distributed on each temporal slice using the same numerical integration scheme used in the standard XFEM. Integration points for space-time interface are set on a space-time interface which has the same dimension as the spatial domain. If the spatial dimension of a system is d , the procedure to set volume and interface integration points for the space-time XFEM is identical to the method for setting the volume integration points for the d -dimensional spatial XFEM. As higher-dimensional decompositions of a space-time slab like the simplex triangulation method are not needed, the proposed space-time XFEM eases significantly the implementation of the space-time integration. The space-time interface condition was prescribed by Nitsche's method. In addition, the face-oriented ghost-penalty method was applied in the space-time XFEM for mitigating the ill-conditioning problem due to small intersected space-time elements.

The proposed space-time XFEM was studied with an elasto-dynamic problem, which assumed a spatially two-dimensional two-phase problem using the finite strain theory and

the hyperelastic material. The comparison of four methods (spatial FEM spatial XFEM, space-time FEM and space-time XFEM) was performed. It was confirmed that results of the space-time XFEM and results of the space-time standard FEM (no interface) were identical. The implementation of Nitsche's method for the space-time interface condition was verified. A faster convergence of L2 errors was achieved using the space-time FEM/XFEM when compared to the spatial FEM/XFEM. This was because the space-time elements have internal temporal integration points and the effective time increment was smaller than the spatial FEM/XFEM.

The space-time XFEM was also applied to spatially two-dimensional transient fluid problems. The incompressible Navier-Stokes fluid was assumed and both fixed and moving interface conditions were computed. As a fixed interface problem, the well-known DFG 2D-3 benchmark problem was studied using both the spatial XFEM and the space-time XFEM. While the numerical accuracy of physical quantities that had a steady-state like behavior was quite similar in both method, the space-time XFEM could evaluate physical quantities that had a dynamic characteristic more precisely than the spatial XFEM using the same time increment. As a moving interface problem, the flow around an in-line oscillating cylinder was studied. The divergence of numerical solution was avoided successfully by the face-oriented ghost-penalty stabilization and it was confirmed that the face-oriented ghost-penalty method was effective to stabilize the numerical computations, especially for moving interface problems. The space-time XFEM overcomes numerical errors due to moving interfaces without any additional treatment such as the ghost-fluid method. Hence, the space-time XFEM predicted the smooth evolution of the in-line force similar to previous works (experiment and results with body-fitted fixed interface problem) using a moving interface problem.

Through these numerical examples, the space-time XFEM has great advantage in terms of stability, accuracy and flexibility for problems with moving interfaces. The space-time XFEM is applicable to complex moving interface problems, such as immiscible multiphase fluid

flow, non-ALE fluid-structure interaction and acoustic analysis around moving structures. The proposed elementwise temporal layer approach can be performed from one to three dimensional problems by using conventional settings of volume integration points of the XFEM. As this thesis focused on spatially two-dimensional problems, the proposed method needs to be studied using spatially three-dimensional problems in the future.

Chapter 4

Fluid-Structure Interaction

4.1 Outline

Transient problems with moving interfaces can be computed by the proposed space-time XFEM with increase accuracy and stability, compared to the XFEM approaches using time stepping schemes (Chapter 3). Robust and stable mathematical treatment for moving interfaces enhances the flexibility of the computational method for fluid-structure interaction (FSI) problems. In this thesis, non-standard FSI methods (non-ALE methods) with moving interfaces are studied, focusing on FSI-contact problems which are difficult to solve by the ALE-FSI. This chapter presents a classification of the numerical methods for FSI problems. More flexible FSI methods than the conventional ALE-FSI method are proposed for multi-physics FSI problems including large deformation and contact.

4.2 Classification of Numerical Methods for FSI

FSI is widely found in the physical world. The physical aspect of FSI is that fluid forces act on a solid and the deformation of the solid reaction affects the fluid flow. Applications of FSI models are widely considered for the design of industrial products, such as tires, airbags, aircraft, trains, vehicles, and biomedical problems such as interactions between organs and blood fluids. From a computational mechanics, there are some combinations of computational methods to solve these problems. Computational FSI methods are categorized by the following four factors; physical description, interface, solver and coupling in Figure 4.1.

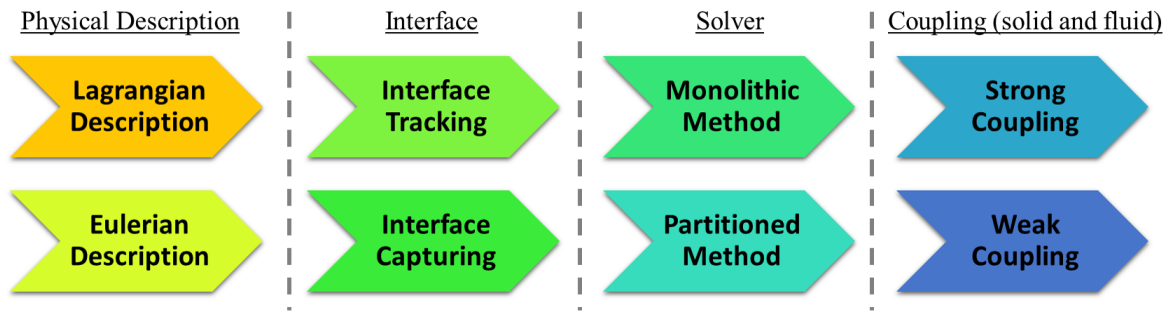


Figure 4.1: Category about numerical methods for FSI

4.3 Solution Method and Coupling

This section focuses on solution methods and couplings described in Figure 4.1. In FSI analysis, how to couple multi-physics phenomena is an essential key for the computation of FSI. In this research, the monolithic method is always used. The monolithic method is the strictest FSI solution method, which couples multi-physics phenomena at each time step. Considering FSI between phases a and b , the physical response in both phases at the next time step is computed by the physical response at previous time step and also current physical quantities mutually. The diagram of this solution method is shown in Figure 4.2. Blue and red arrows represent FSI. Blue arrows represent contribution from the physical response at the previous time step t_n . A red arrow means that a_{n+1} and b_{n+1} are computed simultaneously. This method is also called the strong coupling method and forms the basis for the fully-implicit residual and Jacobian. This method has the ability to treat FSI problems with large nonlinearity.

4.4 Physical Description and Treatment of Interface

Important characteristics to differentiate FSI methods are the physical description and treatment of interface described in Figure 4.1. First, focusing on the physical description. The Lagrangian description is a natural description of solids and also called the material

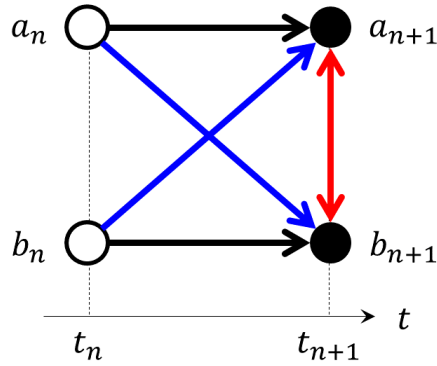


Figure 4.2: Monolithic method
(Strong Coupling)

• Monolithic Method

Residual

$$\mathbf{R}_a = \mathbf{R}_a(a_{n+1}, b_{n+1}, a_n, b_n) \quad (4.1)$$

$$\mathbf{R}_b = \mathbf{R}_b(b_{n+1}, a_{n+1}, b_n, a_n) \quad (4.2)$$

Jacobian

$$J_a = J_a(a_{n+1}, b_{n+1}, a_n, b_n) \quad (4.3)$$

$$J_b = J_b(b_{n+1}, a_{n+1}, b_n, a_n) \quad (4.4)$$

description. Physical quantities are defined at material points and thus, deformable meshes are usually used in this case. On the other hand, the Eulerian description is a natural description of fluids and also called as the field description. As there is no material point in the Eulerian description, physical quantities are defined in a fixed background mesh. Background meshes do not deform and keep their initial shape. For numerically solving FSI problems, the choice of the physical description of the solid and fluid phases has great impact on the numerical implementation and the flexibility such as the treatment of large deformation and contact.

The treatment of the interface is related to the physical description. When the Lagrangian description is applied, one can track the explicit interface defined by the edge of deformable meshes. Therefore, the interface tracking method can be used for the Lagrangian description. In contrast, when the Eulerian description is applied, the immersed boundary modeling is necessary to capture interfaces. The first attempt of the immersed boundary method was the volume of fluid method (VOF). The VOF defines interfaces by referencing the volume fraction of the fluid and is frequently used for FSI analysis. But there is a tendency that the interface fades due to the intermediate volume fraction. This drawback is fatal for complex interface geometries. The level set method does not suffer from this issue. The immersed interface is directly treated by an iso-contour line of the level set function.

Based on the physical description and the treatment of the interface, there are some representative methods for FSI. The most widely used and traditional way is FSI based on the arbitrary Lagrangian-Eulerian (ALE) formulation (Belytschko et al. [58], Huerta et al. [59, 60], Nitikitpaiboon and Bathe [61, 62], Bathe et al. [63]). This approach is called the ALE-FSI method in this thesis. In the ALE-FSI method, the solid domain is defined by deformable mesh based on the Lagrangian description. The fluid domain is also defined by deformable mesh to follow the deformation of the solid like a Lagrangian fashion, but the deformation of fluid mesh is driven by the fictitious velocity. This treatment is called the ALE formulation. FSI interfaces are explicitly defined by deformable meshes in this case. The left column of Figure 4.3 shows an image of mesh deformation in the ALE-FSI method.

The drawback of the ALE-FSI method is the computational limit due to the mesh deformation of the fluid domain. In the ALE-FSI method, the fluid ALE mesh around the solid domain must follow the deformation of the solid. It is difficult to preserve the topology of the fluid ALE mesh when large deformation of the solid occurs and then, the computation fails. Figure 4.4 shows one example of the breakdown of ALE meshes due to large deformation of the solid. The contact is also related to this drawback. Considering a FSI system where a solid Ω_S is initially immersed in a fluid phase Ω_F ; see Figure 4.5 on the left, When the solid contacts on the ground, the fluid mesh at the contact region should be annihilated. Although the ALE-FSI method can approximate this contact phenomenon with thin mesh, this technique does not allow for topological changes of the fluid mesh and becomes unstable and ill-conditioned. Therefore, it is difficult to handle contact phenomenon using the ALE-FSI method.

The full-Eulerian FSI method (Frei and Richter et al. [64, 65], Richter [66], Kamrin et al. [67, 68]), recently enjoys increasing attention. This method applies the Eulerian description for both the solid and fluid phases, and the interface capturing method such as the level set function method is used. Fixed background meshes are used for both the solid and fluid

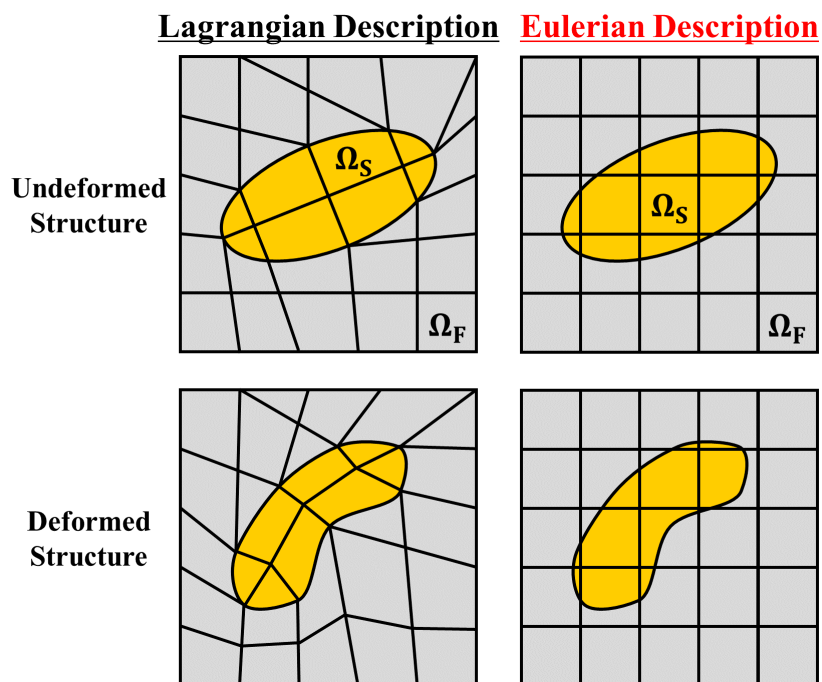
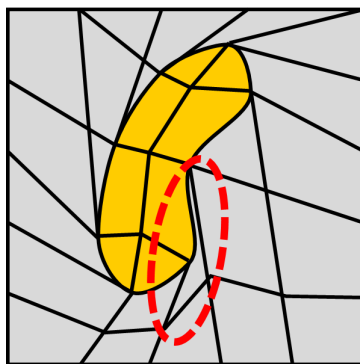
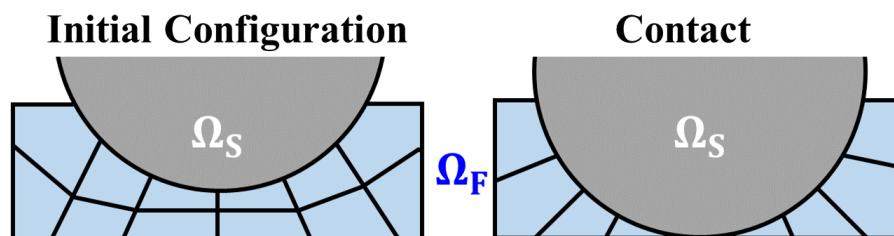


Figure 4.3: Image of mesh for FSI

Figure 4.4: Drawback of ALE-FSI 1
(Breakdown of fluid mesh)Figure 4.5: Drawback of ALE-FSI 2
(Annihilation of fluid mesh due to contact)

phases. The right column of Figure 4.3 shows an image of mesh in the full-Eulerian FSI method. As the background meshes do not deform, larger deformation can be computed than with the ALE-FSI method. In addition, contact can be simulated by the full-Eulerian FSI method because it allows for the topological changes of the fluid phase. One difficulty of this method is a stability issue due to the treatment of the solid phase based on the Eulerian description. The momentum equation of the solid phase includes the convection of material points based on the Eulerian description and thus, the stabilization for the convection term is needed in the solid phase like the fluid phase. Another difficulty is the representation of the FSI interfaces. Using the level set function as an interface capturing method, the interfaces are evolved by the Hamilton-Jacobi equation of the level set function and thus, a smaller time increment is always needed to capture reasonable interfaces.

Another way to compute FSI uses a mixed formulation of the Lagrangian and Eulerian description. Mayer, Wall, et al. [69, 70] proposed the XFEM based fixed grid approach using the ghost-fluid method to handle FSI and contact simultaneously. Miller et al. [91] proposed the oversetgrid method which is the combination of ALE-FSI method and Eulerian fluid analysis. In this thesis, the Lagrangian-immersed FSI method is proposed. The Lagrangian-immersed FSI uses the Lagrangian description for solids and the Eulerian description for fluids respectively. Solid bodies defined by the Lagrangian description are immersed within the Eulerian background meshes. The physical description changes across the interface between the solid and the fluid. This main concept is identical to [69, 70]. The main advantage of this method is that natural physical descriptions are used for both the solid and fluid phases. Interfaces in the fluid system are captured by the deformed interfaces of the solid system. In this case, the deformation of a solid body is trackable due to its deformable meshes based on the Lagrangian description. Therefore, tracking deformation is much easier than the Full-Eulerian FSI method. As solid bodies are completely disconnected from the fluid background mesh, large deformation and contact can be simulated without considering

the breakdown of the fluid ALE mesh in the ALE-FSI method. The challenging point of the Lagrangian-immersed FSI method is the treatment of FSI between the two different physical descriptions. The FSI computation in the Lagrangian-immersed FSI is performed on non-matching interface pairs of the solid and fluid systems.

Table 4.1 summaries computational methods for FSI considering physical description. The full-Eulerian FSI method and the Lagrangian-immersed FSI method are discussed in Chapters 5 and 6, respectively.

Table 4.1: Computational methods for FSI

| | ALE-FSI | Full-Eulerian FSI | Lagrangian-Immersed FSI |
|--------------------|-------------------------------|-----------------------------|---|
| Solid | Lagrangian | Eulerian | Lagrangian |
| Fluid | ALE | Eulerian | Eulerian |
| Interface | interface tracking | interface capturing | solid=interface tracking fluid=interface capturing |
| Challenging Points | large deformation and contact | treatment of Eulerian solid | FSI on non-matching interface pair |

Chapter 5

Full-Eulerian FSI Method using XFEM

5.1 Outline

This chapter focuses on the full-Eulerian FSI method using the XFEM and the time stepping scheme, as a non-standard FSI method for complex FSI-contact problems. There are two physical descriptions for the continuum body. One is the Lagrangian description, and the other is the Eulerian description. Focusing on the Eulerian description, there is no material point and physical quantities are observed on the fixed background points. This formulation bypasses the issues and limitations of the ALE-FSI formulation. As the solid phase is also represented in the fixed meshes, simultaneous treatment of both FSI and contact is possible. This chapter focuses on the FSI based on the Eulerian description, which is called as the full-Eulerian FSI method.

The key challenge of the full-Eulerian FSI method is the treatment of the solid phase based on the Eulerian description. There are several ways to model the deformation of a solid object based on the Eulerian description. For examples, Okazawa et al. [92] performed the Eulerian solid analysis based on the propagation of the deformation gradient F . Based on this research, displacement u_i is not defined and it is hard to reproduce u_i from F . On the other hand, the research of Kamrin et al. [93, 67, 68] and Levin et al. [94, 95] is based on the advection of the material coordinate (initial configuration) X_i , which is called as the reference map. This method can compute the displacement as $u_i = X_i - x_i$. Considering the actual product design, the displacement is one of important quantities of structures and also important for numerical applications such as the optimization. Therefore, this thesis follows the work of [93, 67, 68, 94, 95].

Sections 5.2 and 5.3 discuss the general theory related to the solid phase. In Section 5.4, the Eulerian solid analysis using the standard FEM is summarized. Sections 5.5 - 5.7 discusses the theory, numerical implementation and numerical examples of the Eulerian solid analysis using the XFEM with a standard time stepping scheme. Sections 5.8 and 5.9 provide the theory and numerical examples of the full-Eulerian FSI method using the XFEM and the time stepping scheme. Finally, Section 5.10 summarizes the findings for the full-Eulerian FSI method using the XFEM.

5.2 Mechanical Theory of Solids based on Eulerian Description

As the full-Eulerian FSI applies the Eulerian description to both the solid and fluid phases, it is necessary to describe the response of the solid phase by the Eulerian description. The treatment of the Eulerian description is the conventional way for the fluid phase. On the other hand, the treatment of solid phase based on the Eulerian description is not natural and thus, it is the challenging point of the full-Eulerian FSI method. This section summarizes the mechanical theory of elastic solids based on the Eulerian description.

Considering the conservation of momentum of a continuum body based on the Eulerian description, the Cauchy momentum equation using material derivative is:

$$\rho \frac{Dv_i}{Dt} = \rho \frac{\partial v_i}{\partial t} + \rho v_j \frac{\partial v_i}{\partial x_j} = \frac{\partial \sigma_{ij}}{\partial x_j} + \rho b_i, \quad (5.1)$$

where v_i denotes the solid velocity, ρ the denotes solid density, b_i denotes the body force and σ_{ij} denotes the Cauchy stress tensor. If the material is compressible, σ_{ij} is a function of just the displacements \mathbf{u} . If the material is incompressible, σ_{ij} is a function of \mathbf{u} and the hydrostatic pressure p ; $\sigma_{ij}(\mathbf{u}, p) = -p\delta_{ij} + \bar{\sigma}_{ij}(\mathbf{u})$, where $\bar{\sigma}_{ij}$ is a deviatoric stress tensor. Considering a material point of the Lagrange description with X_i being its spatial coordinates in the initial configuration, the time derivative of X_i is zero based on the Lagrangian

description:

$$\frac{DX_i}{Dt} = \frac{dX_i}{dt} = 0 \quad (\text{Lagrangian description}) , \quad (5.2)$$

where $\frac{D}{Dt}$ denotes a total derivative and $\frac{d}{dt}$ denotes a local time derivative. Using the Eulerian description, a total derivative is interpreted by a material derivative that considers the advection of particles of a continuum body. Therefore, (5.2) is rewritten as follows:

$$\frac{DX_i}{Dt} = \frac{\partial X_i}{\partial t} + v_j \frac{\partial X_i}{\partial x_j} = 0 \quad (\text{Eulerian description}) . \quad (5.3)$$

The displacements at the fixed background points \mathbf{x} are computed as follows:

$$u_i(\mathbf{x}, t) = x_i - X_i(\mathbf{x}, t) . \quad (5.4)$$

Kamrin et al. [93, 67, 68] and Levin et al. [94, 95] call X_i a reference map and use (5.3) and (5.4). From the displacements \mathbf{u} , one can compute strain measures such as the infinitesimal strain $\varepsilon_{ij}(\mathbf{u})$ and the inverse of the deformation gradients $F_{ij}^{-1}(\mathbf{u})$. As the displacements are defined in this method, conventional post processing (stress evaluation) of the standard FEM can be used:

$$\text{Infinitesimal strain:} \quad \varepsilon_{ij}(\mathbf{u}) = \frac{1}{2} \left(\frac{\partial u_i}{\partial x_j} + \frac{\partial u_j}{\partial x_i} \right) , \quad (5.5)$$

$$\text{Finite strain:} \quad F_{ij}^{-1}(\mathbf{u}) = \frac{\partial X_i}{\partial x_j} = \frac{\partial (x_i - u_i)}{\partial x_j} = \delta_{ij} - \frac{\partial u_i}{\partial x_j} . \quad (5.6)$$

However, X_i is not necessary because all strain measures can be computed by the displacement \mathbf{u} . Mathematically, reference maps \mathbf{X} are the linear combinations of displacements \mathbf{u} and current coordinates \mathbf{x} defined on the fixed background meshes like (5.4). As \mathbf{x} is constant, \mathbf{X} is computed from \mathbf{u} . \mathbf{X} contains more excessive information than \mathbf{u} . Consider the advection of 1D rigid body with a constant advective velocity along x direction; v_x , the advection of X_x (5.3) should keep the triangle shape with slope 1 because of $X_x = x$ at $t = 0$. Differential equations which have odd spatial derivatives are numerically unstable because the direction of the propagation is not symmetric, and stabilization methods such as the

SUPG (stream-upwind/Petrov-Galerkin) method is needed to solve (5.3). Using stabilization methods, numerical divergence is suppressed but the dissipation of advected properties due to these stabilization methods cannot be avoided. The advection of X_x using appropriate stabilization method is illustrated in Figure 5.1. Dissipation due to the stabilization method generally occurs on the trailing edge of the wave. As time goes on (from blue to red), a sharp edge in the initial configuration (blue line) becomes round due to the dissipation due to stabilization methods.

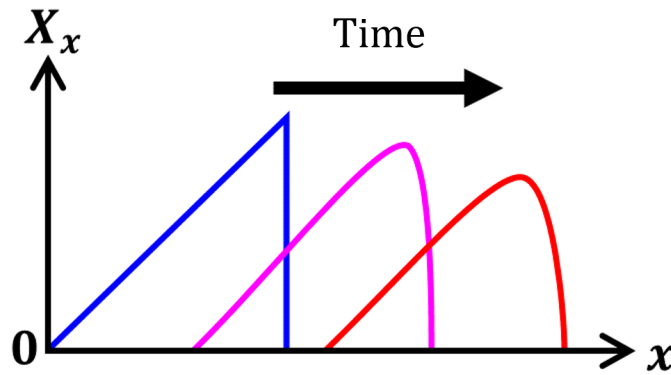


Figure 5.1: Image of 1D advection of reference map X_x using stabilization method

From the fact that the dissipation occurred at the trailing edges of waves, numerical dissipation is suppressed when there is no trailing edge in the initial configuration. Considering the 1D advection of a rigid body ($\frac{\partial u_x}{\partial x} = 0$), the advection of displacement u_x is more stable than (5.3). Therefore, the advection of the displacements is used instead of (5.3) in this research:

$$\frac{\partial u_i}{\partial t} + v_j \frac{\partial u_i}{\partial x_j} = v_i . \quad (5.7)$$

In the Eulerian FEM, interfaces of solid are not defined explicitly and an interface capturing method is essential to define interfaces of solid phase. The level set function ϕ is used as an interface capturing method in this research. The time evolution of the level set

function is also defined by an advection equation as follows:

$$\frac{\partial \phi}{\partial t} + v_j \frac{\partial \phi}{\partial x_j} = 0 . \quad (5.8)$$

5.3 Conservative Level Set Function (CLSF)

The definition of the solid interface by the iso-contour line of the level set function ϕ is the key factor of the Eulerian solid analysis. However, when the level set function is propagated by (5.8) using a stabilization method like the SUPG, leaking of the volume of the level set function frequently occurs. It is hard to conserve the total volume of the level set function. To propagate the level set function accurately, the conservative level set function (CLSF) method (Olsson et al. [96, 97]) is an efficient way. This CLSF method can maintain the conservation of the volume of the level set function by introducing a reinitialization step. A point to be aware of using the CLSF is that the form of the level set function is limited to a Heaviside-like step function. The following equation is an example of a Heaviside-like level set function to represent a circular structure with the radius r :

$$\phi(\mathbf{x}) = \left[1 + \exp\left(\frac{|\mathbf{x} - \mathbf{x}_c| - r}{\varepsilon_\phi}\right) \right]^{-1} \quad (\because \varepsilon_\phi = h^{1-d_\phi}) . \quad (5.9)$$

The value of ϕ is restricted between 0 and 1. ε_ϕ is the characteristic length with $\varepsilon_\phi > 0$ and defined by the spatial element size h and a coefficient d_ϕ ; $0 \leq d_\phi < 1$. When d_ϕ is set to a smaller value, a sharper distribution is obtained. On the other hand, when d_ϕ is set to a larger value, the slope of the level set function becomes small. Generally, functions that change drastically tend to cause the instability in numerical computations, especially due to the calculation of their derivatives. Therefore, d_ϕ is set as 0.1 in this research. This CLSF method consists of the following three steps:

$$\text{Step 1: Advection} \quad \frac{\partial \phi}{\partial t} + v_j \frac{\partial \phi}{\partial x_j} = 0 , \quad (5.10)$$

$$\text{Step 2: Normal Direction} \quad \hat{n}_i = \|\nabla \phi\|^{-1} \frac{\partial \phi}{\partial x_i} , \quad (5.11)$$

$$\text{Step 3: Reinitialization} \quad \frac{\partial \phi}{\partial t} + \frac{1}{\mu_\phi} \frac{\partial}{\partial x_j} \left[\phi(1 - \phi) \hat{n}_j \right] = \frac{\varepsilon_\phi}{\mu_\phi} \frac{\partial}{\partial x_j} \left[\left(\frac{\partial \phi}{\partial x_k} \hat{n}_k \right) \hat{n}_j \right]. \quad (5.12)$$

(5.10) is the basic form of the Hamilton-Jacobi equation. (5.11) and (5.12) are additional treatments by the CLSF. (5.11) is to compute the normal direction based on the result of the advection (5.10). (5.12) is the implicit reinitialization step, making ϕ smoother. μ_ϕ is a fictitious mass coefficient and set as 10 in this research. The values of ϕ are restricted between 0 and 1 due to the second term in the left-hand side.

5.4 Preliminary Study for Eulerian Solid Analysis

This section shows a numerical example of the Eulerian approaches such as the CLSF method and the reference map using the finite element (FEM), as the preliminary study of the Eulerian solid analysis using the XFEM. In this section, the propagation of the level set function around a 1D beam is computed. The beam is modeled by 2-node beam elements (BEAM2). Although the deformation of a continuum body is calculated based on a geometrically 1D beam model, the reference map \mathbf{X} , the level set function ϕ , strains and stresses are calculated in 2D in this case.

5.4.1 2-Node Beam Element (BEAM2)

This section summarizes the isoparametric representation for a BEAM2 element. The following discussion is common in both the Lagrangian approach and the Eulerian approach. The degrees of freedom of BEAM2 are two displacements in y direction and their first derivative with respect to x . A solution vector for the element e is defined as follows:

$$\mathbf{u}^e \equiv \left(u_{y1} \quad \theta_1 \quad u_{y2} \quad \theta_2 \right)^T, \quad (5.13)$$

where θ denotes a derivative of the displacement u_y with respect to x : $\theta = \frac{\partial u_y}{\partial x}$. The shape functions for a BEAM2 element are the Hermitian cubic shape functions:

$$N_{d1} \equiv \frac{1}{4}(1 - \xi)^2(2 + \xi) , \quad (5.14)$$

$$N_{\theta1} \equiv \frac{1}{8}l(1 - \xi)^2(1 + \xi) , \quad (5.15)$$

$$N_{d2} \equiv \frac{1}{4}(1 + \xi)^2(2 - \xi) , \quad (5.16)$$

$$N_{\theta2} \equiv -\frac{1}{8}l(1 + \xi)^2(1 - \xi) . \quad (5.17)$$

The isoparametric coordinate ξ is defined as:

$$\xi \equiv \frac{2}{l}x - 1 . \quad (5.18)$$

The Jacobian for the isoparametric transformation is as follows:

$$J \equiv \frac{dx}{d\xi} = \frac{l}{2} . \quad (5.19)$$

The derivatives of shape functions with respect to the Descartes coordinates are calculated as follows using the Jacobian (5.19):

$$\frac{dN_i}{dx} = J^{-1} \frac{dN_i}{d\xi} = \frac{2}{l} \frac{dN_i}{d\xi} \quad (i = d1, \theta1, d2, \theta2) . \quad (5.20)$$

These derivatives are summarized as follows:

First Derivatives w.r.t x

$$\frac{dN_{d1}}{dx} = -\frac{3}{2l}(1 - \xi^2) , \quad (5.21)$$

$$\frac{dN_{\theta1}}{dx} = -\frac{1}{4}(1 - \xi)(1 + 3\xi) , \quad (5.22)$$

$$\frac{dN_{d2}}{dx} = \frac{3}{2l}(1 - \xi^2) , \quad (5.23)$$

$$\frac{dN_{\theta2}}{dx} = -\frac{1}{4}(1 + \xi)(1 - 3\xi) , \quad (5.24)$$

Second Derivatives w.r.t. x

$$\frac{d^2 N_{d1}}{dx^2} = \frac{6}{l^2} \xi , \quad (5.25)$$

$$\frac{d^2 N_{\theta1}}{dx^2} = \frac{1}{l}(3\xi - 1) , \quad (5.26)$$

$$\frac{d^2 N_{d2}}{dx^2} = -\frac{6}{l^2} \xi , \quad (5.27)$$

$$\frac{d^2 N_{\theta2}}{dx^2} = \frac{1}{l}(3\xi + 1) . \quad (5.28)$$

In the following discussion, row vectors of shape functions are used for the weak form:

$$N \equiv \begin{pmatrix} N_{d1} & N_{\theta1} & N_{d2} & N_{\theta2} \end{pmatrix}, \quad (5.29)$$

$$N_x \equiv \begin{pmatrix} \frac{dN_{d1}}{dx} & \frac{dN_{\theta1}}{dx} & \frac{dN_{d2}}{dx} & \frac{dN_{\theta2}}{dx} \end{pmatrix}, \quad (5.30)$$

$$B \equiv \begin{pmatrix} \frac{d^2N_{d1}}{dx^2} & \frac{d^2N_{\theta1}}{dx^2} & \frac{d^2N_{d2}}{dx^2} & \frac{d^2N_{\theta2}}{dx^2} \end{pmatrix}. \quad (5.31)$$

5.4.2 Static Beam Analysis based on Lagrangian Description

Before discussing the dynamic analysis based on the Eulerian description, this section summarizes the static analysis based on the Lagrangian description. This section assumes infinitesimal strains based on Felippa [98] and Kwon [99].

The static analysis is to calculate the balance of the force and moment, and the corresponding displacements. The total potential energy of the element e has the quadratic form in terms of the nodal displacements:

$$\Pi_e \equiv \frac{1}{2} \mathbf{u}_e^T K_e \mathbf{u}_e - \mathbf{u}_e^T \mathbf{f}_e. \quad (5.32)$$

In (5.32), K_e and \mathbf{f}_e are the local stiffness matrix and the local nodal force vector defined as follows:

$$K_e = \int_0^l dx B^T B = \int_{-1}^1 d\xi \frac{EI}{2} B^T B, \quad (5.33)$$

$$\mathbf{f}_e = \int_0^l dx q N^T = \int_{-1}^1 d\xi \frac{ql}{2} N^T, \quad (5.34)$$

where E is the Young's modulus, I is the moment of inertia and q is the load. These three variables are functions of x in general. If the bending rigidity EI and the load q have an

uniform distribution, (5.33) and (5.34) can be calculated analytically as follows:

$$K_e = \frac{EI}{2} \int_{-1}^1 d\xi B^T B = \frac{EI}{l^3} \begin{pmatrix} 12 & 6l & -12 & 6l \\ & 4l^2 & -6l & 2l^2 \\ & & 12 & -6l \\ \text{Symm} & & & 4l^2 \end{pmatrix}, \quad (5.35)$$

$$\mathbf{f}_e = \frac{ql}{2} \int_{-1}^1 d\xi N^T = \frac{ql}{2} \begin{pmatrix} 1 \\ l/6 \\ 1 \\ l/6 \end{pmatrix}. \quad (5.36)$$

Assuming a deflection of the beam due to the body force with the constant bending rigidity, (5.35) and (5.36) can be used because $q = -g$, which has a constant distribution everywhere. Then, assembling K_e and \mathbf{f}_e of all elements in the system, displacements and rotations (derivative of displacements) of each node are determined by solving the balance of forces and moments. K and \mathbf{f} are the total stiffness matrix and the total force vector. If the beam has N nodes, K is a $2N \times 2N$ matrix and following \mathbf{f} and \mathbf{u} are $2N$ dimension vectors:

$$K\mathbf{u} = \mathbf{f} \quad (5.37)$$

$$\mathbf{f}^T = (f_{y1}, f_{\theta1}, \dots, f_{yN}, f_{\theta N}) \quad (5.38)$$

$$\mathbf{u}^T = (u_{y1}, \theta_1, \dots, u_{yN}, \theta_N) \quad (5.39)$$

By solving (5.37), the stationary solution of the beam deflection is determined.

5.4.3 Dynamic Beam Analysis based on Lagrangian description

The stationary solution of the deflection of a beam can be calculated based on the method outlined above. But the method of the static analysis cannot be applied to the finite element method based on the Eulerian description (Eulerian FEM) because the Eulerian FEM is

inherently a dynamic analysis. This section summarizes the method of the dynamic analysis for BEAM2 elements based on the Lagrangian description.

The governing equation of the dynamic BEAM2 analysis using the FEM is as follows:

$$M \frac{d^2 \mathbf{u}}{dt^2} + C \frac{d\mathbf{u}}{dt} + K \mathbf{u} = \mathbf{f} , \quad (5.40)$$

$$\mathbf{u}^T \equiv \left(u_{y1} \quad \theta_1 \quad \cdots \quad u_{yN} \quad \theta_N \right) , \quad (5.41)$$

where M , C , K and \mathbf{f} are the mass matrix, the damping matrix, the stiffness matrix and the force vector respectively. They are assembled by corresponding local matrices M_e , C_e and K_e , and local force vector \mathbf{f}_e defined as follows based on the continuous Galerkin method:

$$\text{Local mass matrix:} \quad M_e = \int_0^l dx \, m N^T N = \int_{-1}^1 d\xi \frac{ml}{2} N^T N , \quad (5.42)$$

$$\text{Local damping matrix:} \quad C_e = \int_0^l dx \, c N^T N = \int_{-1}^1 d\xi \frac{cl}{2} N^T N , \quad (5.43)$$

$$\text{Local stiffness matrix:} \quad K_e = \int_0^l dx \, B^T B = \int_{-1}^1 d\xi \frac{EI}{2} B^T B , \quad (5.44)$$

$$\text{Local force vector:} \quad \mathbf{f}_e = \int_0^l dx \, q N^T = \int_{-1}^1 d\xi \frac{ql}{2} N^T . \quad (5.45)$$

If the mass and the damping coefficient are constant, the above matrices and vector can be calculated analytically. As (5.44) and (5.45) are the same as (5.33) and (5.34) in the static analysis, the results of analytical integration are identical to (5.35) and (5.36). M_e and C_e are defined as follows:

$$M_e = \frac{ml}{2} \int_{-1}^1 d\xi N^T N = \frac{\rho A l}{420} \begin{pmatrix} 156 & 22l & 54 & 13l \\ & 4l^2 & 13l & -3l^2 \\ & & 156 & -22l \\ \text{Symm} & & & 4l^2 \end{pmatrix} , \quad (5.46)$$

$$C_e = \frac{cl}{2} \int_{-1}^1 d\xi N^T N = \frac{cl}{420} \begin{pmatrix} 156 & 22l & 54 & 13l \\ & 4l^2 & 13l & -3l^2 \\ & & 156 & -22l \\ \text{Symm} & & & 4l^2 \end{pmatrix}. \quad (5.47)$$

The central differencing method is used for the time integration of (5.40):

$$\text{Step 1: } \mathbf{a}^{(n)} \equiv \frac{d^2 \mathbf{u}^{(n)}}{dt^2} = M^{-1}(\mathbf{f}^{(n)} - C\mathbf{v}^{(n)} - K\mathbf{u}^{(n)}), \quad (5.48)$$

$$\text{Step 2: } \mathbf{v}^{(n+1/2)} \equiv \frac{d\mathbf{u}^{(n)}}{dt} = \mathbf{v}^{(n-1/2)} + \Delta t \mathbf{a}^{(n)}, \quad (5.49)$$

$$\text{Step 3: } \mathbf{u}^{(n+1)} = \mathbf{u}^{(n)} + \Delta t \mathbf{v}^{(n+1/2)}. \quad (5.50)$$

where \mathbf{a} , \mathbf{v} and \mathbf{u} denote accelerations, velocities and displacements respectively. The upper subscript (n) denotes the time step. First, the acceleration at the current time step n is calculated and then, the intermediate velocity at the time step $n + 1/2$ is also computed. Finally, the displacement at the time step $n + 1$ is updated. Because the damping matrix exists in this system, the dissipation of the energy occurs. Finally, the deflection of the beam becomes stationary due to this dissipation of the energy. Therefore, the stationary solution of the dynamic analysis is obtained, which is the same as the result of the static analysis mentioned in the previous section.

5.4.4 Dynamic Beam Analysis based on Eulerian Description

The dynamic beam analysis based on the Eulerian description is an extension of the one based on the Lagrangian description. Although the kinematic model is identical to the Lagrangian approach, the deformation of the solid phase is represented by the CLSF method in the Eulerian approach. It should be noted that the Eulerian approaches are used only in the post-processing and the Eulerian approaches do not have an effect on the structural analysis.

The advection velocity is calculated by the beam model outlined above and then, the

Eulerian fields such as the level set function and the reference map, are calculated based on the advection equation using the preceding advective velocity. The computation of the level set function and the reference map is performed by 2D elements. In this case, QUAD4 is used for the 2D spatial discretization. The procedure of this approach is as follows:

Procedure of the dynamic beam analysis based on the Eulerian description

Step 1: Calculate (5.48) - (5.50) \Rightarrow Set the advective velocity \bar{v}_y

$$\text{Step 2: Propagate the level set function} \quad \frac{\partial \phi}{\partial t} + \bar{v}_j \frac{\partial \phi}{\partial x_j} = 0 \quad (5.51)$$

$$\text{Step 3: Propagate the reference map} \quad \frac{\partial X_i}{\partial t} + \bar{v}_j \frac{\partial X_i}{\partial x_j} = 0 \quad (5.52)$$

$$\text{Step 4: Propagate the velocity field} \quad \frac{\partial v_i}{\partial t} + \bar{v}_j \frac{\partial v_i}{\partial x_j} = 0 \quad (5.53)$$

$$\text{Step 5: Calculate the displacement} \quad u_y^{(n+1)}(\mathbf{x}) = y - X_y^{(n+1)}(\mathbf{x}) \quad (5.54)$$

$$\text{Step 6: Calculate the curvature} \quad \kappa = \frac{d^2 u_y}{dx^2} = B \mathbf{u}^e \quad (5.55)$$

$$\mathbf{u}^e = \begin{pmatrix} u_{y1} & \theta_1 & u_{y2} & \theta_2 \end{pmatrix} \quad (5.56)$$

$$\text{Step 7: Calculate the local strain} \quad \bar{\epsilon}^{(n+1)} = -(X_y^{(N+1)} - y_0) \kappa \quad (5.57)$$

$$\text{Step 8: Calculate the local stress} \quad \bar{\sigma}^{(n+1)} = E \bar{\epsilon} \quad (5.58)$$

Step 9: Rotate the local strain and stress into the global coordinate system

\Rightarrow Go back to Step 1

5.4.5 Numerical Example of 2D Beam Analysis

This section compares the dynamic beam problems using the FEM based on both the Lagrangian and the Eulerian description. The benchmark problem is the deflection of a cantilever beam due to the body force. The initial configuration of this cantilever beam is listed in Table 5.1 and shown in Figure 5.2.

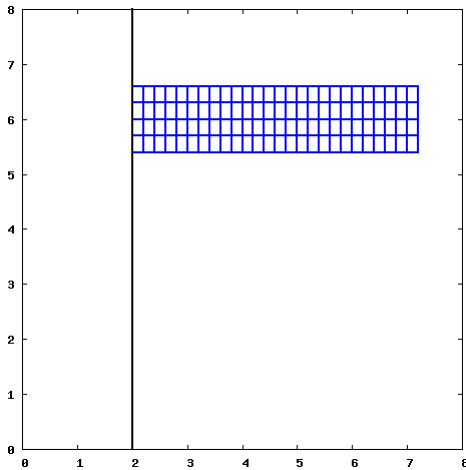


Figure 5.2: Initial configuration of beam

| Parameter | Symbol | Value |
|---------------------|----------------------|-----------|
| length | L | 5 |
| height | h | 1.2 |
| cross section | A | 1 |
| density | ρ | 1 |
| bending rigidity | EI | 100 |
| damping coefficient | c | 0.6 |
| time increment | Δt | 10^{-4} |
| spatial increments | $\Delta x, \Delta y$ | 0.2 |

Figure 5.3 shows the result of the dynamic beam analysis based on the Lagrangian description. The blue mesh shows the deformed Lagrangian mesh and the red line indicates the neutral axis of the analytical solution. The neutral axis of the Lagrangian approach agrees well the one of the analytical solution. Figure 5.4 shows the result of the dynamic beam analysis based on the Eulerian description. The blue shading represents the value of the level set function and the red line is the neutral surface of the analytical solution same as Figure 5.3. The deflection of a beam is identical to the result of the Lagrangian approach because the same BEAM2 model is used in both approaches. The solid phase in the Eulerian approach is appropriately represented by the level set function, comparing with Figure 5.3. The Eulerian approach predicts a similar result of the Lagrangian approach. The drawback of the Eulerian approach using the XFEM jagged interface like Figure 5.4. To represent accurate interfaces, the XFEM is more suitable for the Eulerian analysis.

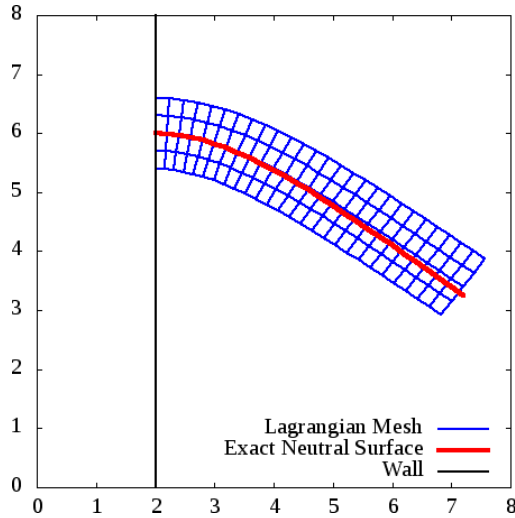


Figure 5.3: Result of Lagrangian FEM
(blue: Lagrangian mesh)

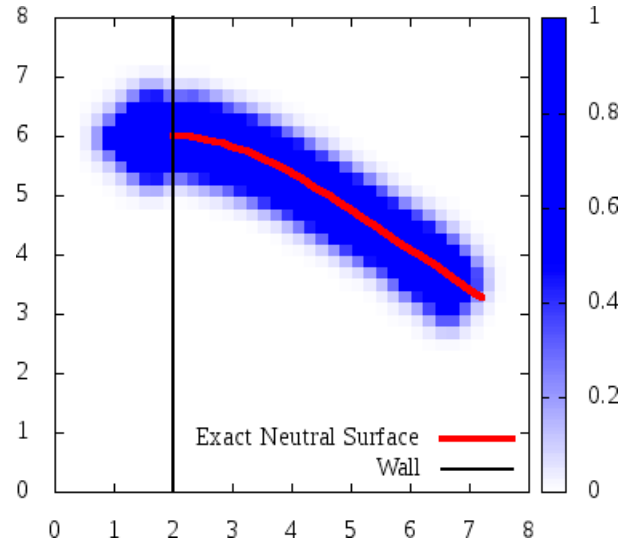


Figure 5.4: Result of Eulerian FEM
(blue: level set function)

5.5 Numerical Implementation of Eulerian Solid Analysis using XFEM

To simulate accurately interfaces of an Eulerian solid, the XFEM is more suitable than the FEM. An interface can be represented by intersected elements of the XFEM more accurately. To apply the XFEM to the Eulerian solid analysis, some special techniques are necessary for the treatment of the void phase and the stabilization of the numerical formulation. Three techniques are explained in this section.

5.5.1 Helmholtz smoothing Method

The momentum equation of the solid (5.1) is computed in the solid phase Ω_S . On the other hand, the propagation of the level set function should be performed in the entire computational domain Ω including the void phase Ω_V . Therefore, defining pseudo velocity fields in the void phase Ω_V is essential for the Eulerian solid analysis. In this research, the Helmholtz smoothing method is used to compute velocity fields in Ω_V . This smoothing is

based on the Helmholtz equation defined as follows:

$$-\Delta a^v + k^2 a^v = 0 \quad \text{in } \Omega_V, \quad (5.59)$$

$$a^s = a^v \quad \text{on } \Gamma_{SV} \quad (5.60)$$

where a^v and a^s are some scalar fields in Ω_V and Ω_S respectively. (5.60) is a boundary condition on the solid-void interface Γ_{SV} . For the velocity fields, $a = v_i$. k is a coefficient of the production term and k^2 is set to 1 in this section. To use this Helmholtz smoothing method, velocity fields in the void Ω_V (outside of the solid structure) connects smoothly to velocity fields in Ω_S and the resulting pseudo velocity field decreases monotonically in void as the distance to the solid domain increases.

5.5.2 Nitsche's Method

This section describes Nitsche's method to enforce the $C0$ continuities on the interfaces. The original objective of the XFEM is to capture discontinuities on the interfaces, focusing on the crack propagation. On the other hand, considering the Eulerian solid analysis, the XFEM is used to represent solid interfaces, not to introduce the discontinuities in state variables. While displacements are computed only in the solid phase Ω_S , velocities are computed in both the solid and void phase by using Helmholtz smoothing method. Therefore, the straightforward application of the XFEM based on a Heaviside enrichment strategy to the Eulerian solid may introduce discontinuity in the velocity fields v_i on the solid-void interface.

To avoid the discontinuity of the velocity fields on the solid-void interface Γ_{SV} , Nitsche's method is applied to velocities v_i in this research. Considering a generic two-phase problem as shown Figure 5.5, the following continuity needs to be enforced:

$$[[v_i]] = v_i^1 - v_i^2 = 0 \quad \text{on } \Gamma_{12}, \quad (5.61)$$

where v_i^1 denotes the velocity in the phase 1: Ω_1 , v_i^2 denotes the velocity in the phase 2: Ω_2 ,

and $[[\cdot]]$ is the jump operator that computes the difference of the physical quantities on Γ_{12} . The image of an intersected element is shown in Figure 5.5. For the pure solid analysis, one of these phases is a solid phase and the other is a void phase, and Γ_{12} is Γ_{SV} .

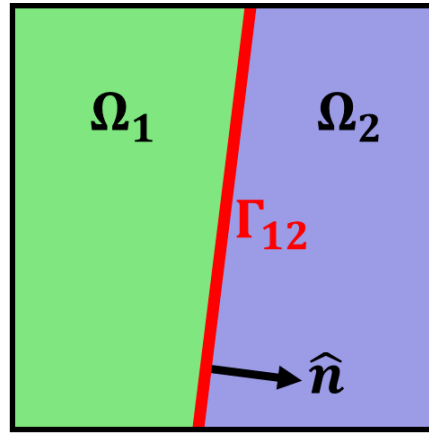


Figure 5.5: Intersected element

Nitsche's method (5.61) is applied to the momentum equation by introducing a penalty factor to enforce weakly that velocity fields v_i satisfy (5.61). Assuming Ω_2 is a solid phase, which is filled by a continuum body, and Ω_1 is a void phase. The strong forms are as follows:

$$-\Delta v_i + v_i = 0 \quad \text{in } \Omega_1 \text{ (Void Phase) ,} \quad (5.62)$$

$$\frac{\partial v_i}{\partial t} + v_j \frac{\partial v_i}{\partial x_j} = \rho^{-1} \frac{\partial \sigma_{ij}}{\partial x_j} + b_i \quad \text{in } \Omega_2 \text{ (Solid Phase) ,} \quad (5.63)$$

$$[[v_i]] = v_i^1 - v_i^2 = 0 \quad \text{on } \Gamma_{12} \text{ (Solid-Void Interface) .} \quad (5.64)$$

Corresponding weak form of (5.62) - (5.64) is summarized as follows based on the formulation of the symmetric Nitsche's method, assuming compressible material as a simple case. The derivation of (5.65) is summarized in Appendix B:

$$\begin{aligned} & (\nabla \delta \mathbf{v}, \rho \nabla \mathbf{v})_1 + (\delta \mathbf{v}, \rho \mathbf{v})_1 + \left(\delta \mathbf{v}, \rho \frac{\partial \mathbf{v}}{\partial t} + \rho \mathbf{v} \cdot \nabla \mathbf{v} - \rho \mathbf{b} \right)_2 + (\nabla \delta \mathbf{v}, \sigma)_2 + \left\langle \delta \mathbf{v}, \rho \nabla \mathbf{v} \cdot \hat{\mathbf{n}}_{1 \rightarrow 2} \right\rangle_{\Gamma_{12}} \\ & + \left\langle \{ \delta \sigma \} \cdot \hat{\mathbf{n}}_{1 \rightarrow 2}, [\mathbf{u}] \right\rangle_{\Gamma_{12}} + \left\langle [[\delta \mathbf{v}]], \{ \sigma \} \cdot \hat{\mathbf{n}}_{1 \rightarrow 2} \right\rangle_{\Gamma_{12}} + \eta^N \left\langle \delta \mathbf{v}^1, [[\mathbf{v}]] \right\rangle_{\Gamma_{12}} = 0 , \end{aligned} \quad (5.65)$$

where $(\cdot)_\alpha$ and $\langle \cdot \rangle_{\Gamma_\beta}$ denote the volume integral and the boundary integral:

$$\text{Volume Integral:} \quad (\mathbf{a}, \mathbf{b})_\alpha \equiv \int_{\Omega_\alpha} d\Omega \mathbf{a}^T \mathbf{b} , \quad (5.66)$$

$$\text{Boundary Integral:} \quad \langle \mathbf{a}, \mathbf{b} \rangle_{\Gamma_\beta} \equiv \int_{\Gamma_\beta} d\Gamma \mathbf{a}^T \mathbf{b} . \quad (5.67)$$

Red terms in (5.65) denote terms related to Nitsche's method. η^N is the penalty factor for Nitsche's method. The test function for the last term at the left-hand side (the Nitsche's penalty term) is the test function of a void phase based on the one-sided Nitsche method. This treatment is because of that the fictitious velocity on the void phase does not affect the solid velocity. $\{\cdot\}$ is the averaging operator defined as follows:

$$\{\mathbf{u}\} \equiv w^1 \mathbf{u}^1 + w^2 \mathbf{u}^2 \quad (\cdot: w^1 + w^2 = 1) , \quad (5.68)$$

$$\{\mathbf{v}\} \equiv w^1 \mathbf{v}^1 + w^2 \mathbf{v}^2 , \quad (5.69)$$

$$\{\delta\sigma\} = w^1 \sigma(\delta\mathbf{v}^1) + w^2 \sigma(\delta\mathbf{v}^2) . \quad (5.70)$$

There are several ways to define these weighting factors w^i . Here are examples of the weighting strategies:

$$\text{Equal Weighting} \quad w^1 = w^2 = 0.5 , \quad (5.71)$$

$$\text{Area Weighting} \quad w^1 = \frac{A_1}{A_1 + A_2}, \quad w^2 = \frac{A_2}{A_1 + A_2} , \quad (5.72)$$

$$\text{Modulus Weighting} \quad w^1 = \frac{E_2}{E_1 + E_2}, \quad w^2 = \frac{E_1}{E_1 + E_2} , \quad (5.73)$$

$$\text{Dolbow et.al. [100]} \quad w^1 = \frac{A_1/E_1}{A_1/E_1 + A_2/E_2}, \quad w^2 = \frac{A_2/E_2}{A_1/E_1 + A_2/E_2} , \quad (5.74)$$

where A_i and E_i are the area and Young's modulus of phase i respectively. To satisfy the traction free boundary condition on Γ_{12} , a weighting strategy which is $w^1 = 1$ and $w^2 = 0$ is appropriate. Therefore, the modulus weighting ($E_1 = 0$) is the appropriate method for the Eulerian solid analysis. In addition, this thesis uses the one-sided Nitsche method, i.e. the test function is constructed by only shape functions in Ω_1 : N^1 , such that the void phase Ω_V does not affect the solution in the solid phase Ω_S .

5.5.3 Face-Oriented Ghost-Penalty Method

The interface of the Eulerian solid is defined by the level set function ϕ on fixed background meshes. Therefore, intersected elements which have very small area (volume in 3D) are generally created around the interfaces. If small elements exist, the condition number of the Jacobian becomes larger and the solution tends to become inaccurate. This ill-conditioning problem leads to the blow-up of the solution, which is a purely computational phenomenon, not a physical problem. To avoid this ill-condition of the Jacobian, the face-oriented ghost-penalty method proposed by Burman [55, 56] is an efficient way to improve the stability.

Here, 2D Eulerian solid system that contains two phases is assumed: one phase is the solid phase and the other is the void phase. The face-oriented ghost-penalty method is only applied on the edges around intersected elements. The face-oriented ghost-penalty method is applied on the faces of intersected elements Γ_{12}^{GP} as shown in 5.6.

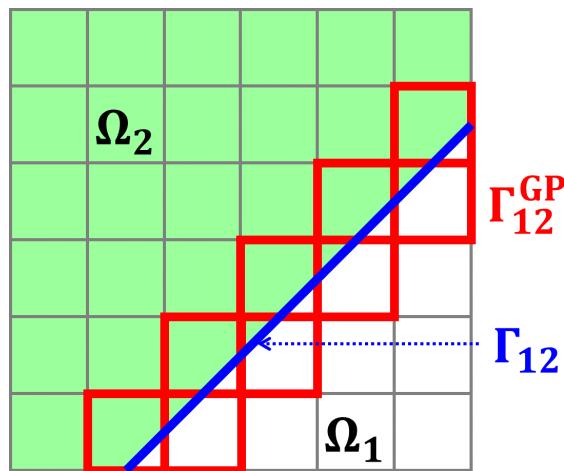


Figure 5.6: Boundaries for face-oriented ghost-penalty method

The objective of this method is to reduce the condition number of the Jacobian by enforcing that the jumps of the flux of solution in both phases are zero. Thus, the following

weak form of the face-oriented ghost-penalty method is added to (5.65):

$$+\eta^{\text{gp}} \left\langle \llbracket \nabla \delta \mathbf{v} \rrbracket \cdot \hat{\mathbf{n}}, \llbracket \nabla \mathbf{v} \rrbracket \cdot \hat{\mathbf{n}} \right\rangle \quad \text{on } \Gamma_{12}^{\text{gp}}, \quad (5.75)$$

where η^{gp} is a penalty factor of the face-oriented ghost-penalty method. In the face-oriented ghost-penalty method, the jump terms are integrated over the entire face, individually for each phase that is considered. Thus, this method integrates twice over an intersected edge in a solid-solid problem, using different interpolation functions and state variables.

5.6 Eulerian Solid Analysis using XFEM

Considering the Helmholtz smoothing, Nitsche's method and the face-oriented ghost-penalty method, the overall governing equations for the Eulerian solid analysis using XFEM are summarized as follows. Section 5.6.1 introduces first strong forms and Section 5.6.2 summarizes the corresponding weak form. In this section, the incompressible solid is assumed as the most complex case.

5.6.1 Strong Form of Eulerian Solid Analysis

The governing equations using velocities as independent state variables are summarized as follows:

- Velocity

- Momentum: $\frac{\partial v_i}{\partial t} + v_j \frac{\partial v_i}{\partial x_j} + \alpha v_i = \rho^{-1} \frac{\partial \sigma_{ij}(\mathbf{u}, p)}{\partial x_j} + b_i \quad \text{in } \Omega_S, \quad (5.76)$

- Continuity: $\frac{\partial v_i}{\partial x_i} = 0 \quad \text{in } \Omega_S, \quad (5.77)$

- Helmholtz: $\Delta v_i + v_i = 0 \quad \text{in } \Omega_V, \quad (5.78)$

- Nitsche: $\llbracket v_i \rrbracket = v_i^1 - v_i^2 = 0 \quad \text{on } \Gamma_{\text{SV}}, \quad (5.79)$

- Ghost-Penalty: $\left[\left[\frac{\partial v_i}{\partial x_j} \right] \right] \hat{n}_j = \left(\frac{\partial v_i^1}{\partial x_j} - \frac{\partial v_i^2}{\partial x_j} \right) \hat{n}_j \quad \text{on } \Gamma_{\text{SV}}^{\text{gp}}. \quad (5.80)$

In this section, σ_{ij} denotes the stress tensor, which is a function of \mathbf{u} and p . The additional viscous term αv_i is introduced in (5.76) such that the structure converges to a steady-state solution the equilibrium state and α is set to 1 in this research.

The governing equations for the displacement field and the level set function are summarized as follows.

- Displacement

- Advection:
$$\frac{\partial u_i}{\partial t} + v_j \frac{\partial u_i}{\partial x_j} - v_i = 0 \quad \text{in } \Omega_S, \quad (5.81)$$

- Conservative Level Set Function (CLSF)

- Advection:
$$\frac{\partial \phi}{\partial t} + v_j \frac{\partial \phi}{\partial x_j} = 0 \quad \text{in } \Omega, \quad (5.82)$$

- Normal Vector:
$$\hat{n}_i \equiv \frac{1}{|\nabla \phi|} \frac{\partial \phi}{\partial x_i} \quad \text{in } \Omega, \quad (5.83)$$

- Reinitialization:
$$\frac{\partial \phi}{\partial t} + \frac{1}{\mu_\phi} \frac{\partial}{\partial x_i} [\phi(1 - \phi)\hat{n}_i] = \frac{\varepsilon_\phi}{\mu_\phi} \frac{\partial}{\partial x_i} [(\nabla \phi \cdot \hat{\mathbf{n}})\hat{n}_i] \quad \text{in } \Omega, \quad (5.84)$$

where Ω denotes the entire computational domain as $\Omega = \Omega_S \cup \Omega_V$.

5.6.2 Weak Form of Eulerian Solid Analysis

The corresponding weak form is defined by applying SUPG and PSPG stabilization methods. Because of the use of the conservative level set function, a staggered approach is necessary for the Eulerian solid analysis. Therefore, the residual \mathcal{R} is divided into following three steps ($\mathcal{R} = \mathcal{R}^1 + \mathcal{R}^2 + \mathcal{R}^3$). \mathcal{R}^1 is the standard residual of the Eulerian solid analysis for the incompressible material. \mathcal{R}^2 and \mathcal{R}^3 are the residuals for the reinitialization of the level set function defined by the conservative level set function method.

Staggered Step 1: Advection
$$\mathcal{R}^1 = \mathcal{R}_v + \mathcal{R}_u + \mathcal{R}_\phi^1 + \mathcal{R}_{gp} \quad (5.85)$$

Staggered Step 2: Normal Direction
$$\mathcal{R}^2 = \mathcal{R}_\phi^2 \quad (5.86)$$

Staggered Step 3: Reinitialization of ϕ
$$\mathcal{R}^3 = \mathcal{R}_\phi^3 \quad (5.87)$$

Details of each residual are provided below. The symmetric Nitsche method is applied in the momentum equation (5.88):

- Velocity

$$\begin{aligned}
\mathcal{R}_v = & (\nabla \delta \mathbf{v}, \rho \nabla \mathbf{v})_V + (\delta \mathbf{v}, \rho \mathbf{v})_V + \left\langle \delta \mathbf{v}, \rho \nabla \mathbf{v} \cdot \hat{\mathbf{n}}_{S \rightarrow V} \right\rangle_{\Gamma_{SV}} \\
& + \left(\delta \mathbf{v}, \rho \frac{\partial \mathbf{v}}{\partial t} + \rho \mathbf{v} \cdot \nabla \mathbf{v} + \alpha \mathbf{v} - \rho \mathbf{b} \right)_S + (\nabla \delta \mathbf{v}, \sigma(\mathbf{u}, p))_S + (\delta p, \nabla \cdot \mathbf{v})_S \\
& + \sum_{n_e \in \Omega_S} \left(\tau_{\text{SUPG}} \mathbf{v} \cdot \nabla \delta \mathbf{v} + \frac{\tau_{\text{PSPG}}}{\rho} \nabla \delta p, \rho \frac{\partial \mathbf{v}}{\partial t} + \rho \mathbf{v} \cdot \nabla \mathbf{v} - \nabla \sigma(\mathbf{u}, p) - \rho \mathbf{b} \right)_S \\
& + \left\langle \{\delta \sigma\} \cdot \hat{\mathbf{n}}_{S \rightarrow V}, [\mathbf{u}] \right\rangle_{\Gamma_{SV}} + \left\langle [[\delta \mathbf{v}], \{\sigma\}] \cdot \hat{\mathbf{n}}_{S \rightarrow V} \right\rangle_{\Gamma_{SV}} + \eta^N \left\langle \delta \mathbf{v}^V, [\mathbf{v}] \right\rangle_{\Gamma_{SV}} \quad (5.88)
\end{aligned}$$

where $\{\sigma\} = w^S \sigma^S(\mathbf{u}, p) + w^V \sigma^V(\mathbf{u}, p)$, $\{\delta \sigma\} = w^S \sigma^S(\delta \mathbf{v}, p) + w^V \sigma^V(\delta \mathbf{v}, p)$ and $w^S + w^V = 1$.

- Displacement

$$\mathcal{R}_u = \left(\delta \mathbf{v}, \frac{\partial \mathbf{u}}{\partial t} + \mathbf{v} \cdot \nabla \mathbf{u} - \mathbf{v} \right)_S + \sum_{n_e \in \Omega_S} \left(\tau_{\text{SUPG}} \mathbf{v} \cdot \nabla \delta \mathbf{u}, \frac{\partial \mathbf{u}}{\partial t} + \mathbf{v} \cdot \nabla \mathbf{u} - \mathbf{v} \right)_S \quad (5.89)$$

- Conservative Level Set Function (CLSF)

$$\mathcal{R}_\phi^1 = \left(\delta \phi, \frac{\partial \phi}{\partial t} + \mathbf{v} \cdot \nabla \phi \right)_{S+V} + \sum_{n_e \in \Omega_{S+V}} \left(\tau_{\text{SUPG}} \mathbf{v} \cdot \nabla \delta \phi, \frac{\partial \phi}{\partial t} + \mathbf{v} \cdot \nabla \phi \right)_{S+V} \quad (5.90)$$

$$\mathcal{R}_\phi^2 = (\delta \hat{\mathbf{n}}, |\nabla \phi| \hat{\mathbf{n}} - \nabla \phi)_{S+V} \quad (5.91)$$

$$\mathcal{R}_\phi^3 = \left(\delta \phi, \frac{\partial \phi}{\partial t} + \frac{1}{\mu_\phi} \nabla \cdot [\phi(1 - \phi) \hat{\mathbf{n}}] - \frac{\varepsilon_\phi}{\mu_\phi} \nabla \cdot [(\nabla \phi \cdot \hat{\mathbf{n}}) \hat{\mathbf{n}}] \right)_{S+V} \quad (5.92)$$

- Face-oriented Ghost-Penalty Method

$$\mathcal{R}_{\text{gp}} = \eta_v^{\text{gp}} \left\langle [[\nabla \delta \mathbf{v}]] \cdot \hat{\mathbf{n}}, [[\nabla \mathbf{v}]] \cdot \hat{\mathbf{n}} \right\rangle_{\Gamma_{SV}^{\text{gp}}} + \eta_p^{\text{gp}} \left\langle [[\nabla \delta p]] \cdot \hat{\mathbf{n}}, [[\nabla p]] \cdot \hat{\mathbf{n}} \right\rangle_{\Gamma_{SV}^{\text{gp}}} \quad (5.93)$$

5.7 Numerical Examples of Eulerian Solid Analysis using XFEM

This section discusses two numerical examples of the two-dimensional Eulerian solid problems using the XFEM. In these examples, QUAD4 elements are used for the spatial discretization and the time evolution is calculated by BDF1 (backward Euler method). At each time step, the nonlinear problem is solved by Newton's method and the convergence criteria requires a drop of the norm of the residual of 10^{-6} relative to the norm of the initial residual. In each Newton step, the system of linearized equations is solved by GMRES.

5.7.1 Free Falling of Cylinder due to Body Force

The first benchmark problem is a falling circular solid structure due to a body force. In this example, no boundary condition is imposed. This solid structure is made by an isotropic linear elastic material and infinitesimal strains are assumed. It should be noted that the small strain assumption is not applicable to a general problem, but this assumption can be used for this particular problem because there is no rigid-body rotation. This circular structure has the initial velocity -0.8m/s in y direction and is accelerated by the body force \mathbf{b} . Table 5.2 is the summary of material parameters. Analytical results of velocity and displacement: \hat{v}_i and \hat{u}_i are as follows:

$$\hat{v}_i(n\Delta t) = v_{i0} + b_i n\Delta t, \quad (5.94)$$

$$\hat{u}_i(n\Delta t) = v_{i0}n\Delta t + \frac{b_i}{2}n^2(\Delta t)^2. \quad (5.95)$$

Table 5.2: Settings of free falling circular solid

| Parameter | Symbol | Value |
|------------------|----------------|-----------------------|
| initial velocity | \mathbf{v}_0 | $(0, -0.8)\text{m/s}$ |
| body force | \mathbf{b} | $(0, -3)\text{m/s}^2$ |
| time increment | Δt | 0.003s |
| modulus | E | 0.1MPa |
| Poisson's ratio | ν | 0.3 |
| density | ρ | 1000kg/m ³ |

Figure 5.7 shows the propagation of the level set function ϕ , the solid phase and the von Mises stress σ_{VM} (Cauchy stress). These results show that the circular shape is preserved at any time step while the solid structure falls due to the body force. In addition, the von Mises stress is almost zero, as it should be since the body undergoes just a rigid body motion.

Figures 5.8 and 5.9 show the comparisons between the numerical results and the analytical solutions (5.94) and (5.95). At the center of this circle, the results of the velocity and displacement in y direction are identical to their analytical solutions (\hat{v}_y and \hat{u}_y). The free fall of a circular solid was computed correctly using the XFEM based on the Eulerian description.

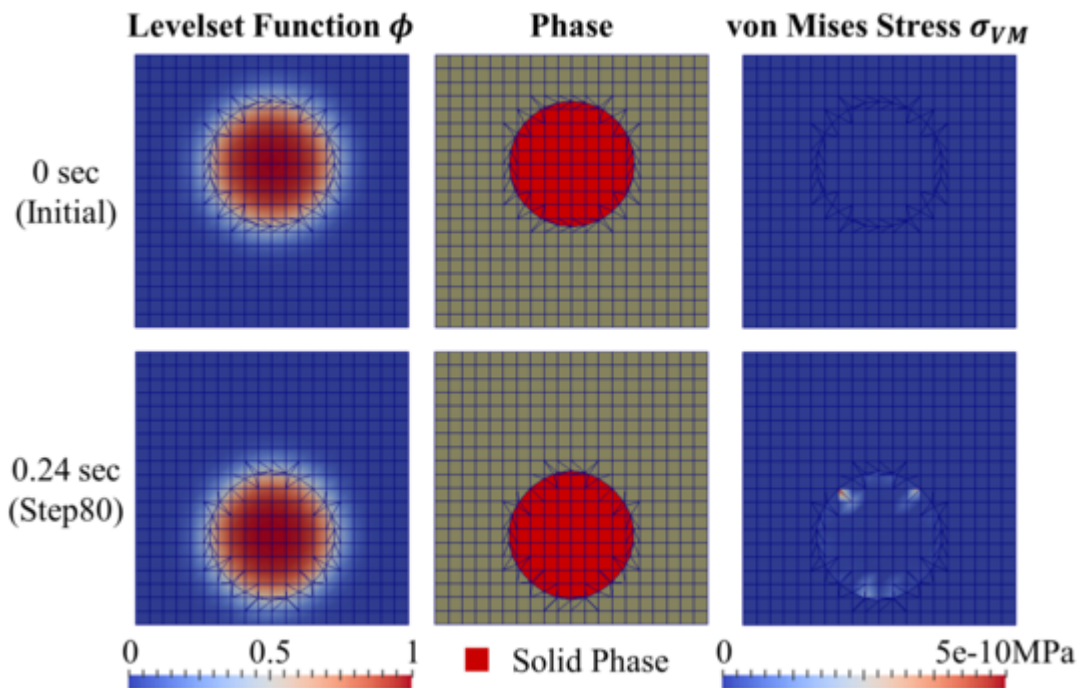
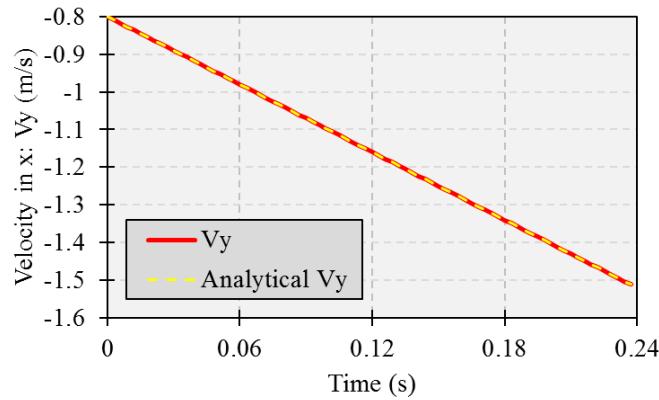
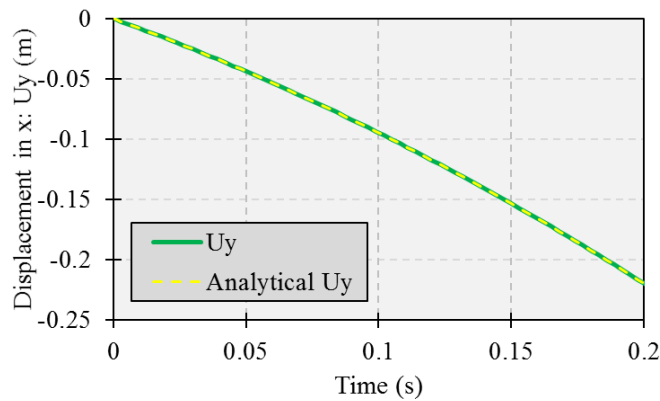


Figure 5.7: Free falling circular structure due to body force

Figure 5.8: History of velocity v_y in timeFigure 5.9: History of displacement u_y in time

5.7.2 Beam Bending due to Body Force (2D Analysis with BCs)

The second benchmark problem is a solid beam subject to a body force. This benchmark problem includes Dirichlet boundary conditions. The geometry and material parameters of the system are given in Figure 5.10 and Table 5.3. There is one solid beam specified as a solid phase Ω_S in Figure 5.10, which is made by the incompressible neo-Hookean material. The incompressible neo-Hookean material is a simplified model of incompressible Mooney-Rivlin model which is defined by the hyperelastic function W as follows:

$$W(\bar{I}_1, \bar{I}_2) = C_{10}(\bar{I}_1 - 3) + C_{01}(\bar{I}_2 - 3) , \quad (5.96)$$

where \bar{I}_i are the reduced invariants of the left Cauchy-Green tensor B (and also right Cauchy-Green tensor C) and $\bar{I}_3 = J = \det F = 1$ due to the incompressibility. C_{10} and C_{01} are

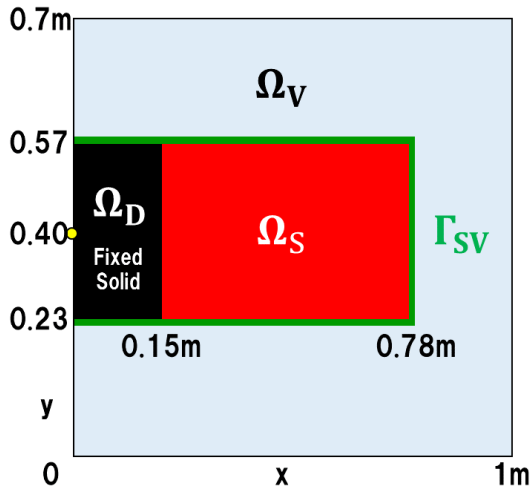


Figure 5.10: System of bending beam

Table 5.3: Parameters of bending beam

| Parameter | Symbol | Value |
|--------------------|----------------------|-------------------------|
| material parameter | C_{10} | 0.0375MPa |
| density | ρ | 1000 kg/m ³ |
| body force | (b_x, b_y) | (0, -3)m/s ² |
| time increment | Δt | 0.075s |
| mesh size | $\Delta x, \Delta y$ | 0.05m |
| number of mesh | n_e | 280 |

Assumptions

- finite strains
- plane strain case
- incompressible neo-Hookean material

material parameters of the Mooney-Rivlin model and if $C_{01} = 0$, this material is referred to the incompressible neo-Hookean model. As the Eulerian FEM is based on the current configuration, the Cauchy stress tensor is an appropriate stress measure. Based on (5.96), the deviatoric Cauchy stress tensor $\bar{\sigma}$ is defined by the derivative of W with respect to the Euler-Almansi strain tensor e , which is the conjugate strain tensor of $\bar{\sigma}$:

$$\bar{\sigma}_{ij} = -\frac{2}{3}(C_{10}I_1 - C_{01}I_2)\delta_{ij} + 2C_{10}B_{ij} - 2C_{01}B_{ij}^{-1}, \quad (5.97)$$

where I_i are invariants of B and $\bar{I}_i = I_i$ because of the incompressible material. In addition, it is necessary to consider the hydrostatic pressure p as a non-deterministic contribution of the force due to the incompressibility. Thus, the Cauchy stress tensor σ_{ij} is defined by p and $\bar{\sigma}_{ij}$:

$$\sigma_{ij} = -p\delta_{ij} + \bar{\sigma}_{ij} = -p\delta_{ij} - \frac{2}{3}(C_{10}I_1 - C_{01}I_2)\delta_{ij} + 2C_{10}B_{ij} - 2C_{01}B_{ij}^{-1}. \quad (5.98)$$

The root of this solid beam defined by the x -coordinate being less than 0.15m, is fixed domain by Dirichlet boundary conditions. The undeformed structure of this solid beam is defined by the following initial level set function ϕ .

$$\phi_s = \min(L_x - |x - x_c|, L_y - |y - y_c|), \quad (5.99)$$

$$\phi = \frac{1}{2} + \frac{1}{2} \tanh\left(\frac{\phi_s}{\varepsilon_\phi}\right). \quad (5.100)$$

Parameters in terms of the initial level set function ϕ are summarized in Table 5.4.

Table 5.4: Parameters about level set function ϕ

| Parameter | Symbol | Value |
|-----------------------------------|--------------------|----------------------------|
| length in x | L_x | 0.78m |
| length in y | L_y | 0.17m |
| center in x | x_c | 0m |
| center in y | y_c | 0.4m |
| slope parameter of ϕ | ε_ϕ | $0.5\Delta x^{0.9}=0.0337$ |
| time scaling for reinitialization | μ_ϕ | 10 |

The phase outside of the solid beam is defined as a void phase Ω_V . The velocity fields in Ω_V are defined by the Helmholtz smoother. The green line in Figure 5.10 shows the interface between the solid and void phase Γ_{SV} . On Γ_{SV} , Nitsche's method is applied. In addition, the face-oriented ghost penalty method is also applied in the vicinity of Γ_{SV} . Coefficients related to Nitsche's method and the ghost penalty method are as follows.

Table 5.5: Parameters about boundary integrals

| Parameter | Symbol | Value |
|--|-------------|---|
| penalty factor of Nitsche's method | η^N | $20E = 2000\text{MPa}$ |
| penalty factor of ghost-penalty method | η^{SP} | $0.0005\Delta x = 2.5 \times 10^{-5}\text{m}$ |

Based on the above parameters, this solid beam system is computed up to 0.675s (9 steps) to reach an equilibrium state. Figure 5.11 shows results of a coarse mesh ($\Delta x = \Delta y = 0.05\text{m}$) based on the Eulerian XFEM and Lagrangian standard FEM. The reinitialization process for ϕ was performed at every four time steps for the Eulerian XFEM. In Figure 5.11, the left three columns are results of the Eulerian XFEM and the right column is the result of the von Mises stress of the Lagrangian FEM. The left column shows the history of the propagation of phase. The interface Γ_{SV} is defined by the iso-contour line at $\phi = 0.5$ and the phases (left figures) are defined by its interface. Even if coarse meshes are used, the smooth interface is obtained by using XFEM. The second column shows the distributions of v_y . It is confirmed

that the equilibrium state is obtained at step 9 because v_y converges to almost zero. The third and fourth columns show the distribution of the von Mises stress σ_{VM} using both the Eulerian and Lagrangian method. The root of the beam has large stresses as expected. It is confirmed that stress distributions at the steady-state (step 9, $t = 0.675s$) of both the Eulerian and Lagrangian method are almost identical.

Finally, the rate of convergence of the proposed Eulerian solid analysis compared against the results of the standard Lagrangian analysis is studied. Models for this convergence check are listed in Table 5.6. The finest Lagrangian model (LAG5 in Table 5.6) is used as a reference model for both the Eulerian and Lagrangian analysis to compute the L2 errors. The definition of the L2 errors are (5.101) - (5.104). These L2 errors are normalized by the reference value (denominator):

Table 5.6: Models for convergence check (Eulerian solid analysis)

| Method | Model Name | Number of Node | Spatial Discretization $h = \Delta x = \Delta y$ (m) |
|-------------------------------|-------------|----------------|---|
| Lagrangian (reference) | LAG1 | 153 | 0.048462 |
| | LAG2 | 338 | 0.031500 |
| | LAG3 | 561 | 0.024231 |
| | LAG4 | 1225 | 0.016154 |
| | LAG5 | 2145 | 0.012155 |
| Eulerian | EUL1 | 315 | 0.05 |
| | EUL2 | 704 | 0.032693 |
| | EUL3 | 1189 | 0.025 |
| | EUL4 | 2623 | 0.016667 |

$$\text{Err}(\mathbf{v}) = \sqrt{\frac{\int_S d\Omega |\mathbf{v} - \mathbf{v}^{\text{ref}}|^2}{\int_S d\Omega |\mathbf{v}^{\text{ref}}|^2}}, \quad (5.101)$$

$$\text{Err}(p) = \sqrt{\frac{\int_S d\Omega (p - p^{\text{ref}})^2}{\int_S d\Omega p^{\text{ref} 2}}}, \quad (5.102)$$

$$\text{Err}(\mathbf{u}) = \sqrt{\frac{\int_S d\Omega |\mathbf{u} - \mathbf{u}^{\text{ref}}|^2}{\int_S d\Omega |\mathbf{u}^{\text{ref}}|^2}}, \quad (5.103)$$

$$\text{Err}(\sigma_{VM}) = \sqrt{\frac{\int_S d\Omega (\sigma_{VM} - \sigma_{VM}^{\text{ref}})^2}{\int_S d\Omega \sigma_{VM}^{\text{ref} 2}}}. \quad (5.104)$$

Figure 5.12 shows the convergence of the L2 errors of main quantities of interest. Blue markers show the results of the Lagrangian FEM and red markers show the results of the Eulerian XFEM. The rates of convergence is computed by the least square fitting. As the finest Lagrangian model is set to a reference model, the rate of convergence of the Lagrangian models is larger than one of the Eulerian models and they are larger than 1. The convergence of the Eulerian XFEM is slower, but the L2 errors converge by mesh refinement. These results suggest that the structural problems using the Eulerian XFEM needs finer meshes than the Lagrangian FEM to achieve the same accuracy.

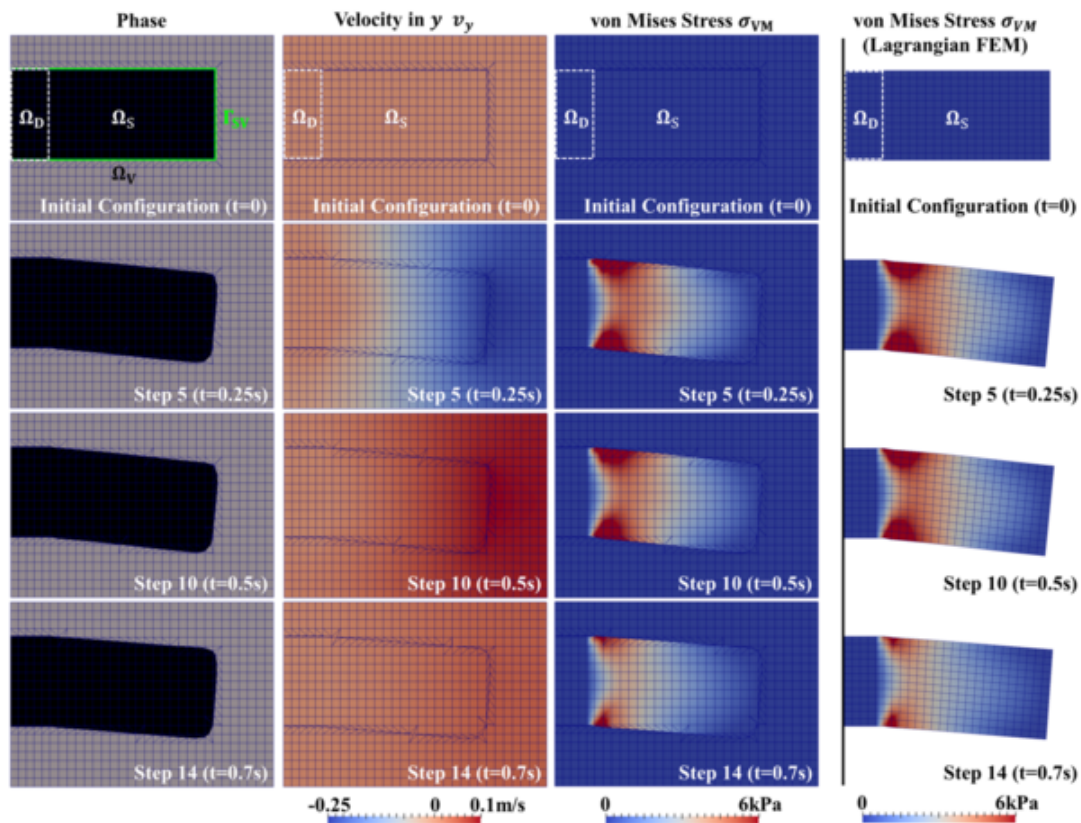


Figure 5.11: History of bending beam (phase, v_y and σ_{VM})

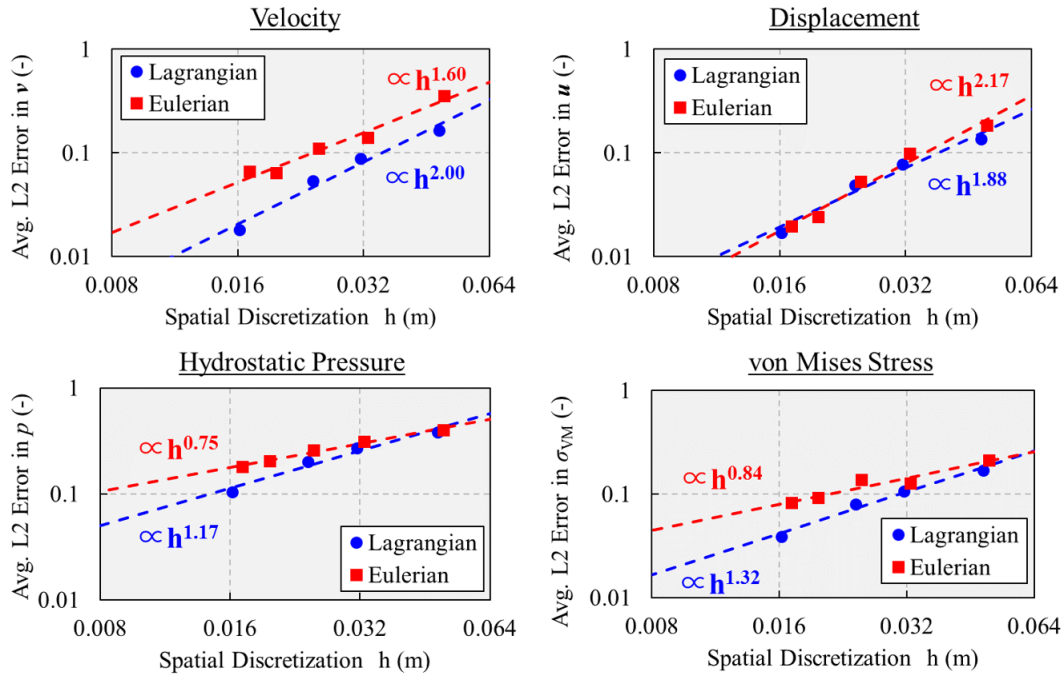


Figure 5.12: Convergence of Eulerian solid analysis (Step 9, $t = 0.675s$)

5.8 Theory of Full-Eulerian FSI Method

This section describes the full-Eulerian FSI method by following building on the Eulerian solid analysis introduced previously. To explain the general theory of the FSI, first a simple system as shown in Figure 5.13 is considered. There is a solid phase Ω_S surrounded by a fluid phase Ω_F . The outer boundary of the computational domain consists of a solid boundary Γ_S and a fluid boundary Γ_F . The interface between Ω_S and Ω_F is denoted by Γ_{SF} .

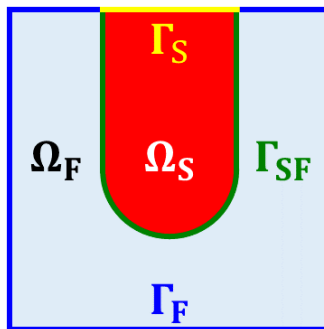


Figure 5.13: Simple system for discussion of FSI theory

5.8.1 Artificial Advective Velocity for Level Set Function

The governing equations in the solid phase Ω_S are identical to the Eulerian solid analysis which is summarized in Section 5.6. The difference from the Eulerian solid analysis is the treatment of the phase outside of Ω_S . In the solid analysis, a void phase is defined to model an artificial advective velocity for the propagation of the level set field ϕ . The Helmholtz smoothing method is used to create this artificial velocity fields. On the other hand, there is a fluid phase Ω_F outside of a solid phase Ω_S in the FSI system. Theoretically, a smoothing operation like the Helmholtz smoothing is not necessary because of the existence of the fluid, and the propagation of ϕ is computed by the solid and fluid velocities as follows:

$$\frac{\partial \phi}{\partial t} + v_i^s \frac{\partial \phi}{\partial x_i} = 0 \quad \text{in } \Omega_S , \quad (5.105)$$

$$\frac{\partial \phi}{\partial t} + v_i^f \frac{\partial \phi}{\partial x_i} = 0 \quad \text{in } \Omega_F . \quad (5.106)$$

A straightforward approach for computing the advective velocities of ϕ is to use the solid velocities \mathbf{v}^s in Ω_S and the fluid velocities \mathbf{v}^f in Ω_F as the advective velocities; see (5.105) and (5.106). While this propagation should work in theory, numerical experiments have shown that it is difficult to represent accurate deformation using (5.105) and (5.106). Figure 5.14 shows an example of the deformation of the solid phase based on (5.105) and (5.106). The top figure shows the deformation of the solid phase (red region). There is a pointed interface at the right edge of the solid phase. This pointed interface is created due to the leakage of the level set function ϕ (bottom left figure) and this leakage of ϕ occurs along the streak line of the fluid. In general, the fluid velocities are much larger than the solid velocities. Therefore, this leakage originates from the large advective velocities in Ω_F , which is identical to the fluid velocities \mathbf{v}^f .

To suppress the leakage of the level set function ϕ due to large fluid velocities, an artificial advective velocity field in the fluid phase $\hat{\mathbf{v}}^f$ is introduced. The governing equations for the

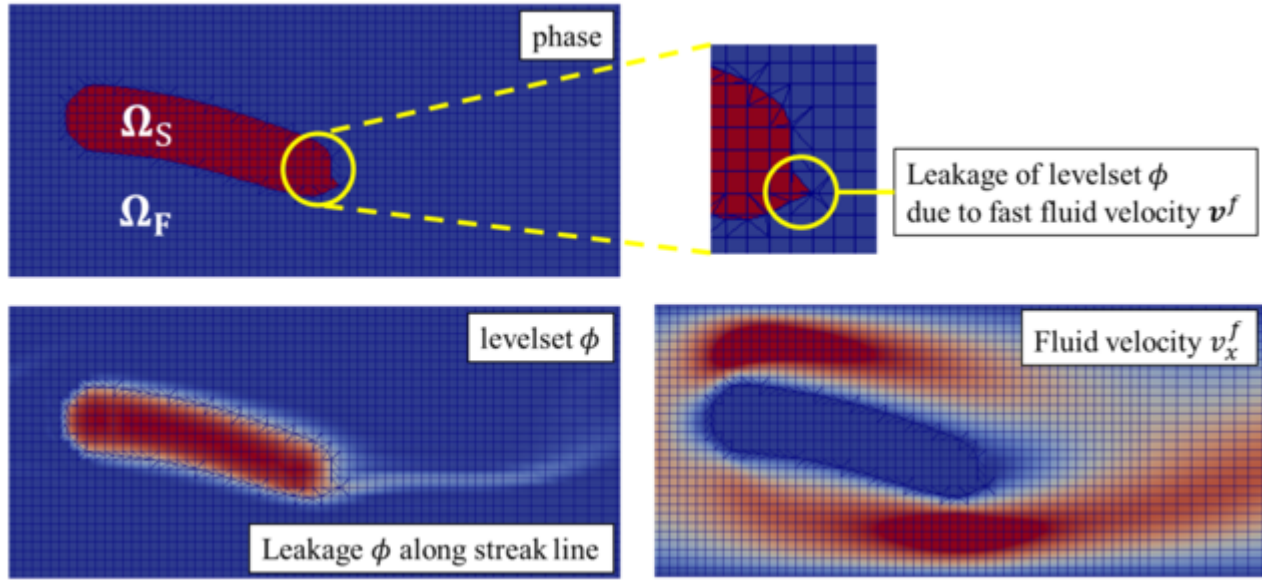


Figure 5.14: Leakage of level set function due to fluid velocity

propagation of ϕ are modified as follows:

$$\frac{\partial \phi}{\partial t} + v_i^s \frac{\partial \phi}{\partial x_i} = 0 \quad \text{in } \Omega_S, \quad (5.107)$$

$$\frac{\partial \phi}{\partial t} + \hat{v}_i^f \frac{\partial \phi}{\partial x_i} = 0 \quad \text{in } \Omega_F. \quad (5.108)$$

Following the techniques of the Eulerian solid analysis, the artificial advective velocities \hat{v}_i^f are computed by the Helmholtz smoothing in the fluid phase Ω_F . In addition, Nitsche's method is applied to \hat{v}_i^f to obtain a smooth velocity field for ϕ . Using this artificial advective velocity in the fluid phase leads to more stable propagation of ϕ in the FSI analysis:

$$\text{Helmholtz smoothing:} \quad -\Delta \hat{v}_i^f + \hat{v}_i^f = 0 \quad \text{in } \Omega_F, \quad (5.109)$$

$$\text{Nitsche's method:} \quad [[\hat{v}_i]] \equiv v_i^s - \hat{v}_i^f = 0 \quad \text{on } \Gamma_{SF}. \quad (5.110)$$

5.8.2 Strong Form of Full-Eulerian FSI

Considering the treatment of the advective velocities for ϕ , the strong forms of the governing equations for the full-Eulerian FSI are as follows, where the solid material is assumed

incompressible and the flow is modeled by the incompressible Navier-Stokes (INS) fluid:

- Momentum equation of the solid:

$$\frac{\partial v_i^s}{\partial t} + v_j^s \frac{\partial v_i^s}{\partial x_j} + \alpha v_i^s = \frac{1}{\rho^s} \frac{\partial \sigma_{ij}^s(\mathbf{u}^s, p^s)}{\partial x_j} + b_i^s \quad \text{in } \Omega_S, \quad (5.111)$$

- Continuity equation of the solid:

$$\frac{\partial v_i^s}{\partial x_i} = 0 \quad \text{in } \Omega_S, \quad (5.112)$$

- Advection of displacements:

$$\frac{\partial u_i^s}{\partial t} + v_j^s \frac{\partial u_i^s}{\partial x_j} = v_i^s \quad \text{in } \Omega_S, \quad (5.113)$$

- Momentum equation of the fluid:

$$\frac{\partial v_i^f}{\partial t} + v_j^f \frac{\partial v_i^f}{\partial x_j} = \frac{1}{\rho^f} \frac{\partial \sigma_{ij}^f(\mathbf{v}^f, p^f)}{\partial x_j} + b_i^f \quad \text{in } \Omega_F, \quad (5.114)$$

- Continuity equation of the fluid:

$$\frac{\partial v_i^f}{\partial x_i} = 0 \quad \text{in } \Omega_F, \quad (5.115)$$

- Helmholtz smoothing for $\hat{\mathbf{v}}^f$:

$$-\Delta \hat{v}_i^f + \hat{v}_i^f = 0 \quad \text{in } \Omega_F, \quad (5.116)$$

- Advection of the level set function:

$$\frac{\partial \phi}{\partial t} + v_j^s \frac{\partial \phi}{\partial x_j} = 0 \quad \text{in } \Omega_S, \quad (5.117)$$

$$\frac{\partial \phi}{\partial t} + \hat{v}_j^f \frac{\partial \phi}{\partial x_j} = 0 \quad \text{in } \Omega_F. \quad (5.118)$$

The Cauchy momentum equations: (5.111) and (5.114) are common governing equations for velocities in both phases Ω_S and Ω_F . The main difference of these momentum equations is the definition of the stress tensor. The stress tensor of the solid σ^s is defined by the displacements \mathbf{u}^s and the solid pressure p^s in Ω_S . The stress tensor of the fluid σ^f is defined

by the fluid velocities \mathbf{v}^f and the fluid pressure p^f . In addition, the artificial viscous term αv_i^s is introduced in Ω_S such that the structural deformations are damped and converge to a steady-state. α is set to 1 in this case. The body forces are applied only in the solid phase Ω_S . As the displacements are defined only in Ω_S , the advection equation of the displacement is performed only in Ω_S . The INS fluid model is used in Ω_F . The continuity equation (5.115) is essential to satisfy the incompressibility. The level set function ϕ is defined in the entire domain $\Omega = \Omega_S \cup \Omega_F$. The advective velocities for ϕ are the solid velocities \mathbf{v}^s in Ω_S and the artificial velocities $\hat{\mathbf{v}}^f$ in Ω_F . This artificial velocity field $\hat{\mathbf{v}}^f$ is defined by the Helmholtz smoothing (5.116). In addition, the reinitialization technique is applied to ϕ once at four time steps. On the interface between solid and fluid Γ_{SF} , the jump between the solid and fluid velocities (5.119) should be zero to satisfy C^0 continuities of the velocity fields. Nitsche's method is applied to the jump of the artificial advective velocities (5.120):

- interface condition:

$$[[v_i]] \equiv v_i^s - v_i^f = 0 \quad \text{on } \Gamma_{SF} , \quad (5.119)$$

$$[[\hat{v}_i]] \equiv v_i^s - \hat{v}_i^f = 0 \quad \text{on } \Gamma_{SF} . \quad (5.120)$$

5.8.3 Weak Form of Full-Eulerian FSI

The weak form of the governing equations introduced in Section 5.8.2 is summarized in this section. Operators of the jump and average are defined by the combination of the solid and fluid phase.

- Jump operator: $[[v_i]] = v_i^s - v_i^f, \quad [[\hat{v}_i]] = v_i^s - \hat{v}_i^f , \quad (5.121)$

- Averaging operator: $\{\sigma\} = w^s \sigma^s + w^f \sigma^f \quad (\because w^s + w^f = 1) . \quad (5.122)$

Consider the spaces of trial functions \mathcal{S}^h and test functions \mathcal{V}^h , the trial and test functions for the full-Eulerian FSI system are defined as follows:

- Trial functions: $\{\mathbf{v}^s, p^s, \mathbf{u}^s, \mathbf{v}^f, p^f, \hat{\mathbf{v}}^f, \phi\} \in \mathcal{S}^h$, (5.123)

- Test functions: $\{\delta \mathbf{v}^s, \delta p^s, \delta \mathbf{u}^s, \delta \mathbf{v}^f, \delta p^f, \delta \hat{\mathbf{v}}^f, \delta \phi\} \in \mathcal{V}^h$. (5.124)

In addition, the following notations in terms of integrals are used for simplicity:

- Volume integral: $(\mathbf{a}, \mathbf{b})_\alpha \equiv \int_{\Omega_\alpha} d\Omega \mathbf{a}^T \mathbf{b}$, (5.125)

- Boundary integral: $\langle \mathbf{a}, \mathbf{b} \rangle_{\Gamma_\beta} \equiv \int_{\Gamma_\beta} d\Gamma \mathbf{a}^T \mathbf{b}$. (5.126)

Using these notations, the residual of the full-Eulerian FSI using the XFEM is summarized as follows:

$$\begin{aligned}
& R_v^s(\{\delta \mathbf{v}^s, \delta p^s\}; \{\mathbf{v}^s, p^s, \mathbf{u}^s\}) + R_u^s(\delta \mathbf{u}^s; \{\mathbf{u}^s, \mathbf{v}^s\}) \\
& + R_v^f(\{\delta \mathbf{v}^f, \delta p^f\}; \{\mathbf{v}^f, p^f\}) + \hat{R}_v^f(\delta \hat{\mathbf{v}}^f; \hat{\mathbf{v}}^f) + R_\phi(\delta \phi; \{\phi, \mathbf{v}^s, \hat{\mathbf{v}}^f\}) \\
& + R_{\text{FSI}}(\{\delta \mathbf{v}^s, \delta p^s, \delta \mathbf{v}^f, \delta p^f, \delta \hat{\mathbf{v}}^f\}; \{\mathbf{v}^s, p^s, \mathbf{u}^s, \mathbf{v}^f, p^f, \hat{\mathbf{v}}^f\}) \\
& + R_{\text{gp}}(\{\delta \mathbf{v}^s, \delta p^s, \delta \mathbf{v}^f, \delta p^f, \delta \hat{\mathbf{v}}^f\}; \{\mathbf{v}^s, p^s, \mathbf{v}^f, p^f, \hat{\mathbf{v}}^f\}) = 0 .
\end{aligned} \tag{5.127}$$

Each term of (5.127) are defined as follows. To stabilize the advective terms, SUPG stabilization is applied to (5.111), (5.113), (5.114) and (5.117). In addition, PSPG stabilization is applied to stabilize the incompressibility of the solid and the fluid. Nitsche's method is applied to the boundary integral on the interface Γ_{SF} in R_{FSI} :

$$\begin{aligned}
R_v^s = & \left(\delta \mathbf{v}^s, \rho^s \frac{\partial \mathbf{v}^s}{\partial t} + \rho^s \mathbf{v}^s \cdot \nabla \mathbf{v}^s + \alpha \mathbf{v}^s - \rho^s \mathbf{b}^s \right)_S + (\nabla \delta \mathbf{v}^s, \sigma^s(\mathbf{u}^s, p^s))_S + (\delta p^s, \nabla \cdot \mathbf{v}^s)_S \\
& + \sum_{n_e \in \Omega_S} \left(\tau_{\text{SUPG}} \mathbf{v}^s \cdot \nabla \delta \mathbf{v}^s + \frac{\tau_{\text{PSPG}}}{\rho^s} \nabla \delta p^s, \tilde{\mathbf{r}}_v^s \right)_S - \langle \delta \mathbf{v}^s, \sigma^s(\mathbf{u}^s, p^s) \cdot \hat{\mathbf{n}}_s \rangle_{\Gamma_S} ,
\end{aligned} \tag{5.128}$$

$$R_u^s = (\delta \mathbf{u}^s, \tilde{\mathbf{r}}_u^s)_S + \sum_{n_e \in \Omega_S} (\tau_{\text{SUPG}} \mathbf{v}^s \cdot \nabla \delta \mathbf{u}^s, \tilde{\mathbf{r}}_u^s)_S , \tag{5.129}$$

$$R_v^f = \left(\delta \mathbf{v}^f, \rho^f \frac{\partial \mathbf{v}^f}{\partial t} + \rho^f \mathbf{v}^f \cdot \nabla \mathbf{v}^f - \rho^f \mathbf{b}^f \right)_F + (\nabla \delta \mathbf{v}^f, \sigma^f(\mathbf{v}^f, p^f))_F + (\delta p^f, \nabla \cdot \mathbf{v}^f)_F$$

$$+ \sum_{n_e \in \Omega_F} \left(\tau_{\text{SUPG}} \mathbf{v}^f \cdot \nabla \delta \mathbf{v}^f + \frac{\tau_{\text{PSPG}}}{\rho^f} \nabla \delta p^f, \tilde{\mathbf{r}}_v^f \right)_F - \langle \delta \mathbf{v}^f, \sigma^f(\mathbf{v}^f, p^f) \cdot \hat{\mathbf{n}}_f \rangle_{\Gamma_F}, \quad (5.130)$$

$$\hat{R}_v^f = (\nabla \delta \hat{\mathbf{v}}^f, \rho^s \nabla \hat{\mathbf{v}}^f)_F + (\delta \hat{\mathbf{v}}^f, \rho^s \hat{\mathbf{v}}^f)_F - \langle \delta \hat{\mathbf{v}}^f, \rho^s \nabla \hat{\mathbf{v}}^f \cdot \hat{\mathbf{n}}^f \rangle_{\Gamma_F}, \quad (5.131)$$

$$R_\phi = (\delta \phi, \tilde{r}_\phi^s)_S + \sum_{n_e \in \Omega_S} (\tau_{\text{SUPG}} \mathbf{v}^s \cdot \nabla \delta \phi, \tilde{r}_\phi^s)_S \\ + (\delta \phi, \tilde{r}_\phi^f)_F + \sum_{n_e \in \Omega_F} (\tau_{\text{SUPG}} \hat{\mathbf{v}}^f \cdot \nabla \delta \phi, \tilde{r}_\phi^f)_F, \quad (5.132)$$

$$R_{\text{FSI}} = \frac{1}{2} \left\langle \sigma^f(\delta \mathbf{v}^f, \delta p^f) \cdot \hat{\mathbf{n}}_{s \rightarrow f}, [\mathbf{v}] \right\rangle_{\Gamma_{\text{SF}}} + \frac{1}{2} \left\langle \sigma^s(\delta \mathbf{v}^s, \delta p^s) \cdot \hat{\mathbf{n}}_{s \rightarrow f}, [\mathbf{u}] \right\rangle_{\Gamma_{\text{SF}}} \\ + \left\langle [[\delta \mathbf{v}]], \{\sigma\} \cdot \hat{\mathbf{n}}_{s \rightarrow f} \right\rangle_{\Gamma_{\text{SF}}} + \eta^N \left\langle [[\delta \mathbf{v}]], [\mathbf{v}] \right\rangle_{\Gamma_{\text{SF}}} \\ + \langle \delta \hat{\mathbf{v}}^f, \nabla \hat{\mathbf{v}}^f \cdot \hat{\mathbf{n}}_{s \rightarrow f} \rangle_{\Gamma_{\text{SF}}} + \eta^N \left\langle \delta \hat{\mathbf{v}}^f, [[\hat{\mathbf{v}}]] \right\rangle_{\Gamma_{\text{SF}}}, \quad (5.133)$$

where η^N is a penalty factor of Nitsche's method. $\tilde{r}_v^s, \tilde{r}_u^s, \tilde{r}_v^f, \tilde{r}_\phi^s$ and \tilde{r}_ϕ^f are the scalar residuals defined previously in Section 5.8.2. Nitsche's penalty term for the artificial advective velocity \hat{v}_i^f (last term of (5.133)) is applied in the fluid phase and thus, the corresponding test function is defined as $\delta \hat{\mathbf{v}}^f$ based on the one-sided Nitsche method:

$$\tilde{r}_v^s \equiv \rho^s \frac{\partial \mathbf{v}^s}{\partial t} + \rho^s \mathbf{v}^s \cdot \nabla \mathbf{v}^s + \alpha \mathbf{v}^s - \nabla \sigma^s(\mathbf{u}^s, p^s) - \rho^s \mathbf{b}^s, \quad (5.134)$$

$$\tilde{r}_u^s \equiv \frac{\partial \mathbf{u}^s}{\partial t} + \mathbf{v}^s \cdot \nabla \mathbf{u}^s - \mathbf{v}^s, \quad (5.135)$$

$$\tilde{r}_v^f \equiv \rho^f \frac{\partial \mathbf{v}^f}{\partial t} + \rho^f \mathbf{v}^f \cdot \nabla \mathbf{v}^f - \nabla \sigma^f(\mathbf{v}^f, p^f) - \rho^f \mathbf{b}^f, \quad (5.136)$$

$$\tilde{r}_\phi^s \equiv \frac{\partial \phi}{\partial t} + \mathbf{v}^s \cdot \nabla \phi, \quad (5.137)$$

$$\tilde{r}_\phi^f \equiv \frac{\partial \phi}{\partial t} + \hat{\mathbf{v}}^f \cdot \nabla \phi. \quad (5.138)$$

Following the works of Hansbo et al. [74], Jenkins et al. [101, 102] and Mayer et al. [70], only the traction from the fluid side is used as the traction at the interface. This approach is consistent with the traditional FSI approach where forces are transferred from the fluid phase to the solid phase rather than its vice versa. Hence, the solid traction is replaced by

the fluid traction:

$$\{\sigma\} = w^s \sigma^s(\mathbf{u}^s, p^s) + w^f \sigma^f(\mathbf{v}^f, p^f) \rightarrow \sigma^f(\mathbf{v}^f, p^f), \quad (5.139)$$

$$\frac{1}{2} \left\langle \sigma^s(\delta \mathbf{v}^s, \delta p^s) \cdot \hat{\mathbf{n}}_{s \rightarrow f}, \llbracket \mathbf{u} \rrbracket \right\rangle_{\Gamma_{\text{SF}}} \rightarrow \frac{1}{2} \left\langle \sigma^f(\delta \mathbf{v}^f, \delta p^f) \cdot \hat{\mathbf{n}}_{s \rightarrow f}, \llbracket \mathbf{v} \rrbracket \right\rangle_{\Gamma_{\text{SF}}}, \quad (5.140)$$

Therefore, (5.133) is simplified as follows:

$$\begin{aligned} R_{\text{FSI}} = & \left\langle \sigma^f(\delta \mathbf{v}^f, \delta p^f) \cdot \hat{\mathbf{n}}_{s \rightarrow f}, \llbracket \mathbf{v} \rrbracket \right\rangle_{\Gamma_{\text{SF}}} + \left\langle \llbracket \delta \mathbf{v} \rrbracket, \sigma^f \cdot \hat{\mathbf{n}}_{s \rightarrow f} \right\rangle_{\Gamma_{\text{SF}}} + \eta^N \left\langle \llbracket \delta \mathbf{v} \rrbracket, \llbracket \mathbf{v} \rrbracket \right\rangle_{\Gamma_{\text{SF}}} \\ & + \left\langle \delta \hat{\mathbf{v}}^f, \nabla \hat{\mathbf{v}}^f \cdot \hat{\mathbf{n}}_{s \rightarrow f} \right\rangle_{\Gamma_{\text{SF}}} + \eta^N \left\langle \delta \hat{\mathbf{v}}^f, \llbracket \hat{\mathbf{v}} \rrbracket \right\rangle_{\Gamma_{\text{SF}}}. \end{aligned} \quad (5.141)$$

The derivation of (5.133) and (5.141) is summarized in Appendix B.

In addition, the face-oriented ghost penalty method is applied to suppress the instability due to small intersected XFEM meshes. This ghost penalty method is applied on the faces of intersected elements which is denoted as Γ_{gp} :

$$\begin{aligned} R_{\text{gp}}(\{\delta \mathbf{v}^s, \delta \mathbf{v}^f, \delta p^f\}; \{\mathbf{v}^s, \mathbf{v}^f, p^f\}) = & \eta_v^{\text{gp}} \left\langle \llbracket \nabla \delta \mathbf{v}^s \rrbracket \cdot \hat{\mathbf{n}}_{s \rightarrow f}, \llbracket \nabla \mathbf{v}^s \rrbracket \cdot \hat{\mathbf{n}}_{s \rightarrow f} \right\rangle_{\Gamma_{\text{gp}}} \\ & + \eta_p^{\text{gp}} \left\langle \llbracket \nabla \delta p^s \rrbracket \cdot \hat{\mathbf{n}}_{s \rightarrow f}, \llbracket \nabla p^s \rrbracket \cdot \hat{\mathbf{n}}_{s \rightarrow f} \right\rangle_{\Gamma_{\text{gp}}} \\ & + \eta_v^{\text{gp}} \left\langle \llbracket \nabla \delta \mathbf{v}^f \rrbracket \cdot \hat{\mathbf{n}}_{s \rightarrow f}, \llbracket \nabla \mathbf{v}^f \rrbracket \cdot \hat{\mathbf{n}}_{s \rightarrow f} \right\rangle_{\Gamma_{\text{gp}}} \\ & + \eta_p^{\text{gp}} \left\langle \llbracket \nabla \delta p^f \rrbracket \cdot \hat{\mathbf{n}}_{s \rightarrow f}, \llbracket \nabla p^f \rrbracket \cdot \hat{\mathbf{n}}_{s \rightarrow f} \right\rangle_{\Gamma_{\text{gp}}} \\ & + \eta_v^{\text{gp}} \left\langle \llbracket \nabla \delta \hat{\mathbf{v}}^f \rrbracket \cdot \hat{\mathbf{n}}_{s \rightarrow f}, \llbracket \nabla \hat{\mathbf{v}}^f \rrbracket \cdot \hat{\mathbf{n}}_{s \rightarrow f} \right\rangle_{\Gamma_{\text{gp}}}, \end{aligned} \quad (5.142)$$

where η_v^{gp} and η_p^{gp} are the penalty factors for the ghost penalty method. Generally, penalty factors for velocity and pressure are distinguished and have different values.

5.9 Numerical Example of Full-Eulerian FSI using XFEM

As a benchmark problem for the full-Eulerian FSI analysis, the system shown in Figure 5.15 is considered. A solid beam immersed in a flow channel is clamped at its left and subject

to a body force.

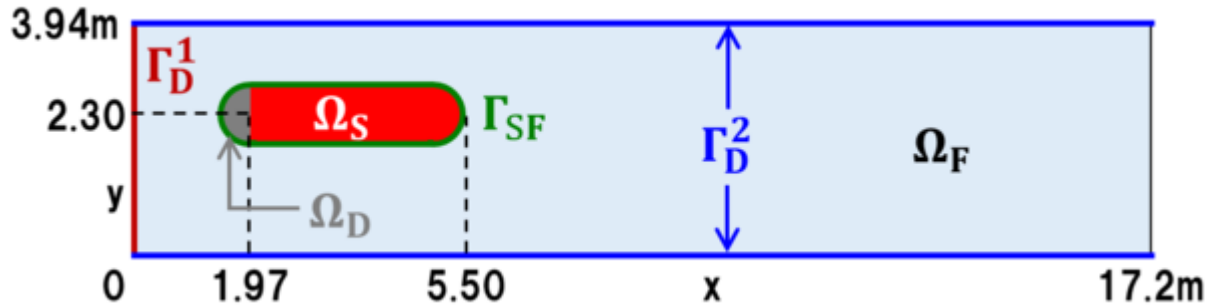


Figure 5.15: System for numerical example of full-Eulerian FSI

The solid and fluid phases are denoted as Ω_S and Ω_F respectively. The region of the root of the solid beam Ω_D is fixed. Ω_D is a part of solid phase Ω_S ($\Omega_D \subset \Omega_S$). Γ_D^1 and Γ_D^2 are Dirichlet boundary conditions (BCs). The hydrostatic pressure p is not constraint by these BCs. The summary of Dirichlet BCs is as follows:

$$v_x = \frac{6}{3.94^2}y(3.94 - y) \text{ m/s}, \quad v_y = 0 \text{ m/s} \quad \text{on } \Gamma_D^1 \quad (\text{inlet flow}), \quad (5.143)$$

$$v_x = 0 \text{ m/s}, \quad v_y = 0 \text{ m/s} \quad \text{on } \Gamma_D^2 \quad (\text{no slip BC}), \quad (5.144)$$

$$v_x = 0 \text{ m/s}, \quad v_y = 0 \text{ m/s} \quad \text{in } \Omega_D \quad (\text{fixed solid}). \quad (5.145)$$

The traction free boundary condition is applied on the right edge. Ω_S is modeled by the incompressible neo-Hookean material (5.146) under the assumption of the finite strains. Ω_F is modeled by the incompressible Navier-Stokes (INS) equations. In addition, the body force \mathbf{b}^s is applied only to the solid phase. The geometry and material parameters of this system are summarized in Table 5.7:

- Incompressible neo-Hookean: $W(I_{C1}) = C_{10}(I_{C1} - 3)$ ($\because I_{C1} = \text{Tr}C$). (5.146)

Table 5.7: Parameters of full-Eulerian FSI analysis (infinitesimal strain case)

| Category | Parameter | Symbol | Value |
|-------------|---------------------------------------|----------------|---|
| Solid | Density | ρ^s | 1000kg/m ³ |
| | parameter of neo-Hookean material | C_{10} | 0.0375MPa |
| | body force | \mathbf{b}^s | (0, -3)m/s ² |
| | thickness | d^s | 1m |
| Fluid | density | ρ^f | 1000kg/m ³ |
| | dynamic viscosity | μ^f | 0.1kg/(m·s) |
| | body force | \mathbf{b}^f | (0, 0)m/s ² |
| | thickness | d^f | 1m |
| Interface | penalty of Nitsche's method | η^N | 200kg/(m ³ ·s) |
| | penalty of GP method for \mathbf{v} | η_v^{gp} | $2.5 \times 10^{-4} \Delta y$ kg/(m·s) |
| | penalty of GP method for p | η_p^{gp} | $6.25 \times 10^{-4} \Delta y^3$ m ³ ·s/kg |
| Calculation | time increment | Δt | 0.005s |
| | mesh size in x | Δx | 0.131m ($x \leq 7.88$ m) |
| | | | 0.262m ($x > 7.88$ m) |
| | mesh size in y | Δy | 0.131m |
| | number of node | n_n | $106 \times 31 = 3286$ |
| | number of mesh | n_e | $105 \times 30 = 3150$ |

Figure 5.16 shows the time evolution of the solid phase Ω_S using the parameters listed in Table 5.7. The left column is the history of the solid velocity in y direction v_y^s . The solid phase is accelerated by the body force at the initial stage, then its velocity decreases due to the fluid traction. Finally, a steady-state is obtained. The corresponding displacement in y : u_y and the von Mises stress σ_{VM} (Cauchy stress) shown in the middle and right columns of Figure 5.16. In this example, the artificial advective velocity fields (Section 5.8.1) are used to propagate the level set function ϕ and the appropriate deformation is obtained. The computational results of the fluid phase Ω_F are summarized in Figure 5.17. The left and middle columns show the history of the fluid velocities \mathbf{v}^f . As the solid phase Ω_S deforms in response to the body force, the distribution of the fluid velocities changes appropriately. v_x^f has large value in the flow channel below the right edge of Ω_S because this flow channel becomes narrow due to the bending of a solid structure. In terms of v_y^f , up and down fluid motion occurs at the left edge of Ω_S because the fluid avoids the solid structure and then, the flow above and below the solid structure joins together at the right edge of Ω_S . The corresponding fluid shear stress is shown in the right column of Figure 5.17.

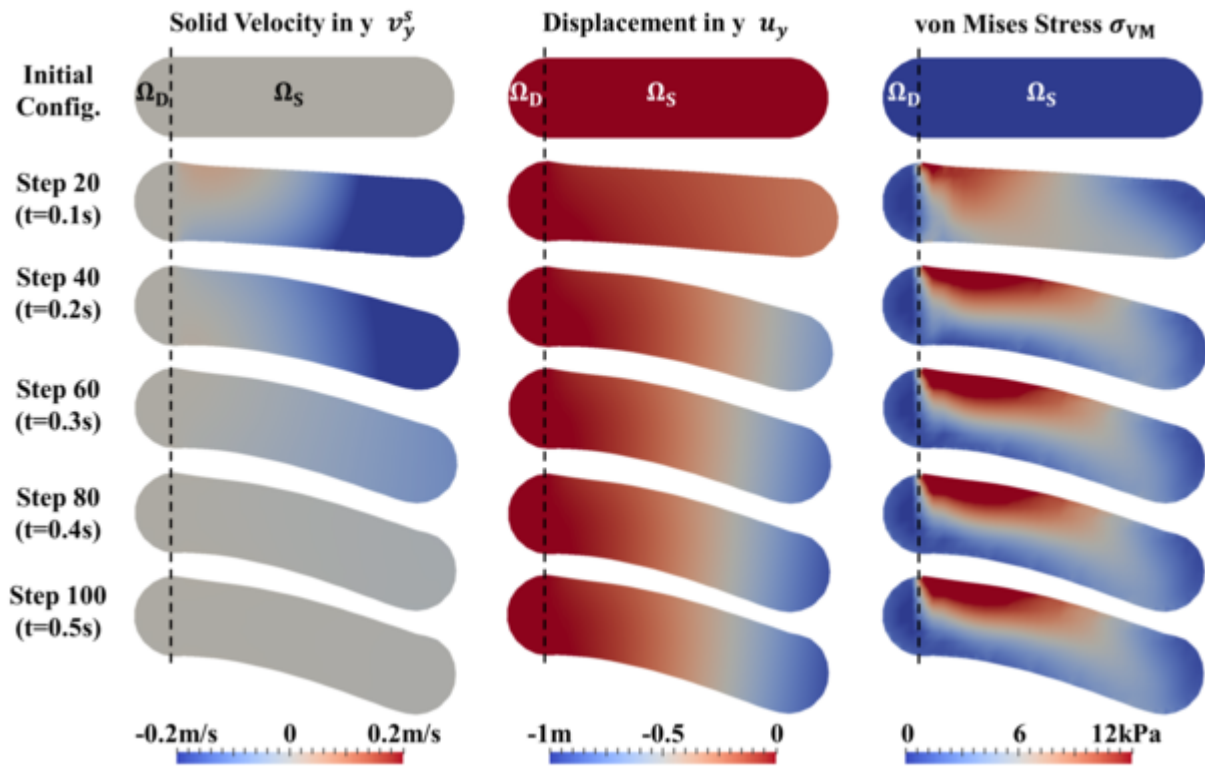


Figure 5.16: History of solid properties

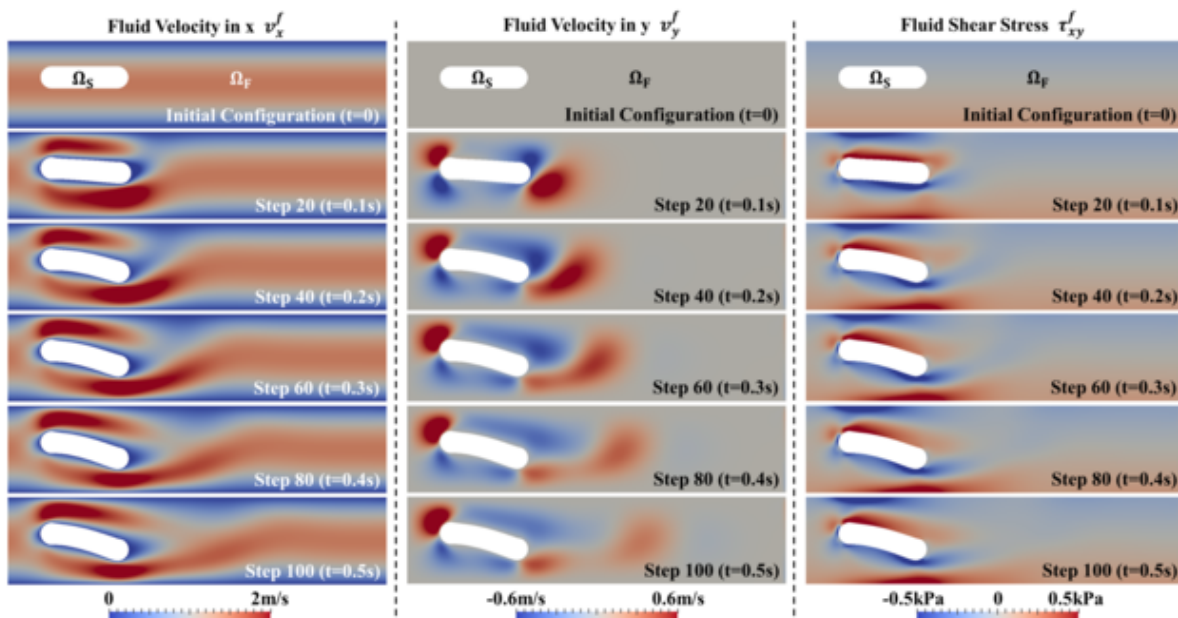


Figure 5.17: History of fluid properties

The convergence of solutions of the full-Eulerian FSI analysis is studied. The models for this analysis are summarized in Table 5.8 and the finest model is used as a reference model to compute the L2 errors.

Table 5.8: Models for convergence check

| | Model | Number of Node | Spatial Discretization h (m) |
|--------------------------------|-------|----------------|--------------------------------|
| coarse model | 1 | 2125 | 0.164263 |
| model of Figures 5.16 and 5.17 | 2 | 3286 | 0.131410 |
| | 3 | 4699 | 0.109509 |
| | 4 | 5781 | 0.098558 |
| finest model (reference) | 5 | 7614 | 0.085702 |

The L2 errors of representative quantities of interest (velocity \mathbf{v} , displacement \mathbf{u} , hydrostatic pressure p and von Mises stress σ_{VM}) for both the solid and fluid phases are defined as follows:

$$\text{Err}(\mathbf{v}) = \sqrt{\frac{\int_S d\Omega |\mathbf{v} - \mathbf{v}^{\text{ref}}|^2}{\int_S d\Omega |\mathbf{v}^{\text{ref}}|^2}}, \quad (5.147)$$

$$\text{Err}(p) = \sqrt{\frac{\int_S d\Omega (p - p^{\text{ref}})^2}{\int_S d\Omega p^{\text{ref} 2}}}, \quad (5.148)$$

$$\text{Err}(\mathbf{u}) = \sqrt{\frac{\int_S d\Omega |\mathbf{u} - \mathbf{u}^{\text{ref}}|^2}{\int_S d\Omega |\mathbf{u}^{\text{ref}}|^2}}, \quad (5.149)$$

$$\text{Err}(\sigma_{VM}) = \sqrt{\frac{\int_S d\Omega (\sigma_{VM} - \sigma_{VM}^{\text{ref}})^2}{\int_S d\Omega \sigma_{VM}^{\text{ref} 2}}}. \quad (5.150)$$

Figure 5.18 illustrates these L2 errors with respect to the size of the spatial discretization h (mesh size) at the final time step ($t = 0.5\text{s}$).

The top left figure shows the L2 errors of the solid velocity \mathbf{v}^s and the fluid velocity \mathbf{v}^f . The top right figure illustrates the L2 error of the displacement \mathbf{u} . As the displacement are defined only in the solid body, the L2 error of the solid phase is only shown. The bottom left figure shows the L2 errors of the hydrostatic pressure in both phases, p^s and p^f . The bottom right figure shows the L2 errors of the von Mises stress σ_{VM}^s in the solid phase, and the corresponding measure of fluid stresses; the in-plane effective shear stress $q = |\sigma_1 - \sigma_2|/2$. The L2 errors in the solid phase are computed by the projecting the quantity of interest

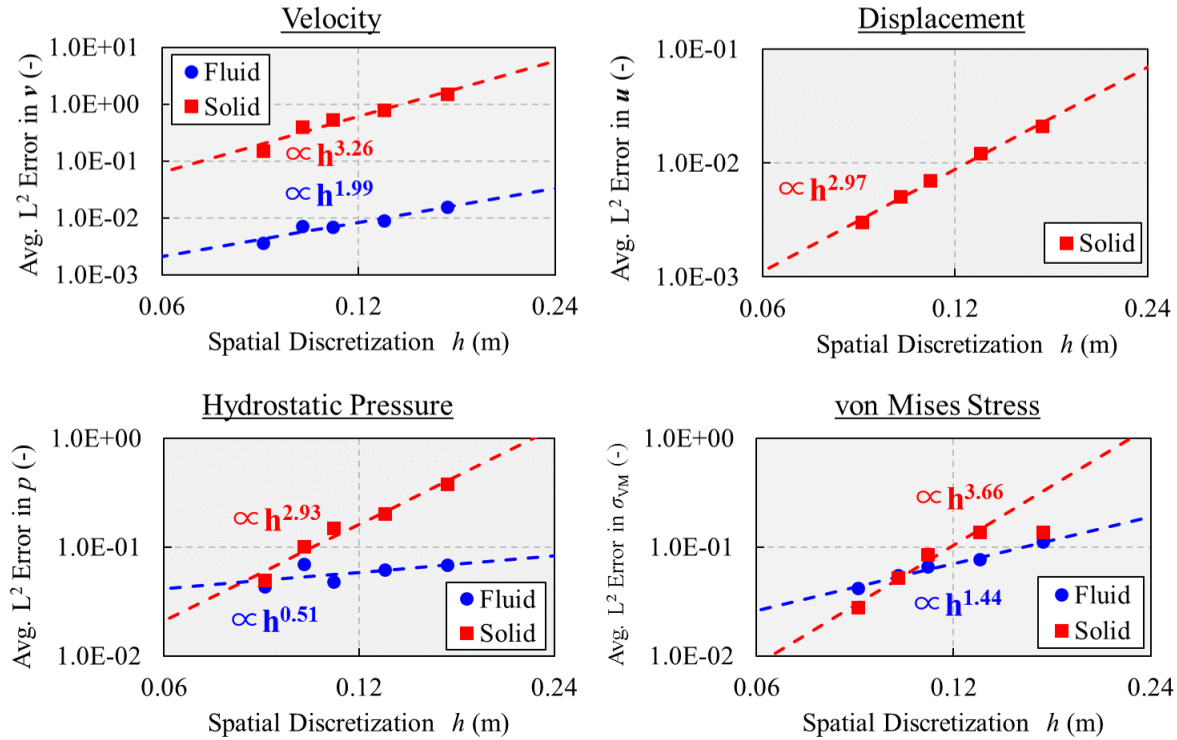


Figure 5.18: Convergence of Eulerian FSI (final time step, $t = 0.5s$)

onto the initial configuration of the reference model. The L^2 errors in the fluid phase are computed by the projection onto the current configuration at the final time step of the reference model. This L^2 errors are computed in the domain belongs to the fluid phase at all models in the steady-state.

All quantities except the hydrostatic pressure of the fluid phase p^f have larger rate of convergence than 1 and thus, this indicates that the proposed Eulerian FSI analysis is computationally efficient. The convergence of the fluid pressure p^f is slower than the other quantities and this is an unclear point.

In terms of the L^2 error of the velocity fields, the L^2 error of the solid phase is larger than the one of the fluid phase. As the results of the final time step are used, the solid velocities v^s are almost zero because the solid structure reaches the steady-state. On the other hand, the fluid velocities v^f at this time are non-zero because there is inlet flow at the left edge of this system. Therefore, the L^2 error of v^s tends to be larger than one of v^f because the

computed L2 error is normalized by a smaller reference value.

There is a reference work (Kamrin et al. [68]) which is similar to this numerical example. The reference work is also based on an Eulerian FSI method but uses a finite difference method and a VOF-like interface capturing method. The difference between current numerical example and reference work is shown in Table 5.9.

Table 5.9: Difference between current computation and reference work

| | Reference Work | Computed Example |
|-----------|--|--------------------------------|
| Method | Eulerian finite difference method blurred-interface method (like VOF) | Eulerian XFEM |
| Interface | isovalue of level set function | isovalue of level set function |
| Solid | Compressible neo-Hookean ($\nu = 0.41$) | incompressible neo-Hookean |
| Fluid | nearly incompressible NS Fluid ($\nu = 0.499$) | incompressible NS Fluid |
| Mesh | Finer meshes are necessary. | Coarse meshes are available. |

The problem studied in the reference works is the deformation of a rotor by incoming fluid flow. Figure 5.19 shows the history of the deformation of the rotor. The center of the rotor is fixed and the rotor is twisted by the rotational flow created by the inlet flow at the left edge (green region) and the outlet flow at the upper edge (sky-blue region). The computed results (Figures 5.16 and 5.17) show a smooth deformation similar to the one in this reference work. Figure 5.20 shows the rate of convergence of the reference work and these results agree qualitatively well with the results found in this thesis in Figure 5.18. However, the rate of convergence of the reference work is much smaller compared with the Eulerian XFEM except the fluid pressure p^f . Although the rate of convergence of p^f is slow, the performance of the proposed method (Eulerian XFEM) seems to be better than the reference work (finite difference method). One reason that the proposed method is better than the reference work, is that the representation of the interface in the proposed method is performed by the XFEM and more accurate than the blurred-interface method like the VOF method used in the reference work.

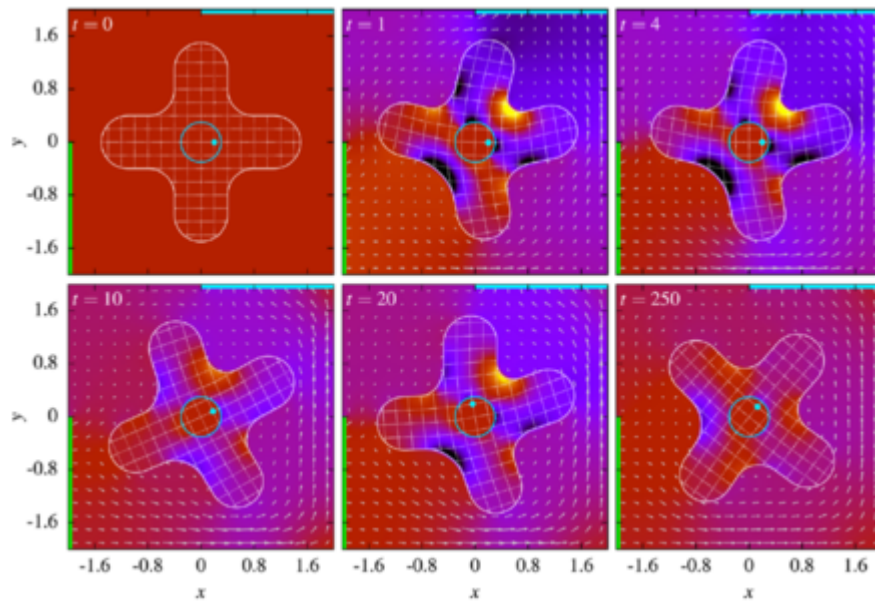


Figure 5.19: reference work [68] (deformation of hyperelastic body in INS fluid)

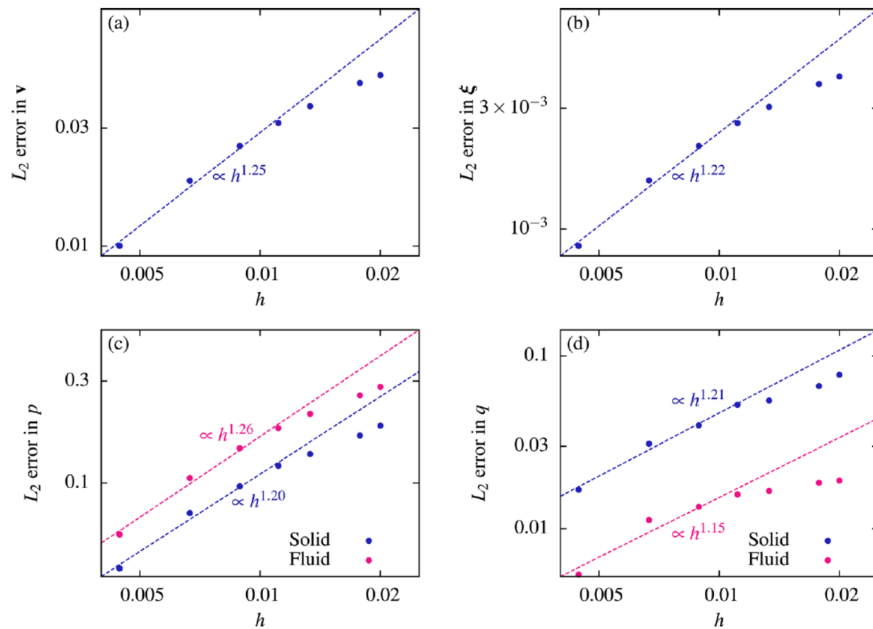


Figure 5.20: Reference work [68] (L_2 error corresponding to Figure 5.19)

5.10 Discussion

In this chapter, studies of the Eulerian solid formulation and the full-Eulerian FSI formulation using the XFEM were discussed. The entire FSI system is described by an Eulerian formulation, including the solid phase. The time evolution of the solid phase based on the Eulerian description was computed using SUPG/PSPG stabilization because of the existence of the advection term. FSI is modeled on the interface in the fixed background meshes using Nitsche's method. In addition, the face-oriented ghost-penalty method is applied for the treatment of small intersected elements created by moving interfaces. The ill-conditioning problem due to moving interfaces is suppressed by the face-oriented ghost-penalty method. The key challenge of the full-Eulerian FSI method is the representation of the interfaces. This research introduced the conservative level set function and obtained stable propagation of deformed solid structures. In consequence, the capability of the full-Eulerian FSI method to treat large deformation was verified.

However, the full-Eulerian FSI method using the XFEM has two fundamental drawbacks. The first drawback is the representation of interfaces of the solid. As the Eulerian description is used in the solid domain, the deformation of the solid structures is captured by the momentum equation with an advective term and the advection of the conservative level set function. In general, the solution of the advection equations needs very fine time increments Δt to represent accurately the deformation of the solid. The steady-state problems cannot be computed efficiently by the full-Eulerian FSI method using the XFEM due to the interface capturing method. The second drawback is the numerical interpolation error due to the XFEM. As the XFEM and the time stepping scheme are used in this chapter, the interpolation error due to moving interfaces always occurs. While all numerical examples summarized in this chapter seemed to be successful, these examples are computationally incorrect because of this error. This drawback can be easily overcome by the application of the space-time XFEM. However, the first drawback is inherent to the full Eulerian model.

Thus, these findings suggest that another FSI approach is needed for the robust and scalable FSI analysis.

Chapter 6

Lagrangian-Immersed FSI Method using XFEM

6.1 Outline

This chapter focuses on the Lagrangian-immersed FSI method. The Lagrangian-immersed FSI method has the ability to handle both FSI and contact simultaneously. In this method, the solid phase is discretized by the Lagrangian meshes (deformable meshes) and the fluid phase is discretized by the Eulerian meshes (fixed background meshes). This method is an intermediate method of the arbitrary Lagrangian-Eulerian FSI method (ALE-FSI method) and the full-Eulerian FSI method. Mayer, Wall, et al. [69, 70] and Miller et al. [91] have been already studied this intermediate approach.

In the ALE-FSI and the full-Eulerian FSI, the solid and fluid elements are defined in the same computational domain and the interfaces between the solid and the fluid match. Therefore, boundary integrals on the interface can be exactly computed within one intersected element. Considering the Lagrangian-immersed FSI with the XFEM, the interfaces between the solid and the fluid are defined in both the Lagrangian and Eulerian meshes because the solid and fluid elements are spatially disconnected. In this chapter, the interfaces of Lagrangian and Eulerian meshes are denoted as Γ_L and Γ_E , respectively. These interfaces do not match as shown in Figure 6.1, because there are two types of meshes based on the Lagrangian and Eulerian description, respectively. Some small but non-zero gap exists between these two interfaces. The way to compute boundary integrals of the Lagrangian-immersed FSI method is similar to methods for computing boundary integrals in computational contact mechanics. Therefore, the more complicated treatment is needed than the ALE-FSI method and the full-Eulerian FSI method.

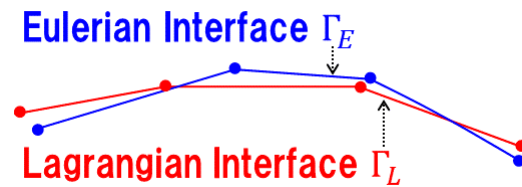


Figure 6.1: Lagrangian and Eulerian interface

A main advantage of the Lagrangian-immersed FSI method is the ability to simulate FSI problems with contact. As the solid and fluid meshes are decoupled and the solid structures are just immersed within the Eulerian system, there is no limitation of the deformation. In addition, as the solid phase is defined by the Lagrangian description, conventional contact formulations are directly applicable and thus, the implementation of the contact formulation is much easier than in the full-Eulerian FSI method.

While the physical model is identical with [69, 70], there are several differences in the actual numerical implementation. [69, 70] updates the interface in the Eulerian system using a geometric approach [103] as an additional technique in addition to a FSI solver. In the Lagrangian-immersed FSI method, the level set projection method is introduced and the update of interfaces in the Eulerian system is automatically performed in a monolithic FSI solver. The update of geometry is included in the weak form of FSI and thus additional techniques in addition to the FSI solver is not needed. FSI is computed between non-matching Lagrangian and Eulerian interfaces and techniques of contact formulation such as the master-slave concept, the node-to-surface (NTS) pairing, and the gap equation are applied. Besides, Nitsche's method is used instead of the Lagrange multiplier method used in [69, 70]. The proposed Lagrangian-immersed FSI method allows for a simpler implementation than [69, 70]. As the solid phase is defined by the Lagrangian description, the stabilized Lagrange multiplier method proposed by [75] is directly applied to this method as a contact formulation.

In this research, the Heaviside-enriched XFEM is used for the Lagrangian-immersed FSI

method. The level set function ϕ used for the Heaviside-enriched XFEM is a Heaviside-type level set function, considering the level set projection explained at the following section:

$$\phi(\mathbf{x}) = \left[1 + \exp\left(\frac{\phi_s}{\varepsilon_\phi}\right) \right]^{-1}, \quad (6.1)$$

where ϕ_s is the signed-distance level set function and ϕ is the Heaviside-type level set function. This ϕ is defined between $0 < \phi < 1$ and the iso-contour $\phi = 0.5$ defines immersed boundaries in the XFEM.

The organization of this chapter is as follows: Section 6.2 summarizes the physical aspects of the Lagrangian-immersed FSI method. FSI between non-matching interfaces and the contact formulation are described in this section. In Section 6.3, the level set projection method is proposed to update the geometry. The finite element discretization of the Lagrangian-immersed FSI method using the XFEM is summarized in Section 6.4. Section 6.5 describes the actual numerical implementation. In Section 6.6, two steady-state FSI problems, a transient multibody contact problem and a transient multibody FSI-contact problem are studied using the XFEM with a standard time stepping scheme. Section 6.7 summarizes the Lagrangian-immersed FSI method using the XFEM. In addition, the drawback of the Lagrangian-immersed FSI method using the XFEM is discussed and the necessity of the combination of the Lagrangian-immersed FSI method and the space-time XFEM is discussed.

6.2 Physics Model

This section summarizes the governing equations of both the Eulerian and Lagrangian systems, and the interface conditions for FSI. In this section, an Eulerian domain Ω_E and a set of Lagrangian domains Ω_L are considered. A fluid domain Ω_F is embedded within Ω_E . Ω_L is separated into multiple meshes Ω_L^i , which correspond to individual solid bodies: $\Omega_L = \sum_i \Omega_L^i$. The fluid and solid meshes are disconnected entities. FSI between the fluid

and solid is modeled at the interface in the Eulerian system Γ_E and the interface in the Lagrangian system Γ_L . In addition, the contact formulation for the Lagrangian description based on the stabilized Lagrange multiplier method is described in this section.

6.2.1 Eulerian System

An Eulerian system Ω_E contains a fluid domain Ω_F and a void domain Ω_V : $\Omega_E = \Omega_F \cup \Omega_V$. Ω_V is the projected domain of deformed solid structures defined in the Lagrangian system Ω_L . The immersed interface in Ω_E is denoted as Γ_E and FSI is computed on this Γ_E . The fluid phase is modeled by the incompressible Navier-Stokes (INS) fluid equations:

$$\frac{\partial v_i^f}{\partial t} + v_j^f \frac{\partial v_i^f}{\partial x_j} = \frac{1}{\rho^f} \frac{\partial \sigma_{ij}^f(\mathbf{v}^f, p^f)}{\partial x_j} + b_i^f \quad \text{in } \Omega_F, \quad (6.2)$$

$$\frac{\partial v_i^f}{\partial x_i} = 0 \quad \text{in } \Omega_F. \quad (6.3)$$

The momentum equation of fluid is (6.2) and the fluid continuity equation is (6.3). In this thesis, physical quantities in the fluid phase Ω_F are denoted by lower cases, such as the fluid velocity v_i^f and the fluid pressure p^f , and they are defined in the current configuration \mathbf{x} based on the Eulerian description. b_i^f is a body force for the fluid and σ_{ij}^f means the Cauchy stress tensor of the fluid defined as follows:

$$\sigma_{ij}^f(\mathbf{v}^f, p^f) = -p^f \delta_{ij} + 2\mu^f \varepsilon_{ij}(\mathbf{v}^f), \quad (6.4)$$

where ε_{ij} is the strain rate tensor of the fluid velocity \mathbf{v}^f :

$$\varepsilon_{ij}(\mathbf{v}^f) = \frac{1}{2} \left(\frac{\partial v_i^f}{\partial x_j} + \frac{\partial v_j^f}{\partial x_i} \right). \quad (6.5)$$

6.2.2 Lagrangian System

The Lagrangian system Ω_L contains multiple solid bodies defined in each Lagrangian mesh Ω_L^i . Each Lagrangian mesh Ω_L^i contains a solid domain Ω_S^i and a dummy displacement domain Ω_D^i . Physical quantities in Ω_L are defined by the Lagrangian description. Ω_S and

Ω_D denote the sets of Ω_S^i and Ω_D^i .

The solid phase Ω_S is governed by the momentum equation based on the initial configuration:

$$\rho^s \frac{\partial^2 U_i^s}{\partial t^2} + \rho^s \alpha^s \frac{\partial U_i^s}{\partial t} = \frac{\partial \Pi_{iJ}^s}{\partial X_J} + \rho^s B_i^s \quad \text{in } \Omega_{S0}, \quad (6.6)$$

where the lower subscript of zero; $(\cdot)_0$, denotes a quantity in the initial configuration. Physical quantities in the Lagrangian system Ω_L are denoted by upper cases and they are defined in the initial configuration \mathbf{X} . U_i^s is solid displacement, B_i^s is a body force for the solid and Π_{iJ}^s is the first Piola-Kirchhoff tensor. Π_{iJ}^s is defined by the solid displacement and solid pressure P^s for the incompressible constitutive law: $\Pi_{iJ}^s = \Pi_{iJ}^s(\mathbf{U}^s, P^s)$. α^s is an artificial viscosity for the steady-state FSI problem, that in the absence of time-varying external forces, causes the structure to converge to a steady-state solution.

In this work, (6.6) is separated into two parts: the momentum equation, similar to the momentum equations in the fluid phase (6.7) and the displacement-velocity relationship (6.8). To simplify the fluid-structure interaction model, the solid velocity V_i^s is introduced as an independent state variable:

$$\rho^s \frac{\partial V_i^s}{\partial t} + \rho^s \alpha^s V_i^s = \frac{\partial \Pi_{iJ}^s}{\partial X_J} + \rho^s B_i^s \quad \text{in } \Omega_{S0}, \quad (6.7)$$

$$\frac{\partial U_i^s}{\partial t} = V_i^s \quad \text{in } \Omega_{S0}. \quad (6.8)$$

The reason to use only first derivative terms with respect to t is motivated by the Lagrangian-immersed FSI method using the space-time XFEM (Chapter 7), because the linear interpolation along time is used in Chapter 7.

The Lagrangian system Ω_L also contains the dummy displacement domain Ω_D , which is related to the projection of deformed structures onto the Eulerian system Ω_E ; see Section 6.3. In the Lagrangian-immersed FSI method, the interface in the Eulerian system is not propagated like the full-Eulerian FSI analysis. Instead, the geometry of the interface in the

Eulerian system (background meshes) is created based on the projection of the level set function in the Lagrangian system (deformable meshes). As the interface is defined by the iso-contour line of the level set function ϕ ($\phi = 0.5$ in this work), the deformed level set function outside of the solid structures is needed to project the interface geometry onto the Eulerian system. The dummy displacement domain Ω_{D0} and the dummy displacement U_i^d are needed to create the level set function ϕ defined on the deformed Lagrangian mesh at the vicinity of the interface. The necessary conditions for this dummy displacement domain are as follows.

- The continuity of solid displacements in Ω_{S0} and dummy displacements in Ω_{D0} should be guaranteed across the interface.
- There is no influence of dummy displacements in Ω_{D0} on the solid displacements in Ω_{S0} .

In this research, the following two methods which satisfy above conditions are used.

The first method is the Helmholtz smoothing method. The dummy displacement U_i^d is governed by the following Helmholtz equation:

$$-\Delta_X U_i^d + U_i^d = -\frac{\partial^2 U_i^d}{\partial X^2} - \frac{\partial^2 U_i^d}{\partial Y^2} + U_i^d = 0 \quad \text{in } \Omega_{D0} , \quad (6.9)$$

where Ω_{D0} means the dummy displacement domain in the initial configuration. Nitsche's method is applied to enforce the continuity of the displacement at the interface of the Lagrangian system in the initial configuration Γ_{L0} between Ω_{S0} and Ω_{D0} :

$$[[U_i]] = U_i^s - U_i^d = 0 \quad \text{on } \Gamma_{L0} , \quad (6.10)$$

where $[[\cdot]]$ is a jump operator.

The second method for the dummy displacement is the dummy solid method. The dummy

solid method uses (6.7) and (6.8) also in Ω_{D0} :

$$\rho^d \frac{\partial V_i^d}{\partial t} + \rho^d \alpha^d V_i^d = \frac{\partial \Pi_{iJ}^d}{\partial X_J} + \rho^d B_i^d \quad \text{in } \Omega_{D0} , \quad (6.11)$$

$$\frac{\partial U_i^d}{\partial t} = V_i^d \quad \text{in } \Omega_{D0} . \quad (6.12)$$

In addition, Nitsche's method is applied considering the traction boundary condition and the continuity of displacement (6.10). The purpose of the dummy solid method is that follow the deformation of the solid domain Ω_{S0} . In general, α^d and B_i^d are set to zero, but the other material parameters are identical to the parameters of the solid phase Ω_{S0} .

Considering the case when a solid structure has the rigid body rotation, the dummy displacement domain Ω_{D0} defined by the dummy solid method can follow its rigid body rotation because the continuity of stress is also considered. Thus, the topology of mesh connectivity is correctly preserved and the negative Jacobian of elements is suppressed. On the other hand, the Helmholtz smoothing method only considers the continuity of the displacement and the continuity of numerical flux (solid stress) is not considered. Thus, it is hard to follow the rigid body rotation using the Helmholtz smoothing. Overall, the dummy solid method is more robust than the Helmholtz smoothing method. However, the Helmholtz method works fine for the case of pinned structures and the case of small rigid body rotation.

6.2.3 Fluid-Structure Interaction (FSI)

The Lagrangian-immersed FSI method uses separate meshes for the Lagrangian and Eulerian systems and thus, a pair of non-matching interfaces is used for the fluid-structure interaction. The key challenge of this FSI is the procedure to set integration points for boundary integrals between non-matching interfaces. A problem where boundary integrals using non-matching interfaces is commonly encountered, is the contact formulation. In contact formulations, there are several approaches to establish contact pairs (pairs of interfaces

for contact). The simplest approach is based on the master-slave concept and the node-to-surface pairing (NTS pairing: slave nodes contacts the surface in master elements).

In this research, the Eulerian interface Γ_E is the master interface, and the Lagrangian interface Γ_L is the slave interface. Boundary integrals of FSI are evaluated on the master interface Γ_E . Master integration points on Γ_E are defined by the quadrature rule on the master interface, and slave integration points on Γ_L are determined by the projection of master integration points Γ_E . The relation between master and slave points is defined by the following “gap equation”:

$$x_{Ei} + g_n n_{Ei}(\phi_E) - X_{Li} - U_{Li}^s(\mathbf{X}_L) = 0, \quad (6.13)$$

where x_{Ei} denotes the current configuration of the Eulerian system, n_{Ei} is the deformed normal of the Eulerian system and ϕ_E is the level set function of the Eulerian system. X_{Li} and U_{Li}^s are the initial configuration and solid displacement of the undeformed Lagrangian system Ω_{L0} . g_n denotes the normal gap between master (Eulerian) integration points and slave (Lagrangian) integration point and thus, slave integration points are determined by the gap g_n and the master normal n_{Ei} . Figures 6.3 and 6.2 show examples of the projection from the master integration points to the slave integration points.

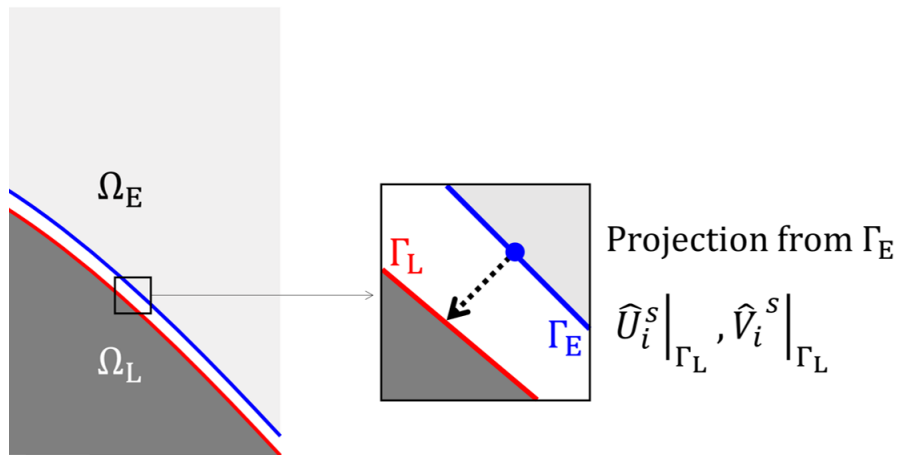


Figure 6.2: Projection of values from master interface Γ_E to slave interface Γ_L

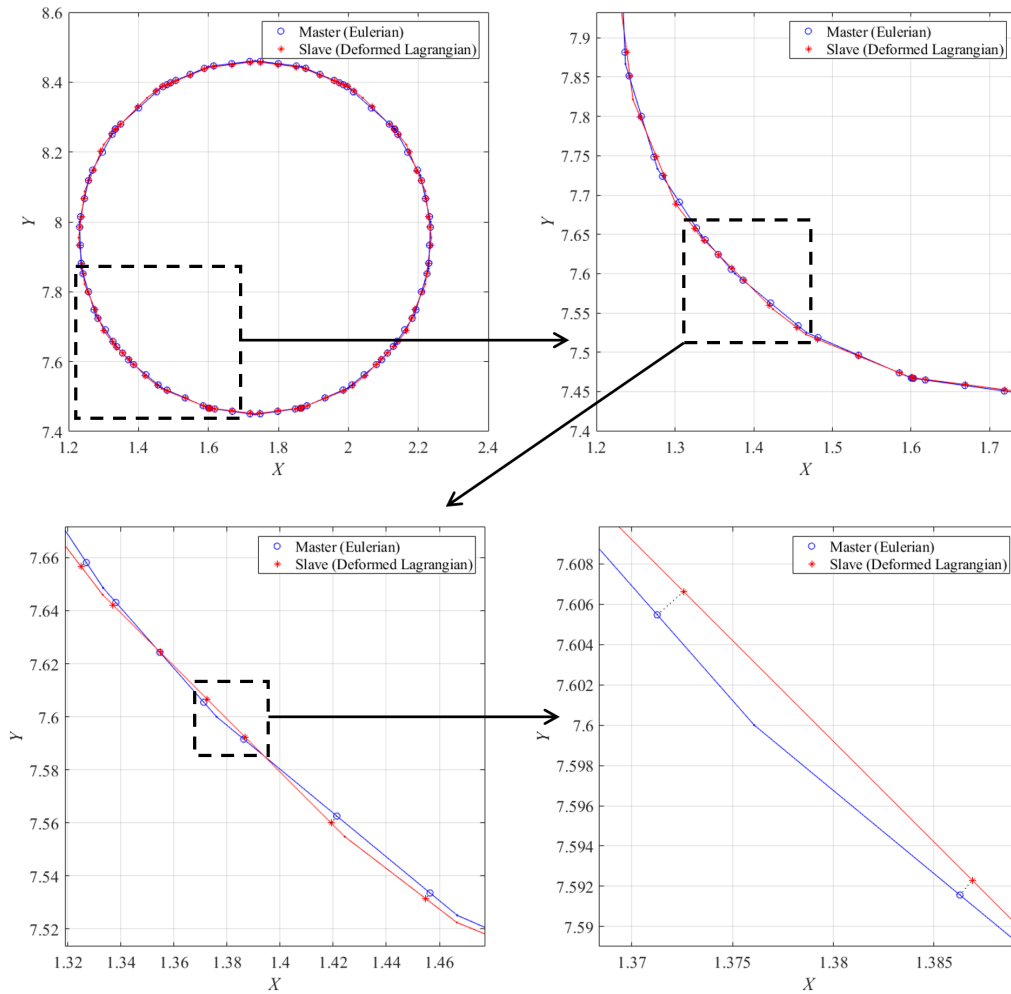


Figure 6.3: Projection from master integration points to slave integration points
 (—: master (Eulerian) interface, —: slave (Lagrangian) deformed interface)
 (○: master integration points, * : slave integration points by projection)

Based on the master-slave concept, the traction boundary condition and the continuity condition of velocity are enforced on the master (Eulerian) interface Γ_E :

$$\hat{T}_i^s|_{\Gamma_L} - t_i^f = 0 \quad \text{on } \Gamma_E, \quad (6.14)$$

$$\hat{V}_i^s|_{\Gamma_L} - v_i^f = 0 \quad \text{on } \Gamma_E. \quad (6.15)$$

Here, T_i^s is the solid traction on Γ_L and t_i^f is the fluid traction on Γ_E defined as follows:

$$T_i^s = \sigma_{ij}^s n_{Lj}^s = \Pi_{iJ}^s n_{L0J}^s \quad \text{on } \Gamma_L, \quad (6.16)$$

$$t_i^f = \sigma_{ij}^f n_{Ej}^f \quad \text{on } \Gamma_E, \quad (6.17)$$

where $\mathbf{n}_L^s = \{n_{Li}^s\}$ and $\mathbf{n}_{L0}^s = \{n_{L0i}^s\}$ are the outward facing normals for the solid on the deformed Lagrangian interface Γ_L and the undeformed Lagrangian interface Γ_{L0} respectively, and $\mathbf{n}_E^f = \{n_{Ei}^f\}$ is the outward facing normal for the fluid on the Eulerian interface Γ_E . As Γ_E is the master interface, $\hat{T}_i^s|_{\Gamma_L}$ and $\hat{V}_i^s|_{\Gamma_L}$ mean projected values from a master integration point onto a corresponding slave integration point.

6.2.4 Contact Model

This section describes the frictionless contact model for the large deformation based on the Lagrangian description. This approach follows the work of Lawry and Maute [75]. In the presence of large relative motion between surfaces of master and slave bodies, the dependence of coincident location along the interface on the displacements of either body needs to be accounted for. To this end, the surfaces of both bodies can be mapped to a parametric space. This parameterization simplifies the definition of coincident surface location by describing the master and slave material coordinates \mathbf{X}^A and \mathbf{X}^B , and subsequently the displacements \mathbf{U}^{sA} and \mathbf{U}^{sB} in a reduced dimensional space, where upper subscripts A and B mean properties of the master and slave bodies. The surfaces of master and slave bodies are parameterized by some surface parameters α and β respectively, as illustrated in Figure 6.4.

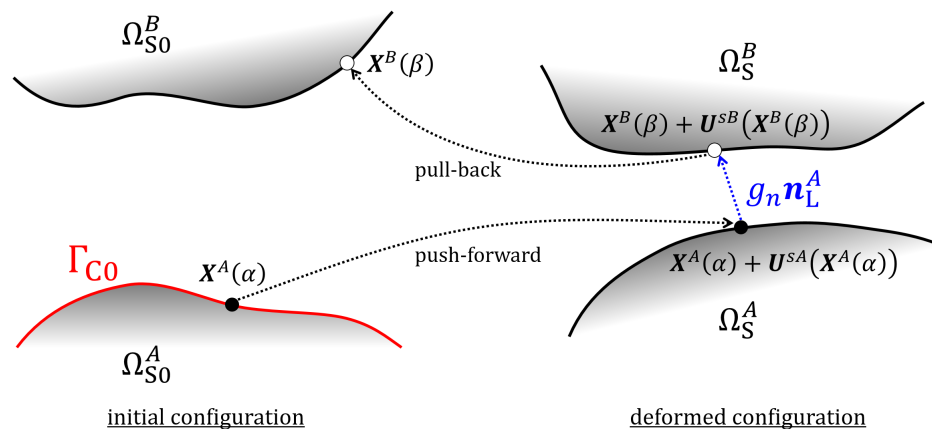


Figure 6.4: Contact interface Γ_{c0} and normal gap g_n (A : master, B : slave)

To provide a continuous representation of coincident surface positions, both surface parameterization schemes are coupled through the following relationship:

$$X_i^A(\alpha) + U_i^{sA}(\mathbf{X}^A(\alpha)) + g_n n_{Li}^A(\mathbf{X}^A, \mathbf{U}^{sA}) - X_i^B(\beta) - U_i^{sB}(\mathbf{X}^B(\beta)) = 0, \quad (6.18)$$

where g_n is the normal gap between deformed bodies A and B in the current configuration, and $\mathbf{n}_L^A = \{n_{Li}^A\}$ is the outward facing normal for the solid domain in the master solid body in the deformed Lagrangian system.

The following non-penetration condition should be satisfied in the current configuration:

$$g_n \lambda = 0, \quad g_n \geq 0, \quad \lambda \leq 0, \quad (6.19)$$

where λ is a Lagrange multiplier in the current configuration. By pulling back (6.19) to the initial configuration, the following non-penetration condition is obtained and used to enforce the contact:

$$g_n^0 \lambda^0 = 0, \quad g_n^0 \geq 0, \quad \lambda^0 \leq 0. \quad (6.20)$$

Here, g_n^0 and λ^0 are the normal gap and the Lagrange multiplier in the initial configuration of the master body A . g_n^0 is transformed from g_n by the Jacobian of the surface area based on the Nanson's formula:

$$g_n^0 = g_n j^A, \quad (6.21)$$

$$j^A = \det(F^A) \|(F^A)^{-T} \mathbf{n}_{L0}^A\|, \quad (6.22)$$

where F^A and $\mathbf{n}_{L0}^A = \{n_{L0I}^A\}$ are the deformation gradient tensor and the normal on the undeformed interface of the master body.

(6.21) is exactly identical to the KKT condition in the initial configuration. λ^0 is the contact pressure on the undeformed master interface based on the standard Lagrange multiplier

method for the contact:

$$\lambda^0 = \mathbf{n}_{L0}^A \text{T} S^A \mathbf{n}_{L0}^A, \quad (6.23)$$

where S^A is the second Piola-Kirchhoff stress tensor of the master body A . The potential of the standard Lagrange multiplier method W_c is defined in the initial configuration:

$$W_c = \int_{\Gamma_{c0}} d\Gamma g_n^0 \lambda^0. \quad (6.24)$$

By taking a variation of W_c , the weak form of the contact condition in the initial configuration Γ_{c0} based on the total Lagrangian formulation is as follows:

$$\int_{\Gamma_{c0}} d\Gamma \delta g_n^0 \lambda^0 + \int_{\Gamma_{c0}} d\Gamma \delta \lambda^0 g_n^0 = 0. \quad (6.25)$$

When the master and slave interfaces are not in contact ($g_n > 0$), λ^0 vanishes. On the other hand, a non-zero contact pressure λ^0 is needed to enforce that g_n^0 is zero and to satisfy the KKT condition (6.21).

Contact analysis based on (6.25) is reported that the distribution of contact pressure tends to become oscillatory [75]. To obtain a stable distribution of the contact pressure, the stabilized Lagrange multiplier method (Wriggers [104]) is effective. The weak form of the stabilized Lagrange multiplier method is a modification of (6.25) as follows:

$$\int_{\Gamma_{c0}} d\Gamma \delta g_n^0 \lambda^0 + \int_{\Gamma_{c0}} d\Gamma \delta \lambda^0 (\lambda^0 - \tilde{\lambda}^0 - \gamma_c g_n^0) = 0, \quad (6.26)$$

$$\tilde{\lambda}^0 = \kappa^A \mathbf{n}_{L0}^A \text{T} S^A \mathbf{n}_{L0}^A + \kappa^B \mathbf{n}_{L0}^B \text{T} S^B \mathbf{n}_{L0}^B (j^B)^{-1} j^A, \quad (6.27)$$

where $\tilde{\lambda}^0$ is an average contact pressure along the normal direction and j^B is the Jacobian of the surface area of the undeformed interface of the slave body. The weights for computing the average contact pressure $\tilde{\lambda}^0$ are defined as follows based on Dolbow et al. [100]:

$$\kappa^p = \frac{|\Omega^p|/E^p}{|\Omega^A|/E^A + |\Omega^B|/E^B} \quad (p = A, B), \quad (6.28)$$

where $|\Omega^p|$ is the elemental volume of the solid phase in the master and slave body ($p = A, B$)

and E^p is the Young's modulus of the master and slave solid phase. In addition, the penalty factor γ_c in the stabilized Lagrange multiplier method (6.26) is defined by Young's modulus E^p and the master element size h^A :

$$\gamma_c = \frac{\alpha_c}{h^A} (E^A + E^B) . \quad (6.29)$$

α_c is a constant and set as $\alpha_c = 5$ in this work. Detailed discussions are summarized in Appendix D.

6.3 Level Set Projection for Fluid-Structure Interaction

In the Lagrangian-immersed FSI method, both the solid and fluid domains are spatially disconnected because the solid and fluid domains are defined in different meshes: the Lagrangian system Ω_L and the Eulerian system Ω_E , respectively. Therefore, the fluid-structure interaction between the solid and fluid phases is modeled with non-matching interfaces: the deformed Lagrangian interface Γ_L and the Eulerian interface Γ_E . As the Lagrangian system Ω_L is defined by deformable meshes, the deformed Lagrangian interface Γ_L is explicitly defined and driven by displacements \mathbf{U} (solid displacements \mathbf{U}^s or dummy displacements \mathbf{U}^d). While Γ_L can be directly defined, some procedures to define a corresponding interface Γ_E in the Eulerian system Ω_E is needed. In this research, the level set projection method is introduced. The main idea of the level set projection method is that the projected level set field solves the following minimization problem:

$$\underset{\phi}{\text{minimize}} \frac{1}{2} \int_{\Omega_E} d\Omega \left(\phi(\mathbf{x}) - \hat{\Phi}(\mathbf{X} + \mathbf{U}) \right)^2 , \quad (6.30)$$

where ϕ is the level set function defined in the Eulerian system Ω_E . In addition, $\hat{\Phi}$ is a projected value of Φ from the deformed Lagrangian system Ω_L onto the Eulerian system Ω_E , and Φ is the level set function defined in the undeformed Lagrangian system Ω_{L0} . Φ is defined based on the initial configuration \mathbf{X} because the solid phase is computed by

the total Lagrangian formulation. As $\Phi(\mathbf{X})$ is fixed in the initial configuration, this Φ is a time-invariant parameter. Therefore, it is necessary to compute the deformed level set function $\hat{\Phi}(\mathbf{x})$ based on the deformed configuration \mathbf{x} using displacement $\mathbf{U}(\mathbf{X}, t)$; $\mathbf{U}^s(\mathbf{X}, t)$ or $\mathbf{U}^d(\mathbf{X}, t)$. The following equation is a relation between Φ and $\hat{\Phi}$:

$$\Phi(\mathbf{X}) = \hat{\Phi}(\mathbf{X} + \mathbf{U}) = \hat{\Phi}(\mathbf{x} - \mathbf{U}) . \quad (6.31)$$

The minimization problem (6.30) is equivalent to the following variational problem:

$$R_\phi = \int_{\Omega_E} d\Omega \delta\phi \left(\phi(\mathbf{x}) - \hat{\Phi}(\mathbf{X} + \mathbf{U}) \right) = 0 . \quad (6.32)$$

This projection method does not depend on the type of the level set function, but the computational efficiency varies by the type of the level set function. The most efficient projection is the projection based on the Heaviside-type level set function (6.1). As the Heaviside-type level set function varies only at the vicinity of interfaces, the projection needs to be only performed in the vicinity of interfaces. On the other hand, the projection based on the signed-distance level set function, which is a standard type of the level set function, has to compute accurate projection in the whole domain, because the signed-distance level set function varies everywhere. Therefore, the Heaviside-type level set function (6.1) is used in the Lagrangian-immersed FSI method.

To capture accurately the interface Γ_E in Ω_E , the weighted projection focusing on the vicinity of interfaces is introduced:

$$\underset{\phi}{\text{minimize}} \frac{1}{2} \int_{\Omega_E} d\Omega f(\hat{\Phi}) \left(\phi(\mathbf{x}) - \hat{\Phi}(\mathbf{X} + \mathbf{U}) \right)^2 , \quad (6.33)$$

where $f(\hat{\Phi})$ is a weighting function. Mathematical characteristics of $f(\hat{\Phi})$ are summarized as follows.

- $f(\hat{\Phi})$ should have the maximum weight at the value which indicates the location of the interface.

- $f(\hat{\Phi})$ should be larger than 0 everywhere.

As Φ is defined by the Heaviside-like level set function between 0 and 1 in this research, and interface is defined by the iso-contour line $\Phi = 0.5$, the following double-well potential is used in this work:

$$f(\hat{\Phi}) = 16a(\hat{\Phi} - 0.5)^4 - 8a(\hat{\Phi} - 0.5)^2 + a + \varepsilon , \quad (6.34)$$

where a is an amplitude and ε is a shifted parameter which is much smaller than a . In this work, $a = 10$ and $\varepsilon = 0.001$ are used. (6.34) is equivalent to the following variational problem:

$$R_\phi = \int_{\Omega_E} d\Omega \delta\phi f(\hat{\Phi}) \left(\phi(\mathbf{x}) - \hat{\Phi}(\mathbf{X} + \mathbf{U}) \right) = 0 . \quad (6.35)$$

To compute (6.35), integration points are defined in Ω_E at first. Then, a corresponding point in Ω_L of each integration point in Ω_E is detected. Finally, $\hat{\Phi}$ is evaluated at the detected point in Ω_L and used in (6.35).

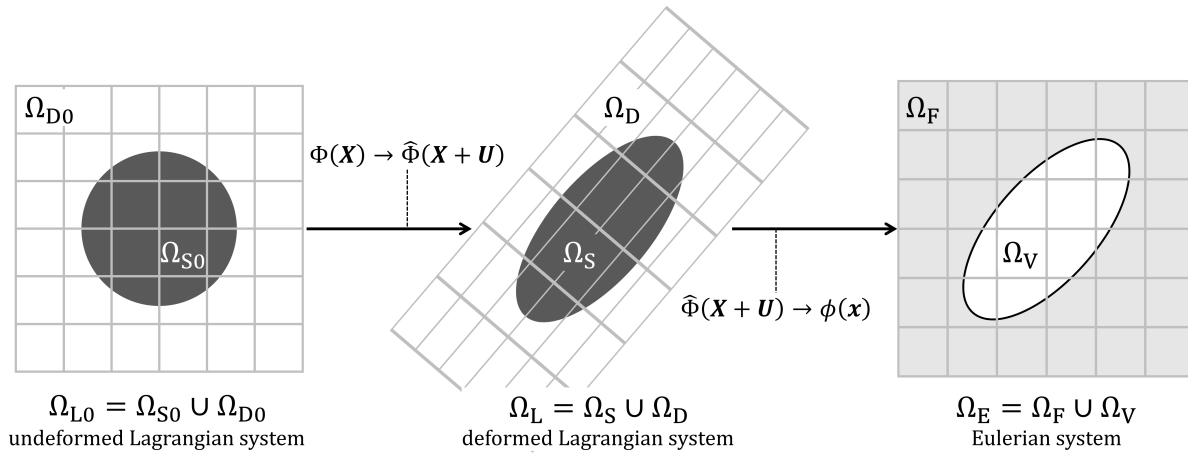


Figure 6.5: Level set projection

6.4 Finite Element Discretization of Lagrangian-Immersed FSI Method using XFEM

This section summarizes the finite element discretization of the FSI-contact problem based on the Lagrangian-immersed FSI method, considering two-dimensional problems. The entire computational domain Ω is the union of the Eulerian and Lagrangian system: $\Omega = \Omega_E \cup \Omega_L$ and discretized spatially by bilinear QUAD4 elements. The temporal discretization is performed by the Newmark method with $\Gamma = 0.9$ and $\beta = 0.5$. Given a trial function space \mathcal{S}^h and an admissible test function space \mathcal{V}^h (lower subscript 0 denotes a space in the initial configuration):

$$\text{Trial functions: } \quad \{\mathbf{U}^s, \mathbf{V}^s, \mathbf{U}^d\} \in \mathcal{S}_0^h, \quad \{\mathbf{v}^f, p^f, \phi\} \in \mathcal{S}^h, \quad (6.36)$$

$$\text{Test functions: } \quad \{\delta \mathbf{U}^s, \delta \mathbf{V}^s, \delta \mathbf{U}^d\} \in \mathcal{V}_0^h, \quad \{\delta \mathbf{v}^f, \delta p^f, \delta \phi\} \in \mathcal{V}^h, \quad (6.37)$$

the variational form of the FSI-contact problem using a compressible material for the solid phase is as follows:

$$\begin{aligned} & R_m^s(\delta \mathbf{U}^s; \{\mathbf{U}^s, \mathbf{V}^s\}) + R_{uv}^s(\delta \mathbf{V}^s; \{\mathbf{U}^s, \mathbf{V}^s\}) + R_u^d(\delta \mathbf{U}^d; \{\mathbf{U}^s, \mathbf{U}^d\}) + R_c^s(\delta \mathbf{U}^s; \mathbf{U}^s) \\ & + R_m^f(\{\delta \mathbf{v}^f, \delta p^f\}; \{\mathbf{v}^f, p^f, \phi\}) + R_\phi(\delta \phi; \{\phi, \hat{\Phi}\}) \\ & + R_L^{\text{fsi}}(\delta \mathbf{U}^s; \{\mathbf{U}^s, \mathbf{V}^s, \mathbf{v}^f, p^f, \phi\}) + R_E^{\text{fsi}}(\{\delta \mathbf{v}^f, \delta p^f\}; \{\mathbf{U}^s, \mathbf{V}^s, \mathbf{v}^f, p^f, \phi\}) \\ & + R_L^{\text{gp}}(\{\delta \mathbf{U}^s, \delta \mathbf{V}^s, \delta \mathbf{U}^d\}; \{\mathbf{U}^s, \mathbf{V}^s, \mathbf{U}^d\}) + R_E^{\text{gp}}(\{\delta \mathbf{v}^f, \delta p^f\}; \{\mathbf{v}^f, p^f\}) = 0. \end{aligned} \quad (6.38)$$

This section discusses the individual terms of (6.38) except the variational form of the stabilization terms R_L^{gp} and R_E^{gp} , for which details are provided in Section 6.5.3.

First, R_m^s , R_{uv}^s and R_u^d are defined in the undeformed Lagrangian system Ω_{L0} and on the corresponding undeformed Lagrangian interface Γ_{L0} . R_m^s and R_{uv}^s are the variational form of the solid momentum equation (6.7) and the displacement-velocity relationship (6.8) in the solid phase of the initial configuration Ω_{S0} . The test functions associated with R_m^s and R_{uv}^s

are δU_i^s , δV_i^s and δU_i^d respectively. The detailed forms of R_m^s and R_{uv}^s are defined as follows:

$$R_m^s = \int_{\Omega_{S0}} d\Omega \delta U_i^s \rho^s \left(\frac{\partial V_i^s}{\partial t} + \alpha^s V_i^s - B_i^s \right) + \int_{\Omega_{S0}} d\Omega \frac{\partial \delta U_i^s}{\partial X_J} \Pi_{iJ}^s(\mathbf{U}^s), \quad (6.39)$$

$$R_{uv}^s = \int_{\Omega_{S0}} d\Omega \delta V_i^s \rho^s \left(\frac{\partial U_i^s}{\partial t} - V_i^s \right). \quad (6.40)$$

Second, R_u^d is the variational form of the governing equation in the dummy displacement domain Ω_{D0} . Based on the Helmholtz smoothing method, the Helmholtz equation (6.9) for the dummy displacement outside of the solid phase Ω_{D0} and the continuity condition of U_i^s and U_i^d (6.10) on the undeformed Lagrangian interface Γ_{L0} based on the one-sided Nitsche method are included in this weak form:

$$R_u^d = \int_{\Omega_{D0}} d\Omega \frac{\partial \delta U_i^d}{\partial X_J} \rho^d \frac{\partial U_i^d}{\partial X_J} + \int_{\Omega_{D0}} d\Omega \delta U_i^d \rho^d U_i^d - \int_{\Gamma_{L0}} d\Gamma \delta U_i^d \rho^d \frac{\partial U_i^d}{\partial X_J} n_{L0J}^d + \int_{\Gamma_{L0}} d\Gamma \delta U_i^d \rho^d \eta^d (U_i^s - U_i^d), \quad (6.41)$$

where η^d is the Nitsche penalty factor for the displacement continuity condition of the Lagrangian system. Based on the dummy solid method, the dummy momentum equation (6.11) and the dummy displacement-velocity relationship (6.12) determine R_u^d , using the one-sided Nitsche method as follows:

$$R_u^d = \int_{\Omega_{D0}} d\Omega \delta U_i^d \rho^d \left(\frac{\partial V_i^d}{\partial t} + \alpha^d V_i^d - B_i^d \right) + \int_{\Omega_{D0}} d\Omega \frac{\partial \delta U_i^d}{\partial X_J} \Pi_{iJ}^d(\mathbf{U}^d) + \int_{\Omega_{D0}} d\Omega \delta V_i^d \rho^d \left(\frac{\partial U_i^d}{\partial t} - V_i^d \right) - \int_{\Gamma_{L0}} d\Gamma \delta U_i^d \{\Pi_{iJ}\} n_{L0J}^{s \rightarrow d} - \int_{\Gamma_{L0}} d\Gamma \Pi_{iJ}^d (\delta \mathbf{U}^d) n_{L0J}^{s \rightarrow d} (U_i^s - U_i^d) + \int_{\Gamma_{L0}} d\Gamma \delta U_i^d \rho^d \eta^d (U_i^s - U_i^d), \quad (6.42)$$

where $\{\Pi_{iJ}\}$ is the weighted average of the first PK stress and the modulus weighting is used in (6.42); see Section 5.5.2. As the modulus weighting is identical to the equal weighting because Young's moduli of the solid and void phases are identical. In general, the weighting proposed by [100], which is used in the contact formulation in this research, works more stably than the other weighting strategies. But no issue is observed by using the modulus

weighting in (6.42) in this research.

Third, R_c^s denotes the variational form of the contact formulation, which is an interface integral between two different solid bodies in Ω_L . R_c^s is performed on the interface of a master body in the initial configuration Γ_{c0} :

$$R_c^s = \int_{\Gamma_{c0}} d\Gamma \delta g_n^0 \lambda^0, \quad (6.43)$$

where δg_n^0 is the variation of the normal gap in the initial Lagrangian system and λ^0 is governed by the following equation based on the stabilized Lagrange multiplier method (Section 6.2.4):

$$R_\lambda^s = \int_{\Gamma_{c0}} d\Gamma \delta \lambda^0 (\lambda^0 - \tilde{\lambda}^0 - \gamma_c g_n^0), \quad (6.44)$$

where the definition of $\tilde{\lambda}^0$ is given by (6.27). λ^0 is computed outside of the monolithic FSI-contact solver and defined elementwise. Detailed discussions about contact and how to compute λ^0 are summarized in Appendix D.

Fourth, R_m^f , and R_ϕ are defined in the Eulerian system Ω_E and on the corresponding interface Γ_E in the current configuration. R_m^f is the variational form of volume contribution of the fluid momentum equation (6.2) and the continuity equation (6.3) in the fluid phase of the current configuration Ω_F :

$$\begin{aligned} R_m^f &= \int_{\Omega_F} d\Omega \delta v_i^f \rho^f \left(\frac{\partial v_i^f}{\partial t} + v_j^f \frac{\partial v_i^f}{\partial x_j} - b_i^f \right) + \int_{\Omega_F} d\Omega \frac{\partial \delta v_i^f}{\partial x_j} \sigma_{ij}^f(\mathbf{v}^f, p^f) \\ &\quad + \int_{\Omega_F} d\Omega \delta p^f \frac{\partial v_i^f}{\partial x_i} + \sum_{e \in \Omega_F} \int_{\Omega_{Fe}} d\Omega \left(\tau_m^f v_j^f \frac{\partial \delta v_i^f}{\partial x_j} + \frac{\tau_m^f}{\rho^f} \frac{\partial \delta p^f}{\partial x_i} \right) \tilde{r}_i^f \\ &\quad + \sum_{e \in \Omega_F} \int_{\Omega_{Fe}} d\Omega \tau_c^f \frac{\partial \delta v_i^f}{\partial x_i} \frac{\partial v_j^f}{\partial x_j}, \end{aligned} \quad (6.45)$$

where $\int_{\Omega_{Fe}}$ denotes a volume integral over an elemental volume of the fluid Ω_{Fe} ($\Omega_{Fe} \in \Omega_F$), and \tilde{r}_i^f is a scalar residual of the momentum equation of the incompressible Navier-Stokes

fluid:

$$\tilde{r}_i^f = \rho^f \frac{\partial v_i^f}{\partial t} + \rho^f v_j^f \frac{\partial v_i^f}{\partial x_j} - \frac{\partial \sigma_{ij}^f(\mathbf{v}^f, p^f)}{\partial x_j} - \rho^f b_i^f. \quad (6.46)$$

In (6.45), terms without summation symbol are the standard Galerkin terms, other terms are the stabilization terms for the convection and the incompressibility. Here, the residual-based variational multiscale (VMS) method is used to suppress the numerical instability due to convection and incompressibility, and τ_m^f and τ_c^f are the stabilization parameters of the VMS method for the momentum and continuity equations respectively:

$$\tau_m^f = \left[\left(\frac{2\rho^f}{\Delta t} \right)^2 + (\rho^f \mathbf{v}^f)^T G(\rho^f \mathbf{v}^f) + \mu^f G : G \right]^{-1/2}, \quad (6.47)$$

$$\tau_c^f = \left[\tau_m^f \text{Tr}(G) \right]^{-1}, \quad (6.48)$$

where $G_{ij} = \sum_{k=1}^2 (\partial \xi_k / \partial x_i)(\partial \xi_k / x_j)$ and ξ_k is the isoparametric coordinate of each element. τ_m^f and τ_c^f correspond to parameters of SUPG/PSPG and LSIC stabilizations, respectively. R_ϕ is the variational form of the level set projection using a weighted projection method (6.35):

$$R_\phi = \int_{\Omega_E} d\Omega \delta \phi f(\hat{\Phi})(\phi - \hat{\Phi}). \quad (6.49)$$

This projection is performed in the entire Eulerian system Ω_E to capture the accurate interface for the fluid phase.

Finally, R_L^{fsi} and R_E^{fsi} are the FSI contributions of the solid and fluid momentum equations; (6.7) and (6.2), based on Nitsche's method. Using the master-slave concept described in Section 6.2.3, boundary integrals of FSI are performed on the master (Eulerian) interface Γ_E . R_L^{fsi} is the FSI contribution for the Lagrangian interface Γ_L and R_E^{fsi} is the FSI contribution for the Eulerian interface Γ_E :

$$R_L^{\text{fsi}} = - \int_{\Gamma_E} d\Gamma \delta U_i^s \{ \sigma_{ij} \}_{\text{fsi}} n_{Lj}^{s \rightarrow f} + \int_{\Gamma_E} d\Gamma \delta U_i^s \eta^{\text{fsi}} (\hat{V}_i^s|_{\Gamma_L} - v_i^f), \quad (6.50)$$

$$\begin{aligned}
R_E^{\text{fsi}} = & \int_{\Gamma_E} d\Gamma \delta v_i^f \{\sigma_{ij}\}_{\text{fsi}} n_{Ej}^{s \rightarrow f} - \int_{\Gamma_E} d\Gamma \sigma_{ij}^f (\delta \mathbf{v}^f \delta p^f) n_{Ej}^{s \rightarrow f}, (\hat{V}_i^s|_{\Gamma_L} - v_i^f) \\
& - \int_{\Gamma_E} d\Gamma \delta v_i^f \eta^{\text{fsi}} (\hat{V}_i^s|_{\Gamma_L} - v_i^f). \tag{6.51}
\end{aligned}$$

Here, $\{\sigma_{ij}\}_{\text{fsi}}$ is the weighted average of the Cauchy stress of solid and fluid phase and defined as follows:

$$\{\sigma_{ij}\}_{\text{fsi}} = \kappa^s \sigma_{ij}^s(\mathbf{U}^s) + \kappa^f \sigma_{ij}^f(\mathbf{v}^f, p^f), \tag{6.52}$$

where κ^s and κ^f are weights for the solid and fluid stresses. In this research, the following weighting strategy based on the shear modulus is used:

$$\kappa^s = \frac{G^f}{G^s + G^f}, \tag{6.53}$$

$$\kappa^f = \frac{G^s}{G^s + G^f}, \tag{6.54}$$

where G^s is the shear modulus of a solid phase and G^f is the effective shear modulus of a fluid phase:

$$G^s = \frac{E^s}{2(1 + \nu^s)}, \tag{6.55}$$

$$G^f = c^f \frac{\mu^f}{\Delta t}. \tag{6.56}$$

In (6.55), E^s and ν^s are the Young's modulus and the Poisson's ration of a solid phase. In (6.56), μ^f is the dynamic viscosity of a fluid phase, Δt is the time increment and c^f is a scaling coefficient. As $\mu^f/\Delta t$ is much smaller than G^s , $c^f = 100$ in this thesis. In general, $\kappa^f \gg \kappa^s$. Therefore, the traction from the fluid side is the dominant contribution of the traction used at the interface integrals. This treatment is similar to the traditional weighting strategy ($\kappa^f = 1, \kappa^s = 0$); see discussions in Section 5.8.3.

The first term of RHS of (6.50) and (6.51) is called as the standard consistency term. The second term of RHS of (6.51) is called as the adjoint consistency term. In this adjoint consistency term, the traditional weighting strategy ($\kappa^f = 1, \kappa^s = 0$) is applied for the sim-

plicity because $\kappa^f \gg \kappa^s$ based on the weighting strategy in this research: (6.53) and (6.54). The last term of RHS of (6.50) and (6.51) is called as the Nitsche penalty term. Detailed discussion of Nitsche's method for the Lagrangian-immersed FSI method is summarized in Appendix C.

6.5 Numerical Implementation

This section discusses the details of the numerical implementation. The overall procedure of Newton iteration used in this method is summarized in Algorithm 1. The FSI problem described above is solved numerically by Algorithm 1 assuming a time step $n + 1$ (time t^{n+1}).

Algorithm 1 Newton solver for the Lagrangian-immersed FSI method using XFEM (time step $n + 1$: t^{n+1})

for $k \leftarrow 1$ **to** (maximum Newton iteration) **do**

(1) Compute global residual and Jacobian: $\mathbf{R}_{(k+1)}^{n+1}$ and $J_{(k+1)}^{n+1}$

(2) Compute relative norm of current residual against the initial residual
 $r_{(k+1)}^{n+1} = \|\mathbf{R}_{(k+1)}^{n+1}\| / \|\mathbf{R}_{(1)}^{n+1}\|$

(3) Solve incremental solution at current Newton iteration
 $\Delta \mathbf{u}_{(k+1)}^{n+1} = - (J_{(k+1)}^{n+1})^{-1} \mathbf{R}_{(k+1)}^{n+1}$

(4) Update solution vector
 $\mathbf{u}_{(k+1)}^{n+1} = \mathbf{u}_{(k)}^{n+1} + \Delta \mathbf{u}_{(k+1)}^{n+1}$

(5) Perform correction of level set projection

if $r_{(k+1)}^{n+1} \geq 0.1$ **then**

(5-a) Define residual and Jacobian only for level set projection: $\mathbf{R}_{\phi}^{\text{post}}$ and J_{ϕ}^{post}

(5-b) Update level set function

$$\Delta \phi^{\text{post}} = - (J_{\phi}^{\text{post}})^{-1} \mathbf{R}_{\phi}^{\text{post}} \quad \text{and} \quad \phi_{(k+1)}^{n+1} = \phi_{(k+1)}^{n+1} + \Delta \phi^{\text{post}}$$

end if

(6) Check convergence criterion

if $r_{(k+1)}^{n+1} < (\text{convergence criterion})$ **then**

exit

end if

end for

6.5.1 Correction of Level Set Projection

A key component within Newton iteration (Algorithm 1) is the correction of the level set projection after the update of solution vector at Step (5) of Algorithm 1. The correction of level set projection is performed when the relative norm of the residual with respect to the initial residual is larger than 10^{-1} .

The purpose of the correction of the level set projection is the correction of the updated Eulerian interface Γ_E at the early stage of the Newton iteration. Figure 6.6 is an image of Lagrangian interface Γ_L and Eulerian interface Γ_E at the early stage of the Newton iteration. Figure 6.6 (a) shows the first iteration of the Newton iteration. At the first iteration, both Γ_L and Γ_E coincide because solution \mathbf{s} at the first iteration is the converged solution at the previous time step n (time t^n). Figure 6.6 (b) shows the state just after the update of the solution vector in Step (4) of Algorithm 1. At this time, Γ_E does not move because the residual of the level set projection in Step (a) is zero. On the other hand, Γ_L moves due to the updated solid displacements. If the correction step (5) of Algorithm 1 is omitted, the FSI system is built in Step (1) and solved in Step (2) using the geometries of the previous iteration. This can lead to a large discrepancy between interfaces and slow convergence of Newton iterations. To accelerate the convergence of the Newton solver, the correction of the level set projection is introduced. Therefore, Γ_E and Γ_L coincide at the beginning of each Newton iteration. The errors associated with the mismatch of the interface geometries in the Lagrangian and Eulerian meshes are reduced, and a fast convergence is achieved.

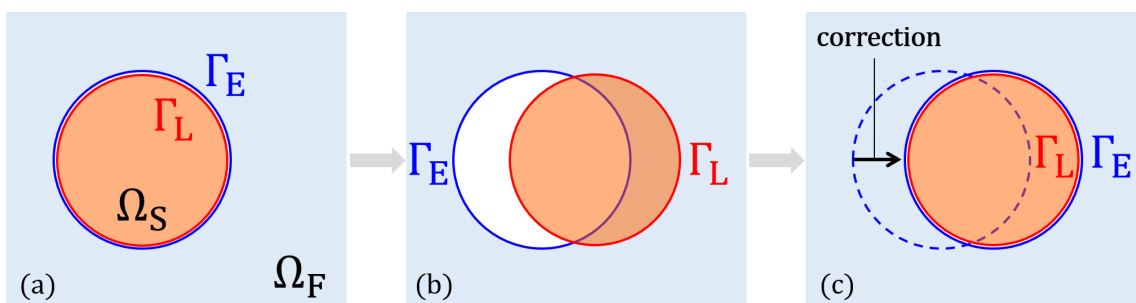


Figure 6.6: Correction of level set projection (early stage of Newton iteration)

6.5.2 Structure of Jacobian

The blocks of the Jacobian (tangential stiffness) corresponding to the weak form (6.38) of the Lagrangian-immersed FSI method using the XFEM are shown in Figure 6.7 (\mathbf{u} denotes the entire state variables). When the norm of the residual is larger than 10^{-1} relative to the norm of the initial residual, an approximate Jacobian, which omits the blue terms in Figure 6.7, is used to solve the system in Step (2) of Algorithm 1. Otherwise, the consistent Jacobian which is the same as shown in Figure 6.7 is used in the Newton iteration. This is because the correction of the level set projection described in Section 6.5.1 is applied when the relative norm of the residual is larger than 10^{-1} , and the blue terms are no more consistent when the correction of the level set projection is applied. In this case, an approximate computation with respect to the level set function should be used, and the computational cost can be reduced by omitting the contribution of blue terms in Figure 6.7. As the location of interfaces at the early stage of the Newton iteration may significantly differ from the converged solution. The blue terms (off-diagonal terms) of the consistent Jacobian sometimes cause the Newton iteration to diverge. Therefore, the usage of the consistent Jacobian should be avoided at the early stage of the Newton iteration.

| | | Column | | | | | |
|-----|----------------|--|--|--|--|---|--|
| | | \mathbf{v}^f | p^f | \mathbf{V}^s | \mathbf{U}^s | \mathbf{U}^d | ϕ |
| Row | \mathbf{v}^f | $\frac{\partial \mathbf{R}_m^f}{\partial \mathbf{v}^f} + \frac{\partial \mathbf{R}_E^{\text{fsi}}}{\partial \mathbf{v}^f}$ | $\frac{\partial \mathbf{R}_m^f}{\partial p^f} + \frac{\partial \mathbf{R}_E^{\text{fsi}}}{\partial p^f}$ | $\frac{\partial \mathbf{R}_E^{\text{fsi}}}{\partial \mathbf{V}^s}$ | $\frac{\partial \mathbf{R}_E^{\text{fsi}}}{\partial \mathbf{U}^s}$ | $\mathbf{0}$ | $\frac{\partial \mathbf{R}_m^f}{\partial \phi} + \frac{\partial \mathbf{R}_E^{\text{fsi}}}{\partial \phi}$ |
| | p^f | | | | | | |
| | \mathbf{V}^s | $\mathbf{0}$ | $\mathbf{0}$ | $\frac{\partial \mathbf{R}_{uv}^s}{\partial \mathbf{V}^s}$ | $\frac{\partial \mathbf{R}_{uv}^s}{\partial \mathbf{U}^s}$ | $\mathbf{0}$ | $\mathbf{0}$ |
| | \mathbf{U}^s | $\frac{\partial \mathbf{R}_L^{\text{fsi}}}{\partial \mathbf{v}^f}$ | $\frac{\partial \mathbf{R}_L^{\text{fsi}}}{\partial p^f}$ | $\frac{\partial \mathbf{R}_m^s}{\partial \mathbf{V}^s} + \frac{\partial \mathbf{R}_L^{\text{fsi}}}{\partial \mathbf{V}^s}$ | $\frac{\partial \mathbf{R}_m^s}{\partial \mathbf{U}^s} + \frac{\partial \mathbf{R}_c^s}{\partial \mathbf{U}^s} + \frac{\partial \mathbf{R}_L^{\text{fsi}}}{\partial \mathbf{U}^s}$ | $\mathbf{0}$ | $\frac{\partial \mathbf{R}_L^{\text{fsi}}}{\partial \phi}$ |
| | \mathbf{U}^d | $\mathbf{0}$ | $\mathbf{0}$ | $\mathbf{0}$ | $\frac{\partial \mathbf{R}_u^d}{\partial \mathbf{U}^s}$ | $\frac{\partial \mathbf{R}_u^d}{\partial \mathbf{U}^d}$ | $\mathbf{0}$ |
| | ϕ | $\mathbf{0}$ | $\mathbf{0}$ | $\mathbf{0}$ | $\frac{\partial R_\phi}{\partial \mathbf{U}^s}$ | $\frac{\partial R_\phi}{\partial \mathbf{U}^d}$ | $\frac{\partial R_\phi}{\partial \phi}$ |

Figure 6.7: Broad structure of Jacobian (Lagrangian-immersed FSI using XFEM)

6.5.3 Face-Oriented Ghost-Penalty Method

As the geometry of the solid and fluid domains is described by the level set function in the XFEM, the XFEM procedure usually creates intersection configurations where certain degrees of freedom interpolate in very small subdomains. These small subdomains produce an ill-conditioning problem, which leads an increase in the condition number of the Jacobian, and may slow-down of the convergence or cause divergence of the Newton iteration. In particular, as the Lagrangian-immersed FSI analysis treats the Eulerian interface as a moving interface projected by the level set projection method (Section 6.3), numerical instability due to small intersection configuration has a large impact.

To mitigate this ill-conditioning problem, the face-oriented ghost-penalty method is applied in this work. This ghost-penalty method is applied at the faces of intersected elements. A face in the Lagrangian mesh of the initial configuration is denoted as Γ_{Lgp0} . A face in the Eulerian mesh is denoted as Γ_{Egp} . The variational forms of the face-oriented ghost-penalty method on Γ_{Lgp0} and Γ_{Egp} are defined as follows:

$$R_L^{gp} = R_{LU^s}^{gp}(\delta \mathbf{U}^s; \mathbf{U}^s) + R_{LV^s}^{gp}(\delta \mathbf{V}^s; \mathbf{V}^s) + R_{LU^d}^{gp}(\delta \mathbf{U}^d; \mathbf{U}^d), \quad (6.57)$$

$$R_E^{gp} = R_{Ev^f}^{gp}(\delta \mathbf{v}^f; \mathbf{v}^f) + R_{Ep^f}^{gp}(\delta p^f; p^f). \quad (6.58)$$

The continuity of fluxes is enforced on the elemental faces by penalizing the jump of fluxes. The contribution of the velocity and the pressure is to suppress numerical instability by considering the associated fluxes across the elemental face:

$$R_{LV^s}^{gp} = \int_{\Gamma_{Lgp0}} d\Omega \left[\left[\frac{\partial \delta V_i^s}{\partial X_J} \right]_{gp} n_{L0J}^{gp} \eta_{V^s}^{gp} \left[\left[\frac{\partial V_i^s}{\partial X_K} \right]_{gp} n_{L0K}^{gp} \right], \quad (6.59)$$

$$R_{Ev^f}^{gp} = \int_{\Gamma_{Egp}} d\Omega \left[\left[\frac{\partial \delta v_i^f}{\partial x_j} \right]_{gp} n_{Ej}^{gp} \eta_{v^f}^{gp} \left[\left[\frac{\partial v_i^f}{\partial x_k} \right]_{gp} n_{Ek}^{gp} \right], \quad (6.60)$$

$$R_{Ep^f}^{gp} = \int_{\Gamma_{Egp}} d\Omega \left[\left[\frac{\partial \delta p^f}{\partial x_i} \right]_{gp} n_{Ei}^{gp} \eta_{p^f}^{gp} \left[\left[\frac{\partial p^f}{\partial x_j} \right]_{gp} n_{Ej}^{gp} \right], \quad (6.61)$$

where the jump operator for the face-oriented ghost-penalty method $[[\cdot]]_{\text{gp}}$ is defined as:

$$[[a]]_{\text{gp}} = a|_{\Omega_e^1} - a|_{\Omega_e^2} , \quad (6.62)$$

and evaluated at the face between two adjacent elements Ω_e^1 and Ω_e^2 intersected by $\Gamma_{\text{Lgp}0}$ or Γ_{Egp} . In the face-oriented ghost-penalty method, the jump terms are integrated over the entire face, individually for each phase that is considered. The face-oriented ghost-penalty method for displacements is defined by the minimization of the jump in the first PK stress on the elemental faces [75]. Applying the following variational forms, the continuity of the stress field is weakly enforced, even if there is a tiny intersected element:

$$R_{LU^s}^{\text{gp}} = \int_{\Gamma_{\text{Lgp}0}} d\Gamma \left[\left[\frac{\partial \delta U_i^s}{\partial X_J} \right]_{\text{gp}} n_{L0J}^{\text{gp}} \eta_{U^s}^{\text{gp}} [[\Pi_{iK}^s]]_{\text{gp}} n_{L0K}^{\text{gp}} \right] , \quad (6.63)$$

$$R_{LU^d}^{\text{gp}} = \int_{\Gamma_{\text{Lgp}0}} d\Gamma \left[\left[\frac{\partial \delta U_i^d}{\partial X_J} \right]_{\text{gp}} n_{L0J}^{\text{gp}} \eta_{U^d}^{\text{gp}} [[\Pi_{iK}^d]]_{\text{gp}} n_{L0K}^{\text{gp}} \right] , \quad (6.64)$$

where Π_{iJ}^s denotes the first Piola-Kirchhoff stress tensor of the solid phase. While there is no physical solid material in the dummy displacement domain $\Omega_{\text{D}0}$, the dummy second PK stress Π_{iJ}^d is assumed by the same material constitutive law as the solid phase.

$\eta_{U^s}^{\text{gp}}$, $\eta_{V^s}^{\text{gp}}$, $\eta_{U^d}^{\text{gp}}$, $\eta_{v^f}^{\text{gp}}$ and $\eta_{p^f}^{\text{gp}}$ are the penalty factors of the ghost penalty method. Following the works of Burman et al. [105], Schott et al. [72], Lawry et al. [75] and Villanueva et al. [106], these penalty factors are defined as follows:

$$\eta_{U^s}^{\text{gp}} = \alpha_{U^s}^{\text{gp}} h , \quad (6.65)$$

$$\eta_{V^s}^{\text{gp}} = \alpha_{V^s}^{\text{gp}} h G^s , \quad (6.66)$$

$$\eta_{U^d}^{\text{gp}} = \alpha_{U^d}^{\text{gp}} h , \quad (6.67)$$

$$\eta_{v^f}^{\text{gp}} = \alpha_{v^f}^{\text{gp}} h \mu^f , \quad (6.68)$$

$$\eta_{p^f}^{\text{gp}} = \alpha_{p^f}^{\text{gp}} h^2 \left(\frac{\mu^f}{h} + \frac{\rho^f \|\mathbf{v}^f\|_{\infty}}{6} \right)^{-1} , \quad (6.69)$$

where h is a representative elemental length, μ^f is a dynamic viscosity of fluid and G^s is a representative shear modulus of solid. $\|\cdot\|_{\infty}$ denotes an infinity norm, which extracts the

maximum amplitude from a vector:

$$\|\mathbf{a}\|_{\infty} \equiv \max(|a_1|, |a_2|, \dots, |a_n|) \quad \text{for } n \text{ dimension vector} \quad (6.70)$$

The penalty factor for the pressure term is to control instability of the pressure considering the inf-sup condition of equal-order approximation for velocity and pressure [72]. α_v^{GP} , α_p^{GP} , α_V^{GP} , α_P^{GP} and α_U^{GP} are constant scaling factors. The typical value of these scaling factor is from 0.001 to 0.05.

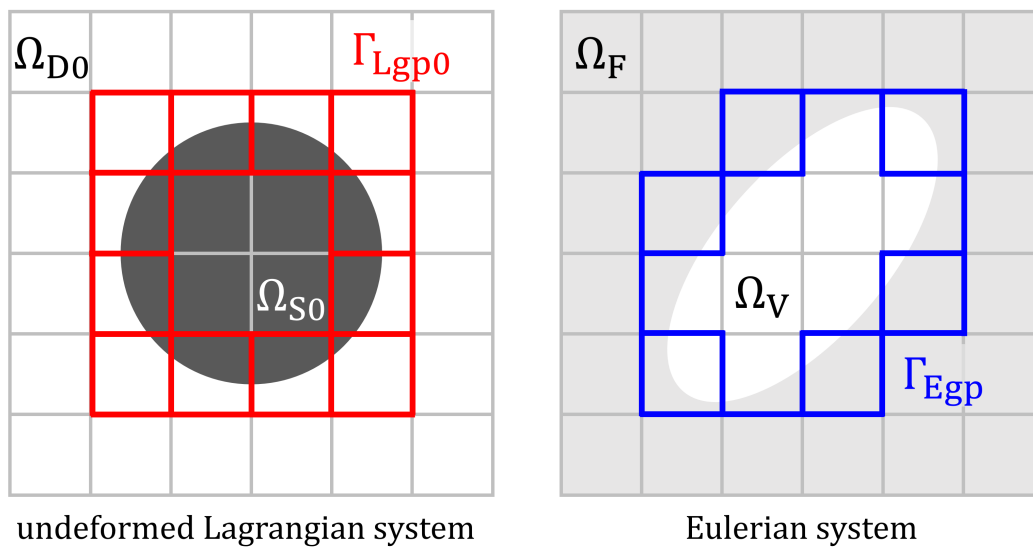


Figure 6.8: Faces for face-oriented ghost-penalty method: Γ_{Lgp0} and Γ_{Egp}

6.6 Numerical Examples

This section studies four numerical examples of the Lagrangian-immersed FSI method using the XFEM and the time stepping scheme. The first and second examples are steady-state FSI problems. These examples demonstrate the capability of the Lagrangian-immersed FSI method for the steady-state FSI problems. The third example is a transient structural problem including multibody contact and this example is a preliminary example for a FSI-contact problem. The fourth example is a transient FSI-contact problem.

In these examples, the plane strain case is assumed. In the first example, a solid structure is made by an isotropic linear elastic material. In the other examples, the solid objects are made by a neo-Hookean material (Belytschko et al. [107]):

$$W^s = \frac{1}{2}\lambda^s (\ln(\det F^s))^2 + \frac{1}{2}\mu^s (\text{Tr}(C^s) - 3) - \mu^s \ln(\det F^s) , \quad (6.71)$$

$$S_{IJ}^s = 2 \frac{\partial W}{\partial C_{IJ}^s} = (\lambda^s \ln(\det F^s) - \mu^s) C_{IJ}^{s-1} + \mu^s \delta_{IJ} . \quad (6.72)$$

Here, W^s is the hyperelastic function of the neo-Hookean material, F^s is the deformation gradient tensor, C^s is the right Cauchy-Green tensor ($C^s = F^{sT} F^s$), S^s is the second Piola-Kirchhoff stress tensor, and λ^s and μ^s are the Lamé's constants defined as follows:

$$\lambda^s = \frac{\nu^s}{(1 + \nu^s)(1 - 2\nu^s)} E^s , \quad (6.73)$$

$$\mu^s = \frac{1}{2(1 + \nu^s)} E^s , \quad (6.74)$$

where E^s is the Young's modulus and ν^s is the Poisson's ratio.

6.6.1 Stationary Beam in a Fluid Channel (COMSOL Benchmark Problem)

The first numerical example is a stationary beam in a fluid channel and focuses on the steady-state response of a fluid-structure interaction problem. This example is one of the benchmark problems of the commercial software COMSOL Multiphysics [108] and also

studied in the Ph.D. thesis of Jenkins [109]. The geometry of this numerical example is shown in Figure 6.9 and the problem parameters are listed in Table 6.1.

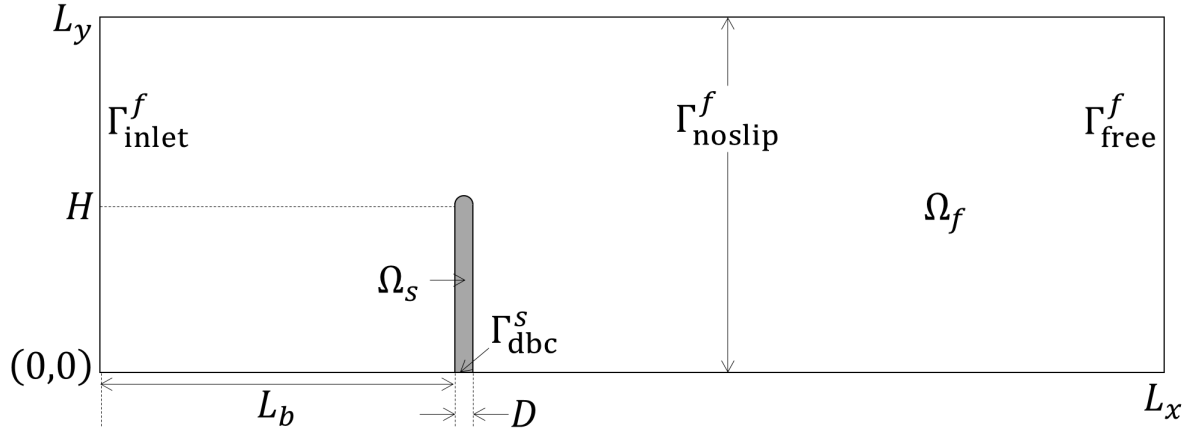


Figure 6.9: System of COMSOL benchmark problem

Table 6.1: Parameters of COMSOL benchmark problem

| Group | Description | Parameter |
|----------|---|--------------------------------------|
| Geometry | system length in x | $L_x = 300\mu\text{m}$ |
| | system length in y | $L_y = 100\mu\text{m}$ |
| | distance of a beam from the origin | $L_b = 100\mu\text{m}$ |
| | beam thickness | $D = 5\mu\text{m}$ |
| | diameter of hemisphere at the tip of a beam | $D = 5\mu\text{m}$ |
| | beam height | $H = 47.5\mu\text{m}$ |
| Solid | density | $\rho^s = 1000\text{kg/m}^3$ |
| | Young's modulus | $E^s = 200\text{kPa}$ |
| | Poisson's ratio | $\nu^s = 0.33$ |
| | body force | $\mathbf{B}^s = (0, 0)\text{m/s}^2$ |
| | artificial viscosity | $\alpha^s = 0\text{kg/s}$ |
| Fluid | density | $\rho^f = 1000\text{kg/m}^3$ |
| | Reynolds number | $\text{Re} = 1.5$ |
| | kinematic viscosity | $\nu^f = 10^{-6}\text{m}^2/\text{s}$ |
| | body force | $\mathbf{b}^f = (0, 0)\text{m/s}^2$ |
| | mean inflow velocity | $\bar{U} = 0.0333\text{m/s}$ |

The beam is made by an isotropic linear elastic material and immersed in the fluid domain. Fixed Dirichlet boundary conditions are applied at the bottom of this beam Γ_{dbc}^s :

$$U_x^s = U_y^s = 0, \quad V_x^s = V_y^s = 0 \quad \text{on } \Gamma_{\text{dbc}}^s. \quad (6.75)$$

The fluid domain has a parabolic inlet flow at Γ_{inlet}^f and a traction free outlet condition is prescribed at Γ_{free}^f . The no-slip boundary condition Γ_{noslip}^f is applied to the upper and lower edges of the fluid domain:

$$v_x^f(0, y) = 6\bar{U} \frac{y(H-y)}{H^2}, \quad v_y^f = 0 \quad \text{on } \Gamma_{\text{inlet}}^f, \quad (6.76)$$

$$v_x^f = v_y^f = 0 \quad \text{on } \Gamma_{\text{noslip}}^f. \quad (6.77)$$

This benchmark problem only focuses on a steady-state solution of a FSI system. Therefore, this example uses an one-step time integration based on the BDF1 method with a large time increment ($\Delta t = 10^{20}$ s). The weak form of this system is as follows (details are described in Section 6.4):

$$\begin{aligned} & R_m^s(\delta \mathbf{U}^s; \{\mathbf{U}^s, \mathbf{V}^s\}) + R_{uv}^s(\delta \mathbf{V}^s; \{\mathbf{U}^s, \mathbf{V}^s\}) + R_u^d(\delta \mathbf{U}^d; \{\mathbf{U}^s, \mathbf{U}^d\}) \\ & + R_m^f(\{\delta \mathbf{v}^f, \delta p^f\}; \{\mathbf{v}^f, p^f\}) + R_\phi(\delta \phi; \{\phi, \hat{\Phi}\}) \\ & + R_L^{\text{fsi}}(\delta \mathbf{U}^s; \{\mathbf{U}^s, \mathbf{V}^s, \mathbf{v}^f, p^f\}) + R_E^{\text{fsi}}(\{\delta \mathbf{v}^f, \delta p^f\}; \{\mathbf{U}^s, \mathbf{V}^s, \mathbf{v}^f, p^f\}) \\ & + R_L^{\text{gp}}(\{\delta \mathbf{U}^s, \delta \mathbf{V}^s, \delta \mathbf{U}^d\}; \{\mathbf{U}^s, \mathbf{V}^s, \mathbf{U}^d\}) + R_E^{\text{gp}}(\{\delta \mathbf{v}^f, \delta p^f\}; \{\mathbf{v}^f, p^f\}) = 0. \end{aligned} \quad (6.78)$$

R_u^d is a residual of the dummy displacement domain Ω_D and R_u^d in this example is defined by the Helmholtz smoothing method. As there is only one solid structure, the contact residual R_c^s is not included in this case. Newton's method using a direct solver is used and the convergence criterion requires a drop of the norm of the residual of 10^{-6} relative to the norm of the initial residual.

The COMSOL benchmark problem [108] uses the moving mesh using the ALE-FSI method (ALE-FSI with remeshing). Jenkins [109] uses the ALE-FSI method without remeshing. [109] compares the body-fitted modeling and the immersed boundary modeling using the ALE-FSI method. Table 6.2 summarizes the computational results for different spatial discretization sizes h and reference solutions. Comparing the finest model of the current work (Model 3) and reference works, the maximum von Mises stress of a solid beam is slightly

larger than reference works. The tip displacement U_x^s in x direction and the norm of the fluid velocity $\|\mathbf{v}^f\|$ of Model 3 are also larger than the reference works.

Table 6.2: Computational results of COMSOL stationary benchmark problem

| Model | h (μm) | U_x^s at beam tip (μm) | $\max(\sigma_{VM}^s)$ (mPa) | $\max(\ \mathbf{v}^f\)$ (m/s) |
|--|--------------------------|--|--------------------------------|-----------------------------------|
| Model 1 ($\Delta t = 10^{20}\text{s}$) | 1.333 | 9.662 | 6.190 | 0.0875 |
| Model 2 ($\Delta t = 10^{20}\text{s}$) | 1.075 | 10.390 | 6.782 | 0.0919 |
| Model 3 ($\Delta t = 10^{20}\text{s}$) | 0.954 | 10.960 | 6.838 | 0.0922 |
| COMSOL, moving mesh | - | 8.388 | 6.480 | 0.0884 |
| Jenkins, body-fitted mesh | - | 8.088 | 6.158 | 0.0628 |
| Jenkins, immersed boundary | - | 8.113 | 6.201 | 0.0624 |

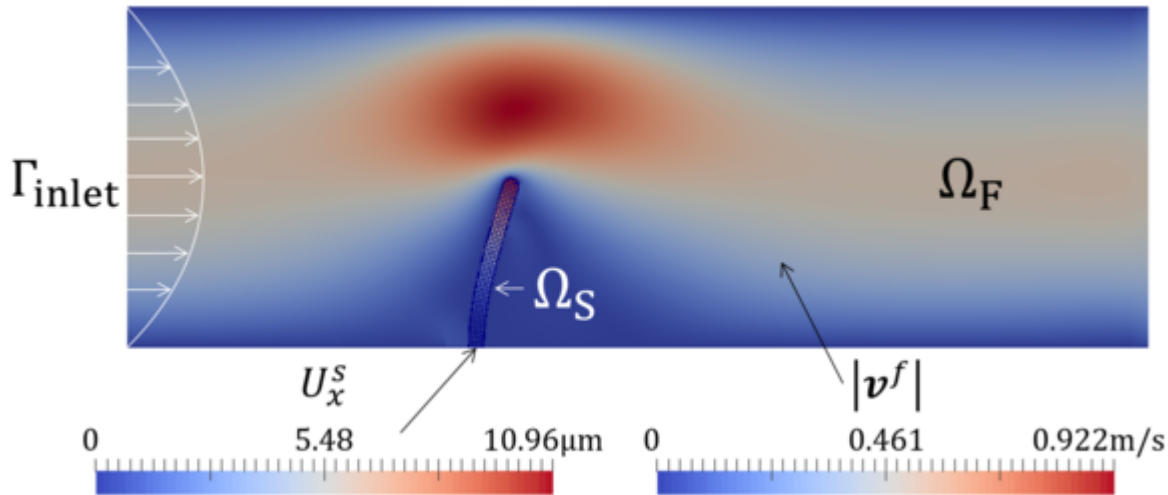


Figure 6.10: Steady-state result of COMSOL benchmark problem (solid displacement in x : U_x^s and norm of fluid velocity $\|\mathbf{v}^f\|$)

Figure 6.10 shows the steady-state result of Model 3 defined in Table 6.2. The region with the mesh superimposed is the deformed solid domain Ω_S . The color of a meshed region shows the solid displacement in x -direction; U_x^s . The other region is the fluid domain. The color in this region represents the norm of the fluid velocity $\|\mathbf{v}^f\|$. The Lagrangian solid is deflected by the parabolic channel flow and the Eulerian fluid field is affected by the solid structure simultaneously. Figure 6.11 shows non-matching interfaces around a tip of the solid beam. The region colored by gray is the deformed solid domain Ω_S based

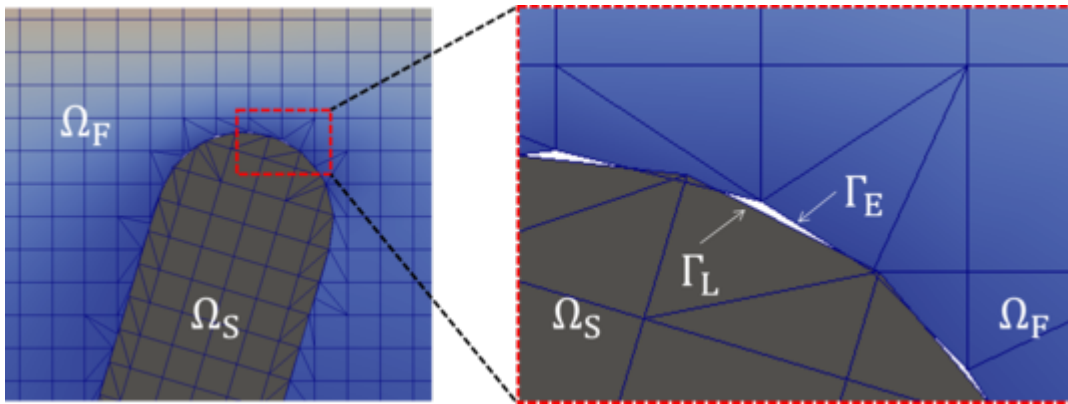


Figure 6.11: Non-matching interfaces

on the Lagrangian description and the outside of Ω_S is a fluid domain Ω_F based on the Eulerian description. As the Lagrangian-immersed FSI method uses separate non-matching interfaces of the Lagrangian and Eulerian mesh, gaps between a Lagrangian interface Γ_L and an Eulerian interface Γ_E always exist. This gap can be reduced by refining the mesh size because the accuracy of the level set projection increases.

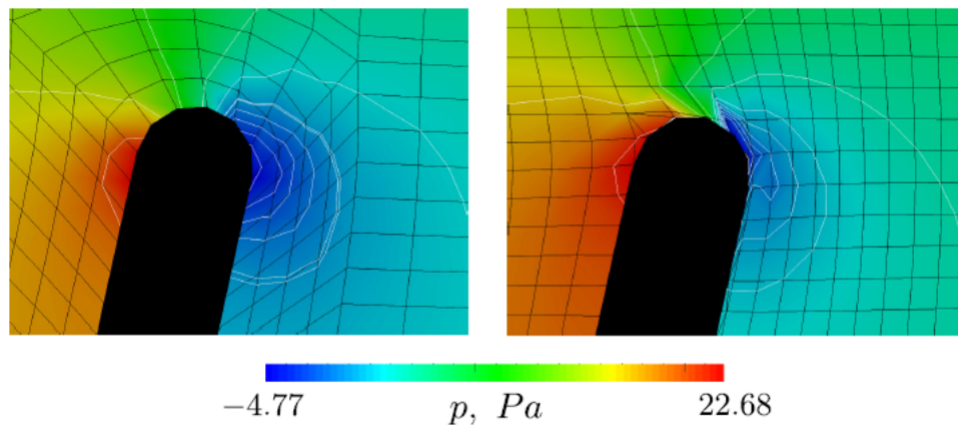


Figure 6.12: Deformation of fluid domain at reference work (Jenkins [109])
 (Left: Deformed body-fitted ALE meshes with pressure contours)
 (Right: Deformed immersed ALE meshes with pressure contours)

The reason why the Lagrangian-immersed FSI method achieved larger deformation than reference works is primarily related to the description of fluid meshes. Figure 6.12 shows examples of the work of Jenkins [109] using the ALE-FSI method without remeshing; the left

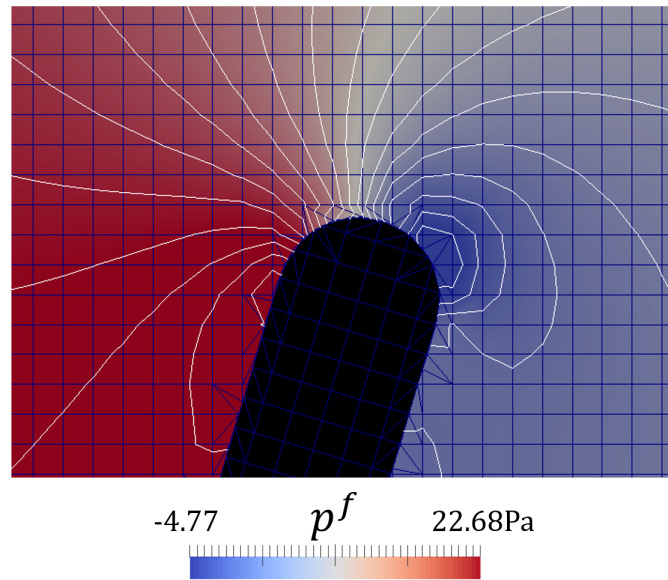


Figure 6.13: Distribution of fluid pressure around a tip
(Corresponding to Figure 6.12)

figure is the result using body-fitted meshes and the right figure is the one using the immersed boundaries. The color shows the fluid pressure and white lines are its iso-contours. The black domain represents a solid beam. Based on the ALE formulation, fluid meshes around the tip of a beam deforms significantly by following the deformation of a beam. In particular, the fluid meshes using the immersed boundary method (right figure of Figure 6.12) deform significantly. While the ALE formulation does not influence the deformation of the solid structures, the ALE formulation suffers from the limits of the deformation of the fluid mesh to avoid negative determinants of Jacobians of fluid elements. The deformation of the fluid mesh tends to degrade the accuracy of the flow solution if a large deformation occurs in the fluid mesh.

The results of Jenkins [109], computed the smallest tip displacement and the von Mises stress in Table 6.2. In addition, the maximum of the norm of the fluid velocity at Jenkins [109], $\max(\|\mathbf{v}^f\|)$ is much smaller than this work and COMSOL. This fact might be related to the above discussion of the limit of the ALE formulation. In the result of COMSOL, the limitation of deformation of fluid meshes is moderated by remeshing and this may lead to

the larger deformation of the solid beam than Jenkins [109] (ALE-FSI without remeshing). Figure 6.13 shows the result using the Lagrangian-immersed FSI method that corresponds to Figure 6.12. The color shows the fluid pressure and white lines are its iso-contours. The shape of the fluid meshes around the tip of the solid beam differs noticeably. As the fluid domain of the Lagrangian-immersed FSI method is defined by the Eulerian description, the shape of fluid meshes is always fixed. In addition, the FSI boundary integral is computed on non-matching interfaces located in separate meshes. As the solid structure and the fluid phase are completely separate, this geometric feature also enhances the deformability of the FSI system. Therefore, the larger deformation is allowed than in the other reference works of Table 6.13.

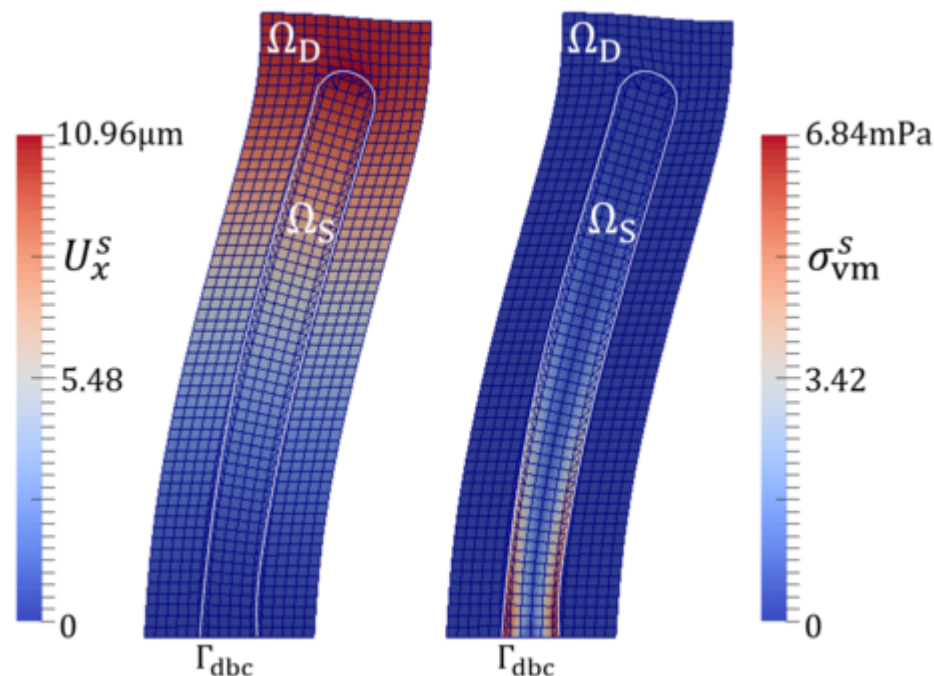


Figure 6.14: Deformation of a Lagrangian mesh
(Left: Solid Displacement in x U_x^s , Right: Von Mises Stress σ_{vm}^s)

The Lagrangian system in the Lagrangian-immersed FSI method consists of the solid phase and the dummy displacement phase. Figure 6.14 illustrates the deformed solid phase Ω_S and the deformed dummy displacement phase Ω_D . White lines show the interface between

the solid and dummy displacement phase, and this interface should correspond to the Eulerian interface by the level set projection. Ω_D is driven by the Helmholtz smoothing method in this example. As shown in Figure 6.14, the continuity of the displacements across the interface in the Lagrangian domain (the white line) is guaranteed by the one-sided Nitsche method; see (6.41). The smooth deformation of the Lagrangian mesh like Figure 6.14 is needed for the accurate level set projection and FSI on non-matching interfaces.

6.6.2 Stationary Beam in a Fluid Channel with Body Force

The second numerical example is also a steady-state FSI problem but the finite strain theory and body forces are applied to the solid phase. A beam structure made by the neo-Hookean material defined in (6.71) - (6.74) is pinned within the fluid channel. This geometry of this example is identical to an example of the full-Eulerian FSI method summarized in Section 5.9. The geometry and material parameters of this numerical example are shown in Figure 6.15 and given in Table 6.3.

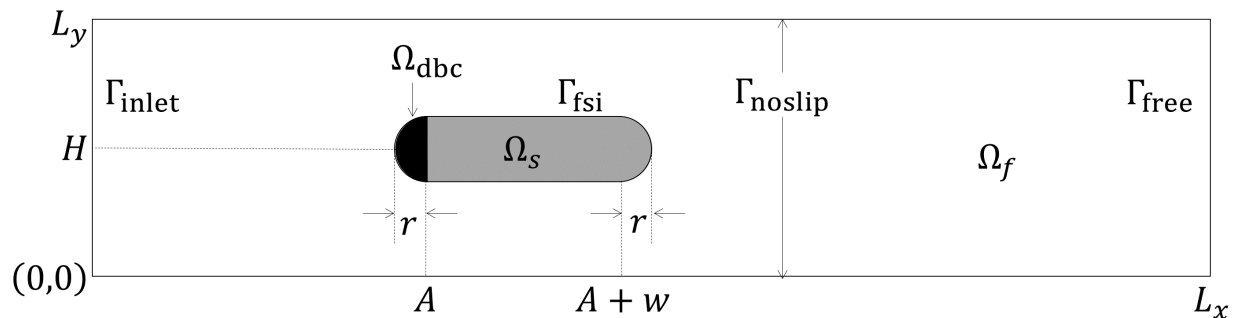


Figure 6.15: System of stationary beam with body force

Table 6.3: Parameters of stationary beam with body force

| Group | Description | Parameter |
|----------|---|--------------------------------------|
| Geometry | system length in x | $L_x = 17.2\text{m}$ |
| | system length in y | $L_y = 3.94\text{m}$ |
| | distance of a beam from the origin | $A = 1.97\text{m}$ |
| | beam width | $w = 3\text{m}$ |
| | center position of beam in y | $H = 2.30\text{m}$ |
| | radius of hemisphere at the tip of beam | $r = 0.5\text{m}$ |
| Solid | density | $\rho^s = 1000\text{kg/m}^3$ |
| | Young's modulus | $E^s = 300\text{kPa}$ |
| | Poisson's ratio | $\nu^s = 0.49$ |
| | body force | $\mathbf{B}^s = (0, -3)\text{m/s}^2$ |
| | artificial viscosity | $\alpha^s = 1\text{s}^{-1}$ |
| Fluid | density | $\rho^f = 1000\text{kg/m}^3$ |
| | Reynolds number | $\text{Re} = 10$ |
| | kinematic viscosity | $\nu^f = 0.1\text{m}^2/\text{s}$ |
| | body force | $\mathbf{b}^f = (0, 0)\text{m/s}^2$ |
| | mean inflow velocity | $\bar{U} = 1\text{m/s}$ |

In Figure 6.15, a solid beam consists of Ω_S and Ω_{dbc} (black domain in Figure 6.15) where the Dirichlet boundary conditions are applied:

$$U_x^s = U_y^s = 0, \quad V_x^s = V_y^s = 0 \quad \text{in } \Omega_{\text{dbc}} . \quad (6.79)$$

The fluid domain has a parabolic inlet flow at Γ_{inlet}^f and a traction free outlet condition is applied at Γ_{free}^f . No-slip boundary conditions are applied at the upper and lower edges Γ_{noslip}^f :

$$v_x^f(0, y) = 6\bar{U} \frac{y(H-y)}{H^2}, \quad v_y^f(0, y) = 0 \quad \text{on } \Gamma_{\text{inlet}} \quad (6.80)$$

$$v_x^f = v_y^f = 0 \quad \text{on } \Gamma_{\text{noslip}} \quad (6.81)$$

The weak form of this system is identical to the one of the previous numerical example. In the dummy displacement domain, the Helmholtz smoothing method is used. As this numerical example also focuses on a steady-state solution, this computation is an one-step BDF1 time integration method with a large time increment ($\Delta t = 10^4\text{s}$). Newton's method with a direct solver is used and the convergence criterion requires a drop of the norm of the residual of

10^{-6} relative to the norm of the initial residual. The weak form of the governing equations is identical to the one of the previous example; (6.78), but the solid model is different and the body force is applied in this example.

Figure 6.16 shows the geometry of the solid and fluid meshes in the deformed configuration. FSI is considered between the non-matching Lagrangian and Eulerian interfaces: Γ_L and Γ_E . In this numerical example, the models listed in Table 6.4 are studied and the convergence study is analyzed via these models.

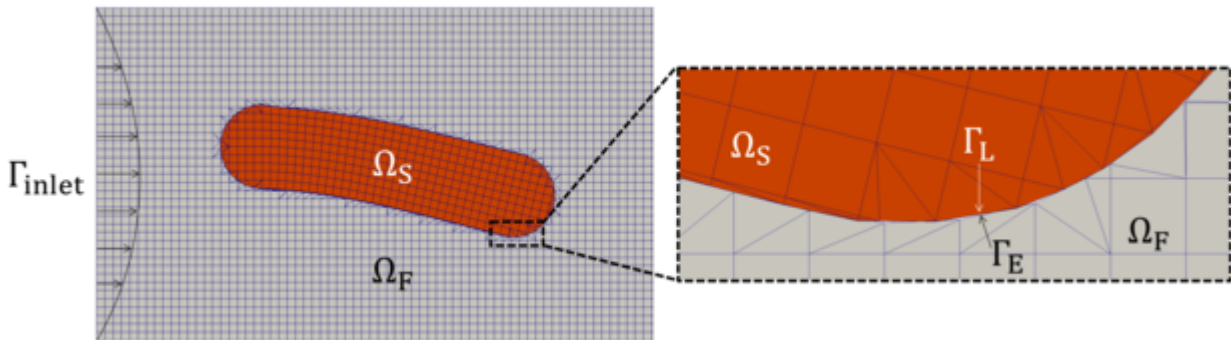


Figure 6.16: Mesh of stationary beam with body force

Table 6.4: Models of numerical example 2 of Lagrangian-immersed FSI using XFEM

| | Model | Number of Nodes | Spatial Discretization h (m) |
|-------------------------------|-------|-----------------|--------------------------------|
| | 1 | 2125 | 0.1971 |
| | 2 | 2125 | 0.1314 |
| Model for Figures 6.17 - 6.19 | 3 | 4699 | 0.1095 |
| | 4 | 5781 | 0.0986 |
| | 5 | 7614 | 0.0857 |
| Reference | 6 | 7614 | 0.0788 |

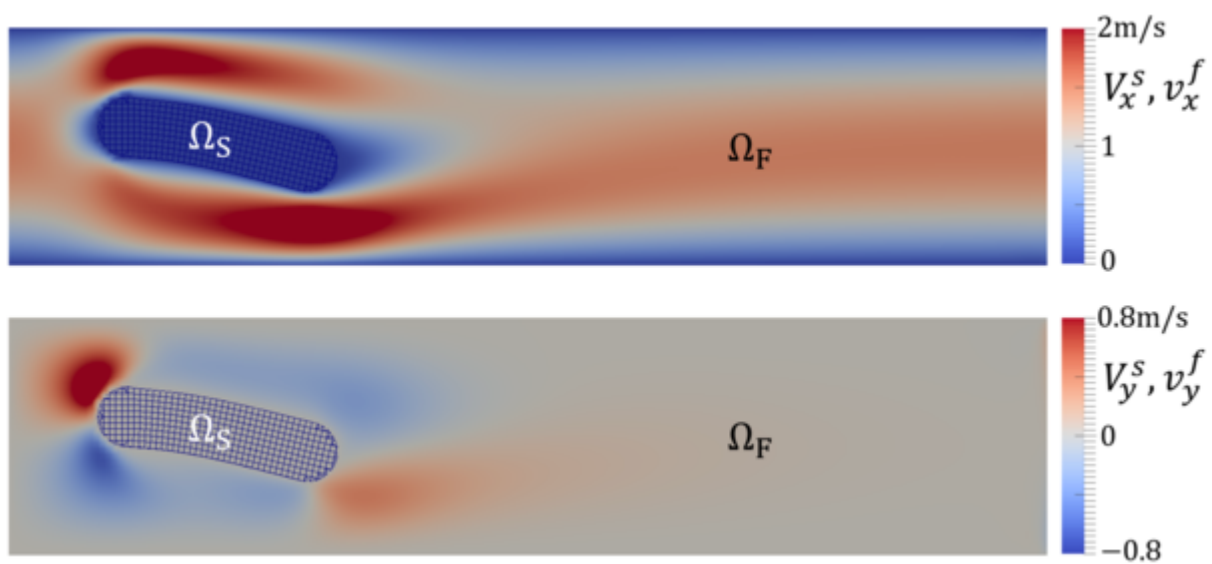


Figure 6.17: Steady-state velocity distribution (Model 3 of Table 6.4)
(Solid: Mesh, Fluid: Surface)

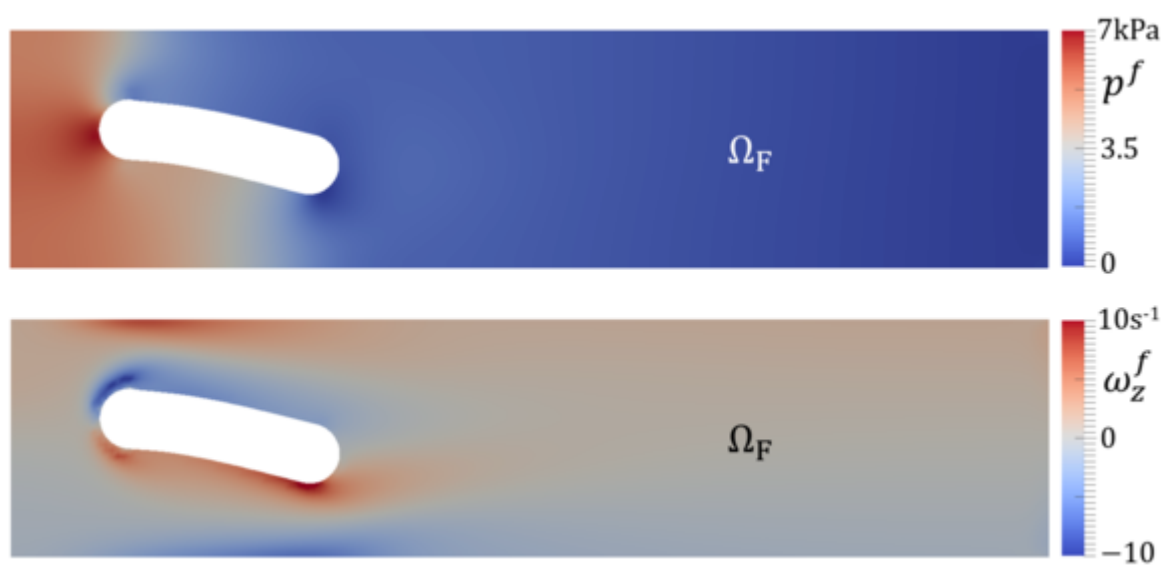


Figure 6.18: Fluid pressure and vorticity (Model 3 of Table 6.4)

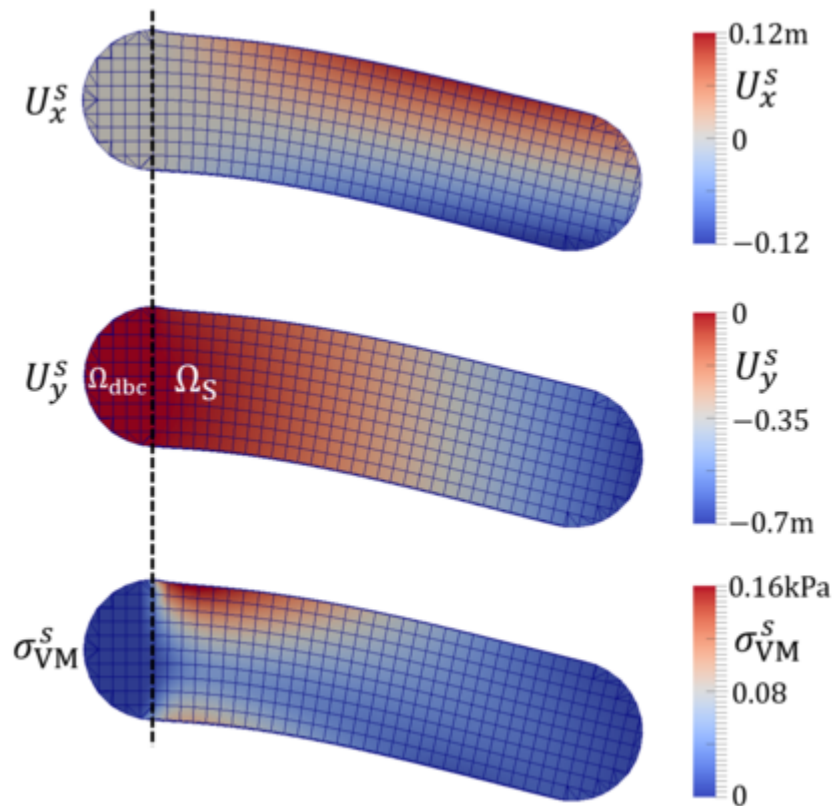


Figure 6.19: Solid displacement and von Mises stress (Model 3 of Table 6.4)

The results for Model 3 in Table 6.4 are shown in Figures 6.17 - 6.19. Figure 6.17 shows the velocity distributions of both the solid and fluid phases. V_i^s and v_i^f denote the velocity of the solid and the fluid, respectively. The solid beam deforms by the body force in y direction, and the fluid flow fits to the deformed solid structure. The results show that the continuity of the solid and fluid velocity is satisfied. Figure 6.18 shows the following fluid quantities: the fluid pressure p^f and the fluid vorticity in z direction; ω_z^f . Figure 6.19 illustrates the solid displacements; U_x^s and U_y^s , and the von Mises stress σ_{VM}^s (Cauchy stress). As the Lagrangian description is used for the solid phase, deformable meshes are used for the solid structure.

As it is described above, this numerical example is similar to the numerical example of the full-Eulerian FSI method described in Section 5.9. The advantage of the Lagrangian-immersed FSI method over the full-Eulerian FSI method is the ability to compute a steady-state problem using a single time step with a large time increment Δt . The representation

of a deformed solid structure in the full-Eulerian FSI method is based on the propagation of the level set function (CLSF method) in time. Therefore, the full-Eulerian FSI method needs to use much smaller time increments $\Delta t = 0.005s$ than the Lagrangian-immersed FSI method ($\Delta t = 10^4s$), and multiple time steps are necessary for the computation based on the full-Eulerian FSI method. On the other hand, it is easy to obtain an accurate solid structure using the Lagrangian-immersed FSI method with a large time increment because the Lagrangian description is used for the solid phase. The steady-state solutions can be easily computed by the Lagrangian-immersed FSI method, similar to the conventional ALE-FSI method.

Using the models described in Table 6.4, the convergence of the L2 error of characteristic physical quantities are studied. The reference solutions are computed with Model 6 in Table 6.4. Evaluated L2 errors of the solid phase are as follows:

$$\text{Err}(\mathbf{V}^s) = \sqrt{\frac{\int_{\Omega_S} d\Omega \|\mathbf{V}^s - \mathbf{V}_{\text{ref}}^s\|^2}{\int_{\Omega_S} d\Omega \|\mathbf{V}_{\text{ref}}^s\|^2}}, \quad (6.82)$$

$$\text{Err}(\mathbf{U}^s) = \sqrt{\frac{\int_{\Omega_S} d\Omega \|\mathbf{U}^s - \mathbf{U}_{\text{ref}}^s\|^2}{\int_{\Omega_S} d\Omega \|\mathbf{U}_{\text{ref}}^s\|^2}}, \quad (6.83)$$

$$\text{Err}(\sigma_{\text{VM}}^s) = \sqrt{\frac{\int_{\Omega_S} d\Omega (\sigma_{\text{VM}}^s - \sigma_{\text{VM-ref}}^s)^2}{\int_{\Omega_S} d\Omega \sigma_{\text{VM-ref}}^s{}^2}}, \quad (6.84)$$

where \mathbf{V}^s , \mathbf{U}^s and σ_{VM}^s are the displacements, the velocities and the von Mises stress (Cauchy stress) of the solid phase Ω_S , respectively. The L2 errors of the fluid phase are as follows:

$$\text{Err}(\mathbf{v}^f) = \sqrt{\frac{\int_{\Omega_F} d\Omega \|\mathbf{v}^f - \mathbf{v}_{\text{ref}}^f\|^2}{\int_{\Omega_F} d\Omega \|\mathbf{v}_{\text{ref}}^f\|^2}}, \quad (6.85)$$

$$\text{Err}(p^f) = \sqrt{\frac{\int_{\Omega_E} d\Omega (p^f - p_{\text{ref}}^f)^2}{\int_{\Omega_F} d\Omega p_{\text{ref}}^f{}^2}}, \quad (6.86)$$

$$\text{Err}(q^f) = \sqrt{\frac{\int_{\Omega_E} d\Omega (q^f - q_{\text{ref}}^f)^2}{\int_{\Omega_F} d\Omega q_{\text{ref}}^f{}^2}}, \quad (6.87)$$

where \mathbf{v}^f and p^f are the velocity and the pressure of the fluid phase Ω_F . q^f is the in-plane

effective shear stress defined by principal stresses σ_1^f and σ_2^f ; $q^f = |\sigma_1 - \sigma_2|/2$, which is a similar measure as the von Mises stress of the solid phase. Figure 6.20 shows the comparison of the L2 errors of the velocity and the stress measures. Red markers represent the solid quantities and blue markers represent the fluid quantities. The rates of convergence are computed by the least square fitting and both dashed lines represents the fitted data of the solid (red) and the fluid (blue), respectively.

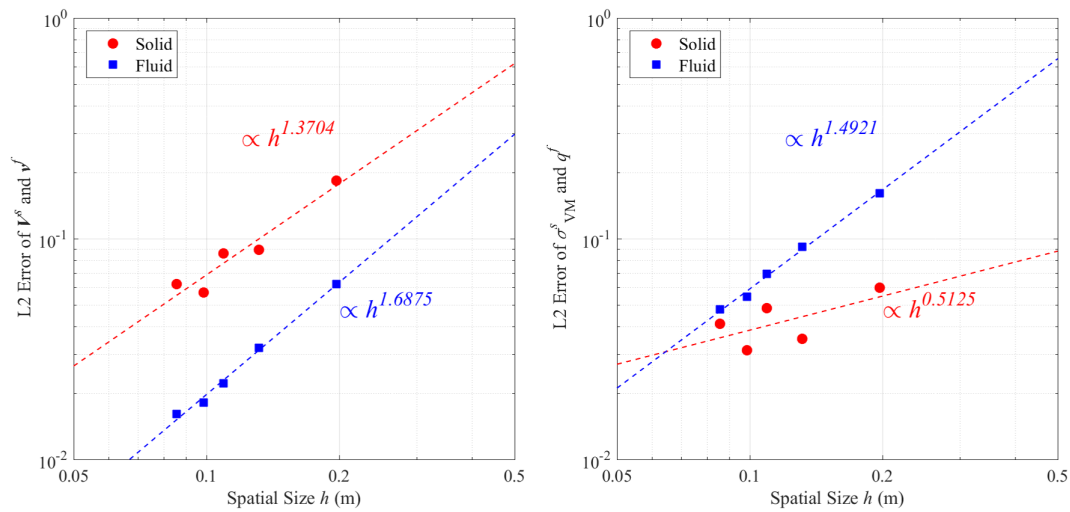


Figure 6.20: L2 error of velocity and stress

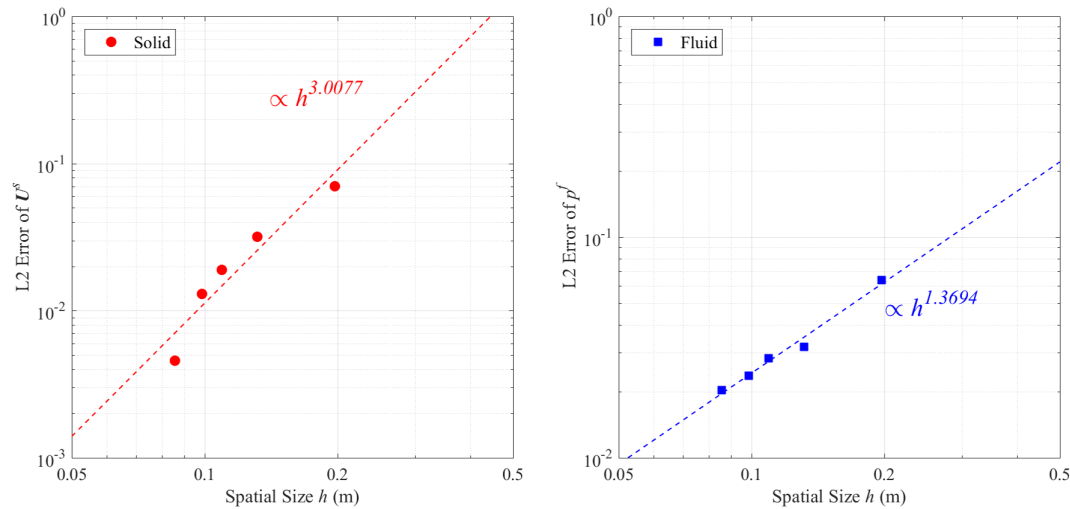


Figure 6.21: L2 error of solid displacement and fluid pressure

Both the solid and fluid velocity have similar rates of convergence (left figure). In terms of

stress measures (right figure), the solid phase has lower convergence rate than the fluid phase in this example. Figure 6.21 illustrates the L2 errors of the fluid pressure p^f and the solid displacement \mathbf{U}^s . Figure 6.22 shows a comparison of the L2 errors of the level set function in both the Lagrangian and Eulerian systems. Φ is the level set function in the undeformed Lagrangian system Ω_{L0} and the purpose of this Φ is to describe the initial solid structures. ϕ is the level set function in the Eulerian system Ω_E . ϕ is defined by the projection of Φ based on the level set projection method (Section 6.3) and the interface used in the FSI boundary integral Γ_E is determined by the iso-contour of ϕ . The L2 error of Φ is defined in the entire Lagrangian system Ω_L and the L2 error of ϕ is defined in the entire Eulerian system Ω_E as follows:

$$\text{Err}(\Phi) = \sqrt{\frac{\int_{\Omega_L} d\Omega (\Phi - \Phi_{\text{ref}})^2}{\int_{\Omega_L} d\Omega \Phi_{\text{ref}}^2}}, \quad (6.88)$$

$$\text{Err}(\phi) = \sqrt{\frac{\int_{\Omega_E} d\Omega (\phi - \phi_{\text{ref}})^2}{\int_{\Omega_E} d\Omega \phi_{\text{ref}}^2}}. \quad (6.89)$$

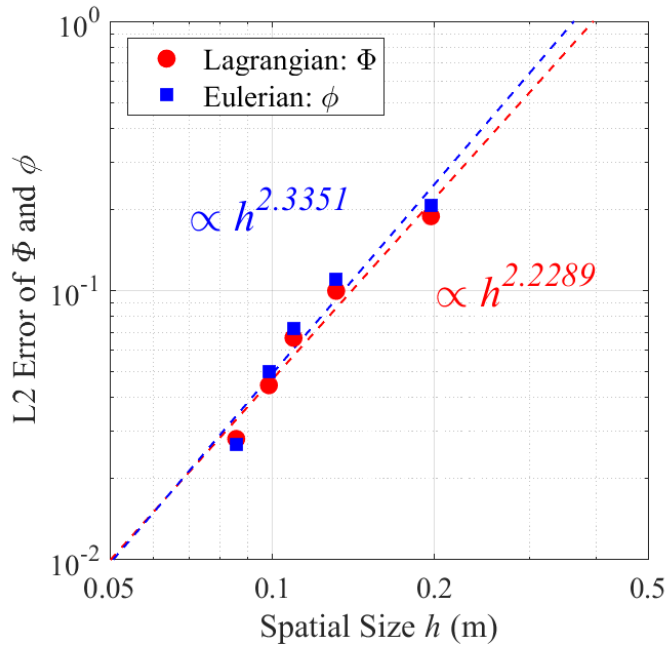


Figure 6.22: L2 error of level set function

The L2 error of Φ : $\text{Err}(\Phi)$ purely indicates the difference in initial designs of the solid beam. The difference of the L2 error of ϕ : $\text{Err}(\phi)$ reflects the accuracy of the level set projection. As can be seen from Figure 6.22, $\text{Err}(\phi)$ and $\text{Err}(\Phi)$ overlap and the rates of convergence of both L2 errors are almost identical; i.e. a factor of around 2.3. These results suggest that the level set projection method performs well in the Lagrangian-immersed FSI method.

6.6.3 Transient Structural Problem with Multibody Contact

The third numerical example is a transient structural problem with multi-body contact. This example studies the characteristics of the stabilized Lagrangian contact formulation (Section 6.2.4) in a transient problem. In this numerical example, three elastic circular solid objects (solid 1, 2 and 3) exist within an elastic ring solid object (solid 4) and they are made by the neo-Hookean material (6.71) - (6.74). The initial geometry and material parameters are shown in Figure 6.23 and listed in Table 6.5.

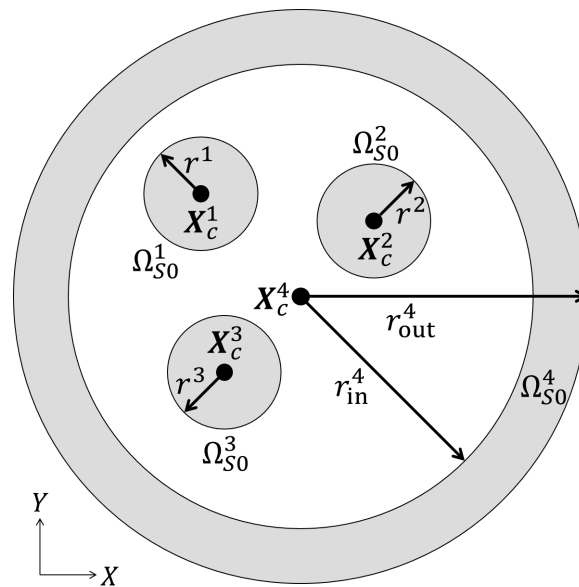


Figure 6.23: Model of transient contact problem

Table 6.5: parameters of multibody contact problem

| Group | Description | Parameter |
|---------|----------------------|---|
| Common | density | $\rho^s = 1000\text{kg/m}^3$ |
| | Poisson's ratio | $\nu^s = 0.4$ |
| | body force | $\mathbf{B}^s = (0, 0)\text{m/s}^2$ |
| | artificial viscosity | $\alpha^s = 0\text{s}^{-1}$ |
| | element size | $h = 0.25\text{m}$ |
| Solid 1 | Young's modulus | $E^{s1} = 300\text{kPa}$ |
| | centroid | $\mathbf{X}_c^1 = (-4/3, 4/3)\text{m}$ |
| | radius | $r^1 = 0.7\text{m}$ |
| | initial velocity | $\mathbf{V}_{\text{ini}}^{s1} = (0.56, -0.24)\text{m/s}$ |
| Solid 2 | Young's modulus | $E^{s2} = 300\text{kPa}$ |
| | centroid | $\mathbf{X}_c^2 = (1, 1)\text{m}$ |
| | radius | $r^2 = 0.7\text{m}$ |
| | initial velocity | $\mathbf{V}_{\text{ini}}^{s2} = (0, 0.8)\text{m/s}$ |
| Solid 3 | Young's modulus | $E^{s3} = 300\text{kPa}$ |
| | centroid | $\mathbf{X}_c^3 = (-1, -1)\text{m}$ |
| | radius | $r^3 = 0.7\text{m}$ |
| | initial velocity | $\mathbf{V}_{\text{ini}}^{s3} = (-1/\sqrt{2}, -1/\sqrt{2})\text{m/s}$ |
| Solid 4 | Young's modulus | $E^{s4} = 30\text{MPa}$ |
| | centroid | $\mathbf{X}_c^4 = (0, 0)\text{m}$ |
| | inner radius | $r_{\text{in}}^4 = 3.40\text{m}$ |
| | outer radius | $r_{\text{out}}^4 = 3.76\text{m}$ |
| | initial velocity | $\mathbf{V}_{\text{ini}}^{s4} = (0, 0)\text{m/s}$ |

The computational domain Ω_0 is constructed by the union of undeformed Lagrangian solid domains based on the total Lagrangian formulation:

$$\Omega_0 = \Omega_{S0}^1 \cup \Omega_{S0}^2 \cup \Omega_{S0}^3 \cup \Omega_{S0}^4 . \quad (6.90)$$

The state variables are the solid displacement U_i^s and the solid velocity V_i^s . The variational form consists of the solid momentum equation R_m^s (6.39), the displacement-velocity relationship R_{uv}^s (6.40), and the contact residual of the stabilized Lagrange multiplier method R_c^s (6.43). In addition, the face-oriented ghost-penalty method is applied to stabilize U_i^s (6.63) and V_i^s (6.59), respectively:

$$\begin{aligned}
& R_m^s(\delta \mathbf{U}^s; \{\mathbf{U}^s, \mathbf{V}^s\}) + R_{uv}^s(\delta \mathbf{V}^s; \{\mathbf{U}^s, \mathbf{V}^s\}) \\
& + R_c^s(\delta \mathbf{U}^s; \mathbf{U}^s) + R_L^{\text{gp}}(\{\delta \mathbf{U}^s, \delta \mathbf{V}^s\}; \{\mathbf{U}^s, \mathbf{V}^s\}) = 0 .
\end{aligned} \tag{6.91}$$

The Newmark method ($\gamma = 0.9, \beta = 0.5$) is used as a time integration scheme and the time increment Δt is set to $\Delta t = 0.2\text{s}$. The nonlinear contact problems are solved by Newton's method and a direct solver is used. The convergence criterion for the Newton iteration requires a drop of the norm of the residual of 10^{-5} relative to the norm of the initial residual. In addition, an adaptive time-stepping scheme is applied to avoid the divergence at the Newton iteration and for the robust contact analysis method. If the norm of the residual increases over 10^4 relative to the norm of the initial residual, Δt is reduced as follows:

$$\Delta t_{\text{new}} = \alpha_{\text{cut}} \Delta t_{\text{old}} , \tag{6.92}$$

where α_{cut} is set to 0.7 in this research. The Newton step when Δt is reduced, is recomputed from scratch.

Representative computational results are shown in Figure 6.24, focusing on times when contact occurs. Figures 6.25 and 6.26 show the history of the momentum of the entire system Ω_{S_0} and momentum of each solid domain $\Omega_{S_0}^1 - \Omega_{S_0}^4$, respectively. The total momentum (black line in Figures 6.25 and 6.26) is constant at any time and thus, the numerical implementation of the transient contact analysis satisfies the conservation of the momentum. The kinks in Figures 6.25 and 6.26 indicate instances in time when contact occurs. The momentum is transmitted across solid bodies. These results suggest that the proposed formulation and computational schemes are able to compute multiple contact phenomena among multiple solid bodies in a stable fashion with acceptable accuracy.

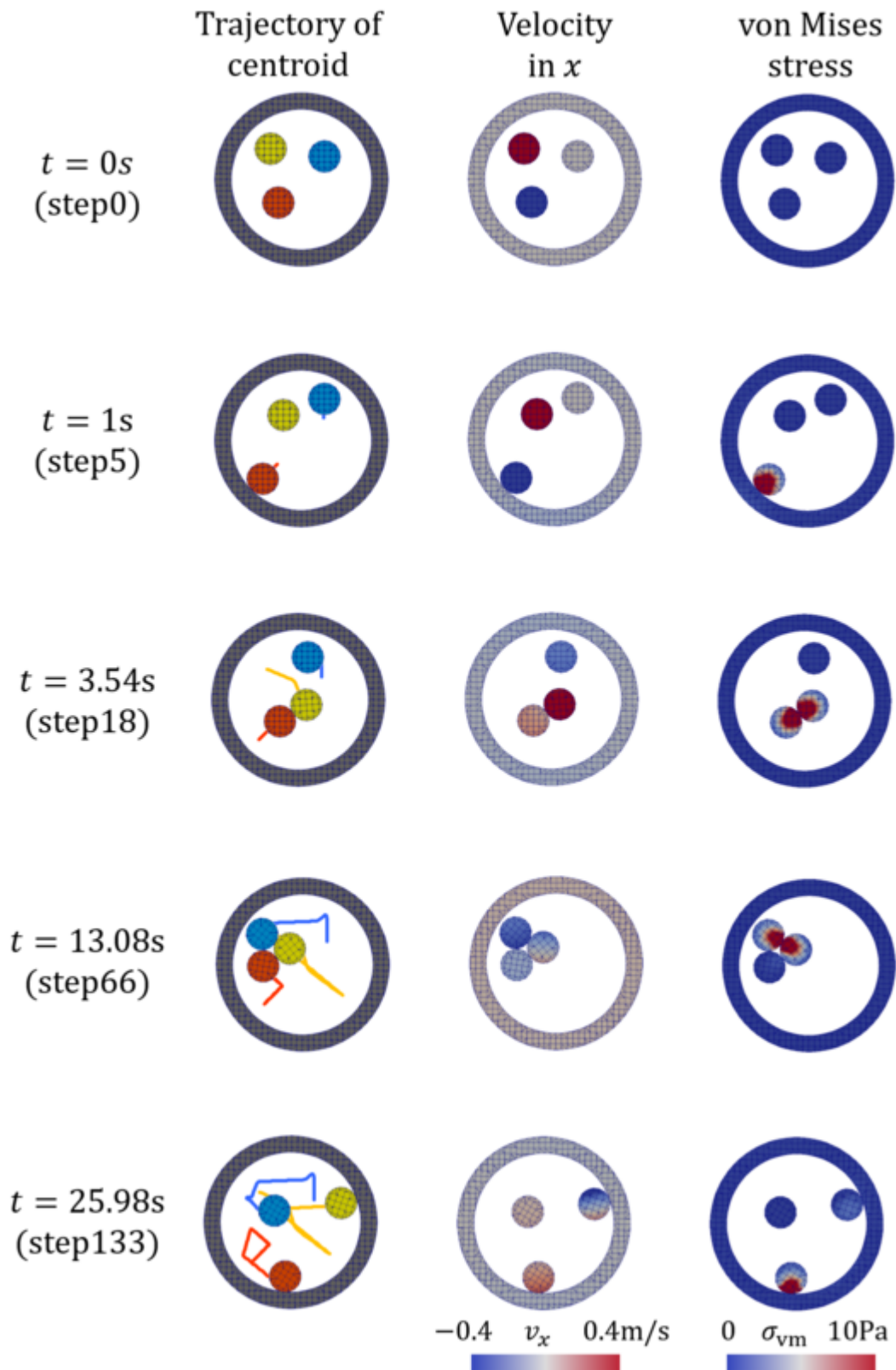
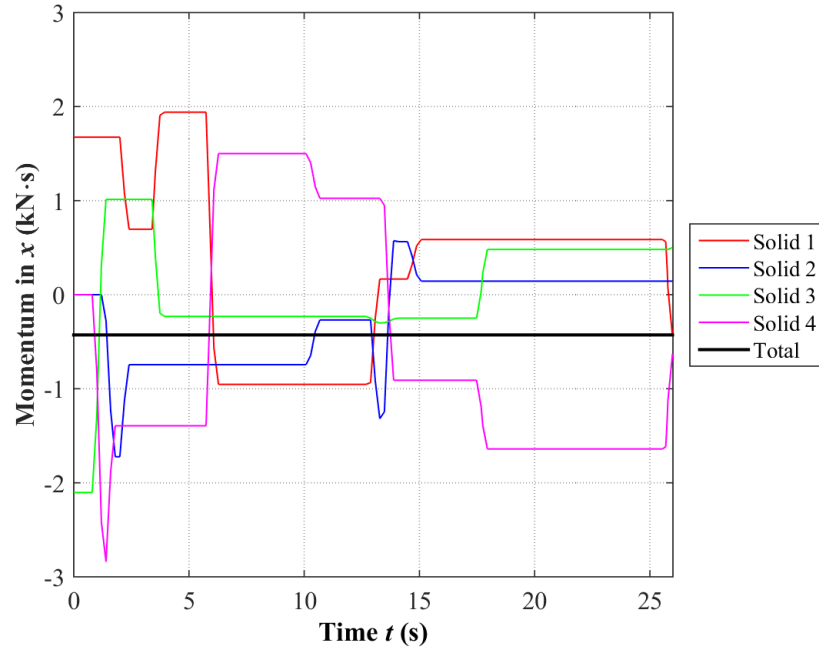
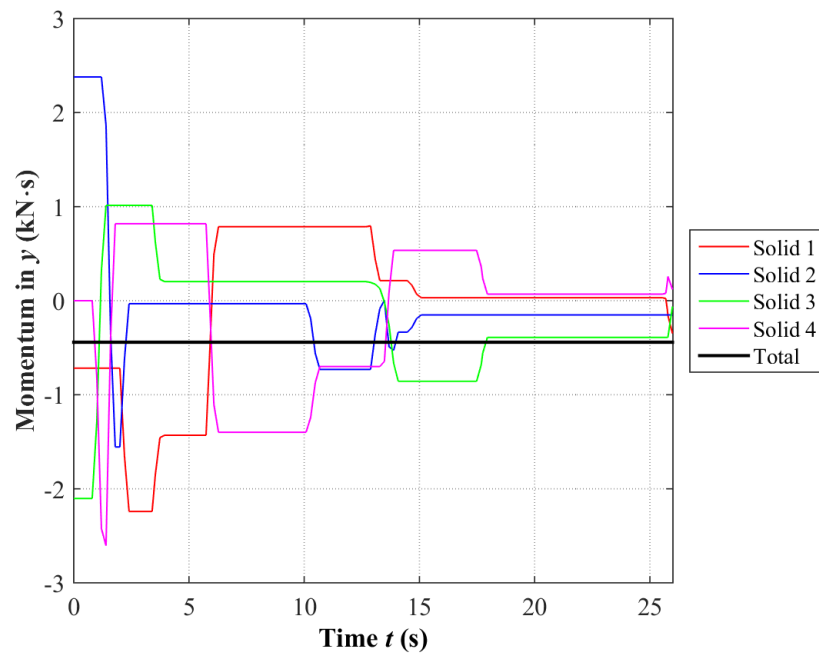


Figure 6.24: Results of transient contact problem

Figure 6.25: History of momentum in x Figure 6.26: History of momentum in y

6.6.4 Multibody FSI-Contact Problem using XFEM

The fourth numerical example is a FSI-contact problem based on the combination of the Lagrangian-immersed FSI method and the stabilized Lagrange multiplier method for contact using the XFEM. In this example, there are five solid structures made by the neo-Hookean material (6.71) - (6.74). These solid structures are defined within individual Lagrangian domain Ω_L^i ($i = 1 \sim 5$). Each Lagrangian domain Ω_L^i contains a solid domain Ω_S^i and a dummy displacement domain Ω_D^i : $\Omega_L^i = \Omega_S^i \cup \Omega_D^i$. Figures 6.27 - 6.31 and Table 6.6 are the geometry of each Lagrangian domain.

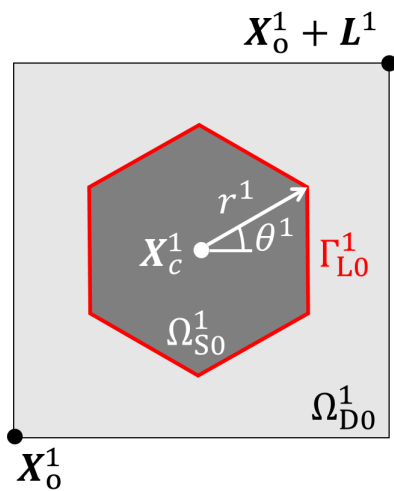


Figure 6.27: Lagrangian system 1: Ω_{L0}^1

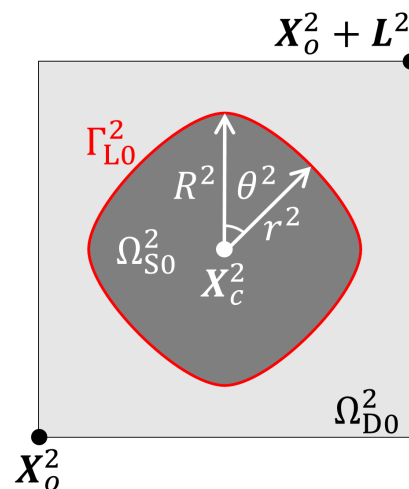


Figure 6.28: Lagrangian system 2: Ω_{L0}^2

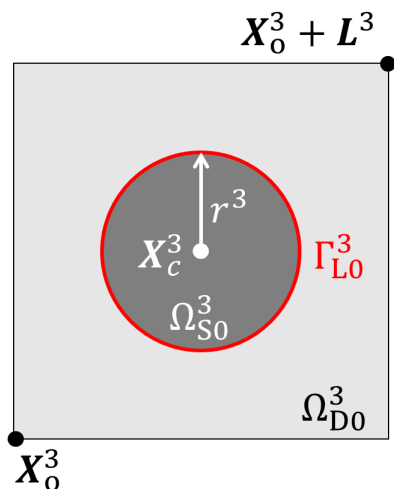


Figure 6.29: Lagrangian system 3: Ω_{L0}^3

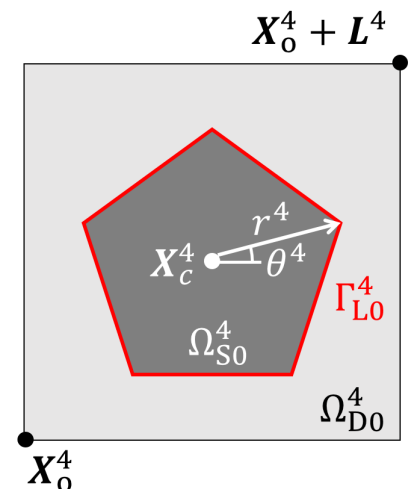


Figure 6.30: Lagrangian system 4: Ω_{L0}^4

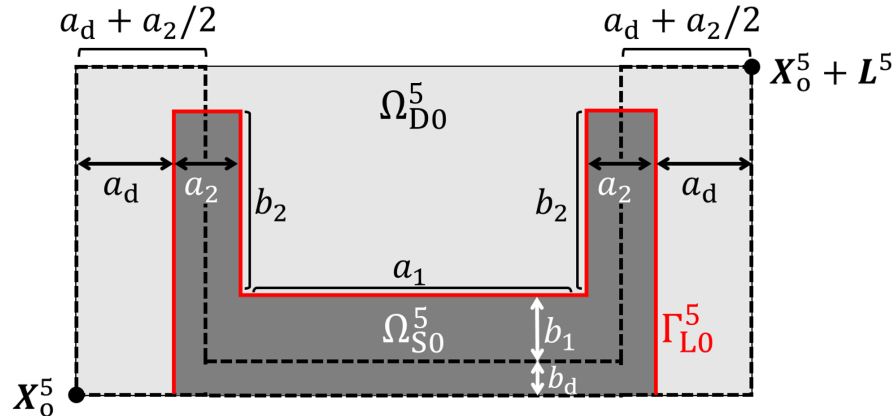


Figure 6.31: Lagrangian system 5: Ω_{L0}^5

The interfaces of the solid structures 1, 2 and 4 are defined by the strain ellipsoidal equation using the exponential function as follows:

$$e^{-b^2x^2} + e^{-c^2y^2} = 2e^{-a^2}, \quad (6.93)$$

where a, b and c are positive real numbers and only a has the following constraint:

$$0 < a < \sqrt{\ln 2} \simeq 0.8326. \quad (6.94)$$

The following results are solutions of (6.93) based on a polar coordinate system (r, θ) (Yamamoto [110]):

$$r(\theta) = r_0 + \frac{1}{c} \sqrt{-\ln \left[2 \exp(-a^2) - \exp \left(-b^2 x_{\max}^2 \sin \left\{ \left(\theta - \frac{\pi}{2} \right) \frac{n}{2} \right\} \right) \right]}, \quad (6.95)$$

$$x_{\max} = \sqrt{-\frac{1}{b^2} \ln \left(2 \exp(-a^2) - 1 \right)}, \quad (6.96)$$

where $r(\theta)$ is a radius from the centroid (X_c, Y_c) as a function of angle θ . Using $r(\theta)$, the signed-distance level set function Φ_s is computed as follows:

$$\Phi_s = d \frac{r(\theta)}{r_0} - \sqrt{(X - X_c)^2 + (Y - Y_c)^2}. \quad (6.97)$$

Finally, the signed-distance level set function ϕ_s is converted into the Heaviside-type level

set function Φ , which is used in the Lagrangian-immersed FSI method:

$$\Phi = \left[1 + \exp\left(\frac{\Phi_s}{\varepsilon_\Phi}\right) \right]^{-1} \quad (\varepsilon_\Phi = 0.5h^{0.9}) . \quad (6.98)$$

The interfaces of the solid structures 1, 2 and 4 are defined by the following parameters which are used in (6.96) and (6.97):

$$\text{Solid 1: } n = 6, a = 0.81, b = 0.01485, c = 1, d = 0.5577, r_0 = 0.1x_{\max} , \quad (6.99)$$

$$\text{Solid 2: } n = 4, a = 0.81, b = 0.01800, c = 1, d = 0.5577, r_0 = 0.1x_{\max} , \quad (6.100)$$

$$\text{Solid 4: } n = 5, a = 0.81, b = 0.02200, c = 1, d = 0.5577, r_0 = 0.1x_{\max} . \quad (6.101)$$

The Eulerian domain Ω_E has a rectangle domain and no-slip boundary conditions are applied on all edges of the rectangle. The geometry parameters are summarized in Table 6.6. The fluid domain Ω_F is included in Ω_E : $\Omega_F \in \Omega_E$. The interface of the fluid domain is denoted as the Eulerian interface Γ_E and automatically created by the level set projection method as shown in Figure 6.32. The fluid domain is modeled by the incompressible Navier-Stokes equations. Material parameters of the solid and fluid phase, and the initial conditions are given in Table 6.7. A body force in y direction is only applied to $\Omega_S^1, \Omega_S^2, \Omega_S^3$ and Ω_S^4 .

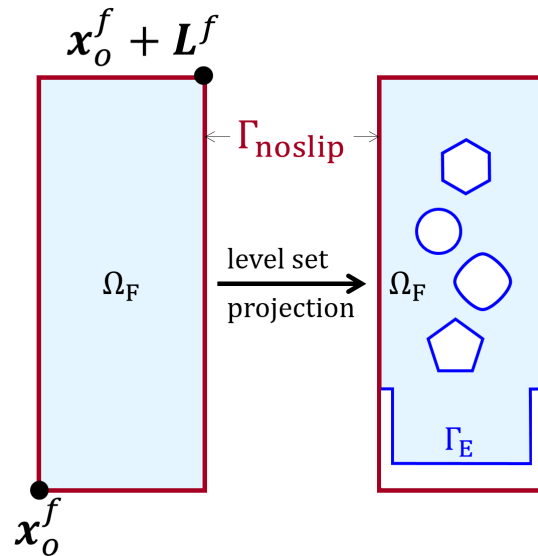


Figure 6.32: Eulerian system: Ω_E

Table 6.6: Geometry parameters

| System | Description | Parameter |
|--------------|-------------------|---|
| Lagrangian 1 | origin | $\mathbf{X}_o^1 = (1.067, 7.067)\text{m}$ |
| | system size | $\mathbf{L}^1 = (1.867, 1.867)\text{m}$ |
| | shape of solid | regular hexagon |
| | centroid of solid | $\mathbf{X}_c^1 = (2.000, 8.000)\text{m}$ |
| | max. radius | $r^1 = 0.641\text{m}$ |
| | angle of r^1 | $\theta^1 = \pi/6$ rad |
| Lagrangian 2 | origin | $\mathbf{X}_o^2 = (1.467, 4.267)\text{m}$ |
| | system size | $\mathbf{L}^2 = (1.867, 1.867)\text{m}$ |
| | shape of solid | rounded square |
| | centroid of solid | $\mathbf{X}_c^2 = (2.400, 5.200)\text{m}$ |
| | max. radius | $R^2 = 0.656\text{m}$ |
| | min. radius | $r^2 = 0.560\text{m}$ |
| | angle | $\theta^2 = \pi/4$ rad |
| Lagrangian 3 | origin | $\mathbf{X}_o^3 = (0.400, 5.467)\text{m}$ |
| | system size | $\mathbf{L}^3 = (1.867, 1.867)\text{m}$ |
| | shape of solid | circle |
| | centroid of solid | $\mathbf{X}_c^3 = (1.333, 6.400)\text{m}$ |
| | radius | $r^3 = 0.509\text{m}$ |
| Lagrangian 4 | origin | $\mathbf{X}_o^4 = (0.788, 2.628)\text{m}$ |
| | system size | $\mathbf{L}^4 = (1.867, 1.867)\text{m}$ |
| | shape of solid | regular pentagon |
| | centroid of solid | $\mathbf{X}_c^4 = (1.733, 3.675)\text{m}$ |
| | max. radius | $r^4 = 0.605\text{m}$ |
| | angle | $\theta^4 = \pi/10$ rad |
| Lagrangian 5 | origin | $\mathbf{X}_o^5 = (-0.400, -0.120)\text{m}$ |
| | system size | $\mathbf{L}^5 = (4.800, 3.180)\text{m}$ |
| | width for DBC | $a_d = 0.087\text{m}$ |
| | base width | $a_1 = 3.374\text{m}$ |
| | wall width | $a_2 = 0.626\text{m}$ |
| | height for DBC | $b_d = 0.330\text{m}$ |
| | base height | $b_1 = 0.341\text{m}$ |
| | wall height | $b_2 = 2.853\text{m}$ |
| Eulerian | origin | $\mathbf{x}_o^f = (0, 0)\text{m}$ |
| | system size | $\mathbf{L}^f = (4, 10)\text{m}$ |

Table 6.7: Physical parameters of solid and fluid

| Domain | Description | Parameter |
|--------|----------------------|---|
| Solid | density | $\rho^s = 1000\text{kg/m}^3$ |
| | Young's modulus | $E^s = 1\text{MPa}$ |
| | Poisson's ratio | $\nu^s = 0.4$ |
| | artificial viscosity | $\alpha^s = 0\text{s}^{-1}$ |
| | body force | $\mathbf{B}^s = (0, -1)\text{m/s}^2$ |
| | initial velocity | $\mathbf{V}_{\text{ini}}^s = (0, -1)\text{m/s}$ |
| Fluid | density | $\rho^f = 1000\text{kg/m}^3$ |
| | kinematic viscosity | $\nu^f = 10^{-2}\text{m}^2/\text{s}$ |
| | body force | $\mathbf{b}^f = (0, 0)\text{m/s}^2$ |
| | initial velocity | $\mathbf{v}_{\text{ini}}^f$: random in $[-10^{-5}, 10^{-5}]\text{m/s}$ |

As the Lagrangian-immersed FSI method uses multiple meshes, each solid objects and fluid system are spatially separate. Therefore, different element sizes for the spatial discretization can be used in each mesh. The spatial discretization of Lagrangian systems 1- 4 is determined based on the size of the spatial discretization in the Eulerian system h as listed in Table 6.8. The size of the spatial discretization of Lagrangian system 5 (fixed structure at the bottom): h_{L0}^5 is constant and independent from h .

Table 6.8: Summary of spatial discretization (multibody FSI-contact problem)

| System | Shape of Solid | Spatial Size |
|-------------------------------|------------------|-----------------------------|
| Eulerian: Ω_E | - | $h_E = h$ |
| Lagrangian 1: Ω_{L0}^1 | regular hexagon | $h_{L0}^1 = \frac{2}{3}h$ |
| Lagrangian 2: Ω_{L0}^2 | rounded square | $h_{L0}^2 = \frac{5}{9}h$ |
| Lagrangian 3: Ω_{L0}^3 | circle | $h_{L0}^3 = h$ |
| Lagrangian 4: Ω_{L0}^4 | regular pentagon | $h_{L0}^4 = \frac{2}{3}h$ |
| Lagrangian 5: Ω_{L0}^5 | concave shape | $h_{L0}^5 = 0.1867\text{m}$ |

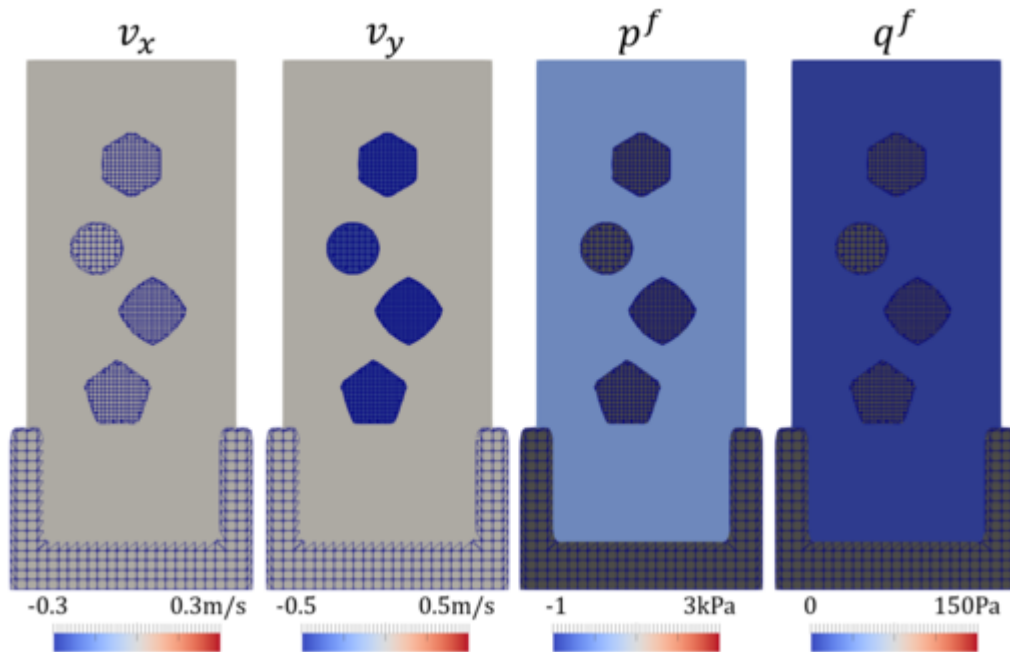
The weak form of this numerical example is identical to (6.38), which contains both the FSI boundary integral and the contact boundary integral. As rigid body rotation of solid structures occurs in this example, the dummy solid method (6.42) is applied and the residual term R_u^d is computed accordingly. The penalty coefficients for Nitsche's method, the face-oriented ghost-penalty method, and the stabilized Lagrangian contact formulation are summarized in Table 6.9.

Table 6.9: Penalty coefficients for multibody FSI-contact problem

| Method | Penalty Coefficients |
|---------------------------------------|---|
| Nitsche's method for FSI | $\eta^{\text{fsi}} = \alpha^{\text{fsi}} E^s$, $\alpha^{\text{fsi}} = 0.1\text{s/m}$ |
| face-oriented ghost-penalty method | $\alpha_{U^s}^{\text{gp}} = \alpha_{U^d}^{\text{gp}} = \alpha_{V^s}^{\text{gp}} = \alpha_{v^f}^{\text{gp}} = 0.05$, $\alpha_{p^f}^{\text{gp}} = 0.005$ |
| stabilized Lagrange multiplier method | $\alpha_c = 5$ |

The Newmark method ($\gamma = 0.9, \beta = 0.5$) is used as a time integration scheme and the time increment Δt is set to $\Delta t = 0.1\text{s}$. Newton's method with a direct solver are used. The convergence criterion for the Newton iteration requires a drop of the norm of the residual of 5×10^{-3} relative to the norm of the initial residual. In addition, the adaptive time-stepping scheme is applied to ensure the convergence of the Newton iteration; see (6.92) in Section 6.6.3.

Figures 6.33 - 6.52 show the distribution of the solid and fluid velocities V_i^s and v_i^f , the fluid pressure p^f and the fluid in-plane effective shear stress q^f ($q^f = |\sigma_1 - \sigma_2|/2$). Figure 6.33 shows the initial configuration of this FSI-contact problem. Figures 6.34 - 6.37 show snapshots when only FSI occurs without contact.

Figure 6.33: FSI-contact problem using XFEM ($t = 0\text{s}$, step0)

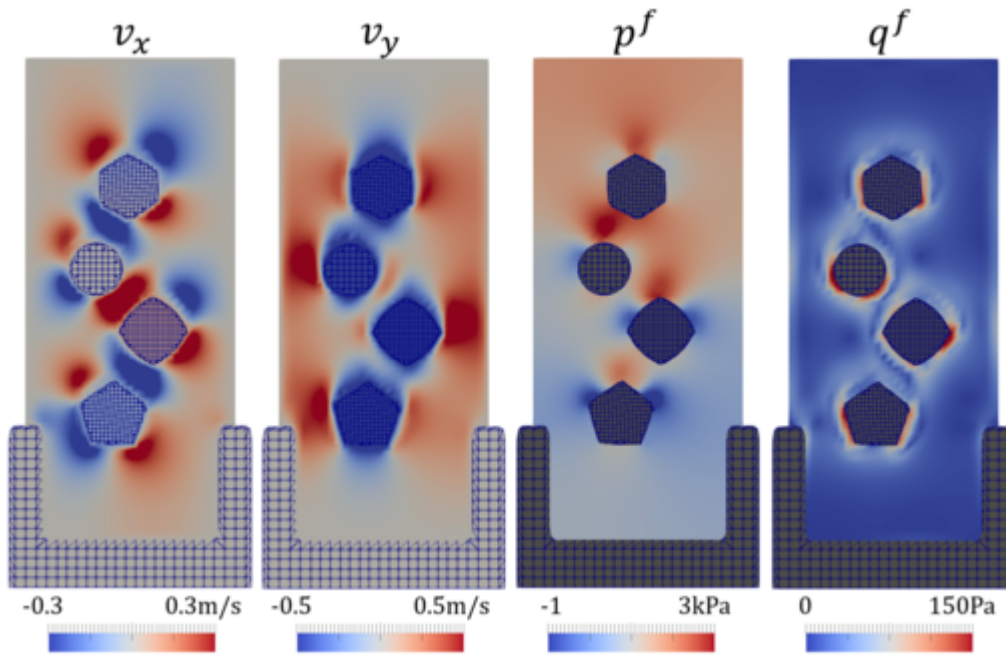


Figure 6.34: FSI-contact problem using XFEM ($t = 1.1s$, step10)

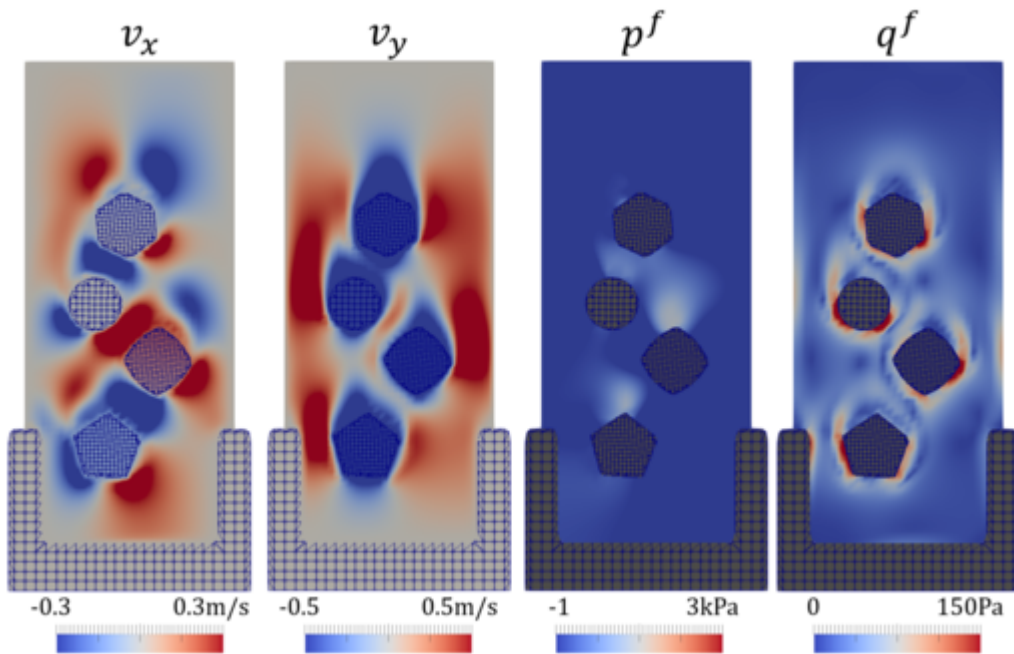


Figure 6.35: FSI-contact problem using XFEM ($t = 2.05s$, step20)

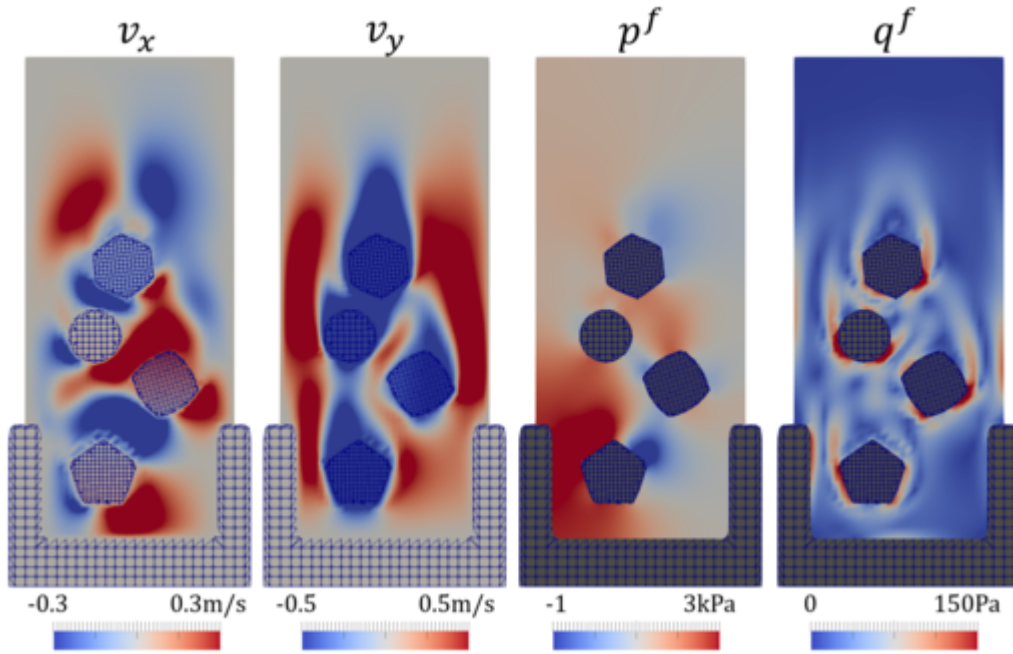


Figure 6.36: FSI-contact problem using XFEM ($t = 3.05\text{s}$, step30)

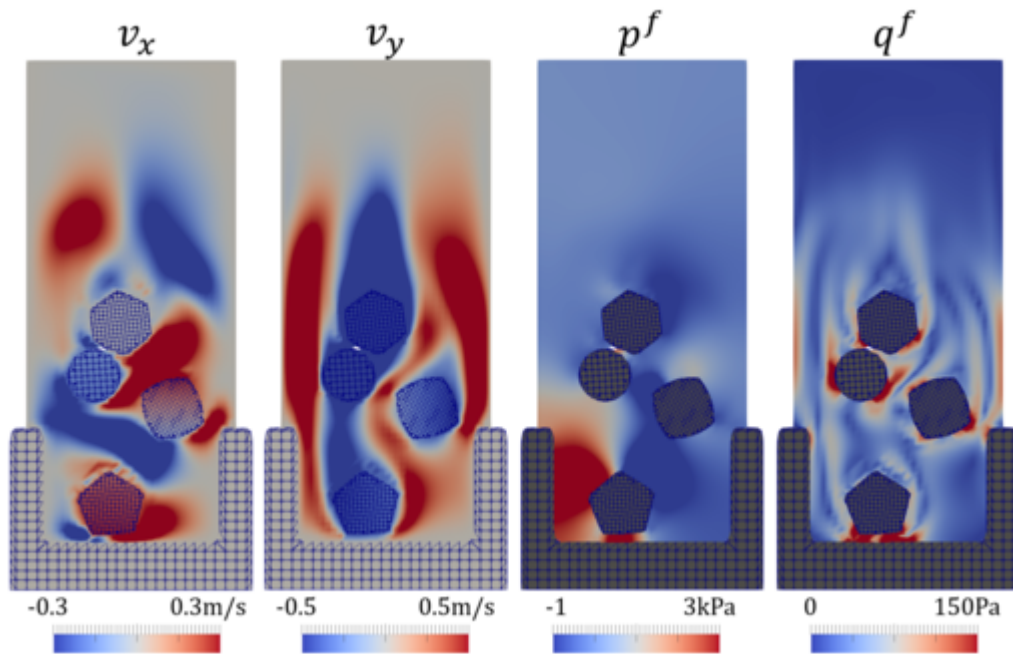


Figure 6.37: FSI-contact problem using XFEM ($t = 4.05\text{s}$, step40)

Figures 6.38 - 6.52 show snapshots when both FSI and contact occur simultaneously. Figure 6.52 shows the final step of the computation. The solid structures contact each other, and the velocity of these structures becomes almost zero in Figure 6.52. The fluid velocity becomes much smaller than values at step 200 (Figure 6.52) and q^f is almost zero in this snapshot. Thus, the equilibrium state is approximately reached at step 347 ($t \simeq 30s$).

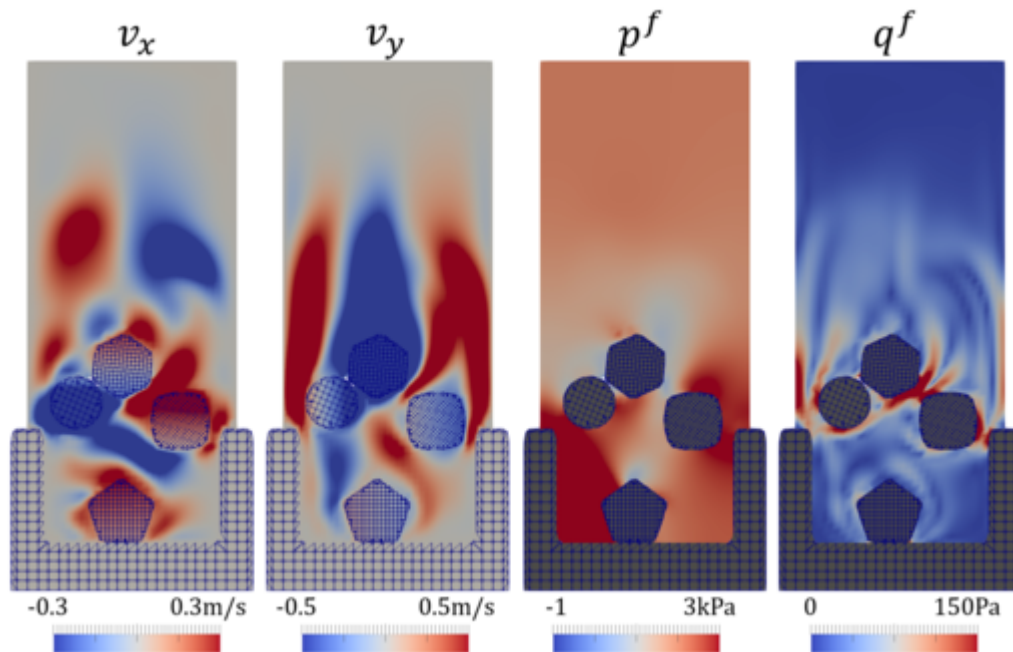


Figure 6.38: FSI-contact problem using XFEM ($t = 4.75s$, step50)

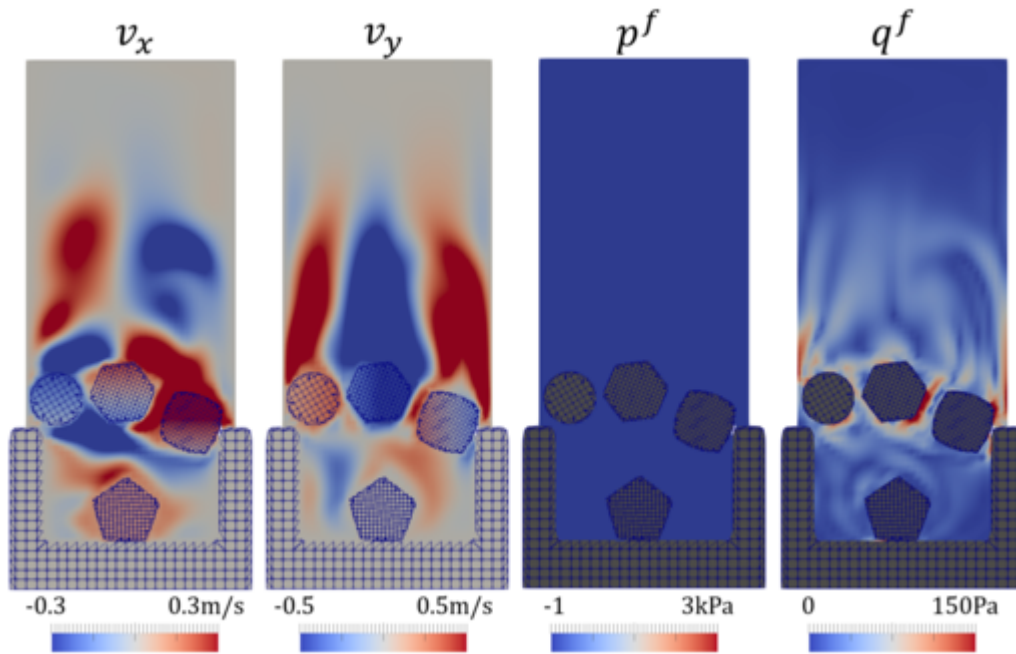


Figure 6.39: FSI-contact problem using XFEM ($t = 5.575s$, step60)

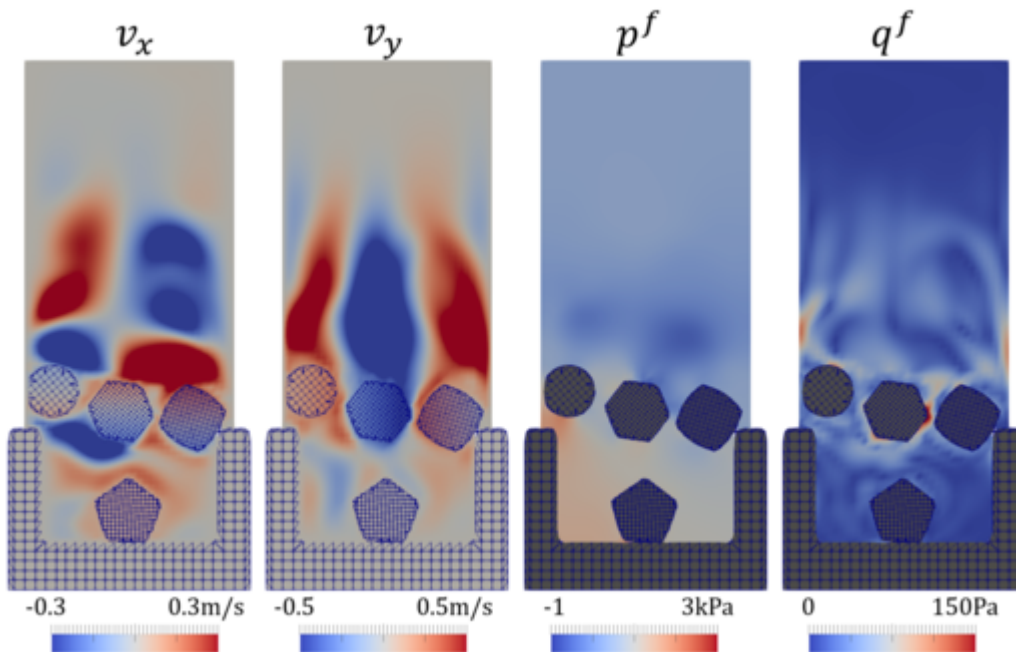


Figure 6.40: FSI-contact problem using XFEM ($t = 6.425s$, step70)

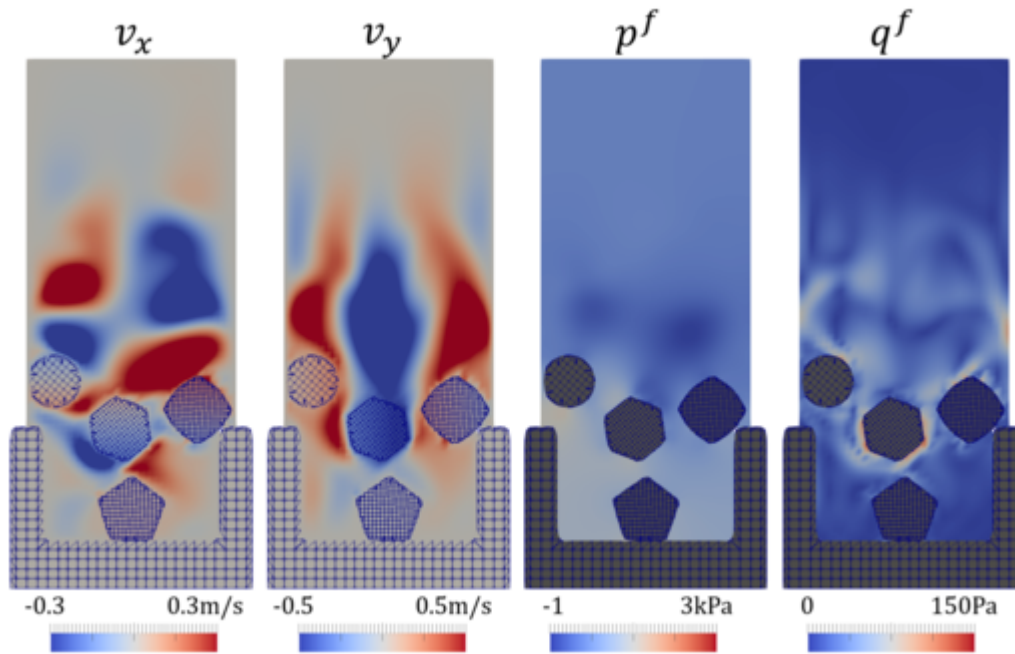


Figure 6.41: FSI-contact problem using XFEM ($t = 7.375\text{s}$, step80)

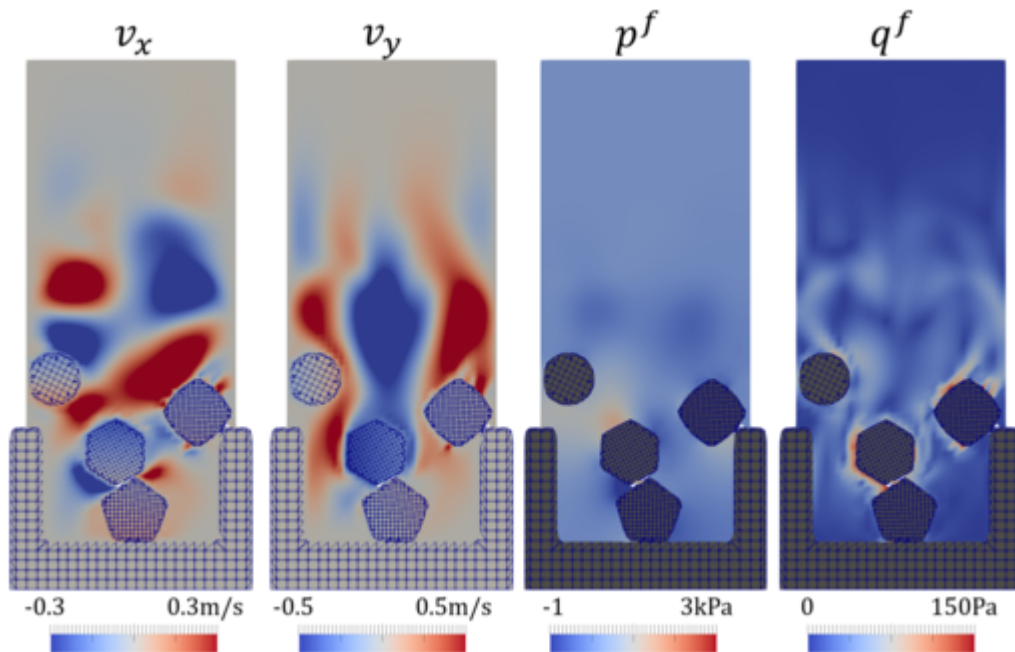


Figure 6.42: FSI-contact problem using XFEM ($t = 8.25\text{s}$, step90)

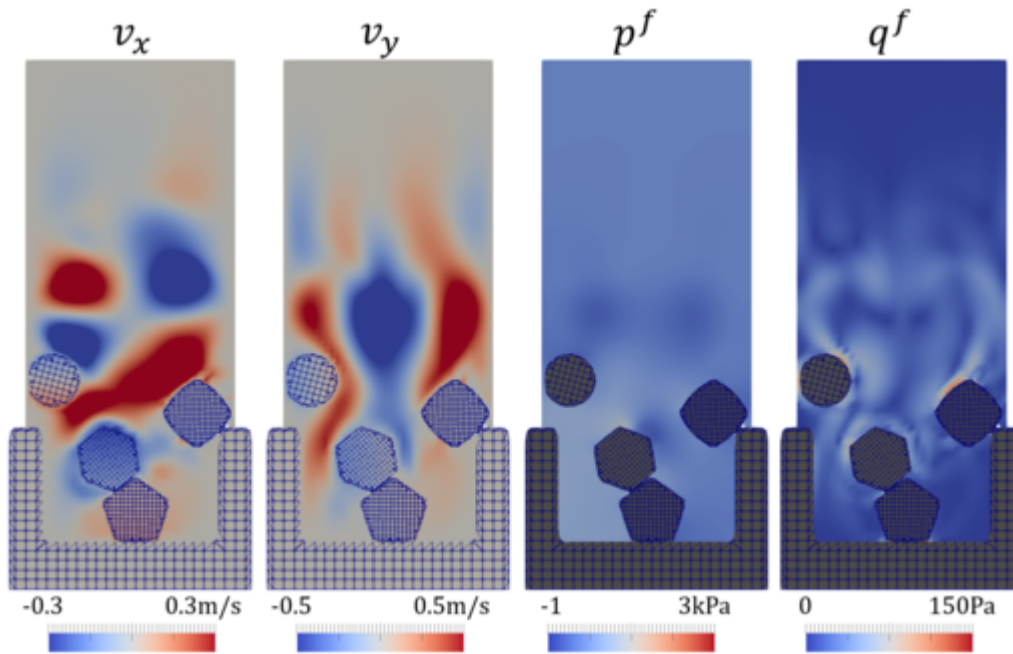


Figure 6.43: FSI-contact problem using XFEM ($t = 9\text{s}$, step100)

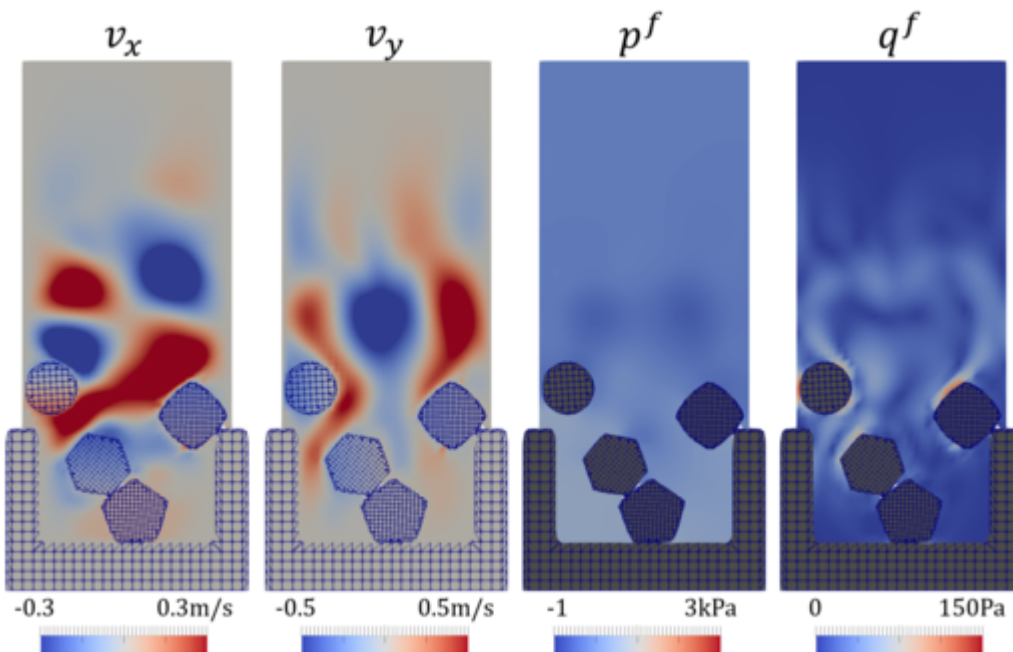


Figure 6.44: FSI-contact problem using XFEM ($t = 10\text{s}$, step110)

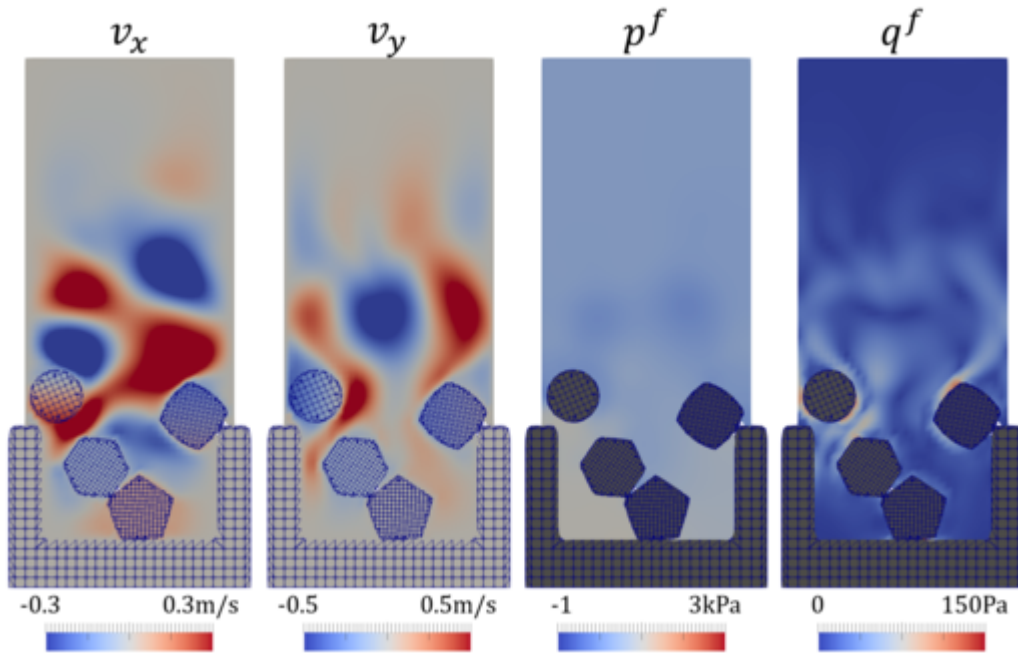


Figure 6.45: FSI-contact problem using XFEM ($t = 11\text{s}$, step120)

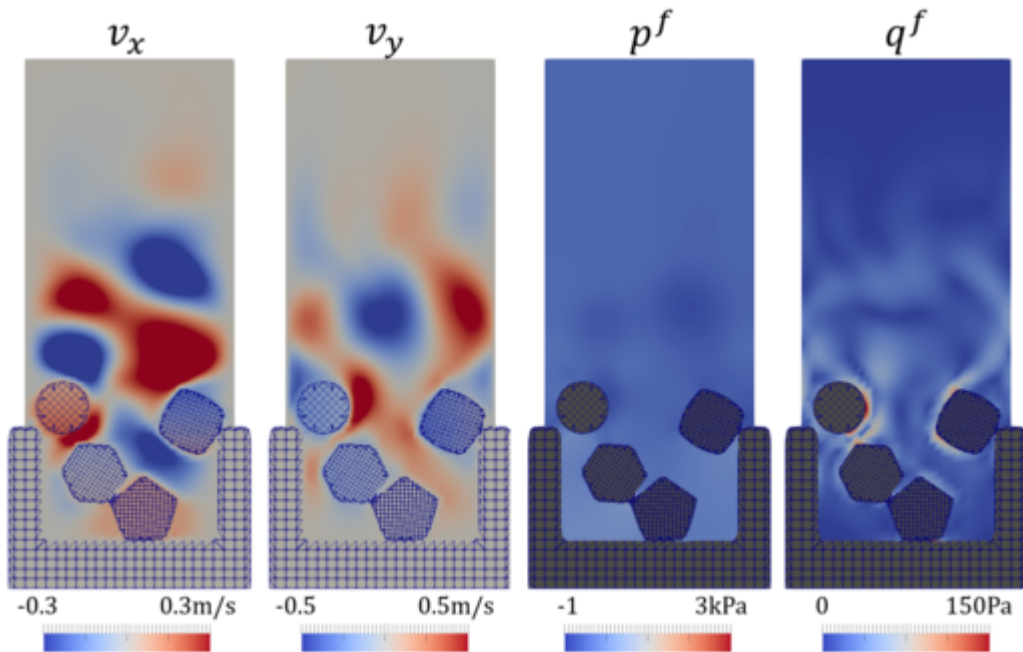


Figure 6.46: FSI-contact problem using XFEM ($t = 11.9\text{s}$, step130)

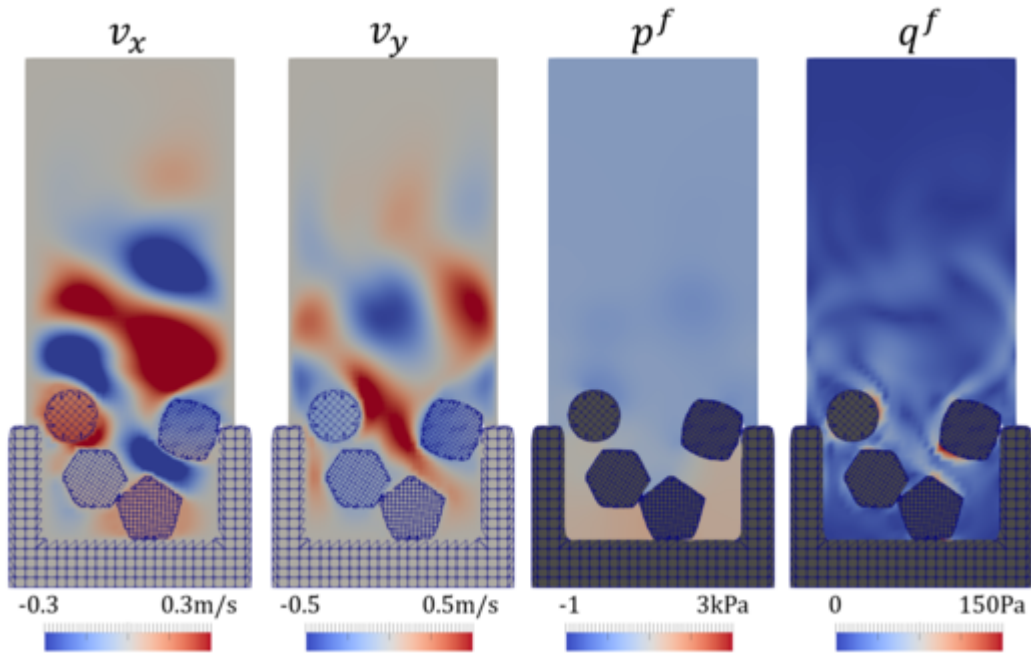


Figure 6.47: FSI-contact problem using XFEM ($t = 12.9\text{s}$, step140)

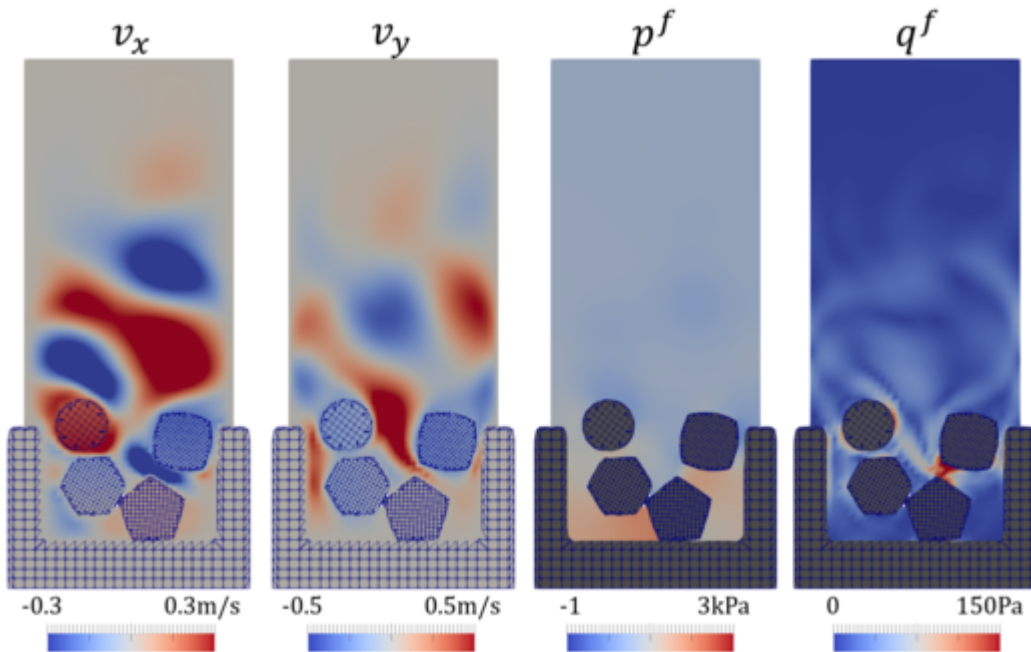


Figure 6.48: FSI-contact problem using XFEM ($t = 13.85\text{s}$, step150)

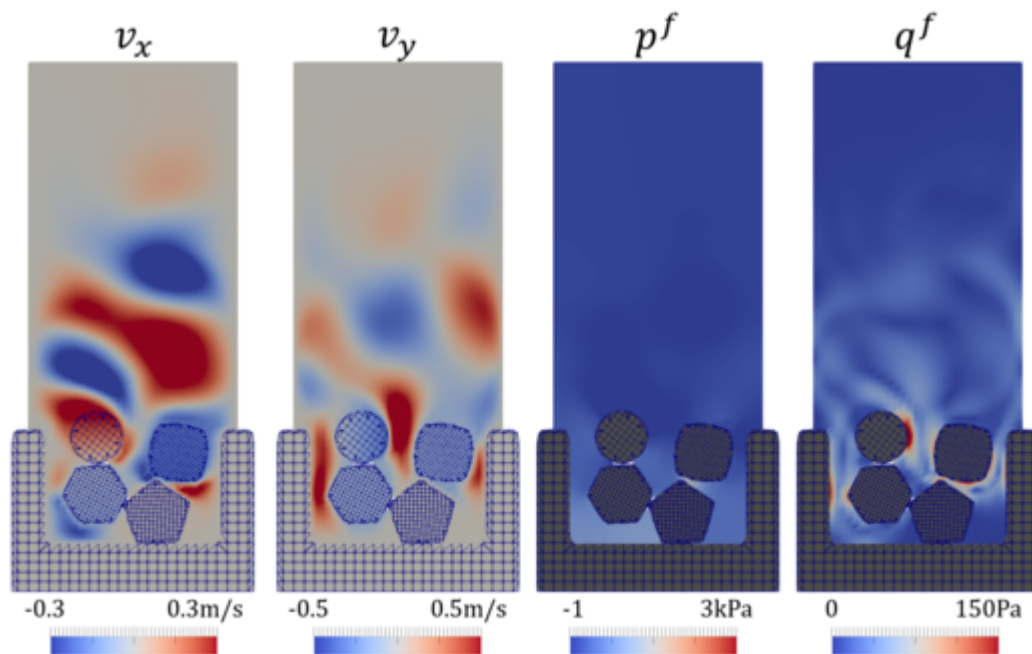


Figure 6.49: FSI-contact problem using XFEM ($t = 14.75\text{s}$, step160)

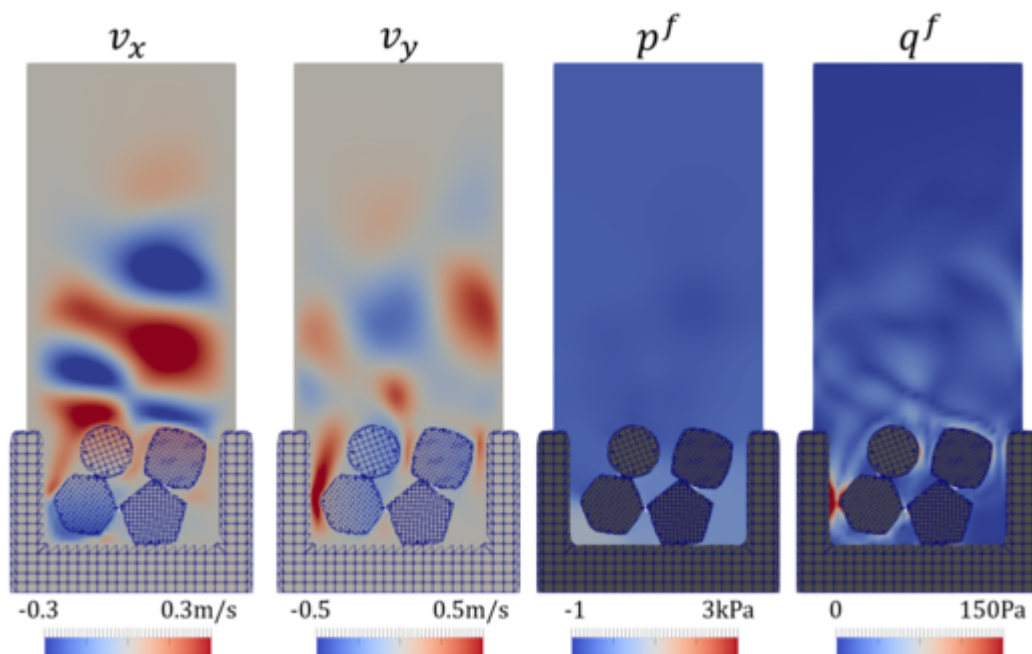


Figure 6.50: FSI-contact problem using XFEM ($t = 16.275\text{s}$, step180)

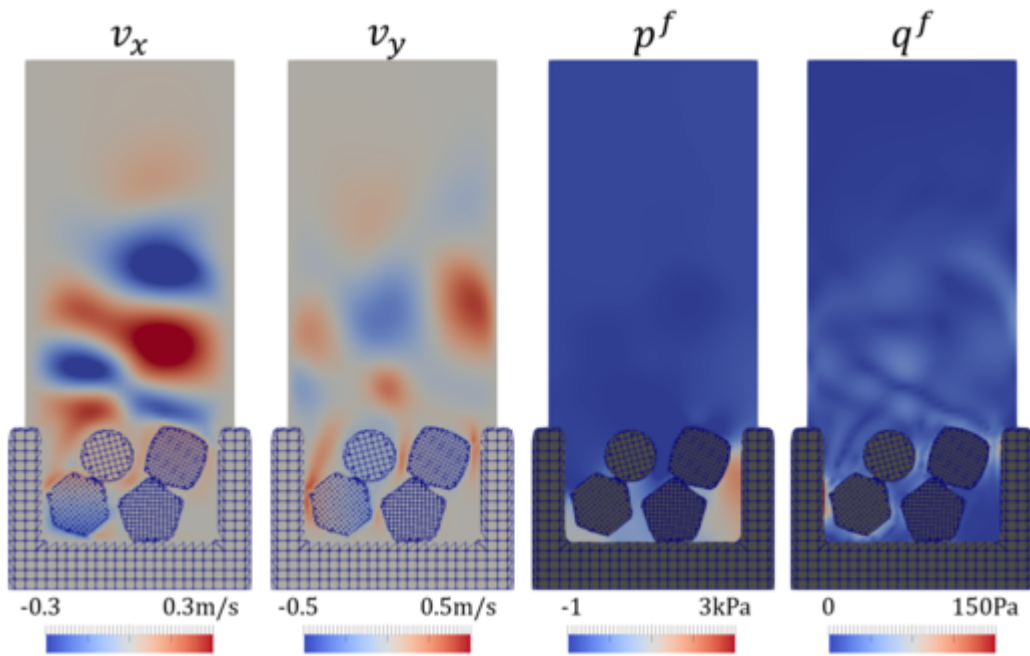


Figure 6.51: FSI-contact problem using XFEM ($t = 17.2\text{s}$, step200)

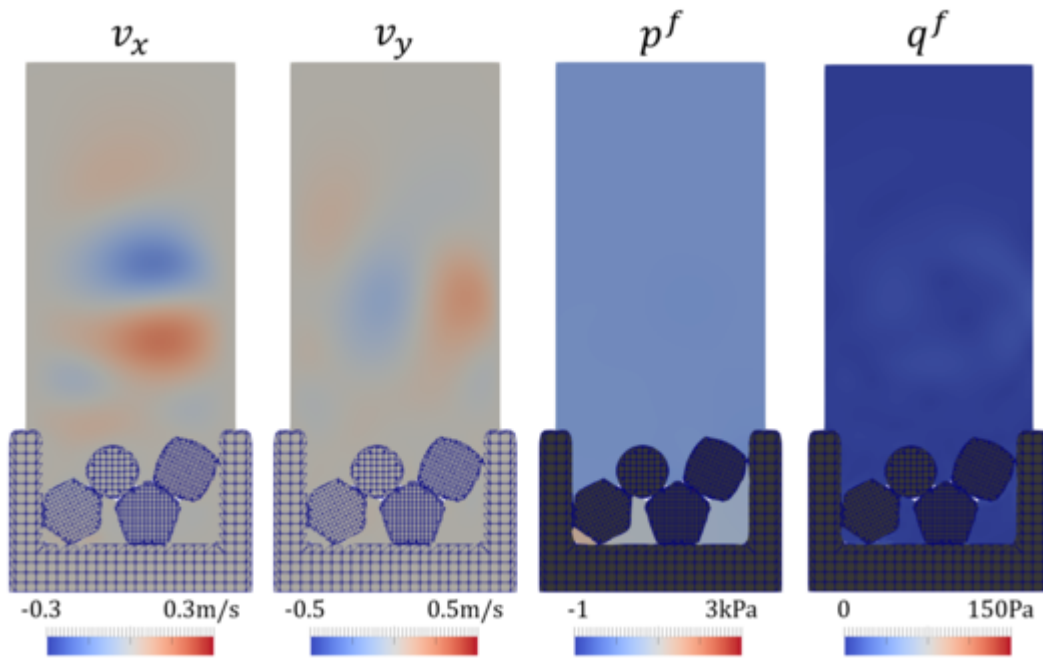


Figure 6.52: FSI-contact problem using XFEM ($t = 30.98125\text{s}$, step347)

The results in Figures 6.33 - 6.52 suggest that the Lagrangian-immersed FSI method using the XFEM has the ability to compute both FSI and contact phenomena simultaneously. As the solid and fluid meshes are spatially separate, a flexible FSI-contact formulation and computational method were developed. However, there is a numerical issue in terms of the XFEM in this example. A typical example of this issue is the oscillation of the fluid velocity and the fluid stress around Solid 4 (pentagon); see Figure 6.53. This figure shows the distribution of the fluid velocity and stress around Solid 4 and non-smooth distribution is observed around Solid 4.

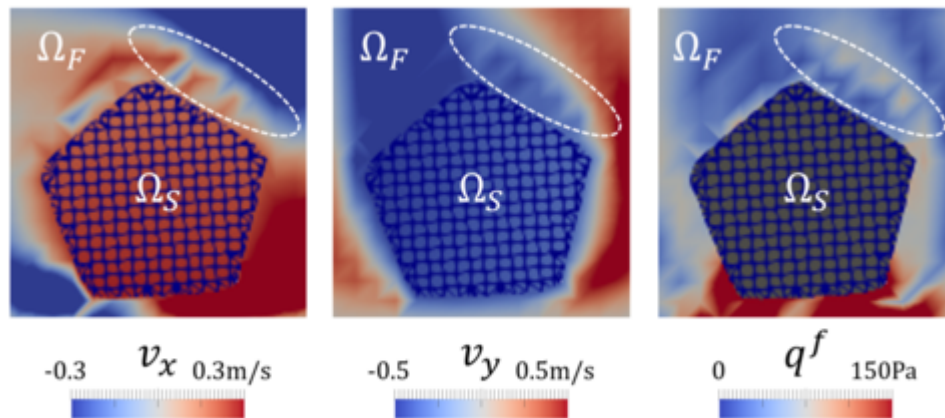


Figure 6.53: Oscillation of fluid velocity and stress ($t = 4.05\text{s}$, step40)

Similar spurious oscillations can be observed in Figure 6.53 is Figures 6.54, 6.55 and 6.56. These figures show the results of a falling cylinder due to the body force within the FSI system. A two-dimensional circular cylinder is immersed within an incompressible fluid. This cylinder has the radius of $r = 0.509\text{m}$ and its centroid \mathbf{X}_c in the initial configuration is $\mathbf{X}_c = (1.73, 8.00)\text{m}$. The geometry parameters of the Eulerian system and material parameters are identical to the problem presented in Section 6.6.3. Focusing on steps 105 and 125 of Figures 6.54 and 6.55, the fluid velocity highly oscillates around the cylinder (see Figure 6.53) and this computation diverges at step 126 due to this oscillation. The fluid pressure oscillates in time; see Figure 6.56.

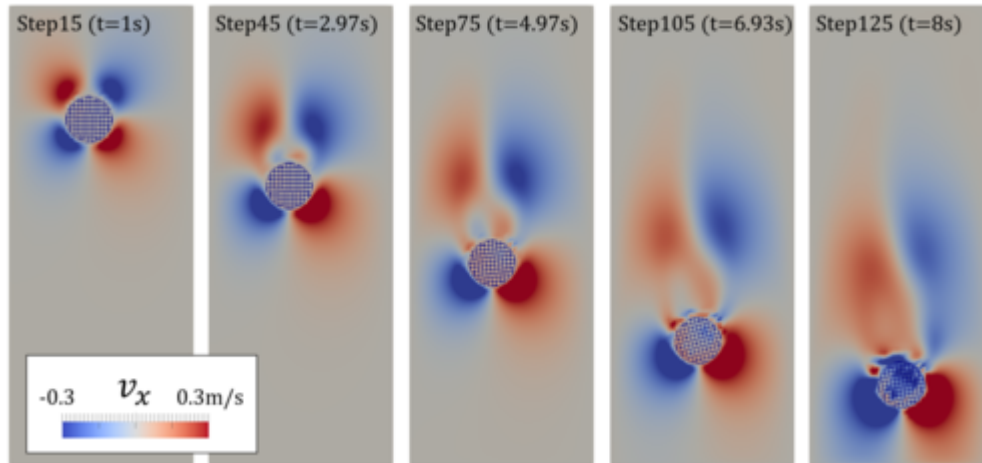


Figure 6.54: Interpolation error due to XFEM (velocity in x)

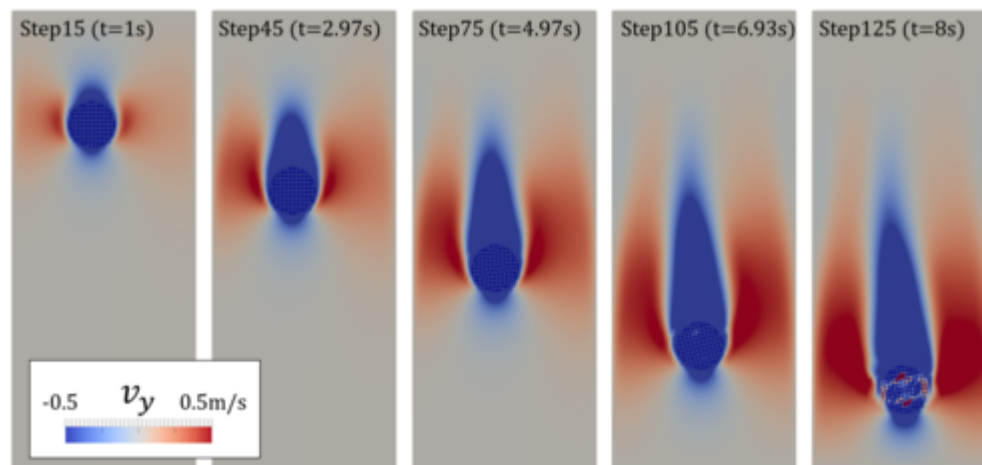


Figure 6.55: Interpolation error due to XFEM (velocity in y)

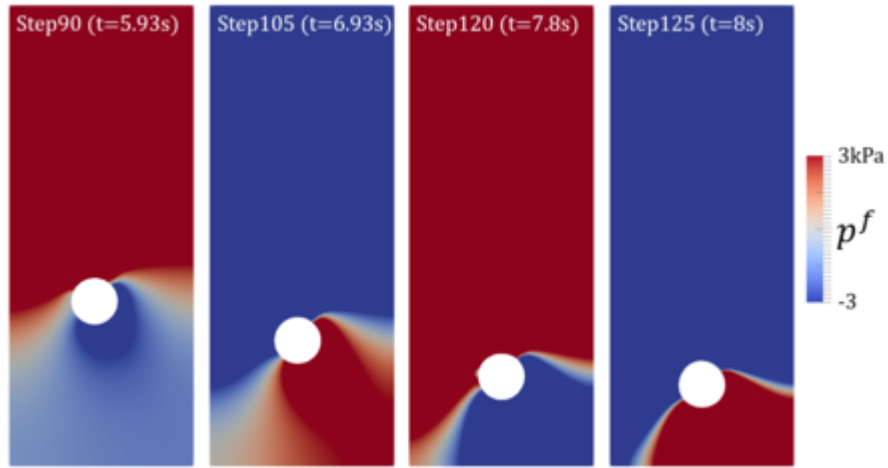


Figure 6.56: Interpolation error due to XFEM (fluid pressure)

These issues are caused by the numerical error due to moving interfaces using the combination of the XFEM and a time stepping scheme. This error has been discussed in Chapter 3. In the Lagrangian-immersed FSI method, the fluid domain is represented by the Eulerian description and background meshes are used. Immersed FSI interfaces follow the motion of the solid structures. The combination of the XFEM and the time stepping scheme cannot handle correctly numerical interpolation due to the phase change as interface moves; see Figure 1.1.

To overcome this numerical error, XFEM based fixed-grid approach for the FSI (Wall et al. [69], Mayer et al. [70]) uses the ghost fluid method (Fedkiw et al. [37], Hong et al. [38], Liu et al. [39] and Nguyen et al. [40]). The ghost fluid method is originally derived from the numerical interpolation of the Eulerian equations with moving interfaces. This method uses the idea of a Lagrangian description within the Eulerian system. The numerical interpolation along time is computed by considering corresponding material coordinates and thus, the effect of moving interface is included in the time evolution of the solution.

Figure 6.57 illustrates the numerical interpolation along time based on the ghost fluid method. A region colored by white is defined as the domain A: Ω_A^n and another region colored by gray is defined as the domain B: Ω_B^n at time t^n . A black solid line and a black

dashed line represent the interfaces between A and B at time t^n and t^{n-1} ; they are denoted by Γ^n and Γ^{n-1} , respectively. At a point \mathbf{x}^n on Γ^n , the solution $\mathbf{u}_B^n(\mathbf{x}^n)$ belongs to the phase B. The time interpolation of $\mathbf{u}_B^n(\mathbf{x}^n)$ needs the information of the corresponding past material point at time t^{n-1} : \mathbf{x}^{n-1} . Because the spatial point $\mathbf{x} = \mathbf{x}^n$ at t^{n-1} belongs to the phase A: Ω_A , computing \mathbf{u}_B^{n-1} is not directly possible. Thus, the ghost fluid method computes $\mathbf{u}_B^n(\mathbf{x}^n)$ considering the corresponding past material coordinate \mathbf{x}^{n-1} using a time increment at time t^n , $\Delta \mathbf{u}$, as follows:

$$\mathbf{u}_B^n(\mathbf{x}^n) = \mathbf{u}_B^{n-1}(\mathbf{x}^{n-1}) + \Delta \mathbf{u} . \quad (6.102)$$

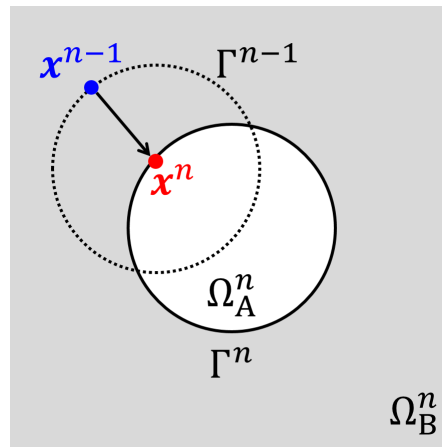


Figure 6.57: Ghost fluid method

An alternative but more generic approach to overcome this issue is the space-time formulation described in Chapter 3. The Lagrangian-immersed FSI method using the space-time XFEM is able to treat FSI and contact phenomena properly without using additional treatments such as the ghost fluid method.

6.7 Discussion

This chapter proposed the Lagrangian-immersed FSI method using the XFEM with a time stepping scheme. In the Lagrangian-immersed FSI method, the solid and fluid phases are defined by the Lagrangian and Eulerian descriptions, respectively. Meshes of the solid and the fluid are spatially disconnected. FSI is computed between non-matching Lagrangian and Eulerian interfaces using techniques from computational contact mechanics, such as the master-slave concept, the node-to-surface pairing, and the gap equation. As the solid phase is defined by the Lagrangian description, conventional contact formulations are directly applicable to the FSI system and thus, the implementation of the contact formulation is much easier than with the full-Eulerian FSI method. Interfaces in the Eulerian system are defined by the level set projection method to capture the deformation of disconnected solid structures correctly. By introducing the level set projection method into a monolithic solution strategy for the FSI system, the update of geometry is automatically performed as the solution converges. The point that no additional operation for the update of interfaces is one advantage over the previous work of the FSI-contact problem of Mayer, Wall, et al. [69, 70]. In addition, Nitsche's method for non-matching interfaces is proposed. The weak boundary conditions on an interface are satisfied without introducing Lagrange multipliers used in [69, 70].

Steady-state FSI problems with large deformations were computed by the Lagrangian-immersed FSI method and the XFEM. There is no limitation on the deformation of the solid structures as the ALE-FSI method has. As a preliminary study for FSI-contact problems, a transient contact problem was also computed based on the stabilized Lagrange multiplier method [75]. Transient multibody contact phenomena were successfully computed by the XFEM and the conservation of the momentum was verified under the multibody contact. Finally, a transient multibody FSI-contact problem was studied. The Lagrangian-immersed FSI method was able to predict the response of a complex FSI-contact system without lim-

itation on large deformation as the ALE-FSI method has. The drawback of the transient analysis of the Lagrangian-immersed FSI method using the XFEM with a time stepping scheme is the presence of numerical interpolation errors due to moving interfaces as discussed in Section 6.6.4. Therefore, the proposed Lagrangian-immersed FSI method should be combined with the space-time XFEM to achieve stable and robust FSI-contact problem. The next chapter (Chapter 7) discusses the Lagrangian-immersed FSI method using the space-time XFEM, as an appropriate and efficient computational method for FSI-contact problems.

Chapter 7

Lagrangian-Immersed FSI Method using Space-Time XFEM

7.1 Outline

The Lagrangian-immersed FSI method using the XFEM has the ability to handle simultaneously fluid-structure interaction (FSI) and contact (Chapter 6). The Lagrangian description for the solid phase and the Eulerian description for the fluid phase, respectively.

However, the combination of the XFEM and the time stepping scheme approximates incorrectly the time derivatives of the fluid velocities when moving interfaces exist because of the phase change. One method to overcome this interpolation issue is to use the ghost-fluid method (Fedkiw et al. [37], Hong et al. [38], Liu et al. [39] and Nguyen et al. [40]) and this method is used in the previous work for FSI-contact problems; XFEM based fixed-grid approach for the FSI (Wall et al. [69], Mayer et al. [70]). The ghost-fluid method is a mixed formulation considering both the Eulerian fixed points and the Lagrangian material points to correctly interpolate in time state variables when the phase changes occurs due to moving interfaces.

A more generic approach to overcome this issue is the space-time formulation described in Chapter 3. As the phase change due to a moving interface is considered in a space-time slab using the space-time XFEM, the Lagrangian-immersed FSI method using the space-time XFEM is able to treat FSI and contact phenomena properly without using additional operations like the ghost fluid method.

This chapter describes the finite element discretization and the numerical implementation of the Lagrangian-immersed FSI method using the space-time XFEM, and its applications to FSI-contact problems. The strong form of governing equations is identical to the Lagrangian-

immersed FSI method using the XFEM summarized in Sections 6.2 and 6.3.

In this chapter, the notations of volume and interface of a space-time slab are Q and P respectively; see Chapter 3. Table 7.1 summarizes the notation of volumes and boundaries of a space-time slab. In general, a space-time volume Q is subdivided into thin slabs, which are denoted by Q^n with the time interval $T^n =]t^n, t^{n+1}[$. The discontinuous Galerkin method is applied in the temporal direction. Figure 7.1 shows a space-time volume and interfaces in a space-time slab Q^n . As the discontinuous Galerkin method is used in time, Q^n does not contain time t^n and t^{n+1} and its lower and upper temporal bounds are denoted as t_+^n and t_-^{n+1} , which deviate from t^n and t^{n+1} by an infinitesimal value δ :

$$t_+^n \equiv t^n + \delta, \quad t_-^{n+1} \equiv t^{n+1} - \delta. \quad (7.1)$$

The Interface P in this slab Q^n is denoted by P^n . $P_-^{n+1,p}$ and $P_+^{n,p}$ denote boundaries on the upper temporal bound t_-^{n+1} and lower temporal bound t_+^n for the phase p . P_{int}^n denotes an interface in a space-time slab Q^n .

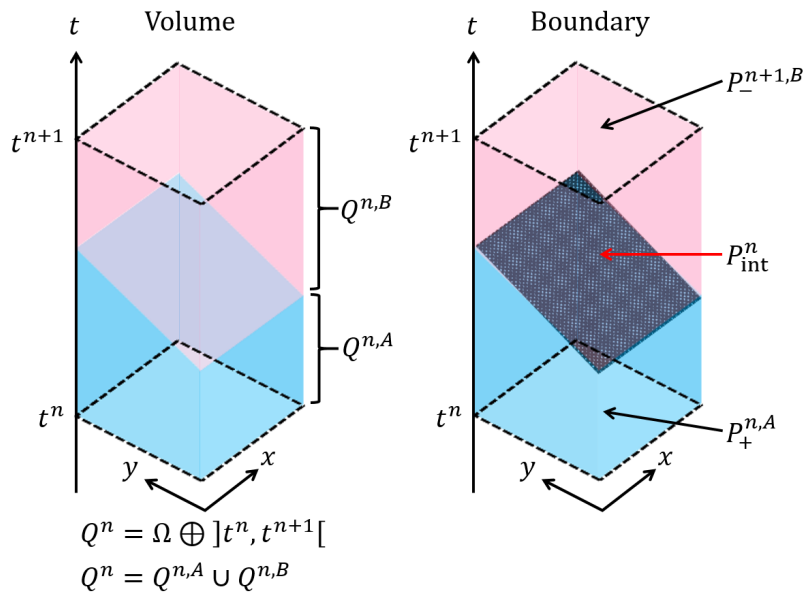


Figure 7.1: Definition of volume and interfaces in a space-time slab (phase A and B)

The organization of this chapter is as follows: Section 7.2 summarizes the finite element discretization of the Lagrangian-immersed FSI method using the space-time XFEM. Section

Table 7.1: Notation of volume and boundary

| | Spatial Domain | Space-Time Slab |
|----------|-------------------|---|
| Volume | $\Omega, d\Omega$ | $Q \equiv \Omega \oplus T, dQ = d\Omega dt$ |
| Boundary | $\Gamma, d\Gamma$ | $P \equiv \Gamma \oplus T, dP = d\Gamma dt$ |

7.3 discusses the integration scheme for the space-time XFEM, including space-time FSI and contact. The level set projection for the space-time XFEM is presented. In Section 7.4, three numerical examples are studied. The fluid phase is modeled by the incompressible Navier-Stokes (INS) equations. Finite strains and the plane strain assumption are considered in the solid phase. The first numerical example is a falling circular cylinder due to a body force in the FSI system. This benchmark problem is a transient FSI analysis with large solid deformation, which is difficult to analyze with the conventional ALE-FSI method. The second numerical example is a well-known transient FSI benchmark problem, named as Turek-Hron FSI3 benchmark problem proposed by Turek and Hron [111]. The final numerical example is a transient multibody FSI-contact problem using the space-time XFEM. This problem is identical to the numerical example described in Section 6.6.4. This chapter will show that the proposed space-time XFEM allows for a stable and robust FSI-contact analysis without interpolation errors due to moving interfaces.

7.2 Finite Element Discretization of Lagrangian-Immersed FSI Method using Space-Time XFEM

This section summarizes the finite element discretization of the FSI-contact problem based on the Lagrangian-immersed FSI method using the space-time XFEM. This section assumes spatially two-dimensional cases and the plain strain case. The entire spatial domain Ω is the union of the Eulerian and Lagrangian system: $\Omega = \Omega_E \cup \Omega_L$ and discretized spatially by bilinear QUAD4 elements. The finite element discretization is also applied to the temporal domain T . The temporal domain is discretized by linear elements. Therefore, the space-time

domain Q : $Q = \Omega \oplus T$ is discretized by trilinear HEXA8 space-time elements. Given a trial function space \mathcal{S}^h and an admissible test function space \mathcal{V}^h defined in a space-time domain:

$$\text{Trial functions:} \quad \{\mathbf{U}^s, \mathbf{V}^s, \mathbf{U}^d\} \in \mathcal{S}_0^h, \quad \{\mathbf{v}^f, p^f, \phi\} \in \mathcal{S}^h, \quad (7.2)$$

$$\text{Test functions:} \quad \{\delta \mathbf{U}^s, \delta \mathbf{V}^s, \delta \mathbf{U}^d\} \in \mathcal{V}_0^h, \quad \{\delta \mathbf{v}^f, \delta p^f, \delta \phi\} \in \mathcal{V}^h, \quad (7.3)$$

where a lower subscript 0 denote a space in the initial configuration. The variational form of FSI-contact problems using the compressible material constitutive law for the solid phase is as follows:

$$\begin{aligned} & \tilde{R}_m^s(\delta \mathbf{U}^s; \{\mathbf{U}^s, \mathbf{V}^s\}) + \tilde{R}_{uv}^s(\delta \mathbf{V}^s; \{\mathbf{U}^s, \mathbf{V}^s\}) + \tilde{R}_u^d(\delta \mathbf{U}^d; \{\mathbf{U}^s, \mathbf{U}^d\}) + \tilde{R}_c^s(\delta \mathbf{U}^s; \mathbf{U}^s) \\ & + \tilde{R}_m^f(\{\delta \mathbf{v}^f, \delta p^f\}; \{\mathbf{v}^f, p^f\}) + \tilde{R}_\phi(\delta \phi; \{\phi, \hat{\Phi}\}) \\ & + \tilde{R}_L^{\text{fsi}}(\delta \mathbf{U}^s; \{\mathbf{U}^s, \mathbf{V}^s, \mathbf{v}^f, p^f\}) + \tilde{R}_E^{\text{fsi}}(\{\delta \mathbf{v}^f, \delta p^f\}; \{\mathbf{U}^s, \mathbf{V}^s, \mathbf{v}^f, p^f\}) \\ & + \tilde{R}_L^{\text{gp}}(\{\delta \mathbf{U}^s, \delta \mathbf{V}^s, \delta \mathbf{U}^d\}; \{\mathbf{U}^s, \mathbf{V}^s, \mathbf{U}^d\}) + \tilde{R}_E^{\text{gp}}(\{\delta \mathbf{v}^f, \delta p^f\}; \{\mathbf{v}^f, p^f\}) = 0, \end{aligned} \quad (7.4)$$

where \tilde{R} denotes a weak form for the space-time XFEM. While the weak form for the XFEM is denoted by R in Section 6.4, a different symbol; \tilde{R} , is used for the space-time XFEM in this chapter to emphasize the difference between weak forms of both the XFEM and the space-time XFEM.

First, \tilde{R}_m^s , \tilde{R}_{uv}^s and \tilde{R}_u^d are defined in the undeformed Lagrangian space-time domain Q_{L0}^n and on the corresponding undeformed Lagrangian space-time interface $P_{L0\text{-int}}^n$, based on the total Lagrangian formulation. \tilde{R}_m^s and \tilde{R}_{uv}^s are the variational forms of the solid momentum equation (6.7) and the displacement-velocity relationship (6.8) in the solid phase of the initial space-time configuration Q_{S0}^n . The test function associated with \tilde{R}_m^s , \tilde{R}_{uv}^s and \tilde{R}_u^d are δU_i^s , δV_i^s and δU_i^d respectively. The detailed forms of \tilde{R}_m^s , \tilde{R}_{uv}^s and \tilde{R}_u^d are defined as follows:

$$\begin{aligned} \tilde{R}_m^s &= \int_{Q_{L0}^{n,s}} dQ \delta U_i^s \rho^s \left(\frac{\partial V_i^s}{\partial t} + \alpha^s V_i^s - B_i^s \right) + \int_{Q_{L0}^{n,s}} dQ \frac{\partial \delta U_i^s}{\partial X_J} \Pi_{iJ}^s(\mathbf{U}^s) \\ &+ \int_{P_{L0+}^{n,s}} d\Omega \delta U_i^s |_{+} \rho^s [V_i^s]_{\pm}^n, \end{aligned} \quad (7.5)$$

$$\tilde{R}_{uv}^s = \int_{Q_{L0}^{n,s}} dQ \delta V_i^s \rho^s \left(\frac{\partial U_i^s}{\partial t} - V_i^s \right) + \int_{P_{L0+}^{n,s}} d\Omega \delta V_i^s |^n \rho^s [[U_i^s]]_{\pm}^n . \quad (7.6)$$

The last terms in (7.5) and (7.6) are additional terms derived from the discontinuous Galerkin method in time.

Second, \tilde{R}_u^d is the variational form of the governing equation in the undeformed dummy displacement domain $Q_0^{n,d}$, based on the total Lagrangian formulation. Based on the Helmholtz smoothing method, the Helmholtz equation (6.9) for the dummy displacement outside of the solid phase Ω_{D0} and the continuity condition of U_i^s and U_i^d (6.10) on the undeformed Lagrangian space-time interface P_{L0-int}^n based on Nitsche's penalty method are included in this weak form:

$$\begin{aligned} \tilde{R}_u^d = & \int_{Q_{L0}^{n,d}} dQ \frac{\partial \delta U_i^d}{\partial X_J} \rho^d \frac{\partial U_i^d}{\partial X_J} + \int_{Q_{L0}^{n,d}} dQ \delta U_i^d \rho^d U_i^d \\ & - \int_{P_{L0-int}^n} dP \delta U_i^d \rho^d \frac{\partial U_i^d}{\partial X_J} \tilde{n}_{L0J}^d + \int_{P_{L0-int}^n} dP \delta U_i^d \rho^d \eta^d (U_i^s - U_i^d) , \end{aligned} \quad (7.7)$$

where η^d is the Nitsche penalty factor for the continuity of the displacements within the Lagrangian system. \tilde{n}_{L0J}^d is the undeformed space-time outward normal from the dummy displacement domain $Q_0^{n,d}$. As a spatially two-dimensional case is assumed, \tilde{n}_{L0J}^d has three components (two spatial directions: x, y and one temporal direction: t). However, the temporal component of the undeformed space-time normal is zero because a space-time interface is always perpendicular to the spatial domain when the total Lagrangian formulation is used (Figure 7.2):

$$\text{Undeformed Spatial Normal:} \quad \mathbf{n}_{L0}^\alpha = (n_{L0x}^\alpha, n_{L0y}^\alpha)^\top , \quad (7.8)$$

$$\text{Undeformed Space-Time Normal:} \quad \tilde{\mathbf{n}}_{L0}^\alpha = (n_{L0x}^\alpha, n_{L0y}^\alpha, 0)^\top . \quad (7.9)$$

Based on the dummy solid method described in Section 6.2.2, the dummy momentum equation (6.11) and the dummy displacement-velocity relationship (6.12) determine R_u^d , using

the one-sided Nitsche method as follows:

$$\begin{aligned}
\tilde{R}_u^d = & \int_{Q_{L0}^{n,d}} dQ \delta U_i^d \rho^d \left(\frac{\partial V_i^d}{\partial t} + \alpha^d V_i^d - B_i^d \right) + \int_{Q_{L0}^{n,d}} dQ \frac{\partial \delta U_i^d}{\partial X_J} \Pi_{iJ}^d(\mathbf{U}^d) \\
& + \int_{Q_{L0}^{n,d}} dQ \delta V_i^d \left(\frac{\partial U_i^d}{\partial t} - V_i^d \right) - \int_{P_{L0\text{-int}}^n} dP \delta U_i^d \{ \Pi_{iJ} \} \tilde{n}_{L0J}^{s \rightarrow d} \\
& - \int_{P_{L0\text{-int}}^n} dP \delta \Pi_{iJ}^d \tilde{n}_{L0J}^{s \rightarrow d} (U_i^s - U_i^d) + \int_{P_{L0\text{-int}}^n} dP \delta U_i^d \eta^d (U_i^s - U_i^d) \\
& + \int_{P_{L0+}^{n,d}} d\Omega \delta U_i^d |_{+} \rho^d \llbracket V_i^d \rrbracket_{\pm}^n + \int_{P_{L0+}^{n,d}} d\Omega \delta V_i^d |_{+} \rho^d \llbracket U_i^d \rrbracket_{\pm}^n , \tag{7.10}
\end{aligned}$$

where $\{\cdot\}$ denotes a weighted average and the representative strategies for the weighting is described in Section 5.5.2. The parameters of the dummy displacement $Q_{L0}^{n,d}$ based on the dummy solid method are identical to the actual solid domain $Q_{L0}^{n,s}$ except for the body force (the body force in $Q_{L0}^{n,d}$ is 0). The last line of (7.10) show the correction terms due to the discontinuous Galerkin method in time.

Third, \tilde{R}_c^s denotes the variational form of the stabilized Lagrange multiplier method for contact, which is an interface integral between two different solid bodies in Q_{L0}^n . \tilde{R}_c^s is evaluated on the interface of the master body in the initial configuration P_{c0}^n :

$$\tilde{R}_c^s = \int_{P_{c0}^n} dP \delta g_n^0 \lambda^0 , \tag{7.11}$$

where δg_n^0 is the variation of the normal gap in the initial Lagrangian system. λ^0 is governed by the following equation based on the stabilized Lagrange multiplier method (Section 6.2.4):

$$\tilde{R}_\lambda^s = \int_{P_{c0}^n} dP \delta \lambda^0 (\lambda^0 - \tilde{\lambda}^0 - \gamma_c g_n^0) = 0 , \tag{7.12}$$

the definition of $\tilde{\lambda}^0$ is (6.27). The numerical implementation of this contact formulation for the space-time XFEM; (7.11) and (7.12), is summarized in Section 7.3.5.

Fourth, \tilde{R}_m^f , and \tilde{R}_ϕ are defined in the Eulerian space-time slab Q_E^n and on the corresponding space-time interface $P_{E\text{-int}}^n$, in the initial configuration. \tilde{R}_m^f is the variational form of a volume contribution of the fluid momentum equation (6.2) and the continuity equation

(6.3) in the fluid phase of the current configuration $Q_E^{n,f}$:

$$\begin{aligned} \tilde{R}_m^f &= \int_{Q_E^{n,f}} dQ \delta v_i^f \rho^f \left(\frac{\partial v_i^f}{\partial t} + v_j^f \frac{\partial v_i^f}{\partial x_j} - b_i^f \right) + \int_{Q_E^{n,f}} dQ \frac{\partial \delta v_i^f}{\partial x_j} \sigma_{ij}^f(\mathbf{v}^f, p^f) + \int_{Q_E^{n,f}} dQ \delta p^f \frac{\partial v_i^f}{\partial x_i} \\ &+ \sum_{e \in Q_E^{n,f}} \int_{Q_{Ee}^{n,f}} dQ \tau_m^f \left(v_j^f \frac{\partial \delta v_i^f}{\partial x_j} + \frac{1}{\rho^f} \frac{\partial \delta p^f}{\partial x_i} \right) \tilde{r}_i^f + \sum_{e \in Q_E^{n,f}} \int_{Q_{Ee}^{n,f}} dQ \tau_c^f \frac{\partial \delta v_i^f}{\partial x_i} \frac{\partial v_j^f}{\partial x_j} \\ &+ \int_{P_{E+}^{n,f}} d\Omega \delta v_i^f |_{+} \rho^f \llbracket v_i^f \rrbracket_{\pm}^n . \end{aligned} \quad (7.13)$$

The last line of (7.13) shows the correction term due to the discontinuous Galerkin method in time. \tilde{r}_i^f in (7.13) is a scalar residual of the momentum equation of the incompressible Navier-Stokes equations:

$$\tilde{r}_i^f = \rho^f \frac{\partial v_i^f}{\partial t} + \rho^f v_j^f \frac{\partial v_i^f}{\partial x_j} - \frac{\partial \sigma_{ij}^f(\mathbf{v}^f, p^f)}{\partial x_j} - \rho^f b_i^f . \quad (7.14)$$

In (7.13), the terms in the first line are the standard Galerkin terms, the terms in the second line are the convection and incompressibility stabilization terms. Here, the residual-based variational multiscale (VMS) method is used to suppress the numerical instability due to the convection and incompressibility of the INS fluid. τ_m^f and τ_c^f denote the elementwise stabilization parameters of the VMS method, defined in (6.47) and (6.48). The stabilized fluid residual denoted in (7.13) does not include $\frac{\partial \delta v_i^f}{\partial t}$ term in the stabilized test function and thus, it is identical to the stabilized fluid residual using the XFEM with an time stepping scheme introduced in Section 6.4. This form is called as the WTSE option ($\partial w / \partial t$ term is excluded; $w = \delta v_i^f$ in (7.13)) proposed by Tezduyar et al. [87].

\tilde{R}_ϕ is the variational form of the level set projection using the weighted projection method (6.35):

$$\tilde{R}_\phi = \int_{Q_E^n} dQ \delta \phi f(\hat{\Phi})(\phi - \hat{\Phi}) . \quad (7.15)$$

This projection is performed in the entire Eulerian space-time slab Q_E^n to capture the motion of the interface in the fluid domain. The detailed numerical implementation of the level set projection method for the space-time XFEM is summarized in Section 7.3.6.

\tilde{R}_L^{fsi} and \tilde{R}_E^{fsi} are the interface contributions of the solid and fluid momentum equations; (6.7) and (6.2), enforced with Nitsche's method. The master-slave concept used in the Lagrangian-immersed FSI method using the XFEM can be directly applied to the FSI interface integral for the space-time XFEM. The master interface is the Eulerian space-time interface $P_{E\text{-int}}^n$ and the slave interface is the deformed Lagrangian space-time interface $P_{L\text{-int}}^n$. Therefore, the interface integrals of FSI are performed on the Eulerian space-time interface $P_{E\text{-int}}^n$. \tilde{R}_L^{fsi} is the FSI contribution from the Lagrangian interface $P_{L\text{-int}}^n$ and \tilde{R}_E^{fsi} is the FSI contribution for the Eulerian interface $P_{E\text{-int}}^n$ in the current configuration:

$$\tilde{R}_L^{\text{fsi}} = - \int_{P_{E\text{-int}}^n} dP \delta U_i^s \{ \sigma_{ij} \}_{\text{fsi}} \tilde{n}_{Lj}^{s \rightarrow f} + \int_{P_{E\text{-int}}^n} dP \delta U_i^s \eta^{\text{fsi}} (\hat{V}_i^s |_{P_{L\text{-fsi}}^n} - v_i^f), \quad (7.16)$$

$$\begin{aligned} \tilde{R}_E^{\text{fsi}} = & \int_{P_{E\text{-int}}^n} dP \delta v_i^f \{ \sigma_{ij} \}_{\text{fsi}} \tilde{n}_{Ej}^{s \rightarrow f} - \int_{P_{E\text{-int}}^n} dP \sigma_{ij}^f (\delta \mathbf{v}^f, \delta p^f) \tilde{n}_{Ej}^{s \rightarrow f} (\hat{V}_i^s |_{P_{L\text{-fsi}}^n} - v_i^f) \\ & - \int_{P_{E\text{-int}}^n} dP \delta v_i^f \eta^{\text{fsi}} (\hat{V}_i^s |_{P_{L\text{-fsi}}^n} - v_i^f). \end{aligned} \quad (7.17)$$

Here, $\{ \sigma_{ij} \}_{\text{fsi}}$ is the weighted average of the Cauchy stress of solid and fluid phase defined in (6.52). In this research, the modulus weighting defined in (6.53) is used. As the current configuration is used for these FSI contribution, the deformed space-time normal of the Lagrangian interface $\tilde{n}_{Lj}^{s \rightarrow f}$ and the one of the Eulerian interface $\tilde{n}_{Ej}^{s \rightarrow f}$ are used in (7.16) and (7.17). In this case, the temporal component of these normals is non-zero because interfaces in the deformed configuration is tilting at the interface moves. Details of the numerical implementation of these FSI integrals are summarized in Section 7.3.4. Equations (7.16) and (7.17) are extensions of Nitsche's method using the XFEM defined by (6.50) and (6.51) with spatial interface integrals being converted into space-time interface integrals. Detailed discussions of the FSI interface integrals in the Lagrangian-immersed FSI method are summarized in Appendix C.

Finally, \tilde{R}_L^{gp} and \tilde{R}_E^{gp} are the weak forms of the face-oriented ghost-penalty method. The face-oriented ghost-penalty method for the space-time XFEM is simply an extension of the

integrals on a spatial interface Γ to integrals on a space-time interface P .

$$\tilde{R}_L^{\text{gp}} = \tilde{R}_{LV^s}^{\text{gp}}(\delta \mathbf{V}^s; \mathbf{V}^s) + \tilde{R}_{LU^s}^{\text{gp}}(\delta \mathbf{U}^s; \mathbf{U}^s) + \tilde{R}_{LU^d}^{\text{gp}}(\delta \mathbf{U}^d; \mathbf{U}^d), \quad (7.18)$$

$$\tilde{R}_E^{\text{gp}} = \tilde{R}_{Ev^f}^{\text{gp}}(\delta \mathbf{v}^f; \mathbf{v}^f) + \tilde{R}_{Ep^f}^{\text{gp}}(\delta p^f; p^f). \quad (7.19)$$

The face-oriented ghost-penalty method for the Lagrangian system Q_L^n is computed based on the total Lagrangian formulation on the undeformed Lagrangian space-time face $P_{L\text{gp}0}^n$.

$$\tilde{R}_{LV^s}^{\text{gp}} = \int_{P_{L\text{gp}0}^n} dP \left[\left[\frac{\partial \delta V_i^s}{\partial Z_J} \right]_{\text{gp}} \tilde{n}_{L0J}^{\text{gp}} \eta_{V^s}^{\text{gp}} \left[\left[\frac{\partial V_i^s}{\partial Z_K} \right]_{\text{gp}} \tilde{n}_{L0K}^{\text{gp}} \right], \quad (7.20)$$

$$\tilde{R}_{LU^s}^{\text{gp}} = \int_{P_{L\text{gp}0}^n} dP \left[\left[\frac{\partial \delta U_i^s}{\partial Z_J} \right]_{\text{gp}} \tilde{n}_{L0J}^{\text{gp}} \eta_{U^s}^{\text{gp}} \llbracket \Pi_{iK}^s \rrbracket_{\text{gp}} \tilde{n}_{L0K}^{\text{gp}} \right], \quad (7.21)$$

$$R_{LU^d}^{\text{gp}} = \int_{P_{L\text{gp}0}^n} dP \left[\left[\frac{\partial \delta U_i^d}{\partial Z_J} \right]_{\text{gp}} \tilde{n}_{L0J}^{\text{gp}} \eta_{U^d}^{\text{gp}} \llbracket \Pi_{iK}^d \rrbracket_{\text{gp}} \tilde{n}_{L0K}^{\text{gp}} \right], \quad (7.22)$$

where $\llbracket \cdot \rrbracket_{\text{gp}}$ means the jump operator for the face-oriented ghost-penalty method between two adjacent space-time elements $Q_{L0e_1}^n$ and $Q_{L0e_2}^n$ ($Q_{L0e_1}^n \in Q_{L0}^n$, $Q_{L0e_2}^n \in Q_{L0}^n$). A generalized undeformed coordinate \mathbf{Z} includes the initial configuration \mathbf{X} and the time t ; $\mathbf{Z} = (\mathbf{X}, t)$. $\tilde{n}_{L0I}^{\text{gp}}$ is the undeformed space-time normal of the faces for the face-oriented ghost-penalty method. As (7.22) is based on the initial configuration, faces for the ghost-penalty method is perpendicular to the spatial domain. Thus, $\tilde{n}_{L0I}^{\text{gp}}$ is parallel to the spatial domain and thus, the temporal component $\tilde{n}_{L0t}^{\text{gp}}$ is zero. Details are summarized in Section 7.3.3. The face-oriented ghost-penalty method for the Eulerian system Q_E^n is computed in the current configuration on the face of the Eulerian space-time element $P_{L\text{gp}}^n$:

$$\tilde{R}_{Ev^f}^{\text{gp}}(\delta \mathbf{v}^f; \mathbf{v}^f) = \int_{P_{E\text{gp}}^n} dP \left[\left[\frac{\partial \delta v_i^f}{\partial z_j} \right]_{\text{gp}} \tilde{n}_{Ej}^{\text{gp}} \eta_{v^f}^{\text{gp}} \left[\left[\frac{\partial v_i^f}{\partial z_k} \right]_{\text{gp}} \tilde{n}_{Ek}^{\text{gp}} \right], \quad (7.23)$$

$$\tilde{R}_{Ep^f}^{\text{gp}}(\delta p^f; p^f) = \int_{P_{E\text{gp}}^n} dP \left[\left[\frac{\partial \delta p^f}{\partial z_i} \right]_{\text{gp}} \tilde{n}_{Ei}^{\text{gp}} \eta_{p^f}^{\text{gp}} \left[\left[\frac{\partial p^f}{\partial z_j} \right]_{\text{gp}} \tilde{n}_{Ej}^{\text{gp}} \right]. \quad (7.24)$$

The definition of the penalty factors in (7.20) - (7.24) is identical to the settings using the XFEM and the time stepping scheme; see (6.65) - (6.69).

7.3 Numerical Implementation

This section focuses on the numerical implementation of the finite element discretization for the Lagrangian-immersed FSI method using the space-time XFEM described above. This section also assumes spatially two-dimensional cases and the plane strain model. For the fundamental concept and implementation of the space-time XFEM, the reader is referred to Chapter 3.

7.3.1 Space-Time Slab for Lagrangian-Immersed FSI Method

In the Lagrangian-immersed FSI method using the XFEM and the time stepping scheme (Chapter 6), solid and fluid domains are spatially separate into different systems; the Lagrangian spatial domain Ω_L and the Eulerian spatial domain Ω_E . Similarly, the Lagrangian-immersed FSI method using the space-time XFEM uses separate space-time slabs; the Lagrangian space-time slab Q_L^n and the Eulerian space-time slab Q_E^n defined between t_+^n and t_-^{n+1} . Figure 7.2 shows an undeformed Lagrangian space-time slab Q_{L0}^n and Q_E^n , along with the summary of notation for volumes and interfaces assuming a two-phase case (phase 1 and 2). P_{L0-int}^n is an undeformed Lagrangian interface that is always perpendicular to the spatial domain (x - y plane) in the initial configuration. The elementwise temporal layer approach is applied to both the undeformed Lagrangian and Eulerian slabs: Q_{L0}^n and Q_E^n .

7.3.2 Integration Schemes for Volume and Standard Interface

Volume integration points in Q_{L0}^n and Q_E^n are set in each temporal slice defined by the elementwise temporal layer approach. On standard interfaces (matching interfaces), which is used for the standard boundary integral within one space-time slab, its integration points are defined independently from temporal layers. A detailed discussion of the setting of integration points and corresponding weights in the volume and on the standard interfaces is summarized in Sections 3.4.2 and 3.4.3.

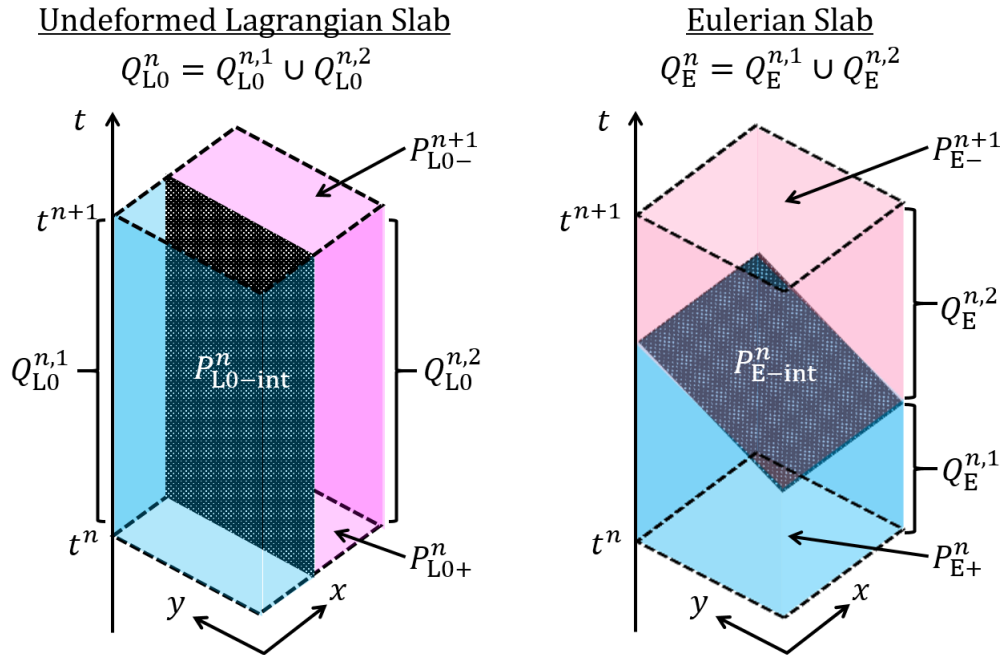


Figure 7.2: Lagrangian and Eulerian space-time slabs

7.3.3 Integration Schemes for Face-Oriented Ghost-Penalty Method

Integration points for the face-oriented ghost-penalty method using the space-time XFEM are defined on the faces of intersected space-time elements. P_{Lgp0}^n is the face of a space-time intersected element in the undeformed Lagrangian slab. P_{Egp}^n is the face of a space-time intersected element in the Eulerian slab. Figure 7.3 shows an example of integration points for the face-oriented ghost-penalty method between two adjacent space-time elements. A detailed discussion about the face-oriented ghost-penalty method for the space-time XFEM is summarized in Section 3.4.4.

7.3.4 Pairing of Integration Points on Non-Matching Space-Time Interfaces for FSI

The Lagrangian-immersed FSI method integrates the weak form of the coupling conditions over non-matching interfaces for FSI. In the Lagrangian-immersed FSI method using the XFEM with a time stepping scheme discussed in Chapter 6, the master-slave concept is

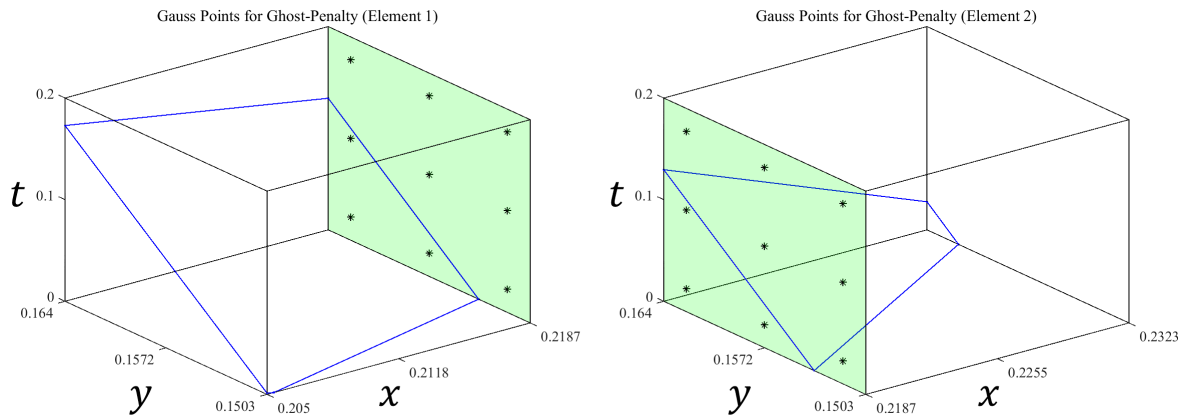


Figure 7.3: Space-time integration points for face-oriented ghost-penalty stabilization

applied. The Eulerian interface Γ_E is the master side and the deformed Lagrangian interface Γ_L is the slave side. The node-to-surface (NTS) pairing is used to define pairs of integration points on separate interfaces for FSI and the following gap equation governs the location of the pairs of the master (Eulerian) integration point \mathbf{x}_E and the slave (Lagrangian) integration point $\mathbf{x}_L = \mathbf{X}_L + \mathbf{U}_L^s$:

$$x_{Ei} + g_n n_{Ei}(\phi_E) - X_{Li} - U_{Li}^s(\mathbf{X}_L) = 0, \quad (7.25)$$

where \mathbf{n}_E is the Eulerian spatial normal and this NTS pairing is performed in the current configuration (between spatial interfaces; Γ_E and Γ_L). The master-slave concept and the NTS pairing are applied to the FSI interface integrals between non-matching space-time interfaces: the Eulerian space-time interface P_{E-int}^n and the deformed Lagrangian space-time interface P_{L-int}^n . As the traction boundary condition and the continuity condition of velocity are purely spatial conditions and instantaneous in time, the NTS pairing of the master and slave integration points for the space-time XFEM is performed by the same manner as the one for the XFEM with a time stepping scheme. Hence, (7.25) can be directly used in the space-time XFEM. The normal in the NTS pairing condition (7.25) for the space-time XFEM should be the Eulerian spatial normal \mathbf{n}_E , not the Eulerian space-time normal $\tilde{\mathbf{n}}_E$ which contains not only spatial components but also temporal component.

Figure 7.4 shows an example of the NTS pairing of integration points on non-matching interfaces P_{E-int}^n and P_{L-int}^n at an intermediate step of the Newton iteration. This figure assumes the case of a spatially circular Lagrangian structure surrounded by the Eulerian fluid. The cylinder moves to downward in y direction due to a body force. First, the intersections are detected and the Delaunay triangulation is performed in both interfaces; P_{E-int}^n and P_{L-int}^n . Blue lines show the triangulation of the Eulerian space-time interface and red lines show the triangulation of the deformed Lagrangian space-time interface. As this figure is at an intermediate step (larger than 1 step) of the Newton iteration, both interfaces are tilting in time due to the motion of the deformed solid structure. Then, the master integration points on the Eulerian interface P_{E-int}^n are defined on each Delaunay triangle by the quadrature rule and represented by blue circles in Figure 7.4. Finally, the NTS pairing is performed for each master (Eulerian) integration point onto a corresponding slave (Lagrangian) integrations point. The slave integration points on the Lagrangian interface P_{L-int}^n are represented by red asterisks in Figure 7.4.

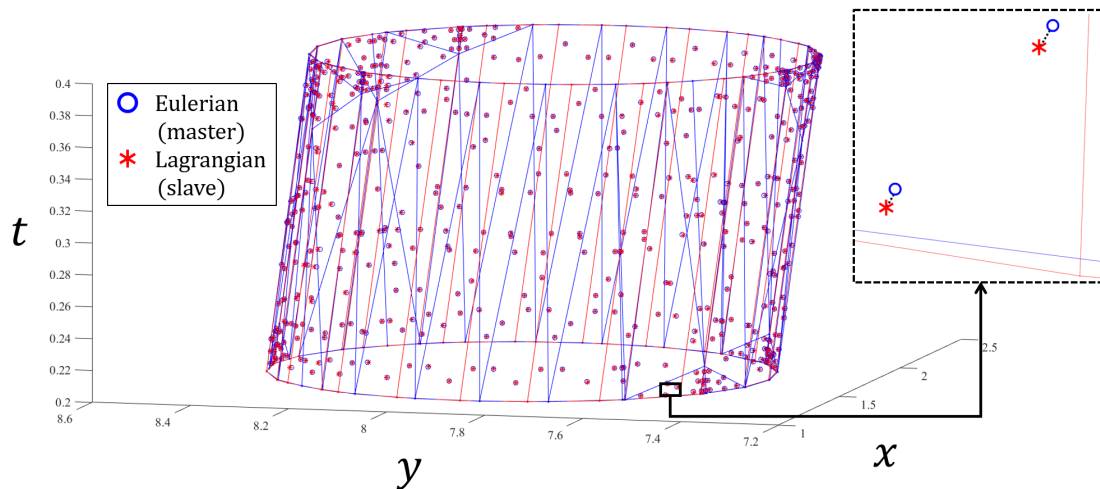


Figure 7.4: Node-to-surface (NTS) pairing between non-matching space-time interfaces (○: master (Eulerian) integration points, *: slave (Lagrangian) integration points) (intermediate step of the Newton iteration)

7.3.5 Contact Formulation for Space-Time XFEM

The stabilized Lagrange multiplier method is used to weakly enforce frictionless contact in this research. As Section 7.2 describes, the weak form of the stabilized Lagrange multiplier method for the space-time XFEM is as follows:

$$\tilde{R}_c^s = \int_{P_{c0}^n} dP \delta g_n^0 \lambda^0, \quad (7.26)$$

$$\tilde{R}_\lambda^s = \int_{P_{c0}^n} dP \delta \lambda^0 (\lambda^0 - \tilde{\lambda}^0 - \gamma_c g_n^0). \quad (7.27)$$

These equations are extensions of the stabilized Lagrange multiplier method using the XFEM with a spatial contact interface Γ_{c0} being converted into the space-time contact interface P_{c0} . The key point of the space-time contact formulation is the integration scheme between space-time contact interfaces. The contact condition is enforced between two Lagrangian space-time interfaces in the initial configuration. P_{c0-m}^n is the master (Lagrangian) space-time contact interface in the initial configuration and equivalent to the notation of P_{c0}^n , which is actually used for the integrals of the contact formulation. P_{c0-s}^n is the slave (Lagrangian) space-time contact interface in the initial configuration. Figure 7.5 shows the master and slave space-time elements, and their contact interfaces; P_{c0-m}^n and P_{c0-s}^n .

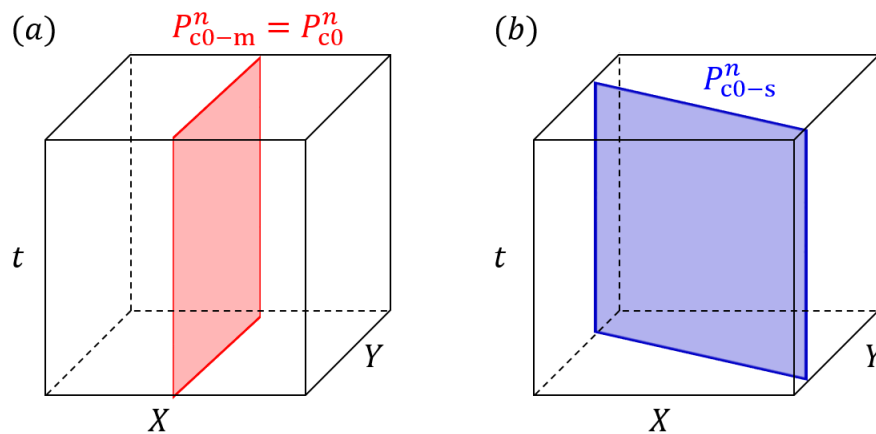


Figure 7.5: Space-time contact interfaces (undeformed configuration)
 (a). master space-time element, (b). slave space-time element

While the contact integrals (7.26) and (7.27) are evaluated in the initial configuration, the evaluation of the contact condition is performed in the current configuration. Figure 7.6 shows an image of contact interfaces in the current configuration. In Figure 7.6, two Lagrangian interfaces are separate at the lower bound in time; t_+^n , and penetrate each other at the upper bound in time; t_-^{n+1} .

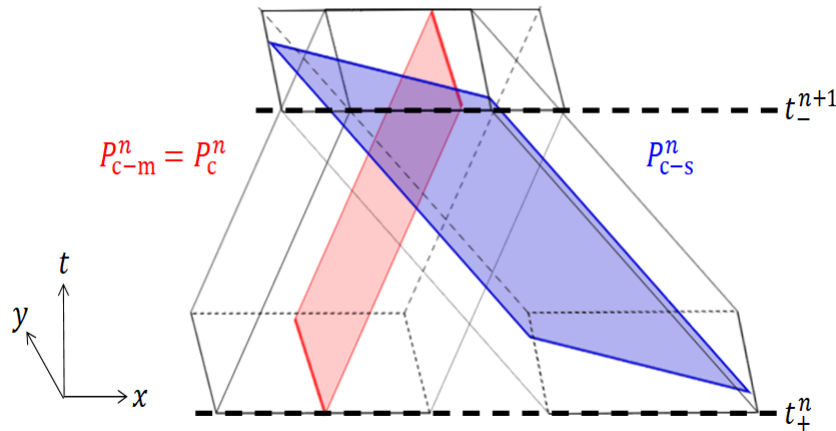


Figure 7.6: Space-time contact interfaces (deformed configuration) (before performing contact formulation)

The purpose of the contact formulation is obviously to avoid the penetration of contact interfaces. As state variables are defined at the lower temporal bound t_+^n and the upper temporal bound t_-^{n+1} , the penetration at t_+^n and t_-^{n+1} must be avoided. Therefore, the setting of integration points for space-time contact is the key to suppress penetration at t_+^n and t_-^{n+1} . Figure 7.7 is a comparison of two settings of integration points for the space-time contact formulation. Black circles represent integration points for the space-time contact formulation. In Figure 7.7 (a), the integration points are placed like the FSI interface integrals described in Section 7.3.4. In this case, the integration points are located between t_+^n and t_-^{n+1} . The contact condition is evaluated on these points and thus, the perfect condition of the contact formulation is not guaranteed at t_+^n and t_-^{n+1} because there is no evaluation point on lines of t_+^n and t_-^{n+1} . On the other hand, the placement in Figure 7.7 (b) is a setting like the standard spatial contact formulation used in the XFEM. The integration points are located

only on the upper and lower bound in time: t_+^n and t_-^{n+1} .

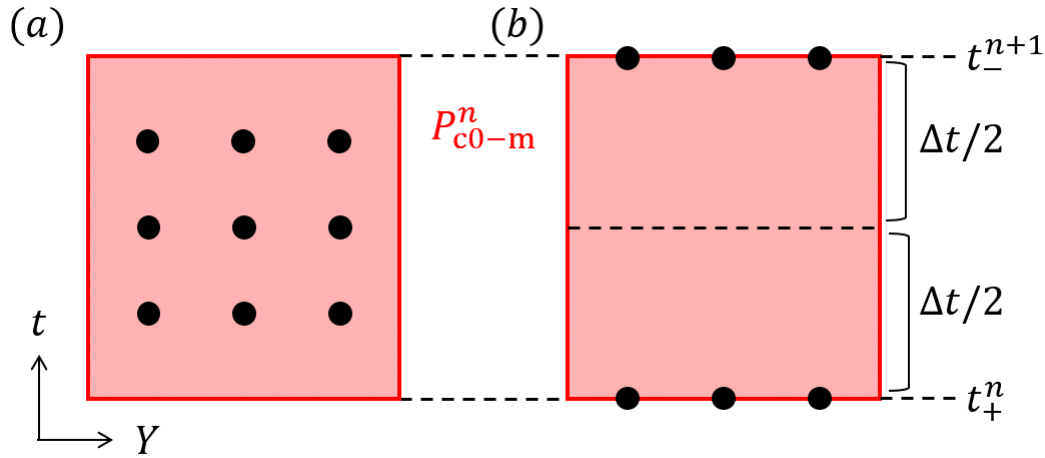


Figure 7.7: Setting of integration points for space-time contact (master interface P_{c0-m}^n)
 (a). Setting like FSI interface integral, (b). Setting like standard contact formulation

An additional benefit of Figure 7.7 (b) is that the conventional contact formulation used in the standard XFEM is directly applicable to the space-time XFEM. Contact integrals at t_+^n and t_-^{n+1} can be computed independently. Thus, (7.26) is described by only spatial boundary integrals in this case, even if when the space-time XFEM is used:

$$\begin{aligned} \tilde{R}_c^s &= \int_{P_{c0}^n} dP \delta g_n^0 \lambda^0 \\ &= \int_{t_+^n}^{t_-^{n+1}} dt \int_{\Gamma_{c0}} d\Gamma \delta g_n^0 \lambda^0 \\ &\simeq \frac{\Delta t}{2} \int_{\Gamma_{c0+}^n} d\Gamma \delta g_n^0 \lambda^0 + \frac{\Delta t}{2} \int_{\Gamma_{c0-}^{n+1}} d\Gamma \delta g_n^0 \lambda^0 \end{aligned} \quad (7.28)$$

$$\simeq \frac{\Delta t}{2} \int_{\Gamma_{c0+}^n} d\Gamma \delta g_n^0 \lambda_1^0 + \frac{\Delta t}{2} \int_{\Gamma_{c0-}^{n+1}} d\Gamma \delta g_n^0 \lambda_2^0 . \quad (7.29)$$

The weak form for contact \tilde{R}_c^s is simplified like (7.28) as the summation of spatial boundary integrals on Γ_{c0+}^n and Γ_{c0-}^{n+1} which indicate spatial contact interfaces at t_+^n and t_-^{n+1} , respectively (lower and upper lines of Figure 7.7 (b)). As the contact integrals are computed based on the total Lagrangian formulation, i.e. the initial configuration, the space-time contact

interfaces $P_{c0}^n = P_{c0-m}^n$ are always perpendicular to the spatial domain. Hence, temporal and spatial integrals can be divided explicitly as shown in (7.28). In (7.29), different Lagrange multipliers are introduced at t_+^n and t_-^{n+1} . λ_1^0 and λ_2^0 are Lagrange multipliers of the stabilized Lagrangian contact formulation at t_+^n and t_-^{n+1} , respectively. Each integral of (7.29) is identical to the stabilized Lagrangian multiplier method for contact using the standard XFEM. In addition, the way to detect slave integration points based on the master-slave concept is also identical to the method for the XFEM described in Section 6.2.4.

To compute (7.29), the constraint equation of the stabilized Lagrange multiplier method (7.27) is split into two integrals at t_+^n and t_-^{n+1} using two Lagrange multipliers λ_1^0 and λ_2^0 :

$$\tilde{R}_{\lambda_1}^s = \frac{\Delta t}{2} \int_{\Gamma_{c0+}^n} d\Gamma \delta\lambda_1^0 (\lambda_1^0 - \tilde{\lambda}_1^0 - \gamma_c g_n^0), \quad (7.30)$$

$$\tilde{R}_{\lambda_2}^s = \frac{\Delta t}{2} \int_{\Gamma_{c0-}^{n+1}} d\Gamma \delta\lambda_2^0 (\lambda_2^0 - \tilde{\lambda}_2^0 - \gamma_c g_n^0), \quad (7.31)$$

where $\tilde{\lambda}_1^0$ and $\tilde{\lambda}_2^0$ are weighted averages of the surface traction along the normal direction at t_+^n and t_-^{n+1} , respectively. The definitions of $\tilde{\lambda}_1^0$ and $\tilde{\lambda}_2^0$ are identical to the one for the spatial contact formulation (6.27).

The space-time contact formulation based on the stabilized Lagrange multiplier method by (7.32) - (7.34) and Figure 7.8. The Detailed discussions in terms of the stabilized Lagrange multiplier method for the XFEM with a time stepping scheme are described in Appendix D:

$$\tilde{R}_c^s = \frac{\Delta t}{2} \int_{\Gamma_{c0+}^n} d\Gamma \delta g_n^0 \lambda_1^0 + \frac{\Delta t}{2} \int_{\Gamma_{c0-}^{n+1}} d\Gamma \delta g_n^0 \lambda_2^0, \quad (7.32)$$

$$\tilde{R}_{\lambda_1}^s = \frac{\Delta t}{2} \int_{\Gamma_{c0+}^n} d\Gamma \delta\lambda_1^0 (\lambda_1^0 - \tilde{\lambda}_1^0 - \gamma_c g_n^0), \quad (7.33)$$

$$\tilde{R}_{\lambda_2}^s = \frac{\Delta t}{2} \int_{\Gamma_{c0-}^{n+1}} d\Gamma \delta\lambda_2^0 (\lambda_2^0 - \tilde{\lambda}_2^0 - \gamma_c g_n^0). \quad (7.34)$$

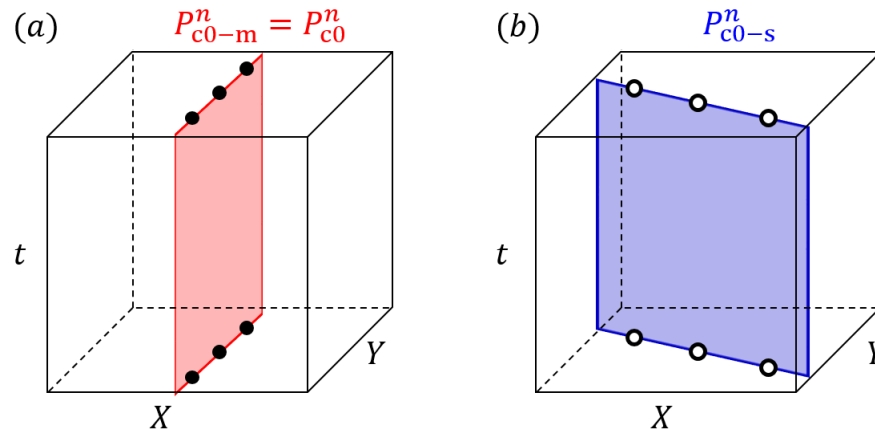


Figure 7.8: Space-time contact interfaces and integration points (undeformed configuration)
 (a). Master space-time element, (b). Slave space-time element
 (●: Master integration points, ○: Slave integration points)

7.3.6 Level Set Projection for Space-Time XFEM

This section presents the numerical implementation of the level set projection method for the space-time XFEM. The original variational form of the level set function is as follows:

$$\tilde{R}_\phi = \int_{Q_E^n} dQ \delta\phi f(\hat{\Phi})(\phi - \hat{\Phi}), \quad (7.35)$$

where ϕ is the level set function in the Eulerian space-time slab Q_E^n , $\hat{\Phi}$ is the level set function in the deformed configuration of the Lagrangian space-time slab Q_L^n and $f(\hat{\Phi})$ is a weighting function defined in (6.34).

Figure 7.9 illustrates the procedure of the level set projection method for the space-time XFEM. The red interface represents a Lagrangian interface in a Lagrangian space-time element. The blue interface represents an Eulerian interface in an Eulerian space-time element. These interfaces are implicitly defined by the nodal level set functions of the space-time elements. The deformed Lagrangian element is mapped from Q_{L0e}^n to Q_{Le}^n , and the level set projection is performed onto the Eulerian element Q_{Ee}^n .

In this research, the level set function at t_+^n in both the Lagrangian and Eulerian slabs is fixed, and the level set projection is performed only for t_-^{n+1} . There are two reasons for

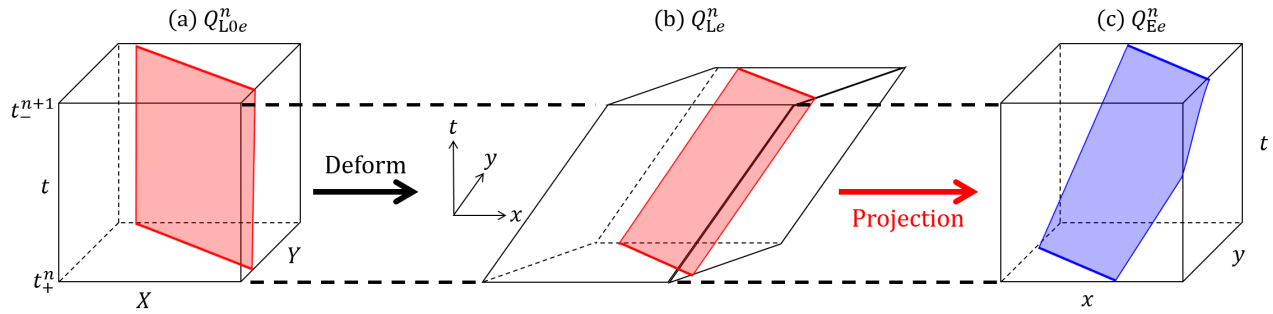


Figure 7.9: Level set projection for space-time XFEM

- (a) Undeformed Lagrangian space-time element Q_{L0e}^n
- (b) Deformed Lagrangian space-time element Q_{Le}^n
- (c) Eulerian space-time element Q_{Ee}^n

this approach. The main reason is related to the correction terms due to the discontinuous Galerkin method in time; see, for example; the last terms of (7.5) and (7.6), or the last lines of (7.10) and (7.13):

$$\text{e.g. in (7.13); } \int_{P_{E+}^{n,f}} d\Omega \delta v_i^f|_+^n \rho^f \llbracket v_i^f \rrbracket_{\pm} = \int_{P_{E+}^{n,f}} d\Omega \delta v_i^f|_+^n \rho^f \left(v_i^f|_+^n - v_i^f|_-^n \right), \quad (7.36)$$

where $\llbracket \cdot \rrbracket_{\pm}$ is the jump operator between t_+^n and t_-^n . In the discontinuous Galerkin method, state variables at the current space-time slab Q^n and the past space-time slab Q^{n-1} are discontinuous, but the continuity of state variables between t_+^n in Q^n and t_-^n in Q^{n-1} is enforced weakly through a correction term, such as (7.36). This term is an integral over the bottom face of the current space-time slab. To compute (7.36), the geometry at t_+^n and t_-^n should be identical and thus, the level set function at t_+^n in both the Lagrangian and Eulerian slabs is fixed as the level set function at t_-^n computed at the past space-time slab Q^{n-1} . The second reason to fix the level set function at t_+^n is that the linear interpolation along time is used for the level set function in the proposed space-time XFEM; see Chapter 3. Thereby, even if the level set function at t_+^n in both the Lagrangian and Eulerian slabs is fixed and the level set projection is performed only on the slice at t_-^{n+1} , the space-time interfaces are accurately created under the assumption of the linear interpolation along time.

The integration points for the level set projection method in the space-time XFEM are

distributed only on the spatial domain at t_-^{n+1} . The spatial domain at t_-^{n+1} in an Eulerian slab Q_E^n and a deformed Lagrangian slab Q_L^n are denoted as P_{E-}^{n+1} and P_{L-}^{n+1} respectively. Figure 7.10 illustrates the level set projection for the space-time XFEM. The level set projection method is only performed on green faces; i.e. spatial domains at t_-^{n+1} ; (P_{E-}^{n+1} and P_{L-}^{n+1}). Figure 7.11 is the detailed procedure of the level set projection method for the space-time XFEM in this research. The associated governing equation (7.35) is rewritten as an integral in the Eulerian spatial volume P_{E-}^{n+1} as follows:

$$\tilde{R}_\phi = \Delta t \int_{P_{E-}^{n+1}} d\Omega \delta\phi f(\hat{\Phi})(\phi - \hat{\Phi}) . \quad (7.37)$$

Another approach to compute the level set projection is the procedure similar to the contact formulation described in Section 7.3.5. In this case, the level set projection is performed at the upper and lower bounds. To guarantee the continuity of the level set function across space-time slabs, an additional treatment such as Nitsche's method is needed for its continuity condition. While this approach is not tested, a strong penalty factor might be needed when Nitsche's method is used. This is because the computation of (7.36) needs consistent spatial geometries between t_+^n and t_-^n .

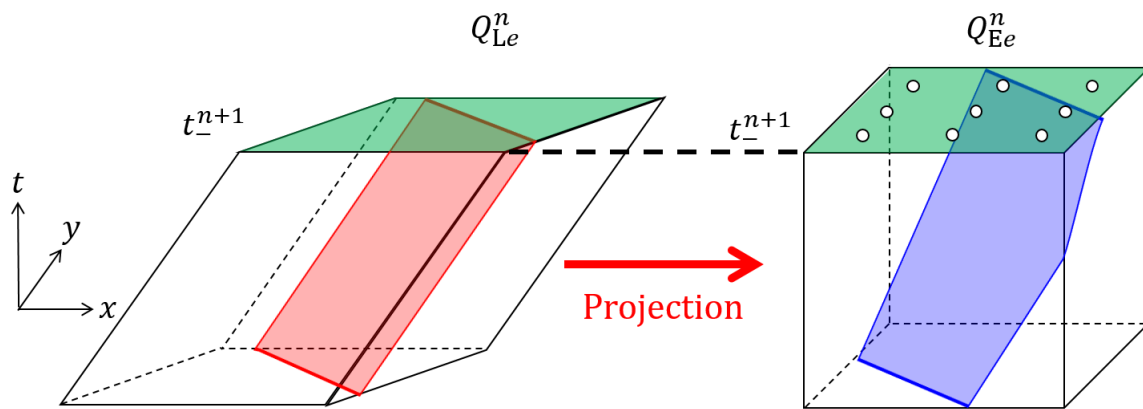
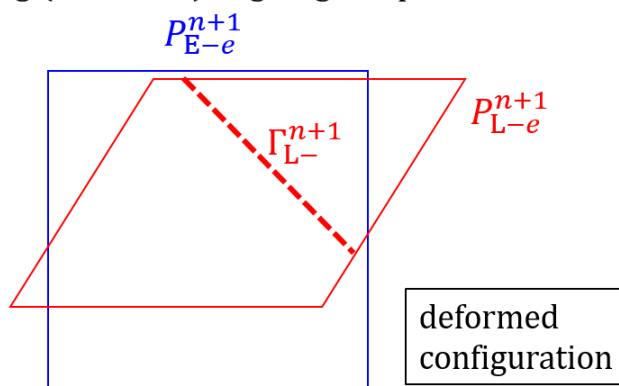
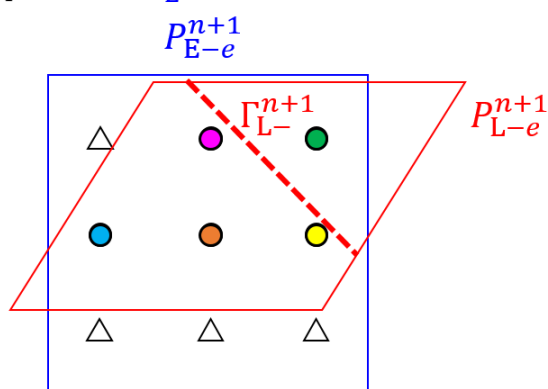


Figure 7.10: Level set projection performed at t_-^{n+1}
(green faces: spatial domain at t_-^{n+1} , \circ : Eulerian integration points)

Step1: Detect a pair of Eulerian spatial domain at t_-^{n+1} : P_{E-e}^{n+1} and overlapping (deformed) Lagrangian spatial domain at t_-^{n+1} : P_{L-e}^{n+1}



Step2: Set Gauss points on P_{E-e}^{n+1}



Step3: Perform the level set projection from P_{L-e}^{n+1} onto P_{E-e}^{n+1}
Determine Eulerian spatial interface at t_-^{n+1} : Γ_{E-}^{n+1}

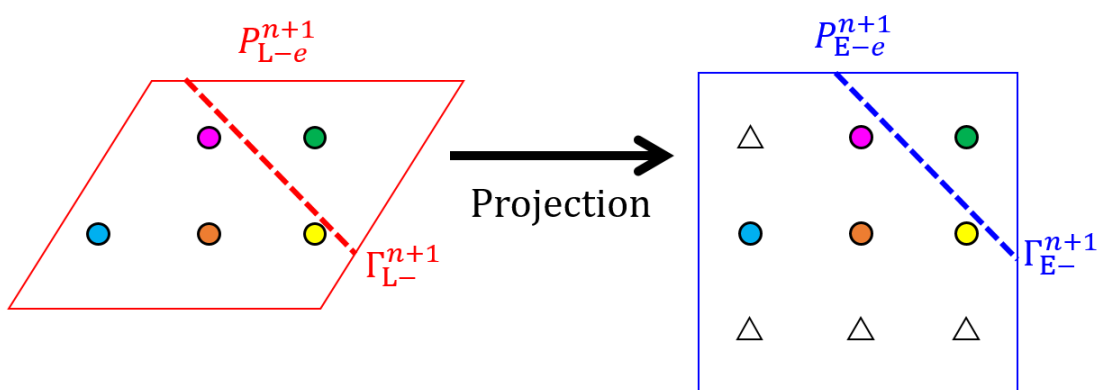


Figure 7.11: Procedure of level set projection for space-time XFEM
(colored circle: active integration points, Δ : inactive integration points)
(dashed lines: spatial interfaces at t_-^{n+1})

7.3.7 Structure of Dynamic Jacobian

The Jacobian (tangential stiffness) corresponding to the weak form (7.4) of the Lagrangian-immersed FSI method using the space-time XFEM is summarized subsequently. The global Jacobian \tilde{J} is decomposed into four block Jacobians as follows:

$$\tilde{J} = \frac{\partial \tilde{\mathbf{R}}}{\partial \tilde{\mathbf{u}}} = \begin{pmatrix} J_n^n & J_n^{n+1} \\ J_{n+1}^n & J_{n+1}^{n+1} \end{pmatrix}, \quad (7.38)$$

where $\tilde{\mathbf{u}}$ is the vector of all state variables including information at t_+^n and t_-^{n+1} . In each block Jacobian J_a^b , rows of J_a^b mean state variables at t^a and columns of J_a^b mean state variables at t^b . In the following discussion, contributions of the face-oriented ghost-penalty method are not shown.

The structure of a diagonal block Jacobian J_n^n is shown in Figure 7.12 ($t_+^n \otimes t_+^n$). As the level set projection is only performed at the upper bound t_-^{n+1} and ϕ is fixed at t_+^n , the contribution of ϕ : \tilde{R}_ϕ is omitted in J_n^n .

| | | Column (nodal values at t_+^n) | | | | | | |
|-----------|-----------------|--|--|--|--|--|--------------|--------------|
| | | \mathbf{v}^f | p^f | \mathbf{V}^s | \mathbf{U}^s | \mathbf{U}^d | ϕ | |
| $J_n^n =$ | Row (t_+^n) | \mathbf{v}^f | $\frac{\partial \tilde{\mathbf{R}}_m^f}{\partial \mathbf{v}^f} + \frac{\partial \tilde{\mathbf{R}}_E^{\text{fsi}}}{\partial \mathbf{v}^f}$ | $\frac{\partial \tilde{\mathbf{R}}_m^f}{\partial p^f} + \frac{\partial \tilde{\mathbf{R}}_E^{\text{fsi}}}{\partial p^f}$ | $\frac{\partial \tilde{\mathbf{R}}_E^{\text{fsi}}}{\partial \mathbf{V}^s}$ | $\frac{\partial \tilde{\mathbf{R}}_E^{\text{fsi}}}{\partial \mathbf{U}^s}$ | $\mathbf{0}$ | $\mathbf{0}$ |
| | p^f | $\mathbf{0}$ | $\mathbf{0}$ | $\frac{\partial \tilde{\mathbf{R}}_{uv}^s}{\partial \mathbf{V}^s}$ | $\frac{\partial \tilde{\mathbf{R}}_{uv}^s}{\partial \mathbf{U}^s}$ | $\mathbf{0}$ | $\mathbf{0}$ | |
| | \mathbf{V}^s | $\mathbf{0}$ | $\mathbf{0}$ | $\mathbf{0}$ | $\frac{\partial \tilde{\mathbf{R}}_m^s}{\partial \mathbf{U}^s} + \frac{\partial \tilde{\mathbf{R}}_c^s}{\partial \mathbf{U}^s} + \frac{\partial \tilde{\mathbf{R}}_L^{\text{fsi}}}{\partial \mathbf{U}^s}$ | $\mathbf{0}$ | $\mathbf{0}$ | |
| | \mathbf{U}^s | $\frac{\partial \tilde{\mathbf{R}}_L^{\text{fsi}}}{\partial \mathbf{v}^f}$ | $\frac{\partial \tilde{\mathbf{R}}_L^{\text{fsi}}}{\partial p^f}$ | $\frac{\partial \tilde{\mathbf{R}}_m^s}{\partial \mathbf{V}^s} + \frac{\partial \tilde{\mathbf{R}}_L^{\text{fsi}}}{\partial \mathbf{V}^s}$ | $\frac{\partial \tilde{\mathbf{R}}_u^d}{\partial \mathbf{U}^s}$ | $\frac{\partial \tilde{\mathbf{R}}_u^d}{\partial \mathbf{U}^d}$ | $\mathbf{0}$ | $\mathbf{0}$ |
| | \mathbf{U}^d | $\mathbf{0}$ | $\mathbf{0}$ | $\mathbf{0}$ | $\mathbf{0}$ | $\mathbf{0}$ | $\mathbf{0}$ | $\mathbf{0}$ |
| | ϕ | $\mathbf{0}$ | $\mathbf{0}$ | $\mathbf{0}$ | $\mathbf{0}$ | $\mathbf{0}$ | $\mathbf{0}$ | $\mathbf{0}$ |

Figure 7.12: Broad structure of diagonal block Jacobian ($J_n^n: t_+^n \otimes t_+^n$)

J_{n+1}^{n+1} is another diagonal block Jacobian at time t_-^{n+1} ($t_-^{n+1} \otimes t_-^{n+1}$). Figure 7.13 shows the structure of J_{n+1}^{n+1} . In this block Jacobian, contributions of the level set function ϕ (blue and red terms) exist. Like the Lagrangian-immersed FSI method using the XFEM (Section

6.5.1), the post level set projection is also applied when the norm of the residual relative to the initial residual is larger than 10^{-1} . Blue terms are omitted when the post level set projection is applied like Section 6.5.2.

| | | Column (nodal values at t_-^{n+1}) | | | | | |
|-------------------|----------|---|---|---|---|---|---|
| | | v^f | p^f | V^s | U^s | U^d | ϕ |
| $J_{n+1}^{n+1} =$ | v^f | $\frac{\partial \tilde{R}_m^f}{\partial v^f} + \frac{\partial \tilde{R}_E^{fsi}}{\partial v^f}$ | $\frac{\partial \tilde{R}_m^f}{\partial p^f} + \frac{\partial \tilde{R}_E^{fsi}}{\partial p^f}$ | $\frac{\partial \tilde{R}_E^{fsi}}{\partial V^s}$ | $\frac{\partial \tilde{R}_E^{fsi}}{\partial U^s}$ | 0 | $\frac{\partial \tilde{R}_m^f}{\partial \phi} + \frac{\partial \tilde{R}_E^{fsi}}{\partial \phi}$ |
| | p^f | | | | | | |
| | V^s | 0 | 0 | $\frac{\partial \tilde{R}_{uv}^s}{\partial V^s}$ | $\frac{\partial \tilde{R}_{uv}^s}{\partial U^s}$ | 0 | 0 |
| | U^s | $\frac{\partial \tilde{R}_L^{fsi}}{\partial v^f}$ | $\frac{\partial \tilde{R}_L^{fsi}}{\partial p^f}$ | $\frac{\partial \tilde{R}_m^s}{\partial V^s} + \frac{\partial \tilde{R}_L^{fsi}}{\partial V^s}$ | $\frac{\partial \tilde{R}_m^s}{\partial U^s} + \frac{\partial \tilde{R}_c^s}{\partial U^s} + \frac{\partial \tilde{R}_L^{fsi}}{\partial U^s}$ | 0 | $\frac{\partial \tilde{R}_L^{fsi}}{\partial \phi}$ |
| | U^d | 0 | 0 | 0 | $\frac{\partial \tilde{R}_u^d}{\partial U^s}$ | $\frac{\partial \tilde{R}_u^d}{\partial U^d}$ | 0 |
| ϕ | 0 | 0 | 0 | $\frac{\partial \tilde{R}_\phi}{\partial U^s}$ | $\frac{\partial \tilde{R}_\phi}{\partial U^d}$ | $\frac{\partial \tilde{R}_\phi}{\partial \phi}$ | |

Figure 7.13: Broad structure of diagonal block Jacobian ($J_{n+1}^{n+1}: t_-^{n+1} \otimes t_-^{n+1}$)

Figure 7.14 shows the structure of an off-diagonal block Jacobian $J_n^{n+1} (t_+^n \otimes t_-^{n+1})$. As the level set function is variable only at t_-^{n+1} and the contact formulation \tilde{R}_c^s is only defined on diagonal block Jacobians based on (7.29), J_n^{n+1} has simple structure. Another off-diagonal block Jacobian $J_{n+1}^n (t_-^{n+1} \otimes t_+^n)$ also has similar structure like Figure 7.14.

| | | Column (nodal values at t_-^{n+1}) | | | | | |
|---------------|----------|---|---|---|---|---|----------|
| | | v^f | p^f | V^s | U^s | U^d | ϕ |
| $J_n^{n+1} =$ | v^f | $\frac{\partial \tilde{R}_m^f}{\partial v^f} + \frac{\partial \tilde{R}_E^{fsi}}{\partial v^f}$ | $\frac{\partial \tilde{R}_m^f}{\partial p^f} + \frac{\partial \tilde{R}_E^{fsi}}{\partial p^f}$ | $\frac{\partial \tilde{R}_E^{fsi}}{\partial V^s}$ | $\frac{\partial \tilde{R}_E^{fsi}}{\partial U^s}$ | 0 | 0 |
| | p^f | | | | | | |
| | V^s | 0 | 0 | $\frac{\partial \tilde{R}_{uv}^s}{\partial V^s}$ | $\frac{\partial \tilde{R}_{uv}^s}{\partial U^s}$ | 0 | 0 |
| | U^s | $\frac{\partial \tilde{R}_L^{fsi}}{\partial v^f}$ | $\frac{\partial \tilde{R}_L^{fsi}}{\partial p^f}$ | $\frac{\partial \tilde{R}_m^s}{\partial V^s} + \frac{\partial \tilde{R}_L^{fsi}}{\partial V^s}$ | $\frac{\partial \tilde{R}_m^s}{\partial U^s} + \frac{\partial \tilde{R}_L^{fsi}}{\partial U^s}$ | 0 | 0 |
| | U^d | 0 | 0 | 0 | $\frac{\partial \tilde{R}_u^d}{\partial U^s}$ | $\frac{\partial \tilde{R}_u^d}{\partial U^d}$ | 0 |
| ϕ | 0 | 0 | 0 | 0 | 0 | 0 | |

Figure 7.14: Broad structure of off-diagonal block Jacobian ($J_n^{n+1}: t_+^n \otimes t_-^{n+1}$)

7.4 Numerical Examples

This section studies numerical examples of the Lagrangian-immersed FSI method using the space-time XFEM. These are spatially two-dimensional transient FSI problems. The fluid phase is modeled by the incompressible Navier-Stokes (INS) equations. In the solid phase, the plane strain case is assumed. The first numerical example is a falling circular cylinder due to a body force surrounded by fluid. This example demonstrates the stability and accuracy of the Lagrangian-immersed FSI method using the space-time XFEM in the presence of large deformations. The second numerical example is the well-known Turek-Hron FSI3 benchmark problem proposed by Turek and Hron [111]. This example demonstrates the applicability of the proposed analysis method for problems with higher Reynolds number. The third numerical example is a transient FSI-contact problem revising the fourth problem of Section 6.6.4. The geometry and material parameters are the same as the one of the problem in Section 6.6.4. This numerical example shows the ability to simulate multiphase contact problems using the space-time formulation. In these numerical examples, following materials are used:

St. Venant-Kirchhoff Material

$$W^s = \frac{1}{2} \lambda^s (\text{Tr}(E^s))^2 + \mu^s \text{Tr}(E^{s2}) , \quad (7.39)$$

$$S_{IJ}^s = \frac{\partial W}{\partial E_{IJ}^s} = \lambda^s \text{Tr}(E^s) \delta_{IJ} + 2\mu^s E_{IJ}^s , \quad (7.40)$$

Neo-Hookean Material (Belytschko et al. [107])

$$W^s = \frac{1}{2} \lambda^s (\ln(\det F^s))^2 + \frac{1}{2} \mu^s (\text{Tr}(C^s) - 3) - \mu^s \ln(\det F^s) , \quad (7.41)$$

$$S_{IJ}^s = 2 \frac{\partial W}{\partial C_{IJ}^s} = (\lambda^s \ln(\det F^s) - \mu^s) C_{IJ}^{s-1} + \mu^s \delta_{IJ} . \quad (7.42)$$

Here, W^s is the hyperelastic function, F^s is the deformation gradient tensor, C^s is the right Cauchy-Green tensor; $C^s = F^{sT} F^s$, E^s is the Green-Lagrange strain tensor; $E^s = (C^s - I)/2$,

and S^s is the second Piola-Kirchhoff stress tensor. λ^s and μ^s are the Lamé's constants defined as follows:

$$\lambda^s = \frac{\nu^s}{(1 + \nu^s)(1 - 2\nu^s)} E^s, \quad (7.43)$$

$$\mu^s = \frac{1}{2(1 + \nu^s)} E^s, \quad (7.44)$$

where E^s is the Young's modulus and ν^s is the Poisson's ratio.

7.4.1 Falling Circular Cylinder due to Body Force

The first numerical example is a falling circular cylinder due to a body force immersed in fluid. The cylinder has a radius of $r = 0.509\text{m}$ and its centroid in the initial configuration is at $\mathbf{X}_c = (1.73, 8.00)\text{m}$. This cylinder is made by a compressible neo-Hookean material. The body force is applied only in y -direction. Figures 7.15 and 7.16 show the undeformed Lagrangian domain Ω_{L0} and the Eulerian domain Ω_E , respectively. No-slip boundary conditions are applied on the outer edges Γ_{noslip} of Ω_E . The two-dimensional circular cylinder is immersed in Ω_E by the level set projection method and the Eulerian interface Γ_E is created. The geometry and material parameters are summarized in Table 7.2.

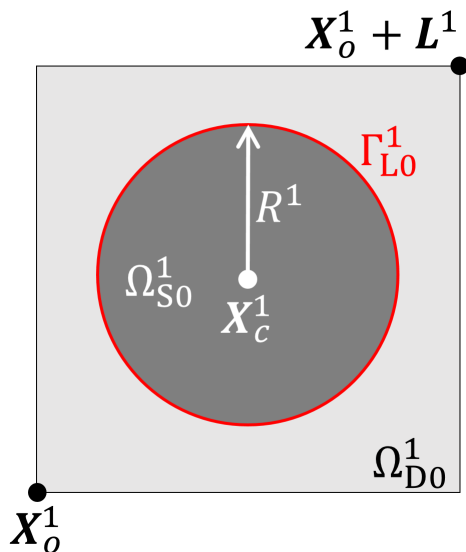


Figure 7.15: Lagrangian system: Ω_{L0}

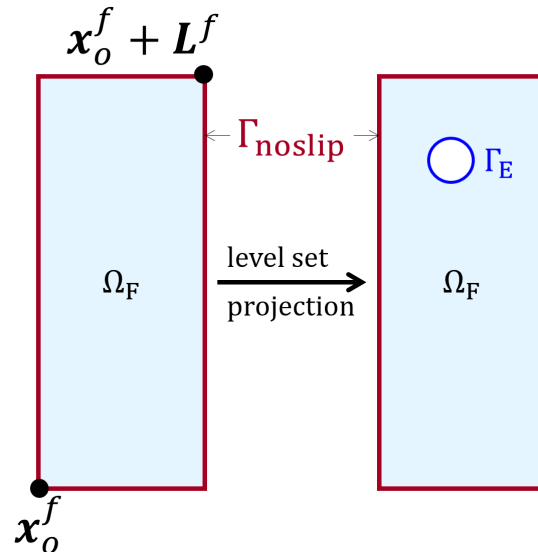


Figure 7.16: Eulerian system: Ω_E

Table 7.2: Geometrical and material parameters for falling cylinder

| Domain | Description | Parameter |
|--------|----------------------|---|
| Solid | origin | $\mathbf{X}_o^1 = (0.8, 7.07)\text{m}$ |
| | system size | $\mathbf{L}^1 = (1.87, 1.87)\text{m}$ |
| | centroid | $\mathbf{X}_c^1 = (1.73, 8)\text{m}$ |
| | radius of cylinder | $R^1 = 0.509\text{m}$ |
| | density | $\rho^s = 1000\text{kg/m}^3$ |
| | Young's modulus | $E^s = 1\text{MPa}$ |
| | Poisson's ratio | $\nu^s = 0.4$ |
| | artificial viscosity | $\alpha^s = 0\text{s}^{-1}$ |
| | body force | $\mathbf{B}^s = (0, -1)\text{m/s}^2$ |
| | initial velocity | $\mathbf{V}_{\text{ini}}^s = (0, -1)\text{m/s}$ |
| Fluid | origin | $\mathbf{x}_o^f = (0, 0)\text{m}$ |
| | system size | $\mathbf{L}^f = (4, 10)\text{m}$ |
| | density | $\rho^f = 1000\text{kg/m}^3$ |
| | kinematic viscosity | $\nu^f = 10^{-2}\text{m}^2/\text{s}$ |
| | body force | $\mathbf{b}^f = (0, 0)\text{m/s}^2$ |
| | initial velocity | $\mathbf{v}_{\text{ini}}^f$: random in $[-10^{-5}, 10^{-5}]\text{m/s}$ |

The weak form of this example does not contain the contribution of the contact \tilde{R}_c^s :

$$\begin{aligned}
& \tilde{R}_m^s(\delta\mathbf{U}^s; \{\mathbf{U}^s, \mathbf{V}^s\}) + \tilde{R}_{uv}^s(\delta\mathbf{V}^s; \{\mathbf{U}^s, \mathbf{V}^s\}) + \tilde{R}_u^d(\delta\mathbf{U}^d; \{\mathbf{U}^s, \mathbf{U}^d\}) \\
& + \tilde{R}_m^f(\{\delta\mathbf{v}^f, \delta p^f\}; \{\mathbf{v}^f, p^f\}) + \tilde{R}_\phi(\delta\phi; \{\phi, \hat{\Phi}\}) \\
& + \tilde{R}_L^{\text{fsi}}(\delta\mathbf{U}^s; \{\mathbf{U}^s, \mathbf{V}^s, \mathbf{v}^f, p^f\}) + \tilde{R}_E^{\text{fsi}}(\{\delta\mathbf{v}^f, \delta p^f\}; \{\mathbf{U}^s, \mathbf{V}^s, \mathbf{v}^f, p^f\}) \\
& + \tilde{R}_L^{\text{gp}}(\{\delta\mathbf{U}^s, \delta\mathbf{V}^s, \delta\mathbf{U}^d\}; \{\mathbf{U}^s, \mathbf{V}^s, \mathbf{U}^d\}) + \tilde{R}_E^{\text{gp}}(\{\delta\mathbf{v}^f, \delta p^f\}; \{\mathbf{v}^f, p^f\}) = 0 . \quad (7.45)
\end{aligned}$$

Details of each residual are summarized in Section 7.2. In this example, the Helmholtz smoothing method (7.7) is used as the residual for the dummy displacement domain; \tilde{R}_u^d , because the rigid body rotation of the cylinder is small. The penalty factors of Nitsche's method for the FSI contributions; \tilde{R}_L^{fsi} and \tilde{R}_E^{fsi} , Nitsche's method for the dummy displacement domain in \tilde{R}_u^d and the face-oriented ghost-penalty method in \tilde{R}_L^{gp} and \tilde{R}_E^{gp} are summarized in Table 7.3.

Three temporal slices are defined in each temporal layer. Newton's method with a direct linear solver is used and the convergence criterion requires a drop of the norm of the residual

Table 7.3: Penalty coefficients for falling cylinder using space-time XFEM

| Method | Penalty Coefficients |
|---|---|
| Nitsche's method for FSI | $\eta^{\text{fsi}} = \alpha^{\text{fsi}} E^s$, $\alpha^{\text{fsi}} = 0.1\text{s/m}$ |
| Nitsche's method for dummy-displacement | $\eta^d = \alpha^d E^s$, $\alpha^d = 20\text{m}^{-1}$ |
| face-oriented ghost-penalty method | $\alpha_{U^s}^{\text{gp}} = \alpha_{U^d}^{\text{gp}} = \alpha_{V^s}^{\text{gp}} = \alpha_{v^f}^{\text{gp}} = 0.05$, $\alpha_{p^f}^{\text{gp}} = 0.005$ |

of 5×10^{-4} relative to the norm of the initial residual.

Figures 7.17 - 7.21 give time histories of the simulation using the Lagrangian-immersed FSI method with the space-time XFEM. The sizes of the spatial and temporal discretization are $h = 1/11\text{m} = 0.009\text{m}$ and $\Delta t = 0.2/3\text{s} = 0.067\text{s}$, respectively. Figures 7.17 and 7.18 are velocity distributions of the solid and fluid phase. The meshed region marks the solid cylinder. Figures 7.19 and 7.20 shows the fluid pressure p^f and the fluid in-line effective shear stress q^f defined by principal stresses: $q^f = |\sigma_1^f - \sigma_2^f|$. Figure 7.21 shows the history of the deformed Lagrangian system Ω_L colored by the displacement U_x^s in x direction. The yellow circles represent the Lagrangian interface and the region outside of this interface is the dummy displacement domain Ω_D . Figures 6.54 - 6.56 in Section 6.6.4 show the results of the same problem when the Lagrangian-immersed FSI method with the XFEM using and time stepping scheme was used, using $h = 1/11\text{m}$ and $\Delta t = 0.2/3\text{s}$. This approach diverged due to the numerical interpolation errors and incorrect approximation of time derivatives caused by the moving interface. On the other hand, the Lagrangian-immersed FSI using the space-time XFEM predicts smooth state variable fields; no oscillations are observed.

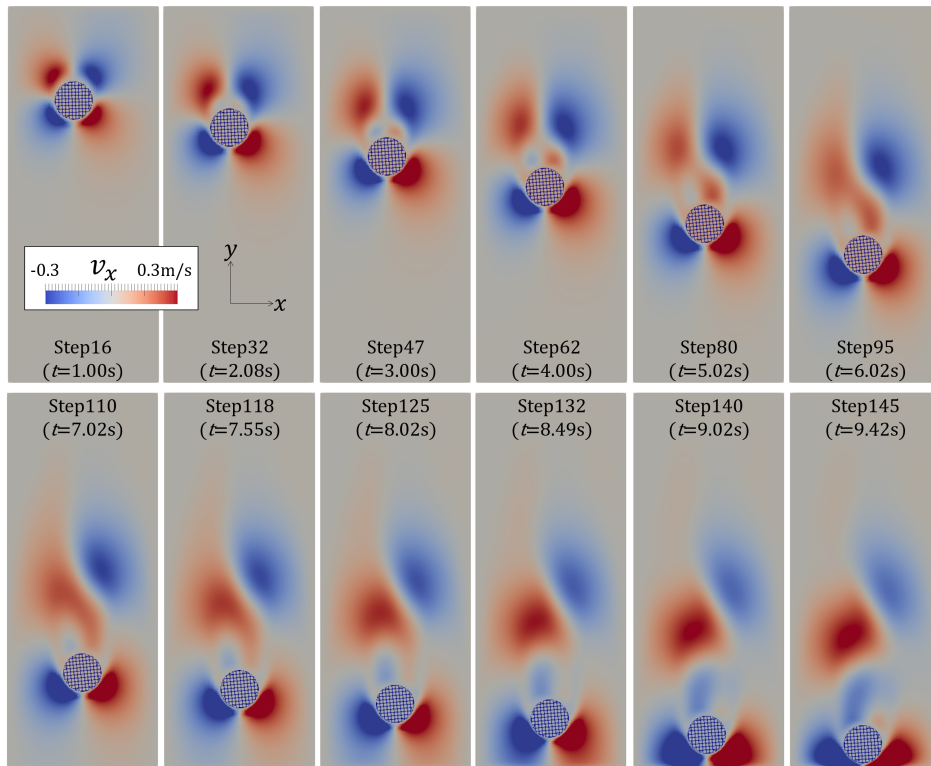


Figure 7.17: History of v_x (Lagrangian-immersed FSI using space-time XFEM)

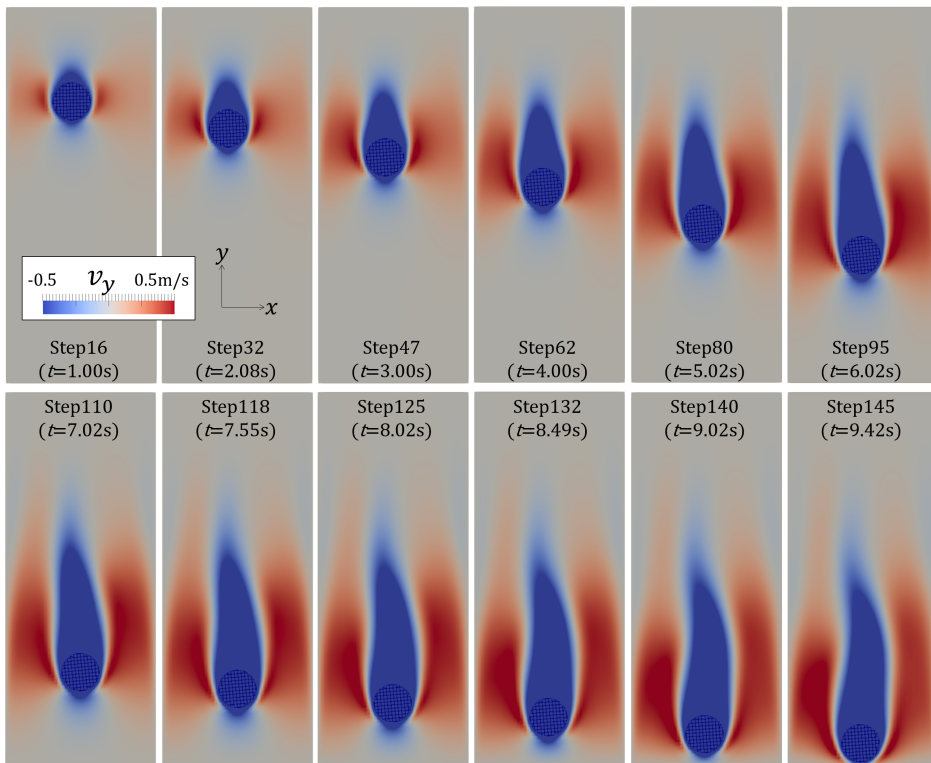


Figure 7.18: History of v_y (Lagrangian-immersed FSI using space-time XFEM)

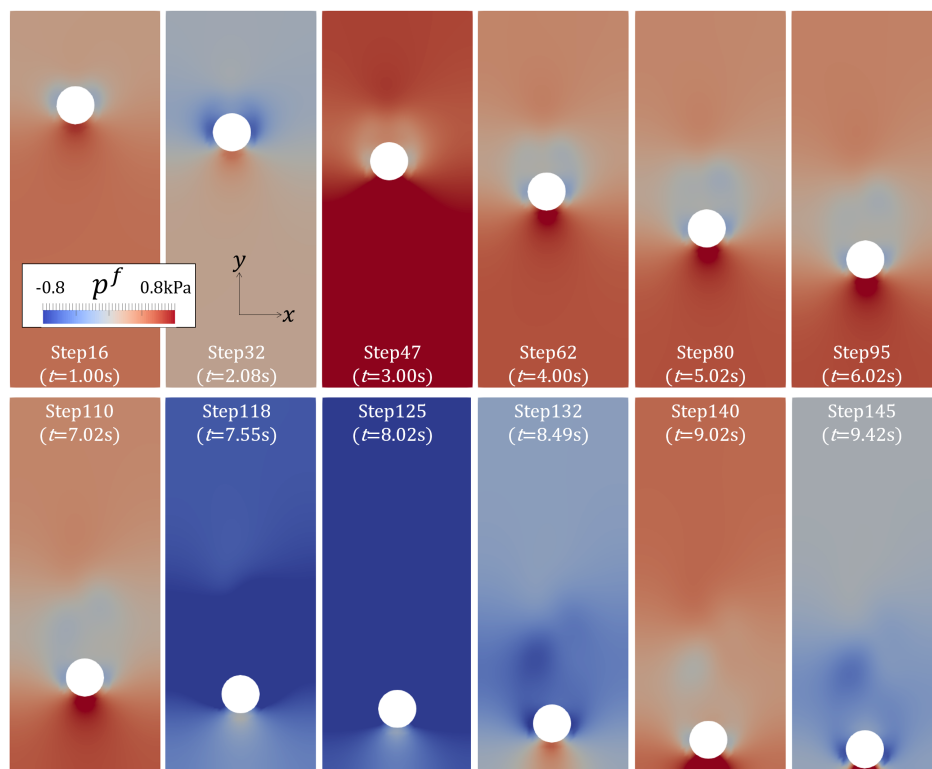


Figure 7.19: History of p^f (Lagrangian-immersed FSI using space-time XFEM)

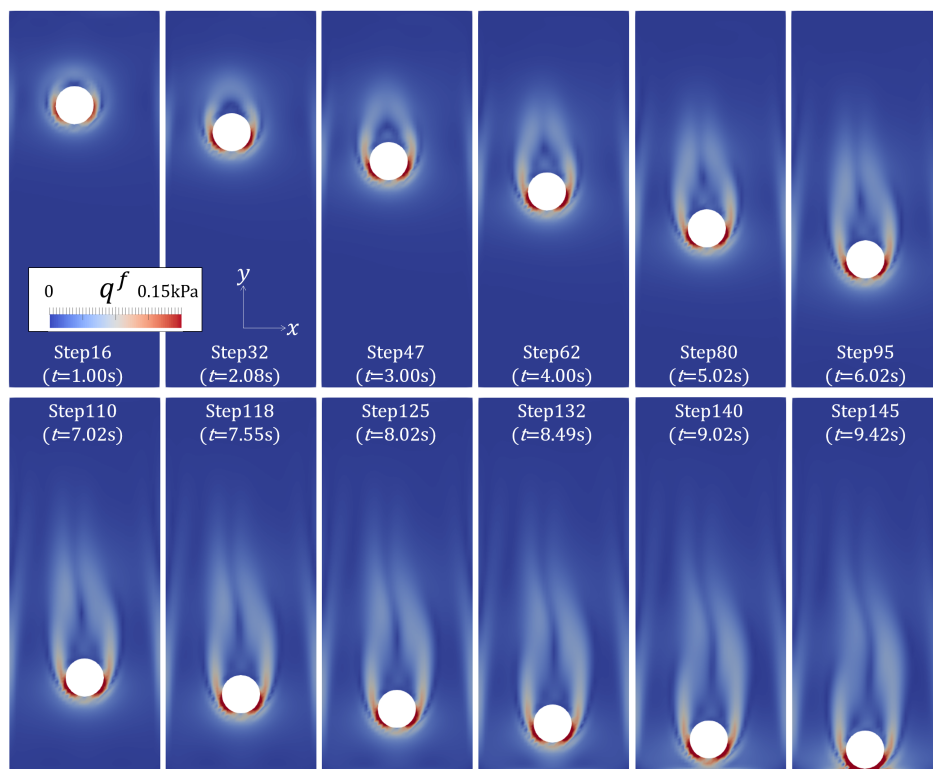


Figure 7.20: History of q^f (Lagrangian-immersed FSI using space-time XFEM)

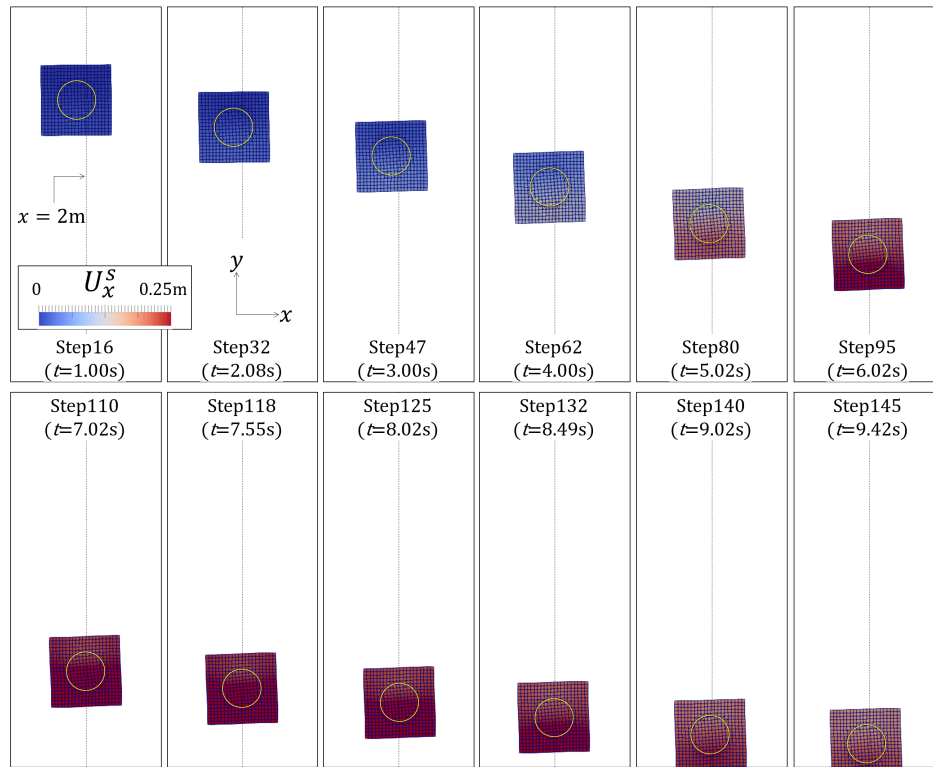
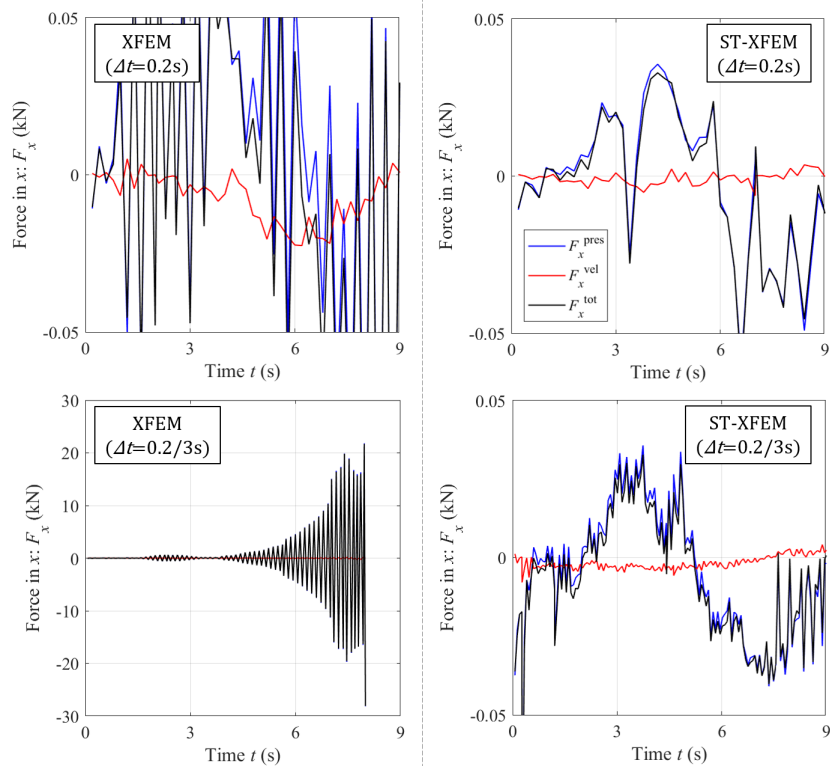
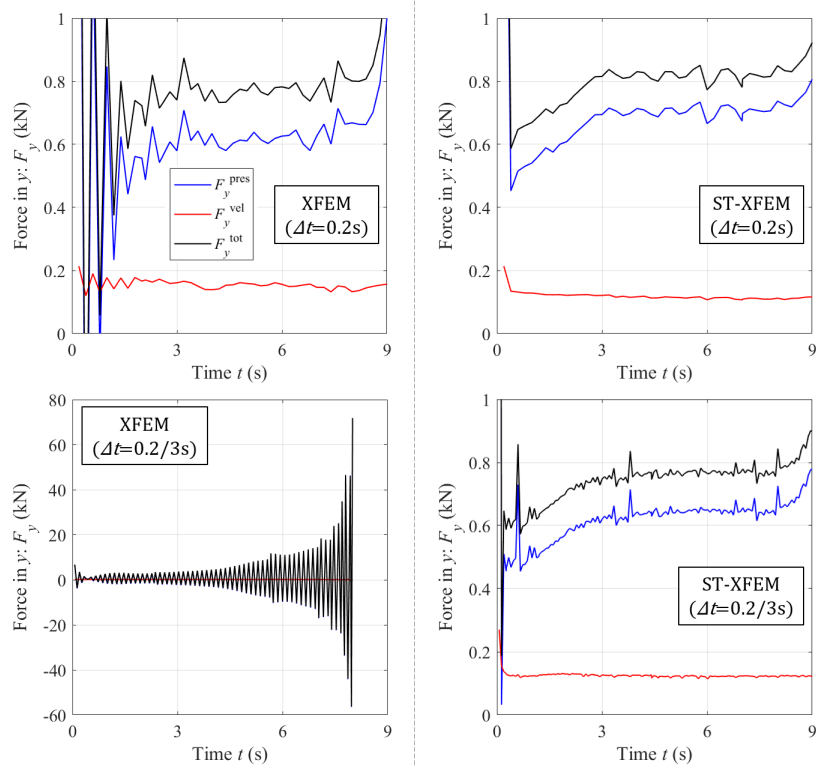


Figure 7.21: History of U_x^s (Lagrangian-immersed FSI using space-time XFEM)

The stability of the Lagrangian-immersed FSI method using the space-time XFEM is remarkable especially when considering the distribution of the fluid force acting on the solid cylinder. Figures 7.22 and 7.23 show the fluid forces F_x and F_y acting on the cylinder. Blue lines represent the contributions of the fluid pressure and red lines represent the contributions of the fluid velocity, respectively. Black lines represent the total fluid force, which is the summation of blue and red lines. In each figure, the left column represents the XFEM with a time stepping scheme, and the right column represents the space-time XFEM. Results in the upper row use a larger time increment $\Delta t = 0.2s$ ($h = 1/11m$). Results in the lower row use a three times smaller time increment $\Delta t = 0.2/3s$. The bottom right graphs correspond to Figures 7.17 - 7.19 (space-time XFEM using $h = 1/11m$ and $\Delta t = 0.2/3s$). The equivalence of the proposed space-time XFEM and the space-time XFEM based on the simplex triangulation is demonstrated in Appendix F.

Figure 7.22: Comparison of F_x (XFEM and space-time XFEM)Figure 7.23: Comparison of F_y (XFEM and space-time XFEM)

Focusing on the graphs in the left columns of Figures 7.22 and 7.23, F_x and F_y computed by the XFEM highly oscillate and the XFEM using finer time increment ($\Delta t = 0.2/3s$: bottom left graph) even diverged. In particular, the oscillation of the contribution of the fluid hydrostatic pressure (blue lines) is significantly larger. On the other hand, the space-time XFEM (right column) does not suffer from the oscillations and no divergence at the smaller time increment.

Figure 7.23 shows the comparison of F_y using the XFEM and the space-time XFEM. Focusing on the upper row ($\Delta t = 0.2s$ and $h = 1/11m$), the general trends in both the standard XFEM (left) and the space-time XFEM (right) are similar. However, the space-time XFEM obtains a smoother distribution of F_x than the XFEM. The difference between the XFEM and the space-time XFEM is remarkable when a smaller time increment $\Delta t = 0.2/3s$ is used. The oscillations of F_y computed by the XFEM using a smaller time increment (bottom left graph) are larger than one of the XFEM using a larger time increment (top left graph). This indicates that the spikes at the top left graph are caused by the temporal interpolation error of the XFEM due to a moving interface. These spikes are not due to an approximation error because of a overly coarse temporal discretization. On the other hand, the space-time XFEM (right column) can get smoother distribution. However, there are some spikes at the bottom right figure (space-time XFEM). These spikes are also observed when the simplex triangulation approach is used for the space-time integration; see Appendix F. Therefore, these spikes are not caused by the proposed elementwise temporal layer approach. Other factors, such as the FSI coupling between non-matching interfaces, enforcing interface conditions by Nitsche's method or Lagrange multiplier method, and the fluid stabilization methods, might cause these spikes.

Forces at non-matching interfaces shown in Figures 7.22 and 7.23 play an important role in FSI. Figures 7.24 and 7.25 illustrate the momentum P_x and P_y in x and y direction of the solid domain, the fluid domain and the total system. P_x and P_y are results of the FSI (force

acting on non-matching interfaces) and transmitted between solid and fluid phase. In these figures, red and blue lines indicate the momentum of the solid and fluid domain, respectively. Black lines show the total momentum of the entire FSI system including both solid and fluid phase. As the entire system is fixed, the total momentum should be zero in both x and y direction. The columns in these figures correspond to the computational method (XFEM or space-time XFEM) and the rows represent different time increments. The upper row is a larger time increment $\Delta t = 0.2s$ and the lower row is a finer time increment $\Delta t = 0.2/3s$. The size of the spatial discretization is $h = 1/11m$.

Figure 7.24 shows the momentum P_x in x direction using the XFEM and the space-time XFEM. The conservation of the total momentum is satisfied when the space-time XFEM is used. The momentum is transmitted between the solid and fluid. The solid cylinder moves towards the positive x direction until 7.22s and then, the direction of the motion is reverted. The momentum of the fluid (blue line) has the opposite tendency compared to the momentum of the solid (red line). On the other hand, oscillations of P_x occur when the standard XFEM with a finer time increment is used (bottom left graph). The oscillations of the momentum are created by the error of the fluid force F_x in Figure 7.22. Furthermore, the conservation of momentum is violated at the bottom left graph. Figure 7.25 illustrates the momentum P_y in y direction. The space-time XFEM (right column) satisfies the conservation of the momentum in y direction without divergence. The results in Figures 7.22 - 7.25 suggest that the space-time XFEM features improved stability and accuracy over the conventional combination of the XFEM with a time stepping scheme.

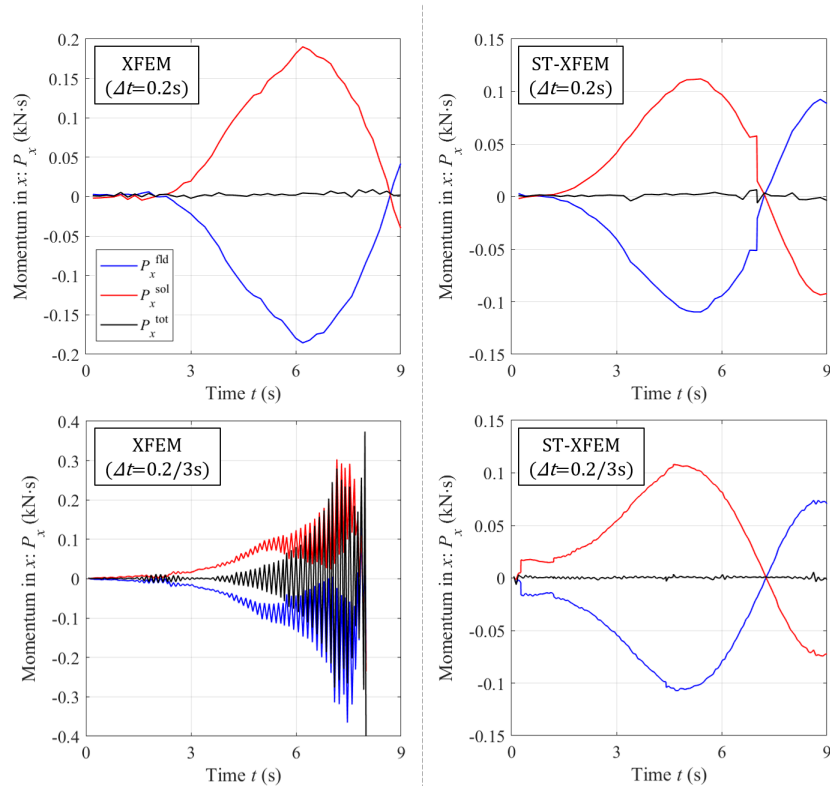


Figure 7.24: Comparison of P_x (XFEM and space-time XFEM)

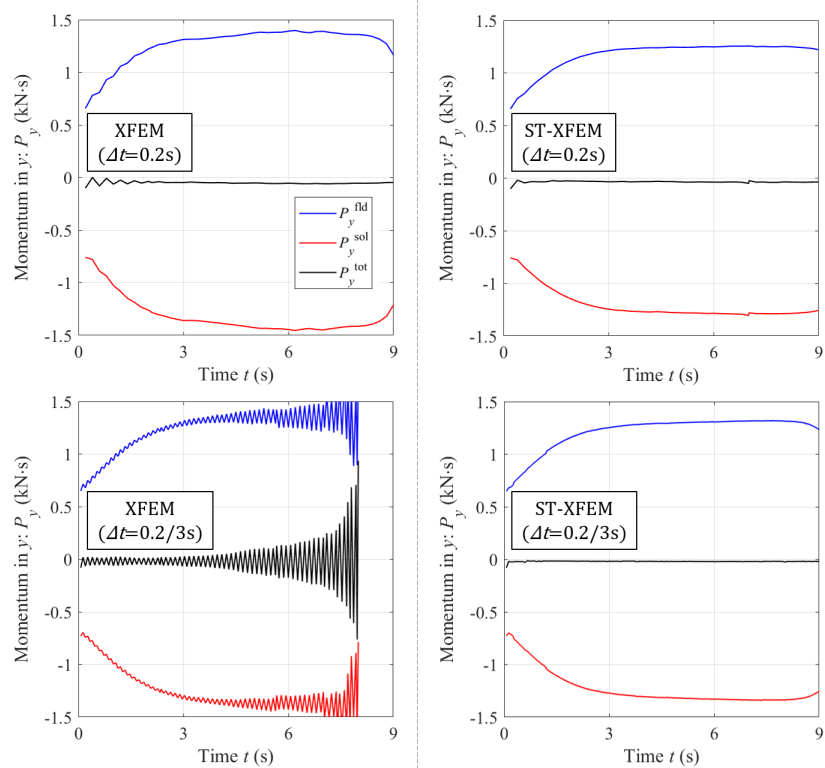


Figure 7.25: Comparison of P_y (XFEM and space-time XFEM)

Finally, the errors of the total fluid force and the total momentum illustrated by black lines in Figures 7.22 - 7.25 are examined. This study uses a time increment $\Delta t = 0.2\text{s}$ as a time increment and the spatial size dependency of the force and momentum errors are computed. The errors of individual force and momentum components are defined as follows:

$$\text{L2Error}(F_x^{\text{tot}}) = \sqrt{\frac{\int_{t_i}^{t_f} dt (F_x^{\text{tot}} - F_{x\text{-ref}}^{\text{tot}})^2}{\int_{t_i}^{t_f} dt F_{x\text{-ref}}^{\text{tot}^2}}}, \quad (7.46)$$

$$\text{L2Error}(F_y^{\text{tot}}) = \sqrt{\frac{\int_{t_i}^{t_f} dt (F_y^{\text{tot}} - F_{y\text{-ref}}^{\text{tot}})^2}{\int_{t_i}^{t_f} dt F_{y\text{-ref}}^{\text{tot}^2}}}, \quad (7.47)$$

$$\text{Error}(P_x^{\text{tot}}) = \sqrt{(t_f - t_i)^{-1} \int_{t_i}^{t_f} dt P_x^{\text{tot}^2}}, \quad (7.48)$$

$$\text{Error}(P_y^{\text{tot}}) = \sqrt{(t_f - t_i)^{-1} \int_{t_i}^{t_f} dt P_y^{\text{tot}^2}}, \quad (7.49)$$

where t_i and t_f are initial and final time for the evaluation of these errors. $t_i = 0.4\text{s}$ and $t_f = 8.5\text{s}$ are used in this numerical example. The L2 force errors are defined using the reference solution. The reference solution is the result using the space-time XFEM with $h = 1/11\text{m}$ and $\Delta t = 0.2\text{s}$. The momentum errors are time averages of the deviation from zero. The reason not to use a relative error for the momentum is that the total momentum P_x^{tot} and P_y^{tot} should be zero based on the conservation law. Blue markers show the errors of the XFEM with a time stepping scheme. Red markers show the errors of the space-time XFEM. The blue and red dashed lines represent the fitting of data using the least square fitting method.

In Figures 7.28 and 7.29, the rate of convergence of the space-time XFEM uses data with $h < 0.133\text{m}$. In addition, data of the error of P_x^{tot} vary widely because the absolute value of P_x^{tot} is much smaller than P_y^{tot} . The computation of the rate of convergence of the XFEM in Figure 7.28 is not computed because its data highly oscillates, and it is hard to extract a trend. The rates of convergence of the standard XFEM are smaller than the ones of the space-time XFEM, due to the temporal interpolation errors by a moving interface. On the

other hand, the errors of the space-time XFEM diminish with the refinement of the spatial discretization and converge quickly with the higher rates of convergence than the standard XFEM.

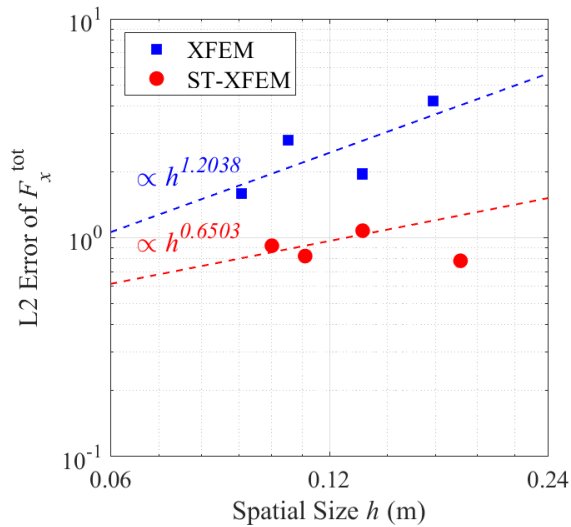


Figure 7.26: L2 error of force in x : F_x^{tot}

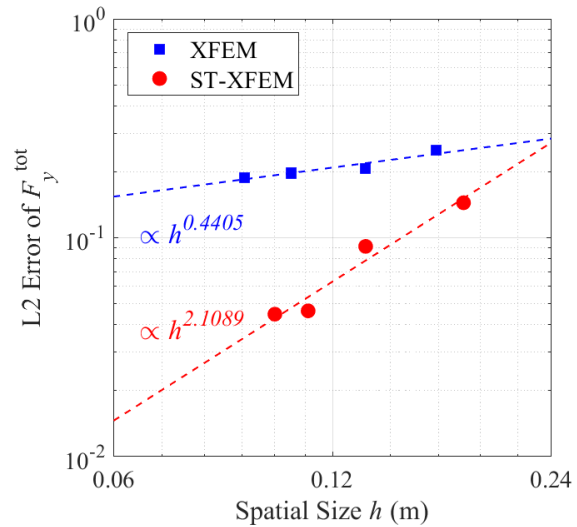


Figure 7.27: L2 error of force in y : F_y^{tot}

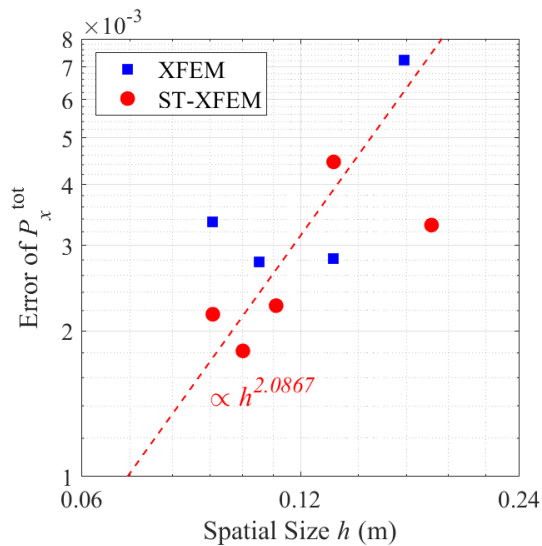


Figure 7.28: Error of momentum in x : P_x^{tot}

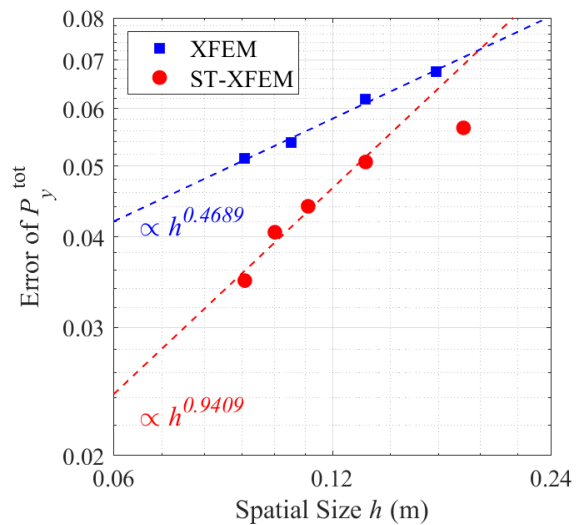


Figure 7.29: Error of momentum in y : P_y^{tot}

7.4.2 Turek-Hron FSI3 Benchmark Problem

The second numerical example of the Lagrangian-immersed FSI method using the space-time XFEM is the well-known transient FSI benchmark problem typically referred to the Turek-Hron FSI3 problem proposed by Turek and Hron [111]. The fluid phase is modeled by the incompressible Navier-Stokes equations and the solid phase is modeled by a compressible St. Venant-Kirchhoff material, (7.39) and (7.40), which considers finite strains but assumes the linear response. In the Turek-Hron FSI3 problem, a fixed cylinder and an elastic flexible beam connected to the cylinder are surrounded by fluid. This benchmark problem is designed to operate in the incompressible laminar regime and periodic oscillations of the flexible beam are obtained due to the self-induced oscillation of fluid flow.

7.4.2.1 Geometry of Turek-Hron FSI3

The geometry of Turek-Hron FSI3 problem is shown in Figures 7.30 and 7.31. Figure 7.30 displays the geometry of the Eulerian system Ω_E in the Lagrangian-immersed FSI method. Ω_E^f is the fluid phase and the entire domain Ω_E is used in the level set projection method. The inlet flow is prescribed at the left edge that is the inlet boundary Γ_{inlet}^f . The right edge is the outlet boundary with “do-nothing” boundary conditions (traction-free boundary conditions) denoted by Γ_{free}^f . The top and bottom edges are the boundaries $\Gamma_{\text{no-slip}}^f$ with no-slip boundary conditions. $\Gamma_{E\text{-fix}}$ refers to the FSI interface where the no-slip boundary conditions are applied around the cylinder. $\Gamma_{E\text{-int}}$ is the standard FSI interface around the elastic beam.

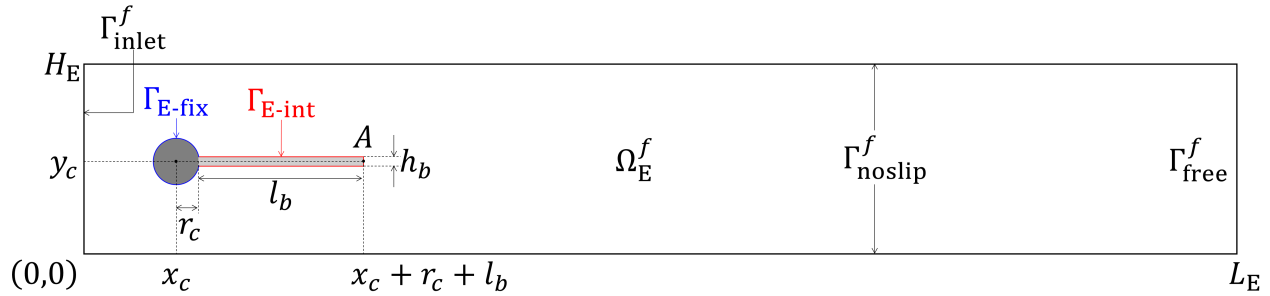


Figure 7.30: Model of Eulerian system Ω_E (Turek-Hron FSI3)

Based on the Lagrangian-immersed FSI method, Lagrangian and Eulerian meshes are independently defined. Figure 7.31 is the geometry of the Lagrangian system Ω_{L0} . The domain colored by light blue is the solid domain Ω_{L0-dbc}^s corresponding to the fixed cylinder. The pink domain is the solid domain Ω_{L0}^s corresponding to the flexible elastic beam. Other domains are the dummy solid domain. The domain colored by dark gray is denoted by Ω_{L0-dbc}^d and always fixed by the Dirichlet boundary condition. The domain colored by light gray is denoted by Ω_{L0}^d is the flexible dummy-displacement domain that follows the deformation of Ω_{L0}^s . Γ_{L0-fix} is the undeformed Lagrangian interface where the no-slip boundary conditions are applied and corresponds to Γ_{E-fix} . Γ_{L0-int} is the undeformed Lagrangian interface for FSI. The FSI boundary integrals are performed between non-matching interfaces Γ_{E-int} and Γ_{L-int} (deformed interface of Γ_{L0-int}). The geometry parameters are summarized in Table 7.4.

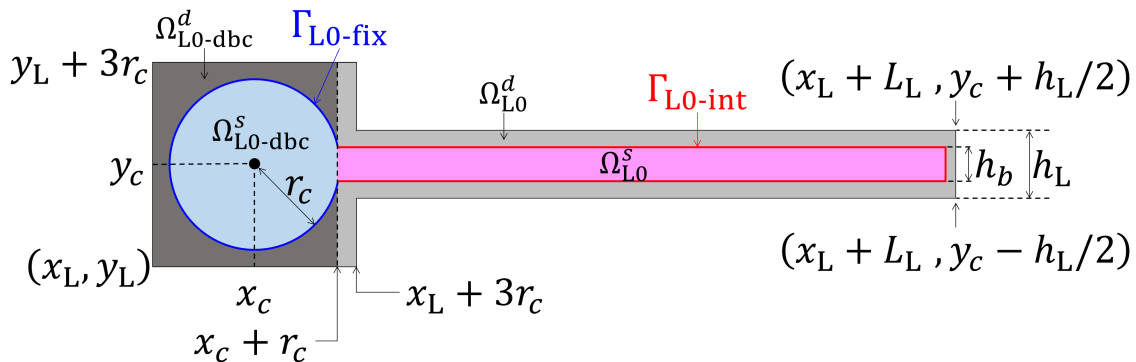


Figure 7.31: Model of undeformed Lagrangian system Ω_{L0} (Turek-Hron FSI3)

Meshes of the Eulerian and Lagrangian system are shown in Figures 7.32 and 7.33. In the Eulerian system (Figure 7.32), finer rectangular elements ($\frac{2}{3}h \times h$: size in x is $\frac{2}{3}h$ and size in y is h) are used in $x < 2H_E$, and coarser rectangular elements ($2h \times h$) are used in another region. In the Lagrangian system (Figure 7.33), finer rectangular elements ($\frac{4}{9}h \times \frac{1}{9}h$) are used in the region of $y_c - h_L/2 \leq y \leq y_c + h_L/2$. Otherwise, square elements ($\frac{4}{9}h \times \frac{4}{9}h$) are used. The representative elemental length is $h = 8.54 \times 10^{-3}$ m in this numerical example.

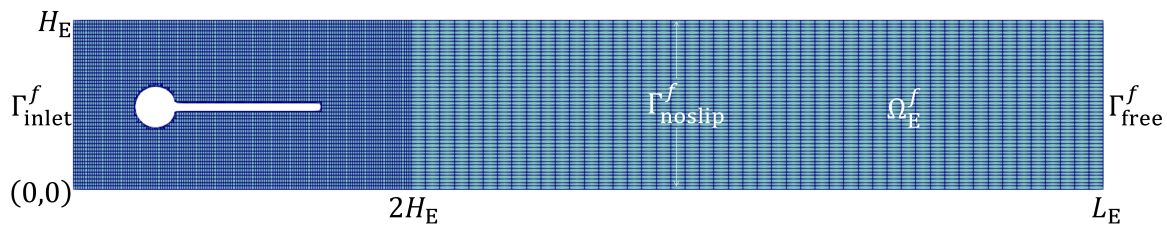


Figure 7.32: Mesh of Eulerian system (Turek-Hron FSI3)

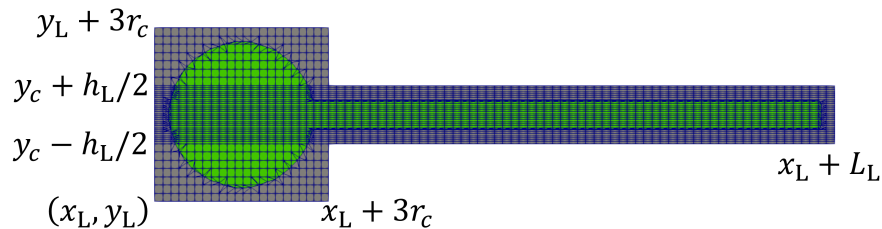


Figure 7.33: Mesh of Lagrangian system (Turek-Hron FSI3)

Table 7.4: Geometry of Turek-Hron FSI3

| Description | Parameter (m) |
|---|-------------------------------|
| cylinder center position | $C = (x_c, y_c) = (0.2, 0.2)$ |
| cylinder radius | $r_c = 0.05$ |
| reference length | $D = 2r_c = 0.1$ |
| elastic beam length | $l_b = 0.35$ |
| elastic beam height | $h_b = 0.02$ |
| reference point (at $t = 0$) | $A = (0.6, 0.2)$ |
| channel length of Eulerian system | $L_E = 2.50$ |
| channel height of Eulerian system | $H_E = 0.41$ |
| origin of Lagrangian system | $(x_L, y_L) = (0.14, 0.14)$ |
| length of Lagrangian system | $L_L = 0.47$ |
| height at right edge of Lagrangian system | $h_L = 0.04$ |

7.4.2.2 Structural Test (Turek-Hron CSM1 Problem)

The structural dynamic response was first computed as a preliminary test for the Turek-Hron FSI3 problem. This structural test is well-known as Turek-Hron CSM1 problem which is a steady-state problem of the elastic beam (red region with $r_c \leq x \leq x_c + r_c + l_b$ in Figure 7.31). The beam is deformed by the body force \mathbf{B}^s within the solid domain $\Omega_{L_0}^s$. This test is a purely structural test and thus, the fluid is omitted. In addition, the dummy displacement domain $\Omega_{L_0}^d$ is also omitted in this test. The elastic beam is modeled by the compressible St. Venant-Kirchhoff material: (7.39) and (7.40), and its material parameters are given in Table 7.5.

Table 7.5: Physical parameters of Turek-Hron CSM1

| | Description | Parameter |
|-------|----------------------|--|
| Solid | Density | $\rho^s = 1000\text{kg/m}^3$ |
| | Young's modulus | $E^s = 5.6\text{MPa}$ |
| | Poisson's ratio | $\nu^s = 0.4$ |
| | artificial viscosity | $\alpha^s = 0\text{s}^{-1}$ |
| | body force | $\mathbf{B}^s = (0, -2)\text{m/s}^2$ |
| | initial velocity | $\mathbf{V}_{\text{ini}}^s = (0, 0)\text{m/s}$ |

As the Turek-Hron CSM1 test is a steady-state problem, the standard XFEM and the backward Euler method (BDF1) are used in this test. The weak form of the governing equations has only the following contributions:

$$R_m^s(\delta\mathbf{U}^s; \{\mathbf{U}^s, \mathbf{V}^s\}) + R_{uv}^s(\delta\mathbf{V}^s; \{\mathbf{U}^s, \mathbf{V}^s\}) + R_L^{\text{gp}}(\{\delta\mathbf{U}^s, \delta\mathbf{V}^s\}; \{\mathbf{U}^s, \mathbf{V}^s\}) = 0. \quad (7.50)$$

Details of (7.50) are discussed in Section 6.4. The penalty coefficients for the face-oriented ghost-penalty method are set as $\alpha_{U^s}^{\text{gp}} = \alpha_{V^s}^{\text{gp}} = 0.05$. The time increment for BDF1 is $\Delta t = 10^{20}\text{s}$ in this case. Newton's method using a direct solver is used as a solution method and the convergence criterion requires a drop of the norm of the residual of 10^{-6} relative to the norm of the initial residual.

Figure 7.34 shows the deformation of the Turek-Hron CSM1 problem. The black domain

shows the initial configuration of the elastic beam and the colored domain shows the deformed configuration with values of displacement U_y^s in y direction. Measures of this problem are the tip displacements at point A marked by the green letter A in Figure 7.34.

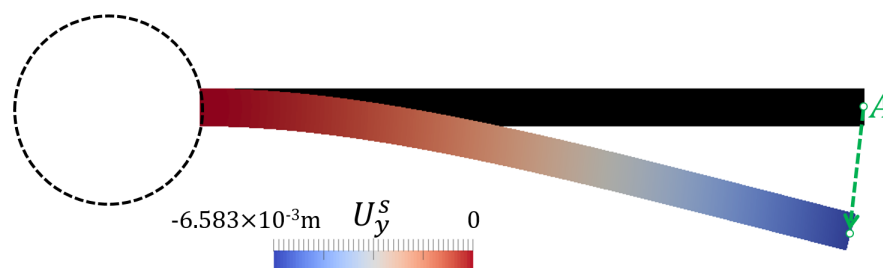


Figure 7.34: Deformation of Turek-Hron CSM1

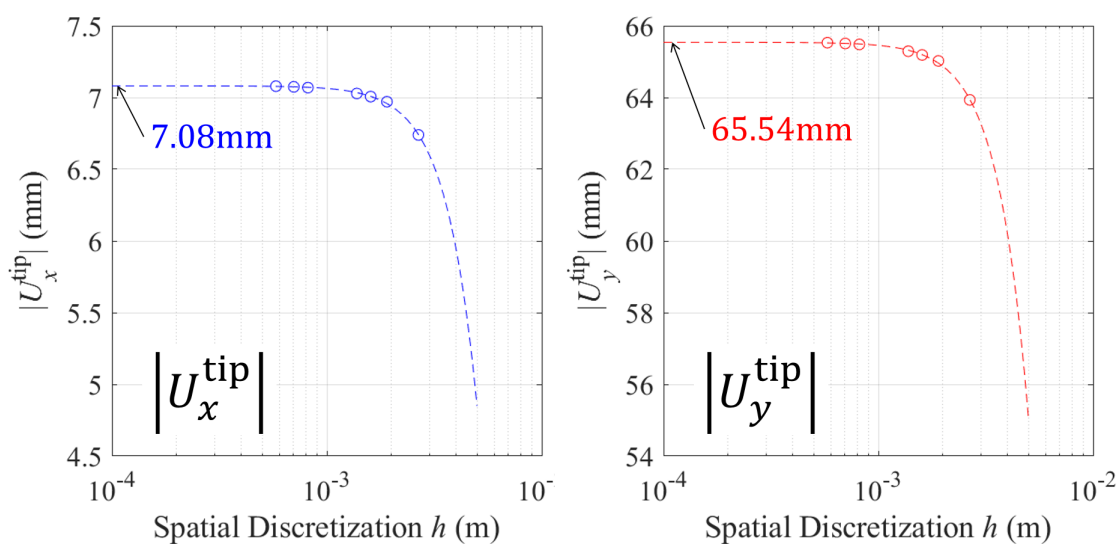


Figure 7.35: Convergence of tip displacements (Turek-Hron CSM1)

Table 7.6: Numerical results of Turek-Hron CSM1

| | U_x^{tip} (mm) | U_y^{tip} (mm) |
|-------|-------------------------|-------------------------|
| [111] | -7.19 | -66.10 |
| Nagai | -7.08 | -65.54 |

Figure 7.35 illustrates the convergence study of the tip displacements U_x^{tip} and U_y^{tip} in x and y direction. As the mesh is refined, converged values of the tip displacements are

obtained. Table 7.6 is the comparison between the reference work (Turek and Hron [111]) and this research (Nagai). As can be seen in Table 7.6, the tip displacements agree well.

7.4.2.3 Turek-Hron FSI3 Problem

In the following, the Turek-Hron FSI3 problem (transient FSI computation) is studied. The summary of physical parameters is given in Table 7.7.

Table 7.7: Physical parameters of Turek-Hron FSI3

| | Description | Parameter |
|--------------------------|----------------------|--|
| Solid | Density | $\rho^s = 1000\text{kg/m}^3$ |
| | Young's modulus | $E^s = 5.6\text{MPa}$ |
| | Poisson's ratio | $\nu^s = 0.4$ |
| | artificial viscosity | $\alpha^s = 0\text{s}^{-1}$ |
| | body force | $\mathbf{B}^s = (0, 0)\text{m/s}^2$ |
| | initial velocity | $\mathbf{V}_{\text{ini}}^s = (0, 0)\text{m/s}$ |
| Fluid | Density | $\rho^f = 1000\text{kg/m}^3$ |
| | kinematic viscosity | $\nu^f = 10^{-3}\text{m}^2/\text{s}$ |
| | body force | $\mathbf{b}^f = (0, 0)\text{m/s}^2$ |
| | reference velocity | $\bar{v}_x = 2\text{m/s}$ |
| Dimensionless Parameters | Reynolds number | $\text{Re} = \bar{v}_x D / \nu^f = 200$ |
| | Strouhal number | $\text{St} = \bar{f} D / \bar{v}_x = 0.05 \quad (\bar{f} = 1\text{s}^{-1})$ |
| | Ratio of density | $\beta = \rho^s / \rho^f = 1$ $\text{Ae} = E^s / (\rho^f \bar{v}_x^2) = 1400$ |

The boundary conditions in the Eulerian space-time slab Q_{E}^n ($Q_{\text{E}}^n = \Omega_{\text{E}} \oplus T^n$) are as follows:

$$\text{No-slip BCs:} \quad v_x^f = v_y^f = 0 \text{ on } P_{\text{E-noslip}}^{n,f} \text{ and } P_{\text{E-fix}}^n, \quad (7.51)$$

$$\text{Parabolic inlet flow:} \quad v_x^f(0, y, t) = 6\bar{v}_x \frac{y(y - H_{\text{E}})}{H_{\text{E}}^2} \theta(t) \text{ on } P_{\text{E-inlet}}^{n,f}, \quad (7.52)$$

$$v_y^f(0, y, t) = 0 \text{ on } P_{\text{E-inlet}}^{n,f}, \quad (7.53)$$

where $P_{\text{E-noslip}}^{n,f}$ and $P_{\text{E-inlet}}^{n,f}$ are the space-time interfaces corresponding to Γ_{noslip}^f and Γ_{inlet}^f in Figure 7.30 respectively. The inlet velocity is ramped up by the following smoothing function

$\theta(t)$:

$$\theta(t) = \begin{cases} \frac{1-\cos(\pi t/2)}{2} & \text{if } t < 2s , \\ 1 & \text{otherwise .} \end{cases} \quad (7.54)$$

The boundary conditions in the undeformed Lagrangian space-time slab Q_{L0}^n ($Q_{L0}^n = \Omega_{L0} \oplus T^n$) are as follows:

$$\text{Fixed Lagrangian domain: } U_x^s = U_y^s = 0 \text{ in } Q_{L0\text{-dbc}}^{n,s} \text{ and } Q_{L0\text{-dbc}}^{n,d} , \quad (7.55)$$

$$V_x^s = V_y^s = 0 \text{ in } Q_{L0\text{-dbc}}^{n,s} \text{ and } Q_{L0\text{-dbc}}^{n,d} , \quad (7.56)$$

$$\text{No-slip BCs: } V_x^s = V_y^s = 0 \text{ on } P_{L0\text{-fix}}^n , \quad (7.57)$$

where $Q_{L0\text{-dbc}}^{n,s}$, $Q_{L0\text{-dbc}}^{n,d}$ and $P_{L0\text{-fix}}^n$ correspond to spatial properties $\Omega_{L0\text{-dbc}}^s$, $\Omega_{L0\text{-dbc}}^d$ and $\Gamma_{L0\text{-fix}}$ in Figure 7.31, respectively.

The weak form of Turek-Hron FSI3 problem is residuals without the contribution of the contact \tilde{R}_c^s and identical to the weak form of the first numerical example, (7.45). The Helmholtz smoothing method (7.7) is applied in the dummy displacement domain because the structure does not undergo rigid body rotations. The penalty factors for the Turek-Hron FSI3 problem are summarized in Table 7.8.

Table 7.8: Penalty coefficients for Turek-Hron FSI3

| Method | Penalty Coefficients |
|---|--|
| Nitsche's method for FSI | $\eta^{\text{fsi}} = \alpha^{\text{fsi}} E^s$, $\alpha^{\text{fsi}} = 1/56\text{s/m}$ |
| Nitsche's method for dummy-displacement | $\eta^d = \alpha^d E^s$, $\alpha^d = 20\text{m}^{-1}$ |
| face-oriented ghost-penalty method | $\alpha_{U^s}^{\text{gp}} = \alpha_{U^d}^{\text{gp}} = \alpha_{V^s}^{\text{gp}} = \alpha_{v^f}^{\text{gp}} = 10^{-2}$, $\alpha_{p^f}^{\text{gp}} = 10^{-3}$ |

In this numerical example, the size of the temporal discretization is set to either $\Delta t = 0.005\text{s}$ or $\Delta t = 0.0025\text{s}$. Three temporal slices are defined in each temporal layer based on the elementwise temporal layer approach. Newton's method with a direct solver is used. The convergence criterion at the Newton iteration is a drop of the norm of the residual of 5×10^{-3} relative to the norm of the initial residual.

In this Turek-Hron FSI3 problem, periodic oscillations of the flexible beam are excited by the fluid flow. Figures 7.36 - 7.40 show the time histories within one period (from 7.09s to 7.27s) using $\Delta t = 0.005s$. Figures 7.36 and 7.37 shows the evolutions of the velocity fields in the solid and fluid phases. The meshed areas represent the deformed solid domain Ω_L^s defined in the Lagrangian system, and the fluid domain Ω_E^f is defined in the Eulerian system. The numerical results show that oscillations of the solid beam are excited by the fluid flow and the distribution of fluid velocity is affected by the deformation of the beam. In addition, the continuity of velocities between solid and fluid is enforced. Figure 7.38 shows the evolution of the fluid vorticity ω_z^f in z direction. The lines colored by gray represent the contour line of the fluid vorticity. Vortex shedding is observed as the flow passes the flexible solid beam.

Figures 7.39 and 7.40 focus on the time histories of the structural response. The left column is the velocity in y direction in the fluid phase. The meshed areas represent the deformed solid domain $\Omega_L^{n,s}$ and the other domain is the fluid domain $\Omega_E^{n,f}$. The middle and right columns are the displacement U_y^s in y direction and the von Mises stress σ_{VM}^s (Cauchy stress) of the solid domain. The domain without mesh is the dummy displacement domain $\Omega_L^{n,d}$ in the middle and right columns of Figures 7.39 and 7.40.

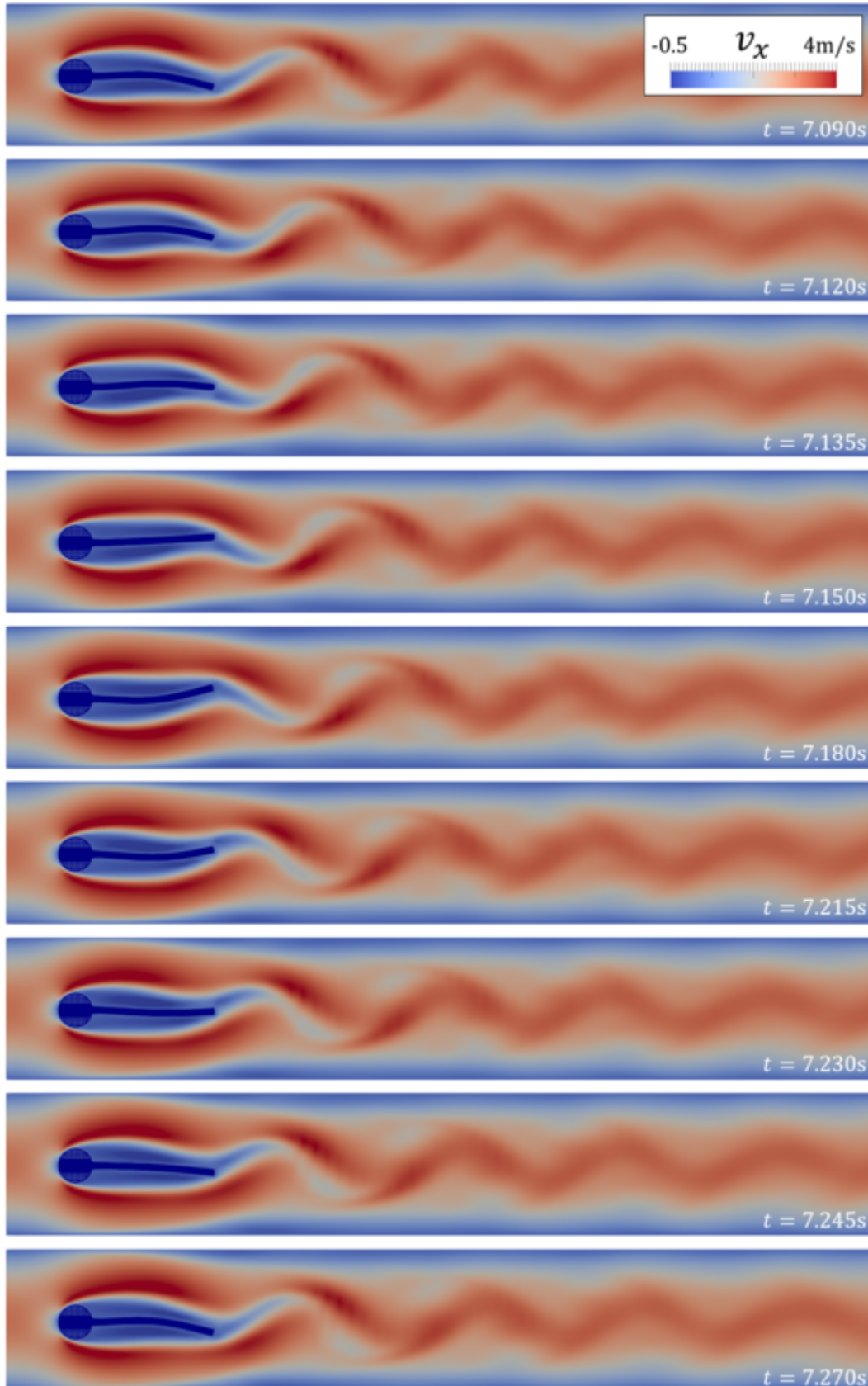


Figure 7.36: History of velocity in x (Turek-Hron FSI3, $\Delta t = 0.005s$)

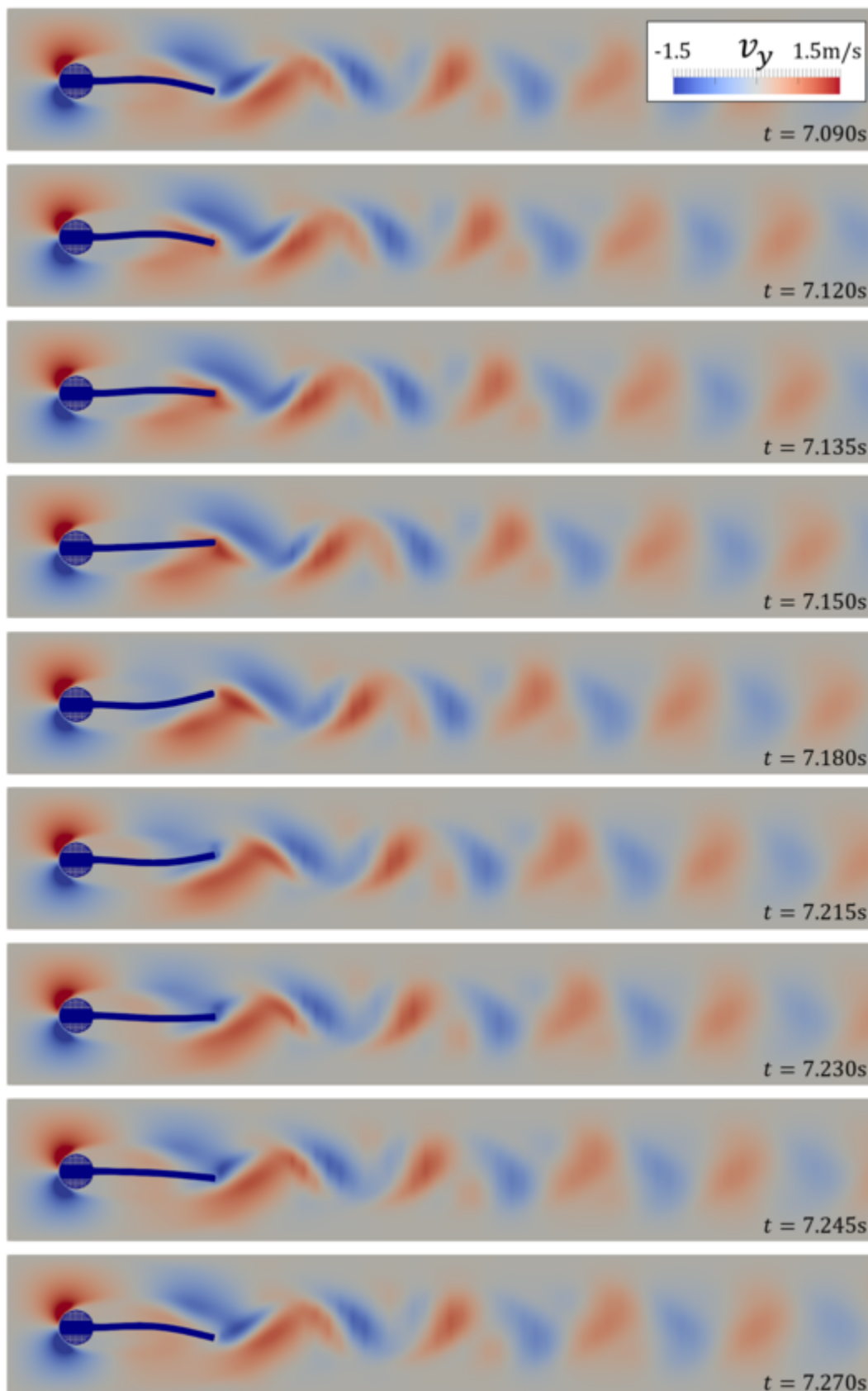


Figure 7.37: History of velocity in y (Turek-Hron FSI3, $\Delta t = 0.005\text{s}$)

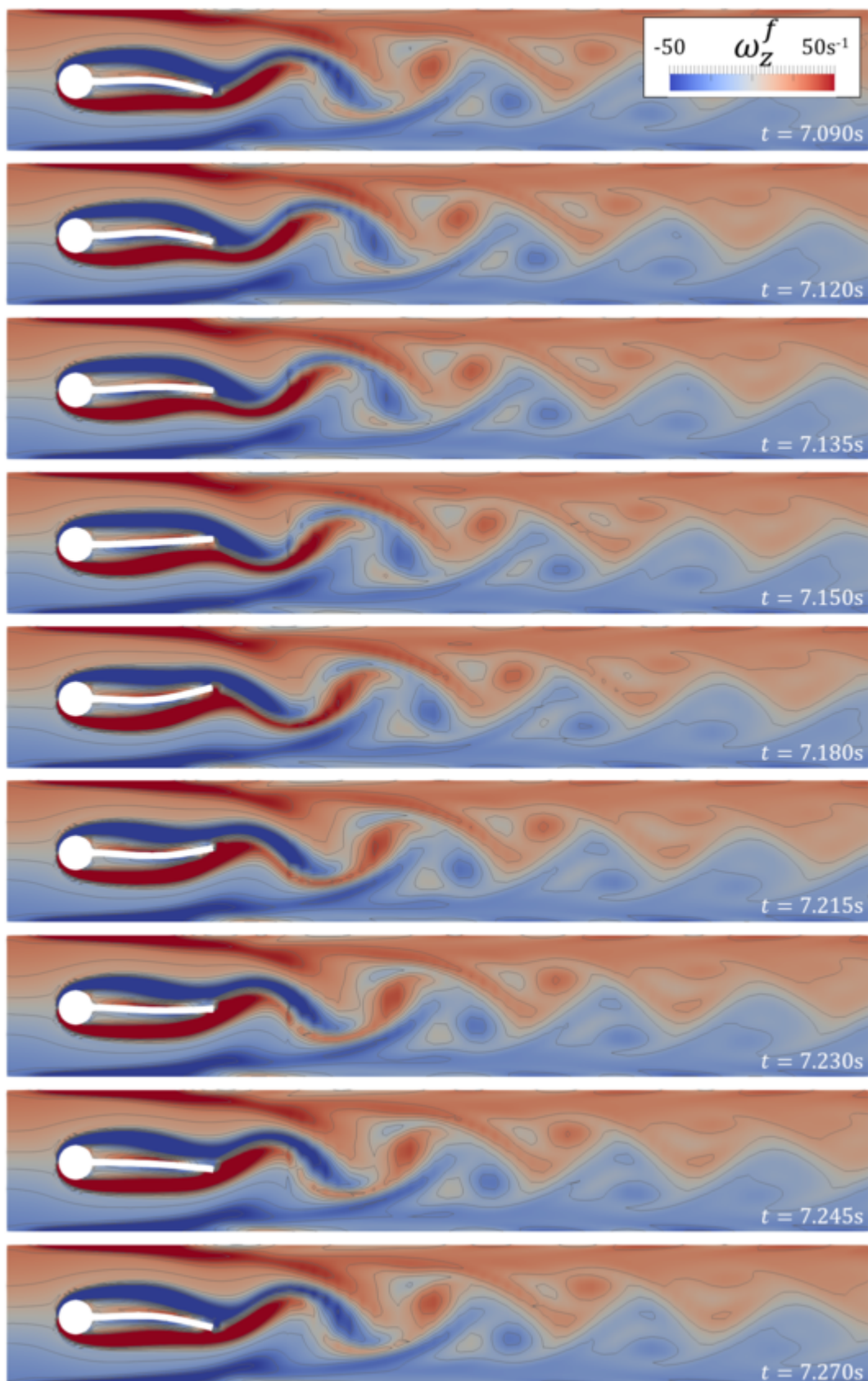


Figure 7.38: History of fluid vorticity ω_z^f (Turek-Hron FSI3, $\Delta t = 0.005s$)

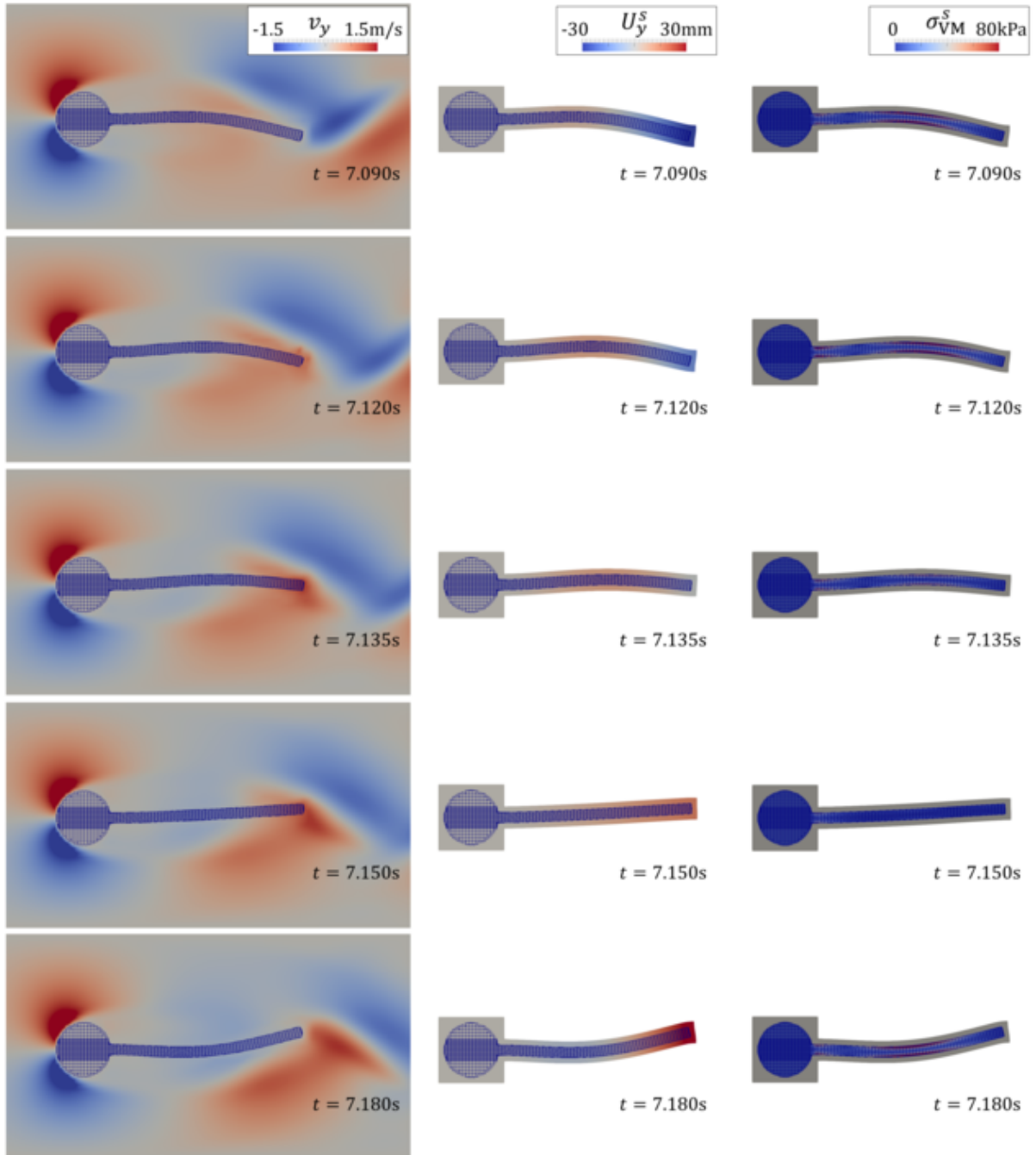


Figure 7.39: Structural deformations (Turek-Hron FSI3, 7.09s-7.18s, $\Delta t = 0.005s$)

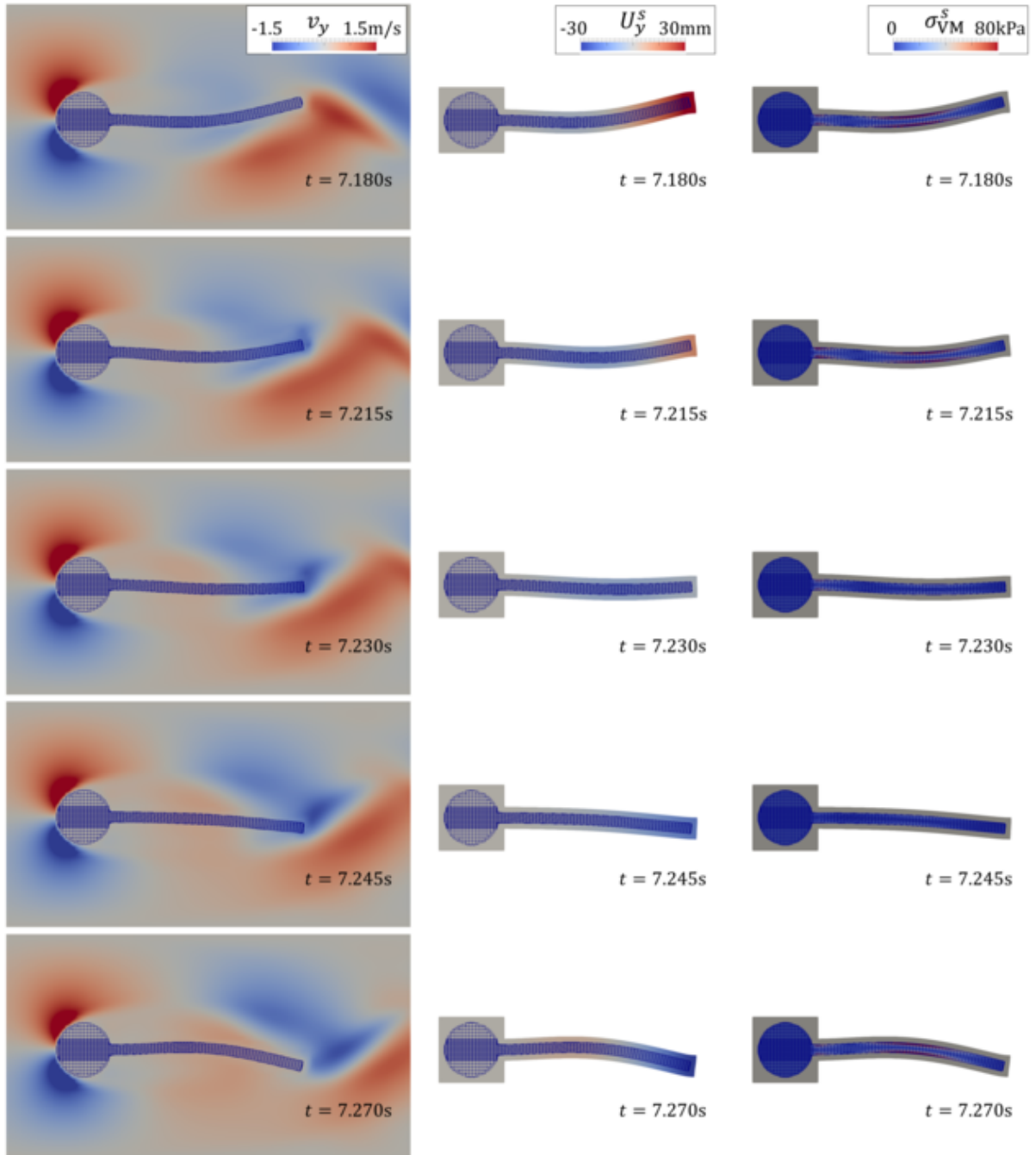


Figure 7.40: Structural deformations (Turek-Hron FSI3, 7.18s-7.27s, $\Delta t = 0.005s$)

The accuracy of the simulation results for the Turek-Hron FSI3 problem is monitored by the tip displacements, U_x^{tip} and U_y^{tip} , at point A of Figure 7.30, the drag force F_D and the lift force F_L on the interface Γ_{solid} around the solid structure including both the cylinder and beam. F_D and F_L are computed by the fluid traction as follows:

$$(F_D \ F_L)^T = \int_{\Gamma_{\text{solid}}} d\Gamma \ \sigma^f \mathbf{n}^f \quad (7.58)$$

The reference results are taken from [111] and shown in Figure 7.41. These results are computed by the ALE-FSI method and the FEM with $\Delta t = 0.0005\text{s}$. The displacement in x direction and the corresponding drag force have about a frequency that is twice as large than the displacement in y direction and the lift force. Smooth oscillations were obtained for all quantities of interest.

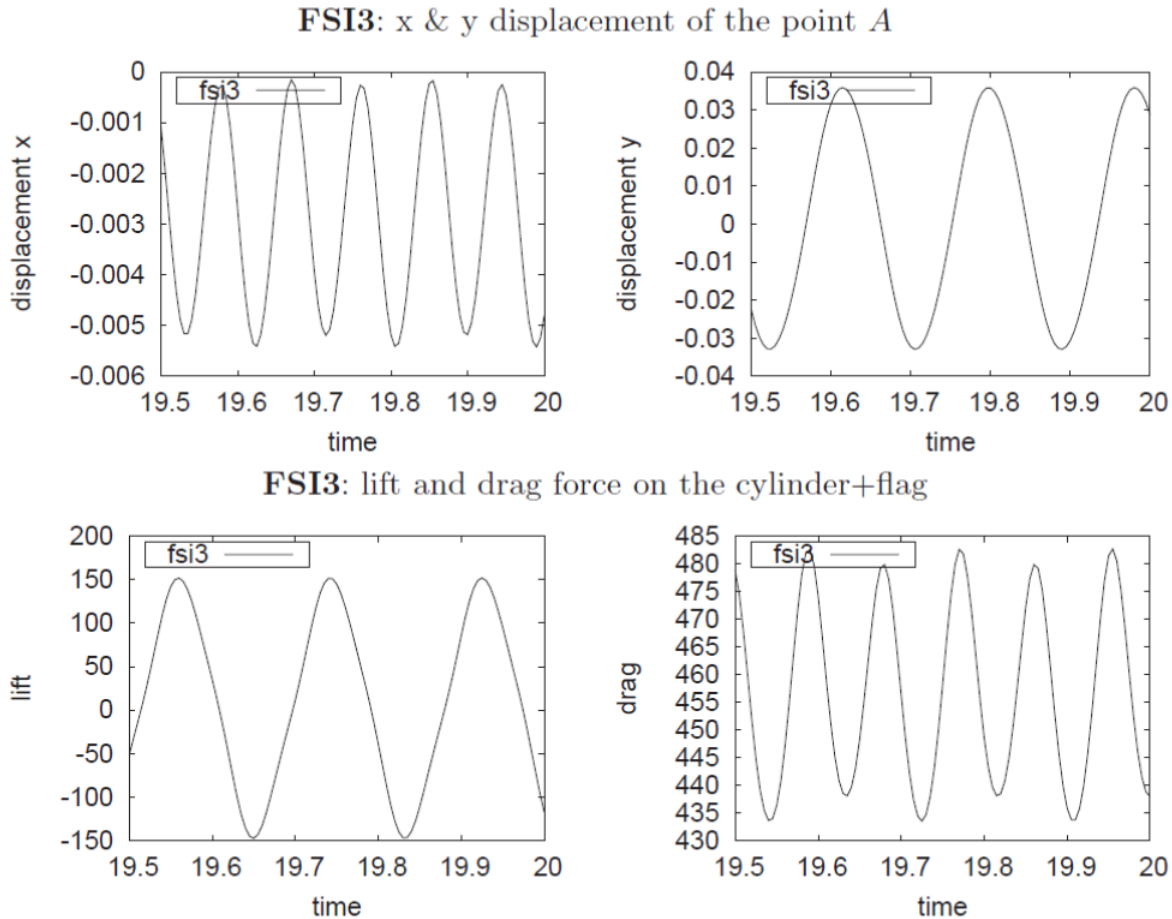


Figure 7.41: Reference results of Turek-Hron FSI3 (Turek and Hron[112], $\Delta t = 0.0005\text{s}$) (unit of displacement = [m], unit of force = [N])

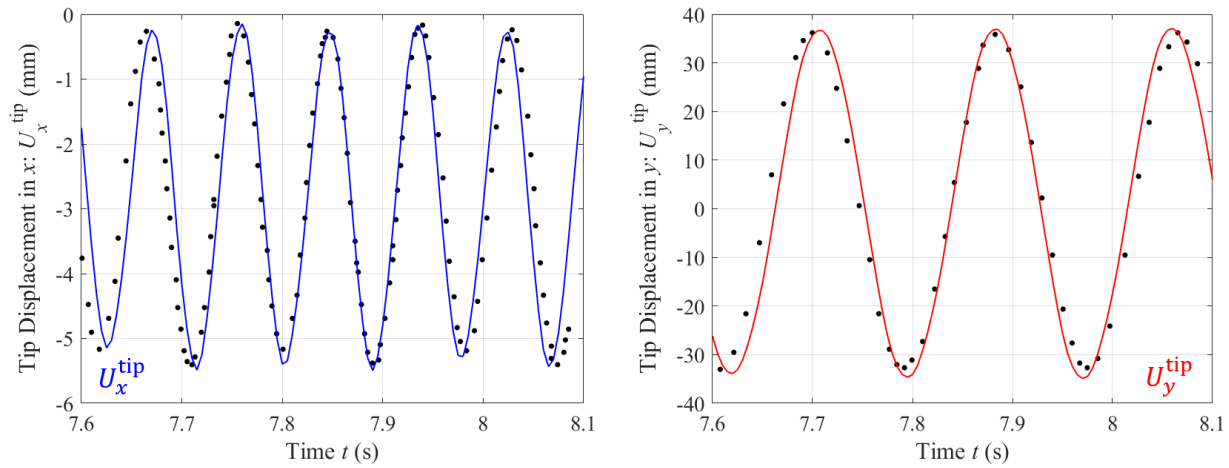


Figure 7.42: Tip displacements using Lagrangian-immersed FSI (Turek-Hron FSI3, $\Delta t = 0.005s$)

(●: referenced data [111] digitized from Figure 7.41)

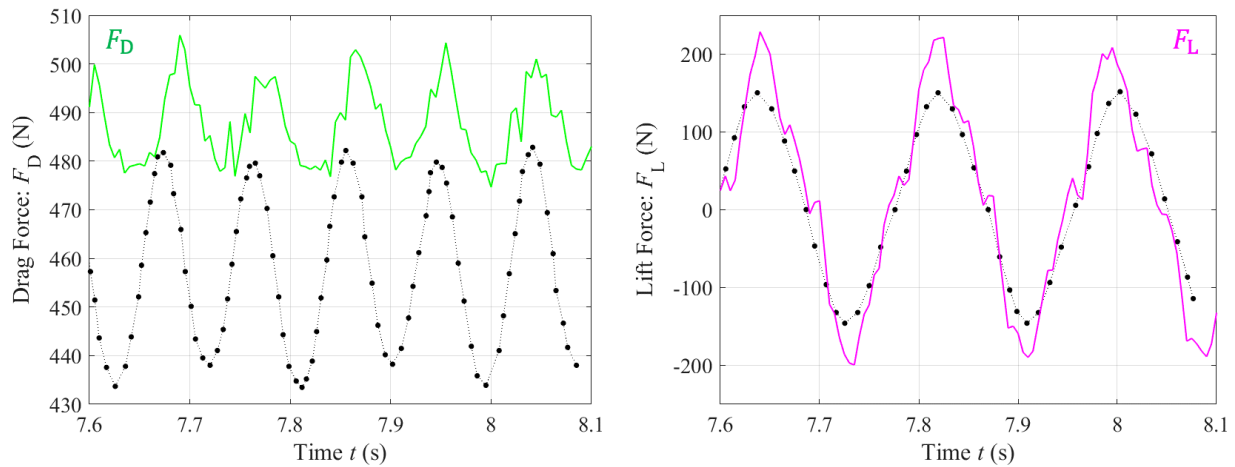


Figure 7.43: Drag and lift forces using Lagrangian-immersed FSI (Turek-Hron FSI3, $\Delta t = 0.005s$)

(●: referenced data [111] digitized from Figure 7.41)

Figures 7.42 and 7.43 show the results of U_x^{tip} , U_y^{tip} , F_D and F_L based on the proposed Lagrangian-immersed FSI method using the space-time XFEM with $\Delta t = 0.005s$. The time increment used in these figures is ten times larger than the one in the reference results. The black dots represent the digitized reference data [111] from Figure 7.41 and shifted along time to overlap onto current results. Before reaching the developed stage such as Figures 7.42 and

7.43, the path of the time evolution is not unique because of the high nonlinearity of geometry. Thus, shifting data along time is reasonable in order to compare the results of the developed stage. From Figure 7.42, one can observe that the amplitude of the tip displacement at point A agrees well with the reference [111]. While the period of the oscillation is slightly shorter than the reference, the overall tendency in terms of amplitude and period is correctly reproduced by the Lagrangian-immersed FSI method using the space-time XFEM. In Figure 7.43, the history of the lift force F_L has almost the same period as the reference, but its amplitude is larger than the reference. The reason for the difference of the amplitude of F_L is the difference of the time increment Δt . As proposed computational results using the space-time XFEM are computed by ten times larger Δt than the reference work, peaks of F_L become sharper because $\frac{\partial F_L}{\partial t}$ changes around the peaks and larger Δt prevent capturing smooth distribution around the peaks. The fact that the slope around $F_L = 0$ is similar to the reference work supports this discussion. The period of F_D is also almost identical to the reference work. On the other hand, there is a big discrepancy between current results and reference results in terms of the value of F_D . This discrepancy is discussed later.

Figures 7.44 and 7.45 show the results with $\Delta t = 0.0025s$. In these figures, a smaller time increment $\Delta t = 0.0025s$ is used to check the influence of the temporal discretization on the convergence of the space-time XFEM.

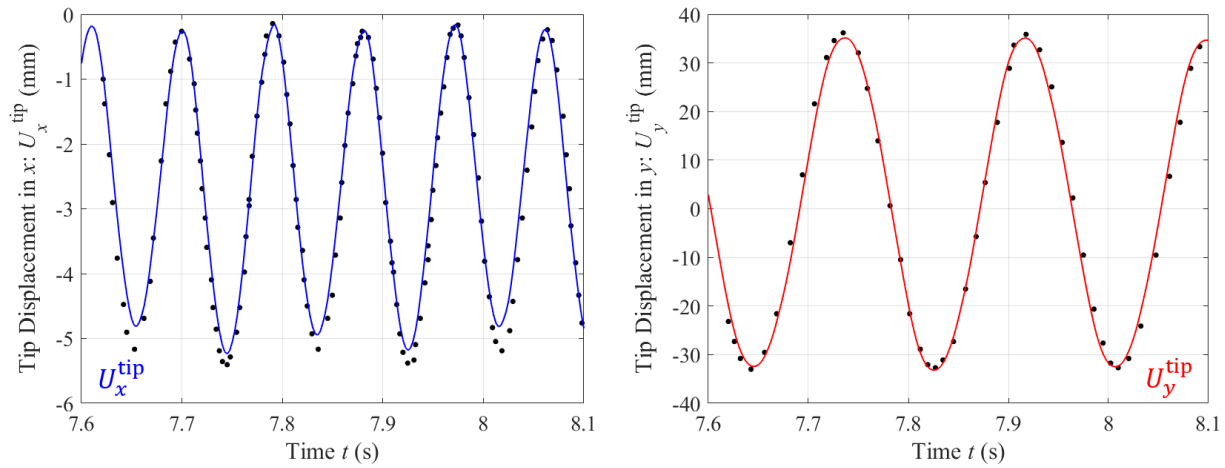


Figure 7.44: Tip displacement using Lagrangian-immersed FSI (Turek-Hron FSI3, $\Delta t = 0.0025s$)

(●: referenced data [111] digitized from Figure 7.41)

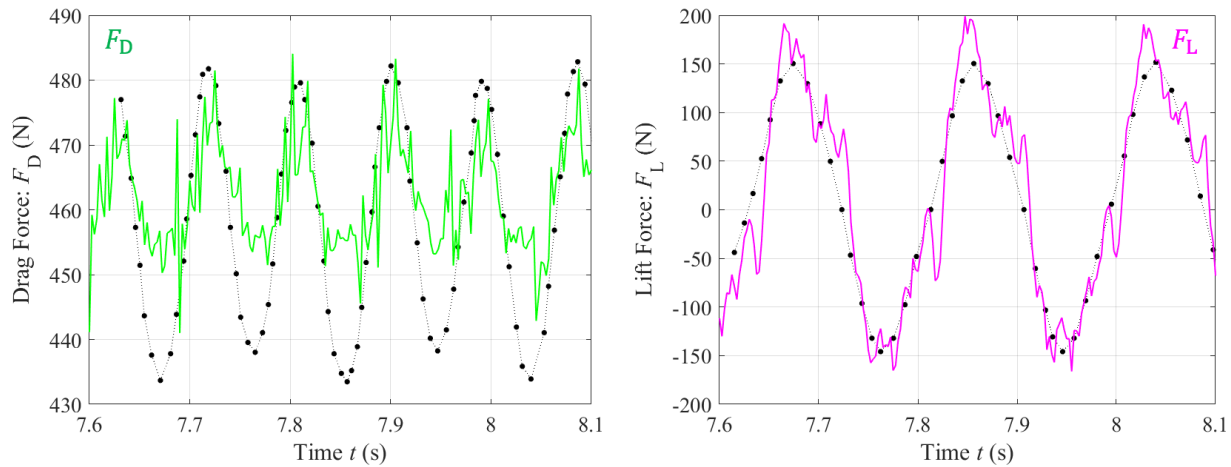


Figure 7.45: Drag and lift forces using Lagrangian-immersed FSI (Turek-Hron FSI3, $\Delta t = 0.0025s$)

(●: referenced data [111] digitized from Figure 7.41)

There is no significant difference with respect to the tip displacements U_x^{tip} and U_y^{tip} (Figures 7.42 and 7.44). On the other hand, differences exist in the time evolution of the drag force F_D and the lift force F_L (Figures 7.43 7.45). F_L computed by smaller time increment $\Delta t = 0.0025s$ is closer to the reference solution than F_L computed by $\Delta t = 0.005s$, especially at its peaks. This is because a smaller Δt could capture more accurately the change of

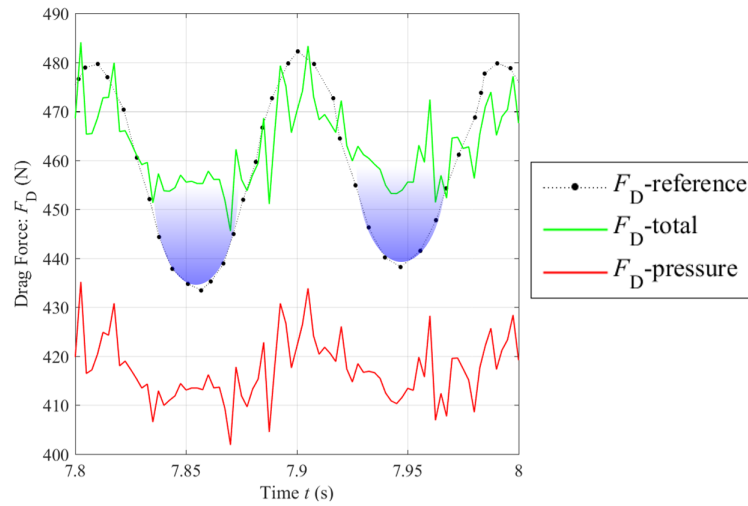


Figure 7.46: Difference of drag force from reference (Turek-Hron FSI3, $\Delta t = 0.0025s$)
 (●: referenced data [111] digitized from Figure 7.41)

$F_L: \frac{\partial F_L}{\partial t}$. F_D computed by a smaller time increment $\Delta t = 0.0025s$ is much closer to the reference solution than F_D computed by $\Delta t = 0.005s$. While F_D at the peak has a similar value as the reference solution, smaller F_D values still differ significantly. Figure 7.46 shows the individual contributions of F_D . The green and red lines represent the total F_D and the contribution of pressure for F_D , respectively. Domains colored by blue denote domains where there is big difference between the computed total F_D (green line) and the reference total F_D (black dots). These results suggest that the lower half of the oscillation of total F_D has a flat distribution which causes the discrepancy from the reference solution. 90% of F_D is the contribution of fluid pressure p^f (red line) and this flat distribution is originated from this pressure contribution. This discrepancy is also observed in the computation using the space-time XFEM based on the simplex triangulation approach (Chapter F) and thus, this issue is not caused by the proposed space-time integration. The difference in the stabilization method for convection term and incomprehensibility of the INS fluid, the method of the FSI integral (ALE-FSI and non-matching interface integral using the Lagrangian-immersed FSI method) and the treatment of interface (fixed interface and moving interface) may cause this discrepancy against the reference work. This issue is still unclear and needs more attention.

Focusing on the smoothness of F_D and F_L , Figures 7.43 and 7.45 are less smooth than the reference work (Figure 7.41). As discussed in Section 7.4.1, the roughness in Figures 7.43 and 7.45 might be caused by FSI between non-matching interfaces based on the Lagrangian-immersed FSI method, the coupling methods (Nitsche’s method of Lagrange multiplier method) and the stabilization method for fluid. The discussion of Figure 7.45 above suggests that the fluid pressure causes the roughness of F_D and F_L in Figure 7.45. This instability of the fluid pressure should be examined in the future. It should be noted that the proposed space-time integration based on the elementwise temporal layer is not the cause of this instability (Appendix F).

Table 7.9 summarizes the accuracy study of the Turek-Hron FSI3 problem. Each measure is shown by “mean \pm amplitude [frequency]”. The mean and amplitude of these measures are computed by taking maximum and minimum values. In addition, the frequency of the oscillations of these measures is computed from their periods:

$$\text{mean} = \frac{1}{2}(\max + \min) , \quad (7.59)$$

$$\text{amplitude} = \frac{1}{2}(\max - \min) , \quad (7.60)$$

$$\text{frequency} = \frac{1}{\text{period}} . \quad (7.61)$$

In Table 7.9, ‘A’ and ‘B’ in the first column are the results of the Lagrangian-immersed FSI method using the space-time XFEM with $\Delta t = 0.005\text{s}$ and $\Delta t = 0.0025\text{s}$ respectively. Computed values are obtained by fitting data from 7.9s to 8.1s where the oscillations are completely developed. As the Turek-Hron FSI3 problem is a well-known benchmark problem, there are several numerical studies of this problem. Reference results summarized in Table 7.9 are Turek, Hron, et al. [111, 112], Breuer, Mayer, et al. [113], Chabannes et al. [114], Sandboge [115], and Frei and Richter [116]. The last paper [116] uses the full-Eulerian FSI method and others are based on the ALE-FSI method.

The results of [111, 112, 114, 115] agree well. The results of [113, 116] deviate from

Table 7.9: Numerical results of Turek-Hron FSI3
(mean \pm amplitude [frequency(Hz)])

| | U_x^{tip} (mm) | U_y^{tip} (mm) | F_D (N) | F_L (N) |
|-------|-------------------------|-------------------------|--------------------------|-------------------------|
| [111] | -2.69 ± 2.53 [10.9] | 1.48 ± 34.38 [5.3] | 457.3 ± 22.66 [10.9] | 2.22 ± 149.78 [5.3] |
| [112] | -2.88 ± 2.72 [10.9] | 1.47 ± 34.99 [5.5] | 460.5 ± 27.74 [10.9] | 2.50 ± 153.91 [5.5] |
| [113] | -4.54 ± 4.34 [10.1] | 1.50 ± 42.50 [5.1] | 467.5 ± 39.50 [10.1] | 16.2 ± 188.70 [5.1] |
| [114] | -2.88 ± 2.75 [10.9] | 1.35 ± 34.72 [5.4] | 459.3 ± 29.84 [10.9] | 3.19 ± 171.20 [5.4] |
| [115] | -2.83 ± 2.78 [10.8] | 1.35 ± 34.75 [5.4] | 458.5 ± 24.00 [10.8] | 2.50 ± 147.50 [5.4] |
| [116] | -2.23 ± 2.16 [-] | 1.90 ± 30.86 [-] | 468.9 ± 22.80 [-] | -9.40 ± 193.6 [-] |
| A | -2.80 ± 2.63 [11.1] | 1.10 ± 36.00 [5.6] | 489.5 ± 14.86 [11.1] | 9.44 ± 199.23 [5.6] |
| B | -2.63 ± 2.44 [11.1] | 1.11 ± 33.59 [5.6] | 461.8 ± 20.00 [11.1] | 9.79 ± 181.01 [5.6] |

([111, 112, 113, 114, 115]: ALE-FSI, [116]: Full-Eulerian FSI)

(A: result using $\Delta t = 0.005\text{s}$, B: result using $\Delta t = 0.0025\text{s}$)

[111, 112, 114, 115] and are there for not further considered. As it can be seen from Figure 7.42 and Table 7.42, the deformations of the flexible beam using the Lagrangian-immersed FSI method and the space-time XFEM agree well with the reference results. On the other hand, the results of F_D and F_L deviate from [111, 112, 114, 115]. The deviation of F_L is likely due to the larger time increment ([111, 112]: $\Delta t = 5 \times 10^{-4}\text{s}$, [116]: $\Delta t = 2.5 \times 10^{-4}\text{s}$, A: $\Delta t = 5 \times 10^{-3}\text{s}$, B: $\Delta t = 2.5 \times 10^{-3}\text{s}$). But the time evolution of F_L is similar to [111] as compared in Figure 7.45. The reason of the deviation of F_D from the reference results is likely due to instability of the fluid pressure as discussed previously.

As the Turek-Hron FSI3 benchmark problem is a very challenging numerical problem, some of FSI method cannot compute this benchmark problem or do not show quantitative argument as shown in Table 7.9. The full-Eulerian FSI method [116] could not compute reasonable deformations in comparison with the reference result of [111], even if a much smaller time increment is used ($\Delta t = 2.5 \times 10^{-4}\text{s}$). This indicates the limitation of the capability of the Eulerian approach for FSI analysis.

Consequently, the Lagrangian-immersed FSI method using the space-time XFEM is a promising method to compute FSI problems with large deformations. The issue in terms of the evaluation of the fluid forces acting on a structure must be examined as a future task.

7.4.3 Multibody FSI-contact problem using space-time XFEM

The last numerical example is a multibody FSI-contact problem based on the combination of the Lagrangian-immersed FSI method and the stabilized Lagrange multiplier method for contact using the space-time XFEM.

The geometry and the material of this example is identical to the numerical example described in Section 6.6.4. There are five solid structures modeled by a neo-Hookean material, (6.71) - (6.74), and these solid structures are defined within separate Lagrangian domains Ω_L^i ($i = 1 \sim 5$). Each Lagrangian domain Ω_L^i contains a solid domain Ω_S^i and a dummy displacement domain Ω_D^i : $\Omega_L^i = \Omega_S^i \cup \Omega_D^i$. Figures 6.27 - 6.31 and Table 6.6 report on the geometry of each Lagrangian domain. The physical quantities are summarized in Table 6.7. The spatial discretizations in each Lagrangian and the Eulerian systems are summarized in Table 6.8.

The weak form of the governing equations for this example is identical to (7.4) including the stabilized Lagrange multiplier method for contact. Details of the weak form is given in Section 7.2. In addition, penalty coefficients for Nitsche's method, the face-oriented ghost-penalty method and the stabilized Lagrange multiplier method are summarized in Table 7.10. The penalty factor γ_c for the stabilized Lagrange multiplier method is defined as follows:

$$\gamma_c = \alpha_c \frac{E_i^s + E_j^s}{h_i^s + h_j^s} \quad (i, j = 1 \sim 5, i \neq j), \quad (7.62)$$

where E_i^s and h_i^s are the Young's modulus and the size of the spatial discretization of the solid domain Ω_S^i defined in the i -th Lagrangian domain Ω_L^i . \bar{E}^s is a representative value of the Young's modulus and set as $\bar{E}^s = 1\text{MPa}$ in this example.

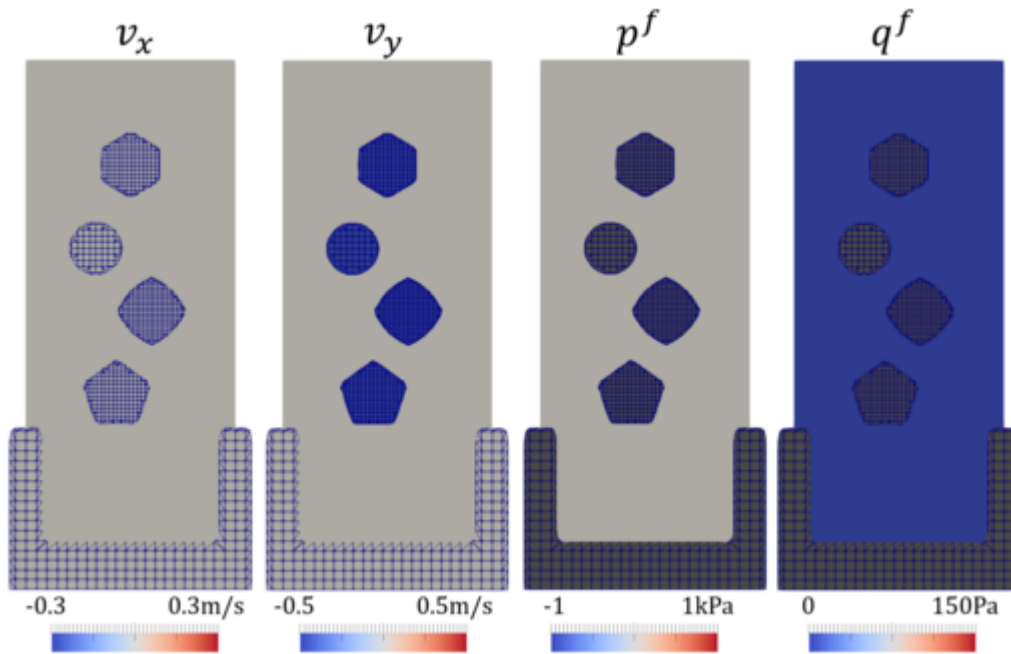
In this numerical example, the size of the temporal discretization is set to $\Delta t = 0.1\text{s}$ and three temporal slices are defined in each temporal layer based on the elementwise temporal layer approach. Newton's method with a direct solver are used. The convergence criterion for the Newton iteration requires a drop of the norm of the residual of 5×10^{-3} relative to

Table 7.10: Penalty coefficients for FSI-contact problem using space-time XFEM

| Method | Penalty Coefficients |
|---|---|
| Nitsche's method for FSI | $\eta^{\text{fsi}} = \alpha^{\text{fsi}} E^s$, $\alpha^{\text{fsi}} = 0.1\text{s/m}$ |
| Nitsche's method for dummy-displacement | $\eta^d = \alpha^d \bar{E}^s$, $\alpha^d = 20\text{m}^{-1}$ |
| stabilized Lagrange multiplier method | $\gamma_c = \alpha_c (E_i^s + E_j^s) / (h_i^s + h_j^s)$, $\alpha_c = 5\text{m}^{-1}$ |
| face-oriented ghost-penalty method | $\alpha_{U^s}^{\text{gp}} = \alpha_{U^d}^{\text{gp}} = \alpha_{V^s}^{\text{gp}} = \alpha_{v^f}^{\text{gp}} = 0.05$, $\alpha_{p^f}^{\text{gp}} = 0.005$ |

the norm of the initial residual. In addition, the adaptive time-stepping scheme is applied to ensure the convergence of the Newton iteration; see (6.92) in Section 6.6.3.

Figures 7.47 - 7.61 illustrate the history of the distributions of the velocity of both the solid and fluid; V_i^s and v_i^f , the fluid pressure p^f and the fluid in-plane effective shear stress q^f ($q^f = |\sigma_1 - \sigma_2|/2$) using $\Delta t = 0.1\text{s}$ and $h = 1/11\text{m}$. Figure 7.47 shows the initial configuration of the FSI-contact problem. Figures 7.48 - 7.50 are snapshots in the time range dominated by FSI without contact. Figures 7.51 - 7.61 are snapshots of the FSI-contact response. Figure 7.61 shows the final time step of this numerical example ($t \simeq 30\text{s}$). Solid structures are in contact with each other and the velocity of both the solid and fluid approaches zero.

Figure 7.47: FSI-contact problem using space-time XFEM ($t = 0\text{s}$, step0)

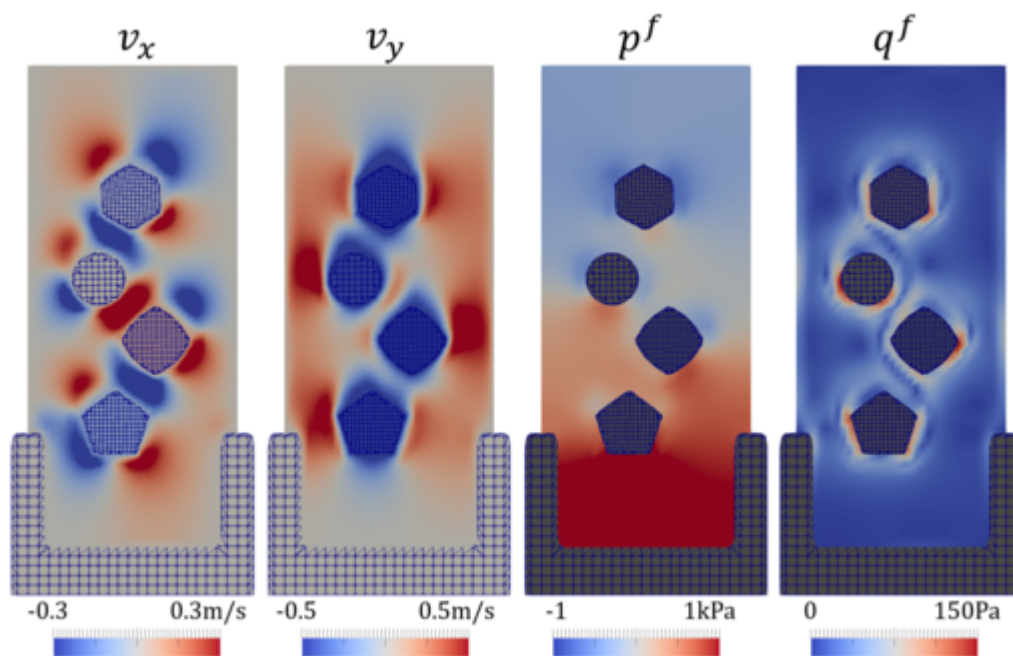


Figure 7.48: FSI-contact problem using space-time XFEM ($t = 1\text{s}$, step10)

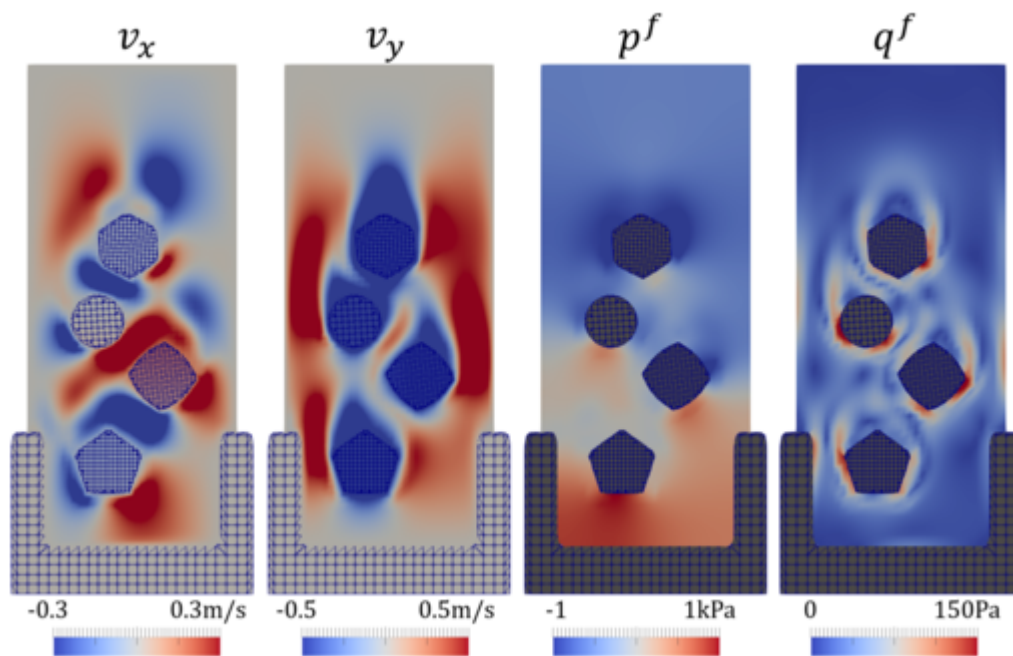


Figure 7.49: FSI-contact problem using space-time XFEM ($t = 2.01875\text{s}$, step23)

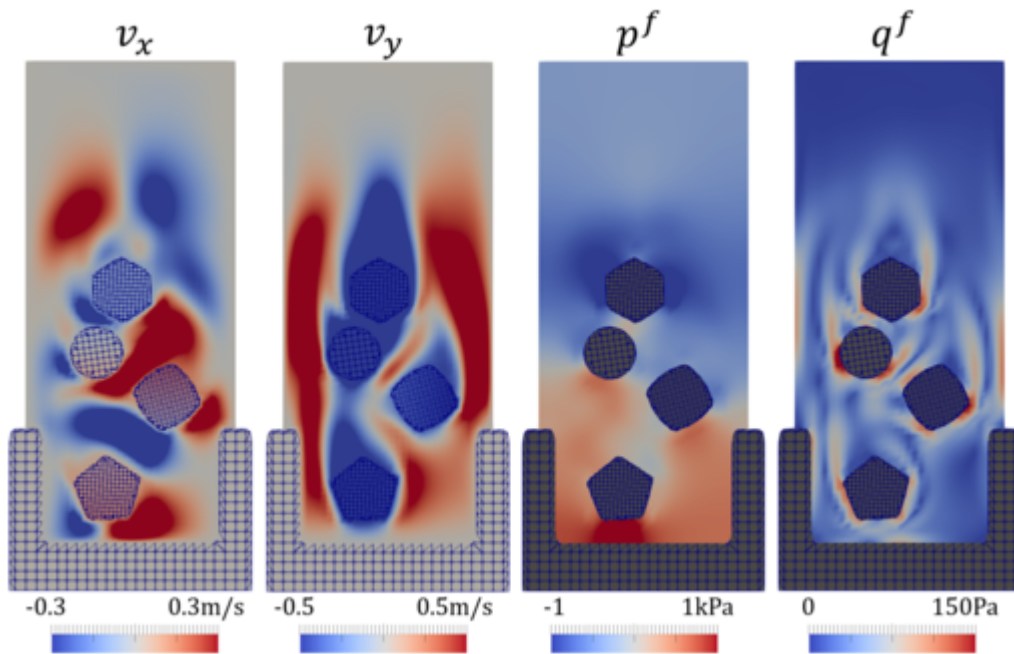


Figure 7.50: FSI-contact problem using space-time XFEM ($t = 3.01875s$, step33)

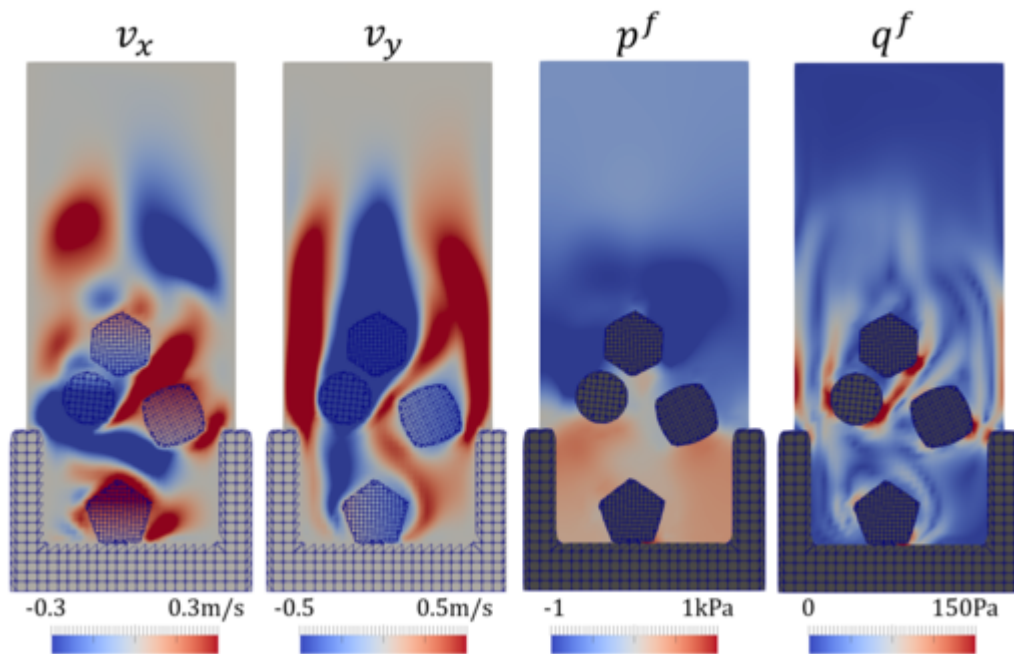


Figure 7.51: FSI-contact problem using space-time XFEM ($t = 4.025s$, step44)

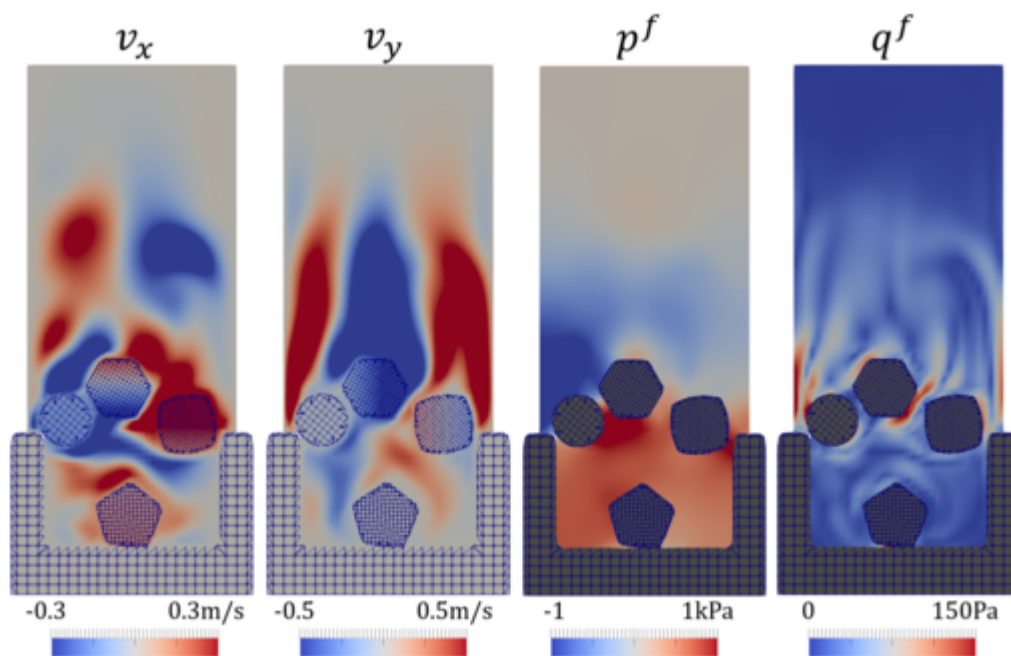


Figure 7.52: FSI-contact problem using space-time XFEM ($t = 4.975s$, step54)

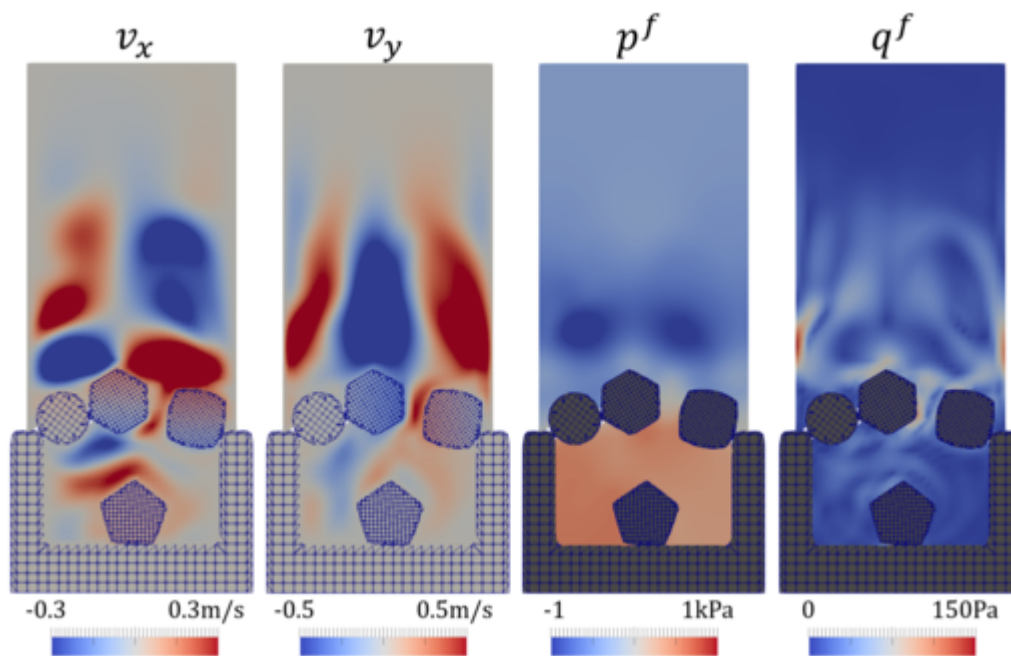


Figure 7.53: FSI-contact problem using space-time XFEM ($t = 5.9875s$, step66)

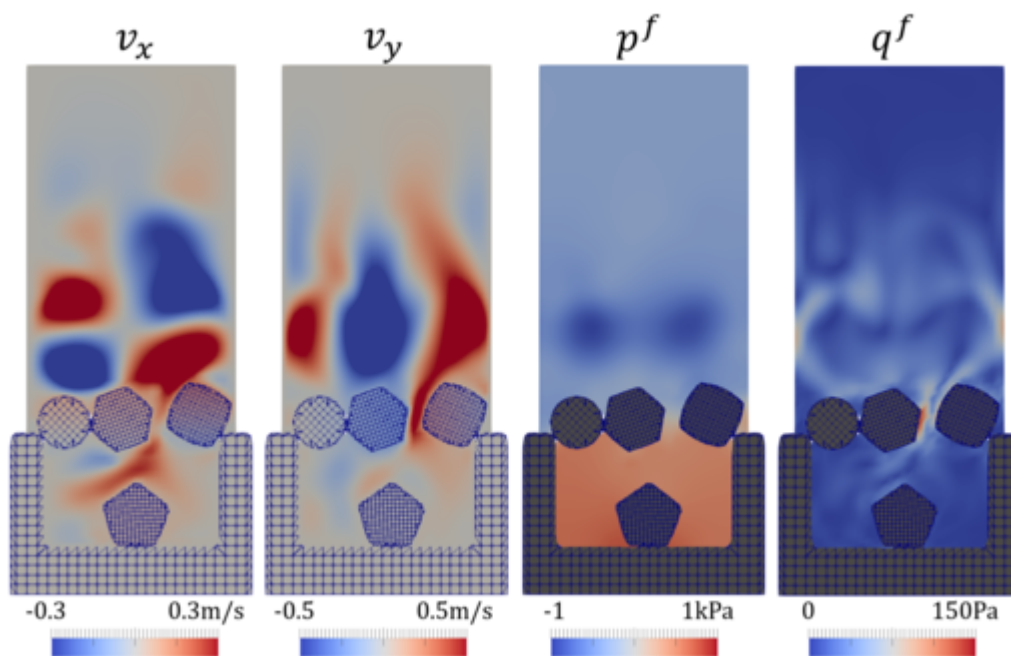


Figure 7.54: FSI-contact problem using space-time XFEM ($t = 7.0625s$, step81)

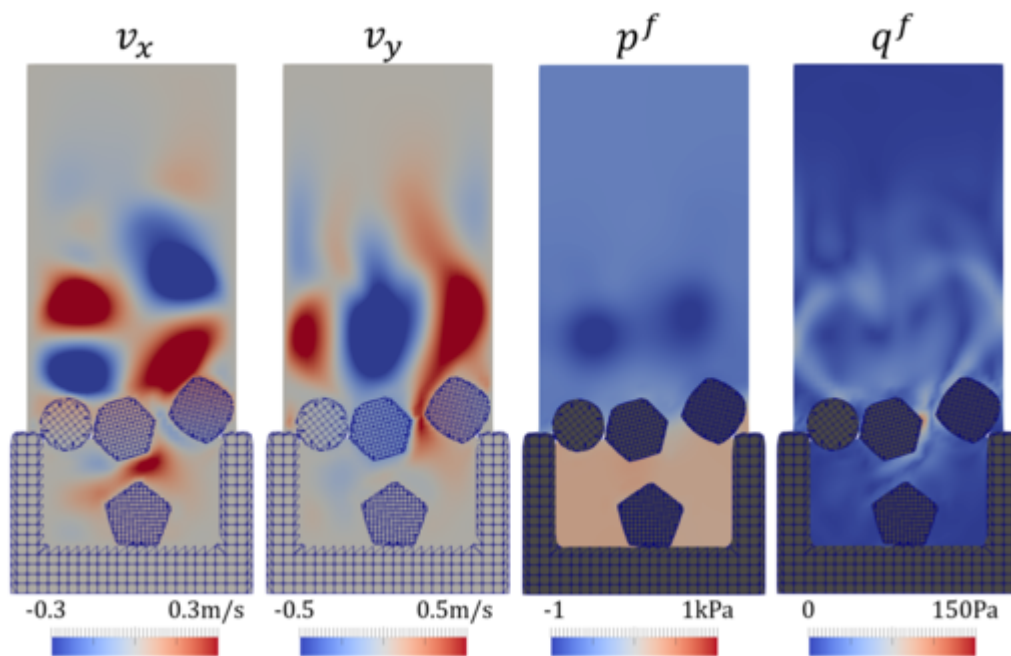


Figure 7.55: FSI-contact problem using space-time XFEM ($t = 8.06875s$, step92)

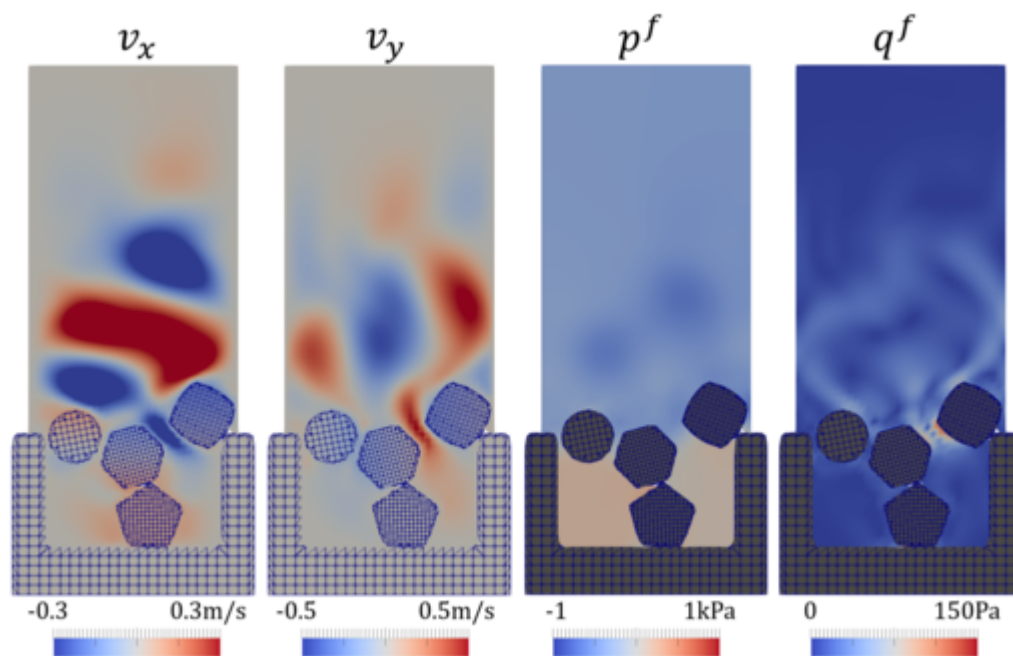


Figure 7.56: FSI-contact problem using space-time XFEM ($t = 11.0625\text{s}$, step129)

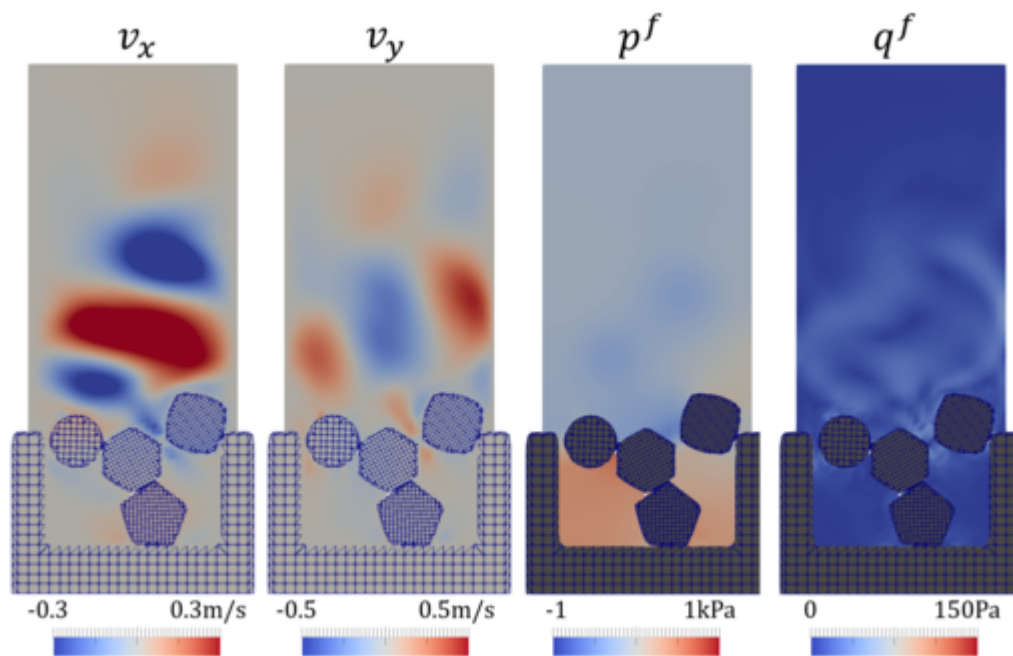


Figure 7.57: FSI-contact problem using space-time XFEM ($t = 13.16785\text{s}$, step150)

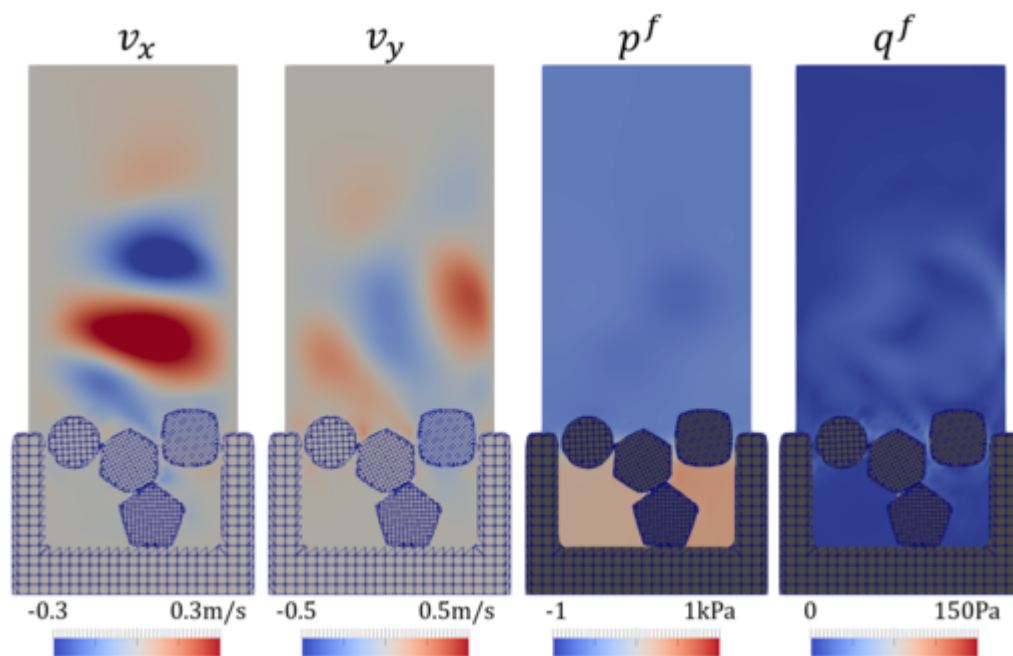


Figure 7.58: FSI-contact problem using space-time XFEM ($t = 15.5125s$, step180)

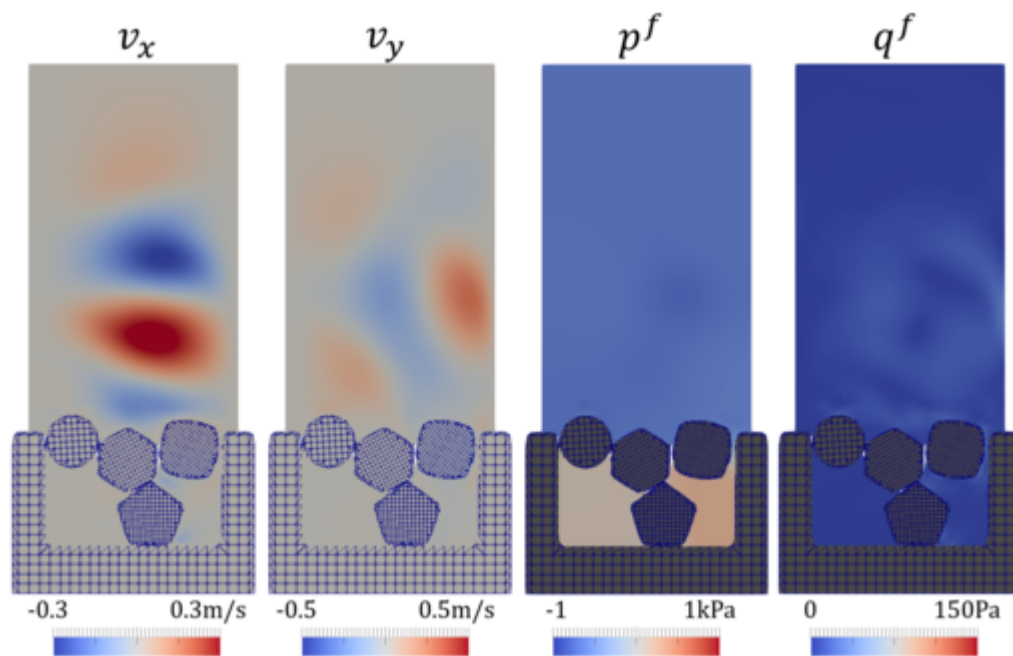


Figure 7.59: FSI-contact problem using space-time XFEM ($t = 18.33125s$, step220)

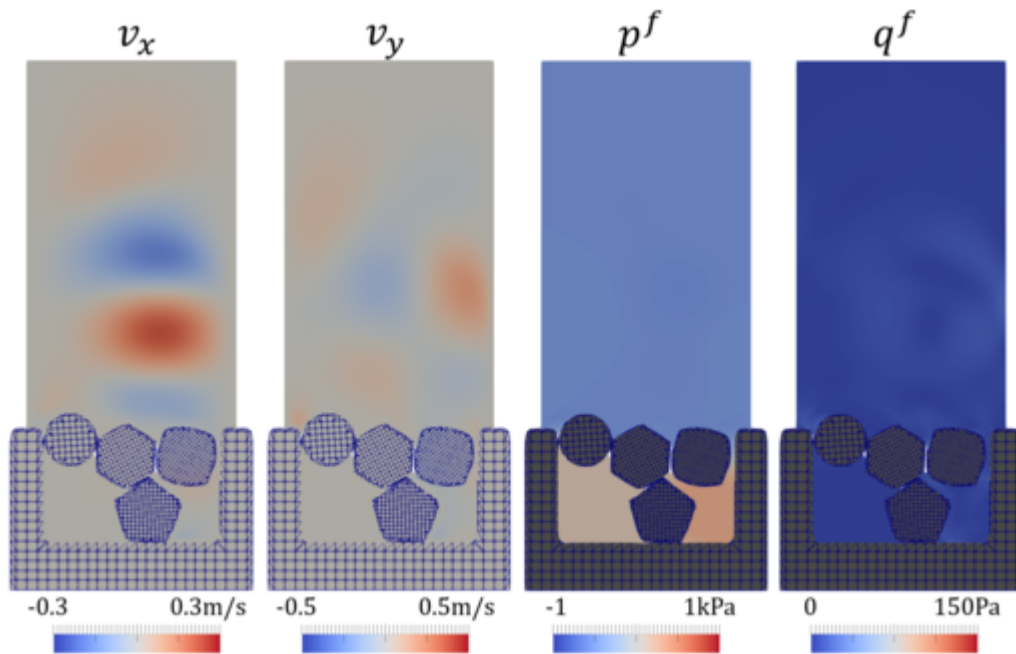


Figure 7.60: FSI-contact problem using space-time XFEM ($t = 25\text{s}$, step297)

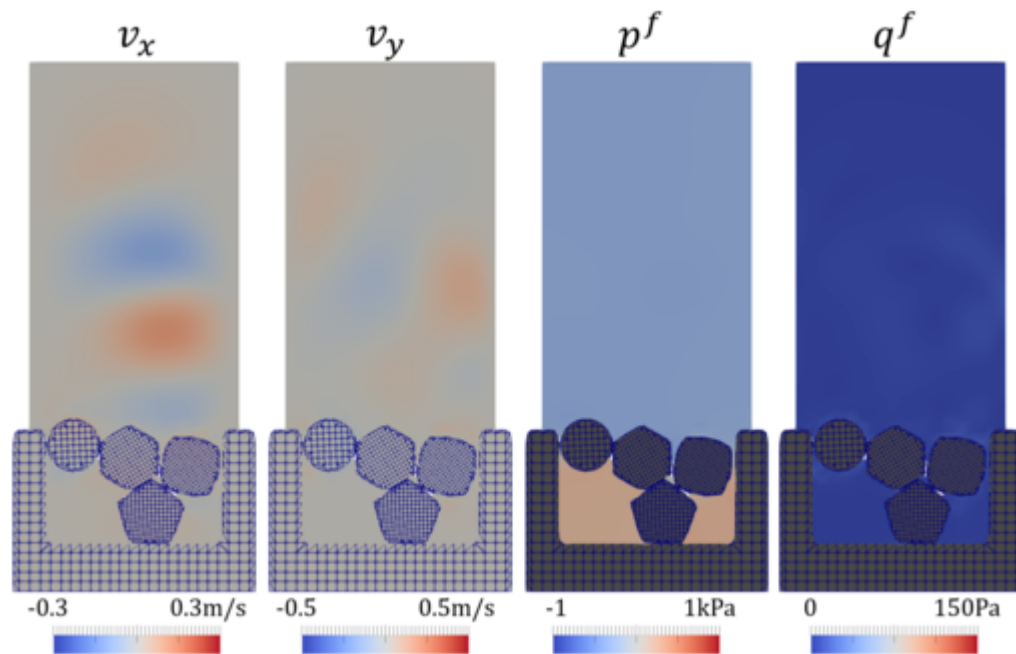


Figure 7.61: FSI-contact problem using space-time XFEM ($t = 30.39375\text{s}$, step385)

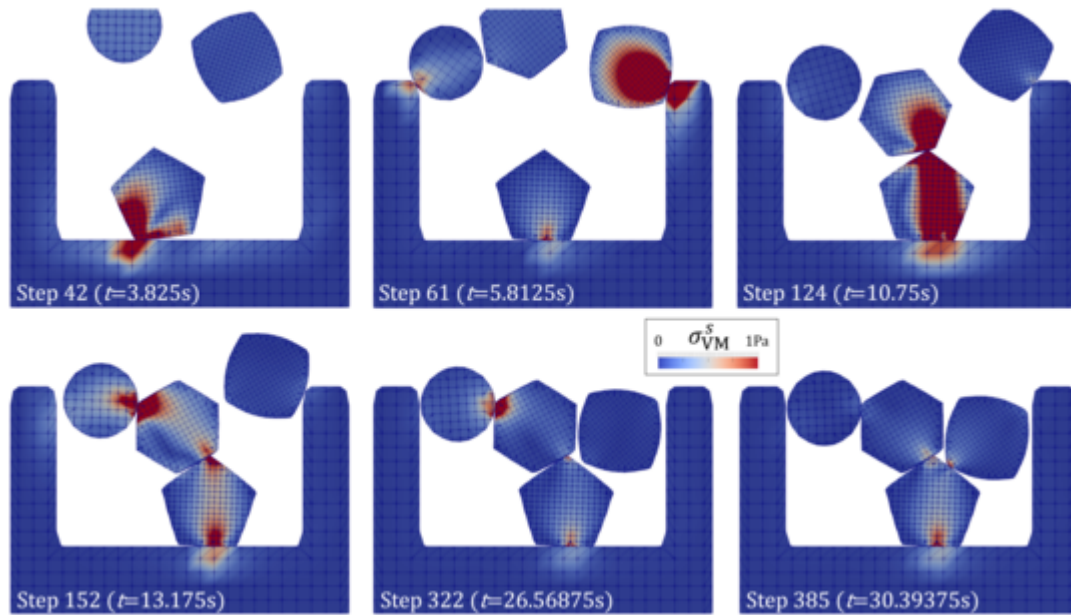


Figure 7.62: Multibody contact in FSI-contact problem using space-time XFEM (von Mises stress contours; Fluid is not visualized.)

Figure 7.62 shows von Mises stress (Cauchy stress) when the solid bodies are in contact. After step 124 ($t > 10$ s), contact among more than two objects occurs.

The results in Figures 7.47 - 7.62 show that the Lagrangian-immersed FSI method using the space-time XFEM can handle both fluid-structure interaction and complex multibody contact simultaneously. These figures look similar to results of the Lagrangian-immersed FSI method using the XFEM with a time stepping scheme described in Section 6.6.4. However, the difference between the results using the space-time XFEM and the previous results using the XFEM is highlighted by comparing the fluid forces and the momentum.

Figures 7.63 and 7.64 are comparisons of the fluid forces using the XFEM and the space-time XFEM, respectively. The blue and red lines are contributions of the fluid hydrostatic pressure and the fluid velocity, respectively. The black lines represent the total fluid forces acting on solid structures and defined as the summation of blue and red lines. At the range of $0 \leq t \leq 25$ s, the Eulerian interfaces Γ_E move due to the deformations of the Lagrangian solid structures. The fluid forces computed by the standard XFEM (left graphs) oscillate due to the temporal interpolation errors caused by moving interfaces.

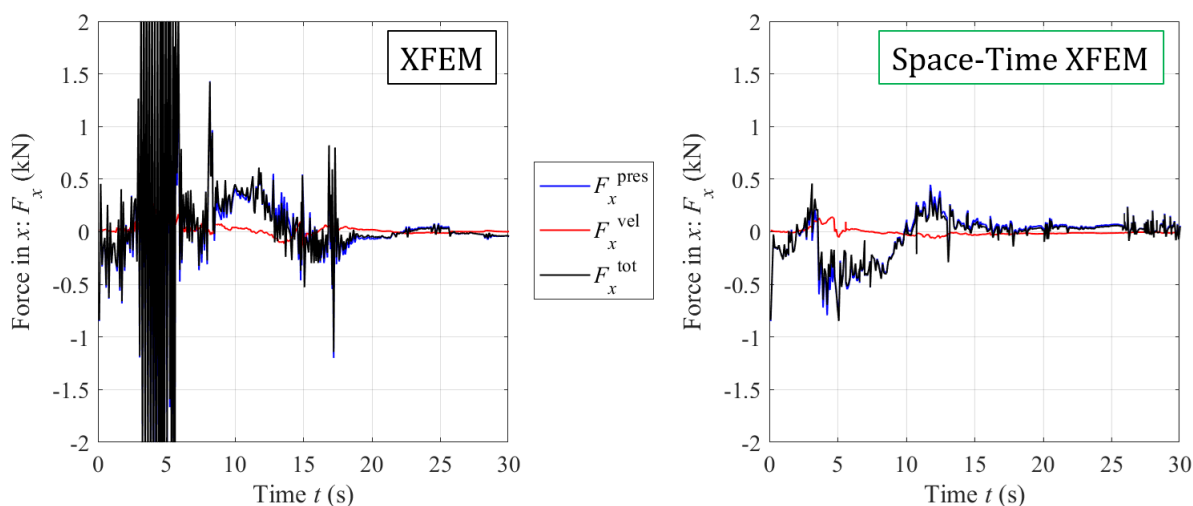


Figure 7.63: Comparison of F_x (FSI-contact with XFEM and space-time XFEM)

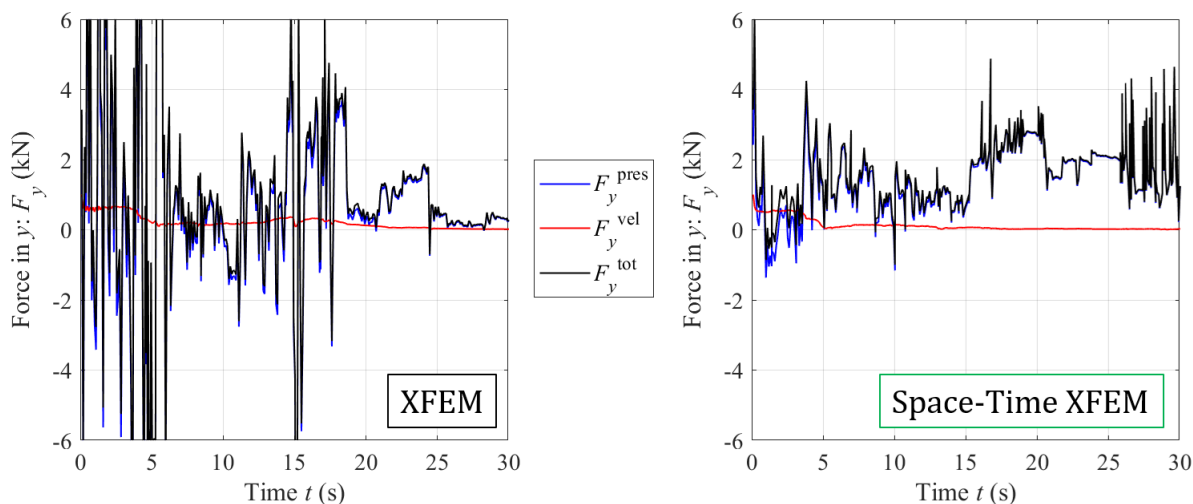


Figure 7.64: Comparison of F_y (FSI-contact with XFEM and space-time XFEM)

In particular, these forces highly oscillate until 10s because the motion of the interfaces is large in this region. On the other hand, the fluid forces F_y computed by the space-time XFEM (right graphs) have not spurious oscillations. This indicates that the space-time XFEM correctly integrates the response in time even for moving interfaces. Small oscillations using the space-time XFEM can be observed; these oscillations are assumed to be caused by the non-matching space-time interfaces and multibody contact. In the range of $25 < t \leq 30$ s, the velocities of both the solid and fluid become very small and the system response is dominated by contact. In this region, the fluid forces computed by the space-time XFEM oscillate more

largely than forces computed by the XFEM. This may indicate that the conventional contact formulation for the XFEM is more stable than the current contact formulation for the space-time XFEM described in Section 7.3.5. This issue is still unclear and needs more attention.

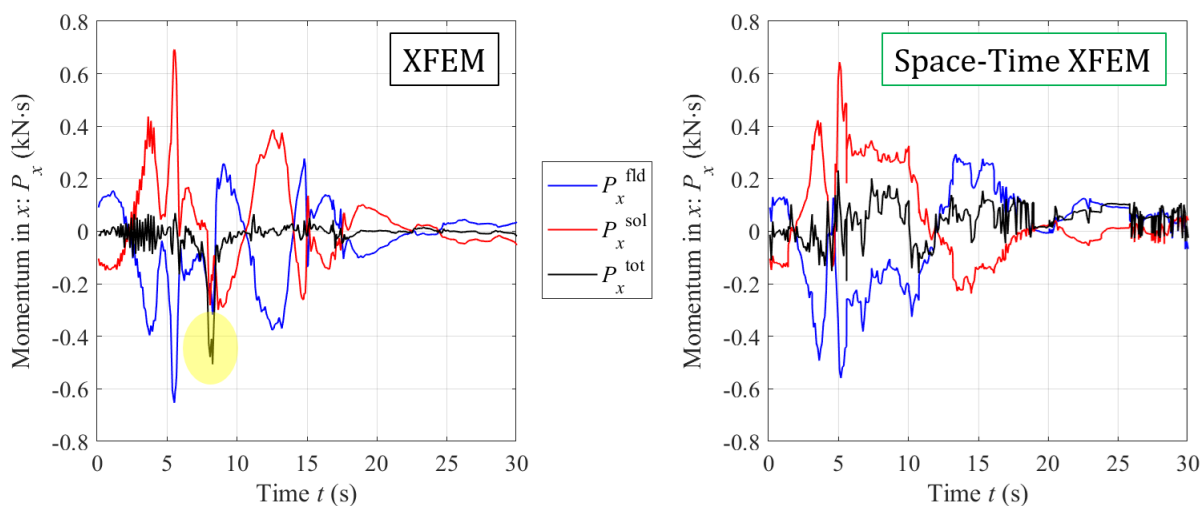


Figure 7.65: Comparison of P_x (FSI-contact with XFEM and space-time XFEM)

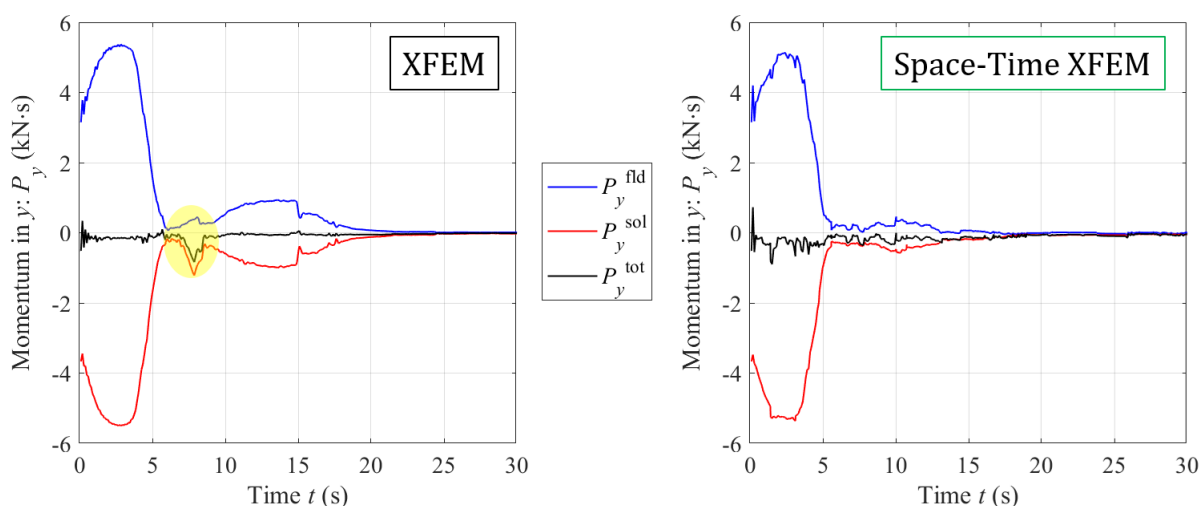


Figure 7.66: Comparison of P_y (FSI-contact with XFEM and space-time XFEM)

Figures 7.65 and 7.66 show the comparisons of the momentum computed by the XFEM and the space-time XFEM, respectively. The blue and red lines represent the momentum of the fluid and solid phase, respectively. The total momentum is shown by black lines as the summation of the solid and fluid momentum. These results show that the XFEM and the space-time XFEM converge to the steady-states. Like the first numerical example

(Section 7.4.1), the momentum P_x and P_y in x and y direction, are transmitted between the solid and fluid. The conservation of the total momentum (summation of solid and fluid momentum) should be satisfied. As the momentum is a result of the solid and fluid forces, the fluid forces in Figures 7.63 and 7.64 influence the evolution of the momentum P_x and P_y . A remarkable point is the violation of the conservation of momentum using the XFEM. The yellow shaded regions in left graphs show large discrepancies from zero in the total momentum using the XFEM. Such a large violation of the conservation is not observed in results of the space-time XFEM. Oscillations using the space-time XFEM can be observed in Figure 7.65; these oscillations are assumed to be caused by the non-matching space-time interfaces and multibody contact, similar to the oscillations of the fluid forces. In the range of $25 < t \leq 30$ s, the oscillations seem to be due to contact. While multibody contact is correctly captured using the proposed contact formulation in the space-time XFEM, reconsideration of the contact formulation for the space-time XFEM will be necessary to enhance the stability of the FSI-contact problem.

Finally, the convergence of the Lagrangian-immersed FSI method using the space-time XFEM is studied. Four models which have different size of the spatial discretization ($h = 4/11, 7/2, 4/19$ and $2/11$ m $\simeq 0.364, 0.286, 0.211$ and 0.182 m) are used. As a remainder, h is the representative size of the spatial discretization in this example and identical to the size of the spatial discretization in the Eulerian system h_E . The sizes of the spatial discretization h_{L0}^i of the Lagrangian systems 1-4 ($i = 1 \sim 4$), are proportional to h as defined in Table 6.8. The spatial discretization of Lagrangian system 5, which is a fixed concave structure at the bottom, is constant ($h_{L0}^5 = 0.1867$ m).

Figure 7.67 illustrates the trajectories of centroids of solid structures 1-4 using different sizes of the spatial discretization. Figures 7.68 and 7.69 show comparisons of total fluid force and total momentum using different sizes of the spatial discretization.

For the convergence study, the L2 errors of the solid displacements and the velocity at

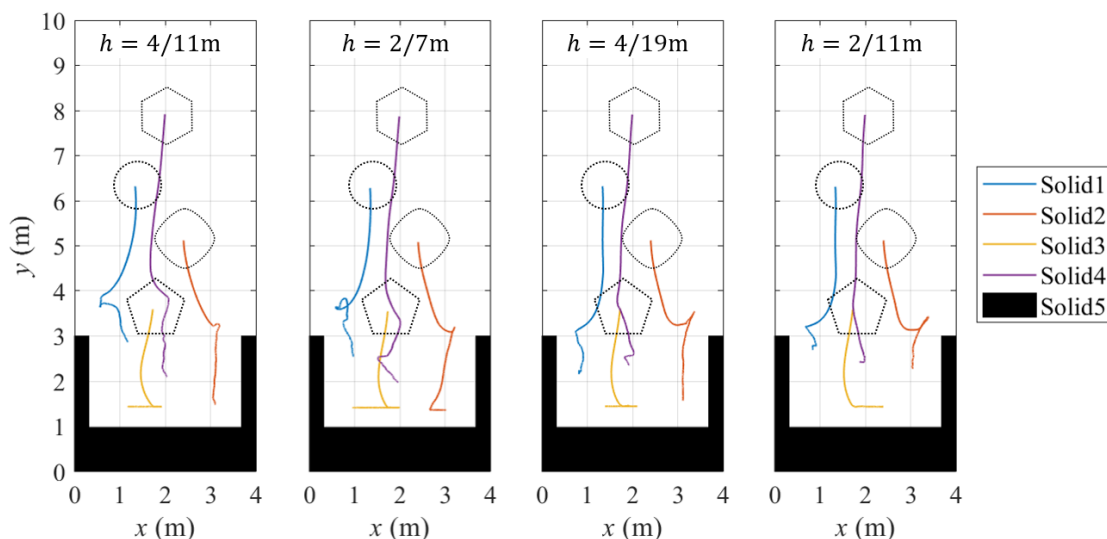


Figure 7.67: Trajectory of centroids of solid structures (space-time XFEM, $\Delta t = 0.1s$)

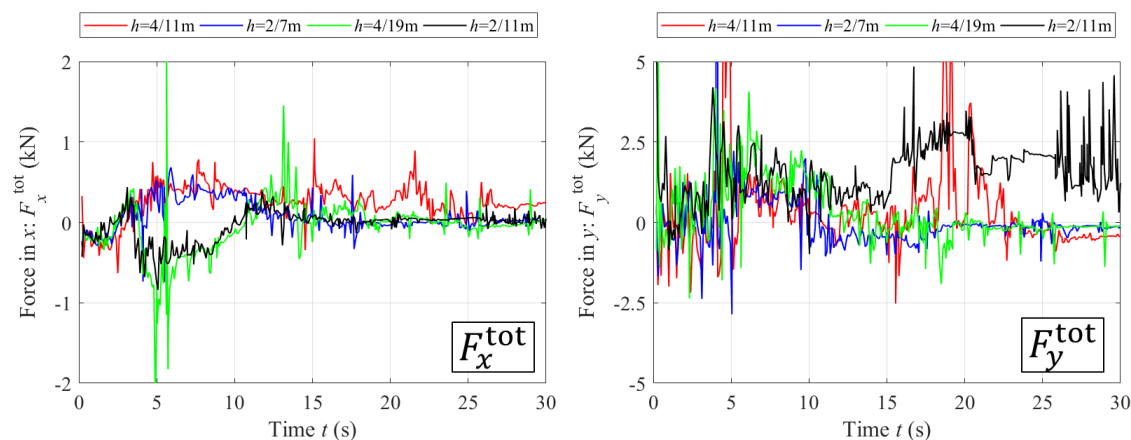


Figure 7.68: Spatial size dependency of force (space-time XFEM, $\Delta t = 0.1s$)

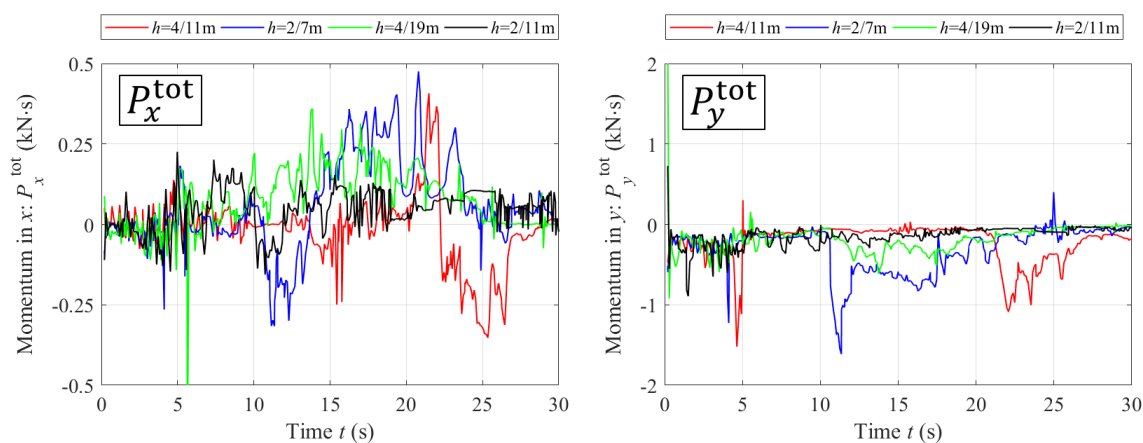


Figure 7.69: Spatial size dependency of momentum (space-time XFEM, $\Delta t = 0.1s$)

each centroid corresponding to Figure 7.67, the L2 errors of the fluid forces corresponding to Figure 7.68, and the deviation of the total momentum from zero corresponding to Figure 7.69. The definitions of these errors are as follows:

$$\text{L2Error}(\mathbf{U}_{\text{cent}}) = \sqrt{\frac{\sum_{j=1}^4 \int_{t_i}^{t_f} dt \|\mathbf{U}_{\text{cent}}^j - \mathbf{U}_{\text{cent-ref}}^j\|^2}{\sum_{j=1}^4 \int_{t_i}^{t_f} dt \|\mathbf{U}_{\text{cent-ref}}^j\|^2}}, \quad (7.63)$$

$$\text{L2Error}(\mathbf{V}_{\text{cent}}) = \sqrt{\frac{\sum_{j=1}^4 \int_{t_i}^{t_f} dt \|\mathbf{V}_{\text{cent}}^j - \mathbf{V}_{\text{cent-ref}}^j\|^2}{\sum_{j=1}^4 \int_{t_i}^{t_f} dt \|\mathbf{V}_{\text{cent-ref}}^j\|^2}}, \quad (7.64)$$

$$\text{L2Error}(F_x^{\text{tot}}) = \sqrt{\frac{\int_{t_i}^{t_f} dt (F_x^{\text{tot}} - F_{x\text{-ref}}^{\text{tot}})^2}{\int_{t_i}^{t_f} dt F_{x\text{-ref}}^{\text{tot}2}}, \quad (7.65)$$

$$\text{L2Error}(F_y^{\text{tot}}) = \sqrt{\frac{\int_{t_i}^{t_f} dt (F_y^{\text{tot}} - F_{y\text{-ref}}^{\text{tot}})^2}{\int_{t_i}^{t_f} dt F_{y\text{-ref}}^{\text{tot}2}}, \quad (7.66)$$

$$\text{Error}(P_x^{\text{tot}}) = \sqrt{(t_f - t_i)^{-1} \int_{t_i}^{t_f} dt P_x^{\text{tot}2}}, \quad (7.67)$$

$$\text{Error}(P_y^{\text{tot}}) = \sqrt{(t_f - t_i)^{-1} \int_{t_i}^{t_f} dt P_y^{\text{tot}2}}, \quad (7.68)$$

where t_i and t_f are initial and final times for the evaluation of errors. $t_i = 0.4\text{s}$ and $t_f = 30\text{s}$ are used to evaluate these errors. $\mathbf{U}_{\text{cent}}^i$ and $\mathbf{V}_{\text{cent}}^i$ represent the displacement and velocity vectors at the centroid of the solid structure i defined in Ω_{L0}^i . $\mathbf{U}_{\text{cent-ref}}^i$, $\mathbf{V}_{\text{cent-ref}}^i$, $F_{x\text{-ref}}^{\text{tot}}$ and $F_{y\text{-ref}}^{\text{tot}}$ denote the reference solutions using the finest model: $h = 2/11\text{m}$.

Figure 7.70 shows the L2 errors of the solid displacements and the velocities at each centroid. The convergence rates of both the displacements and velocities are almost identical because of the linear relationship between the solid displacements and velocities in the governing equations; i.e. the displacement-velocity relationship (6.8).

Figure 7.71 shows the L2 errors of the fluid forces. The convergence of F_y^{tot} is slower than the one of F_x^{tot} . As the contact is dominant in y direction because of the fall of the solid structures, the high nonlinearity due to contact exists mainly in y direction and this complex nonlinearity might cause the slower convergence in F_y^{tot} .

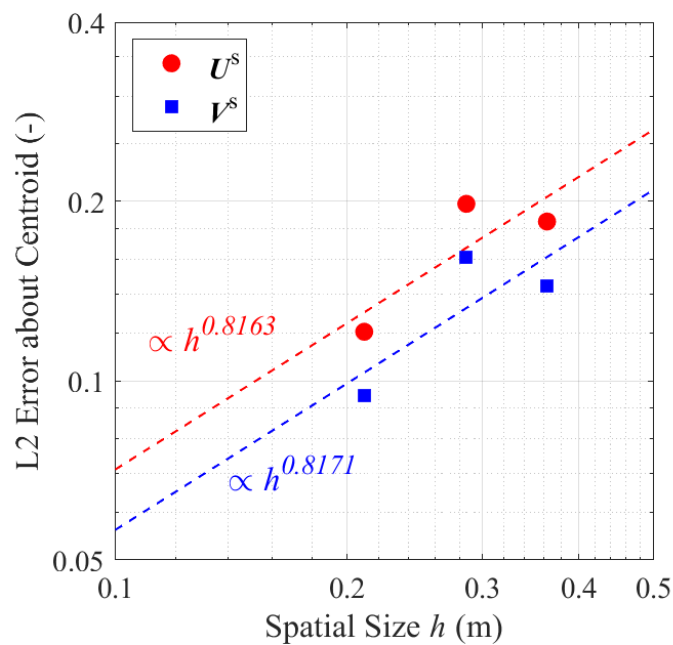


Figure 7.70: L2 error of quantities at centroids (space-time XFEM, $\Delta t = 0.1s$)
(reference model: $h = 2/11m$ and $\Delta t = 0.1s$ using space-time XFEM)

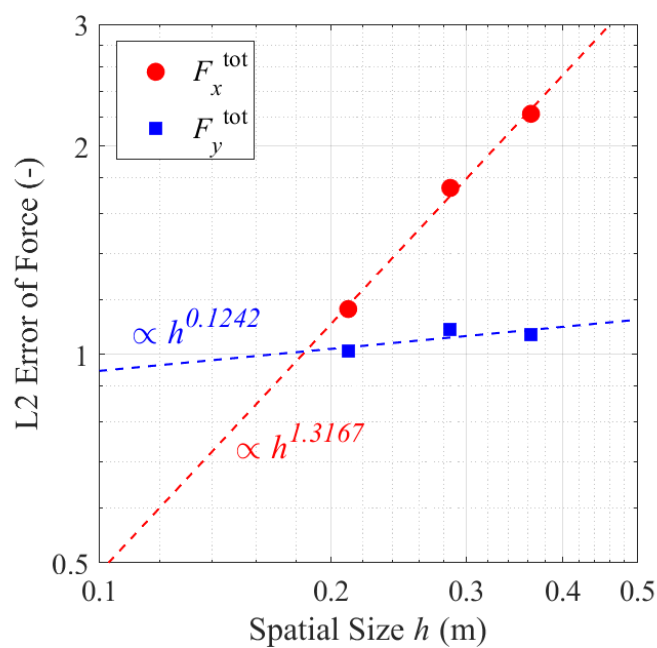


Figure 7.71: L2 error of force (space-time XFEM, $\Delta t = 0.1s$)
(reference model: $h = 2/11m$ and $\Delta t = 0.1s$ using space-time XFEM)

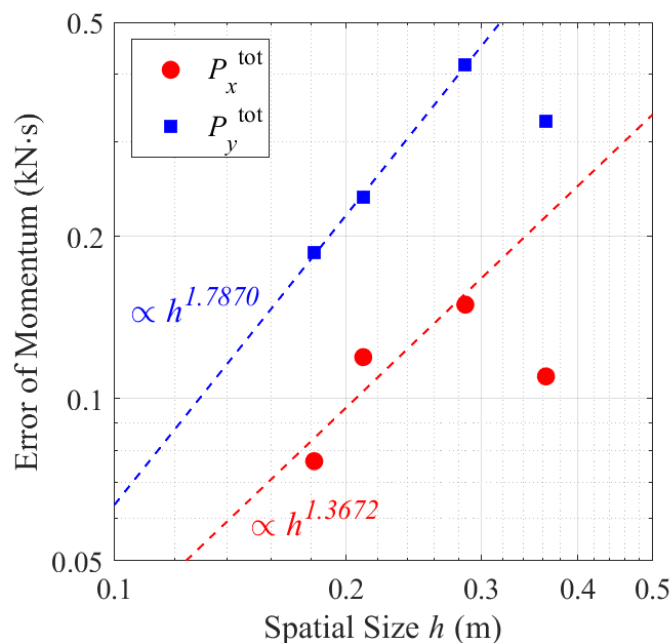


Figure 7.72: Error of momentum (space-time XFEM, $\Delta t = 0.1\text{s}$)

Figure 7.72 shows the error of the conservation of the total momentum. The approximation to compute the rates of convergence in this figure uses only three points with $h < 0.3\text{m}$. The violation of the conservation of momentum is reduced by mesh refinement for both P_x^{tot} and P_y^{tot} . These studies suggest that the combination of the space-time XFEM and the Lagrangian-immersed FSI method correctly treats the complex nonlinearity due to both FSI and multibody contact.

7.5 Discussion

This chapter presented the Lagrangian-immersed FSI method using the space-time XFEM. The space-time XFEM based on the elementwise temporal layer approach (Chapter 3) is applied to the Lagrangian-immersed FSI method. The finite element discretization and the XFEM enrichment is applied in both space and time. A simple implementation for integrating the space-time discretization is realized based on the elementwise temporal layer approach.

FSI is modeled between non-matching space-time interfaces defined by separate Lagrangian and Eulerian space-time slabs. The integration scheme for space-time FSI uses techniques of computational contact mechanics, such as the master-slave concept, the node-to-surface pairing and the gap equation for contact. The stabilized Lagrange multiplier method and the level set projection method are expanded into the space-time formulations.

Three transient numerical examples were studied based on the Lagrangian-immersed FSI method using the space-time XFEM. The first numerical example was a falling cylinder within a fluid domain. This problem poses severe challenges for the conventional ALE-FSI method because of large deformation. The second numerical example was a challenging FSI problem known as the Turek-Hron FSI3 benchmark problem. It should be noted that some of non-standard FSI methods cannot pass this benchmark problem. The Lagrangian-immersed FSI method using the space-time XFEM could capture the complex deformations of a flexible solid beam due to self-induced oscillation by fluid flow. The obtained results agreed reasonably well with the ALE-FSI method. The deformation of the proposed approach agrees well with the reference works. However, the fluid forces acting on the solid structure have oscillatory behaviors and the drag force has a big discrepancy from the reference works. This issue is still unclear and needs more attention. These two examples illustrate the potential of the proposed method for FSI with large deformation without remeshing and any additional treatment like the ghost fluid method. The third numerical example was

a multibody FSI-contact problem. As an interface in the Eulerian system is treated as a moving interface, there is no limitation with respect to contact and large deformations in the Lagrangian-immersed FSI method. The space-time XFEM avoids temporal interpolation errors due to moving interfaces. Stable and robust FSI-contact computation was achieved by the proposed method.

Owing to the elegance of the fixed grid approach in a fluid domain and the space-time formulation, the Lagrangian-immersed FSI method using the space-time XFEM is a promising method which has interesting capabilities for complex FSI-contact problems. The ability to model large deformations and contact simultaneously within the FSI system presents a significant process in simulating complex FSI problems. This method is not limited to the fluid-structure interaction and also applicable to various types of complex multi-physics problems including moving interfaces, such as the interaction between the Lagrangian and Eulerian solids, the interaction of structure and electromagnetic fields and acoustic-structure interaction. Unresolved issues of the Lagrangian-immersed FSI method using the space-time XFEM include the presence of small fluctuations of the fluid forces around moving interfaces as shown in Figures 7.22 and 7.23. This problem is assumed to be caused by non-matching space-time interfaces. Revisiting the integration method between non-matching interfaces might be necessary. Other coupling method for FSI like the Lagrange multiplier method is worth considering instead of Nitsche's method. While the studies in this chapter only focus on spatially two-dimensional problems, it is necessary to expand this method into three-dimensional problems.

Chapter 8

Conclusions

8.1 Summary

This thesis presented a space-time extended finite element method (space-time XFEM) based on the elementwise temporal layer approach and its applications to fluid-structure interaction (FSI) and contact problems.

The proposed space-time XFEM applies the Heaviside-enrichment strategy in both the space and time. A simple space-time integration based on the summation of spatial integration at multiple temporal quadrature points was introduced as the elementwise temporal layer approach. Each space-time element is subdivided into multiple temporal layers along time by considering its intersection configuration. Furthermore, temporal integration points are defined in each temporal layer. Each temporal layer is cut by planes on these points parallel to the spatial domain. The cross sections created by this cut are called as the temporal slices in this thesis. As the number of temporal slices in each temporal layer affects the effective time increment, a larger number of slices is beneficial from the viewpoint to get a faster convergence in terms of the time evolution. Integration points for a space-time volume are distributed on each temporal slice using the same numerical integration scheme used in the standard XFEM. Integration points for space-time interface are set on a space-time interface which has the same dimension as the spatial domain. As higher-dimensional decompositions of a space-time slab like the simplex triangulation method are not needed, the proposed space-time XFEM eases significantly the implementation of the space-time integration. The space-time interface conditions are prescribed by Nitsche's method. In addition, the face-oriented ghost-penalty method is applied in the space-time XFEM for mitigating

the ill-conditioning problem due to small intersected space-time elements.

The proposed space-time XFEM was applied to transient, spatially two-dimensional problems. The accuracy and stability of Nitsche's method and the face-oriented ghost-penalty stabilization for the space-time XFEM was studied with an elasto-dynamic problem and a fluid problem known as DFG 2D-3 benchmark problem. While the numerical accuracy of physical quantities that had a steady-state like behavior was quite similar in both methods, the space-time XFEM could evaluate physical quantities that had a dynamic characteristic more precisely than the spatial XFEM using the same time increment. The proposed space-time XFEM was applied to a fluid problem with moving interfaces. The divergence of the numerical solution was avoided successfully by the face-oriented ghost-penalty stabilization and it was confirmed that the face-oriented ghost-penalty method was effective in the space-time XFEM to stabilize the numerical computations, especially for moving interface problems. As the XFEM suffer from temporal interpolation errors due to moving interfaces, and additional treatments such as the ghost-fluid method are necessary for the stable temporal interpolation. The space-time XFEM overcomes temporal interpolation errors due to moving interfaces without the ghost-fluid method, and obtains dynamical quantities stably. The space-time XFEM has a great advantage in terms of stability, accuracy and flexibility for problems with moving interfaces.

The benefit of robust and stable mathematical treatment of moving interfaces using the space-time XFEM enhances the flexibility of the computational methods for the FSI problems. In this thesis, non-standard FSI methods (non-ALE methods) using moving interfaces were studied by considering the FSI-contact problems which are difficult to solve by the conventional ALE-FSI method. As a preliminary study for the combination of the flexible FSI method and the space-time XFEM, two non-standard FSI methods using the XFEM were examined.

The full-Eulerian FSI method using the XFEM is one method which has the ability

to treat the FSI-contact problems. The Eulerian description is applied in both the solid and fluid domains and thus, its computation is performed in the fixed background mesh. There is no limitation in terms of large deformation and contact. The conservative level set function (CLS F) method is introduced to represent the FSI interfaces. While the full-Eulerian FSI method was confirmed as an attractive method to compute FSI and large deformations, a fine-scale time increment is needed for the computation of the convection equations used in the level set function and the momentum equations. In addition, the steady-state problems cannot be computed efficiently by the full-Eulerian FSI method. This feature is a big disadvantage for the applications such as the optimization scheme.

The Lagrangian-immersed FSI method using the XFEM was also proposed as a more flexible computational method for the FSI-contact problems than the Full-Eulerian FSI method. In the Lagrangian-immersed FSI method, the solid and fluid phases are defined by the Lagrangian and Eulerian descriptions, respectively. Meshes of the solid and the fluid are spatially disconnected. FSI is computed between non-matching Lagrangian and Eulerian interfaces using techniques of computational contact mechanics, such as the master-slave concept, the node-to-surface pairing, and the gap equation. As the solid phase is defined by the Lagrangian description, conventional contact formulations are directly applicable to the FSI system, and the stabilized Lagrange multiplier method is used in this research. Thus, the implementation of the contact formulation is much easier than with the full-Eulerian FSI method. Interfaces in the Eulerian system are defined by the level set projection method to capture the deformation of disconnected solid structures correctly. By introducing the level set projection method into a monolithic solution strategy for the FSI system, the update of geometry is automatically performed as the solution converges. Steady-state FSI problems with large deformations were computed by the Lagrangian-immersed FSI method and the XFEM. The ability to compute steady-state FSI problems with large deformations is a great advantage for the applications such as the optimization. A transient multibody FSI-contact

problem was also studied. The Lagrangian-immersed FSI method using the XFEM was able to predict the response of a complex FSI-contact system without the limitation on large deformation as the ALE-FSI method has. While the Lagrangian-immersed FSI method using the XFEM is an attractive method in terms of the high capability for the FSI-contact problems and the easiness of the implementation, the drawback of temporal interpolation errors by moving interfaces exist due to the time stepping schemes. Thus, this method should be combined with the space-time XFEM for the accurate evaluation of the effect of moving interfaces used in the fluid domain.

Finally, the combination of the space-time XFEM and the Lagrangian-immersed FSI method was proposed. FSI is modeled between non-matching space-time interfaces defined by separate Lagrangian and Eulerian space-time slabs. The integration scheme for space-time FSI uses techniques of computational contact mechanics. The stabilized Lagrange multiplier method and the level set projection method are expanded into the space-time formulations. From the studies using two numerical examples; a falling cylinder within a fluid domain and the Turek-Hron FSI3 benchmark problem, the potential of the proposed combination for FSI with large deformation was demonstrated. A multibody FSI-contact problem was also computed. As the space-time XFEM can avoid temporal interpolation errors due to moving interfaces, stable and robust computation for the FSI-contact problems was achieved.

Owing to the elegance of the fixed grid approach in a fluid domain and the space-time formulation, the Lagrangian-immersed FSI method using the space-time XFEM is a promising method which has interesting capabilities for complex FSI-contact problems. The ability to model large deformations and contact simultaneously within the FSI system presents a significant process in simulating complex FSI problems. This method is not limited to the fluid-structure interaction and also applicable to various types of complex multi-physics problems including moving interfaces, such as the interaction between the Lagrangian and Eulerian solids, the immiscible multiphase fluid problem, the interaction of a structure and

electromagnetic fields, and acoustic-structure interaction. Based on the proposed method, the realization of the flexible computation for complex multi-physics analysis is able to extend greatly the range of the product design in the industrial world.

8.2 Future Works

The computational methods presented in this thesis are promising for complex geometries and multi-physics systems, but these methods are still in the developing stage. This section summarizes future prospects and open questions to be clarified for the space-time XFEM and the Lagrangian-immersed FSI method.

(1) Extension to spatially three-dimensional problems

In this thesis, the space-time XFEM and the Lagrangian-immersed FSI method were studied using spatially two-dimensional problems. To demonstrate the versatility of the proposed methods, the extension of the proposed methods into spatially three-dimensional problems should be the next step. As the elementwise temporal layer approach and the FSI between non-matching space-time interfaces based on the node-to-surface method are directly applicable to 3D, there are no fundamental hurdles for this extension. The challenging point is the contact formulation. Currently, the surface-to-surface pairing is used in the contact formulation, following the work of Lawry and Maute [75]. The contact algorithm based on the node-to-surface pairing is preferable for 3D analysis. Furthermore, the combination of the proposed method and hierarchical mesh refinement would enhance both the accuracy and computational efficiency for large-scale 3D problems.

(2) Modification of FSI between non-matching interfaces

FSI in the Lagrangian-immersed FSI method is computed by boundary integrals between non-matching interfaces based on Nitsche's method. In some cases, physical quantities of the

Eulerian system (e.g. drag and lift force) have non-physical fluctuations in time even if when the space-time XFEM is used. It is assumed that these fluctuations mainly originate from FSI on non-matching interfaces. Enhancing the accuracy and stability of the FSI boundary integrals is recommended. Studies could include: the parameter study of the penalty coefficients for Nitsche's method, and the change of the coupling method from Nitsche's method to other methods, such as the Lagrange multiplier method.

(3) Optimization based on Lagrangian-immersed FSI method

This thesis presented only forward analysis. As an application, topology optimization of steady-state and transient FSI problems including large deformation and contact could be computed by the Lagrangian-immersed FSI method. As Lagrangian and Eulerian systems are completely disconnected in the Lagrangian-immersed FSI method, this feature simplifies the adjoint sensitivity analysis for the gradient-based design optimization.

(4) Application to various multi-physics problems

The proposed combination of the space-time XFEM and the Lagrangian-immersed FSI method is not limited to fluid-structure interaction, but it provides a computational framework for complex multi-physics problems. Tire simulation on snow or soil could be computed as the interaction between Lagrangian and Eulerian solids based on the proposed method. The proposed method would be directly applicable to acoustic-structure interaction in the presence of moving interfaces [117], and interaction between a structure and the electromagnetic field. The latter would allow studying the Meissner effect (superconductivity) and applications to industrial products, such as Maglev systems [118].

Bibliography

- [1] G.D. Smith. Numerical Solution of Partial Differential Equations: Finite Difference Methods. Oxford Applied Mathematics and. Clarendon Press, 1985.
- [2] A. Iserles. A First Course in the Numerical Analysis of Differential Equations. Cambridge Texts in Applied Mathematics. Cambridge University Press, 1996.
- [3] J.D. Hoffman and S. Frankel. Numerical Methods for Engineers and Scientists, Second Edition,. Taylor & Francis, 2001.
- [4] P. Majumdar. Computational Methods for Heat and Mass Transfer. Series in Computational and Physical Processes in Mechanics and Thermal Sciences. Taylor & Francis, 2005.
- [5] C. Grossmann, H.G. Roos, and M. Stynes. Numerical Treatment of Partial Differential Equations. Universitext. Springer Berlin Heidelberg, 2007.
- [6] Y. Jaluria. Computational Heat Transfer. CRC Press, 2017.
- [7] A. Hrennikoff. Solution of problems of elasticity by the framework method. Journal of Applied Mechanics, 8(4):0–0, 1941.
- [8] R. Courant. Variational Methods for the Solution of Problems of Equilibrium and Vibrations. [s.n.] @, 1943.
- [9] E. Hinton and B. Irons. Least squares smoothing of experimental data using finite elements. Strain, 4(1):24–27, 1968.
- [10] G. Strang and G. Fix. An Analysis of the Finite Element Method. Wellesley-Cambridge Press, 2008.
- [11] O.C. Zienkiewicz, R.L. Taylor, and J.Z. Zhu. The Finite Element Method: Its Basis and Fundamentals, Sixth Edition. Butterworth-Heinemann, 6 edition, May 2005.
- [12] K.J. Bathe. Finite Element Procedures. Prentice Hall, 2006.
- [13] G. Allaire. Numerical Analysis and Optimization: An Introduction to Mathematical Modelling and Numerical Simulation. Numerical Mathematics and Scientific Computation. Oxford University Press, 2007.
- [14] T.J.R. Hughes. The Finite Element Method: Linear Static and Dynamic Finite Element Analysis. Dover Publications, 2000.
- [15] N.H. Kim. Introduction to Nonlinear Finite Element Analysis. SpringerLink : Bücher. Springer US, 2014.

- [16] R. Eymard, T. Gallouët, and R. Herbin. The finite volume method. In Philippe Ciarlet and Jean-Louis Lions, editors, Handbook of Numerical Analysis, pages 713–1020. North Holland, 2000. This paper appeared as a technical report four years ago.
- [17] R.J. LeVeque. Finite-Volume Methods for Hyperbolic Problems. Cambridge University Press, 2002.
- [18] E.F. Toro. Riemann Solvers and Numerical Methods for Fluid Dynamics: A Practical Introduction. Springer Berlin Heidelberg, 2009.
- [19] S.V. Patankar. Numerical heat transfer and fluid flow. Series on Computational Methods in Mechanics and Thermal Science. Hemisphere Publishing Corporation (CRC Press, Taylor & Francis Group), 1980.
- [20] C. Hirsch and C. Hirsch. Numerical Computation of Internal and External Flows: Computational methods for inviscid and viscous flows. Wiley series in numerical methods in engineering. Wiley, 1990.
- [21] R.H. Pletcher, J.C. Tannehill, and D. Anderson. Computational Fluid Mechanics and Heat Transfer, Second Edition. Series in Computational and Physical Processes in Mechanics and Thermal Sciences. Taylor & Francis, 1997.
- [22] J.A. Cottrell, T.J.R. Hughes, and Y. Bazilevs. Isogeometric Analysis: Toward Integration of CAD and FEA. Wiley, 2009.
- [23] E.A. Cohen, R.F.A. Riesenfeld, and G.A. Elber. Geometric Modeling With Splines: An Introduction. Ak Peters Series. Peters, 2001.
- [24] G. Farin. Curves and Surfaces for CAGD: A Practical Guide. The Morgan Kaufmann Series in Computer Graphics. Elsevier Science, 2001.
- [25] L. Piegl and W. Tiller. The NURBS Book. Monographs in Visual Communication. Springer Berlin Heidelberg, 2012.
- [26] D.F. Rogers. An Introduction to NURBS: With Historical Perspective. The Morgan Kaufmann Series in Computer Graphics. Elsevier Science, 2000.
- [27] S. Osher and J.A. Sethian. Fronts propagating with curvature-dependent speed: Algorithms based on Hamilton-Jacobi formulations. Journal of Computational Physics, 79(1):12–49, 1988.
- [28] M. Sussman, P. Smereka, and S. Osher. A level set approach for computing solutions to incompressible 2-phase flow. Journal of Computational Physics, 114(1):146–159, 1994.
- [29] A. Hansbo and P. Hansbo. A finite element method for the simulation of strong and weak discontinuities in solid mechanics. Computer Methods in Applied Mechanics and Engineering, 193(33-35):3523–3540, 2004.

- [30] T.P. Fries and T. Belytschko. The extended/generalized finite element method: An overview of the method and its applications. International Journal for Numerical Methods in Engineering, 84(3):253–304, 2010.
- [31] T.P. Fries and T. Belytschko. The intrinsic XFEM: a method for arbitrary discontinuities without additional unknowns. International Journal for Numerical Methods in Engineering, 68(13):1358–1385, 2006.
- [32] A.R. Khoei. Extended Finite Element Method: Theory and Applications, pages 1–565. Wiley, 01 2015.
- [33] S. Mohammadi. Extended Finite Element Method: for Fracture Analysis of Structures. Wiley, 2008.
- [34] D. Makhija and K. Maute. Numerical instabilities in level set topology optimization with the extended finite element method. Structural and Multidisciplinary Optimization, 49(2):185–197, 2014.
- [35] K. Terada, M. Asal, and M. Yamagishi. Finite cover method for linear and non-linear analyses of heterogeneous solids. International Journal for Numerical Methods in Engineering, 58(9):1321–1346, 2003.
- [36] A.B. Tran, J. Yvonnet, Q.C. He, C. Toulemonde, and J. Sanahuja. A multiple level set approach to prevent numerical artefacts in complex microstructures with nearby inclusions within XFEM. International Journal for Numerical Methods in Engineering, 85(11):1436–1459, 2011.
- [37] R.P. Fedkiw, T. Aslam, B. Merriman, and S. Osher. A non-oscillatory Eulerian approach to interfaces in multimaterial flows (the ghost fluid method). Journal of Computational Physics, 152(2):457–492, 1999.
- [38] J.M. Hong, T. Shinar, M.J. Kang, and R. Fedkiw. On boundary condition capturing for multiphase interfaces. Journal of Scientific Computing, 31(1-2):99–125, 2007.
- [39] X.D. Liu, R.P. Fedkiw, and M.J. Kang. A boundary condition capturing method for Poisson’s equation on irregular domains. Journal of Computational Physics, 160(1):151–178, 2000.
- [40] D.Q. Nguyen, R.P. Fedkiw, and M. Kang. A boundary condition capturing method for incompressible flame discontinuities. Journal of Computational Physics, 172(1):71–98, 2001.
- [41] T.E. Tezduyar, M. Behr, and J. Liou. A new strategy for finite-element computations involving moving boundaries and interfaces - the deforming-spatial-domain space-time procedure: 1. the concept and the preliminary numerical tests. Computer Methods in Applied Mechanics and Engineering, 94(3):339–351, 1992.

- [42] T.E. Tezduyar, M. Behr, S. Mittal, and J. Liou. A new strategy for finite-element computations involving moving boundaries and interfaces - the deforming-spatial-domain space-time procedure: 2. computation of free-surface flows, 2-liquid flows, and flows with drifting cylinders. Computer Methods in Applied Mechanics and Engineering, 94(3):353–371, 1992.
- [43] T.E. Tezduyar. Computation of moving boundaries and interfaces and stabilization parameters. International Journal for Numerical Methods in Fluids, 43(5):555–575, 2003.
- [44] T.J.R. Hughes and G.M. Hulbert. Space-time finite-element methods for elastodynamics - formulations and error-estimates. Computer Methods in Applied Mechanics and Engineering, 66(3):339–363, 1988.
- [45] J. Chessa and T. Belytschko. Arbitrary discontinuities in space-time finite elements by level sets and X-FEM. International Journal for Numerical Methods in Engineering, 61(15):2595–2614, 2004.
- [46] J. Chessa and T. Belytschko. A local space-time discontinuous finite element method. Computer Methods in Applied Mechanics and Engineering, 195(13-16):1325–1343, 2006.
- [47] C. Lehrenfeld. The Nitsche XFEM-DG space-time method and its implementation in three space dimensions. Siam Journal on Scientific Computing, 37(1):A245–A270, 2015.
- [48] M. Behr. Simplex space-time meshes in finite element simulations. International Journal for Numerical Methods in Fluids, 57(9):1421–1434, 2008.
- [49] M. Neumüller and O. Steinbach. Refinement of flexible space-time finite element meshes and discontinuous Galerkin methods. Computing and Visualization in Science, 14(5):189–205, Jun 2011.
- [50] S. Zahedi. A space-time cut finite element method with quadrature in time. In Stéphane P. A. Bordas, Erik Burman, Mats G. Larson, and Maxim A. Olshanskii, editors, Geometrically Unfitted Finite Element Methods and Applications, pages 281–306, Cham, 2017. Springer International Publishing.
- [51] E. Bechet, H. Minnebol, N. Moes, and B. Burgardt. Improved implementation and robustness study of the X-FEM for stress analysis around cracks. International Journal for Numerical Methods in Engineering, 64(8):1033–1056, 2005.
- [52] C. Lang, D. Makhija, A. Doostan, and K. Maute. A simple and efficient preconditioning scheme for heaviside enriched XFEM. Computational Mechanics, 54(5):1357–1374, 2014.
- [53] A. Menk and S.P.A. Bordas. A robust preconditioning technique for the extended finite element method. International Journal for Numerical Methods in Engineering, 85(13):1609–1632, 2011.

- [54] H. Sauerland and T.P. Fries. The stable XFEM for two-phase flows. Computers and Fluids, 87:41–49, 2013.
- [55] E. Burman and P. Hansbo. Fictitious domain finite element methods using cut elements: II. a stabilized Nitsche method. Applied Numerical Mathematics, 62(4):328–341, 2012.
- [56] E. Burman and P. Hansbo. Fictitious domain methods using cut elements: III. a stabilized nitsche method for stokes’ problem. Esaim-Mathematical Modelling and Numerical Analysis-Modelisation Mathematique Et Analyse Numerique, 48(3):859–874, 2014.
- [57] C.H. Zhang. Research on thin film lubrication: state of the art. Tribology International, 38(4):443–448, 2005.
- [58] K.J. Bathe, C. Nitikitpaiboon, and X. Wang. A mixed displacement-based finite-element formulation for acoustic fluid-structure interaction. Computers and Structures, 56(2-3):225–237, 1995.
- [59] K.J. Bathe, H. Zhang, and M.H. Wang. Finite-element analysis of incompressible and compressible fluid-flows with free surfaces and structural interactions. Computers and Structures, 56(2-3):193–213, 1995.
- [60] T. Belytschko, D.P. Flanagan, and J.M. Kennedy. Finite-element methods with user-controlled meshes for fluid structure interaction. Computer Methods in Applied Mechanics and Engineering, 33(1-3):669–688, 1982.
- [61] A. Huerta and W.K. Liu. Viscous-flow structure interaction. Journal of Pressure Vessel Technology-Transactions of the Asme, 110(1):15–21, 1988.
- [62] A. Huerta and W.K. Liu. Viscous-flow with large free-surface motion. Computer Methods in Applied Mechanics and Engineering, 69(3):277–324, 1988.
- [63] C. Nitikitpaiboon and K.J. Bathe. An arbitrary Lagrangian-Eulerian velocity potential formulation for fluid-structure interaction. Computers and Structures, 47(4-5):871–891, 1993.
- [64] S. Frei, T. Richter, and Wick T. Eulerian techniques for fluid-structure interactions - Part I: Modeling and simulation. Lecture Notes in Computational Science and Engineering, 103(1):745–753, 2014.
- [65] S. Frei, T. Richter, and Wick T. Eulerian techniques for fluid-structure interactions - Part II: Applications. Lecture Notes in Computational Science and Engineering, 103(1):755–762, 2014.
- [66] T. Richter. A fully Eulerian formulation for fluid-structure-interaction problems. Journal of Computational Physics, 233:227–240, 2013.

- [67] K. Kamrin, C. H. Rycroft, and J.C. Nave. Reference map technique for finite-strain elasticity and fluid-solid interaction. Journal of the Mechanics and Physics of Solids, 60(11):1952–1969, 2012.
- [68] B. Valkov, C.H. Rycroft, and K. Kamrin. Eulerian method for multiphase interactions of soft solid bodies in fluids. Journal of Applied Mechanics-Transactions of the Asme, 82(4), 2015.
- [69] W.A. Wall, A. Gerstenberger, U. Küttler, and U.M. Mayer. An XFEM based fixed-grid approach for 3D fluid-structure interaction. In H.J. Bungartz, M. Mehl, and M. Schäfer, editors, Fluid Structure Interaction II, pages 327–349, Berlin, Heidelberg, 2010. Springer Berlin Heidelberg.
- [70] U.M. Mayer, A. Popp, A. Gerstenberger, and W.A. Wall. 3D fluid-structure-contact interaction based on a combined XFEM FSI and dual mortar contact approach. Computational Mechanics, 46(1):53–67, 2010.
- [71] T.J.R. Hughes, G. Scovazzi, and L.P. Franca. Multiscale and Stabilized Methods, pages 1–64. American Cancer Society, 2017.
- [72] B. Schott, U. Rasthofer, V. Gravemeier, and W.A. Wall. A face-oriented stabilized Nitsche-type extended variational multiscale method for incompressible two-phase flow. International Journal for Numerical Methods in Engineering, 104(7):721–748, 2015.
- [73] B. Schott, S. Shahmiri, R. Kruse, and W.A. Wall. A stabilized Nitsche-type extended embedding mesh approach for 3D low-and high-reynolds-number flows. International Journal for Numerical Methods in Fluids, 82(6):289–315, 2016.
- [74] P. Hansbo, J. Hermansson, and T. Svedberg. Nitsche’s method combined with space-time finite elements for ale fluid-structure interaction problems. Computer Methods in Applied Mechanics and Engineering, 193(39-41):4195–4206, 2004.
- [75] M. Lawry and K. Maute. Level set topology optimization of problems with sliding contact interfaces. Structural and Multidisciplinary Optimization, 52(6):1107–1119, 2015.
- [76] T.P. Fries. <http://www.xfem.rwth-aachen.de/index.php>, 2013.
- [77] J.H. Song, P.M. A. Areias, and T. Belytschko. A method for dynamic crack and shear band propagation with phantom nodes. International Journal for Numerical Methods in Engineering, 67(6):868–893, 2006.
- [78] J.M. Melenk and I. Babuska. The partition of unity finite element method: Basic theory and applications. Computer Methods in Applied Mechanics and Engineering, 139(1-4):289–314, 1996.
- [79] I. Babuska and J.M. Melenk. The partition of unity method. International Journal for Numerical Methods in Engineering, 40(4):727–758, 1997.

- [80] M. Schäfer, S. Turek, F. Durst, E. Krause, and R. Rannacher. Benchmark computations of laminar flow around a cylinder (flow simulation with high-performance computers II: DFG priority research programme results 1993–1995), 1996.
- [81] Los Alamos Scientific Laboratory, United States. Department of Energy. Technical Information Center, United States. Department of Energy. Office of Scientific, and Technical Information. Triangular Mesh Methods for the Neutron Transport Equation. United States. Department of Energy. Technical Information Center, 1973.
- [82] P. Lasaint and P.A. Raviart. On a finite element method for solving the neutron transport equation. In B. Carl, editor, Mathematical Aspects of Finite Elements in Partial Differential Equations, pages 89 – 123. Academic Press, 1974.
- [83] Y. Saad and M.H. Schultz. GMRES: a generalized minimal residual algorithm for solving nonsymmetric linear systems. SIAM J. Sci. Stat. Comput., 7(3):856–869, July 1986.
- [84] T. Belytschko, W.K. Liu, B. Moran, and K. Elkhodary. Nonlinear Finite Elements for Continua and Structures. Wiley, 2013.
- [85] H. Dutsch, F. Durst, S. Becker, and H. Lienhart. Low-reynolds-number flow around an oscillating circular cylinder at low Keulegan-Carpenter numbers. Journal of Fluid Mechanics, 360:249–271, 1998.
- [86] E. Guilmineau and P. Queutey. A numerical simulation of vortex shedding from an oscillating circular cylinder. Journal of Fluids and Structures, 16(6):773–794, 2002.
- [87] T.E. Tezduyar and S. Sathe. Modelling of fluid-structure interactions with the space-time finite elements: Solution techniques. International Journal for Numerical Methods in Fluids, 54(6-8):855–900, 2007.
- [88] V. John. Higher order finite element methods and multigrid solvers in a benchmark problem for the 3D Navier-Stokes equations. International Journal for Numerical Methods in Fluids, 40(6):775–798, 2002.
- [89] M. Tatsuno and P.W. Bearman. A visual study of the flow around an oscillating circular-cylinder at low keulegan-carpenter numbers and low stokes numbers. Journal of Fluid Mechanics, 211:157–182, 1990.
- [90] S. Chakrabarti. Handbook of Offshore Engineering, Volumes 1-2. Elsevier, 2005.
- [91] S. Miller, R.L. Campbell, C. Elsworth, J. Pitt, and D. Boger. An overset grid method for fluid-structure interaction. World Journal of Mechanics, 4:217–237, 07 2014.
- [92] S. Okazawa, K. Kashiyaama, and Y. Kaneko. Eulerian formulation using stabilized finite element method for large deformation solid dynamics. International Journal for Numerical Methods in Engineering, 72(13):1544–1559, 2007.

- [93] K. Kamrin and J.C. Nave. An Eulerian approach to the simulation of deformable solids: Application to finite-strain elasticity. [arXiv:0901.3799v2](https://arxiv.org/abs/0901.3799v2), 2009.
- [94] D.I.W. Levin, J. Litven, G.L. Jones, S. Sueda, and D.K. Pai. Eulerian solid simulation with contact. *Acm Transactions on Graphics*, 30(4), 2011.
- [95] Y. Fan, J. Litven, D.I.W. Levin, and D.K. Pai. Eulerian-on-Lagrangian simulation. *Acm Transactions on Graphics*, 32(3), 2013.
- [96] E. Olsson and G. Kreiss. A conservative level set method for two phase flow. *Journal of Computational Physics*, 210(1):225–246, 2005.
- [97] E. Olsson, G. Kreiss, and S. Zahedi. A conservative level set method for two phase flow ii. *Journal of Computational Physics*, 225(1):785–807, 2007.
- [98] C. Felippa. Variational formulation of plane beam element, 2013. <http://www.colorado.edu/engineering/CAS/courses.d/IFEM.d/IFEM.Ch12.d/IFEM.Ch12.pdf>.
- [99] Y.W. Kwon and H. Bang. *The Finite Element Method Using MATLAB*. CRC Press, Inc., Boca Raton, FL, USA, 2nd edition, 2000.
- [100] C. Annavarapu, M. Hautefeuille, and J.E. Dolbow. A robust Nitsches formulation for interface problems. *Computer Methods in Applied Mechanics and Engineering*, 225-228:44 – 54, 2012.
- [101] N. Jenkins and K. Maute. Level set topology optimization of stationary fluid-structure interaction problems. *Structural and Multidisciplinary Optimization*, 52(1):179–195, 2015.
- [102] N. Jenkins and K. Maute. An immersed boundary approach for shape and topology optimization of stationary fluid-structure interaction problems. *Structural and Multidisciplinary Optimization*, 54(5):1191–1208, 2016.
- [103] U.M. Mayer, A. Gerstenberger, and W.A. Wall. Interface handling for three-dimensional higher-order XFEM-computations in fluidstructure interaction. *International Journal for Numerical Methods in Engineering*, 79(7):846–869, 2009.
- [104] P. Wriggers. *Computational Contact Mechanics*. Wiley, 2002.
- [105] E. Burman and M.A. Fernandez. Continuous interior penalty finite element method for the time-dependent Navier-Stokes equations: space discretization and convergence. *Numerische Mathematik*, 107(1):39–77, 2007.
- [106] C.H. Villanueva and K. Maute. CutFEM topology optimization of 3D laminar incompressible flow problems. *Computer Methods in Applied Mechanics and Engineering*, 320:444 – 473, 2017.
- [107] T. Belytschko, W.K. Liu, B. Moran, and K. Elkhodary. *Nonlinear Finite Elements for Continua and Structures*. No Longer used. Wiley, 2013.

- [108] COMSOL. Comsol multiphysics 5.3a fluid-structure interaction, 2011. https://www.comsol.com/model/download/471221/models.mems.fluid_structure_interaction.pdf.
- [109] N. Jenkins. Immersed boundary methods for optimization of strongly coupled fluid-structure systems. *Aerospace Engineering Sciences Graduate Theses & Dissertations*, 140, 2017.
- [110] N. Yamamoto. Equation expressing star or flower graphics. http://www.geocities.jp/nyjp07/index_asteroid_E.html.
- [111] S. Turek and J. Hron. Proposal for numerical benchmarking of fluid-structure interaction between an elastic object and laminar incompressible flow. In H.J. Bungartz and M. Schäfer, editors, *Fluid-Structure Interaction*, pages 371–385, Berlin, Heidelberg, 2006. Springer Berlin Heidelberg.
- [112] S. Turek, J. Hron, M. Mádlík, M. Razzaq, H. Wobker, and J.F. Acker. Numerical simulation and benchmarking of a monolithic multigrid solver for fluid-structure interaction problems with application to hemodynamics. In H.J. Bungartz, M. Mehl, and M. Schäfer, editors, *Fluid Structure Interaction II*, pages 193–220, Berlin, Heidelberg, 2010. Springer Berlin Heidelberg.
- [113] M. Breuer, G. De Nayer, M. Munsch, T. Gallinger, and R. Wuchner. Fluid-structure interaction using a partitioned semi-implicit predictor-corrector coupling scheme for the application of large-eddy simulation. *Journal of Fluids and Structures*, 29:107–130, 2012.
- [114] V. Chabannes, G. Pena, and C. Prud'homme. High-order fluid-structure interaction in 2D and 3D application to blood flow in arteries. *Journal of Computational and Applied Mathematics*, 246:1–9, 2013.
- [115] R. Sandbode. Fluid-structure interaction with opensitm and md nastrantm structural solver. *Ann Arbor*, 1001:48105, 2010.
- [116] S. Frei and T. Richter. 3. An accurate Eulerian approach for fluid-structure interactions: modeling, adaptive discretisations and solvers. *Fluid-Structure Interaction*, 11 2017.
- [117] J. Friedrich and M. Schäfer. Acoustics simulation in the presence of moving interfaces in multiphase flows, 2018. <http://www.eccm-ecfd2018.org/admin/files/filePaper/p742.pdf>.
- [118] Public Relations Office (Government of Japan). Tokyo to nagoya city in 40 minutes, 2017. https://www.gov-online.go.jp/eng/publicity/book/hlj/html/201704/201704_03_en.html.
- [119] Japan Association for Nonlinear CAE. *Yokuwaku Renzokutai-Rikigaku Note (Japanese book about continuum mechanics)*. Morikita Publishing, 2008.

- [120] N.H. Kim. Introduction to Nonlinear Finite Element Analysis. Springer US, 2014.
- [121] D. Schillinger, I. Harari, M.C. Hsu, D. Kamensky, S.K.F. Stoter, Y. Yu, and Y. Zhao. The non-symmetric Nitsche method for the parameter-free imposition of weak boundary and coupling conditions in immersed finite elements. Computer Methods in Applied Mechanics and Engineering, 309:625–652, 9 2016.

Appendix A

Material Constitutive Laws

This appendix summarizes the theory and the numerical implementation of the material constitutive laws related to this thesis.

A.1 Isotropic Linear Elastic Material Constitutive Law

The most basic constitutive law is the isotropic linear elastic material constitutive law based on the infinitesimal small strain theory. The general form of the linear elastic material is as follows:

$$\sigma_{ij} = D_{ijkl}\varepsilon_{kl} , \quad (\text{A.1})$$

$$\varepsilon_{kl} = \frac{1}{2} \left(\frac{\partial u_i}{\partial x_j} + \frac{\partial u_j}{\partial x_i} \right) , \quad (\text{A.2})$$

where ε_{kl} and σ_{ij} are the infinitesimal small strain tensor and the Cauchy stress tensor, respectively. D_{ijkl} is the constitutive tensor. By applying the assumption of the isotropic material, the following symmetries are required based on the symmetry of the stress tensor σ_{ij} and the strain tensor ε_{kl} :

$$D_{ijkl} = D_{jikl} = D_{ijlk} = D_{klij} . \quad (\text{A.3})$$

Using the engineering strain ε , the following representation is mainly used for the isotropic linear elastic material constitutive law (assuming two-dimensional case):

$$\boldsymbol{\sigma} = \begin{pmatrix} \sigma_{xx} \\ \sigma_{yy} \\ \sigma_{xy} \end{pmatrix} = \begin{pmatrix} D_{11} & D_{12} & 0 \\ D_{12} & D_{22} & 0 \\ 0 & 0 & D_{33} \end{pmatrix} \begin{pmatrix} \varepsilon_{xx} \\ \varepsilon_{yy} \\ 2\varepsilon_{xy} \end{pmatrix} = D\boldsymbol{\varepsilon} . \quad (\text{A.4})$$

The tangential operators for the isotropic linear elastic material with respect to the nodal displacement \mathbf{u} is as follows:

$$\frac{\partial \boldsymbol{\sigma}}{\partial \mathbf{u}} = D \frac{\partial \boldsymbol{\varepsilon}}{\partial \mathbf{u}} . \quad (\text{A.5})$$

A.2 Hyperelastic Material Constitutive Law

Section A.1 is limited to the case of the infinitesimal small strain. The assumption of the infinitesimal small strain is valid when the rigidity of the structure is high enough and the applicable deformation is relatively small. In general, the structures made by metals fit into this assumption. On the other hand, the structures affected by the large deformation, especially in the case that the elastic modulus is relatively small, its assumption breaks down. It is essential to treat finite strains and consider the geometric nonlinearity of the material. The most common example of this kind of material is the rubber.

While there are several nonlinear constitutive laws, the most popular type is the hyperelastic material constitutive law. The hyperelastic material is defined by the hyperelastic function (strain energy density function) W . The discussion of this section based on Kyoya [119] and Kim [120]. In addition, the following notations are used in this section.

Table A.1: Notation for material constitutive law

| Notation | Property |
|------------------------|--------------------------------------|
| W | hyperelastic function |
| $F = F_{iJ}$ | deformation gradient tensor |
| $C = C_{IJ}$ | right Cauchy-Green tensor |
| $B = B_{ij}$ | left Cauchy-Green tensor |
| $E = E_{IJ}$ | Green-Lagrange strain tensor |
| $e = e_{iJ}$ | Euler-Almansi strain tensor |
| $P = P_{iJ}$ | first Piola-Kirchhoff stress tensor |
| $S = IJ$ | second Piola-Kirchhoff stress tensor |
| $\sigma = \sigma_{ij}$ | Cauchy stress tensor |

A.2.1 Objectivity of Hyperelastic Material Constitutive Law

An important characteristic of the hyperelastic material constitutive law is the objectivity. The objectivity means that the hyperelastic function (strain energy density function) W does not have the influence of the rigid-body rotation. This is because that W should have the unique value for all observers.

Assuming the deformation gradient tensor F is given at a material point \mathbf{X} , the hyperelastic function can be interpreted by the function of F :

$$W = W(F(\mathbf{X})) , \quad (\text{A.6})$$

Based on (A.6), the first Piola-Kirchhoff (first PK) stress tensor P , which is the conjugate stress tensor of the deformation gradient F , is computed by differencing W with respect to F :

$$P_{iJ} = \frac{\partial W}{\partial F_{iJ}} . \quad (\text{A.7})$$

However, the deformation gradient F has the influence of the rigid-body rotation R . F is decomposed by the appropriate rotation tensor R and the stretch tensor U (or V) by the

polar decomposition:

$$F = RU = VR . \quad (\text{A.8})$$

Satisfying the objectivity, W should be a function of the stretch part U (or V):

$$W = W(F) = W(RU) = W(U) . \quad (\text{A.9})$$

The left Cauchy-Green tensor C and the Green-Lagrange strain tensor E also have the rotational invariance because C and E are defined only by the stretch part of F :

$$C = F^T F = (RU)^T RU = U^T R^T RU = U^T IU = U^T U \quad (\because R^T = R^{-1}) , \quad (\text{A.10})$$

$$E = \frac{1}{2}(C - I) = \frac{1}{2}(U^T U - I) . \quad (\text{A.11})$$

Therefore, the second Piola-Kirchhoff (second PK) stress tensor S is directly computed by differencing W with respect to its conjugate strain tensor E , by satisfying the objectivity of the constitutive law:

$$S_{IJ} = \frac{\partial W}{\partial E_{IJ}} . \quad (\text{A.12})$$

The first PK stress P and the Cauchy stress σ are computed from S as follows:

$$P = FS , \quad (\text{A.13})$$

$$\sigma = J^{-1} F S F^T , \quad (\text{A.14})$$

where $J = \det F$. Based on the total Lagrangian formulation, P is the appropriate stress measure. Based on the updated Lagrangian formulation, σ is the appropriate stress measure.

A.2.2 Tangential Operator of Stress Tensor

For the computation of the momentum equation, tangential operators of the stress with respect to the nodal displacement \mathbf{u} are essential. Followings are the tangential operators of P and σ for the total and updated Lagrangian formulation respectively:

$$\frac{\partial P}{\partial \mathbf{u}} = \frac{\partial F}{\partial \mathbf{u}} S + F \frac{\partial S}{\partial \mathbf{u}} , \quad (\text{A.15})$$

$$\frac{\partial \sigma}{\partial \mathbf{u}} = J^{-1} \frac{\partial F}{\partial \mathbf{u}} S F^T + J^{-1} F \frac{\partial S}{\partial \mathbf{u}} F^T + J^{-1} F S \frac{\partial F^T}{\partial \mathbf{u}} - J^{-2} \frac{\partial J}{\partial \mathbf{u}} F S F^T . \quad (\text{A.16})$$

In the following section, $\frac{\partial S}{\partial \mathbf{u}}$ is only denoted. (A.15) and (A.16) are used for the computation of the tangential operators. In addition, following derivatives of C and C^{-1} are beneficial for the above tangential operators:

$$\frac{\partial C}{\partial \mathbf{u}} = \frac{\partial F^T}{\partial \mathbf{u}} F + F^T \frac{\partial F}{\partial \mathbf{u}} , \quad (\text{A.17})$$

$$\frac{\partial C^{-1}}{\partial \mathbf{u}} = -C^{-1} \frac{\partial C}{\partial \mathbf{u}} C^{-1} . \quad (\text{A.18})$$

A.2.3 Hyperelastic Constitutive Law based on F , C and E

This section summarizes the representative hyperelastic constitutive laws defined by C and E directly.

A.2.3.1 Compressible St. Venant-Kirchhoff Material

The St. Venant-Kirchhoff material is a geometrically-nonlinear materially-linear hyperelastic material constitutive law. W and S are defined as follows:

$$W = \frac{1}{2} \lambda (\text{Tr}(E))^2 + \mu \text{Tr}(E^2) , \quad (\text{A.19})$$

$$S_{IJ} = \frac{\partial W}{\partial E_{IJ}} = \lambda \text{Tr}(E) \delta_{IJ} + 2\mu E_{IJ} , \quad (\text{A.20})$$

where λ and μ are the Lamé's constants defined as follows:

$$\lambda = \frac{\nu^s}{(1 + \nu^s)(1 - 2\nu^s)} E^s, \quad (\text{A.21})$$

$$\mu = \frac{1}{2(1 + \nu^s)} E^s, \quad (\text{A.22})$$

where E^s is the Young's modulus and ν^s is the Poisson's ratio. The tangential operator of S with respect to the nodal displacement \mathbf{u} is as follows:

$$\frac{\partial S_{IJ}}{\partial \mathbf{u}} = (\lambda \delta_{IJ} + 2\mu) \frac{\partial E_{IJ}}{\partial \mathbf{u}} = \frac{1}{2} (\lambda \delta_{IJ} + 2\mu) \frac{\partial C_{IJ}}{\partial \mathbf{u}}. \quad (\text{A.23})$$

A.2.3.2 Compressible Neo-Hookean Material (Belytchko's Form)

Belytchko et al. [107] proposed a geometrically and materially nonlinear material constitutive law using C directly. $J = \det F$ also has the objectivity. This constitutive law is widely used in this thesis for FSI and contact. W and S are defined as follows:

$$\begin{aligned} W &= \frac{1}{2} \lambda (\ln(\det F))^2 + \frac{1}{2} \mu (\text{Tr}(C) - 3) - \mu \ln(\det F) \\ &= \frac{1}{2} \lambda (\ln J)^2 + \frac{1}{2} \mu (\text{Tr}(C) - 3) - \mu \ln J, \end{aligned} \quad (\text{A.24})$$

$$S_{IJ} = 2 \frac{\partial W}{\partial C_{IJ}} = (\lambda \ln J - \mu) C_{IJ}^{-1} + \mu \delta_{IJ}. \quad (\text{A.25})$$

where λ and μ are the Lamé's constants. The tangential operator of S with respect to nodal displacement \mathbf{u} is as follows:

$$\frac{\partial S_{IJ}}{\partial \mathbf{u}} = \frac{\lambda}{J} \frac{\partial J}{\partial \mathbf{u}} C_{IJ}^{-1} + (\lambda \ln J - \mu) \frac{\partial C_{IJ}^{-1}}{\partial \mathbf{u}}. \quad (\text{A.26})$$

A.2.4 Hyperelastic Constitutive Law based on Reduced Invariants of C

Widely-used hyperelastic constitutive laws are defined by the invariants of the right Cauchy-Green tensor C . This section first summarizes the hyperelastic constitutive laws based on the standard invariants of the Cauchy-Green tensor. The second Piola-Kirchhoff

(second PK) stress tensor S_{IJ} (A.12) is modified as follows:

$$S_{IJ} = \frac{\partial W}{\partial E_{IJ}} = 2 \frac{\partial W}{\partial C_{IJ}} . \quad (\text{A.27})$$

From here, the hyperelastic functions defined by standard invariants of the right Cauchy-Green tensor C are assumed and then, (A.13) is modified as follows:

$$S_{IJ} = 2 \frac{\partial W}{\partial C_{IJ}} = 2 \frac{\partial I_{C1}}{\partial C_{IJ}} \frac{\partial W}{\partial I_{C1}} + 2 \frac{\partial I_{C2}}{\partial C_{IJ}} \frac{\partial W}{\partial I_{C2}} + 2 \frac{\partial I_{C3}}{\partial C_{IJ}} \frac{\partial W}{\partial I_{C3}} , \quad (\text{A.28})$$

where I_{C1} , I_{C2} and I_{C3} are the standard invariants of C , and $I_{C3} = J^2$:

$$I_{C1} = \text{Tr}C , \quad (\text{A.29})$$

$$I_{C2} = \frac{1}{2} \left[(\text{Tr}C)^2 - \text{Tr}C^2 \right] = \frac{1}{2} (I_{C1}^2 - \text{Tr}C^2) , \quad (\text{A.30})$$

$$I_{C3} = \det C = (\det F)^2 = J^2 . \quad (\text{A.31})$$

Derivatives of the standard invariants with respect to C are denoted as follows:

$$\frac{\partial I_{C1}}{\partial C_{IJ}} = \frac{\partial(\text{Tr}C)}{\partial C_{IJ}} = \frac{\partial C_{KK}}{\partial C_{IJ}} = \delta_{IJ} , \quad (\text{A.32})$$

$$\begin{aligned} \frac{\partial I_{C2}}{\partial C_{IJ}} &= I_{C1} \frac{\partial I_{C1}}{\partial C_{IJ}} - \frac{1}{2} \frac{\partial(\text{Tr}C^2)}{\partial C_{IJ}} = I_{C1} \delta_{IJ} - \frac{1}{2} \frac{\partial(C_{KL}C_{LK})}{\partial C_{IJ}} \\ &= I_{C1} \delta_{IJ} - \frac{1}{2} \frac{\partial(C_{KL}C_{KL})}{\partial C_{IJ}} = I_{C1} \delta_{IJ} - \delta_{KI} \delta_{LJ} C_{KL} = I_{C1} \delta_{IJ} - C_{IJ} , \end{aligned} \quad (\text{A.33})$$

$$\frac{\partial I_{C3}}{\partial C_{IJ}} = \frac{\partial(\det C)}{\partial C_{IJ}} = \det C (C^{-T})_{IJ} = \det C (C^{-1})_{IJ} . \quad (\text{A.34})$$

(A.34) is derived from the Gâteaux derivative (directional derivative) and the detail is summarized in Appendix A.3. Therefore, the second PK stress tensor S is computed as follows (\tilde{I} denotes an identity matrix):

- Second PK Stress (Index Notation)

$$S_{IJ} = 2 \frac{\partial W}{\partial I_{C1}} \delta_{IJ} + 2 \frac{\partial W}{\partial I_{C2}} (I_{C1} \delta_{IJ} - C_{IJ}) + 2 J^2 \frac{\partial W}{\partial I_{C3}} (C^{-1})_{IJ} , \quad (\text{A.35})$$

- Second PK Stress (Matrix Notation)

$$S = 2 \frac{\partial W}{\partial I_{C1}} \tilde{I} + 2 \frac{\partial W}{\partial I_{C2}} (I_{C1} \tilde{I} - C) + 2J^2 \frac{\partial W}{\partial I_{C3}} C^{-1} . \quad (\text{A.36})$$

Many popular hyperelastic material constitutive laws are defined by reduced invariants \mathcal{I}_{C_i} ($i = 1 \sim 3$) of C . For example, the Mooney-Rivlin (MR) material should be defined by the reduced invariants \mathcal{I}_{C_i} , not by the standard invariants I_{C_i} . If a MR material is defined by the standard invariants, stresses are evaluated as non-zero values when there is no deformation (zero strain state). To escape from this problem, the definition by reduced invariants is an efficient way. In the following discussion, the hyperelastic material constitutive law is defined by the reduced invariants of C is discussed. First, the reduced invariants \mathcal{I}_{C_i} are defined by the standard invariants I_{C_i} as follows:

$$\mathcal{I}_{C1} \equiv \mathcal{I}_{C3}^{-2/3} I_{C1} = I_{C3}^{-1/3} I_{C1} , \quad (\text{A.37})$$

$$\mathcal{I}_{C2} \equiv \mathcal{I}_{C3}^{-4/3} I_{C2} = I_{C3}^{-2/3} I_{C2} , \quad (\text{A.38})$$

$$\mathcal{I}_{C3} \equiv I_{C3}^{1/2} = (\det C)^{1/2} = \det F = J . \quad (\text{A.39})$$

Derivatives of the above reduced invariants with respect to C are computed as follows, using (A.31) - (A.34):

$$\frac{\partial \mathcal{I}_{C1}}{\partial C_{IJ}} = I_{C3}^{-1/3} \frac{\partial I_{C1}}{\partial C_{IJ}} - \frac{1}{3} I_{C3}^{-4/3} I_{C1} \frac{\partial I_{C3}}{\partial C_{IJ}} \quad (\text{A.40})$$

$$= I_{C3}^{-1/3} \delta_{IJ} - \frac{1}{3} I_{C3}^{-4/3} I_{C1} I_{C3} (C^{-1})_{IJ} \quad (\text{A.41})$$

$$= I_{C3}^{-1/3} \left(\delta_{IJ} - \frac{1}{3} I_{C1} (C^{-1})_{IJ} \right) , \quad (\text{A.42})$$

$$\frac{\partial \mathcal{I}_{C2}}{\partial C_{IJ}} = I_{C3}^{-2/3} \frac{\partial I_{C2}}{\partial C_{IJ}} - \frac{2}{3} I_{C3}^{-5/3} I_{C2} \frac{\partial I_{C3}}{\partial C_{IJ}} \quad (\text{A.43})$$

$$= I_{C3}^{-2/3} (I_{C1} \delta_{IJ} - C_{IJ}) - \frac{2}{3} I_{C3}^{-5/3} I_{C2} I_{C3} (C^{-1})_{IJ} \quad (\text{A.44})$$

$$= I_{C3}^{-2/3} \left(I_{C1} \delta_{IJ} - C_{IJ} - \frac{2}{3} I_{C2} (C^{-1})_{IJ} \right) , \quad (\text{A.45})$$

$$\frac{\partial \mathcal{I}_{C3}}{\partial C_{IJ}} = \frac{1}{2} I_{C3}^{-1/2} \frac{\partial I_{C3}}{\partial C_{IJ}} = \frac{1}{2} I_{C3}^{1/2} (C^{-1})_{IJ} . \quad (\text{A.46})$$

The second PK stress defined by the reduced invariants is as follows:

$$S_{IJ} = 2 \frac{\partial W}{\partial C_{IJ}} = 2 \frac{\partial \mathcal{I}_{C1}}{\partial C_{IJ}} \frac{\partial W}{\partial \mathcal{I}_{C1}} + 2 \frac{\partial \mathcal{I}_{C2}}{\partial C_{IJ}} \frac{\partial W}{\partial \mathcal{I}_{C2}} + 2 \frac{\partial \mathcal{I}_{C3}}{\partial C_{IJ}} \frac{\partial W}{\partial \mathcal{I}_{C3}} . \quad (\text{A.47})$$

By substituting (A.42) - (A.46), the second PK stress tensor S is computed as follows using $I_{C3} = J^2$. These equations are corresponding to (A.35) and (A.36):

- Second PK Stress (Index Notation)

$$S_{IJ} = 2 \frac{\partial W}{\partial \mathcal{I}_{C1}} \left(J^{-2/3} \delta_{IJ} - \frac{1}{3} \mathcal{I}_{C1} (C^{-1})_{IJ} \right) + 2 \frac{\partial W}{\partial \mathcal{I}_{C2}} \left(J^{-2/3} \mathcal{I}_{C1} \delta_{IJ} - J^{-4/3} C_{IJ} - \frac{2}{3} \mathcal{I}_{C2} (C^{-1})_{IJ} \right) + \frac{\partial W}{\partial \mathcal{I}_{C3}} J (C^{-1})_{IJ} , \quad (\text{A.48})$$

- Second PK Stress (Matrix Notation)

$$S = 2 \frac{\partial W}{\partial \mathcal{I}_{C1}} \left(J^{-2/3} \tilde{I} - \frac{1}{3} \mathcal{I}_{C1} C^{-1} \right) + 2 \frac{\partial W}{\partial \mathcal{I}_{C2}} \left(J^{-2/3} \mathcal{I}_{C1} \tilde{I} - J^{-4/3} C - \frac{2}{3} \mathcal{I}_{C2} C^{-1} \right) + \frac{\partial W}{\partial \mathcal{I}_{C3}} J C^{-1} . \quad (\text{A.49})$$

A.2.4.1 Compressible Material

This section denotes some popular hyperelastic material constitutive laws based on reduced invariants for the compressible material. The general form of the hyperelastic function is defined as follows:

$$W(\mathcal{I}_{C1}, \mathcal{I}_{C2}, J) = \sum_{m+n+p=1}^{\infty} C_{mnp} (\mathcal{I}_{C1} - 3)^m (\mathcal{I}_{C2} - 3)^n (J - 1)^p , \quad (\text{A.50})$$

where C_{mnp} is a coefficient of each term.

• Compressible Mooney-Rivlin Material

The hyperelastic function W of the Mooney-Rivlin model and its derivatives with respect to reduced invariants as follows:

$$W(\mathcal{I}_{C1}, \mathcal{I}_{C2}, J) = c_{10}(\mathcal{I}_{C1} - 3) + c_{01}(\mathcal{I}_{C2} - 3) + D_1(J - 1)^2 , \quad (\text{A.51})$$

$$\frac{\partial W}{\partial \mathcal{I}_{C1}} = \frac{\partial W}{\partial \mathcal{I}_{B1}} = c_{10} , \quad (\text{A.52})$$

$$\frac{\partial W}{\partial \mathcal{I}_{C2}} = \frac{\partial W}{\partial \mathcal{I}_{B2}} = c_{01} , \quad (\text{A.53})$$

$$\frac{\partial W}{\partial \mathcal{I}_{C3}} = \frac{\partial W}{\partial \mathcal{I}_{B3}} = 2D_1(J - 1) . \quad (\text{A.54})$$

The second PK stress tensor and its tangential operator are defined as follows based on matrix forms:

$$S = - 2J^{-4/3}c_{10}C + 2J^{-2/3}(c_{10} + \mathcal{I}_{C1}c_{01})\tilde{I} + \left[-\frac{2}{3}(\mathcal{I}_{C1}c_{10} + \mathcal{I}_{C2}c_{01}) + 2D_1(J - 1)J \right] C^{-1} , \quad (\text{A.55})$$

$$\frac{\partial S}{\partial \mathbf{u}} = \frac{4}{3}J^{-4/3} \left[2c_{10}\tilde{I} - (c_{10} + 2\mathcal{I}_{C1}c_{01})C^{-1} \right] \frac{\partial C}{\partial \mathbf{u}} - \left[\frac{4}{9}(2\mathcal{I}_{C1}c_{10} + 5\mathcal{I}_{C2}c_{01}) + D_1J \right] \frac{\partial C^{-1}}{\partial \mathbf{u}} . \quad (\text{A.56})$$

A.2.4.2 Incompressible Material

Considering the incompressible solid material ($\nu = 0.5$), the third invariant I_3 is always 1 ($I_3 = J^2 = 1$). Therefore, the standard invariants and the reduced invariants are exactly identical in this case:

$$\mathcal{I}_{C1} = I_{C3}^{-1/3} I_{C1} = I_{C1} , \quad (\text{A.57})$$

$$\mathcal{I}_{C2} = I_{C3}^{-2/3} I_{C2} = I_{C2} , \quad (\text{A.58})$$

$$\mathcal{I}_{C3} = I_{C3}^{1/2} = J = 1 . \quad (\text{A.59})$$

The hyperelastic function W is defined by the standard invariants in this discussion. In addition, the hydrostatic pressure p should be introduced as a volume and non-deterministic contribution from the deformation. Therefore, the hyperelastic function for the incompressible material is denoted as follows:

$$W(I_{C1}, I_{C2}) = \sum_{m+n=1}^{\infty} \left(C_{mn}(I_{C1} - 3)^m (I - 3)^n \right) - p(J - 1). \quad (\text{A.60})$$

As denoted at the above equation, the hydrostatic pressure p is a Lagrange multiplier for the incompressibility $J = 1$ mathematically.

• Incompressible Mooney-Rivlin Material

The hyperelastic function W of the incompressible Mooney-Rivlin model and its derivatives with respect to the standard invariants are as follows:

$$W(I_{C1}, I_{C2}) = c_{10}(I_{C1} - 3) + c_{01}(I_{C2} - 3) - p(J - 1) \quad (\text{A.61})$$

$$\frac{\partial W}{\partial I_{C1}} = \frac{\partial W}{\partial I_{B1}} = c_{10} \quad (\text{A.62})$$

$$\frac{\partial W}{\partial I_{C2}} = \frac{\partial W}{\partial I_{B2}} = c_{01} \quad (\text{A.63})$$

$$\frac{\partial W}{\partial J} = -p \quad (\text{A.64})$$

The second PK stress tensor and its tangential operator are defined as follows based on matrix forms:

$$S = -pC^{-1} + S_{\text{dev}} \quad (\text{A.65})$$

$$S_{\text{dev}} = -2c_{01}C + 2(c_{10} + I_{C1}c_{01})\tilde{I} - \frac{2}{3}(I_{C1}c_{10} + 2I_{C2}c_{01})C^{-1} \quad (\text{A.66})$$

$$\frac{\partial S_{\text{dev}}}{\partial \mathbf{u}} = \left[-\frac{2}{3}(c_{10} + 2I_{C1}c_{01})C^{-1} + \frac{4}{3}c_{01}\tilde{I} \right] \frac{\partial C}{\partial \mathbf{u}} - \frac{2}{3}(I_{C1}c_{10} + 2I_{C2}c_{01}) \frac{\partial C^{-1}}{\partial \mathbf{u}} \quad (\text{A.67})$$

where S_{dev} represents the deviatoric part of S .

• **Incompressible Yeoh Material**

$$W(I_{C1}) = C_{10}(I_{C1} - 3) + C_{20}(I_{C1} - 3)^2 + C_{30}(I_{C1} - 3)^3 + p(J - 1) \quad (\text{A.68})$$

$$\frac{\partial W}{\partial I_{C1}} = \frac{\partial W}{\partial I_{B1}} = C_{10} + 2C_{20}(I_{C1} - 3) + 3C_{30}(I_{C1} - 3)^2 \quad (\text{A.69})$$

$$\frac{\partial W}{\partial J} = p \quad (\text{A.70})$$

• **Incompressible Ogden Material**

$$W(\lambda_1, \lambda_2, \lambda_3) = \sum_{i=1}^N \frac{\mu_i}{\alpha_i} (\lambda_1^{\alpha_i} + \lambda_2^{\alpha_i} + \lambda_3^{\alpha_i} - 3) + p(J - 1) \quad (\text{A.71})$$

A.3 Derivative of Determinant

Considering the derivative of the determinant of a tensor C with respect to C , this derivative is derived from the Gâteaux derivative (directional derivative) of the following scalar triplet product. Assuming arbitrary vectors \mathbf{a}_1 , \mathbf{a}_2 and \mathbf{a}_3 , then:

$$\mathcal{F}(C) \equiv (C\mathbf{a}_1)^T(C\mathbf{a}_2 \times C\mathbf{a}_3) \equiv |C\mathbf{a}_1, C\mathbf{a}_2, C\mathbf{a}_3| = \det C |\mathbf{a}_1, \mathbf{a}_2, \mathbf{a}_3| \quad (\text{A.72})$$

The Gâteaux derivative of (A.72) is defined as follows:

$$D\mathcal{F}(C)[\Delta C] = \left. \frac{d\mathcal{F}(C + h\Delta C)}{dh} \right|_{h=0} \quad (\text{A.73})$$

$$= \left. \frac{d}{dh} |(C + h\Delta C)\mathbf{a}_1, (C + h\Delta C)\mathbf{a}_2, (C + h\Delta C)\mathbf{a}_3| \right|_{h=0} \quad (\text{A.74})$$

$$= |\Delta C\mathbf{a}_1, C\mathbf{a}_2, C\mathbf{a}_3| + |C\mathbf{a}_1, \Delta C\mathbf{a}_2, C\mathbf{a}_3| + |C\mathbf{a}_1, C\mathbf{a}_2, \Delta C\mathbf{a}_3| \quad (\text{A.75})$$

$$= |(\Delta C)C^{-1}C\mathbf{a}_1, C\mathbf{a}_2, C\mathbf{a}_3| + |C\mathbf{a}_1, (\Delta C)C^{-1}C\mathbf{a}_2, C\mathbf{a}_3| \\ + |C\mathbf{a}_1, C\mathbf{a}_2, (\Delta C)C^{-1}C\mathbf{a}_3| \quad (\text{A.76})$$

$$= \text{Tr}(\Delta C C^{-1}) |C\mathbf{a}_1, C\mathbf{a}_2, C\mathbf{a}_3| \quad (\text{A.77})$$

$$= \text{Tr}(\Delta C C^{-1}) \det C |\mathbf{a}_1, \mathbf{a}_2, \mathbf{a}_3| \quad (\text{A.78})$$

$$= (\det C)C^{-T} : \Delta C | \mathbf{a}_1, \mathbf{a}_2, \mathbf{a}_3 | . \quad (\text{A.79})$$

On the other hand, this Gâteaux derivative can be solved by the different way as follows:

$$D\mathcal{F}(C)[\Delta C] = \left. \frac{d\mathcal{F}(C + h\Delta C)}{dh} \right|_{h=0} \quad (\text{A.80})$$

$$= \left. \frac{d(\det(C + h\Delta C))}{dh} \right|_{h=0} | \mathbf{a}_1, \mathbf{a}_2, \mathbf{a}_3 | \quad (\text{A.81})$$

$$= \frac{\partial(\det C)}{\partial C_{ij}} (\Delta C)_{ij} | \mathbf{a}_1, \mathbf{a}_2, \mathbf{a}_3 | \quad (\text{A.82})$$

$$= \frac{\partial(\det C)}{\partial C_{ij}} \hat{\mathbf{e}}_i \hat{\mathbf{e}}_j^T : (\Delta C)_{kl} \hat{\mathbf{e}}_k \hat{\mathbf{e}}_l^T | \mathbf{a}_1, \mathbf{a}_2, \mathbf{a}_3 | \quad (\text{A.83})$$

$$= \frac{\partial(\det C)}{\partial C} : \Delta C | \mathbf{a}_1, \mathbf{a}_2, \mathbf{a}_3 | . \quad (\text{A.84})$$

Therefore, the derivative of the determinant of C is defined as follows based on the comparison of (A.79) and (A.84):

$$\frac{\partial(\det C)}{\partial C} = (\det C)C^{-T} = (\det F)^2 C^{-1} = J^2 C^{-1} \quad (\because C^T = C) . \quad (\text{A.85})$$

□

Appendix B

Nitsche's Method for Cauchy Momentum Equation

In this appendix, Nitsche's formulation for the Cauchy momentum equation is summarized by referencing [121, 72]. This appendix assumes the infinitesimal small strain in the solid phase for simplicity.

B.1 Cauchy Momentum Equation

The following Cauchy momentum equation is derived from the conservation of the momentum:

$$\rho \frac{Dv_i}{Dt} = \frac{\partial \sigma_{ij}}{\partial x_j} + b_i, \quad (\text{B.1})$$

where v_i is the velocity, b_i is the body force, ρ is the density, and σ_{ij} is the Cauchy stress tensor. The generalized constitutive equation is defined by the fourth order constitutive tensor D_{ijkl} and the generalized strain tensor e_{ij} :

$$\sigma_{ij} = \sigma_{ij}(\mathbf{a}) = D_{ijkl} e_{kl}(\mathbf{a}), \quad (\text{B.2})$$

where e_{ij} is defined as follows:

$$e_{ij}(\mathbf{a}) = e_{ji}(\mathbf{a}) = \frac{1}{2} \left(\frac{\partial a_i}{\partial x_j} + \frac{\partial a_j}{\partial x_i} \right). \quad (\text{B.3})$$

In (B.3), a_i are the characteristic physical quantities. In the solid analysis, e_{ij} is the strain tensor and a_i is the solid displacement u_i . In the fluid analysis, e_{ij} is the strain rate tensor and a_i is the fluid velocity v_i .

B.2 Constitutive Tensor

The constitutive D_{ijkl} has the following symmetries to meet the request of the symmetry of the Cauchy stress tensor σ_{ij} , the strain tensor e_{ij} and the definition of the strain energy function W :

$$D_{ijkl} = D_{jikl} = D_{ijlk} = D_{klij} . \quad (\text{B.4})$$

Followings are the basic constitutive laws of the solid and the fluid.

• Isotropic Linear Elastic Solid Material

$$a_i = u_i , \quad (\text{B.5})$$

$$D_{ijkl} = \lambda^s \delta_{ij} \delta_{kl} + 2\mu^s \delta_{ik} \delta_{jl} , \quad (\text{B.6})$$

$$b_i = \rho g_i , \quad (\text{B.7})$$

where λ^s and μ^s are the Lamé's constants of the solid material. g_i is the body force constant.

• Compressible Newtonian Fluid

$$a_i = v_i , \quad (\text{B.8})$$

$$D_{ijkl} = -\frac{2}{3}\mu^f \delta_{ij} \delta_{kl} + 2\mu^f \delta_{ik} \delta_{jl} , \quad (\text{B.9})$$

$$b_i = \rho g_i - \frac{\partial p}{\partial x_i} , \quad (\text{B.10})$$

where μ^f is the dynamic viscosity and p is the pressure of the fluid. Note that the Stokes assumption is applied to (B.9). Using these definition, the Cauchy momentum equation (B.1) is identical to the Navier-Stokes (NS) equation.

• **Incompressible Newtonian Fluid**

$$a_i = v_i , \quad (\text{B.11})$$

$$D_{ijkl} = 2\mu^f \delta_{ik} \delta_{jl} , \quad (\text{B.12})$$

$$b_i = \rho g_i - \frac{\partial p}{\partial x_i} . \quad (\text{B.13})$$

Using these definition, the Cauchy momentum equation (B.1) is identical to the incompressible Navier-Stokes (INS) equation.

B.3 Weak Form of Cauchy Momentum Equation

In this section, the weak form of the Cauchy momentum equation is considered. First, the Cauchy momentum equation is divided as follows:

$$-\frac{\partial \sigma_{ij}(\mathbf{a})}{\partial x_j} = -\rho \frac{Dv_i}{Dt} + b_i \equiv f_i , \quad (\text{B.14})$$

$$\sigma_{ij}(\mathbf{a}) = D_{ijkl} e_{kl}(\mathbf{a}) = \frac{1}{2} D_{ijkl} \left(\frac{\partial a_k}{\partial x_l} + \frac{\partial a_l}{\partial x_k} \right) . \quad (\text{B.15})$$

The weak form of (B.14) is modified as follows:

$$\int_{\kappa} d\Omega w \left(-\frac{\partial \sigma_{ij}(\mathbf{a})}{\partial x_j} - f_i \right) = \int_{\kappa} d\Omega \frac{\partial w}{\partial x_j} \sigma_{ij}(\mathbf{a}) - \int_{\partial\kappa} d\Gamma w \sigma_{ji}(\mathbf{a}) \hat{n}_j - \int_{\kappa} d\Omega w f_i = 0, \quad (\text{B.16})$$

$$\therefore \int_{\kappa} d\Omega \frac{\partial w}{\partial x_j} \sigma_{ij}(\mathbf{a}) = \int_{\kappa} d\Omega w f_i + \int_{\partial\kappa} d\Gamma w \sigma_{ji}(\mathbf{a}) \hat{n}_j , \quad (\text{B.17})$$

where w is an admissible test function. Similarly, the weak form of (B.15) is as follows, using other test functions q_j :

$$\int_{\kappa} d\Omega q_j \sigma_{ij}(\mathbf{a}) = \int_{\kappa} d\Omega q_j D_{ijkl} e_{kl}(\mathbf{a}) . \quad (\text{B.18})$$

The summary of these weak forms are:

$$\int_{\kappa} d\Omega \frac{\partial w}{\partial x_j} \sigma_{ij}(\mathbf{a}) = \int_{\kappa} d\Omega w f_i + \int_{\partial\kappa} d\Gamma w \sigma_{ji}(\mathbf{a}) \hat{n}_j, \quad (\text{B.19})$$

$$\int_{\kappa} d\Omega q_j \sigma_{ij}(\mathbf{a}) = \int_{\kappa} d\Omega q_j D_{ijkl} e_{kl}(\mathbf{a}). \quad (\text{B.20})$$

Based on the standard Galerkin method, $w = \delta v_i$ and $q_j = \frac{\partial w}{\partial x_j} = \frac{\partial \delta v_i}{\partial x_j}$, then:

$$\int_{\kappa} d\Omega \frac{\partial \delta v_i}{\partial x_j} \sigma_{ij}(\mathbf{a}) = \int_{\kappa} d\Omega \delta v_i f_i + \int_{\partial\kappa} d\Gamma \delta v_i \sigma_{ji}(\mathbf{a}) \hat{n}_j, \quad (\text{B.21})$$

$$\begin{aligned} \int_{\kappa} d\Omega \frac{\partial \delta v_i}{\partial x_j} \sigma_{ij}(\mathbf{a}) &= \int_{\kappa} d\Omega \frac{\partial \delta v_i}{\partial x_j} D_{ijkl} e_{kl}(\mathbf{a}) = \int_{\kappa} d\Omega e_{ij}(\delta \mathbf{v}) D_{ijkl} e_{kl}(\mathbf{a}) \\ &= \int_{\kappa} d\Omega e_{ij}(\delta \mathbf{v}) D_{klij} e_{kl}(\mathbf{a}) = \int_{\kappa} d\Omega \sigma_{ij}(\delta \mathbf{v}) e_{ij}(\mathbf{a}) \\ &= -\frac{1}{2} \int_{\kappa} d\Omega \frac{\partial \sigma_{ij}(\delta \mathbf{v})}{\partial x_j} a_i + \frac{1}{2} \int_{\partial\kappa} d\Gamma \sigma_{ij}(\delta \mathbf{v}) \hat{n}_j a_i \\ &\quad - \frac{1}{2} \int_{\kappa} d\Omega \frac{\partial \sigma_{ij}(\delta \mathbf{v})}{\partial x_i} a_j + \frac{1}{2} \int_{\partial\kappa} d\Gamma \sigma_{ij}(\delta \mathbf{v}) \hat{n}_i a_j. \end{aligned} \quad (\text{B.22})$$

B.4 Weak Form for Nitsche's Method

The main idea of Nitsche's method is to introduce the numerical flux into the boundary integrals of (B.19) and (B.20):

$$\int_{\kappa} d\Omega \frac{\partial \delta v_i^m}{\partial x_j} \sigma_{ij}^m(\mathbf{a}^m) = \int_{\kappa} d\Omega \delta v_i^m f_i^m + \int_{\partial\kappa} d\Gamma \delta v_i^m \tilde{\sigma}_{ji}^m(\mathbf{a}^m) \hat{n}_j^m, \quad (\text{B.23})$$

$$\begin{aligned} \int_{\kappa} d\Omega \frac{\partial \delta v_i^m}{\partial x_j} \sigma_{ij}^m(\mathbf{a}^m) &= -\frac{1}{2} \int_{\kappa} d\Omega \frac{\partial \sigma_{ij}^m(\delta \mathbf{v}^m)}{\partial x_j} a_i^m + \frac{1}{2} \int_{\partial\kappa} d\Gamma \sigma_{ij}^m(\delta \mathbf{v}^m) \hat{n}_j^m a_i^m \\ &\quad - \frac{1}{2} \int_{\kappa} d\Omega \frac{\partial \sigma_{ij}^m(\delta \mathbf{v}^m)}{\partial x_i} a_j^m + \frac{1}{2} \int_{\partial\kappa} d\Gamma \sigma_{ij}^m(\delta \mathbf{v}^m) \hat{n}_i^m a_j^m. \end{aligned} \quad (\text{B.24})$$

$\tilde{\sigma}_{ij}^m$ and \tilde{u}_k^m are the approximated values at the boundary integrals. The upper subscript m represents the phase ($m = 1, 2$). The first and third terms of the RHS of (B.24) can be rewritten as follows using (B.22):

$$-\frac{1}{2} \int_{\kappa} d\Omega \frac{\partial \sigma_{ij}^m(\delta \mathbf{v}^m)}{\partial x_j} a_i^m - \frac{1}{2} \int_{\kappa} d\Omega \frac{\partial \sigma_{ij}^m(\delta \mathbf{v}^m)}{\partial x_i} a_j^m$$

$$= \int_{\kappa} d\Omega \frac{\partial \delta v_i^m}{\partial x_j} \sigma_{ij}^m(\mathbf{a}^m) - \frac{1}{2} \int_{\partial\kappa} d\Gamma \sigma_{ij}^m(\delta \mathbf{v}^m) \hat{n}_j^m a_i^m - \frac{1}{2} \int_{\partial\kappa} d\Gamma \sigma_{ij}^m(\delta \mathbf{v}^m) \hat{n}_i^m a_j^m \quad (\text{B.25})$$

$$= \int_{\kappa} d\Omega e_{ij}^m(\delta \mathbf{v}^m) \sigma_{ij}^m(\mathbf{a}^m) - \frac{1}{2} \int_{\partial\kappa} d\Gamma \sigma_{ij}^m(\delta \mathbf{v}^m) \hat{n}_j^m a_i^m - \frac{1}{2} \int_{\partial\kappa} d\Gamma \sigma_{ij}^m(\delta \mathbf{v}^m) \hat{n}_i^m a_j^m \quad (\text{B.26})$$

$$= \int_{\kappa} d\Omega \sigma_{ij}^m(\delta \mathbf{v}^m) e_{ij}^m(\mathbf{a}^m) - \frac{1}{2} \int_{\partial\kappa} d\Gamma \sigma_{ij}^m(\delta \mathbf{v}^m) \hat{n}_j^m a_i^m - \frac{1}{2} \int_{\partial\kappa} d\Gamma \sigma_{ij}^m(\delta \mathbf{v}^m) \hat{n}_i^m a_j^m, \quad (\text{B.27})$$

(B.27) do not include the numerical flux. Substituting (B.27) to (B.24), then the weak form is summarized as follows:

$$\int_{\kappa} d\Omega \frac{\partial \delta v_i^m}{\partial x_j} \sigma_{ij}^m(\mathbf{a}^m) = \int_{\kappa} d\Omega \sigma_{ij}^m(\delta \mathbf{v}^m) e_{ij}^m(\mathbf{a}^m) - \int_{\partial\kappa} d\Gamma \sigma_{ij}^m(\delta \mathbf{v}^m) \hat{n}_j^m (a_i^m - \tilde{a}_i^m) \quad (\text{B.28})$$

$$= \int_{\kappa} d\Omega \delta v_i^m f_i^m + \int_{\partial\kappa} d\Gamma \delta v_i^m \tilde{\sigma}_{ji}^m(\mathbf{a}^m) \hat{n}_j^m, \quad (\text{B.29})$$

$$\begin{aligned} \therefore \int_{\kappa} d\Omega \sigma_{ij}^m(\delta \mathbf{v}^m) e_{ij}^m(\mathbf{a}^m) - \int_{\kappa} d\Omega \delta v_i^m f_i^m \\ - \int_{\partial\kappa} d\Gamma \sigma_{ij}^m(\delta \mathbf{v}^m) \hat{n}_j^m (a_i^m - \tilde{a}_i^m) - \int_{\partial\kappa} d\Gamma \delta v_i^m \tilde{\sigma}_{ji}^m(\mathbf{a}^m) \hat{n}_j^m = 0. \end{aligned} \quad (\text{B.30})$$

B.5 Symmetric Nitsche Formulation

This section focuses on the symmetric Nitsche formulation. Based on the symmetric Nitsche formulation, the numerical fluxes; \tilde{u}_i^m and $\tilde{\sigma}_{ij}^m$, are defined as follows. Γ_D and Γ_I mean the Dirichlet boundary and the interface between two phases, respectively:

On Dirichlet Boundary (Γ_D)

$$\tilde{a}_i^1 = \tilde{a}_i^2 = \bar{a}_i \quad \text{on } \Gamma_D, \quad (\text{B.31})$$

$$\tilde{\sigma}_{ij}^1 = \sigma_{ij}^1, \quad \tilde{\sigma}_{ij}^2 = \sigma_{ij}^2 \quad \text{on } \Gamma_D, \quad (\text{B.32})$$

On Interface between Two Phases (Γ_I)

$$\tilde{a}_i^1 = \tilde{a}_i^2 = \frac{1}{2}(a_i^1 + a_i^2) \equiv \{a_i\} \quad \text{on } \Gamma_I, \quad (\text{B.33})$$

$$\tilde{\sigma}_{ij}^1 = \tilde{\sigma}_{ij}^2 = \frac{1}{2}(\sigma_{ij}^1 + \sigma_{ij}^2) - \alpha(v_i^1 - v_i^2)\hat{n}_j^1 \equiv \{\sigma_{ij}\} - \alpha[[v_i]]\hat{n}_j^1 \quad \text{on } \Gamma_I . \quad (\text{B.34})$$

By introducing these definition of the numerical flux (B.31) - (B.34) into (B.30), the weak form for one element is denoted as follows:

$$\begin{aligned} & \int_{\kappa} d\Omega \sigma_{ij}^m(\delta\mathbf{v}^m)e_{ij}^m(\mathbf{a}^m) - \int_{\kappa} d\Omega \delta v_i^m f_i^m \\ & - \int_{\partial\kappa \subset \Gamma_D} d\Gamma \sigma_{ij}^m(\delta\mathbf{v}^m)\hat{n}_j^m(a_i^m - \bar{a}_i^m) - \int_{\partial\kappa \subset \Gamma_D} d\Gamma \delta v_i^m \bar{\sigma}_{ji}^m(\mathbf{a}^m)\hat{n}_j^m \\ & - \int_{\partial\kappa \subset \Gamma_I} d\Gamma \sigma_{ij}^m(\delta\mathbf{v}^m)\hat{n}_j^m(a_i^m - \{a_i\}) - \int_{\partial\kappa \subset \Gamma_I} d\Gamma \delta v_i^m \{\sigma_{ji}\}\hat{n}_j^m \\ & + \alpha \int_{\partial\kappa \subset \Gamma_I} d\Gamma \delta v_i^m [[v_i]](\hat{n}_j^1 \hat{n}_j^m) = 0 . \end{aligned} \quad (\text{B.35})$$

By integrating over all elements, (B.35) is summarized as follows.

$$\begin{aligned} & \int_{\Omega^m} d\Omega \sigma_{ij}^m(\delta\mathbf{v}^m)e_{ij}^m(\mathbf{a}^m) - \int_{\Omega^m} d\Omega \delta v_i^m f_i^m \\ & - \int_{\Gamma_D^m} d\Gamma \sigma_{ij}^m(\delta\mathbf{v}^m)\hat{n}_j^m(a_i^m - \bar{a}_i^m) - \int_{\Gamma_D^m} d\Gamma \delta v_i^m \bar{\sigma}_{ji}^m(\mathbf{a}^m)\hat{n}_j^m \\ & - \int_{\Gamma_I} d\Gamma \sigma_{ij}^m(\delta\mathbf{v}^m)\hat{n}_j^m(a_i^m - \{a_i\}) - \int_{\Gamma_I} d\Gamma \delta v_i^m \{\sigma_{ji}\}\hat{n}_j^m \\ & + \alpha \int_{\Gamma_I} d\Gamma \delta v_i^m [[v_i]](\hat{n}_j^1 \hat{n}_j^m) = 0 , \end{aligned} \quad (\text{B.36})$$

where Ω^m represents the volume of the phase m and Γ_D^m is the Dirichlet boundary of the phase m . The boundary integrals of (B.36) at the interface for each phase ($m = 1, 2$) are simplified as follows:

Boundary Integral on Interface for Phase 1

$$- \int_{\Gamma_I} d\Gamma \sigma_{ij}^1(\delta\mathbf{v}^1)\hat{n}_j^1(a_i^1 - \{a_i\}) - \int_{\Gamma_I} d\Gamma \delta v_i^1 \{\sigma_{ji}\}\hat{n}_j^1 + \alpha \int_{\Gamma_I} d\Gamma \delta v_i^1 [[v_i]](\hat{n}_j^1 \hat{n}_j^1) \quad (\text{B.37})$$

$$= - \frac{1}{2} \int_{\Gamma_I} d\Gamma \sigma_{ij}^1(\delta\mathbf{v}^1)\hat{n}_j^1 [[a_i]] - \int_{\Gamma_I} d\Gamma \delta v_i^1 \{\sigma_{ji}\}\hat{n}_j^1 + \alpha \int_{\Gamma_I} d\Gamma \delta v_i^1 [[v_i]] , \quad (\text{B.38})$$

where $\hat{n}_j^1 \hat{n}_j^1 = \hat{\mathbf{n}}^{1\Gamma} \hat{\mathbf{n}}^1 = 1$ is used.

Boundary Integral on Interface for Phase 2

$$- \int_{\Gamma_I} d\Gamma \sigma_{ij}^2(\delta \mathbf{v}^2) \hat{n}_j^2 (a_i^2 - \{a_i\}) - \int_{\Gamma_I} d\Gamma \delta v_i^2 \{\sigma_{ji}\} \hat{n}_j^2 + \alpha \int_{\Gamma_I} d\Gamma \delta v_i^2 \llbracket v_i \rrbracket (\hat{n}_j^2 \hat{n}_j^1) \quad (\text{B.39})$$

$$= \int_{\Gamma_I} d\Gamma \sigma_{ij}^2(\delta \mathbf{v}^2) \hat{n}_j^1 \frac{1}{2} (a_i^2 - a_i^1) + \int_{\Gamma_I} d\Gamma \delta v_i^2 \{\sigma_{ji}\} \hat{n}_j^1 - \alpha \int_{\Gamma_I} d\Gamma \delta v_i^2 \llbracket v_i \rrbracket (\hat{n}_j^1 \hat{n}_j^1) \quad (\text{B.40})$$

$$= -\frac{1}{2} \int_{\Gamma_I} d\Gamma \sigma_{ij}^2(\delta \mathbf{v}^2) \hat{n}_j^1 \llbracket a_i \rrbracket + \int_{\Gamma_I} d\Gamma \delta v_i^2 \{\sigma_{ji}\} \hat{n}_j^1 - \alpha \int_{\Gamma_I} d\Gamma \delta v_i^2 \llbracket v_i \rrbracket, \quad (\text{B.41})$$

where $\hat{n}_j^2 = -\hat{n}_j^1$ is used at the interface.

B.5.1 Symmetric Nitsche Method for Pure Structural or Pure Fluid Analysis

This section considers the pure solid analysis or the pure fluid analysis, which does not include fluid-structure interaction (FSI). Using (B.36), (B.38) and (B.41), the weak form for the whole system is summarized as follows:

$$\begin{aligned} & \sum_{m=1}^2 \int_{\Omega^m} d\Omega \sigma_{ij}^m(\delta \mathbf{v}^m) e_{ij}^m(\mathbf{a}^m) - \sum_{m=1}^2 \int_{\Omega^m} d\Omega \delta v_i^m f_i^m \\ & - \sum_{m=1}^2 \int_{\Gamma_B^m} d\Gamma \sigma_{ij}^m(\delta \mathbf{v}^m) \hat{n}_j^m (a_i^m - \bar{a}_i^m) - \sum_{m=1}^2 \int_{\Gamma_B^m} d\Gamma \delta v_i^m \bar{\sigma}_{ji}^m(\mathbf{a}^m) \hat{n}_j^m \\ & - \int_{\Gamma_I} d\Gamma \{\delta \sigma_{ij}\} \hat{n}_j^1 \llbracket a_i \rrbracket - \int_{\Gamma_I} d\Gamma \llbracket \delta v_i \rrbracket \{\sigma_{ji}\} \hat{n}_j^1 + \alpha \int_{\Gamma_I} d\Gamma \llbracket \delta v_i \rrbracket \llbracket v_i \rrbracket = 0, \end{aligned} \quad (\text{B.42})$$

where a_i is the displacement u_i in the solid phase or the velocity v_i in the fluid phase. $\{\delta \sigma_{ij}\}$ means the averaged stress. The strategy for the averaged stress is described in Section 5.5.2.

B.5.2 Symmetric Nitsche Method for FSI Analysis

This section considers the weak form of the symmetric Nitsche formulation for the FSI analysis. Assuming the phase f as the fluid phase and the phase s as the solid phase, respectively, Then, the weak form is denoted as follows:

$$\sum_{m=f,s} \int_{\Omega^m} d\Omega \sigma_{ij}^m(\delta \mathbf{v}^m) e_{ij}^m(\mathbf{a}^m) - \sum_{m=f,s} \int_{\Omega^m} d\Omega \delta v_i^m f_i^m$$

$$\begin{aligned}
& - \sum_{m=f,s} \int_{\Gamma_D^m} d\Gamma \sigma_{ij}^m(\delta \mathbf{v}^m) \hat{n}_j^m (a_i^m - \bar{a}_i^m) - \sum_{m=f,s} \int_{\Gamma_D^m} d\Gamma \delta v_i^m \bar{\sigma}_{ji}^m(\mathbf{a}^m) \hat{n}_j^m \\
& - \frac{1}{2} \int_{\Gamma_1} d\Gamma \sigma_{ij}^f(\delta \mathbf{v}^f) \hat{n}_j^f \llbracket v_i \rrbracket - \int_{\Gamma_1} d\Gamma \delta v_i^f \{\sigma_{ji}\} \hat{n}_j^f - \alpha \int_{\Gamma_1} d\Gamma \delta v_i^f \llbracket v_i \rrbracket \\
& - \frac{1}{2} \int_{\Gamma_1} d\Gamma \sigma_{ij}^s(\delta \mathbf{v}^s) \hat{n}_j^s \llbracket u_i \rrbracket + \int_{\Gamma_1} d\Gamma \delta v_i^s \{\sigma_{ji}\} \hat{n}_j^s + \alpha \int_{\Gamma_1} d\Gamma \delta v_i^s \llbracket v_i \rrbracket \quad (B.43) \\
& = \sum_{m=f,s} \int_{\Omega^m} d\Omega \sigma_{ij}^m(\delta \mathbf{v}^m) e_{ij}^m(\mathbf{a}^m) - \sum_{m=f,s} \int_{\Omega^m} d\Omega \delta v_i^m f_i^m \\
& - \sum_{m=f,s} \int_{\Gamma_D^m} d\Gamma \sigma_{ij}^m(\delta \mathbf{v}^m) \hat{n}_j^m (a_i^m - \bar{a}_i^m) - \sum_{m=f,s} \int_{\Gamma_D^m} d\Gamma \delta v_i^m \bar{\sigma}_{ji}^m(\mathbf{a}^m) \hat{n}_j^m \\
& - \frac{1}{2} \int_{\Gamma_1} d\Gamma \sigma_{ij}^f(\delta \mathbf{v}^f) \hat{n}_j^f \llbracket v_i \rrbracket - \frac{1}{2} \int_{\Gamma_1} d\Gamma \sigma_{ij}^s(\delta \mathbf{v}^s) \hat{n}_j^s \llbracket u_i \rrbracket \\
& - \int_{\Gamma_1} d\Gamma \llbracket \delta v_i \rrbracket \{\sigma_{ji}\} \hat{n}_j^f + \alpha \int_{\Gamma_1} d\Gamma \llbracket \delta v_i \rrbracket \llbracket v_i \rrbracket = 0 , \quad (B.44)
\end{aligned}$$

Following the works of Hansbo et al.[74], Jenkins et al.[102] and Mayer et al.[70], the traction from the fluid side is used as the traction at the interface, which is the traditional FSI approach that forces are transferred from the fluid phase to the solid phase rather than its vice versa:

$$\{\sigma_{ij}\} = \frac{1}{2} \left(\sigma_{ij}^f(\mathbf{v}^f) + \sigma_{ij}^s(\mathbf{u}^s) \right) \rightarrow \sigma_{ij}^f(\mathbf{v}^f) , \quad (B.45)$$

$$\frac{1}{2} \int_{\Gamma_1} d\Gamma \sigma_{ij}^s(\delta \mathbf{v}^s) \hat{n}_j^s \llbracket u_i \rrbracket \rightarrow \frac{1}{2} \int_{\Gamma_1} d\Gamma \sigma_{ij}^f(\delta \mathbf{v}^f) \hat{n}_j^f \llbracket v_i \rrbracket . \quad (B.46)$$

Substituting (B.45) and (B.46) to (B.44), the weak form for FSI is summarized as follows:

$$\begin{aligned}
& \sum_{m=f,s} \int_{\Omega^m} d\Omega \sigma_{ij}^m(\delta \mathbf{v}^m) e_{ij}^m(\mathbf{a}^m) - \sum_{m=f,s} \int_{\Omega^m} d\Omega \delta v_i^m f_i^m \\
& - \sum_{m=f,s} \int_{\Gamma_D^m} d\Gamma \sigma_{ij}^m(\delta \mathbf{v}^m) \hat{n}_j^m (a_i^m - \bar{a}_i^m) - \sum_{m=f,s} \int_{\Gamma_D^m} d\Gamma \delta v_i^m \bar{\sigma}_{ji}^m(\mathbf{a}^m) \hat{n}_j^m \\
& - \int_{\Gamma_1} d\Gamma \sigma_{ij}^f(\delta \mathbf{v}^f) \hat{n}_j^f \llbracket v_i \rrbracket - \int_{\Gamma_1} d\Gamma \llbracket \delta v_i \rrbracket \sigma_{ji}^f(\mathbf{v}^f) \hat{n}_j^f + \alpha \int_{\Gamma_1} d\Gamma \llbracket \delta v_i \rrbracket \llbracket v_i \rrbracket = 0 . \quad (B.47)
\end{aligned}$$

If the normal vector from the solid phase to the fluid phase $\hat{\mathbf{n}}^s$ is used, then (B.47) is as follows:

$$\begin{aligned}
& \sum_{m=f,s} \int_{\Omega^m} d\Omega \sigma_{ij}^m(\delta \mathbf{v}^m) e_{ij}^m(\mathbf{a}^m) - \sum_{m=f,s} \int_{\Omega^m} d\Omega \delta v_i^m f_i^m \\
& - \sum_{m=f,s} \int_{\Gamma_D^m} d\Gamma \sigma_{ij}^m(\delta \mathbf{v}^m) \hat{n}_j^m (a_i^m - \bar{a}_i^m) - \sum_{m=f,s} \int_{\Gamma_D^m} d\Gamma \delta v_i^m \bar{\sigma}_{ji}^m(\mathbf{a}^m) \hat{n}_j^m \\
& + \int_{\Gamma_1} d\Gamma \sigma_{ij}^f(\delta \mathbf{v}^f) \hat{n}_j^s [[v_i]] + \int_{\Gamma_1} d\Gamma [[\delta v_i]] \sigma_{ji}^f(\mathbf{v}^f) \hat{n}_j^s + \alpha \int_{\Gamma_1} d\Gamma [[\delta v_i]] [[v_i]] = 0 . \quad (\text{B.48})
\end{aligned}$$

Appendix C

Nitsche's Method for Non-Matching Interfaces

This appendix summarizes the derivation of the FSI boundary integrals for the Lagrangian-immersed FSI method denoted in Section 6.4. The Lagrangian-immersed FSI method performs the FSI boundary integrals between the non-matching Eulerian and Lagrangian interfaces. Based on the master-slave concept, the Eulerian interface is the master interface and the Lagrangian interface is the slave interface. The boundary contributions of the solid and fluid momentum equations are enforced by Nitsche's method. These boundary contributions R_L^{fsi} and R_E^{fsi} originate from the boundary integrals of the momentum equations, and they are defined on the different interfaces; the Lagrangian interface Γ_L and the Eulerian interface Γ_E :

$$R_L^{\text{fsi}} = - \int_{\Gamma_{L0}} d\Gamma \delta U_i^s \Pi_{iJ}^s(\mathbf{U}^s) n_{L0J}^s = - \int_{\Gamma_L} d\Gamma \delta U_i^s \sigma_{ij}^s(\mathbf{U}^s) n_{Lj}^s, \quad (\text{C.1})$$

$$R_E^{\text{fsi}} = - \int_{\Gamma_E} d\Gamma \delta v_i^f \sigma_{ij}^f(\mathbf{v}^f, p^f) n_{Ej}^f, \quad (\text{C.2})$$

where Π_{iJ}^s is the first Piola-Kirchhoff stress tensor of the solid phase, σ_{ij}^s is the Cauchy stress tensor of the solid phase, and σ_{ij}^f is the Cauchy stress tensor of the fluid phase. n_{L0J}^s and n_{Lj}^s represent the undeformed and deformed Lagrangian normals from the solid phase. n_{Ej}^f is the Eulerian normal from the fluid phase. (C.1) denotes both the total and update Lagrangian formulations. In the following discussion, the updated Lagrangian formulation, i.e. the last term of (C.1), is used. In (C.1) and (C.2), the compressible solid and the incompressible Navier-Stokes fluid are assumed. The key operation of Nitsche's method is to replace the actual stress tensors; σ_{iJ}^s and σ_{ij}^f , with the stress tensors with artificial numerical fluxes; $\tilde{\sigma}_{ij}^s$

and $\tilde{\sigma}_{ij}^f$. In addition, the numerical fluxes of the fluid velocity \tilde{v}_i^f is introduced to enforce the continuity of the velocity on the interface. \tilde{v}_i^f is an approximation of v_i^f on an interface ($v_i^f - \tilde{v}_i^f = 0$), then:

$$R_L^{\text{fsi}} = - \int_{\Gamma_L} d\Gamma \delta U_i^s \tilde{\sigma}_{ij}^s n_{Lj}^s - \int_{\Gamma_L} d\Gamma \{ \delta \sigma_{ij} \} n_{Lj}^s (U_i^s - \tilde{U}_i^s) , \quad (\text{C.3})$$

$$R_E^{\text{fsi}} = - \int_{\Gamma_E} d\Gamma \delta v_i^f \tilde{\sigma}_{ij}^f n_{Ej}^f - \int_{\Gamma_E} d\Gamma \{ \delta \sigma_{ij} \} n_{Ej}^f (v_i^f - \tilde{v}_i^f) , \quad (\text{C.4})$$

where $\delta \sigma_{ij}^p$ denotes a tangential stress operator of the Cauchy stress σ_{ij}^p for phase $p = \{s, f\}$. The numerical flux of the solid displacement \tilde{U}_i^s will be removed later. In this section, $[[\cdot]]$ denotes the jump operator and $\{\cdot\}$ denotes the weighted-average operator between the solid and fluid phase:

$$[[a]] = a^s - a^f , \quad (\text{C.5})$$

$$\{a\} = \kappa^s a^s + \kappa^f a^f \quad (\kappa^s + \kappa^f = 1) . \quad (\text{C.6})$$

In this research, the shear modulus weighting (6.52) - (6.56) is used as a strategy for the weighted-average operator $\{\cdot\}$.

In addition, the master-slave concept is used in the Lagrangian-immersed FSI; see Section 6.2.3. The boundary integrals on the Lagrangian interface R_L^{fsi} are computed on the master (Eulerian) interface Γ_E . Therefore, (C.3) is modified as follows:

$$R_L^{\text{fsi}} = - \int_{\Gamma_E} d\Gamma \delta U_i^s \tilde{\sigma}_{ij}^s n_{Lj}^s - \int_{\Gamma_E} d\Gamma \{ \delta \sigma_{ij} \} n_{Lj}^s (U_i^s - \tilde{U}_i^s) , \quad (\text{C.7})$$

$$R_E^{\text{fsi}} = - \int_{\Gamma_E} d\Gamma \delta v_i^f \tilde{\sigma}_{ij}^f n_{Ej}^f - \int_{\Gamma_E} d\Gamma \{ \delta \sigma_{ij} \} n_{Ej}^f (v_i^f - \tilde{v}_i^f) . \quad (\text{C.8})$$

The symmetric Nitsche's method for the standard interface, such as the multiphase flow, the ALE-FSI method and the full-Eulerian FSI method, assumes the numerical fluxes

as follows:

$$\tilde{v}_i^f = \frac{1}{2}(V_i^s + v_i^f) , \quad (\text{C.9})$$

$$\tilde{\Pi}_{iJ}^s = \{\Pi_{iJ}\} - \eta^{\text{fsi}}[[v_i]]n_{0J}^s , \quad (\text{C.10})$$

$$\tilde{\sigma}_{ij}^f = \{\sigma_{ij}\} - \eta^{\text{fsi}}[[v_i]]n_j^s . \quad (\text{C.11})$$

where $[[v_i]] = V_i^s - v_i^f$ and the normal of the solid phase is used above. The Lagrangian-immersed FSI method uses the non-matching interfaces for fluid-structure interaction. As the solid displacement U_i^s and the solid velocity V_i^s are defined only on Γ_L , the projected values of U_i^s and V_i^s are necessary from the viewpoint of integrals on the master interface Γ_E . Hence, the more precise descriptions of (C.9) - (C.11) for the Lagrangian-immersed FSI analysis can be denoted as follows:

$$\tilde{v}_i^f = \frac{1}{2}(\hat{V}_i^s|_{\Gamma_L} + v_i^f) \quad \text{on } \Gamma_E , \quad (\text{C.12})$$

$$\tilde{\sigma}_{ij}^s = \{\sigma_{ij}\} - \eta^{\text{fsi}}(\hat{V}_i^s|_{\Gamma_L} - v_i^f)n_{Lj}^s \quad \text{on } \Gamma_E , \quad (\text{C.13})$$

$$\tilde{\sigma}_{ij}^f = \{\sigma_{ij}\} - \eta^{\text{fsi}}(\hat{V}_i^s|_{\Gamma_L} - v_i^f)n_{Ej}^s \quad \text{on } \Gamma_E . \quad (\text{C.14})$$

where $\cdot|_{\Gamma_L}$ denotes a projected value from Γ_E onto Γ_L . Substituting (C.12) - (C.14) into (C.7) and (C.8), R_L^{fsi} and R_E^{fsi} are modified as follows:

$$\begin{aligned} R_L^{\text{fsi}} = & - \int_{\Gamma_E} d\Gamma \delta U_i^s \{\sigma_{iJ}\} n_{Lj}^s - \frac{1}{2} \int_{\Gamma_E} d\Gamma \{\delta \sigma_{ij}\} n_{Lj}^s (U_i^s - \tilde{U}_i^s) \\ & + \int_{\Gamma_E} d\Gamma \delta U_i^s \eta^{\text{fsi}} (\hat{V}_i^s|_{\Gamma_L} - v_i^f) , \end{aligned} \quad (\text{C.15})$$

$$\begin{aligned} R_E^{\text{fsi}} = & \int_{\Gamma_E} d\Gamma \delta v_i^f \{\sigma_{ij}\} n_{Ej}^s - \frac{1}{2} \int_{\Gamma_E} d\Gamma \{\delta \sigma_{ij}\} n_{Ej}^s (\hat{V}_i^s|_{\Gamma_L} - v_i^f) \\ & - \int_{\Gamma_E} d\Gamma \delta v_i^f \eta^{\text{fsi}} (\hat{V}_i^s|_{\Gamma_L} - v_i^f) , \end{aligned} \quad (\text{C.16})$$

where the following relationships are used: $n_{Ei}^f = -n_{Ei}^s$, $\mathbf{n}_E^{sT} \mathbf{n}_E^s = 1$, and $\mathbf{n}_L^{sT} \mathbf{n}_L^s = 1$. The first integrals of (C.15) and (C.16) are the standard consistency terms, the second integrals

are the adjoint consistency terms and the third integrals are Nitsche's penalty terms.

In this work, the adjoint consistency term of the solid side is replaced by the one of the fluid side for simplicity:

$$-\frac{1}{2} \int_{\Gamma_E} d\Omega \{\delta\sigma_{ij}\} n_{Lj}^s (U_i^s - \tilde{U}_i^s) \rightarrow -\frac{1}{2} \int_{\Gamma_E} d\Gamma \{\delta\sigma_{ij}\} n_{Ej}^s (\hat{V}_i^s|_{\Gamma_L} - v_i^f). \quad (\text{C.17})$$

This treatment is reasonable because the shear modulus weighting is used and thus, the fluid stress is dominant at the weighted average of the stress $\{\sigma_{ij}\}$ ($\because \kappa^f \gg \kappa^s$). In addition, the test function of the adjoint consistency term is replaced by the tangential operator of the fluid stress by following the works of Hansbo et al. [74], Jenkins et al. [101, 102] and Mayer et al. [70]. This approximation means that the traction from the fluid side is assumed as the traction at the interface, which is the traditional FSI approach that forces are transferred from the fluid phase to the solid phase rather than its vice versa:

$$-\frac{1}{2} \int_{\Gamma_E} d\Gamma \{\delta\sigma_{ij}\} n_{Ej}^s (\hat{V}_i^s|_{\Gamma_L} - v_i^f) \rightarrow -\frac{1}{2} \int_{\Gamma_E} d\Gamma \sigma_{ij}^f (\delta v^f, \delta p^f) n_{Ej}^s (\hat{V}_i^s|_{\Gamma_L} - v_i^f). \quad (\text{C.18})$$

Thus, R_L^{fsi} and R_E^{fsi} for non-matching interfaces are simplified based on the master-slave concept and the traditional approximation of averaged traction for the adjoint consistency term:

$$R_L^{\text{fsi}} = - \int_{\Gamma_E} d\Gamma \delta U_i^s \{\sigma_{ij}\} n_{Lj}^s + \int_{\Gamma_E} d\Gamma \delta U_i^s \eta^{\text{fsi}} (\hat{V}_i^s|_{\Gamma_L} - v_i^f), \quad (\text{C.19})$$

$$R_E^{\text{fsi}} = \int_{\Gamma_E} d\Gamma \delta v_i^f \{\sigma_{ij}\} n_{Ej}^s - \int_{\Gamma_E} d\Gamma \sigma_{ij}^f (\delta v^f, \delta p^f) n_{Ej}^s (\hat{V}_i^s|_{\Gamma_L} - v_i^f) - \int_{\Gamma_E} d\Gamma \delta v_i^f \eta^{\text{fsi}} (\hat{V}_i^s|_{\Gamma_L} - v_i^f). \quad (\text{C.20})$$

Assuming the case that both interfaces Γ_L and Γ_E are perfectly identical like ALE-FSI method; i.e. $\Gamma_L = \Gamma_E = \Gamma_{\text{fsi}}$, the summation of R_L^{fsi} and R_E^{fsi} ((C.19) and (C.20)) results in

the well-known Nitsche's interface integral:

$$\begin{aligned}
 R^{\text{fsi}} &= R_{\text{L}}^{\text{fsi}} + R_{\text{E}}^{\text{fsi}} \\
 &= - \int_{\Gamma_{\text{fsi}}} d\Gamma (\delta U_i^s - \delta v_i^f) \{\sigma_{ij}\} (\mathbf{v}^f, p^f) n_j^s - \int_{\Gamma_{\text{fsi}}} d\Gamma \sigma_{ij}^f (\delta \mathbf{v}^f, \delta p^f) n_j^s \llbracket v_i \rrbracket \\
 &\quad + \int_{\Gamma_{\text{fsi}}} d\Gamma (\delta U_i^s - \delta v_i^f) \eta^{\text{fsi}} \llbracket v_i \rrbracket .
 \end{aligned} \tag{C.21}$$

It should be noted that the summation like (C.21) is not appropriate because $R_{\text{L}}^{\text{fsi}}$ and $R_{\text{E}}^{\text{fsi}}$ have different physical dimensions; i.e. $R_{\text{L}}^{\text{fsi}}$ is the work, and $R_{\text{E}}^{\text{fsi}}$ is the power. The separate forms like (C.19) and (C.20) are physically more precise.

Appendix D

Contact Formulation based on Lagrangian Description

D.1 Outline

This chapter summarizes the theory of the contact formulation for the XFEM based on Lawry and Maute [75]. The method proposed by Lawry and Maute [75] succeeded in to compute contact using the XFEM based on the Lagrangian description. In this method, the frictionless contact model is assumed. There are mainly four steps to deal with contact in this method. The outline is shown in Figure D.1. In this figure and following description, upper subscripts m and s represents properties of the master and slave objects. Table D.1 summarizes the notation related to the contact formulation. To represent accurate contact phenomenon, the following non-penetration condition should be satisfied:

$$g_n \lambda = 0, \quad g_n \geq 0, \quad \lambda \leq 0, \quad (D.1)$$

where λ is the Lagrange multiplier and corresponds to the contact pressure based on the standard Lagrange multiplier method. g_n is the gap between contact interfaces on both master and slave surface. \mathbf{x}^m is the integration point on the master surface and \mathbf{x}^s is the integration point on the slave surface. g_n is defined by the material coordinates \mathbf{X} and the displacements \mathbf{U} :

$$\lambda_n = \sigma_{ij} n_i^m n_j^m = t_i n_i^m, \quad (D.2)$$

$$g_n = (x_i^s - x_i^m) n_i^m = (X_i^s + U_i^s - X_i^m - U_i^m) n_i^m. \quad (D.3)$$

(D.1) is identical to the KKT condition. The weak form of the standard Lagrange multiplier method is as follows:

$$\int_{\Gamma_{c0}} d\Gamma \delta g_n^0 \lambda^0 + \int_{\Gamma_{c0}} d\Gamma \delta \lambda^0 g_n^0 = 0 . \quad (\text{D.4})$$

The weak forms are evaluated on the contact interface in the initial configuration, Γ_{c0} , based on the total Lagrangian formulation. Here, the gap and the Lagrange multiplier are denoted as g_n^0 and λ^0 as properties in the initial configuration.

Although contact analysis based on (D.4) can compute the deformation with accurate contact (accurate displacement field), it is reported that the distribution of contact pressure tends to become oscillatory [75]. To get the smooth distribution of the contact pressure, the stabilized Lagrange multiplier method (Wriggers [104], also called as the Uzawa method) is used in [75]. The weak form of the stabilized Lagrange multiplier method is defined as follows:

$$\int_{\Gamma_{c0}} d\Gamma \delta g_n^0 \lambda^0 + \int_{\Gamma_{c0}} d\Gamma \delta \lambda^0 (\lambda^0 - \tilde{\lambda}^0 - \gamma_c g_n^0) = 0 , \quad (\text{D.5})$$

$$\tilde{\lambda}^0 = \kappa^m \mathbf{n}^{mT} S^m \mathbf{n}^m + \kappa^s \mathbf{n}^{sT} S^s \mathbf{n}^s (j^s)^{-1} j^m , \quad (\text{D.6})$$

where $\tilde{\lambda}^0$ is the weighted average of the surface traction along the normal direction, and j^p is the Jacobian of surface area computed by the Nanson's formula. The condition of weights is $\kappa^M + \kappa^S = 1$. γ_c is the penalty factor to prevent penetration. If both interfaces are separate each other ($g_n^0 > 0$), λ^0 vanishes and thus, the KKT condition (D.1) is satisfied. If interfaces penetrate each other, g_n^0 becomes zero to satisfy the KKT condition (D.1).

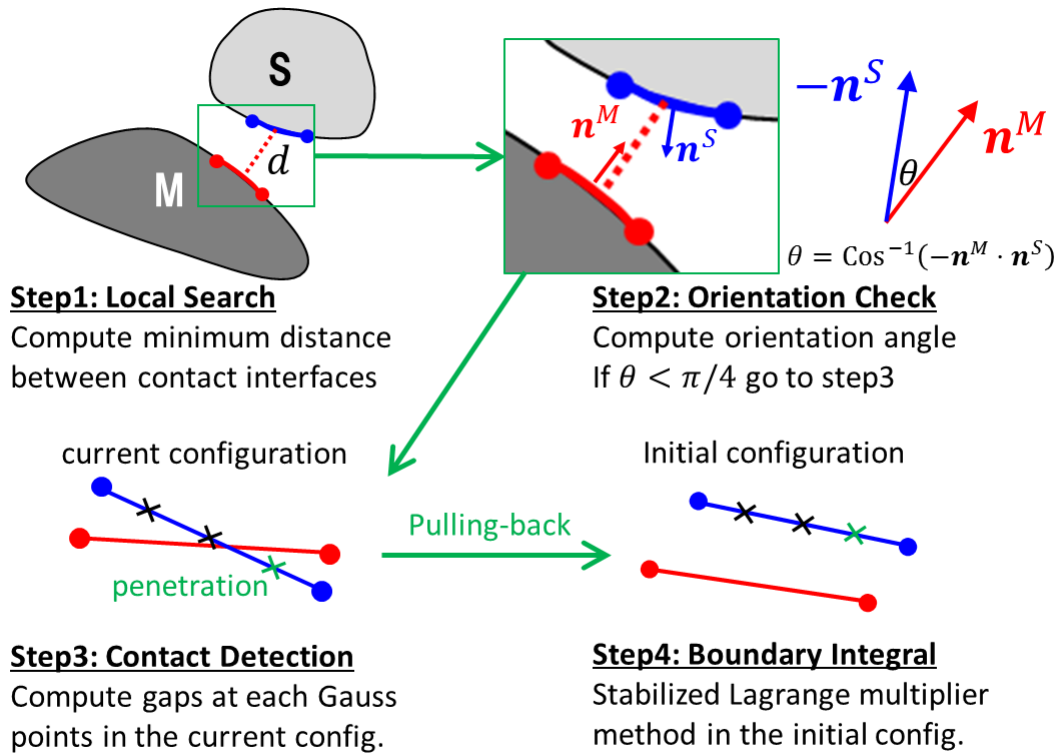


Figure D.1: Contact mechanics for Lagrangian XFEM based on [75]

Table D.1: Notation for frictionless contact mechanics

| Property | Symbol | Relation |
|---|-----------------|--|
| interface type | p | m : Master, s : Slave |
| undeformed configuration | X_i^p | |
| undeformed normal | n_{0i}^p | |
| displacement | U_i^p | |
| deformation gradient | F^p | $F_{ij}^p = \frac{\partial x_i^p}{\partial X_j^p} = \delta_{ij} + \frac{\partial U_i^p}{\partial X_j^p}$ |
| current configuration | x_i^p | $x_i^p = X_i^p + U_i^p$ |
| deformed normal | n_i^p | |
| contact interface in deformed configuration | Γ_c^p | |
| normal gap in deformed configuration | g_n | |
| Lagrange multiplier in deformed configuration | λ | |
| Jacobian of surface area | j^p | (D.71) |
| contact interface in undeformed configuration | Γ_{c0}^p | |
| normal gap in undeformed configuration | g_n^0 | $g_n^0 = j^m g_n$ |
| Lagrange multiplier in undeformed configuration | λ^0 | |

D.2 Numerical Implementation of Frictionless Contact Model (FCM)

This section summarizes the numerical implementation of the frictionless contact model (FCM). In this case, the tangential friction constant is zero.

D.2.1 Gap Equation

The governing equation of the gap g_n^0 is defined as follows:

$$\mathbf{R}_g = \mathbf{x}^m + g_n^0 \mathbf{n}^m - \mathbf{x}^s(\alpha) = \mathbf{X}^m + \mathbf{U}^m + g_n^0 \mathbf{n}^m - \mathbf{x}^s(\alpha) = \mathbf{0} , \quad (\text{D.7})$$

where α is the local coordinate that determines the integral bounds on the slave interface, and defined by properties on the master interface. Considering a solution vector of (D.7) as $\mathbf{s} = (g_n^0, \alpha)^T$ and the Newton iteration, the updated solution vector \mathbf{s}_{n+1} is computed from the previous solution vector \mathbf{s}_n . Assuming $\Delta \mathbf{s}$ is the solution increment of \mathbf{s} , the Taylor expansion of \mathbf{R}_g is defined as follows:

$$\begin{aligned} \mathbf{R}_g(\mathbf{s}_{n+1}) &= \mathbf{R}_g(\mathbf{s}_n + \Delta \mathbf{s}) \\ &= \mathbf{R}_g(\mathbf{s}_n) + \left. \frac{\partial \mathbf{R}_g}{\partial \mathbf{s}} \right|_{\mathbf{s}=\mathbf{s}_n} \Delta \mathbf{s} + O(\Delta \mathbf{s}^2) \simeq \mathbf{R}_g(\mathbf{s}_n) + \left. \frac{\partial \mathbf{R}_g}{\partial \mathbf{s}} \right|_{\mathbf{s}=\mathbf{s}_n} \Delta \mathbf{s} = \mathbf{0} . \end{aligned} \quad (\text{D.8})$$

Therefore, the governing equation for the incremental solution vector $\Delta \mathbf{s} = (\Delta g_n^0, \Delta \alpha)^T$ is:

$$\frac{\partial \mathbf{R}_g}{\partial \mathbf{s}} \Delta \mathbf{s} = J_g \begin{pmatrix} \Delta g_n^0 \\ \Delta \alpha \end{pmatrix} = \begin{pmatrix} n_x^m & -\frac{\partial x^s}{\partial \alpha} \\ n_y^m & -\frac{\partial y^s}{\partial \alpha} \end{pmatrix} \begin{pmatrix} \Delta g_n^0 \\ \Delta \alpha \end{pmatrix} = -\mathbf{R}_g . \quad (\text{D.9})$$

g_n^0 is determined by the solution increment computed by Newton's method.

D.2.2 Residuals of Contact Formulation

The weak forms for the contact formulation based on the stabilized Lagrange multiplier method (Uzawa method) are as follows:

$$r_c = \int_{\Gamma_{c0}^m} d\Gamma \delta g_n^0 \lambda^0 = 0 , \quad (\text{D.10})$$

$$r_\lambda = \int_{\Gamma_{c0}^m} d\Gamma \delta \lambda^0 g_n^0 \rightarrow \int_{\Gamma_{c0}^m} d\Gamma \delta \lambda^0 (\lambda^0 - \tilde{\lambda}^0 - \gamma_c g_n^0) = 0 . \quad (\text{D.11})$$

In (D.11), the averaged normal traction $\tilde{\lambda}^0$ is introduced and its definition is:

$$\tilde{\lambda}^0 = \kappa^m \mathbf{n}_0^{mT} S^m \mathbf{n}_0^m + \kappa^s \mathbf{n}_0^{sT} S^s \mathbf{n}_0^s (j^s)^{-1} j^m \quad (\because \kappa^m + \kappa^s = 1) , \quad (\text{D.12})$$

where κ^m and κ^s are weights for the weighted average. Using the local coordinate along the master interface α , (D.10) and (D.11) are represented as follows:

$$r_c = \int_{\alpha_1}^{\alpha_2} d\alpha \delta g_n^0 \lambda^0 \left\| \frac{\partial \mathbf{X}^m}{\partial \alpha} \right\| = 0 , \quad (\text{D.13})$$

$$r_\lambda = \int_{\alpha_1}^{\alpha_2} d\alpha \delta \lambda^0 (\lambda^0 - \tilde{\lambda}^0 - \gamma_c g_n^0) \left\| \frac{\partial \mathbf{X}^m}{\partial \alpha} \right\| = 0 . \quad (\text{D.14})$$

In the following discussion, the finite element discretization of this frictionless contact model is discussed. The variations in r_c and r_λ can be denoted as follows:

$$\delta g_n^0 = \frac{\partial g_n^0}{\partial \mathbf{U}_t^a} |U_t^a\rangle \equiv \frac{\partial g_n^0}{\partial \mathbf{U}_t^s} |U_t^s\rangle + \frac{\partial g_n^0}{\partial \mathbf{U}_t^m} |U_t^m\rangle , \quad (\text{D.15})$$

$$\delta \lambda^0 = N_{\lambda 0}^T , \quad (\text{D.16})$$

where $|\cdot\rangle$ represents the components of a column vector (based on the notation of quantum mechanics). In the following discussion, $\langle \cdot |$ also means the components of a row vector. \mathbf{U}_t^m and \mathbf{U}_t^s are the nodal displacement vector of the master and slave contact interfaces, including both x and y displacements. \mathbf{U}_t^a means the union of \mathbf{U}_t^m and \mathbf{U}_t^s . $N_{\lambda 0}$ is the shape function vector for the nodal Lagrange multipliers. Using this notation, discretized forms of

(D.13) and (D.14) by the finite element discretization are denoted by the column vectors:

$$\mathbf{R}_c \equiv \int_{\alpha_1}^{\alpha_2} d\alpha \frac{\partial g_n^0}{\partial \mathbf{U}_t^a} \lambda^0 \left\| \frac{\partial \mathbf{X}^m}{\partial \alpha} \right\| |U_t^a\rangle, \quad (\text{D.17})$$

$$\mathbf{R}_\lambda \equiv \int_{\alpha_1}^{\alpha_2} d\alpha N_{\lambda 0}^T (\lambda^0 - \tilde{\lambda}^0 - \gamma_c g_n^0) \left\| \frac{\partial \mathbf{X}^m}{\partial \alpha} \right\| |\lambda^0\rangle. \quad (\text{D.18})$$

D.2.3 Computation of Lagrange Multiplier

In the reference work [75], (D.18) is computed by condensing (D.18) into the elementwise evaluation. Then, the Lagrange multiplier that is computed elementwise, is applied into (D.17) to compute contact. The computation of the nodal Lagrange multiplier λ^0 is as follows:

$$\left(\int_{\alpha_1}^{\alpha_2} d\alpha N_{\lambda 0}^T N_{\lambda 0} \left\| \frac{\partial \mathbf{X}^m}{\partial \alpha} \right\| |\lambda^0\rangle \langle \lambda^0| \right) \lambda^0 = \int_{\alpha_1}^{\alpha_2} d\alpha N_{\lambda 0}^T (\tilde{\lambda}^0 + \gamma_c g_n^0) \left\| \frac{\partial \mathbf{X}^m}{\partial \alpha} \right\| |\lambda^0\rangle, \quad (\text{D.19})$$

$$\lambda^0 = \left(\int_{\alpha_1}^{\alpha_2} d\alpha N_{\lambda 0}^T N_{\lambda 0} \left\| \frac{\partial \mathbf{X}^m}{\partial \alpha} \right\| \right)^{-1} \int_{\alpha_1}^{\alpha_2} d\alpha N_{\lambda 0}^T (\tilde{\lambda}^0 + \gamma_c g_n^0) \left\| \frac{\partial \mathbf{X}^m}{\partial \alpha} \right\| |\lambda^0\rangle. \quad (\text{D.20})$$

The Lagrange multiplier at an arbitrary point α : $\lambda^0(\alpha)$, is computed by the above nodal Lagrange multiplier λ^0 and $N_{\lambda 0}$:

$$\lambda^0(\alpha) = N_{\lambda 0}(\alpha) \lambda^0. \quad (\text{D.21})$$

The first derivatives of λ^0 are needed for the computation of the Jacobian for contact:

$$\frac{\partial \lambda^0}{\partial \alpha_1} = \left(\int_{\alpha_1}^{\alpha_2} d\alpha N_{\lambda 0}^T N_{\lambda 0} \left\| \frac{\partial \mathbf{X}^m}{\partial \alpha} \right\| \right)^{-1} \left[N_{\lambda 0}^T (\lambda^0 - \tilde{\lambda}^0 - \gamma_c g_n^0) \left\| \frac{\partial \mathbf{X}^m}{\partial \alpha} \right\| \right]_{\alpha=\alpha_1} |\lambda^0\rangle, \quad (\text{D.22})$$

$$\frac{\partial \lambda^0}{\partial \alpha_2} = - \left(\int_{\alpha_1}^{\alpha_2} d\alpha N_{\lambda 0}^T N_{\lambda 0} \left\| \frac{\partial \mathbf{X}^m}{\partial \alpha} \right\| \right)^{-1} \left[N_{\lambda 0}^T (\lambda^0 - \tilde{\lambda}^0 - \gamma_c g_n^0) \left\| \frac{\partial \mathbf{X}^m}{\partial \alpha} \right\| \right]_{\alpha=\alpha_2} |\lambda^0\rangle, \quad (\text{D.23})$$

$$\frac{\partial \lambda^0}{\partial \mathbf{U}_t^a} = \left(\int_{\alpha_1}^{\alpha_2} d\alpha N_{\lambda 0}^T N_{\lambda 0} \left\| \frac{\partial \mathbf{X}^m}{\partial \alpha} \right\| \right)^{-1} \int_{\alpha_1}^{\alpha_2} d\alpha N_{\lambda 0}^T \left(\frac{\partial \tilde{\lambda}^0}{\partial \mathbf{U}_t^a} + \gamma_c \frac{\partial g_n^0}{\partial \mathbf{U}_t^a} \right) \left\| \frac{\partial \mathbf{X}^m}{\partial \alpha} \right\| |\lambda^0\rangle, \quad (\text{D.24})$$

where (D.22) and (D.23) are the derivatives with respect to the upper bound α_2 and the lower bound α_1 . (D.24) is the derivative with respect to the displacement. Moreover, the derivatives of Lagrange multiplier at an arbitrary point α are computed as follows:

$$\frac{\partial \lambda^0}{\partial \alpha_1}(\alpha) = N_{\lambda^0}(\alpha) \frac{\partial \lambda^0}{\partial \alpha_1}, \quad (\text{D.25})$$

$$\frac{\partial \lambda^0}{\partial \alpha_2}(\alpha) = N_{\lambda^0}(\alpha) \frac{\partial \lambda^0}{\partial \alpha_2}, \quad (\text{D.26})$$

$$\frac{\partial \lambda^0}{\partial \mathbf{U}_t^a}(\alpha) = N_{\lambda^0}(\alpha) \frac{\partial \lambda^0}{\partial \mathbf{U}_t^a}. \quad (\text{D.27})$$

D.2.4 Jacobian of Contact Formulation

Using pre-computed Lagrangian multiplier and its derivatives, the Jacobian corresponding to the contact residual \mathbf{R}_c is computed as follows:

$$\frac{d\mathbf{R}_c}{d\mathbf{U}_t^a} = \frac{\partial \mathbf{R}_c}{\partial \mathbf{U}_t^a} + \frac{\partial \mathbf{R}_c}{\partial \alpha_1} \frac{\partial \alpha_1}{\partial \mathbf{U}_t^a} + \frac{\partial \mathbf{R}_c}{\partial \alpha_2} \frac{\partial \alpha_2}{\partial \mathbf{U}_t^a} \equiv J_{c-u} + J_{c-a1} \frac{\partial \alpha_1}{\partial \mathbf{U}_t^a} + J_{c-a2} \frac{\partial \alpha_2}{\partial \mathbf{U}_t^a}. \quad (\text{D.28})$$

J_{c-u} is a contribution of the partial derivative with respect to the displacement. J_{c-a1} and J_{c-a2} are contributions of the upper and lower bounds of the contact integration. Detailed forms of J_{c-u} , J_{c-a1} and J_{c-a2} are as follows:

$$J_{c-u} = \int_{\alpha_1}^{\alpha_2} d\alpha \frac{\partial g_n^0}{\partial \mathbf{U}_t^a} N_{\lambda^0} \frac{\partial \lambda^0}{\partial \mathbf{U}_t^a} \left\| \frac{\partial \mathbf{X}^m}{\partial \alpha} \right\| |U_t^a\rangle \langle U_t^a| + \int_{\alpha_1}^{\alpha_2} d\alpha \frac{\partial^2 g_n^0}{\partial \mathbf{U}_t^{a2}} N_{\lambda^0} \lambda^0 \left\| \frac{\partial \mathbf{X}^m}{\partial \alpha} \right\| |U_t^a\rangle \langle U_t^a|, \quad (\text{D.29})$$

$$J_{c1-a1} = \int_{\alpha_1}^{\alpha_2} d\alpha \frac{\partial g_n^0}{\partial \mathbf{U}_t^a} N_{\lambda^0} \frac{\partial \lambda^0}{\partial \alpha_1} \left\| \frac{\partial \mathbf{X}^m}{\partial \alpha} \right\| |U_t^a\rangle \langle \alpha_1| - \left[\frac{\partial g_n^0}{\partial \mathbf{U}_t^a} N_{\lambda^0} \lambda^0 \left\| \frac{\partial \mathbf{X}^m}{\partial \alpha} \right\| \right]_{\alpha=\alpha_1} |U_t^a\rangle \langle \alpha_1|, \quad (\text{D.30})$$

$$J_{c1-a2} = \int_{\alpha_1}^{\alpha_2} d\alpha \frac{\partial g_n^0}{\partial \mathbf{U}_t^a} N_{\lambda^0} \frac{\partial \lambda^0}{\partial \alpha_2} \left\| \frac{\partial \mathbf{X}^m}{\partial \alpha} \right\| |U_t^a\rangle \langle \alpha_2| + \left[\frac{\partial g_n^0}{\partial \mathbf{U}_t^a} N_{\lambda^0} \lambda^0 \left\| \frac{\partial \mathbf{X}^m}{\partial \alpha} \right\| \right]_{\alpha=\alpha_2} |U_t^a\rangle \langle \alpha_2|. \quad (\text{D.31})$$

D.2.5 Derivatives related to Residual and Jacobian

Necessary derivatives related to the above residuals and Jacobians are summarized in this section.

- Derivatives of deformed normal: $\frac{\partial n_x^m}{\partial \mathbf{U}_t^m}, \frac{\partial n_y^m}{\partial \mathbf{U}_t^m}, \frac{\partial^2 n_x^m}{\partial \mathbf{U}_t^{m2}}, \frac{\partial^2 n_y^m}{\partial \mathbf{U}_t^{m2}}$
- Derivatives of gap: $\frac{\partial g_n^0}{\partial \mathbf{U}_t^a}, \frac{\partial^2 g_n^0}{\partial \mathbf{U}_t^{a2}}$
- Derivatives of bounds of master interface: $\frac{\partial \alpha_1}{\partial \mathbf{U}_t^a}, \frac{\partial \alpha_2}{\partial \mathbf{U}_t^a}$

D.2.5.1 First Derivative of Deformed Master Normal

This section describes the first derivatives of the deformed master normal. There are several ways to compute the deformed normal. In this section, the way starting from the undeformed tangential vector is summarized. First, the undeformed tangential vector \mathbf{t}_0 , which corresponds to a vector along the master interface and not normalized, is defined as follows:

$$\mathbf{t}_0^m = \begin{pmatrix} t_{0x}^m & t_{0y}^m \end{pmatrix}^T . \quad (\text{D.32})$$

The undeformed normal \mathbf{n}_0^m is computed by \mathbf{t}_0^m :

$$\mathbf{n}_0^m = \|\mathbf{t}_0^m\|^{-1} \begin{pmatrix} t_{0y}^m & -t_{0x}^m \end{pmatrix}^T , \quad (\text{D.33})$$

The deformed tangential vector is computed by using the deformation gradient tensor F :

$$\mathbf{t}^m = F \mathbf{t}_0^m . \quad (\text{D.34})$$

Similar to (D.33), the deformed normal \mathbf{n}^m is also computed by the deformed tangential vector \mathbf{t}^m :

$$\mathbf{n}^m = \|\mathbf{t}^m\|^{-1} \begin{pmatrix} t_x^m & t_y^m \end{pmatrix}. \quad (\text{D.35})$$

To compute the first derivative of \mathbf{n}^m , the first derivative of the tangential vector \mathbf{t}^m is used:

$$\frac{\partial \mathbf{t}^m}{\partial \mathbf{U}_t^m}{}^T = \begin{pmatrix} \frac{\partial t_x^m}{\partial \mathbf{U}_t^m}{}^T \\ \frac{\partial t_y^m}{\partial \mathbf{U}_t^m}{}^T \end{pmatrix} = \begin{pmatrix} \frac{\partial F_{xx}}{\partial \mathbf{U}_t^m} & \frac{\partial F_{xy}}{\partial \mathbf{U}_t^m} \\ \frac{\partial F_{yx}}{\partial \mathbf{U}_t^m} & \frac{\partial F_{yy}}{\partial \mathbf{U}_t^m} \end{pmatrix} \begin{pmatrix} t_{0x}^m \\ t_{0y}^m \end{pmatrix} = \begin{pmatrix} t_{0x}^m \frac{\partial N_m}{\partial x} + t_{0y}^m \frac{\partial N_m}{\partial y} \langle U_x^m | \\ t_{0x}^m \frac{\partial N_m}{\partial x} + t_{0y}^m \frac{\partial N_m}{\partial y} \langle U_y^m | \end{pmatrix}, \quad (\text{D.36})$$

where N_m is the shape function vector on the master interface. Using (D.36), the first derivative of the deformed normal, $\frac{\partial \mathbf{n}^m}{\partial \mathbf{U}_t^m}$, is computed as follows:

$$\frac{\partial n_x^m}{\partial \mathbf{U}_t^m} = -\|\mathbf{t}^m\|^{-3} t_x^m t_y^m \frac{\partial t_x^m}{\partial \mathbf{U}_t^m} + \|\mathbf{t}^m\|^{-3} t_x^{m2} \frac{\partial t_y^m}{\partial \mathbf{U}_t^m}, \quad (\text{D.37})$$

$$\frac{\partial n_y^m}{\partial \mathbf{U}_t^m} = -\|\mathbf{t}^m\|^{-3} t_y^{m2} \frac{\partial t_x^m}{\partial \mathbf{U}_t^m} + \|\mathbf{t}^m\|^{-3} t_x^m t_y^m \frac{\partial t_y^m}{\partial \mathbf{U}_t^m}. \quad (\text{D.38})$$

D.2.5.2 Second Derivative of Deformed Master Normal

The second derivative of the deformed master normal is also necessary to compute the Jacobian for contact. The second derivative of the deformed master normal is also computed by the tangential vector \mathbf{t}^m as follows:

$$\begin{aligned} \frac{\partial^2 n_x^m}{\partial \mathbf{U}_t^{m2}} = \|\mathbf{t}^m\|^{-5} & \left[t_y^m (2t_x^{m2} - t_y^{m2}) \frac{\partial t_x^m}{\partial \mathbf{U}_t^m} \frac{\partial t_x^m}{\partial \mathbf{U}_t^m}{}^T - t_x^m (t_x^{m2} - 2t_y^{m2}) \frac{\partial t_x^m}{\partial \mathbf{U}_t^m} \frac{\partial t_y^m}{\partial \mathbf{U}_t^m}{}^T \right. \\ & \left. - t_x^m (t_x^{m2} - 2t_y^{m2}) \frac{\partial t_y^m}{\partial \mathbf{U}_t^m} \frac{\partial t_x^m}{\partial \mathbf{U}_t^m}{}^T - 3t_x^{m2} t_y^m \frac{\partial t_y^m}{\partial \mathbf{U}_t^m} \frac{\partial t_y^m}{\partial \mathbf{U}_t^m}{}^T \right], \quad (\text{D.39}) \end{aligned}$$

$$\begin{aligned} \frac{\partial^2 n_y^m}{\partial \mathbf{U}_t^{m2}} = \|\mathbf{t}^m\|^{-5} & \left[3t_x^m t_y^{m2} \frac{\partial t_x^m}{\partial \mathbf{U}_t^m} \frac{\partial t_x^m}{\partial \mathbf{U}_t^m}{}^T - t_y^m (2t_x^{m2} - t_y^{m2}) \frac{\partial t_x^m}{\partial \mathbf{U}_t^m} \frac{\partial t_y^m}{\partial \mathbf{U}_t^m}{}^T \right. \\ & \left. - t_y^m (2t_x^{m2} - t_y^{m2}) \frac{\partial t_y^m}{\partial \mathbf{U}_t^m} \frac{\partial t_x^m}{\partial \mathbf{U}_t^m}{}^T + t_x^m (t_x^{m2} - 2t_y^{m2}) \frac{\partial t_y^m}{\partial \mathbf{U}_t^m} \frac{\partial t_y^m}{\partial \mathbf{U}_t^m}{}^T \right]. \quad (\text{D.40}) \end{aligned}$$

D.2.5.3 First Derivative of Gap

The first derivative of the gap g_n^0 with respect to the displacement is computed from the gap equation:

$$\mathbf{R}_g = \mathbf{x}^m + g_n^0 \mathbf{n}^m - \mathbf{x}^s(\alpha) = \mathbf{X}^m + \mathbf{U}^m + g_n^0 \mathbf{n}^m - \mathbf{X}^s(\alpha) - \mathbf{U}^s(\alpha) = \mathbf{0} . \quad (\text{D.41})$$

Taking derivatives with respect to master and slave displacements: \mathbf{U}_t^m and \mathbf{U}_t^s , then:

$$\begin{aligned} \frac{\partial \mathbf{R}_g}{\partial \mathbf{U}_t^m} &= \begin{pmatrix} N_m \langle U_x^m | \\ N_m \langle U_y^m | \end{pmatrix} + \begin{pmatrix} n_x^m \\ n_y^m \end{pmatrix} \frac{\partial g_n^0}{\partial \mathbf{U}_t^m}{}^T \langle U_t^m | + g_n^0 \begin{pmatrix} \frac{\partial n_x^m}{\partial \mathbf{U}_t^m}{}^T \\ \frac{\partial n_y^m}{\partial \mathbf{U}_t^m}{}^T \end{pmatrix} \langle U_t^m | - \frac{\partial \mathbf{x}^s}{\partial \alpha} \frac{\partial \alpha}{\partial \mathbf{U}_t^m}{}^T \langle U_t^m | \\ &\equiv \begin{pmatrix} n_x^m \\ n_y^m \end{pmatrix} \frac{\partial g_n^0}{\partial \mathbf{U}_t^m}{}^T \langle U_t^m | - \frac{\partial \mathbf{x}^s}{\partial \alpha} \frac{\partial \alpha}{\partial \mathbf{U}_t^m}{}^T \langle U_t^m | + \begin{pmatrix} \mathbf{C}_{gx}^{mT} \\ \mathbf{C}_{gy}^{mT} \end{pmatrix} = \mathbf{0} , \end{aligned} \quad (\text{D.42})$$

$$\begin{aligned} \frac{\partial \mathbf{R}_g}{\partial \mathbf{U}_t^s} &= \begin{pmatrix} n_x^m \\ n_y^m \end{pmatrix} \frac{\partial g_n^0}{\partial \mathbf{U}_t^s}{}^T \langle U_t^s | - \begin{pmatrix} N_s \langle U_x^s | \\ N_s \langle U_y^s | \end{pmatrix} - \frac{\partial \mathbf{x}^s}{\partial \alpha} \frac{\partial \alpha}{\partial \mathbf{U}_t^s}{}^T \langle U_t^s | \\ &\equiv \begin{pmatrix} n_x^m \\ n_y^m \end{pmatrix} \frac{\partial g_n^0}{\partial \mathbf{U}_t^s}{}^T \langle U_t^s | - \frac{\partial \mathbf{x}^s}{\partial \alpha} \frac{\partial \alpha}{\partial \mathbf{U}_t^s}{}^T \langle U_t^s | + \begin{pmatrix} \mathbf{C}_{gx}^{sT} \\ \mathbf{C}_{gy}^{sT} \end{pmatrix} = \mathbf{0} . \end{aligned} \quad (\text{D.43})$$

(D.42) and (D.43) are summarized as the following matrix form:

$$J_g \begin{pmatrix} \frac{\partial g_n^0}{\partial \mathbf{U}_t^p} \\ \frac{\partial \alpha}{\partial \mathbf{U}_t^p} \end{pmatrix} = - \begin{pmatrix} \mathbf{C}_{gx}^p \\ \mathbf{C}_{gy}^p \end{pmatrix} \quad (\because p = \{m, s\}) , \quad (\text{D.44})$$

where J_g is the Jacobian for (D.41) and \mathbf{C}_{gi}^p are defined as follows:

$$J_g = \begin{pmatrix} n_x^m & -\frac{\partial x^s}{\partial \alpha} \\ n_y^m & -\frac{\partial y^s}{\partial \alpha} \end{pmatrix} , \quad (\text{D.45})$$

$$\mathbf{C}_{gx}^m = N_m^T |U_x^m\rangle + g_n^0 \frac{\partial n_x^m}{\partial \mathbf{U}_t^m} |U_t^m\rangle , \quad (\text{D.46})$$

$$\mathbf{C}_{gy}^m = N_m^T |U_y^m\rangle + g_n^0 \frac{\partial n_y^m}{\partial \mathbf{U}_t^m} |U_t^m\rangle , \quad (\text{D.47})$$

$$\mathbf{C}_{gx}^s = -N_s^T |U_x^s\rangle, \quad (\text{D.48})$$

$$\mathbf{C}_{gy}^s = -N_s^T |U_y^s\rangle, \quad (\text{D.49})$$

where N_m and N_s are the shape function vectors for the master and slave interfaces, respectively. The following augmented first derivative of the gap $\frac{\partial g_n}{\partial \mathbf{U}_t^a}$, which includes the derivatives of both the master and slave displacements, is used for the Jacobian:

$$\frac{\partial g_n^0}{\partial \mathbf{U}_t^a} = \begin{pmatrix} \frac{\partial g_n^0}{\partial \mathbf{U}_t^s} \\ \frac{\partial g_n^0}{\partial \mathbf{U}_t^m} \end{pmatrix}. \quad (\text{D.50})$$

D.2.5.4 Second Derivative of Gap

The second derivative of the gap g_n^0 is computed from (D.41). The first derivatives of (D.41) with respect to master and slave displacements: \mathbf{U}_t^m and \mathbf{U}_t^s , are summarized as follows:

$$\begin{aligned} \frac{\partial \mathbf{R}_g}{\partial \mathbf{U}_t^m} &= \begin{pmatrix} N_m \langle U_x^m | \\ N_m \langle U_y^m | \end{pmatrix} + \begin{pmatrix} n_x^m \\ n_y^m \end{pmatrix} \frac{\partial g_n^0}{\partial \mathbf{U}_t^m}{}^T \langle U_t^m | + g_n^0 \begin{pmatrix} \frac{\partial n_x^m}{\partial \mathbf{U}_t^m}{}^T \\ \frac{\partial n_y^m}{\partial \mathbf{U}_t^m}{}^T \end{pmatrix} \langle U_t^m | \\ &\quad - \frac{\partial \mathbf{x}^s}{\partial \alpha} \frac{\partial \alpha}{\partial \mathbf{U}_t^m}{}^T \langle U_t^m |, \end{aligned} \quad (\text{D.51})$$

$$\frac{\partial \mathbf{R}_g}{\partial \mathbf{U}_t^s} = \begin{pmatrix} n_x^m \\ n_y^m \end{pmatrix} \frac{\partial g_n^0}{\partial \mathbf{U}_t^s}{}^T \langle U_t^s | - \begin{pmatrix} N_s \langle U_x^s | \\ N_s \langle U_y^s | \end{pmatrix} - \frac{\partial \mathbf{x}^s}{\partial \alpha} \frac{\partial \alpha}{\partial \mathbf{U}_t^s}{}^T \langle U_t^s |. \quad (\text{D.52})$$

The second derivatives of (D.41) is computed by taking the derivative of (D.51) and (D.52) with respect to \mathbf{U}_t^m and \mathbf{U}_t^s as follows:

$$\begin{aligned} \frac{\partial^2 R_{gx}}{\partial \mathbf{U}_t^{m2}} &= \left(\frac{\partial^2 g_n^0}{\partial \mathbf{U}_t^{m2}} n_x^m + \frac{\partial g_n^0}{\partial \mathbf{U}_t^m} \frac{\partial n_x^m}{\partial \mathbf{U}_t^m}{}^T + \frac{\partial n_x^m}{\partial \mathbf{U}_t^m} \frac{\partial g_n^0}{\partial \mathbf{U}_t^m}{}^T + \frac{\partial^2 n_x^m}{\partial \mathbf{U}_t^{m2}} g_n^0 \right) |U_t^m\rangle \langle U_t^m| \\ &\quad - \left(\frac{\partial \mathbf{x}^s}{\partial \alpha} \frac{\partial^2 \alpha}{\partial \mathbf{U}_t^{m2}} + \frac{\partial^2 \mathbf{x}^s}{\partial \alpha^2} \frac{\partial \alpha}{\partial \mathbf{U}_t^m} \frac{\partial \alpha}{\partial \mathbf{U}_t^m}{}^T \right) |U_t^m\rangle \langle U_t^m| \\ &\equiv n_x^m \frac{\partial^2 g_n^0}{\partial \mathbf{U}_t^{m2}} |U_t^m\rangle \langle U_t^m| - \frac{\partial \mathbf{x}^s}{\partial \alpha} \frac{\partial^2 \alpha}{\partial \mathbf{U}_t^{m2}} |U_t^m\rangle \langle U_t^m| + D_{gx}^{mm}, \end{aligned} \quad (\text{D.53})$$

$$\begin{aligned}
\frac{\partial^2 R_{gy}}{\partial \mathbf{U}_t^{m2}} &= \left(\frac{\partial^2 g_n^0}{\partial \mathbf{U}_t^{m2}} n_y^m + \frac{\partial g_n^0}{\partial \mathbf{U}_t^m} \frac{\partial n_y^m}{\partial \mathbf{U}_t^m}{}^T + \frac{\partial n_y^m}{\partial \mathbf{U}_t^m} \frac{\partial g_n^0}{\partial \mathbf{U}_t^m}{}^T + \frac{\partial^2 n_y^m}{\partial \mathbf{U}_t^{m2}} g_n^0 \right) |U_t^m\rangle \langle U_t^m| \\
&\quad - \left(\frac{\partial y^s}{\partial \alpha} \frac{\partial^2 \alpha}{\partial \mathbf{U}_t^{m2}} + \frac{\partial^2 y^s}{\partial \alpha^2} \frac{\partial \alpha}{\partial \mathbf{U}_t^m} \frac{\partial \alpha}{\partial \mathbf{U}_t^m}{}^T \right) |U_t^m\rangle \langle U_t^m| \\
&\equiv n_y^m \frac{\partial^2 g_n^0}{\partial \mathbf{U}_t^{m2}} |U_t^m\rangle \langle U_t^m| - \frac{\partial y^s}{\partial \alpha} \frac{\partial^2 \alpha}{\partial \mathbf{U}_t^{m2}} |U_t^m\rangle \langle U_t^m| + D_{gy}^{mm} , \tag{D.54}
\end{aligned}$$

$$\begin{aligned}
\frac{\partial^2 R_{gx}}{\partial \mathbf{U}_t^{s2}} &= \left(\frac{\partial^2 g_n^0}{\partial \mathbf{U}_t^{s2}} n_x^m - \frac{\partial x^s}{\partial \alpha} \frac{\partial^2 \alpha}{\partial \mathbf{U}_t^{s2}} - \frac{\partial^2 x^s}{\partial \alpha^2} \frac{\partial \alpha}{\partial \mathbf{U}_t^s} \frac{\partial \alpha}{\partial \mathbf{U}_t^s}{}^T \right) |U_t^s\rangle \langle U_t^s| - 2 \operatorname{sym} \left\{ \frac{\partial \alpha}{\partial \mathbf{U}_t^s} \frac{\partial N_s}{\partial \alpha} |U_t^s\rangle \langle U_x^s| \right\} \\
&\equiv n_x^m \frac{\partial^2 g_n^0}{\partial \mathbf{U}_t^{s2}} |U_t^s\rangle \langle U_t^s| - \frac{\partial x^s}{\partial \alpha} \frac{\partial^2 \alpha}{\partial \mathbf{U}_t^{s2}} |U_t^s\rangle \langle U_t^s| + D_{gx}^{ss} , \tag{D.55}
\end{aligned}$$

$$\begin{aligned}
\frac{\partial^2 R_{gy}}{\partial \mathbf{U}_t^{s2}} &= \left(\frac{\partial^2 g_n^0}{\partial \mathbf{U}_t^{s2}} n_y^m - \frac{\partial y^s}{\partial \alpha} \frac{\partial^2 \alpha}{\partial \mathbf{U}_t^{s2}} - \frac{\partial^2 y^s}{\partial \alpha^2} \frac{\partial \alpha}{\partial \mathbf{U}_t^s} \frac{\partial \alpha}{\partial \mathbf{U}_t^s}{}^T \right) |U_t^s\rangle \langle U_t^s| - 2 \operatorname{sym} \left\{ \frac{\partial \alpha}{\partial \mathbf{U}_t^s} \frac{\partial N_s}{\partial \alpha} |U_t^s\rangle \langle U_y^s| \right\} \\
&\equiv n_y^m \frac{\partial^2 g_n^0}{\partial \mathbf{U}_t^{s2}} |U_t^s\rangle \langle U_t^s| - \frac{\partial y^s}{\partial \alpha} \frac{\partial^2 \alpha}{\partial \mathbf{U}_t^{s2}} |U_t^s\rangle \langle U_t^s| + D_{gy}^{ss} , \tag{D.56}
\end{aligned}$$

$$\begin{aligned}
\frac{\partial^2 R_{gx}}{\partial \mathbf{U}_t^m \partial \mathbf{U}_t^s} &= \left(\frac{\partial^2 g_n^0}{\partial \mathbf{U}_t^m \partial \mathbf{U}_t^s} n_x^m + \frac{\partial n_x^m}{\partial \mathbf{U}_t^m} \frac{\partial g_n^0}{\partial \mathbf{U}_t^s}{}^T - \frac{\partial x^s}{\partial \alpha} \frac{\partial^2 \alpha}{\partial \mathbf{U}_t^m \partial \mathbf{U}_t^s} - \frac{\partial^2 x^s}{\partial \alpha^2} \frac{\partial \alpha}{\partial \mathbf{U}_t^m} \frac{\partial \alpha}{\partial \mathbf{U}_t^s}{}^T \right) |U_t^m\rangle \langle U_t^s| \\
&\quad - \frac{\partial \alpha}{\partial \mathbf{U}_t^s} \frac{\partial N_s}{\partial \alpha} |U_t^m\rangle \langle U_x^s| \tag{D.57}
\end{aligned}$$

$$\equiv n_x^m \frac{\partial^2 g_n^0}{\partial \mathbf{U}_t^m \partial \mathbf{U}_t^s} |U_t^m\rangle \langle U_t^s| - \frac{\partial x^s}{\partial \alpha} \frac{\partial^2 \alpha}{\partial \mathbf{U}_t^m \partial \mathbf{U}_t^s} |U_t^m\rangle \langle U_t^s| + D_{gx}^{ms} , \tag{D.58}$$

$$\begin{aligned}
\frac{\partial^2 R_{gy}}{\partial \mathbf{U}_t^m \partial \mathbf{U}_t^s} &= \left(\frac{\partial^2 g_n^0}{\partial \mathbf{U}_t^m \partial \mathbf{U}_t^s} n_y^m + \frac{\partial n_y^m}{\partial \mathbf{U}_t^m} \frac{\partial g_n^0}{\partial \mathbf{U}_t^s}{}^T - \frac{\partial y^s}{\partial \alpha} \frac{\partial^2 \alpha}{\partial \mathbf{U}_t^m \partial \mathbf{U}_t^s} - \frac{\partial^2 y^s}{\partial \alpha^2} \frac{\partial \alpha}{\partial \mathbf{U}_t^m} \frac{\partial \alpha}{\partial \mathbf{U}_t^s}{}^T \right) |U_t^m\rangle \langle U_t^s| \\
&\quad - \frac{\partial \alpha}{\partial \mathbf{U}_t^m} \frac{\partial N_s}{\partial \alpha} |U_t^m\rangle \langle U_y^s| \tag{D.59}
\end{aligned}$$

$$\equiv n_y^m \frac{\partial^2 g_n^0}{\partial \mathbf{U}_t^m \partial \mathbf{U}_t^s} |U_t^m\rangle \langle U_t^s| - \frac{\partial y^s}{\partial \alpha} \frac{\partial^2 \alpha}{\partial \mathbf{U}_t^m \partial \mathbf{U}_t^s} |U_t^m\rangle \langle U_t^s| + D_{gy}^{ms} . \tag{D.60}$$

Finally, the second derivatives of the gap g_n^0 are computed by (D.52) - (D.60), using the identical Jacobian J_g (D.45) for the first derivatives of the gap as follows:

$$J_g \left(\begin{array}{c} \frac{\partial^2 g_n^0}{\partial \mathbf{U}_t^p \partial \mathbf{U}_t^q} \\ \frac{\partial^2 \alpha}{\partial \mathbf{U}_t^p \partial \mathbf{U}_t^q} \end{array} \right) = - \left(\begin{array}{c} D_{gx}^{pq} \\ D_{gy}^{pq} \end{array} \right) \quad (\because p = \{m, s\}, q = \{m, s\}) . \tag{D.61}$$

In (D.61), $D_{g_i}^{pq}$ are defined as follows:

$$D_{gx}^{mm} = \left(\frac{\partial g_n^0}{\partial \mathbf{U}_t^m} \frac{\partial n_x^m}{\partial \mathbf{U}_t^m}{}^T + \frac{\partial n_x^m}{\partial \mathbf{U}_t^m} \frac{\partial g_n^0}{\partial \mathbf{U}_t^m}{}^T + \frac{\partial^2 n_x^m}{\partial \mathbf{U}_t^{m2}} g_n^0 - \frac{\partial^2 x^s}{\partial \alpha^2} \frac{\partial \alpha}{\partial \mathbf{U}_t^m} \frac{\partial \alpha}{\partial \mathbf{U}_t^m}{}^T \right) |U_t^m\rangle \langle U_t^m|, \quad (\text{D.62})$$

$$D_{gy}^{mm} = \left(\frac{\partial g_n^0}{\partial \mathbf{U}_t^m} \frac{\partial n_y^m}{\partial \mathbf{U}_t^m}{}^T + \frac{\partial n_y^m}{\partial \mathbf{U}_t^m} \frac{\partial g_n^0}{\partial \mathbf{U}_t^m}{}^T + \frac{\partial^2 n_y^m}{\partial \mathbf{U}_t^{m2}} g_n^0 - \frac{\partial^2 y^s}{\partial \alpha^2} \frac{\partial \alpha}{\partial \mathbf{U}_t^m} \frac{\partial \alpha}{\partial \mathbf{U}_t^m}{}^T \right) |U_t^m\rangle \langle U_t^m|, \quad (\text{D.63})$$

$$D_{gx}^{ss} = - \frac{\partial^2 x^s}{\partial \alpha^2} \frac{\partial \alpha}{\partial \mathbf{U}_t^s} \frac{\partial \alpha}{\partial \mathbf{U}_t^s}{}^T |U_t^s\rangle \langle U_t^s| - \frac{\partial \alpha}{\partial \mathbf{U}_t^s} \frac{\partial N_s}{\partial \alpha} |U_t^s\rangle \langle U_x^s| - \frac{\partial N_s}{\partial \alpha}{}^T \frac{\partial \alpha}{\partial \mathbf{U}_t^s}{}^T |U_x^s\rangle \langle U_t^s|, \quad (\text{D.64})$$

$$D_{gy}^{ss} = - \frac{\partial^2 y^s}{\partial \alpha^2} \frac{\partial \alpha}{\partial \mathbf{U}_t^s} \frac{\partial \alpha}{\partial \mathbf{U}_t^s}{}^T |U_t^s\rangle \langle U_t^s| - \frac{\partial \alpha}{\partial \mathbf{U}_t^s} \frac{\partial N_s}{\partial \alpha} |U_t^s\rangle \langle U_y^s| - \frac{\partial N_s}{\partial \alpha}{}^T \frac{\partial \alpha}{\partial \mathbf{U}_t^s}{}^T |U_y^s\rangle \langle U_t^s|, \quad (\text{D.65})$$

$$D_{gx}^{ms} = \left(\frac{\partial n_x^m}{\partial \mathbf{U}_t^m} \frac{\partial g_n^0}{\partial \mathbf{U}_t^s}{}^T - \frac{\partial^2 x^s}{\partial \alpha^2} \frac{\partial \alpha}{\partial \mathbf{U}_t^m} \frac{\partial \alpha}{\partial \mathbf{U}_t^s}{}^T \right) |U_t^m\rangle \langle U_t^s| - \frac{\partial \alpha}{\partial \mathbf{U}_t^m} \frac{\partial N_s}{\partial \alpha} |U_t^m\rangle \langle U_x^s|, \quad (\text{D.66})$$

$$D_{gy}^{ms} = \left(\frac{\partial n_y^m}{\partial \mathbf{U}_t^m} \frac{\partial g_n^0}{\partial \mathbf{U}_t^s}{}^T - \frac{\partial^2 y^s}{\partial \alpha^2} \frac{\partial \alpha}{\partial \mathbf{U}_t^m} \frac{\partial \alpha}{\partial \mathbf{U}_t^s}{}^T \right) |U_t^m\rangle \langle U_t^s| - \frac{\partial \alpha}{\partial \mathbf{U}_t^m} \frac{\partial N_s}{\partial \alpha} |U_t^m\rangle \langle U_y^s|. \quad (\text{D.67})$$

The augmented second derivative of the gap, which includes derivatives of the master and slave displacements, is summarized as follows:

$$\frac{\partial^2 g_n^0}{\partial \mathbf{U}_t^{a2}} = \begin{pmatrix} \frac{\partial^2 g_n^0}{\partial \mathbf{U}_t^{s2}} & \frac{\partial^2 g_n}{\partial \mathbf{U}_t^m \partial \mathbf{U}_t^s} \\ \frac{\partial^2 g_n^0}{\partial \mathbf{U}_t^s \partial \mathbf{U}_t^m} & \frac{\partial^2 g_n}{\partial \mathbf{U}_t^{m2}} \end{pmatrix} = \begin{pmatrix} \frac{\partial^2 g_n^0}{\partial \mathbf{U}_t^{s2}} & \frac{\partial^2 g_n}{\partial \mathbf{U}_t^m \partial \mathbf{U}_t^s} \\ \frac{\partial^2 g_n^0}{\partial \mathbf{U}_t^m \partial \mathbf{U}_t^s}{}^T & \frac{\partial^2 g_n}{\partial \mathbf{U}_t^{m2}} \end{pmatrix}. \quad (\text{D.68})$$

D.2.5.5 First Derivative of Upper and Lower Bounds in Local Coordinate

The computation for the first derivatives of the local coordinates on the integral bounds; α_1 and α_2 , is identical to the computation of the first derivative of the gap:

$$J_g|_{\alpha=\alpha_i} \begin{pmatrix} \frac{\partial g_{mi}}{\partial \mathbf{U}_t^p} \\ \frac{\partial \alpha_i}{\partial \mathbf{U}_t^p} \end{pmatrix} = - \begin{pmatrix} \mathbf{C}_{gx}^p \\ \mathbf{C}_{gy}^p \end{pmatrix} \Big|_{\alpha=\alpha_i} \quad (\because p = \{m, s\}, i = \{1, 2\}), \quad (\text{D.69})$$

where $J_g|_{\alpha=\alpha_i}$ represents a Jacobian on an integral bound. The definition of J_g , \mathbf{C}_{gx}^p and \mathbf{C}_{gy}^p is summarized at (D.45) - (D.49). The augmented first derivative of α_i is defined as follows:

$$\frac{\partial \alpha_i}{\partial \mathbf{U}_t^a} = \begin{pmatrix} \frac{\partial \alpha_i}{\partial \mathbf{U}_t^s} \\ \frac{\partial \alpha_i}{\partial \mathbf{U}_t^m} \end{pmatrix}. \quad (\text{D.70})$$

D.3 Jacobian of Surface Area (Nanson's Formula)

The definition of the Jacobian of the surface area is denoted as follows:

$$j^p = J^p \|(F^p)^{-T} \mathbf{n}_0\| = \det(F^p) \|(F^p)^{-T} \mathbf{n}_0\| . \quad (\text{D.71})$$

The brief derivation of (D.71) is summarized in the following discussion. First, consider the traction boundary integral of phase p ($p = \{m, s\}$) in the deformed configuration (on Γ) and the initial configuration (on Γ_0):

$$\int_{\Gamma} d\Gamma \delta v_i^p \sigma_{ij}^p n_j^p = \int_{\Gamma_0} d\Gamma \delta V_i^p P_{ij}^p n_{0j}^p = \int_{\Gamma_0} d\Gamma \delta V_i^p J^p \sigma_{ik}^p F_{jk}^{p-1} n_{0j}^p , \quad (\text{D.72})$$

where $\mathbf{n}^p = \{n_i^p\}$ and $\mathbf{n}_0^p = \{n_{0i}^p\}$ are the deformed normal and the undeformed normal of phase p , respectively. The last term of (D.72) uses the relation between the first Piola-Kirchhoff stress P^p and the Cauchy stress σ^p via the deformation gradient F^p . By removing the integral symbol and extracting infinitesimal small region ($\Delta\Gamma$ and $\Delta\Gamma_0$) along this integral, the deformed normal is denoted as follows:

$$\mathbf{n}^p \Delta\Gamma^p = J^p (F^p)^{-T} \mathbf{n}_0^p \Delta\Gamma_0^p \quad \Rightarrow \quad \mathbf{n}^p = J^p (F^p)^{-T} \mathbf{n}_0^p \frac{\Delta\Gamma_0^p}{\Delta\Gamma^p} . \quad (\text{D.73})$$

Finally, (D.71) is derived by taking the norm of \mathbf{n}^p :

$$\|\mathbf{n}^p\| = J^p \|(F^p)^{-T} \mathbf{n}_0^p\| \frac{\Delta\Gamma_0^p}{\Delta\Gamma^p} = 1 \quad \Rightarrow \quad \Delta\Gamma^p = J^p \|(F^p)^{-T} \mathbf{n}_0^p\| \Delta\Gamma_0^p \equiv j^p \Delta\Gamma_0^p , \quad (\text{D.74})$$

$$\therefore j^p = J^p \|(F^p)^{-T} \mathbf{n}_0\| = \det(F^p) \|(F^p)^{-T} \mathbf{n}_0\| . \quad (\text{D.75})$$

Appendix E

Correction Term due to Discontinuous Galerkin Method in Time

This appendix is a brief summary of the correction term due to the discontinuous Galerkin method in time, which is used in the space-time XFEM. Assuming a following equation which has a first derivative in terms of time as a strong form:

$$\alpha(u) \frac{\partial u}{\partial t} - f(u) = 0 . \quad (\text{E.1})$$

Mathematically, a time integration should be performed by the continuous time integration methods such as the continuous Galerkin method. In the following discussion, space-time slabs for both the continuous and discontinuous Galerkin methods are denoted as follows:

$$\text{Slab (continuous Galerkin):} \quad \bar{Q}^n = \Omega \oplus [T_-^n, T_-^{n+1}], \quad (\text{E.2})$$

$$\text{Slab (discontinuous Galerkin):} \quad Q^n = \Omega \oplus [T_-^n, T_-^{n+1}] = \Omega \oplus [T_+^n, T_-^{n+1}] \in \bar{Q}^n. \quad (\text{E.3})$$

The weak form R that corresponds to (E.1) should be defined in \bar{Q}^n as follows:

$$R = \int_{\bar{Q}^n} dQ w \left(\alpha(u) \frac{\partial u}{\partial t} - f(u) \right), \quad (\text{E.4})$$

where w is an admissible test function. The weak form for discontinuous Galerkin method is a modification of (E.4). First, (E.4) is split into two parts (Q^n and the rest):

$$R \simeq \int_{Q^n} dQ w \left(\alpha(u) \frac{\partial u}{\partial t} - f(u) \right) + \int_{t_-^n}^{t_+^n} dt \int_{P_+^n} d\Omega \left(\alpha(u) \frac{\partial u}{\partial t} - f(u) \right). \quad (\text{E.5})$$

The first term of RHS is an integral within a space-time slab for the discontinuous Galerkin method: Q^n . The last term is the correction term due to the discontinuous Galerkin method

in time. The last term of (E.5) is an integral in a thin slice with a temporal width δ_t :

$$\delta_t \equiv t_+^n - t_-^n \ll 1. \quad (\text{E.6})$$

Then, the last term of (E.5) is modified as follows:

$$\begin{aligned} & \int_{t_-^n}^{t_+^n} dt \int_{P_+^n} d\Omega w \left(\alpha(u) \frac{\partial u}{\partial t} - f(u) \right) \\ &= \int_{t_-^n}^{t_+^n} dt \int_{P_+^n} d\Omega w \alpha(u) \frac{\partial u}{\partial t} - \int_{t_-^n}^{t_+^n} dt \int_{P_+^n} d\Omega w f(u) \\ &\simeq \int_{t_-^n}^{t_+^n} dt \int_{P_+^n} d\Omega w \alpha(u) \frac{\partial u}{\partial t} - \delta_t \int_{P_+^n} d\Omega w f(u) \\ &\simeq \int_{P_+^n} d\Omega \int_{t_-^n}^{t_+^n} dt \frac{\partial}{\partial t} (w \alpha(u) u) - \int_{t_-^n}^{t_+^n} dt \int_{P_+^n} d\Omega \left(\frac{\partial w}{\partial t} \alpha(u) + w \frac{\partial \alpha(u)}{\partial t} \right) u \\ &\simeq \int_{P_+^n} d\Omega \int_{t_-^n}^{t_+^n} dt \frac{\partial}{\partial t} (w \alpha(u) u) - \delta_t \int_{P_+^n} d\Omega \left(\frac{\partial w}{\partial t} \alpha(u) + w \frac{\partial \alpha(u)}{\partial t} \right) u \\ &\simeq \int_{P_+^n} d\Omega (w|_+^n \alpha(u)|_+^n u|_+^n - w|_-^n \alpha(u)|_-^n u|_-^n) \\ &\simeq \int_{P_+^n} d\Omega w|_+^n (\alpha(u)|_+^n u|_+^n - \alpha(u)|_-^n u|_-^n) \\ &= \int_{P_+^n} d\Omega w|_+^n \llbracket \alpha(u) u \rrbracket_{\pm}^n, \end{aligned} \quad (\text{E.7})$$

where $\cdot|_+^n$ and $\cdot|_-^n$ denote values at t_+^n and t_-^n , respectively. The blue terms at the above equation vanish because $\delta_t \ll 1$. Therefore, the weak form for the discontinuous Galerkin method is summarized as follows:

$$R = \int_{Q^n} dQ w \left(\alpha(u) \frac{\partial u}{\partial t} - f(u) \right) + \int_{P_+^n} d\Omega w|_+^n \llbracket \alpha(u) u \rrbracket_{\pm}^n, \quad (\text{E.8})$$

where the red term is the correction term due to the discontinuous Galerkin method in time. By using the above weak form, the continuity between the current and past space-time slabs is guaranteed using the discontinuous Galerkin method in time.

Appendix F

Comparison between Simplex Triangulation Approach and Elementwise Temporal Layer Approach

The elementwise temporal layer approach is used in the proposed space-time XFEM (Chapter 3). The advantage of the elementwise temporal layer approach is the easy implementation in terms of the setting of volume integration points. The conventional settings of spatial volume integration points used in the standard XFEM can be directly applicable for the space-time XFEM. On the other hand, Lehrenfeld [47] proposed the space-time XFEM using the simplex triangulation approach. The simplex triangulation approach is a method that uses the direct decomposition of a space-time slab. A space-time slab is decomposed by simplices, considering space-time intersection configuration. The simplex triangulation approach is sophisticated but more complex implementation is essential than the elementwise temporal layer approach.

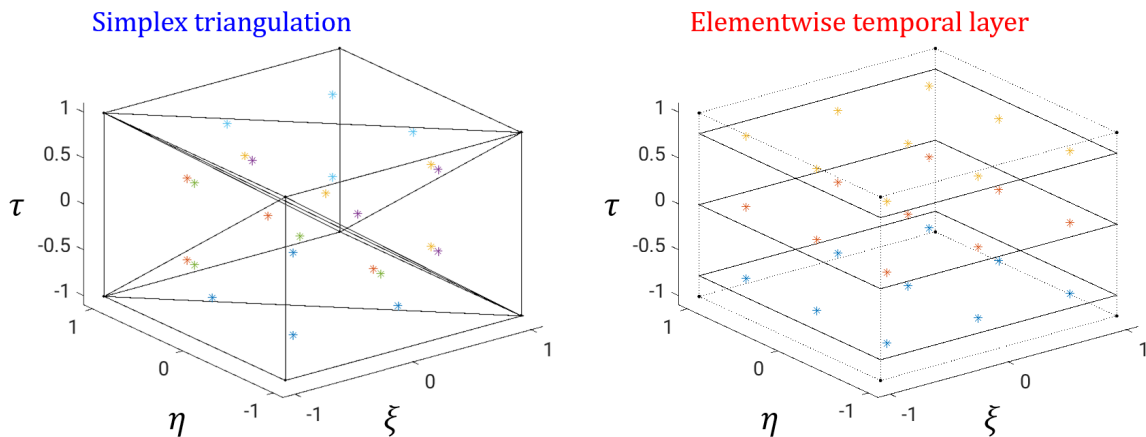


Figure F.1: Comparison of settings of space-time volume integration points (1)
(non-intersected space-time element)

This appendix is the comparison between the simplex triangulation approach and the

elementwise temporal layer approach. This appendix assumes spatially two-dimensional cases. Figure F.1 is the comparison of the settings of the space-time volume integration points in a standard (non-intersected) space-time element. (ξ, η, τ) are isoparametric coordinates of (x, y, t) , respectively. In the simplex triangulation approach (left figure), an entire space-time element is firstly decomposed by three-dimensional Delaunay triangulation. Then, space-time volume integration points are defined within three-dimensional simplices (tetrahedrons) based on the quadrature rule. Four integration points are defined in each simplex and thus, there are 24 integration points at the left figure. The right figure is the setting of space-time volume integration points based on the elementwise temporal layer approach. The space-time volume integration points distribute on each temporal slice using the conventional settings of spatial volume integration points in the standard XFEM. Three temporal slices are defined in each temporal layer and nine integration points in each temporal slice. Thus, 27 integration points for the space-time volume are defined at the right figure. As three-dimensional Delaunay triangulation is not necessary, this implementation is much easier than the simplex triangulation approach.

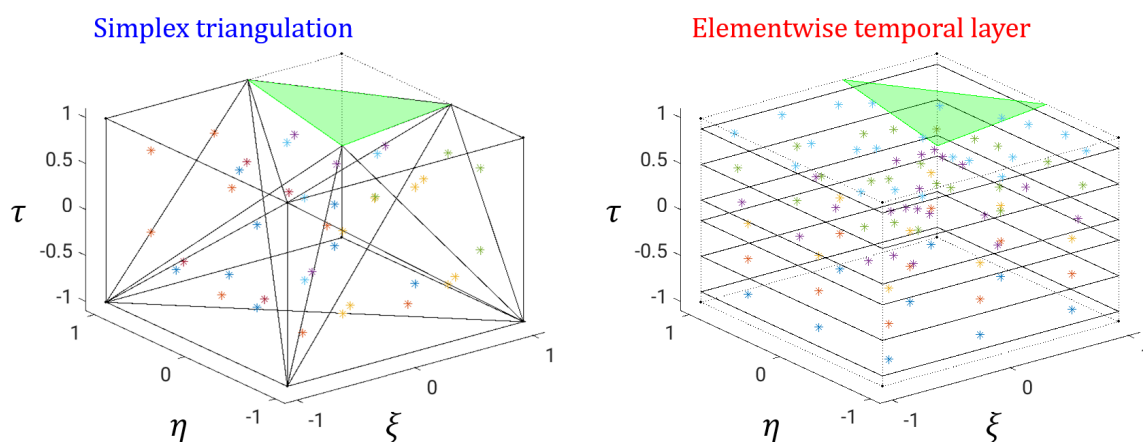


Figure F.2: Comparison of settings of space-time volume integration points (2)
(intersected space-time element, phase 1)

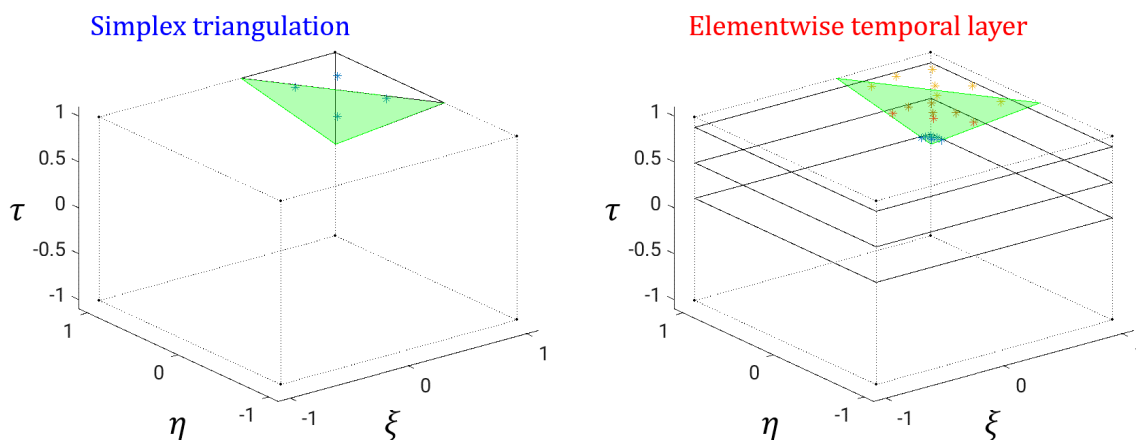


Figure F.3: Comparison of settings of space-time volume integration points (3) (intersected space-time element, phase 2)

Figures F.2 and F.3 are comparisons of the settings of space-time volume integration points in a intersected space-time element. Assuming a two-phase case, Figure F.2 is about phase 1 (negative phase) and Figure F.3 is about phase 2 (positive phase), respectively. The green face shows a space-time interface. The simplex triangulation approach (left figures) is based on three-dimensional Delaunay triangulation. Black solid lines denote edges of three-dimensional simplices. In the elementwise temporal layer approach (right figures), each temporal layer is corresponding to different spatial configurations. At these figures, two temporal layers are defined and six temporal slices are determined (three slices in each layer). Each slice represents the spatial configuration at different time. Black solid lines denote edges of elementwise temporal slices. The elementwise temporal layer approach is based on the conventional setting of the standard XFEM. First, the spatial intersection configuration is created on each temporal slice. Then, two-dimensional Delaunay triangulation is performed on each slice. The space-time volume integration points on each temporal slice are distributed on each triangle created by Delaunay triangulation. Therefore, the number of integration points based on the elementwise temporal layer approach is generally larger than one based on the simplex triangulation approach.

Table F.1 is the summary of numbers of space-time volume integration points in Figures F.1, F.2 and F.3 to compare two methods. As mentioned above, the elementwise temporal layer approach has more integration points than the simplex triangulation approach at the case of space-time intersected elements in general. However, the dominant part of space-time elements in the space-time XFEM is standard (non-intersected) elements like Figure F.1. As the numbers of space-time volume integration points using both approach are almost identical in the case of non-intersected space-time elements, the difference in computational cost is small between two approaches. Moreover, the elementwise temporal layer approach does not need the direct decomposition of a space-time slab. In particular, the simplex triangulation for spatially three-dimensional cases using four-dimensional simplices is complex because Delaunay triangulation is not applicable in the four-dimensional space. The elementwise temporal layer approach has the beauty to reduce computational costs because the higher-dimensional simplex triangulation is not needed. In addition, individual temporal slices are independent from other slices. As the communication between different slices is not necessary, the elementwise temporal layer approach has a high affinity for the efficient parallel computations.

Table F.1: Number of integration points in each figure

| Element-Type | Figure | Simplex Triangulation | Temporal Layer |
|-----------------|------------|-----------------------|----------------|
| Non-intersected | Figure F.1 | 24 | 27 |
| Intersected | Figure F.2 | 40 | 90 |
| Intersected | Figure F.3 | 4 | 21 |

The rest of this appendix demonstrates the comparisons between the simplex triangulation approach and the elementwise temporal layer approach using two numerical examples discussed at preceding chapters. Figure F.4 is a comparison of the DFG 2D-3 benchmark problem using the space-time XFEM based on both approaches. This numerical example

is summarized in Section 3.6.2. This figure shows the histories of quantities of interest; the drag coefficient C_D , the lift coefficient C_L , and the pressure drop around a fixed cylinder Δp . The results are computed by a model with the temporal discretization $\Delta t = 0.2s$ and the spatial discretization $h/D = 0.1105$ (see Tables 3.4 and 3.7).

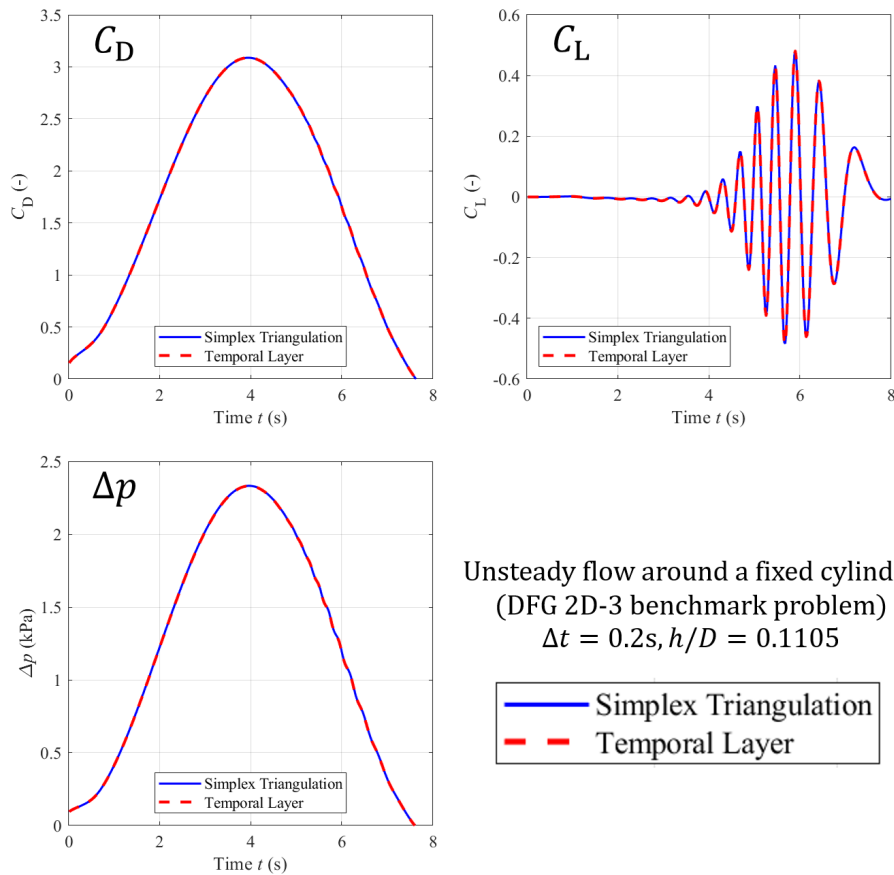


Figure F.4: Comparison of DFG 2D-3 benchmark problem using space-time XFEM (blue: simplex triangulation approach, red: elementwise temporal layer approach) (Details of this problem are summarized in Section 3.6.2.)

Table F.2: Comparison of C_D^{\max} , C_L^{\max} and Δp^{fin}

| Approach | C_D^{\max} (-) | C_L^{\max} (-) | Δp^{fin} (kPa) | $t(C_D^{\max})$ (s) | $t(C_L^{\max})$ (s) |
|----------------------------|---------------------|---------------------|----------------------------------|------------------------|------------------------|
| Simplex triangulation | 3.0876 | 0.4812 | -0.1049 | 3.9600 | 5.9000 |
| Elementwise temporal layer | 3.0877 | 0.4809 | -0.1050 | 3.9400 | 5.9000 |

($\Delta t = 0.2s, h/D = 0.1105, 11718$ DOFs, 400 time steps)

In this example, this problem is a fixed interface problem; the unsteady flow around a

fixed cylinder. As can be seen, the histories of these quantities using both approaches are identical. Table F.2 is a comparison of representative quantities (maximum C_D , maximum C_L and final Δp at $t = 8s$). Although these representative measures are very sensitive quantities because they are defined by values at one time; i.e. non-integrated quantities, both approaches reproduced almost identical solutions. Thereby, the equivalence between the simplex triangulation approach and the elementwise temporal layer approach was verified.

Following examples are computation using moving interfaces. Figure F.5 is a comparison using a FSI problem based on the Lagrangian-immersed FSI method with the space-time XFEM. There is a falling elastic cylinder due to a body force in y direction, within the incompressible Navier-Stokes (INS) fluid. This numerical example is summarized in Section 7.4.1. Figure F.5 shows the histories of the fluid force acting on a cylinder.

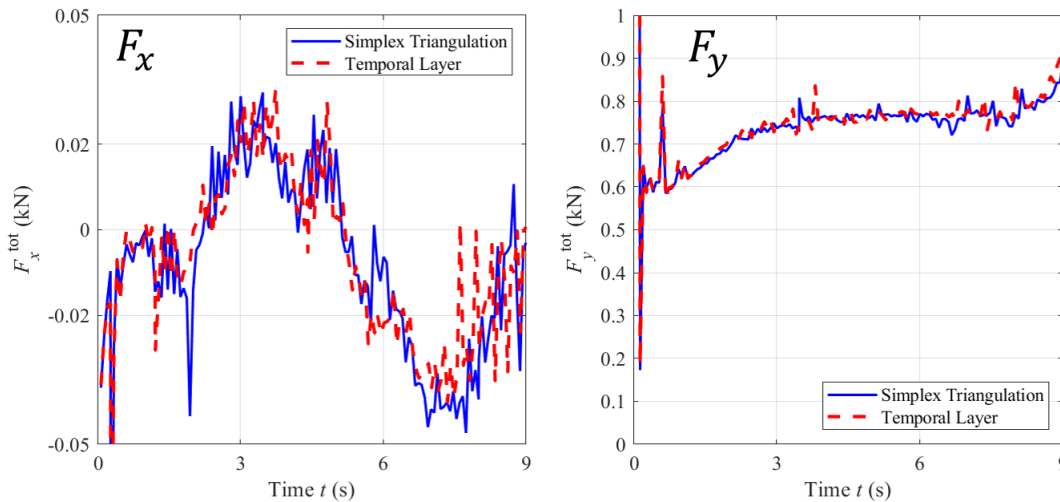


Figure F.5: Comparison of a falling elastic cylinder in INS fluid (method: Lagrangian-immersed FSI method using space-time XFEM) (blue: simplex triangulation approach, red: elementwise temporal layer approach) (Details of this problem are summarized in Section 7.4.1.)

The overall tendency of two approaches in this figure is almost identical. As spikes exist in both cases, the setting of the space-time volume integration points does not cause these spikes in the Lagrangian-immersed FSI method. This indicates that other factors such as

FSI between non-matching interfaces, the coupling method (Nitsche's method or Lagrange multiplier method), and stabilization method, might cause these spikes.

The last example is the Turek-Hron FSI3 benchmark problem. This numerical example is studied by the Lagrangian-immersed FSI method using the space-time XFEM. Details are summarized in Section 7.4.2. Figures F.6 and F.7 are the histories of quantities of interest; the tip displacements U_x^{tip} and U_y^{tip} , the drag force F_D and the lift force F_L . This figure shows results in the completely developed stage ($7.6\text{s} \leq t \leq 8.1\text{s}$).

In these figures, the black dots represent the reference solution [111]. The blue solid line and red dashed line denote the results using $\Delta t = 0.0025\text{s}$ based on the simplex triangulation approach and the elementwise temporal layer approach, respectively. As can be seen, both the simplex triangulation approach and the elementwise temporal layer approach computed almost identical solution. The summary of the mean, the amplitude and the frequency of representative quantities is listed in Table F.3. While there is small difference between two approaches, both approaches compute almost identical results.

Table F.3: Comparison using Turek-Hron FSI3
(mean \pm amplitude [frequency(Hz)])

| | U_x^{tip} (mm) | U_y^{tip} (mm) | F_D (N) | F_L (N) |
|-------|-------------------------|-------------------------|--------------------------|-------------------------|
| [111] | -2.69 ± 2.53 [10.9] | 1.48 ± 34.38 [5.3] | 457.3 ± 22.66 [10.9] | 2.22 ± 149.78 [5.3] |
| ST | -2.63 ± 2.45 [11.1] | 1.17 ± 33.69 [5.6] | 463.4 ± 18.85 [11.1] | 9.84 ± 180.50 [5.6] |
| TL | -2.63 ± 2.44 [11.1] | 1.11 ± 33.59 [5.6] | 461.8 ± 20.00 [11.1] | 9.79 ± 181.01 [5.6] |

([111]: ALE-FSI, ST: Simplex Triangulation, TL: Elementwise Temporal Layer)

The equivalence of the simplex triangulation approach and the elementwise temporal layer approach in the space-time XFEM is verified using both fixed and moving interface problems. It should be noted that spikes in drag and lift forces (Figure F.7) are caused by other factors mentioned at the previous example (Figure F.5).

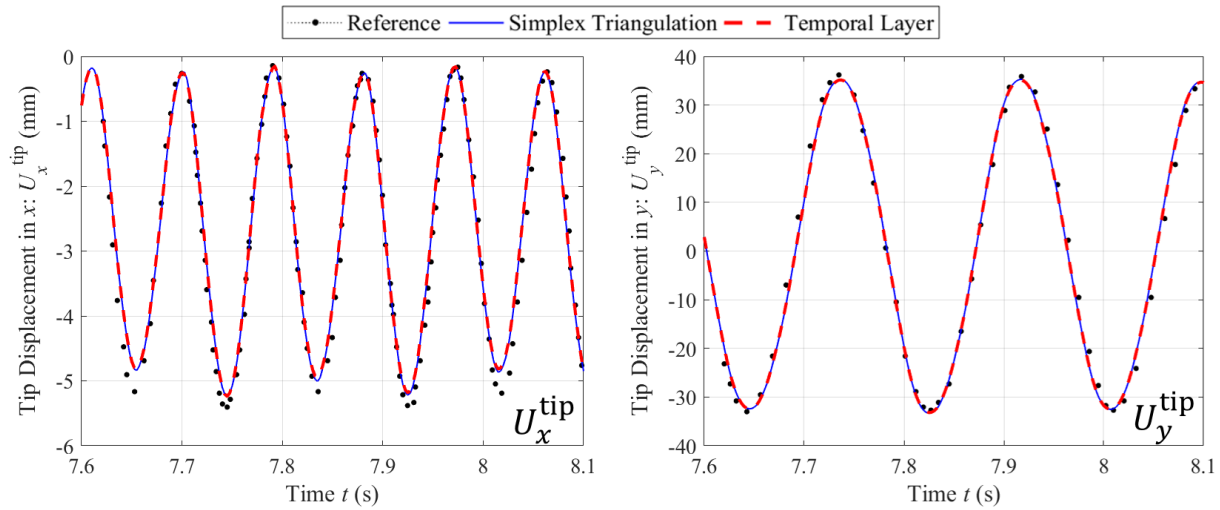


Figure F.6: Comparison of tip displacements (Turek-Hron FSI3 Problem)

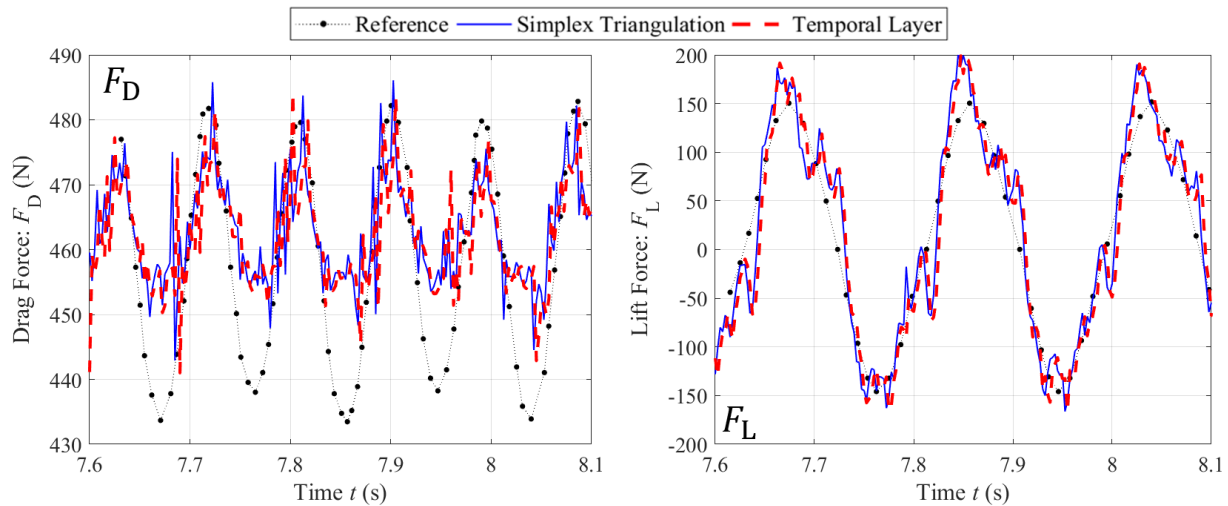


Figure F.7: Comparison of drag and lift forces (Turek-Hron FSI3 Problem)
 (method: Lagrangian-immersed FSI method using space-time XFEM)
 (Details of this problem are summarized in Section 7.4.1.)